Radio Surveys for Galactic Planetary Nebulae (PNe)

Tonye Irabor

Department of Physics and Astronomy

University of Leeds

Submitted in accordance with the
requirements for the degree of

Doctor of Philosophy

July 31, 2019

Declaration

The author, Tonye Irabor, confirms that the work submitted is her own, except where work from a jointly authored publication is included. The author confirms that appropriate credit has been given within this thesis, where reference has been made to the work of others.

This thesis is dedicated to the loving memory
of my late sister and late mother.
They gave me all the kicks that have propelled me thus far,
without holding back.

knowledge unveils itself to any eye that dares look upon it
—Janesoki

...the reach of our consciousness is like an hourglass with two empty sides.
—Janesoki

Life happens and smiles at us in different ways;
Giving us different projected faces;
Life makes us naked and makes us aimless wanderers through time;
Peering through its windy terror and bleak agelessness;
Falling through this space that mocks us through frozen fire;
and then we realise the beauty in the cycle of hoping and loosing pages;
Learning to bear the weight of raw engraved memories
—Janesoki

Preface

This thesis includes data and text from a jointly authored paper that is published in the Monthly Notices of the Royal Astronomical Society:

"The coordinated radio and infrared survey for high-mass star formation - IV. A new radio-selected sample of compact galactic planetary nebulae". The co-authors are M.G. Hoare, R. D. Oudmaijer, J. S. Urquhart, S. Kurtz, S. L. Lumsden, C. R. Purcell, A. A. Zijlstra and G. Umana.

The data was obtained by the CORNISH Team led by M. G. Hoare. Data reduction and measurements of the properties were primarily carried out by C. R. Purcell. The author carried out the analysis on the PNe sample and obtained the results. The manuscript was written by the author, including figures, discussion and conclusion sections. M. G. Hoare gave advice on the final classification of the PNe and provided feedback and comments to improve the initial manuscript. Co-authors provided comments for the final version of the manuscript before submission.

This paper constitutes the Chapter 2 of this thesis and includes comments from the co-authors of the paper and the referee.

Abbreviations

2MASS	2 Micron All Sky Survey
AGB	Asymptotic Giant Branch
ATCA	Australia Telescope Compact Array
AT20G	Australia Telescope 20 GHz Survey
ATLASGAL	APEX Telescope Large Area Survey of the Galaxy
A_v	Extinction in the Visual band
BGPS	Bolocam Galactic Plane Survey
CORNISH	Co-ordinate Radio 'n' Infrared Survey for High Mass Stars
FIR	Far-infrared
GLIMPSE	Galactic Legacy Infrared Mid-Plane Extraordinaire
H_2	Molecular hydrogen
Hα	Hydrogen-Alpha
HII	HII region
HI-Gal	Herschel Infrared Galactic Plane Survey
IFMR	Initial to Final Mass Relationship
IPHAS	INT (Isaac Newton Telescope) Photometric Hα Survey of the Galactic Plane
IRAS	Infrared Astronomical Satellite
MASH	Macquarie /AAO /Strasbourg Hα Planetary Galactic Catalogue
MAGPIS	The Multi-Array Galactic Plane Imaging Survey
MSX	Midcourse Space Experiment
MYSO	Massive Young Stellar Object
MIR	Mid-Infrared
MIPS	Multiband Imaging Photometer for Spitzer
MGPS	Molonglo Galactic Plane Survey
MS	Main Sequence
M_*	Stellar mass
$M_\odot$	Solar mass
NRAO	National Radio Astronomy Observatory
NIR	Near-Infrared
OTF	On the Fly
PAH	Polycyclic Aromatic Hydrocarbon
PN	Planetary Nebula

Continued on next page

– continued from previous page

PNe	Planetary Nebulae
pPN	Proto-Planetary Nebula
pPNe	Proto-Planetary Nebulae
RFI	Radio Frequency Interference
RMS	Red MSX Source (Survey)
Roche lobe	Smallest surface of gravitational equi-potential that encloses the binary system
RRL	Radio Recombination Line
SED	Spectral Energy Distribution
SHS	SuperCosmos Hα Survey
SKA	Square Kilometre Array
SNR	Signal-to-Noise Ratio
SGPS	Southern Galactic Plane Survey
UCHII	Ultra-Compact HII region
UKIDSS	UKIRT Infrared Deep Sky Survey
UV	Ultra-Violet
VLA	Karl G. Jansky Very Large Array
VVV	VISTA Variables in the Via Lactea
WISE	The Wide-Field Infrared Survey Explorer
YSO	Young Stellar Object

Acknowledgements

I am grateful to God who oversees the affairs of men and granted me life to go through this phase. To my supervisors, Melvin Hoare and Rene Oudmaijer, thank you for the support, patience, priceless experience and knowledge you shared with me. I cannot thank you enough. Katherine Johnston, thanks for some useful discussions. To the other academic and non-academic staff, thanks for providing extra support.

To my colleagues, you all made my PhD time at Leeds beautiful. Ivayla Kalcheva, thanks for the friendship. Fernando Olguin, thanks for the many python advices. Wafa, thanks for the shoulder in my time of confusion. Robert Pomohaci, thanks for all the help.

To my 'big baby', thanks for being the engine that kept me functioning and not letting me give up. Thanks for being strong for us. I love you now and always. I see you.

Finally, I would like to thank the Nigerian government for funding my PhD through the office of the special adviser on Niger Delta (OSAPND).

This research made use of Montage, funded by the National Aeronautics and Space Administration's Earth Science Technology Office, Computational Technnologies Project, under Cooperative Agreement Number NCC5-626 between NASA and the California Institute of Technology. The code is maintained by the NASA/IPAC Infrared Science Archive." and the SIMBAD database, operated at CDS, Strasbourg, France.

Finally, this research also made use of TOPCAT in the processing and formatting of tables presented: M. B. Taylor, "TOPCAT STIL: Starlink Table/VOTable Processing Software", in Astronomical Data Analysis Software and Systems XIV, eds. P Shopbell et al., ASP Conf. Ser. 347, p. 29 (2005)

Abstract

This research presents a new radio-selected sample of compact Galactic PNe from the CORNISH survey, a radio continuum survey of the inner Galactic plane. The northern counterpart of the CORNISH survey covers the $10^\circ < l < 65^\circ$; $|b| \leq 1^\circ$ region with a resolution of $1.5''$ and a sensitivity that is better than 0.4 mJy/beam at 5 GHz, using the VLA. The southern counterpart observed the $295^\circ < l < 350^\circ$; $|b| \leq 1^\circ$ region of the southern Galactic plane, using the ATCA array. It achieved a resolution of $2.5''$ and sensitivity better than 0.2 mJy/beam at 5.5 GHz. Candidate PNe, above a 7σ detection limit, were selected through visual inspection of multi-wavelength images. A detailed multi-wavelength investigation using properties such as radio spectral indices, MIR-to-radio ratio, and infrared colours, including near-infrared, mid-infrared and far-infrared colours, were used to confirm the PNe nature of the selected candidates. Some of the detected PNe were found to be compact and dense, having physical diameters < 0.06 pc and closer than 6 kpc, with $T_B > 1000$ K. In the northern Galactic plane, 169 candidate PNe were analysed. 90 were classified as new PNe, out of which 12 PNe were newly detected and 78 were newly classified as PNe. A further 47 objects, previously classified as probable PNe were confirmed as such from the analysis and 24 known PNe were recovered. Eight sources were classified as possible PNe or other source types based on insufficient data. In the southern Galactic plane, 184 sources were classified as PNe. Four previously classified as probable PNe were confirmed and 29 previously known PNe were recovered. 151 were classified as new PNe, out of which 97 were newly classified as PNe and 54 have no astronomical records in the SIMBAD database, hence are classified as being detected for the first time. At

5 - 5.5 GHz, the CORNISH PNe are evenly distributed in Galactic latitude and have significantly increased ($\sim 200\%$) the number of PNe within the $|b| < 1^{\circ}$ region, compared to the distribution of known PNe. Based on Galactic PNe population sythesis, the number of PNe within the CORNISH survey region was synthesized to test Moe & De Marco's binary and single stellar model. Comparison of the Galactic latitude distribution of the CORNISH PNe sample with the distribution of the synthesized population gave a best fit scale height of 550 pc and 600 pc for the northern and southern PNe, respectively. Within the limits of the assumptions made in building the model and the predictions from population synthesis models, the modelled parameters that fit the angular size, flux density distributions and observed number of the CORNISH PNe support the formation of observable PNe through binary interactions. This model is the first of its kind and forms a basis for indepth future investigations that compare observed radio properties with predictions from population synthesis models.

Contents

List of Figures

List of Tables

Chapter 1

Introduction

1.1 What is a Planetary Nebula?

Towards the end of its life, the outer layers of an intermediate mass star ($0.8 \rightarrow 8M_{\odot}$; Peimbert 1990) are gradually ejected in the form of stellar winds, forming an envelope of gas and dust around the stellar core (central star). The central star evolves towards higher temperatures and attains a temperature that is high enough (usually $>$ 25 kK; Schonberner & Blocker 1993 and Bloecker 1995) to ionize the circum-stellar envelope (Paczyński 1970; Shklovskii 1957). This ionized envelope is called a planetary nebula (hereafter PN and PNe for the plural form). The central star continues its evolution and eventually ends up as a white dwarf. The ejected and ionized envelope expands with velocities in the range of 20 - 50 km/s and gradually fades into the interstellar medium (Bloecker, 1995; Choi *et al.*, 2008; Jacob *et al.*, 2013; Schönberner *et al.*, 2014). PNe are short lived, usually $< 10^4$ yrs (Jacob *et al.*, 2013) and $>$ 90% of the stars in our Galaxy are expected to go through the PN phase (Gesicki *et al.*, 2018; Peimbert, 1990). PNe form the evolutionary link between the post Asymptotic Giant Branch (post-AGB) and the white dwarf phase in the life of an intermediate mass star. Traditionally, PNe are identified from their optical spectra, which show recombination lines (hydrogen and helium) and forbidden lines ([OII] and [OIII]) from the ionized volume (see Aller & Minkowski 1956; Osterbrock 1964; Seaton 1960).

PNe and their progenitors are one of the major drivers of chemical evolution and mass return to the Galaxy, forming the materials for next generation stars (Costa & Maciel, 2006; Habing & Olofsson, 2004; Herwig, 2005; Iben, 1995). They are considered good probes of the evolved star population and generally good objects in the study of stellar and galaxy evolution (Ciardullo, 2006; Stanghellini, 2004, 2006). This is because PNe are usually bright ojects and outside the Local Group (gravitationally-bound group of galaxies that includes the Milky Way), they can be readily observed from the ground and studied spectroscopically. Additionally, because stars older than $\sim 10^8$ yrs form PNe, more PNe are available for studies in large galaxies. They are also useful tracers in Galactic kinematics (Durand *et al.*, 1998; Maciel & Lago, 2005; Schneider & Terzian, 1983). From the study and understanding of PNe we should be able to better understand and address the late phase evolution and the physics of mass-loss for intermediate-mass stars (Iben, 1995).

1.2 Evolution of Intermediate Mass Stars

1.2.1 Main Sequence to Asymptotic Giant Branch

Intermediate-mass stars typically go through the Red Giant Branch (RGB) phase and the Asymptotic Giant Branch phase (AGB) on their journey to becoming PNe. Evolution off the main-sequence (MS) starts when the helium density in the core is high enough to interfere with hydrogen fusion or when hydrogen is exhausted in the core. This results in gravitational collapse of the core, causing it to heat up as it contracts. When this happens, an intermediate-mass star starts its journey through to the RGB phase.

Hydrogen burning moves to an outer thin shell as the helium filled core contracts further and heats up, causing more helium to be deposited in the core. The shell burning hydrogen increases in mass and the core gets denser, resulting in mass-loss in the form of stellar winds (Mauas *et al.*, 2006), which causes the outer envelopes to expand and cool with increase in luminosity (Refsdal & Weigert,

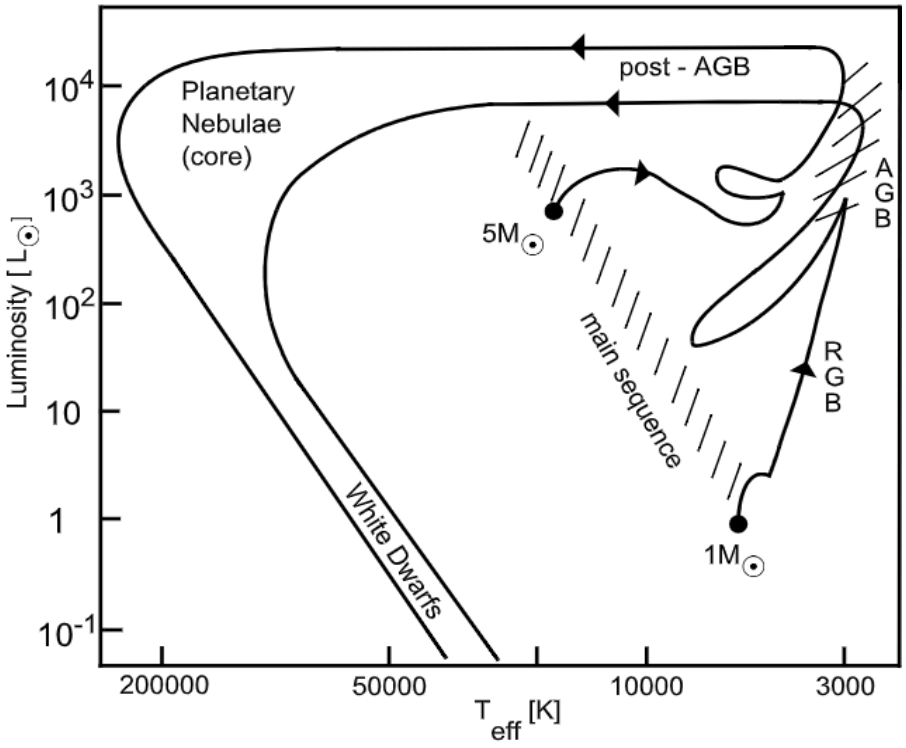

Figure 1.1: *Evolution path for* $1M_\odot$ *and* $5M_\odot$ *star. The evolution from the main-sequence through to the mass-loss phase (RGB and AGB), PN phase and the evolution of the central star to becoming a white dwarf is shown. Source : Engels (2005).*

1970). At the tip of the RGB phase (Figure 1.1), the core becomes dense and acquires the right temperature ($> 10^8$ K) to initiate helium fusion into carbon and oxygen, through the triple-α process (equation 1.1). The energy released in this process is in the form of gamma-ray (γ). When helium fusion starts in the core, the star enters the Horizontal Branch Phase. Soon after, helium in the core becomes exhausted and the star enters the AGB Phase. Helium burning moves to an outer shell like hydrogen burning, while the core collapses further. Because the cores of stars with masses $< 8M_\odot$ cannot attain the required temperature for carbon fusion, a degenerate core of C-O is formed. The exact path of evolution depends on the mass of the star (Kippenhahn & Weigert, 1994), as illustrated in Figure 1.1 for a $1M_\odot$ and $5M_\odot$ star.

$$\begin{aligned} {}^{4}\mathrm{He} \; + \; {}^{4}\mathrm{He} &\leftrightharpoons {}^{8}\mathrm{Be}, \\ {}^{8}\mathrm{Be} \; + \; {}^{4}\mathrm{He} &\rightarrow {}^{12}\mathrm{C} + \gamma \\ {}^{12}\mathrm{C} \; + \; {}^{4}\mathrm{He} &\rightarrow {}^{16}\mathrm{O} + \gamma \end{aligned} \tag{1.1}$$

1.2.2 Asymptotic Giant Branch (AGB) to PNe

The star enters the AGB phase when double shell burning starts, where helium is burning in a shell surrounding the the electron-degenerate C-O core and hydrogen burning in an outer shell. AGB stars usually have temperatures lower than 3000 K and luminosities in the range of $2200 \lesssim \mathrm{L/L_{\odot}} \lesssim 55000$ (Engels, 2005). During this AGB phase, the star undergoes flashes or thermal pulses caused by thermally unstable helium burning and the size of the star grows much bigger than in the RGB phase (Karakas & Lattanzio, 2007; Werner & Herwig, 2006). This results in the build up of dust grains in the cool atmosphere.

The AGB phase is characterised by intense mass-loss, which could be as high as $10^{-4}\mathrm{M_{\odot}yr^{-1}}$ (Balick & Frank, 2002; Engels, 2005; Hoogzaad *et al.*, 2002). Mass-loss during this phase is thought to be a result of time-dependent processes, which include thermal pulsation and radiation pressure (Faulkner, 1970; Iben & Renzini, 1983; Jones *et al.*, 1983; Kwok, 1975, 2000). Stellar pulsations push materials off from the star and as the radiation pressure acts on the dust grains, gas is carried along with a speed that is in the order of 10 km/s to 15 km/s (Griffiths, 2012; Jacob *et al.*, 2013; Kwok, 2011; Maercker *et al.*, 2010; Schönberner *et al.*, 2014). In view of the collimated outflows and non-spherical mass-loss patterns observed in these objects, Morris (1987) considered a binary companion as an additional driver of mass-loss and Pascoli (1997) also suggested that magnetic activities present in the core could also drive mass-loss.

At the end of the AGB phase, the mass-loss rate decreases to about $10^{-8}\mathrm{M_{\odot}yr^{-1}}$ but continues until almost all its outer layer is removed (Kwok *et al.*, 1978). The mass of the envelope is reduced to about $10^{-3}\mathrm{M_{\odot}}$ during this period and the central star contracts further and heats up rapidly. With decreased mass-loss rate, the central star is believed to generate faster and hotter winds with

velocities of about 10^3 kms^{-1}, in contrast to the velocity of the previously ejected circum-stellar envelope of about 10 kms^{-1} to 15 kms^{-1} (Balick & Frank, 2002; Kwok, 2000; Perinotto, 1989). This is the beginning of the post-AGB phase, where the fast wind interacts with the slowly moving envelope ejected in the AGB phase. When these winds subside, the hot central star is surrounded by a dense circum-stellar envelope of carbon and silicate dust, and molecular gas. The gas is dominated by molecular hydrogen (H_2, Glassgold & Huggins 1983), followed by CO. The abundance of CO (carbon monoxide) in the circum-stellar envelope depends on the abundance of C (carbon) and O (oxygen).

Post-AGB phase

The post-AGB phase is brief ($\sim 10^3$ yrs; Bujarrabal *et al.* 2001; Kwok 1993a) but has the key to unlocking the mysteries of the shaping and observed morphologies of PNe. The circum-stellar envelopes formed during the AGB phase could be very massive, depending on the mass-loss rate and processes. This could result in obscuration in the optical regime of these stars (Suárez *et al.*, 2006b) but will readily be observable in the infrared and at mm wavelengths as thermal dust continuum, molecular radio line emission (e.g. CO) and maser emission lines, such as OH, H_2O and SiO (Kim *et al.*, 2016; Lagadec *et al.*, 2011). Large detached shells have been observed around these stars (Waters, 1994), indicating periodic mass-loss have formed these shells (see also Maercker *et al.* 2010).

During the post-AGB phase, the central star continues its journey with constant luminosity and increasing temperature (Figure 1.1). The luminosity is dependent on the core mass such that stars with more massive cores have higher luminosities (Bloecker, 1995; Vassiliadis & Wood, 1994). Eventually, the central star becomes hot (> 20 kK) enough to ionize the circum-stellar envelope, which is now called a PN. The rate at which the central star heats up and ionizes the ejected envelope also depends on the core mass (Bloecker, 1995). Objects in this phase of evolution are called post-AGB stars. It should be noted that post-AGB stars are also referred to as proto-planetary nebulae (pPNe) in some literature (Kwok, 1993a). After complete ionization, the central star continues its evolution and ends up as a

white dwarf, while the PN continues to expand and gradually fades into the ISM, with a decrease in luminosity and surface brightness. This is due to decreasing emission measure and increasing transparency to the ionizing photons.

1.2.3 Dust Features of AGB and Post-AGB Stars

Dust observed in post-AGB stars and PNe is mainly formed during the mass-loss regime in the AGB phase. Originally, the photosphere of the star from the MS to AGB phase is oxygen rich but dredge-ups of carbon atoms by deep convective envelopes, during the AGB phase, change the composition of the stellar photosphere. Depending on the ratio of carbon to oxygen abundance in their photosphere, AGB stars are classified as oxygen-rich or M-type (C/O $<$ 1), carbon-rich (C/O $>$ 1) and transition stars or S-stars with C/O = 1 (Barlow, 1993; Kwok, 1993a; Lattanzio & Wood, 2004). The elements in the photosphere of these stars are dependent on the mass of the star and the core nuclear burning, such that low mass stars are dominated by carbon, while intermediate mass stars are dominated by oxygen, nitrogen and silicates (Maciel & Costa, 2003).

Circum-stellar envelopes that are oxygen-rich (O-rich) are dominated by silicate dust features (e.g 10 and 18μm) in amorphous and crystalline forms, observed through infrared spectroscopy, and oxygen bearing molecules that dominate the chemistry of these objects (OH, H_2O and SiO: Kwon & Suh 2012; Yung *et al.* 2014). In addition, there is amorphous and crystalline H_2O ice at the highest mass-loss rates (Lombaert *et al.*, 2013). The abundance of CO in O-rich circum-stellar envelopes depends on the abundance of C and O. However, CO emission is stronger in carbon-rich (C-rich) envelopes (Olofsson *et al.*, 1988). Circum-stellar envelopes that are C-rich show amorphous carbon, graphite, SiC and MgS (11.3 and 30 μm) dust features (Barlow, 1993; Lombaert *et al.*, 2012) and carbon bearing molecules such as CO, CN, and C_2H_2. In C-rich circum-stellar envelope of post-AGB stars and PNe, PAH (polycyclic aromatic hydrocarbons) features have also been observed in the 3.3, 6.2, 7.7, 8.6, and 11.32 μm bands (Barlow, 1983; Buss *et al.*, 1993; Oudmaijer *et al.*, 1995) and even fullerenes (C_{60} and C_{70}) have also been detected in PNe (Cami *et al.*, 2010; García-Hernández *et al.*,

2010; Sloan *et al.*, 2014). Circum-stellar envelopes of transition stars have dust chemistry between the O-rich and C-rich AGB stars (Danilovich *et al.*, 2014).

1.3 Morphology

One of the characteristics of a PN is its morphology. Observed morphologies of PNe can reflect the environment in which they were formed, including the interaction of the stellar winds, ISM interaction (Wareing *et al.*, 2005) and changes in ionization (Kwok, 2000; Soker, 1992). However, observed morphologies could be biased by line-of-sight, exposure (longer exposure may reveal additional features), limited field of view, projection angle and sensitivity of the observing instrument, such that an elliptical or a bipolar PN may appear round when viewed through its axes of symmetry (Kwok, 2012). According to Chong *et al.* (2012), true morphology can be truly determined by considering all three dimensions in space. Morphologies of observed PNe range from simple to complex with a good degree of symmetry, $> 80\%$ of which are not spherical (Parker *et al.*, 2006; Sahai *et al.*, 2007, 2011; Stanghellini *et al.*, 1993).

Classification of PNe morphology was first made by Curtis (1918), who classified PNe into helical, annular, disk, and amorphous (see Perek & Kohoutek 1967). With a dataset of 255 PNe, Stanghellini *et al.* (1993) classified observed morphologies of PNe based on their Hα images into stellar, bipolar and point-symmetric (see Schwarz *et al.* 1993). Other authors that have classified PNe morphology include Balick (1987), Manchado *et al.* (1996), Corradi & Schwarz (1995b) and Balick & Frank (2002). Using the images of very young PNe from the HST (Hubble Space Telescope) surveys, Sahai *et al.* (2011) modified the classification of PNe morphology. They classified PNe morphology into primary classes of round, bipolar, multi-polar, elongated, irregular, collimated lobe pair and spiral (see Figure 1.2). Furthermore, from compact PNe of angular sizes $< 4''$ using narrow-band images, Stanghellini *et al.* (2016) classified PNe into major morphological classes of round, elliptical, bipolar and point symmetric. They have a

comparable classification scheme with Sahai *et al.* (2011). These observed morphologies resulted in the formulation of models and theories in attempt to explain the deviation from spherical AGB stars. However, it has been observed that AGB and post-AGB star possess non-spherical morphologies (Bujarrabal *et al.*, 1992, 2001; Manchado *et al.*, 2012). This would imply that shaping agents are already present during the AGB to post-AGB evolutionary phases.

Stanghellini *et al.* (1993, 2002) suggested that different morphologies could represent PNe from different progenitors. They also suggested a relationship between the distribution of PNe and their morphology, such that bipolar PNe tend to be located closer to the Galactic plane, where extinction is at a maximum. Manchado (2003) determined mean scale heights from the Galactic plane of 647, 276 and 100 pc for the round, elliptical and bipolar PNe. This confirms the results of Stanghellini *et al.* (2002) that bipolar PNe are closer to the Galactic plane. The mass and spectral type of the central stars of PNe have also been linked to their observed morphology (Corradi & Schwarz, 1995b; Stanghellini *et al.*, 2002). This suggests that the population of PNe from the more massive progenitors will require a survey that has sufficient resolution to probe dense compact ionized regions, and at a wavelength not affected by extinction. Such a population of PNe that would be missed in the optical regime, especially when they are still very young.

1.4 Formation and Shaping Mechanisms of PNe

1.4.1 Interacting Stellar Wind Model

PNe are generally accepted to be formed by interacting stellar winds as proposed by Kwok *et al.* (1978). According to this theory, PNe are formed by the interaction between the fast wind from the central star that takes over during the post-AGB phase, and the slowly expanding envelope that is ejected during the AGB phase. The fast wind compresses the slowly moving materials into a dense shell, clearing up the inner part of the nebulae, which is observed as a PN

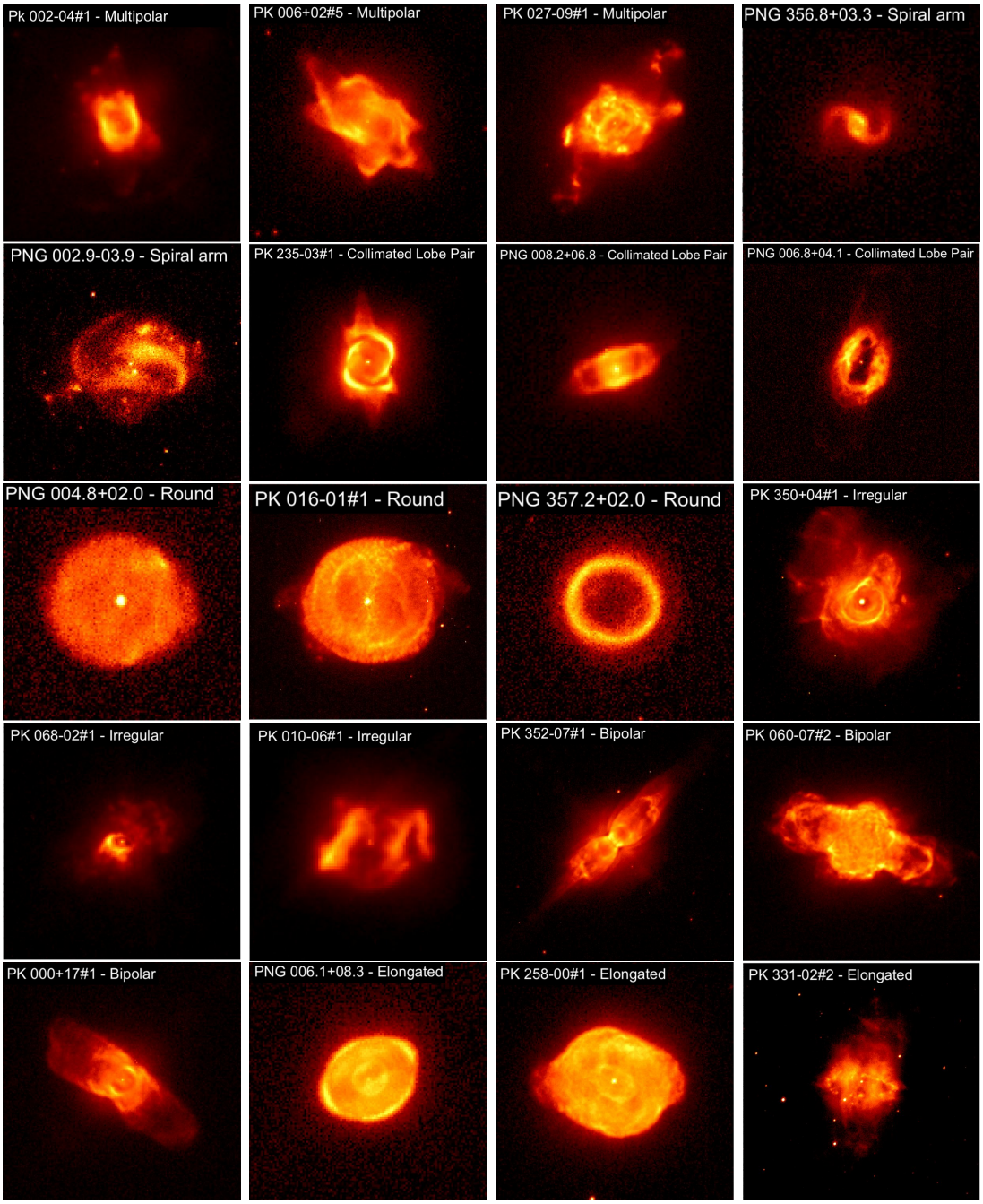

Figure 1.2: *Examples of PNe morphology and classification according to Sahai et al. (2011). Individual images are taken from Sahai et al. 2011.*

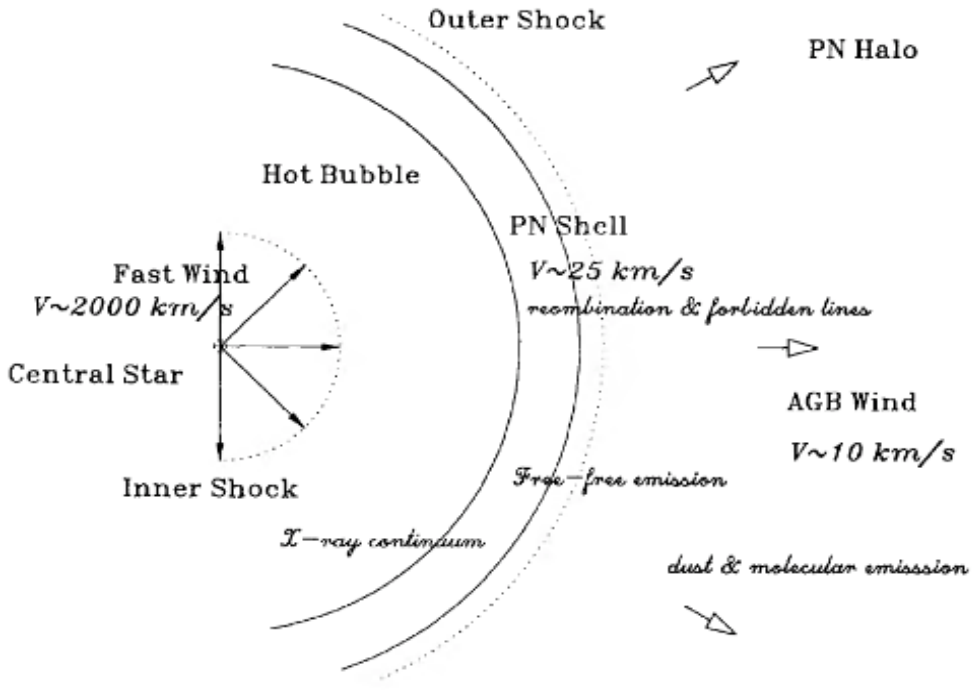

Figure 1.3: *Schematic of a PN structure. It shows the ionized shell that emits free-free emission, recombination and forbidden lines. Dust and molecular emissions are traced by regions just outside the ionized region, while X-ray is within the inner shocked region. Source: Kwok (1994)*

when ionized. This model (see a schematic description in Figure 1.3) assumed an isotropic wind and accounted for the simple, spherical morphology but was not sufficient to explain non-spherical morphologies.

The interacting stellar wind model was later modified to account for some other simple morphological types that were not spherical, observed at the time. Kahn & West (1985) considered a mass-loss that is enhanced towards the equator, such that the ionization front will escape at the pole before the equator. Subsequent model modifications that considered aspherical circum-stellar envelope are presented in Balick (1987); Balick *et al.* (1987); Frank (1994); Icke *et al.* (1989, 1992); Mellema (1995); Mellema & Frank (1995); Soker & Livio (1989) and García-Segura *et al.* (1999). These modifications accounted for non-spherical morpholo-

gies, such as elliptical to bipolar morphologies and became known collectively as the generalized interacting stellar winds (GISW) (Balick & Frank, 2002; Kwok, 2000). The GISW theory, however, could not account for complex morphologies like very collimated bipolar, collimated lobes, point symmetric, multi-polar or irregular morphologies.

1.4.2 Jets or Collimated Fast Wind (CFW)

With the knowledge that AGB and post-AGB show collimated morphologies and the inefficiency of radiation pressure alone to drive observed energetic outflows observed in post-AGB stars (Balick & Frank, 2002; Bujarrabal *et al.*, 2001; Garc´ıa-Segura *et al.*, 2005; Leal Ferreira, 2014; Sahai & Patel, 2015; Sahai *et al.*, 2007), jets are considered another possible mechanism of mass-loss and shaping mechanism. During the late AGB to post-AGB evolution, jets are believed to eject gas and dust in an energetic manner and create cavities or shape the circum-stellar envelopes (Akashi, 2009; Akashi & Soker, 2013; Bujarrabal *et al.*, 2001; Sahai & Patel, 2015; Sahai & Trauger, 1998). The characteristics of the jets such as opening angle, strength, direction and temporal history are thought to play a major role in the observed morphology of the PNe when photoionization starts (Sahai & Trauger, 1998). These jets could be multiple events, episodic or acting in pairs such that they could result in very collimated multi-polar morphologies (Yung *et al.*, 2011). These jet activities could also result in micro-structures such as FLIERS (Fast low-ionization emission regions), observed in PNe (Dyson & Redman, 2000; Soker & Regev, 1998).

The beginning of the collimated jet activities and the driving mechanism are not exactly known. However, they are thought to be the maser pumping mechanism in post-AGB stars and very young PNe i.e. PNe that are $<$ 1000 yrs, where ionization has just started (Sahai *et al.*, 2011; Umana, G. *et al.*, 2004). Masers have been observed to trace these high velocity, collimated outflows in AGB, post-AGB and young PNe (de Gregorio-Monsalvo *et al.*, 2004; Desmurs, 2012; Gómez *et al.*, 2012; Imai *et al.*, 2007; Miranda *et al.*, 2001a; Orosz *et al.*, 2018; Sahai *et al.*, 2003; Suárez *et al.*, 2012; Vlemmings & Diamond, 2006). Two proposed

mechanisms for the launching of jets are magnetic fields (Garc´ıa-Segura *et al.* 2005; see also Tocknell *et al.* 2014) and a binary companion that creates an accretion disk (see Morris 1987; Nordhaus & Blackman 2006; Reyes-Ruiz & López 1999; Soker & Livio 1994 and Section 1.5). Both mechanisms are, however, not entirely independent, such that in the presence of magnetic fields, disk-driven outflows are launched and collimated (Blandford & Payne, 1982; Nordhaus & Blackman, 2007; Reyes-Ruiz & López, 1999). H_2O masers have been observed to trace disks in PNe (Tafoya *et al.*, 2009; Uscanga *et al.*, 2008). Subsequently, magnetic fields have been observed to collimate H_2O jets in post-AGB stars (Amiri *et al.*, 2010; Pérez-Sánchez *et al.*, 2013). According to Pérez-Sánchez *et al.* (2013), magnetic fields are important in launching and driving high-velocity jets in post-AGB stars.

Magnetic fields have been observed in post-AGB stars (Vlemmings & Diamond, 2006; Vlemmings *et al.*, 2006) and Gonidakis *et al.* (2014) reported increasing magnetic field strength with the age of post-AGB stars. Synchrotron emission has also been observed towards a post-AGB star with magnetic field and jets (Pérez-Sánchez *et al.*, 2013). However, the origin of the magnetic fields is still unclear. According to Blackman *et al.* (2001), magnetic fields can be generated, in single stars, by a dynamo at the interface between the stellar core and the circum-stellar envelope, as a result of differential rotation. A binary companion (see section 1.5), however, may be needed to sustain the dynamo and produce a strong magnetic field, capable of collimating outflows (Nordhaus, 2010; Nordhaus & Blackman, 2007; Nordhaus *et al.*, 2007).

1.4.3 Interaction With the ISM

For observed morphologies where the outer shells depart from symmetry or had suffered some form of distortion, Soker *et al.* (1991) and Borkowski *et al.* (1990) suggested an interaction with the ISM. PNe were previously thought to have faded away before any notable distortion by the ISM could occur (Isaacman, 1979; Smith, 1976). Results from numerical simulations show that interaction

with the ISM distorts the outer region of the PNe and actually starts during the AGB phase (Villaver *et al.*, 2003; Wareing *et al.*, 2007).

Interaction of the AGB star or PNe would depend on the density and velocity of the nebular shell relative to the ISM (Borkowski *et al.*, 1990). Using numerical simulations, Villaver *et al.* (2003) showed that interaction with the ISM could also be influenced by the strength of Galactic magnetic field, resulting in bow shocks and cometary-like structures (Ali *et al.*, 2012; Dgani & Soker, 1998a; van Marle *et al.*, 2014; Villaver *et al.*, 2012, 2014). By imploring a triple wind hydrodynamical model, Wareing *et al.* (2005, 2006, 2007) were able to reproduce the shape of PN Sh 2188. The triple wind model considers a third wind due to motion of the AGB star through the ISM in addition to the interacting stellar wind model (see van Marle *et al.* 2014). They found that 90% of the mass-loss on the AGB is swept downstream, suggesting a possible way to account for the missing mass in PNe (see Villaver *et al.* 2003). The missing mass is the mass lost during the evolution of the AGB to becoming a PN that is not accounted for during the formation of a PN or ionization of the circum-stellar envelope.

Observationally, different authors have reported interaction of PNe with the ISM (Ali *et al.*, 2000; Borkowski *et al.*, 1990; Guerrero *et al.*, 1998; Sabin *et al.*, 2012). From the analysis of 117 PNe, Ali *et al.* (2012) found PNe interacting with the ISM to be concentrated in the thin disk and younger i.e. in the mid stage of their evolution than previously thought, which would indeed agree with model results that ISM interaction is present during the AGB phase. Figure 1.4 shows three examples of PN interacting with the ISM, including Sh 2188.

No single shaping mechanism fits all of the observed morphologies of PNe. It follows that a number of shaping processes may be operating with different strengths and at different stages of the evolution of any individual object (Balick & Frank, 2002). It is also possible that the variety of observed morphologies is a result of combining mechanisms such that in order to explain some of the presently observed PNe morphologies, more than one shaping mechanism may be present or responsible.

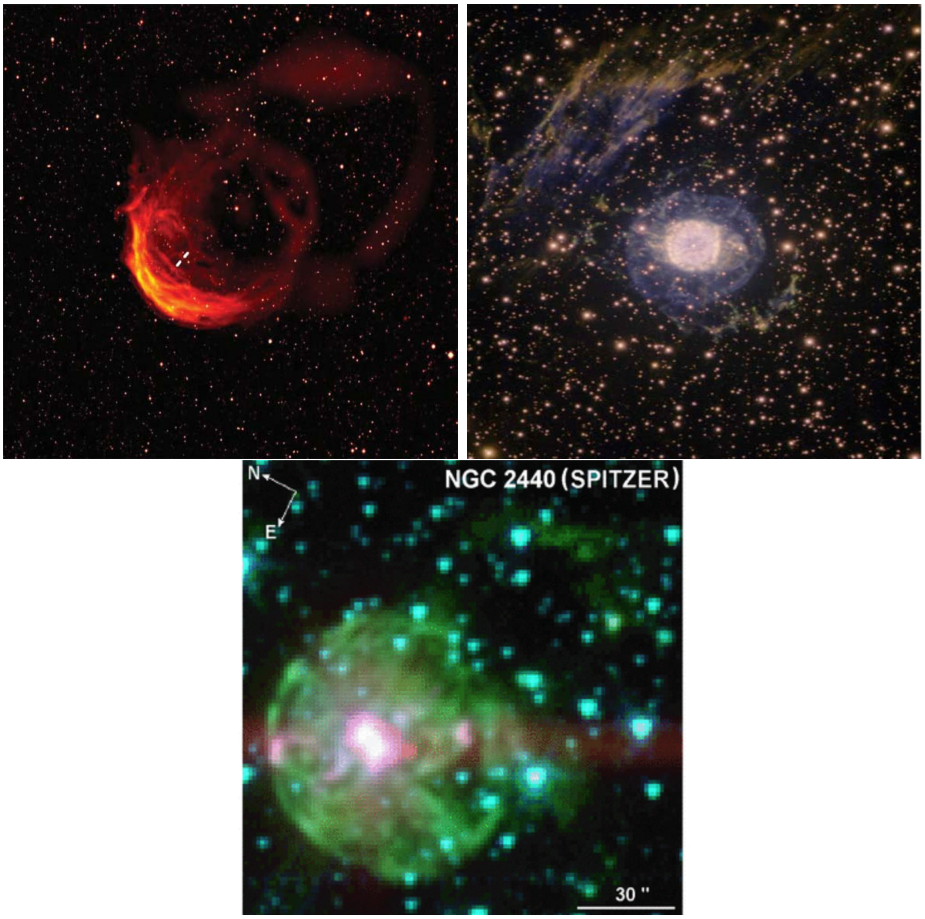

Figure 1.4: *Examples of PN interacting with the ISM. Top left: False colour image of PN Sh 2-188 (Wareing et al., 2007). The central star is indicated by the marker towards the arc region. Top right: NGC 6751. Analysis of ISM interaction is presented in Clark et al. (2010). Image credit: Image credits are Daniel Tran (PAL College), Travis Rector (University of Alaska, Anchorage), Terry Bridges (Queen's University), and the Australian Gemini Office (http://www.gemini.edu/node/11329). Bottom: Mid-infrared false colour image of NGC 2440 (Ramos-Larios & Phillips 2009: 3.6 μm = blue, 4.5 μm = green and 8.0 μm = red).*

1.5 Binary versus Single Stellar System

From the GISW model, it is suggested that non-spherical PNe can be produced if equatorially enhanced mass-loss or density contrast in the circum-stellar envelope is assumed. Magnetic fields (Garc´ıa-Segura *et al.*, 2005) and/or rotation of the AGB stars (Dijkstra & Speck, 2006) are proposed to be responsible for the needed density contrast, eventually resulting in the formation of PNe that deviate from spherical morphology. Such a scenario is supported by the observation of magnetic fields in AGB and post-AGB stars (Pérez-Sánchez *et al.*, 2013; Vlemmings *et al.*, 2005; Vlemmings & Diamond, 2006). From hydrodynamical and magnetohydrodynamical simulations, García-Segura *et al.* (1999); Garc´ıa-Segura *et al.* (2005) considered both rotation and magnetic fields in the formation of observed PNe morphologies. They showed that rotation and magnetic fields could influence mass-loss and result in collimated bipolar morphologies. They, however, noted that single stars with masses $< 1.3 M_{\odot}$ can not result in bipolar PNe. It is still not clear if or how single stellar systems could produce very collimated PNe, where jets and/or strong magnetic fields are believed to be the shaping agents.

Binary stellar systems are thought to be involved in both the formation and shaping of observable PNe (De Marco, 2009; Jones & Boffin, 2017; Zijlstra, 2007). A binary stellar system involves an interaction with a companion, which could be a star, brown dwarf or even a planet (Soker, 1997). Binary interactions, according to De Marco (2009) and Soker (1997) are classified into very wide interactions, wide interactions, common-envelope interactions that results in a merger, common-envelope interactions that do not result in a merger and close interactions. Such interactions could enhance mass-loss and influence the morphology, depending on the interaction type. The resulting effect of a companion on the morphology would depend on the influence of the companion, which in turn depends on the interaction distance (De Marco, 2009; Soker, 1997).

Common-Envelope Interactions

According to Soker (1997), common envelope interactions would account for 79% of PNe and they are thought to have the highest effect on the mass-loss and shape of a PN (Nordhaus & Blackman, 2007; Soker & Livio, 1989). A common envelope is formed when the primary star transfers mass to the secondary or binary companion, after filling its Roche lobe, at a rate that is greater than the accretion rate of the companion, such that both become engulfed in a single or common envelope (Iben & Livio, 1993; Ivanova *et al.*, 2013; Paczynskii, 1976). The primary star in this case, could be an AGB or post-AGB star. Common envelope interactions could result in a close binary interaction or a merger (NGC 6826; De Marco *et al.* 2015a). Once in a common envelope, the companion (e.g. a main sequence star) spirals in towards the core of the primary, depositing angular momentum and orbital energy in the common envelope. The in spiral of the companion is due to the differential velocity between the low density envelope and the companion that results in a drag force. Depending on the mass of the secondary, the in spiral of the companion could supply the required orbital energy to eject the common envelope, which is concentrated around the orbital plane, resulting in close binaries (companion and core of the primary). If the orbital energy supplied by the companion is not enough to eject the common envelope, it spirals inwards until it is tidally shredded, forming an accretion disk around the core of the primary (Nordhaus & Blackman, 2006). Such disks could produce jets and result in highly collimated morphologies (Moe & De Marco, 2006; Soker & Livio, 1994; Zijlstra, 2007).

An accretion disk can also be formed around the binary companion through the accretion of materials lost by the AGB star before filling its Roche lobe. Such an accretion disk could also produce jets. Eventually, if the AGB star fills its Roche lobe, the accretion disk will be destroyed along with any jets produced (Mastrodemos & Morris, 1998; Miranda *et al.*, 2001b; Morris, 1987; Soker & Livio, 1994). Additionally, a triple stellar system has been suggested to explain the morphologies of some irregular PNe (see Bear & Soker 2017; Soker 2016 and references therein).

From the formation rate of PNe ($\sim 1/3$ the formation rate of white dwarfs), Soker (2006) estimated that only one-third of all PNe that evolve to become white dwarfs are bright enough to be observed, 97% of which are from binary interactions. Furthermore, it was suggested that the majority ($\sim 60-70\%$) of the hidden PNe population, mostly from single stars, are hardly bright enough to be observed (Moe & De Marco, 2012). From observation, using photometric variability, only 10% - 20% of the central stars of PNe were found to be close binaries (Bond, 2000; De Marco *et al.*, 2015b; Han *et al.*, 1995; Miszalski *et al.*, 2009). Miszalski *et al.* (2009) concluded that close binaries may play a role in the shaping of PNe but not a major role and neither do they necessarily account for all observed PNe, given the observed percentage ($\sim$ 20%) of close binaries (see Hrivnak *et al.* 2017).

1.6 Galactic PNe

1.6.1 PNe Population and Distribution

From a population synthesis model, Moe & De Marco (2006) estimated a total Galactic PNe population of 46000 ± 15000 (with radii < 0.9 pc), assuming single and binary stellar systems result in PNe and 8100 ± 2300 (Moe & De Marco, 2012), assuming PNe are formed through bnary interactions. This population corresponds to visibility time of 35000 years and average expansion velocity of 25 km/s. Moe & De Marco (2006) estimated the population of Galactic PNe by dividing the galaxy into four components (thin disk, thick disk, spheroid and bulge). For each of the components they have defined different star formation rates, mean ages, metallicities and initial mass function (IMF). The number of Galactic stars that produce PNe was then determined by estimating the luminous mass of each component and using the IMF to determine the number of objects. Zijlstra & Pottasch (1991) had previously estimated $\sim 23000 \pm 6000$ PNe in the Galactic disk, based on local column densities.

About 3500 PNe have been identified so far, including true, likely and possible PNe as catalogued in the Hong Kong/AAO/Strasbourg/Hα catalogue (HASH[1]; Parker *et al.* 2017). This population excludes the CORNISH PNe candidates on the HASH database. If the population of Moe & De Marco (2006) is adopted, the known PNe population makes up $\sim 8\%$ of the predicted number (singles + binaries). Since PNe are mainly a disk population, the column density estimate of Zijlstra & Pottasch (1991) ($\sim 23000 \pm 6000$) still requires $\sim 85\%$ more PNe. This could be an indication that quite a number of PNe are still missing, assuming the majority ($\sim 90\%$) of the stars in our Galaxy are of intermediate mass and expected to go through the PN phase (Gesicki *et al.*, 2018). It could also mean, that not all stars thought to go through the PN phase actually do. However, if observable PNe are assumed to come from binary systems, then 44% have been observed, so far.

Reconciling the the number of observed Galactic PNe population to population synthesis predictions is challenging. This could be because we cannot rightly account for the number of low surface brightness PNe that cannot be observed due to present instrumental limitations (sensitivity and resolution). These could be PNe from low mass stars or PNe from progenitors who do not drive sufficient mass-loss, such that they do not get bright enough to be detected. Soker (2006) suggested that these could be the population formed by single mass stars, hence would require deeper surveys to detect. They could also be PNe whose brightness have been diluted because they have become very extended or old. Additionally, there is also the issue of the number of PNe hiding behind large amounts of dust, and even the very distant PNe that may have been observed but not recognized or classified as PNe yet, due to confusion. How do we account for the number of PNe that are short lived?

The Galactic latitude and longitude distributions of known true PNe are shown in Figures 1.5 and 1.6. Figure 1.5 shows a distribution that peaks towards the Galactic mid-plane as expected. However, because known PNe are mainly optical detections, the effect of extinction is observed about 0° latitude. The angular size distribution of the known PNe is also shown in Figure 1.7, taken from the HASH

[1] hashpn.space

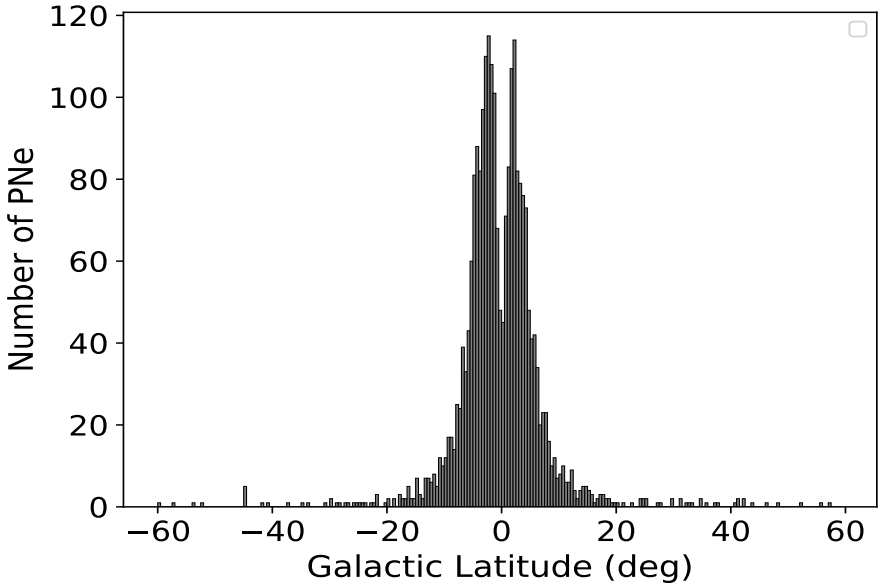

Figure 1.5: *Galactic latitude distribution of known true PNe from the HASH catalogue (Parker* et al.*, 2017).*

catalogue for PNe with catalogued sizes. The distribution shows a mean of $44''$ and a median of $15''$. This describes a PN population that is either close by or extended.

1.6.2 Multi-Wavelength Detections

The processes involved in PNe formation results in a range of emission mechanisms that are dominant at different wavelengths. Emission from a PN is a summation of emission from the central star, ionized gas, molecular gas or neutral gas, and dust component (see Figure 1.8). Each of these regions can be probed at wavelengths including infrared and radio (Zhang & Kwok, 1991). Figure 1.8 shows the spectral energy distribution (SED) of a typical PN (NGC 7027), from the radio to far-infared (Planck Collaboration *et al.*, 2015). Some PNe, especially young PNe, also have molecular emission that can be viewed at milli-metre or sub-millimetre wavelengths (Bujarrabal, 2016; Isaacman, 1984; Zhang, 2017).

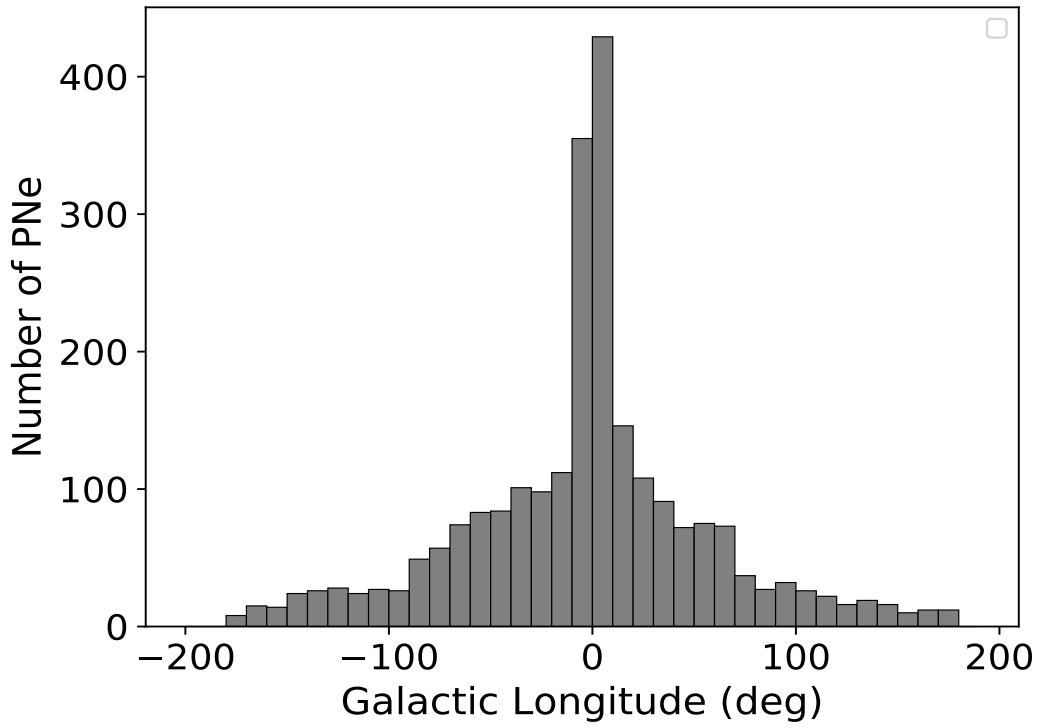

Figure 1.6: *Galactic longitude distribution of known true PNe from the HASH catalogue (Parker* et al.*, 2017).*

Optical and Infrared Detections

Optical surveys such as the SuperCOSMOS Hα survey (SHS: Frew *et al.* 2014; Parker *et al.* 2005), Macquarie/AAO/Strasbourg Hα Planetary Nebula survey (MASH I and II:Miszalski *et al.* 2008; Parker *et al.* 2006) and the INT Photometric Hα survey (IPHAS: Drew *et al.* 2005) have contributed significantly to the number of known Galactic PNe. PNe identification from these surveys include visual inspection of images, the use of difference imaging, quotient imaging, 3-colour combined images, combination of Hα and mid-infrared images, and spectroscopy (Miszalski *et al.*, 2008; Parker *et al.*, 2006; Sabin *et al.*, 2014).

The search for PNe at optical wavelengths is, however, limited by dust extinction, especially towards the Galactic mid-plane. This limitation makes it difficult to detect PNe that are closer to the Galactic mid-plane, especially when they are

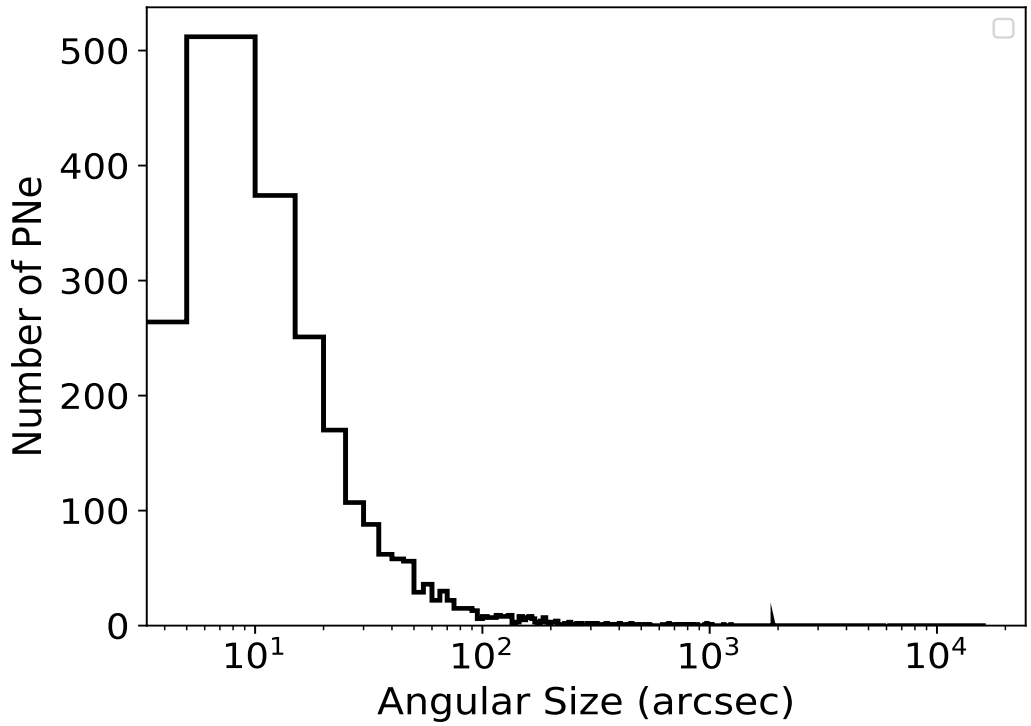

Figure 1.7: *Angular Size distribution of known true PNe from the HASH catalogue (Parker* et al.*, 2017).*

compact. PNe from high-mass stars ($> 0.6 M_{\odot}$) that are closer to the Galactic plane (Stanghellini *et al.*, 1993, 2002), are believed to evolve so fast that the central star ionizes the nebula while it is still compact and dense. Such PNe will also be missed at optical wavelengths. Additionally, an optical survey cannot always distinguish between young and compact PNe from other compact, ionized objects such as H II regions (Frew & Parker, 2010) and symbiotic systems (Kwok, 2003).

To overcome the limitation of extinction, there is the need for observations at longer wavelengths (e.g. infrared wavelengths), where the ISM is more transparent. Infrared surveys such as the Infrared Astronomical Satelite (IRAS: Neugebauer *et al.* 1984) survey provided new ways to search for PNe hidden by dust (Garcia-Lario *et al.*, 1993, 1997; Pottasch *et al.*, 1988; Reddy & Parthasarathy, 1997), at four different bands (12, 25, 60, and 100 μm). After the era of the

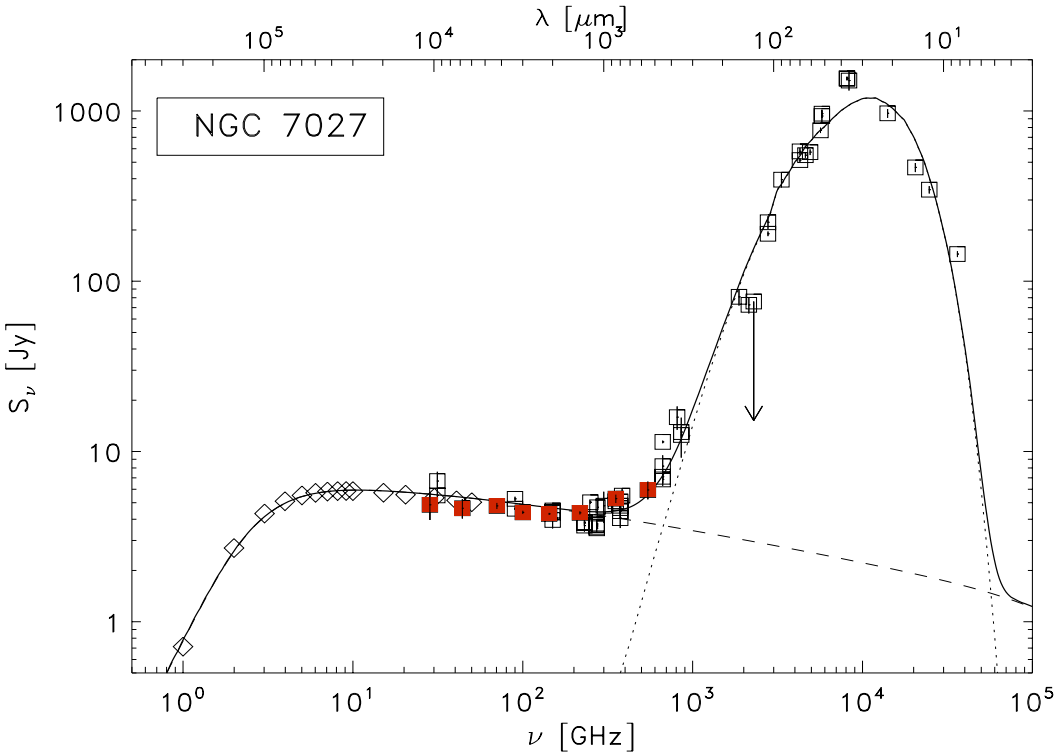

Figure 1.8: *Spectral energy distribution of a typical PN (NGC 7027) from the radio to the far-infrared. The continous line shows the model of the SED (free-free and thermal dust emission). The dust emission is traced by the dotted line, while free-free emission is traced by the dashed line. The red squares represent the Planck data, while the open squares represent measurements from different instruments and the diamonds represent the radio spectrum of NGC 7027 taken from Zijlstra* et al. *(2008a). Source: Planck Collaboration* et al. *(2015).*

IRAS survey, infrared surveys with better resolution and sensitivity such as the GLIMPSE (Churchwell *et al.*, 2009), WISE (Wright *et al.*, 2010) and Hi-Gal (Molinari *et al.*, 2010), covering the mid-infrared to the far-infrared, have made available a wealth of data that have now provided new ways to search for PNe and study their dust content (Kwok *et al.*, 2008). In the near-infrared, surveys such as the 2MASS (Skrutskie *et al.*, 2006a), VVV (Minniti *et al.*, 2010) and UKIDSS (Lawrence *et al.*, 2007) have also provided useful tools in probing deeper for PNe population. Additionally, molecular hydrogen (H_2) in the near-infrared provides an alternative way to search for hidden PNe population by probing their molecu-

lar gas content (Froebrich *et al.*, 2011, 2015; Gledhill *et al.*, 2018; Guerrero *et al.*, 2000; Kastner *et al.*, 1996; Ramos-Larios *et al.*, 2017).

The combination of optical and infrared studies has proven to be a very useful tool in the search and identification of PNe and has improved the census of known PNe (Hsia & Kwok, 2012; Viironen *et al.*, 2009a,c). The use of infrared data, however, has its limitations. This is because infrared selections can be biased towards more embedded PNe. Pottasch *et al.* (1988) recommended instead, that PNe should be searched for at infrared and radio wavelengths, where the ionized region and dust content can be probed without the bias of dust extinction. This will result in a more complete and deeper search for PNe. There are already existing multi-wavelength surveys with good resolution and sensitivity, providing an unbiased view of the Galactic plane in the near-infrared, mid-infrared and far-infrared. Consequently, a co-ordinated search for PNe using a radio survey, covering the same area with matching resolution will be invaluable in discovering the population PNe that are hidden by dust extinction and very compact.

Radio and Infrared Detections

Because the onset of ionization marks the formation of a PN, the probe of the free-free emission from the ionized volume at radio wavelengths, not limited by extinction will provide an unbiased search for PNe. The combination of radio and infrared data, hence provides a method to identify and discriminate PNe from other astronomical objects they share similar observational characteristics with e.g. HII regions and young stellar objects (YSO). YSO are embedded objects in the infrared with weak radio emission from their ionized stellar winds that are usually less than a few mJy (Hoare, 2002; Hoare *et al.*, 1994). HII regions on the other hand, who are the chief contaminants of PNe, can be distinguished using the ratio of the mid-infrared to radio (Cohen *et al.*, 2011) and their infrared colours (Anderson *et al.*, 2012; Cohen *et al.*, 2011; Parker *et al.*, 2012b).

van de Steene & Pottasch (1995) demonstrated the strength of using radio emisision and infrared colours in identifying new PNe. They found 20 new PNe using a combination of IRAS colours and 5 GHz radio emission (see also Filipović *et al.*

2009a). The first large scale radio survey that was used to construct a sample of PNe unbiased by extinction is the NRAO VLA sky survey (NVSS), with a resolution of $45''$ (Condon *et al.*, 1998). Within the coverage of this survey (full sky survey north of $\delta - 40$), 702 of the then known 885 PNe in the Strasbourg-ESO catalogue of Galactic planetary nebulae (Acker *et al.*, 1992) were detected at the time (Condon & Kaplan, 1998; Condon *et al.*, 1999). With a sensitivity of ~ 2.5 mJy/beam, this survey was also used to reject contaminants and detect free-free emission towards 454 candidate PNe in the IRAS point source catalogue, 332 of which were known PNe and 122 sources were identified as candidate PNe (Condon *et al.*, 1999).

1.7 Radio Surveys

1.7.1 Emission Mechanism

Radiation that travels from a source to an observer or a detector through a medium (gas + dust), is governed by the equation of radiative transfer (Equation 1.2), which can be written in terms of the optical depth, τ_ν (dimensionless) as equation 1.3.

$$\frac{dI_\nu}{ds} = -k_\nu I_\nu + \varepsilon_\nu \tag{1.2}$$

$$\frac{dI_\nu}{d\tau_\nu} = I_\nu - \frac{\varepsilon_\nu}{k_\nu} \tag{1.3}$$

where ds is a change in unit length and $d\tau_\nu = -kds$. Iν ($Wm^{-2}Hz^{-1}sr^{-1}$) is the specific intensity of radiation, ε_ν ($Wm^{-3}Hz^{-1}sr^{-1}$) is the emission co-efficient, and k_ν (m^{-1}) is the linear absorption coefficient. The term $\varepsilon_\nu/k_\nu = S_\nu$ is called the source function and the general solution to equation 1.3, considering a homogenous medium is given by equation 1.4.

$$I_\nu(\tau_\nu) = I_\nu(0)e^{-\tau} + S_\nu(1 - e^{-\tau_\nu}) \tag{1.4}$$

For a system in thermal equilibrium (Kirchhoff's law) equation 1.3 can be written as:

$$I_\nu(T) = \frac{\varepsilon_\nu}{k_\nu} = S_\nu \approx B_\nu(T) \tag{1.5}$$

and the radiation can be approximated by a blackbody (Planck's law) as given in equation 1.6.

$$B_\nu(Wm^{-2}sr^{-1}Hz^{-1}) = \frac{2h\nu^3}{c^2}\frac{1}{e^{h\nu/kT} - 1} \tag{1.6}$$

Thermal emission

The dominant emission mechanism at radio frequencies in an ionized region is the thermal free-free continuum emission, also known as bremsstrahlung emission. It is produced as a result of the interaction between an electron and an ion (Burke & Graham-Smith, 2010; Lawrence, 1991; Osterbrock & Ferland, 2006). In such interactions, the electron is free before interaction and still free after interaction. This emission is thermal, which means it is controlled by the temperature of the ionized gas, such that electrons move at thermal speeds.

At radio frequencies, Equation 1.6 can then be replaced by the Rayleigh Jeans approximation (equation 1.7, where $h\nu << kT$). T is the temperature of the radiating source.

$$I_\nu(T) \approx \frac{2kT\nu^2}{c^2} \tag{1.7}$$

The flux density can then be expressed as:

$$F_\nu(Jy) = \int I_\nu d\Omega \tag{1.8}$$

where F_ν is in units of Jy (Jansky[2]) and Ω is the solid angle measured in steradians.

From equation 1.7, the brightness temperature, T_B can be defined as:

$$T_B(\nu) = \frac{c^2 I_\nu}{2k\nu^2} = \frac{c^2}{2k\nu^2}\frac{F_\nu}{\Omega} \tag{1.9}$$

Substituting for T_B in equation 1.3 will result in the expression given by equation 1.10, where T_e is the electron temperature of the source.

$$\frac{dT_B}{d\tau_\nu} = T_B - T_e \tag{1.10}$$

Following equation 1.4, the solution can be written as:

$$T_B = T_B(0)e^{-\tau} + T_e(1 - e^{-\tau_\nu}) \tag{1.11}$$

This equation shows that the brightness temperature is dependent on the optical depth. $T_B(0)e^{-\tau}$ expresses the brightness temperature of the background. Substituting into equation 1.9 and ignoring the background at radio frequencies, the flux density can then be written as:

$$F_\nu = \frac{2k\nu^2\Omega}{c^2}T_B \tag{1.12}$$

where $T_B = T_e(1 - e^{-\tau_\nu})$.

Optical Depth

The optical depth, τ_ν of an ionized region describes the distance over which a photon with frequency ν can travel before been absorbed. It is the integral of the

[2] $1\text{Jy} = 10^{-26}\text{Wm}^{-2}\text{Hz}^{-1} = 10^{-23}\text{ergs}^{-1}\text{cm}^{-2}\text{Hz}^{-1}$

opacity, k, along the line of sight and expressed as:

$$\tau_\nu = \int -k ds \propto n_e^2 \tag{1.13}$$

τ_ν can be expressed in terms of the emission measure (EM), given by equation 1.14.

$$\tau_\nu \approx 3.014 \times 10^{-2} \left(\frac{T_e}{K}\right)^{-3/2} \left(\frac{\nu}{GHz}\right)^{-2} \left(\frac{EM}{pc\ cm^{-6}}\right) \langle g_{ff} \rangle \tag{1.14}$$

where g_{ff} is the free-free gaunt factor (quantum-mechanical correction factor) that is weakly dependent on ν i.e. $\langle g_{ff} \rangle \propto \nu^{-0.1}$ and is given by equation 1.15 and EM is given by equation 1.16.

$$\langle g_{ff} \rangle (\nu, T_e) \approx \ln \left[4.955 \times 10^{-2} \left(\frac{\nu}{GHz}\right)^{-1}\right] + 1.5 \ln \left(\frac{T_e}{K}\right) \tag{1.15}$$

$$\frac{EM}{pc\ cm^{-6}} \equiv \int_{los} \left(\frac{n_e}{cm^{-3}}\right)^2 \left(\frac{ds}{pc}\right) \tag{1.16}$$

Numerically, τ_ν can be approximated by equation 1.17 (Mezger & Henderson, 1967). Thus $\tau_\nu \propto \nu^{-2.1}$.

$$\tau_\nu = 8.235 \times 10^{-2} \left(\frac{T_e}{K}\right)^{-1.35} \left(\frac{\nu}{GHz}\right)^{-2.1} \left(\frac{EM}{pc\ cm^{-6}}\right) \tag{1.17}$$

Considering an ionized region, equation 1.12 has two limiting cases that depend on the optical depth. In the optically thick regime (low frequencies), where $\tau \to \infty$: equation 1.12 can be expressed as equation 4.5, such that $T_B = T_e$. In this regime, the spectrum of the free-free emission can be approximated by a black-body corresponding to the electron temperature and the flux density will obey the Rayleigh-Jeans approximation, such that the free-free emission will increase with increasing frequency as ν^2 (Burke & Graham-Smith, 2010).

$$F_\nu = 2k\nu^2 c^{-2} \Omega T_e \propto \nu^2 \tag{1.18}$$

In the optically thin regime (at high frequencies), where $\tau \rightarrow 0$: The free-free emission shows weak dependence on frequency (flat spectrum) and equation 1.12 can be expressed as equation 1.19, such that $T_B = \tau_\nu Te$. In this regime, the nebulae is nearly transparent and shows little or no dependence on frequency, such that the free-free emission does not change much with frequency.

$$F_\nu = 2k\nu^2 c^{-2} \Omega T_e \tau_\nu \propto \nu^{-0.1} \tag{1.19}$$

where $\tau_\nu \propto \nu^{-2.1}$. Based on equations 1.16 and 1.17, equation 1.19 can also be expressed as:

$$F_\nu \propto \vartheta_s^2 T_e^{-0.35} n_e^2 R_s \nu^{-0.1} \tag{1.20}$$

where ϑ_s (arcsec) is the angular size of the ionized region ($\Omega = \pi\vartheta_s^2$) and R_s is the physical size (pc) of the ionized region. R_s and ϑ_s are related through the distance. In terms of the distance, d, equation 1.19 can be further expressed as:

$$F_\nu \propto T_e^{-0.35} n_e^2 R_s^3 d^{-2} \nu^{-0.1} \tag{1.21}$$

Equation 1.21 expresses the dependence of the observed flux density, F_ν on the electron density and the volume of the ionized region, and the distance to the ionized region.

Non-thermal Emission

The dominant emission in PNe is believed to be thermal. However, non-thermal emission processes could dominate the radio continuum in very young PNe and give rise to synchrotron emission (Suárez *et al.*, 2015), such as in transition PNe. Non-thermal emission is produced in an ionized region when particles are accelerated in the presence of magnetic field, such that the electrons are constrained to move in spiral motion about the magnetic fields lines in a helical path (Figure 1.9). Such interaction will result in synchrotron emission, where the electrons are

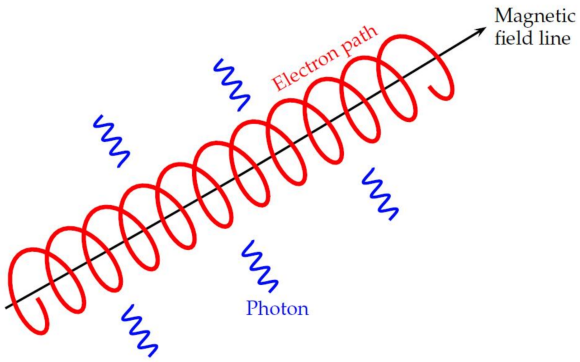

Figure 1.9: *Illustration of synchrotron radiation from charged particle accelerated in a magnetic field. Image credit: Dr. Adrian Jannetta* `http://spiff.rit.edu/classes/ast613/lectures/radio_i/radio_i.html`.

accelerated to relativistic velocities. The spectrum is described by a power law, described by:

$$I_\nu = A(KB^{1+\alpha})\nu^{-\alpha} \tag{1.22}$$

where α is the spectral index, B is the magnetic field, K is the total energy of the electrons and A is a constant.

Strong magnetic fields ($\sim$ 200 mG) have been observed in post-AGB stars (Vlemmings & Diamond, 2006; Vlemmings *et al.*, 2006) and Gonidakis *et al.* (2014) reported increasing magnetic field strength with the age of post-AGB stars. Synchrotron emission has also been observed towards the magnetically collimated jets of a post-AGB star e.g. IRAS 15445-5449 (Pérez-Sánchez *et al.* 2013; see also Miranda *et al.* 2001a; Sabin *et al.* 2007). However, there has been only one direct observational evidence of non-thermal synchrotron radio emission dominating the radio spectrum of a young PN, observed towards IRAS I15103 (Gómez *et al.*, 2015).

The physical processes such as jets or shocks and magnetic fields involved in the shaping of PNe can provide an environment for synchrotron radio emission (Achterberg, 2000). Dgani & Soker (1998b) predicted that radio synchrotron

emission from PNe, having fast winds and a high mass-loss rate, can be detected by resolving the central region of the PNe. However, the free-free emission from the nebulae appears to dominate the radio spectrum, such that synchrotron emission if present may be too weak to be detected. It is possible that observation of such non-thermal emission in PNe could be possible within a small time window ($<$ 100 yrs; Gómez *et al.* 2018), before full ionization, in which case, free-free thermal emission becomes dominant.

1.7.2 Interferometry

Theoretically, the spatial resolution of a single dish (equation 1.23), limited by its diameter, is governed by the Rayleigh criterion. At radio wavelengths, however, it is not practical to achieve sub-arcsecond resolution with single dishes. This results in difficulties in cross-matching with observations at other wavelengths e.g. optical, and discriminating between compact sources. Consequently, multi-wavelength studies and desired science are limited. The need for better resolution, sensitivity[3], and positional accuracy, informed the need for radio interferometry (see Ryle 1968).

$$\vartheta(\text{radians}) = \frac{1.22\lambda}{\mathrm{D}} \tag{1.23}$$

Radio interferometry allows the effective synthesis of a large telescope by combining two or more single radio dishes using aperture synthesis (Ryle, 1955; Ryle & Hewish, 1960). In this case, the diameter of the telescope, D, in equation 1.23 becomes the largest distance between the telescopes ($\mathrm{B_{max}}$). The angular scales an interferometer is sensitive to lie in the range of $\lambda/\mathrm{B_{max}} < \vartheta < \lambda/\mathrm{B_{min}}$. The long baselines are sensitive to small structures, while the short baselines are sensitive to extended or large structures.

An interferometer measures the interference patterns or coherence, called complex visibility (V(u,v)) in amplitude and phase, of an incident electric field. The

[3]smallest radio flux that can be detected, which is determined by the collecting area and the integration time.

complex visibilities, V(u,v) are a function of the baseline coordinates (u,v), produced by pairs of antennas (i,j) in spatial frequencies. This interference pattern or visibility is related to the sky brightness or brightness of the observed source, I(l,m) through the Van Cittert-Zernike theorem (Thompson, 1986), expressed as equations 1.24, 1.25 and 1.26.

The assumptions are that the source being observed is spatially incoherent and the observed field is small. Details on radio interferometry can be found in Cornwell *et al.* (1999); Thompson *et al.* (2001) and Thompson *et al.* (2017).

$$\mathrm{V(u,v)} = \mathrm{Ae^{-i\varphi}} = \int\int \mathrm{I(l,m)e^{-2\pi i(ul+vm)}dldm} \tag{1.24}$$

$$\mathrm{V(u,v)} \rightarrow \mathrm{F} \rightarrow \mathrm{I(l,m)} \tag{1.25}$$

$$\mathrm{I(l,m)} = \int\int \mathrm{V(u,v)e^{2\pi i(ul+vm)}dudv} \tag{1.26}$$

Calibration and Imaging

The observed visibilities can be altered in amplitude and phase by instrument, propagation and radio frequency interference (RFI), hence the need for calibration. Calibration basically accounts for, and restores the visibilities, in amplitude and phase, to be close to what is expected if the observation was done in a vacuum with an ideal instrument. This involves observing well characterized radio point sources that can be easily modelled with little error (known true visibilities) and the corrections in both phase and amplitude that allow the observations to fit the model are determined. These corrections are then applied to the observed visibilities of the target data.

Calibration seeks to solve equation 1.27, such that $\mathrm{G_{ij}}(\nu)$ accounts for variations in amplitude or phase with frequency (bandpass) and $\mathrm{G_{ij}}(t)$ accounts for variations

with time.

$$V_{ij}(t,\nu)_{obs} = V_{ij}(t,\nu)_{true} G_{ij}(t,\nu) \tag{1.27}$$

The process of re-constructing the sky brightness is referred to as imaging. It is an inverse process in which the observed data or visibilities are inverted to recover the brightness distribution of the sky. Inverting the visibilities through Fourier transform (see equations 1.24, 1.25 and 1.26), however, does not directly give the image of the sky. It results in a dirty image (equation 1.28 and 1.29), which is the convolution of the true image and the dirty beam, given by equations 1.29 and 1.30. This introduces the sampling function (Briggs *et al.*, 1999), S(u,v), such that $s(l,m) \rightarrow F \rightarrow S(u,v)$ (equation 1.31).

The uv-plane is usually not completely filled. Therefore, for the observed visibilities to be inverted using the Fourier transform algorithm, they need to be sampled onto a regular grid, thus, multiplying the visibilities by a sampling function (equation 1.29). S(u,v) is 1 where there are data and zero in other parts of the uv-plane.

$$I_D(l,m) = \int\int V(u,v) S(u,v) e^{2\pi i(ul+vm)} dudv \tag{1.28}$$

$$S(u,v)V(u,v) \rightarrow F \rightarrow I_D(l,m) \tag{1.29}$$

$$I_D(l,m) = I(l,m) * s(l,m) \tag{1.30}$$

$$s(l,m) = \int\int S(u,v) e^{2\pi i(ul+vm)} dudv \tag{1.31}$$

Each sample point of the uv-plane contains information about the sky brightness, however, a high quality image of the sky brightness will require a well sampled uv-plane or filled uv-coverage. For N radio telescopes, there will be $N(N-1)/2$ interferometric pairs or samples that provide a set of visibilities, V_{ij}. This set of

visibilities (V_{ij} - sample points) can be increased to get a better u-v coverage by observing for a longer time, thereby allowing the Earth's rotation to fill in the uv-plane. A good uv-coverage should be well sampled, resulting in more sampled points. This is because the more information about the spatial frequencies i.e uv-coverage, the better the brightness distribution of the sky can be approximated.

The process of recovering the true image from equation 1.30 is a deconvolution process, which is non-linear and the common algorithm used is the CLEAN algorithm by Högbom (1974). It assumes the sky image to be a collection of point sources, defined by peak strength and positions. The peak strength is subtracted iteratively from the dirty image, $I_D(l, m)$ using a scaled dirty beam, s(l,m), until the remaining peak is below a defined threshold. These are called CLEAN components, which are then convolved with a restoring beam or clean beam and added to the residual image. The restoring beam is an elliptical Gaussian fitted to the central region of the dirty beam, s(l,m) in order to suppress higher spatial frequencies (Cornwell *et al.*, 1999; Högbom, 1974). The resulting map gives an estimate of the sky brightness or image in Jy/beam.

1.7.3 Previous Radio Surveys of the Galactic Plane

Observations with interferometers like the work of Thompson *et al.* (1967), improved on the limitations of single dish observations (Hughes, 1967; Lynds, 1961) in the radio studies of PNe. They were able to estimate the angular widths of PNe at 10 cm (3 GHz) and 21 cm (1.4 GHz), using the interferometer at Owens Valley Radio Observatory. Their results were comparable to those estimated from optical observations. Kwok (1985) observed ten compact PNe with an angular resolution of $\sim 0.4''$ using the Very Large Array (VLA) in 'A' configuration at 5 GHz, with a sensitivity of 0.5 mJy/beam. Over the years, the resolution and sensitivity of radio observations of PNe have improved, depending on the goal of the survey. In addition, the reliability of cross-matching radio surveys at different frequencies has also improved. Condon *et al.* (1998) carried out a radio continuum sky survey (NVSS) at 20 cm with the VLA in D and D 'n' C configuration. They achieved a resolution of $45''$ and sensitivity limit of ~ 2.5

mJy/beam^{-1}. They were able to detect PNe with low surface brightness but their resolution was not suitable for compact PNe. In the southern Galactic plane, the MGPS (Green, 1999) observed an area of 2400 deg^2, defined by Galactic longitude $245^\circ < l < 365^\circ$ and latitude $|b| \leq 10^\circ$ at 843 MHz. This survey achieved a sensitivity of 1-2 mJy/beam and resolution of $45''$. The $45''$ beam is not suitable for compact PNe like the NVSS survey and most PNe are optically thick at their observing frequency.

Radio surveys carried out between 1982 and 1991 are presented in a comprehensive catalogue put together by White *et al.* (2005) (see paper for individual surveys). At 1.4 GHz, the surveys covered a region of ~ 331 deg^2 defined by longitude $-20^\circ < l < 120^\circ$ and latitude $2.^\circ 7$. At 5 GHz, the surveys observed the region defined by longitude $-10^\circ < l < 42^\circ$, and latitude $|b| < 0.4^\circ$ with a flux density sensitivity of 2.9 mJy. They achieved a resolution of $\sim 6''$ for both the 1.4 GHz and 5 GHz surveys. These surveys are, however, limited in coverage and resolution, compared to the available high-resolution and high-sensitivity multi-wavelength surveys of the Galactic plane. This limits proper source characterization that could be achieved with cross-matching.

1.8 Motivation and Thesis Outline

Understanding PNe formation and how they evolve is key to understanding the late phase evolution of intermediate-mass stars in our galaxy, including their mass-loss history. Achieving this, however, requires a representative sample that is free from contaminants. Such sample should include PNe that are very young, where the physical processes associated with formation and shaping may still be active, and PNe from massive progenitors that are ionized, while they are still very compact.

To overcome dust extinction and incompleteness associated with optical surveys, it is necessary that PNe are searched for at longer wavelengths, where extinction is negligible. In this research, the CORNISH survey (Co-ordinate Radio 'n' Infrared survey for High-mass Star Formation) is used to search for PNe in the Galactic

plane. The CORNISH survey is designed to probe compact ionized regions along the Galactic plane (Hoare *et al.*, 2009). Owing to the suggested correlation between massive PNe progenitors and scale heights (Stanghellini *et al.*, 2002), very compact PNe are expected to be within the CORNISH region. No previous radio survey has observed the Galactic plane at such frequency, resolution and coverage and so detection of new and compact PNe is expected.

The new PNe population from this work should improve the census of known compact PNe. The study of the very young ones, either individually or collectively, especially the ones where the formation mechanism may still be active, are important and will better inform our understanding of the formation processes in these objects. A sample of PNe not affected by extinction will be particularly important in models of PNe evolution and good to compare with population synthesis models.

The rest of the thesis is organized as follows:

- Chapter 2 presents multi-wavelength techniques to confirm the PNe nature of candidate PNe in the northern Galactic plane. Multi-wavelength properties of the candidate PNe are presented and a catalogue with final classifications is also presented.
- Chapter 3 outlines the calibration and imaging of the CORNISH survey in the southern Galactic plane. Source finding and properties of sources are presented. Following the multi-wavelength analysis of the PNe sample in the northern Galactic plane in chapter 2, candidate PNe were selected.
- Chapter 4 is concerned with the comparison of PN population synthesis model to the observed properties of PNe from the CORNISH survey. Angular sizes and radio flux densities are compared, as well as the numbers of predicted PNe within the CORNISH survey region.
- Chapter 5 concludes the findings from this research and makes recommendations for future work.

Chapter 2

Multi-Wavelength Properties of the CORNISH North PNe

2.1 Introduction

The sample of known PNe is not homogeneous. They possess different morphologies, central star masses, evolutionary stages, ionization characteristics and are formed in different environments. This makes the identification of PNe, in the absence of optical spectra, more challenging. To eliminate possible sample contamination by other sources that share similar observational properties with them e.g. HII regions, and apply a proper constraint on source classification, there is a need for multi-wavelength techniques (Frew & Parker, 2010). This is possible because PNe have associated ionized gas, dust emission and some even have molecular emission (Kwok, 2007; Ramos-Larios *et al.*, 2017), making them strong emitters at infrared and radio wavelengths. At these wavelengths, PNe do not suffer from extinction biases associated with the optical regime. Infrared surveys can be used to search for PNe that are not visible at optical wavelengths by probing their dust and molecular content, and free-free emission from their associated ionized gas can be explored at radio wavelengths. The use of multi-wavelength data in the studies of PNe not only provides a possible way to confirm

the PN nature of sources but also provides a way to infer the evolution stages of PNe in a sample (Anderson *et al.*, 2012; Cohen & Green, 2001; Cohen & Parker, 2003; Cohen *et al.*, 2011).

In this chapter, the nature of the candidate PNe (169), detected by the CORNISH survey in the northern Galactic plane is examined. Their multi-wavelength properties are explored to classify and identify possible contaminants within the sample. In order to do this, the PNe candidates from the CORNISH survey are cross-matched with available high resolution, high sensitivity surveys of the Galactic plane (Section 2.2.2). A catalogue of northern Galactic PNe with final classifications is also presented.

2.2 Observation Overview and Data

2.2.1 The CORNISH Survey (6 cm)

The CORNISH survey is a radio continuum survey of the northern Galactic plane at 5 GHz, covering 110 $\deg^2$ area and defined by $10^\circ < l < 65^\circ$ and $|b| < 1^\circ$. It probed free-free emission towards the ionized regions of compact Galactic sources, using the B and BnA configurations of the VLA (Hoare *et al.*, 2012). Observations were carried out between 2006 and 2008. The CORNISH survey provides a combination of high resolution and depth compared to previous radio surveys of the Galactic plane (see section 1.7.3). With its resolution of $1.5''$ and sensitivity better than 0.4 mJy/beam, it forms the radio continuum part of a series of high-resolution, high-sensitivity, multi-wavelength surveys of the northern Galactic plane. This makes the survey well suited for the search and characterization of compact ionized sources, such as compact PNe.

Objects identified in the CORNISH survey include H II regions, PNe, radio galaxies with lobes and radio stars (see Figure 2.1). Details of the survey design, scientific motivation, data reduction and measurements of properties are provided in Hoare *et al.* (2012) and Purcell *et al.* (2013).

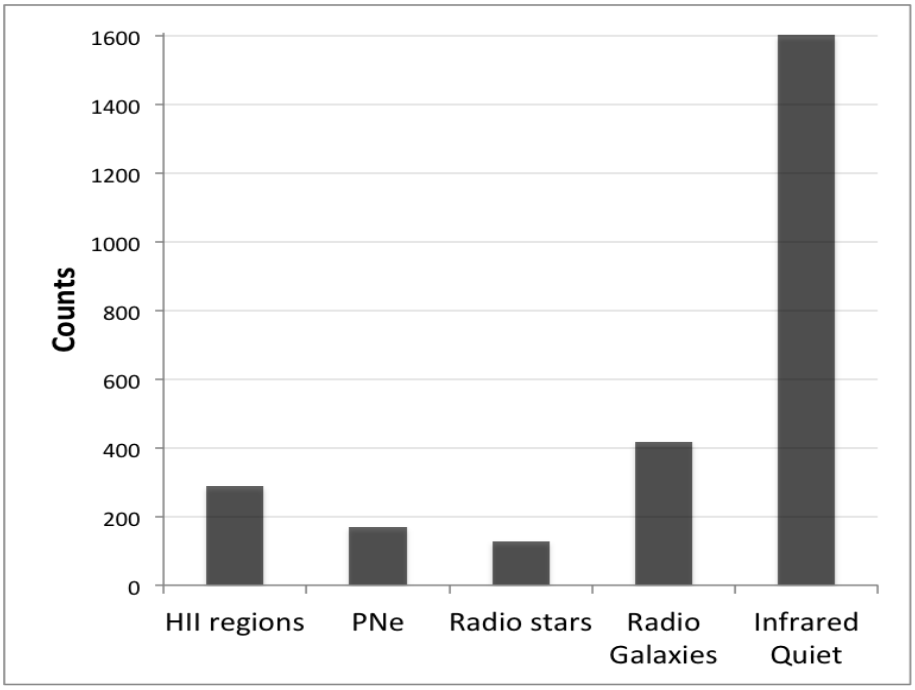

Figure 2.1: *Different source classes and their numbers identified in the CORNISH survey of the northern Galactic plane. Infrared-quiet sources are extragalactic radio sources that are relatively bright at radio wavelengths and not detected or extremely faint at infrared wavelengths (Norris* et al., *2006). Examples of infrared-quiet sources include radio-loud active galactic nuclei (AGNs) at redshifts,* $z \gtrsim 3$ *(Norris* et al., *2011a).*

2.2.2 Multi-Wavelength Data

The CORNISH survey provides information at a single frequency (5 GHz), which is not sufficient to determine the nature and discriminate between compact source types in the CORNISH north catalogue. To search for CORNISH counterparts at other wavelengths, data from other surveys were queried using the CORNISH coordinates (positional accuracy of $0.1''$; see Purcell *et al.* 2013). Data query and cross-matching is generally limited by coverage and resolution, and so the choice of surveys considered is based on comparable resolution and coverage. A summary of the complementary survey data, in the northern Galactic plane, used in the selection of the PNe sample and analysis in this study are presented below.

MAGPIS Survey (20 cm)

The MAGPIS survey at 20 cm, is a radio continuum survey of the northern Galactic plane. Multi-epoch archival data covers the Galactic longitude, $-20^\circ < l < 120^\circ$ and latitude, $|b| < 0^\circ.8$ region. Observations were made using the VLA (Very Large Array) with an average angular resolution of $\sim 6''$. Between 2001 and 2004, an additional survey to improve the data of some regions and fill in some poorly covered areas was carried out by Helfand *et al.* (2006). This survey, at 20 cm, covered Galactic longitude, $5^\circ < l < 32^\circ.5$ and latitude, $|b| < 0^\circ.8$ region, with a resolution of $\sim 5''$ and threshold of $1-2$ mJy. The catalogue queried for the CORNISH-PNe (see section 2.3) is the $> 5\sigma$ catalogue, which is a combination of the multi-epoch survey data, put together by White *et al.* (2005).

GLIMPSE Survey (Mid-Infrared)

The GLIMPSE survey, as one of the Spitzer legacy science programs, is a survey of the inner Galaxy in the mid-infrared. It covers an area of 220 deg^2, defined by longitude, $10^\circ < l < 65^\circ$, $-10^\circ > l > -65^\circ$ and latitude, $|b| \leq 1^\circ$ with a spatial resolution of $\sim 2''$. This survey made use of the infrared array camera (IRAC) mounted on the Spitzer Space Telescope (SST), centred on 3.6 μm, 4.5 μm, 5.8 μm and 8.0 μm. It achieved a 3σ point source sensitivity of 0.2 mJy, 0.2 mJy, 0.4 mJy

and 0.4 mJy for the four bands respectively (Benjamin *et al.*, 2003; Churchwell *et al.*, 2009).

UKIDSS Survey (Near-Infrared)

The GPS (Galactic plane survey), which is one of the five UKIDSS surveys, covers an area of 1868 deg^2, defined by Galactic latitude, $|b| \leq 5^\circ$ and longitude, $15^\circ < l < 107^\circ$, and $142^\circ < l < 230^\circ$ with a seeing of $\sim 1.0''$. These regions were imaged in the J, H and K bands centred on 1.25 μm, 1.65 μm and 2.20 μm, to a depth of 20 mag, 19.1 mag and 19.0 mag, respectively. Full details of the survey and data release are given in Lucas *et al.* (2008).

MIPSGAL, WISE and Hi-Gal Surveys (Mid/Far-infrared)

The MIPSGAL survey is one of the Spitzer Galactic plane surveys covering 278 deg^2 of Galactic longitude, $5^\circ < l < 63^\circ$, and $298^\circ < l < 355^\circ$ and latitude, $|b| < 1^\circ$ regions. This survey was carried out using the MIPS (Multiband Infrared Photometer for Spitzer) on the Spitzer Space Telescope at 24 μm and 70 μm, achieving a resolution of $6''$ and $18''$, respectively. From this survey, only the 24 μm data was used within the $5^\circ < l < 63^\circ$ region, having a point source sensitivity at 3σ of 2 mJy (Carey *et al.*, 2009).

The Wide-field Infrared Survey Explorer (WISE) is an infrared all-sky survey in four bands, centred on 3.4 μm, 4.6 μm, 12 μm, and 22 μm. This survey achieved a 5σ point source sensitivity better than 0.08 mJy, 0.11 mJy, 1.0 mJy, and 6.0 mJy with angular resolutions of $6''.1$, $6''.4$, $6''.5$, and $12''.0$ across the four bands, respectively (Wright *et al.*, 2010). From this survey, the 12 and 22 μm data were used to complement the GLIMPSE and MIPSGAL data.

The Hi-Gal is a far-infrared survey of the Galactic plane, covering $-70^\circ \leq l \leq +68^\circ$; $|b| \leq 1^\circ$ region (first data release) in five wavebands. This survey used the PACS (Poglitsch *et al.*, 2008) and SPIRE (Griffin *et al.*, 2009) photometric cameras of the Herschel Space Observatory centred on 70 μm, 160 μm, 250 μm, 350 μm and 500 μm. It achieved a spatial resolution of $6.0''$, $12.0''$, $18.0''$, $24.0''$ and $35.0''$

across the five bands, respectively. Full details about observation, processing and data release are given in Molinari *et al.* (2010, 2016).

IPHAS Survey (Optical)

The IPHAS survey is a 1800 deg^2 CCD survey, covering Galactic latitude, $|b| < 5^\circ$ and longitude, $30^\circ < l < 215^\circ$ region, in the sloan broad-bands r, i and narrow-band Hα filters. The WFC (wide field camera) of the 2.5 m INT with a pixel scale of $0.33''$ was used for this survey. It is the first fully photometric Hα survey of the Galactic plane with mean 5σ depths of 21.2, 20.0 and 20.3 for the r, i and Hα bands in the Vega magnitude system, respectively (Barentsen *et al.*, 2014; Drew *et al.*, 2005; González-Solares *et al.*, 2008). This survey has a median seeing of $\sim 1.0''$ and has detected both unresolved and resolved PNe (Sabin *et al.*, 2014; Viironen *et al.*, 2009b,c), including PNe with lower surface brightness than previously known (Mampaso *et al.*, 2006).

2.3 PNe Candidate Selection

PNe emission at radio and infrared wavelengths is due to their associated ionized gas and dust. Despite the different morphologies, ionization characteristics and central star masses, PNe typically appear red and isolated in the infrared. However, they are sometimes confused with HII regions and both can get mixed up in the same sample, depending on the distance and how compact and/or young the HII regions are. This is because HII regions also emit at radio and infrared wavelengths from associated ionized gas and dust.

In the infrared, these two classes of objects can be distinguished by inspecting their local environment and morphology. HII regions, unlike PNe, are associated with larger amount of dust and dense molecular material, which becomes very evident in the MIR as strong PAH (polycyclic aromatic hydrocarbon) emission. This also gives them strong millimetre (mm) dust continuum/CO emission (Urquhart *et al.*, 2013), whereas PNe are usually very faint or not detected. A

comparison of the CORNISH and ATLASGAL survey [4] revealed only a handful of PNe candidates (see Urquhart *et al.* 2013). HII regions also show regions of strong dust extinction and usually form in complexes. PNe, on the other hand, usually do not show any form of association with dense molecular material or form in complexes. Furthermore, HII regions usually show a variety of irregular morphologies (Wood & Churchwell, 1989b) as opposed to PNe whose morphologies usually show a good degree of symmetry (Sahai *et al.*, 2011). This difference in morphology is also clearly seen in the MIR. In the near-infrared, HII regions are redder than PNe due to the amount of dust emission and sometimes they are not even detected, owing to high dust extinction.

The SEDs of PNe usually peak between 20 μm and 100 μm (see Figure 1.8; Planck Collaboration *et al.* 2015). However, some PNe could peak above 100 μm (see Urquhart *et al.* 2013), due to the range of dust temperatures ($30\ \mathrm{K} \gtrsim \mathrm{T_d} > 100\ \mathrm{K}$) in their circum-stellar shell (Kwok *et al.*, 1986; Pottasch *et al.*, 1984; Villaver *et al.*, 2002). HII regions, on the other hand, peak at longer wavelengths of about 70 μm and above because they possess a larger fraction of cooler dust (Anderson *et al.*, 2012; Wood & Churchwell, 1989a). This would result in an overlap in the SED of some PNe with HII regions.

Using these observational differences across the different wavelengths over which PNe emit, the CORNISH team, from visual inspection of multi-wavelength image data, classified 169 of the detected sources in the 7σ catalogue as candidate PNe (CORNISH-PNe). These criteria were also used by Urquhart *et al.* (2009a) to distinguish between PNe and HII regions in the Red MSX Source survey (Lumsden *et al.*, 2013). The CORNISH-PNe make up $\sim 6\%$ of the CORNISH catalogue (see Figure 2.1). The use of a multi-wavelength approach provides a good constraint on the visual classification of compact objects (see Figure 2.2), especially towards the Galactic mid-plane, where source crowding is a problem. Observational differences at different wavelengths used by the CORNISH team in selecting the PNe sample are illustrated in Figure 2.2.

[4] http://www3.mpifr-bonn.mpg.de/div/atlasgal/

With the visual classification, it is expected that radio stars, radio galaxies and other extra-galactic sources have been eliminated. However, having done visual classification of these objects, there is a possibility that the sample is still not contaminant-free. Possible contaminants are dusty radio stars and HII regions, especially when they are distant and still very young.

2.4 Aperture Photometry

For uniformity, and to measure the magnitudes and flux densities of extended sources, absent in published point source catalogues, from surveys like the UKIDSS and GLIMPSE, aperture photometry was performed. In order to estimate the integrated flux densities/magnitudes of corresponding infrared sources, the CORNISH-PN aperture was used as a reference. In measuring the integrated flux densities of the CORNISH sources, a 2D Gaussian was used for point sources and manually drawn polygons for extended sources, using aperture photometry (See Purcell *et al.* 2013 for specific details).

A contribution to the MIR emission is from the warm dust component of the nebulae and extends beyond the ionized gas region. For some PNe, especially the young ones, excited molecular components could also contribute to the MIR and NIR emission (e.g. PAH and molecular hydrogen). These molecular emissions are expected from regions larger than the ionized gas region, hence the need for a larger aperture for the UKIDSS and GLIMPSE data. A parameter was defined that allows the size of the reference aperture (CORNISH aperture) to be adjusted accordingly by adding an optimal value. For extended sources, the hand drawn polygons are used as the reference aperture, while the major and minor axes are used to form an ellipse for sources with Gaussian fits. Figure 2.3 shows an illustration of the radio aperture and the increased aperture size on the GLIMPSE data for a Gaussian fitted source and an extended source. The optimal parameter value, which in turn defines an optimal aperture size, was determined from a curve of growth. The need for an optimal aperture was to avoid larger errors due to poor background subtraction. Different apertures sizes were used

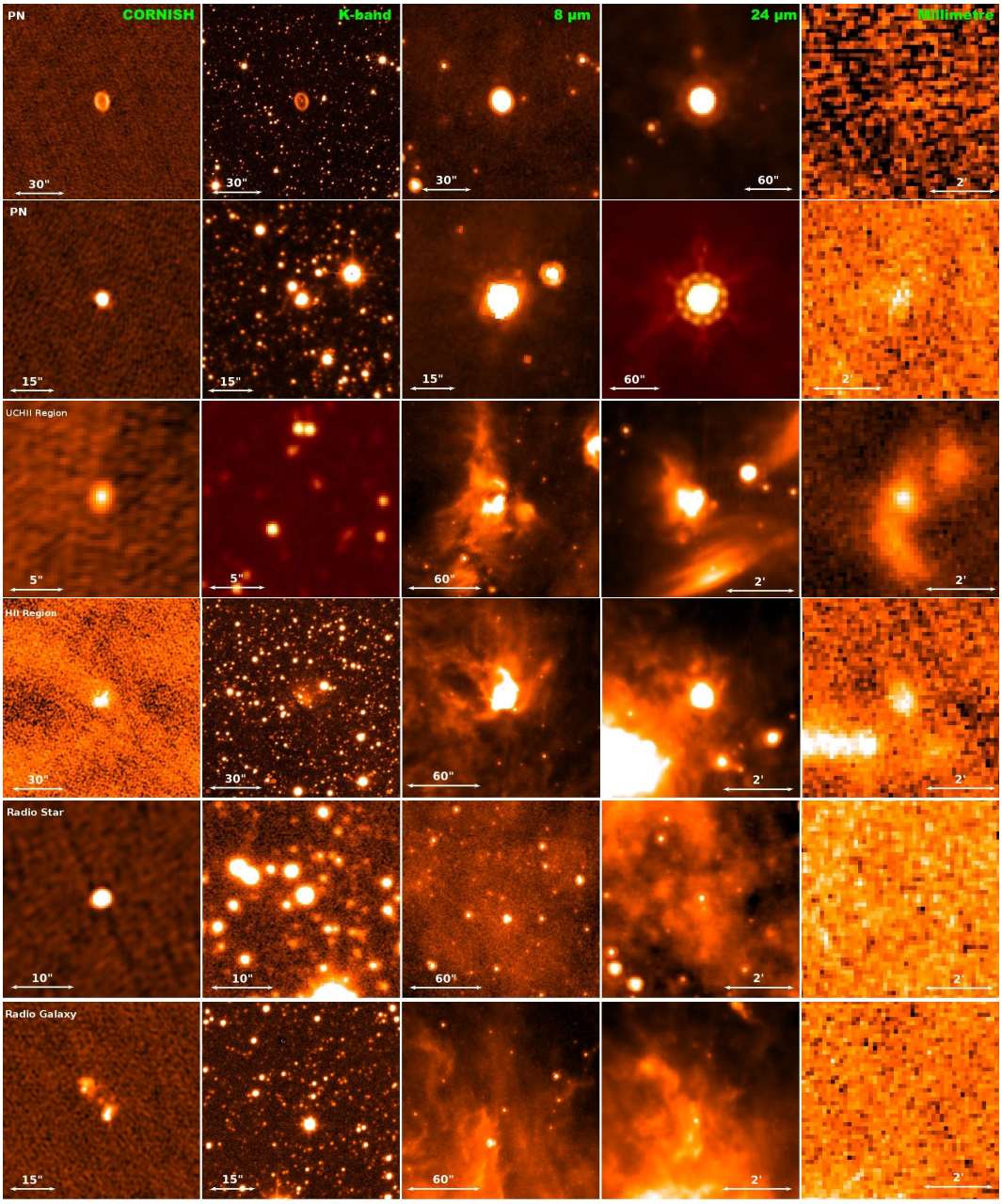

Figure 2.2: *Multi-wavelength observational differences between PNe and other sources identified in the CORNISH survey. Surveys from left to right: CORNISH 5 GHz radio, UKIDSS-GPS (K band), GLIMPSE (8 μm), MIPSGAL (24 μm) and BGPS 1.1 mm dust continuum. The sources from top to bottom are PNe: G051.5095+00.1686 and G035.4719–00.4365; UCHII region: G010.3204–00.2586; HII region: G053.1865+00.2085; Radio star: G045.3657–00.2193 and Radio galaxy: G054.1703–00.0092.*

for the four IRAC bands due to the varying resolution and the varying strength of these emissions across the four bands. The reference apertures for the four IRAC bands were increased by 2.5″, 2.5″, 3.5″ and 4.5″ for the 3.6 μm, 4.5 μm, 5.8 μm and 8.0 μm, respectively. For the near infrared and optical data, the reference aperture sizes were increased by adding 1″.

The background level for each source was measured by means of an annulus, which provides a good estimate of the background level around a source. Due to the background variations across the different wavelengths, the median background level was used, since it is not sensitive to extreme values or bright sources in the background. An annulus width of 10″, with an offset of 5″ from the source aperture was used to estimate the median background level. This ensures that the area of the annulus is greater than the source aperture area, allowing a better estimate of the median background level (Reach *et al.*, 2005). Aperture photometry was performed using equations 2.1 and 2.2 (Purcell *et al.*, 2013), based on python scripts written by C. Purcell.

$$S_{int} = \left(\sum_{i=1}^{N_{src}} S_i - (B_{med} N_{src}) \right) \Big/ a_{bm} \tag{2.1}$$

$$\sigma_{S_{int}} = \sqrt{N_{src}\sigma_g^2 + \frac{\pi N_{src}^2 \sigma_g^2}{2N_{sky}}} \tag{2.2}$$

where S_{int} is the intergrated flux density, $\sum_{i=1}^{N_{src}} S_i$ is the total intensity within the source aperture, N_{src} is the number of pixels in the source aperture, N_{sky} is the number of pixels in the sky annulus, B_{med} is the median background count per pixel in the annulus, a_{bm} is the beam area in pixels, σ_{Sint} is the error on the integrated flux density (S_{int}) and σ_g^2 is the variance in the sky annulus.

For all data considered, the CORNISH positions were used to obtain uniform image cut-outs from the latest processed and final calibrated images, where available. Cross-matching of the CORNISH PNe with individual survey catalogues (UKIDSS and GLIMPSE) was done to compare point source integrated flux densities/magnitudes with results of the aperture photometry. In all cases, the results

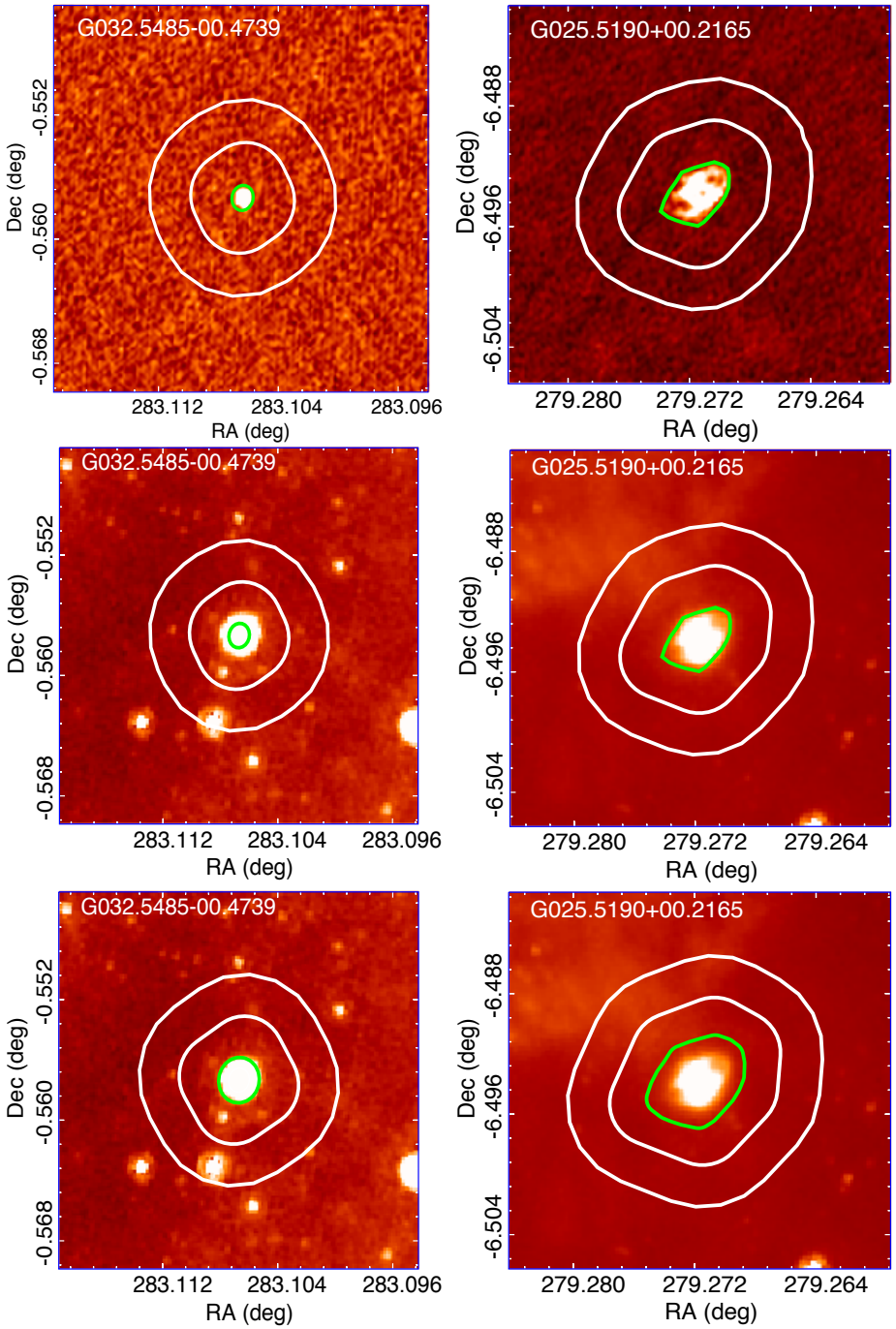

Figure 2.3: *Aperture sizes used for aperture photometry on a Gaussian fitted source and an extended source. The green inner circle is the source aperture, while the annulus used to measure the sky properties is white. Top: The original CORNISH aperture. Middle: The CORNISH aperture on the GLIMPSE images (8* umum*). Bottom: Extended CORNISH aperture on the GLIMPSE images (8* umum*).*

were similar and showed good agreement for point sources. Figure 2.4 (colour coded with the CORNISH angular sizes) shows the comparison of integrated flux densities from aperture photometry described here and the integrated flux densities from the published point source catalogue across the IRAC bands. Point sources show a good agreement across the four bands as illustrated by the one-to-one line. For slightly extended or extended sources, the aperture photometry results in higher flux densities. For the UKIDSS, a plot of the magnitudes and the errors is shown in Figure A.1 (appendix A). Fainter sources have higher errors across the three bands.

The UKIDSS survey has a positional accuracy of $\sim 0.1''$ and the point source catalogue[5] was queried within a $2''$ radius. The option of nearest objects only was used to ensure correct matches. The positional offsets from the cross-match of the CORNISH with the UKIDSS and GLIMPSE point source catalogues were estimated using equations 2.3 and 2.4. The cross-matched positions revealed no systematic offsets for both the UKIDSS and GLIMPSE (see Figure 2.5). Aperture photometry was not done for the MAGPIS survey, where the published catalogue values were used, due to its resolution of $\sim 6''$ compared to the CORNISH resolution of $1.5''$. This also applies to the Hi-Gal, MIPSGAL and WISE data.

$$\Delta\alpha = (\alpha_1 - \alpha_2)\cos(\delta_2) \tag{2.3}$$

$$\Delta\delta = \delta_1 - \delta_2 \tag{2.4}$$

where $\Delta\alpha$ and $\Delta\delta$ represent offsets in right ascension (α) and declination (δ) and the subscripts (1 and 2) represent the reference positions.

2.5 Radio Properties

From a continuum observation, the primary properties of a radio source are its flux density and angular size. Details of equations used and procedures in the

[5] http://wsa.roe.ac.uk:8080/wsa/crossID_form.jsp

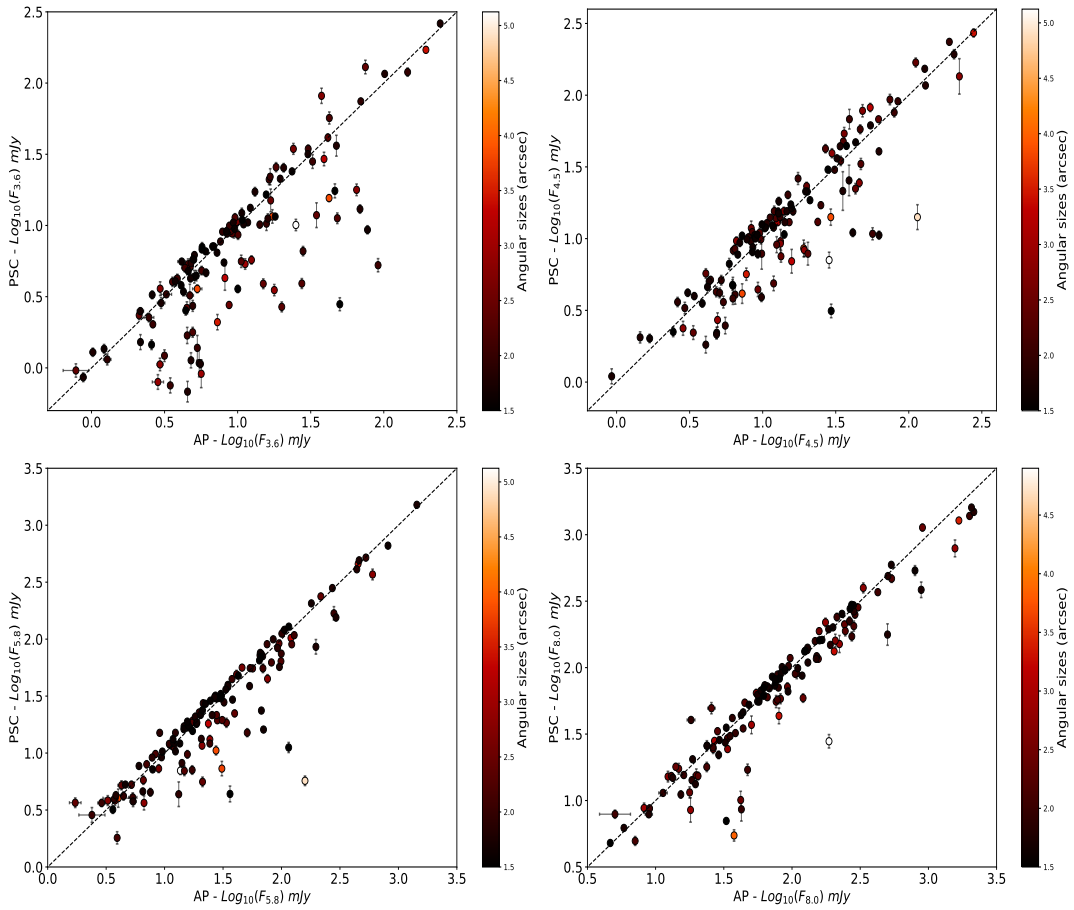

Figure 2.4: *Comparison of the integrated flux densities from the GLIMPSE point source catalogue and integrated flux densities using aperture photometry, across the four bands.*

properties measurement of the CORNISH north sources are given in Purcell *et al.* (2013) and briefly summarized here.

Source detection and photometry was performed using OBIT[6] FndSou. FndSou works by finding and identifying neighbouring islands of emission above a set intensity cut-off and it attempts to fit one or more 2D Gaussians to these emissions. The Gaussian parameters, including flux density are retained for simple sources fitted by single Gaussians. For extended sources, indicated by a cluster of Gaussian fits, the fitted parameters were replaced with single measurements under a

[6]http://www.cv.nrao.edu/bcotton/Obit.html

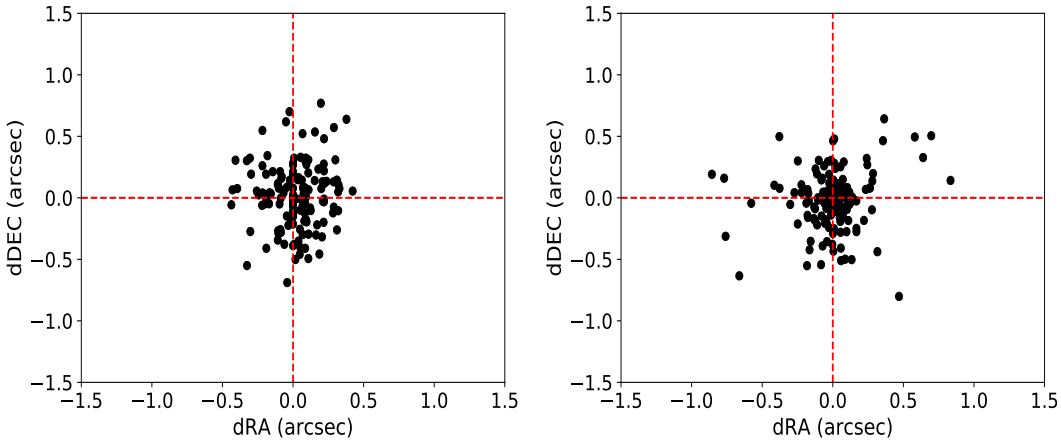

Figure 2.5: *Offset positions in ra and dec between the CORNISH-PNe and point source counterparts in the GLIMPSE (left) and UKIDSS (right).*

manually drawn polygon around the emission. For such extended sources, the fitted Gaussian axes are replaced with intensity-weighted diameters ($\vartheta_{\rm d}$) given by equation 2.5 (Purcell *et al.*, 2013).

$$\vartheta_{\rm d} = 2 \sum_{\rm i=1}^{\rm N_{src}} {\rm r_i A_i} \Bigg/ \sum_{\rm i=1}^{\rm N_{src}} {\rm A_i} \tag{2.5}$$

where $\rm A_i$ is the intensity of the ith pixel and $\rm r_i$ is the angular distance from the ith pixel to the center of the source.

The catalogued angular size is the geometric mean of the fitted Gaussian axes ($\sqrt{\vartheta_{\rm M}\vartheta_{\rm m}}$, where $\vartheta_{\rm M}$ and $\vartheta_{\rm m}$ are the fitted major and minor axes, respectively) or intensity-weighted diameter for extended sources. The intensity weighted sizes would make the extended sources appear smaller than they would in optical catalogues. The deconvolved sizes may also underestimate the sizes of extended sources (see van Hoof 2000). To estimate the true angular sizes, a correction factor at 6 cm was used, according to van Hoof (2000). With this method, $\vartheta_{\rm true} = \gamma\vartheta_{\rm d}$ and γ is estimated using Equation 2.6 (van Hoof, 2000), where $\beta = \vartheta_{\rm d}/\vartheta_{\rm beam}$ ($\vartheta_{\rm d}$

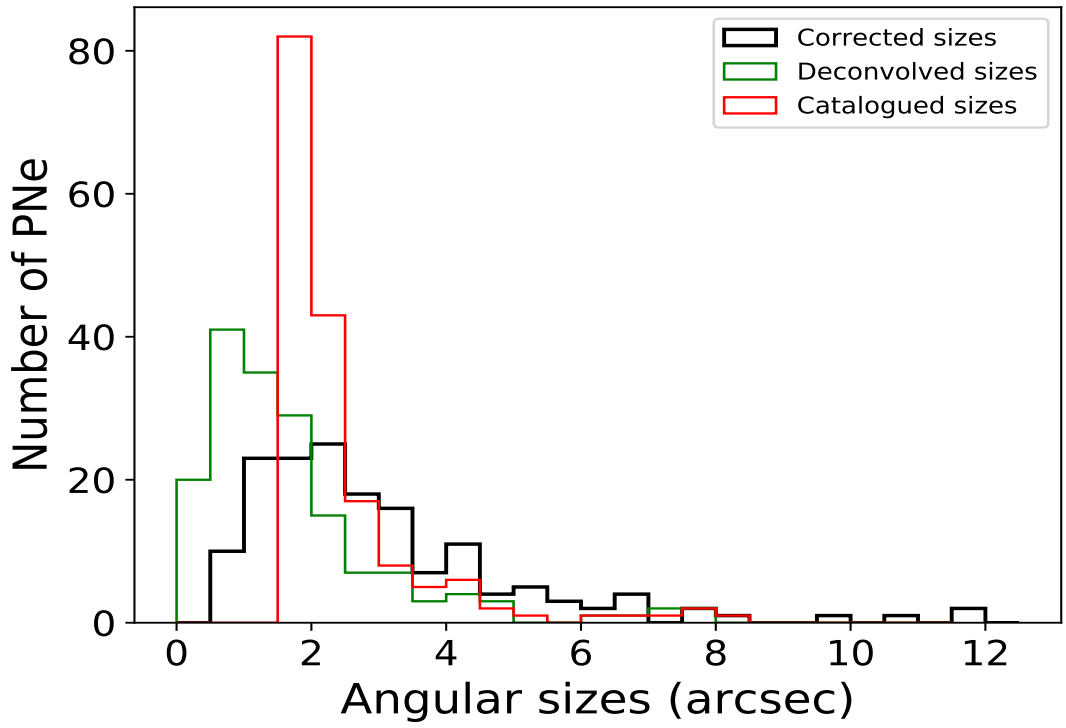

Figure 2.6: *Comparison of the corrected sizes (black), deconvolved sizes (green) and catalogued sizes (red) for the CORNISH-PNe.*

is the deconvolved size).

$$\gamma(\beta) = \frac{0.3429}{1 + 0.7860\beta^2} + 1.6067 \tag{2.6}$$

Table 2.1 shows a comparison of the catalogued sizes, deconvolved sizes, estimated true sizes and corresponding optical sizes for a few PNe. The optical sizes are taken from the MASH (Miszalski *et al.*, 2008; Parker *et al.*, 2006) and IPHAS (Sabin *et al.*, 2014) catalogues. For three of the sources, the optical sizes are 10 to 20 times larger. These sources have bipolar morphologies (G027.6635-00.8267, G050.4802+00.7056 and G062.7551-00.7262) and the CORNISH survey has detected only the bright cores. On the average, the corrected sizes show better agreement with the optical sizes. Figure 2.6 shows the distributions of the catalogued, deconvolved and corrected sizes. The deconvolved sizes tend towards

Table 2.1: *The measured radio sizes (ϑ_{cat}), deconvolved sizes (ϑ_{d}), corrected sizes (ϑ_{true}) compared to the optical angular sizes (ϑ_{Lit}) from the MASH (Miszalski et al., 2008; Parker et al., 2006) and IPHAS (Sabin et al., 2014) catalogues are presented. Where available, the major and minor optical sizes are reported. Bipolar PNe are indicated with *.*

CORNISH Name	ϑ_{cat} (arcsec)	ϑ_{d} (arcsec)	ϑ_{true} (arcsec)	ϑ_{Lit} (arcsec)
G014.5851+00.4613	3.28 ± 0.04	2.91 ± 0.05	4.93 ± 0.08	6.0×5.0
G018.2402–00.9152	8.08 ± 0.03	7.94 ± 0.03	12.88 ± 0.05	12.0×12.0
G026.8327–00.1516	2.52 ± 0.07	2.03 ± 0.08	3.55 ± 0.15	7.0×5.0
G027.6635–00.8267*	1.67 ± 0.06	0.73 ± 0.14	1.38 ± 0.26	35.0×12.0
G032.5485–00.4739	2.16 ± 0.04	1.55 ± 0.05	2.78 ± 0.09	9.0×9.0
G035.5654–00.4922	6.24 ± 0.03	6.05 ± 0.03	9.88 ± 0.05	11.0×11.0
G050.4802+00.7056*	1.60 ± 0.06	0.56 ± 0.16	1.08 ± 0.31	19.0
G051.8341+00.2838	2.25 ± 0.03	1.68 ± 0.05	2.98 ± 0.08	6.0
G062.7551–00.7262*	2.27 ± 0.07	1.71 ± 0.09	3.04 ± 0.16	27.0

smaller sizes and the corrected sizes show a broader distribution. Hereafter, these corrected angular sizes will be used, unless stated otherwise.

All the CORNISH-PNe (sources classified in the northern half of the CORNISH survey as PNe) have flux densities $> 7\sigma$, of which 91% have flux densities $\leq$ 100 mJy (Figure 2.7, right panel), and $\sim 35\%$ are unresolved ($\vartheta < 1.8''$). The distribution of the angular sizes with a median of $2.5''$ (see left panel in Figure 2.7) indicates a preferentially compact and/or distant sample. Figure 2.8 (upper panel) shows a Galactic latitude distribution that is approximately flat (left panel of Figure 2.8), indicating a fairly uniform detection of known PNe within this region. At such low latitudes, detections of PNe from more massive progenitors that are usually dense and compact, are expected (Stanghellini *et al.*, 2002). The longitude distribution (Figure 2.8, Right panel) shows an increase in the CORNISH-PNe population towards the Galactic bulge ($l < 10°$; Valenti *et al.* 2016). This agrees with the observed distribution of PNe (see section 1.6.1), as we would expect more PNe towards the Galactic centre.

The radio continuum emission from a PN can be expressed in terms of its brightness temperature (T_B), a property that can be used to infer the evolution of PNe.

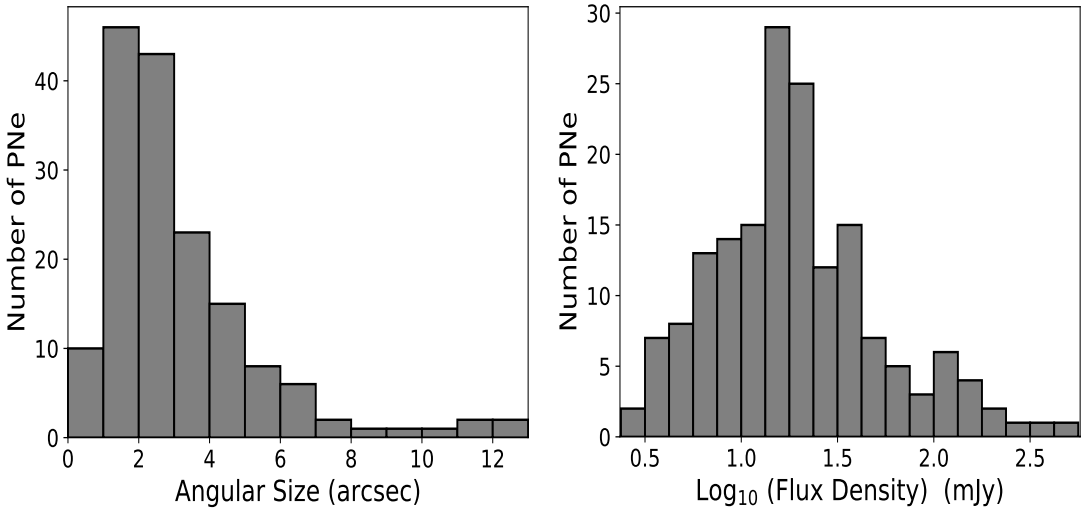

Figure 2.7: *The angular size (left) and integrated flux density (right) distribution of the CORNISH-PNe.*

At 6 cm, most PNe are optically thin and so, T_B (see section 1.7.1) decreases with continuous expansion of the nebulae. Otherwise, PNe that are optically thick will show high T_B ($\sim 10^4$ K). Consequently, more evolved and optically thin PNe should have lower brightness temperatures compared to younger and more compact PNe. Nonetheless, young PNe from low-mass progenitors could show low T_B ($\sim$ 100K) because the envelope may have been mostly dispersed before the central star becomes hot enough to initiate ionization.

$$T_B(K) \propto \frac{\lambda^2(cm)S_\nu(mJy)}{2k\pi\vartheta^2(arcsec^2)} \tag{2.7}$$

The average T_b across each CORNISH-PNe at 5 GHz was estimated using Equation 2.7, where ϑ is the angular radius (arcsec), S_ν is the integrated flux density (mJy) and other symbols have the usual meaning. The CORNISH-PNe show T_b between 20 K and 7000 K (Figure 2.9, left panel) with a median of $\sim$ 200 K. Figure 2.9 (right panel) also shows the variation of the angular sizes with corresponding flux densities and lines of constant T_b. It can be seen that there are a few PNe that can be considered younger. These younger CORNISH-PNe have small angular sizes and T_b that lie within the region of $10^3 K < T_b < 10^4 K$ (see

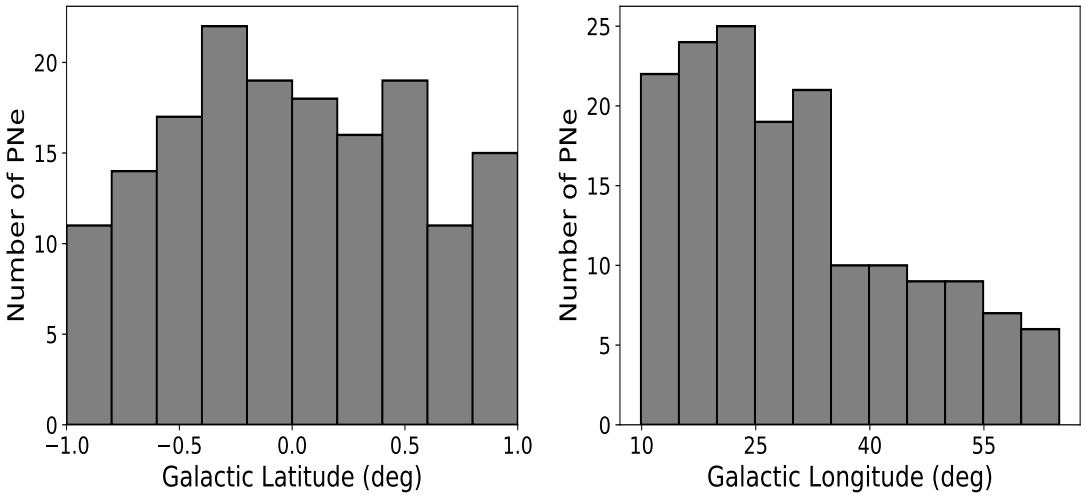

Figure 2.8: *Galactic latitude (upper panel) and longitude (lower panel) distribution of the CORNISH-PNe.*

Kwok 1985). These young compact PNe also show the highest integrated flux densities for the CORNISH-PNe.

2.5.1 Spectral Index

Having shown the possible existence of some young CORNISH-PNe in Figure 2.9, it is also important to determine the nature of their radio emission. The CORNISH survey at 6 cm was cross-matched with the MAGPIS radio survey at 20 cm, within a radius of $5''$. This resulted in a total of 67 matches out of the 169 CORNISH-PNe. 85% of the cross-matched sources have angular separations less than $1''$ and a distribution that peaks about $0.5''$ (see Figure 2.10).

For the purpose of spectral indices estimation, there is a need to exclude very extended sources, whose emission could have been spatially filtered out due to the design of the CORNISH survey. Spatially filtered out emission will result in underestimated flux densities. To exclude extended PNe, the CORNISH-PNe integrated flux densities were compared to their corresponding peak fluxes (Figure 2.11, right panel). Sources with angular sizes larger than $9''$, corresponding to $F_{int}/F_{peak} > 10$ were considered too extended. Additionally, the flux densities

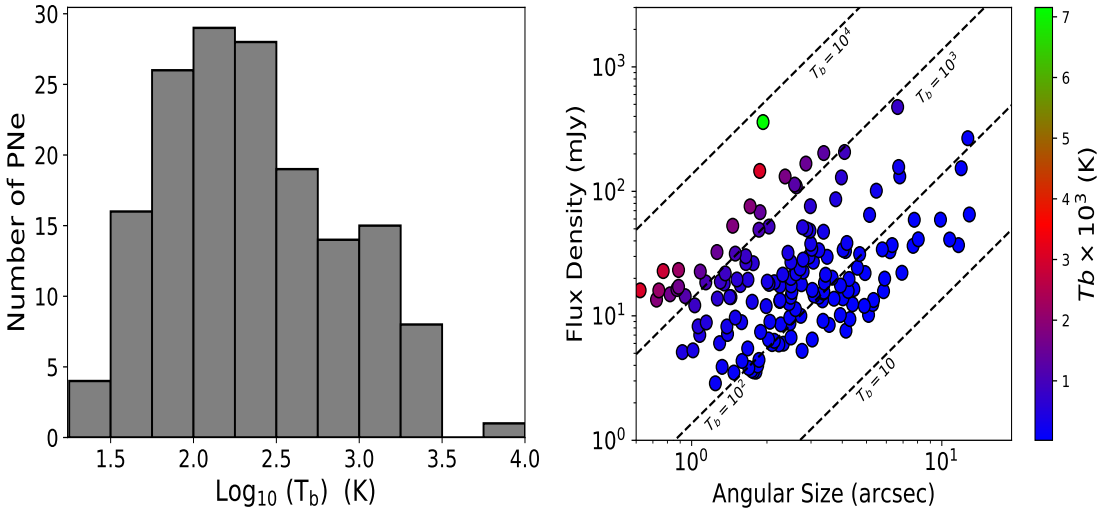

Figure 2.9: *Left panel: Brightness temperature distribution. Right panel: Flux density versus angular size, showing lines of constant brightness temperature and colour coded by the brightness temperature.*

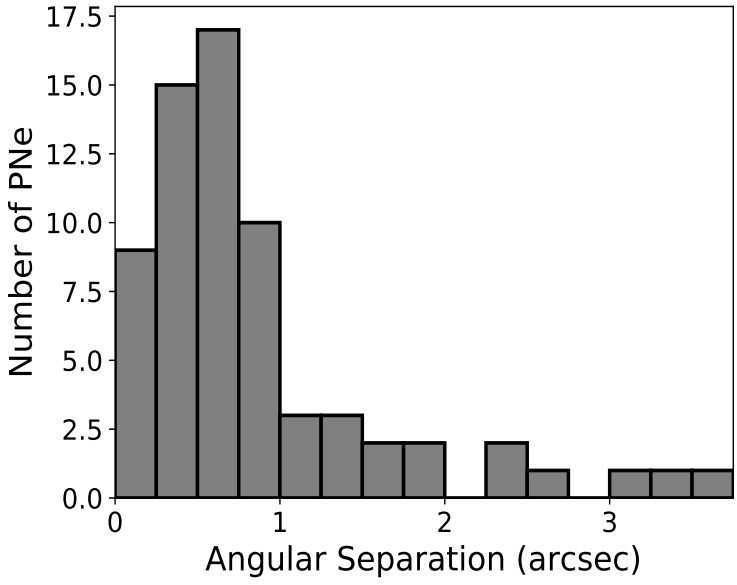

Figure 2.10: *Distribution of the angular separation of the 67 CORNISH-PNe found in the MAGPIS survey within a cross-matching radius of* $5''$.

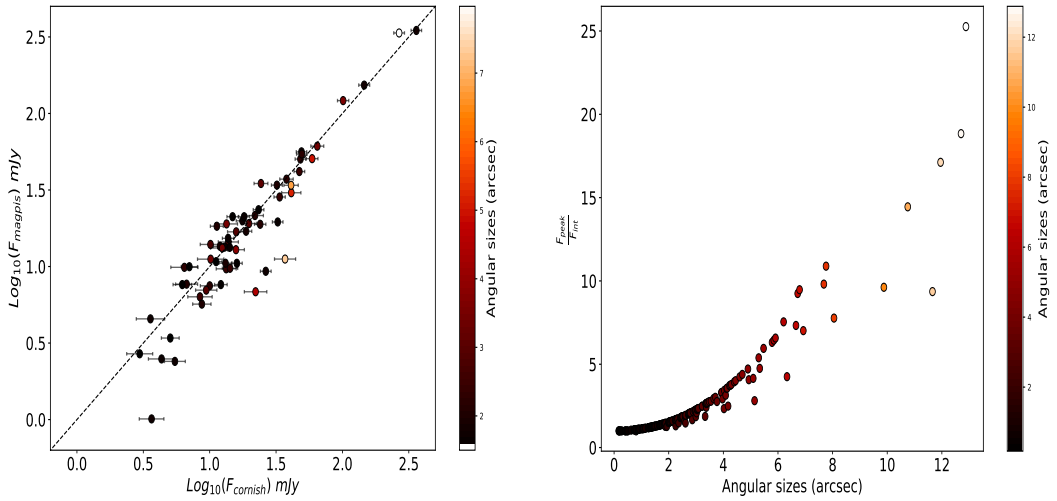

Figure 2.11: *Left: Comparison of the MAGPIS 6 cm and CORNISH 6 cm integrated flux densities. Right: A plot of the ratio of the peak to integrated flux densities for the CORNISH PNe.*

and angular sizes of the CORNISH-PNe were compared with their counterparts in the 6 cm MAGPIS catalogue (at a lower resolution of $6''$, White *et al.* 2005). Figure 2.11 (left) shows a comparison of the 6 cm integrated flux densities of the CORNISH and MAGPIS. This reduced our sample to 61, after excluding 6 sources considered to be very extended.

To get a more complete sample, the flux densities of the CORNISH-PNe absent from the MAGPIS catalogue were measured as described in Section 2.4, using the CORNISH-PNe positions on the MAGPIS 20 cm image data. This brought the CORNISH-PNe sample to a total of 127 out of 169 PNe. Measured 20 cm flux densities are given in Table A.1. The spectral indices and associated errors of the 127 CORNISH-PNe were estimated using Equations 2.8 and 2.9, where S_1 and S_2 are the flux densities in mJy, and ν_1 and ν_2 are the corresponding frequencies.

$$\alpha = \frac{\ln(S_1/S_2)}{\ln(\nu_1/\nu_2)} \tag{2.8}$$

$$\delta\alpha = \frac{1}{\ln(\nu_1/\nu_2)}\sqrt{\left(\frac{\delta S_1}{S_1}\right)^2 + \left(\frac{\delta S_2}{S_2}\right)^2} \tag{2.9}$$

If the radio-continuum emission observed towards PNe is from free-free interactions, the spectral index range is expected to be between –0.1 and 2, where it is optically thin and optically thick, respectively. Figure 2.12 (top panel) shows the distribution of the CORNISH-PNe with a peak ~ 0.1, which agrees with optically thin free-free emission. In Figure 2.12 (middle panel), $\sim 84\%$ of the 127 CORNISH-PNe have spectral indices within the theoretical range. However, two PNe have spectral indices below –0.1 at a 3σ significance level, which is indicative of non-thermal emission (discussed in Section 2.9.3). These are shown in Figure 2.12 (lower) as red filled circles, where spectral indices is plotted against the log of the CORNISH angular sizes.

If the integrated flux density at 1.4 GHz and 5 GHz are are assumed to come from the same solid angle, the spectral index (1.4 GHz and 5 GHz) can be modelled at constant electron temperatures of $T_e = 0.5 \times 10^4$ K, 1.0×10^4 K and 1.5×10^4 K as in Siódmiak & Tylenda (2001) (see their Equations 2 and 5). Results are shown in Figure 2.13, where the modelled spectral indices are plotted against T_B at 5 GHz, laid over the CORNISH-PNe data. At 5 GHz, the CORNISH-PNe generally show a scatter around the theoretical, optically thin region of the model. Above $T_B = 1000$ K, the CORNISH-PNe follow the trend of the model as spectral indices increases with T_B (excluding the two outliers). There are a few PNe that approach the optically thick limit with increasing T_B. This trend is also observed in Figure 2.12 (lower panel) and Figure 2.9 (right panel), where CORNISH-PNe with smaller angular sizes show higher T_B. The observed radio emission of the outliers, marked A (G052.1498–00.3758) and B (G030.2335–00.1385), obviously, cannot be explained by a simple model, where the emission is characterized by a single optical thickness and constant electron temperature (see Siódmiak & Tylenda 2001). G019.2356+00.4951 (non-thermal emission), G030.2335–00.1385 (non-thermal emission) and G052.1498–00.3758 are further discussed in Sections 2.9.2 and 2.9.3. The radio properties from this section are summarized in Table A.1.

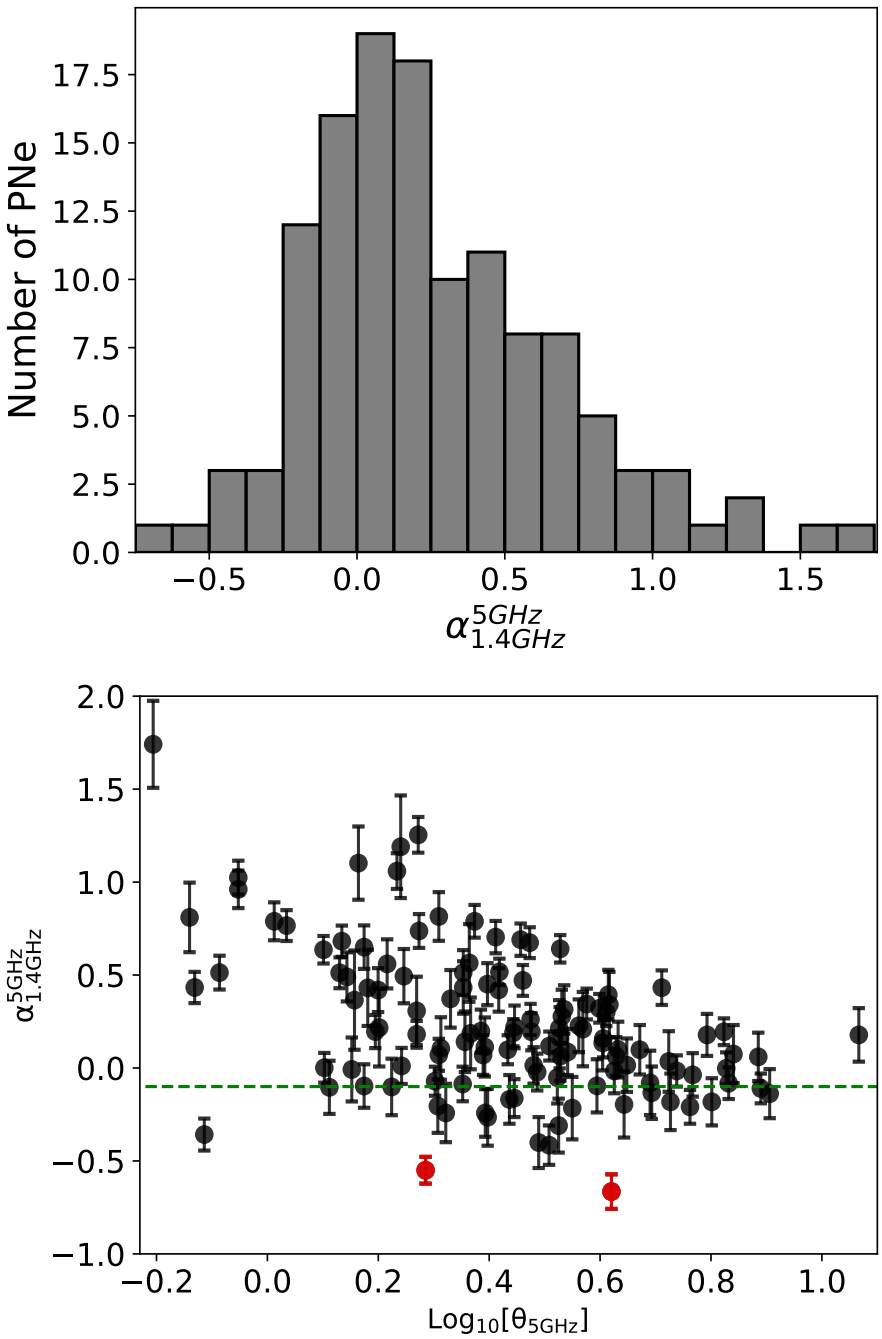

Figure 2.12: *Top: Spectral index distribution of the CORNISH-PNe. Bottom: Distribution of the spectral indices vs. the log of the angular sizes. The red filled circles are the PNe with non-thermal emission at a 3σ significance level.*

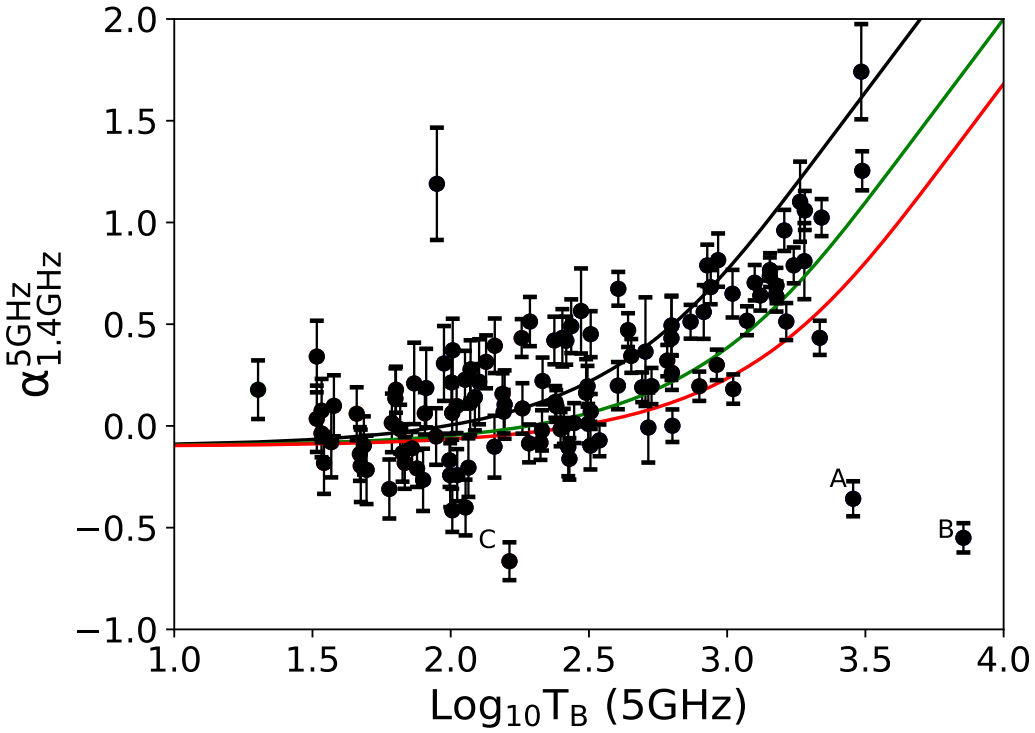

Figure 2.13: *Shows the* T_B *CORNISH-PNe data overlaid on a model of spectral index (5 GHz to 1.4 GHz) against the brightness temperature,* T_B *at 5 GHz. The curves show predictions of the model for* T_e *at* 0.5×10^4 *K (black),* 1.0×10^4 *K (green) and* 1.5×10^4 *K (red). The observed radio emission of the outliers, marked A (G052.1498–00.3758) and B (G030.2335–00.1385), cannot be explained by a simple model, where the emission characterized by a single optical thickness and constant electron temperature (see Siódmiak & Tylenda 2001).*

2.5.2 Mid-Infrared to Radio Continuum Ratio

It is expected that as the PN evolves with an increase in size, the ratio of the MIR to radio flux density (MIR/radio) will decrease. This is as a result of increased ionized volume compared to the amount of dust and excited PAH (polycyclic aromatic hydrocarbon) emission present in the 8.0 μm band. Observed PAH emission present in this band is from the excited PAH molecules just outside the ionized regions. As the ionization front spreads out, the PAH emission decreases (Cerrigone *et al.*, 2009; Cohen *et al.*, 2007; Guzman-Ramirez *et al.*, 2014) for PNe

dominated by carbon dust, causing a decrease in the total flux in the 8 μm band. Carbon rich PNe, however, show stronger PAH emission compared to oxygen rich PNe (Cox *et al.*, 2016). Following this, compared to more evolved ones, younger PNe should have stronger 8μm emission, resulting in higher values of the MIR/radio values. Irrespective of larger angular sizes as a result of evolution, bipolar PNe have high MIR/radio values due to the relatively larger amount of gas and dust and the presence of a torus that could remain molecular for a longer time (Cox *et al.*, 2016; Guzman-Ramirez *et al.*, 2014). Cohen *et al.* (2007, 2011); Matsuura *et al.* (2004) used this ratio (MIR/radio) to discriminate between PNe and HII regions. HII regions are brighter in the MIR compared to PNe due to the larger amount of dust associated with them.

Cohen *et al.* (2011) reported a median of 4.7 ± 1.1 for their PNe sample using $F_{8.0\mu m}/F_{0.848GHz}$. For the CORNISH-PNe, the IRAC 8 μm band (GLIMPSE survey) on the CORNISH 5 GHz ($F_{8.0\mu m}/F_{5GHz}$) was used. The distribution is shown in Figure 2.14 with a median of 3.9 ± 0.90 (161 PNe). If the 5 GHz flux densities is converted to 0.848 Hz, assuming the CORNISH-PNe are all optically thin, the median obtained is 3.3 ± 0.70 (stated error is the standard error on the median). These estimates show a reasonable agreement within 1σ with the Cohen *et al.* (2011) value. Using the same method, Filipović *et al.* (2009b) found a median value of 9.0 ± 2.0 ($F_{8.0\mu m}/F_{1.4GHz}$) for 14 Magellanic cloud PNe, which is consistent with the CORNISH-PNe value and Cohen *et al.* (2011) within 2σ. For the CORNISH-PNe, there is no obvious trend or variation of the $F_{8.0\mu m}/F_{5GHz}$ with angular sizes.

2.6 Multi-Wavelength Colours

The use of multi-wavelength colour-colour diagrams to distinguish between PNe and their contaminants (e.g. HII regions), in the absence of optical data, has been explored by Cohen *et al.* (2011) and Parker *et al.* (2012a). Colour-colour plots allow separation of sources based on their colours. The CORNISH-PNe are

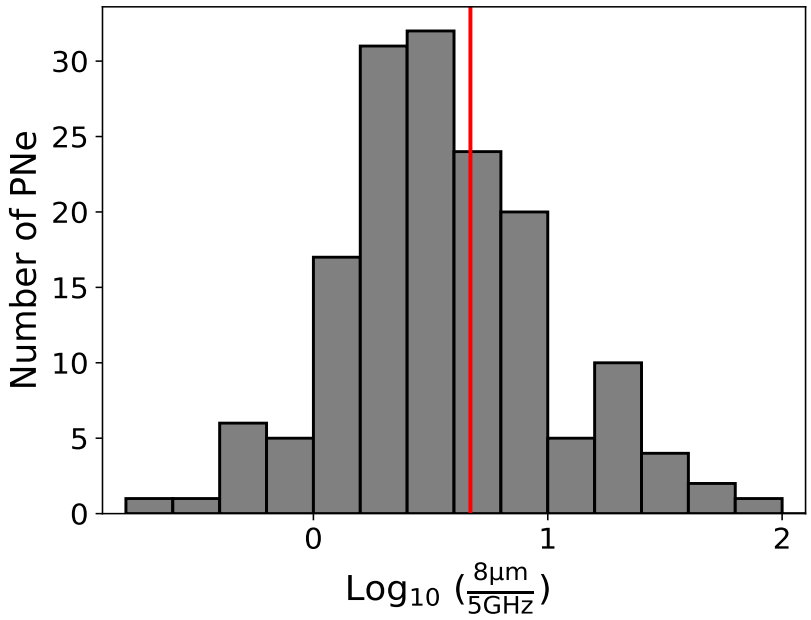

Figure 2.14: *Distribution of the* $F_{8.0\mu m}/F_{5GHz}$ *showing the median (red line) from Cohen* et al. *2011.*

placed on different colour-colour planes and, where necessary, they are compared with other Galactic sources that could be contaminants.

2.6.1 Near-Infrared (NIR) Colours

The measured emission of PNe in the J, H and K bands is a combination of emission from the ionized nebulae, including free-bound and free-free emission, hot dust emission, stellar continuum from the central star and emission lines. The emission from the ionized gas and hot dust is expected to dominate the emission. In some cases, however, stellar continuum could be mostly responsible for the observed emission (Garcia-Lario *et al.*, 1997; Phillips & Zepeda-García, 2009; Ramos-Larios & Phillips, 2005; Whitelock, 1985).

The measured fluxes from aperture photometry were converted to magnitudes

using equations 2.10 and their associated errors using Equation 2.11.

$$m_{cal} = -2.5 \times \log_{10}(F_{uncal}) + m_{zpt} \tag{2.10}$$

$$\sigma m_{cal} = 1.086 \times \frac{\sigma f}{f} \tag{2.11}$$

f is the measured flux, σf is the error on the measured flux, m_{cal} and σm_{cal} are the corresponding magnitude and error and m_{zpt} is the zero point magnitude.

Figure 2.15 shows the distribution of the CORNISH-PNe in the J – H vs. H – K colour-colour plane (measured magnitudes and errors are presented in Table A.2). The colours of PNe from the IPHAS catalogue (IPHAS-PNe; Sabin *et al.* 2014; Viironen *et al.* 2009b,c), symbiotic stars, the intrinsic colours of an O9 star from Ducati *et al.* (2001) and the modelled intrinsic colour of NGC 7027 (0.21, 0.41) and NGC 6720 (0.62, 0.0) from Weidmann *et al.* (2013) are also shown. The IPHAS-PNe NIR colours were estimated from their 2MASS magnitudes (Skrutskie *et al.*, 2006b) presented in the Sabin *et al.* (2014) and Viironen *et al.* (2009b) catalogues. The magnitudes were converted to the WFCAM magnitudes according to the transformation equations in Hewett *et al.* (2006), to fit the UKIDSS magnitudes of the CORNISH-PNe in Figure 2.15. The distribution of the CORNISH-PNe shows a broader range of colours compared to the IPHAS-PNe. Compared to the IPHAS-PNe, more of the CORNISH-PNe show colours that are consistent with symbiotic and post-AGB stars (Garcia-Lario *et al.*, 1997) and some CORNISH-PNe also show higher reddening. The broad distribution of the CORNISH-PNe can be mostly explained by the range of PNe intrinsic colours (see Phillips & Zepeda-García 2009; Ramos-Larios & Phillips 2005) and differing amounts of extinction. The overlap of PNe colours with symbiotic stars makes it difficult to rely solely on the NIR colour-colour plane in differentiating between them.

Categorically, younger PNe with hot dust have redder colours, resulting in higher H – K values. A contribution to the K-band could also arise from the molecular

gas emission, H_2, believed to be mainly excited by shocks and ultra-violet fluorescence, in some cases (Marquez-Lugo *et al.*, 2015). The contribution of this emission to the K-band could also result in large excesses in the H – K colour. The colour distribution of the CORNISH-PNe is similar to the IPHAS-PNe, but with more CORNISH-PNe showing a higher reddening. Compared to the MASH PNe sample analysed by Phillips & Zepeda-García (2009) and PNe from the VVV survey by Weidmann *et al.* (2013), the CORNISH-PNe show a higher reddening. The median colours for the CORNISH-PNe are 1.23 ± 0.05 (H – K) and 1.25 ± 0.07 (J – H).

2.6.2 Optical Colours

CORNISH-PNe counterparts were searched for within the region of the IPHAS survey that overlaps with the CORNISH survey, using the CORNISH positions. Owing to the Galactic position of these PNe, confusion with other sources in the background or foreground is possible. For this reason, the Hα images were visually checked, aided with false 3-colour images. None of the images showed complexes or diffuse emission, usually associated with HII regions. A total of 23 out of the 76 CORNISH-PNe within the IPHAS survey region were found to have genuine counterparts. The Hα, r and i magnitudes were measured following section 2.4 and measurements are presented in Table 2.2.

PNe are good emitters of Hα emission, so they can be easily identified on the [r - Hα] vs. [r – i] colour-colour plane, where normal PNe have large [r-Hα] colours. The region occupied by PNe in the optical colour-colour plane is discussed in Corradi *et al.* (2008) and Viironen *et al.* (2009a), using PNe from the IPHAS survey. Figure 2.16 shows the distribution of the CORNISH-PNe in the [r - Hα] vs. [r – i] colour-colour plane. Reddened PNe should be located towards the right, where higher [r – i] values occur. The positions of some Galactic PNe from the IPHAS survey and symbiotic stars are also shown. This is to show the distribution of the CORNISH-PNe within another PNe sample and possible contaminants like the symbiotic stars. Out of the 23 CORNISH-PNe with IPHAS counterparts, 22 seem to have normal PNe colours (Figure 2.16). An exception

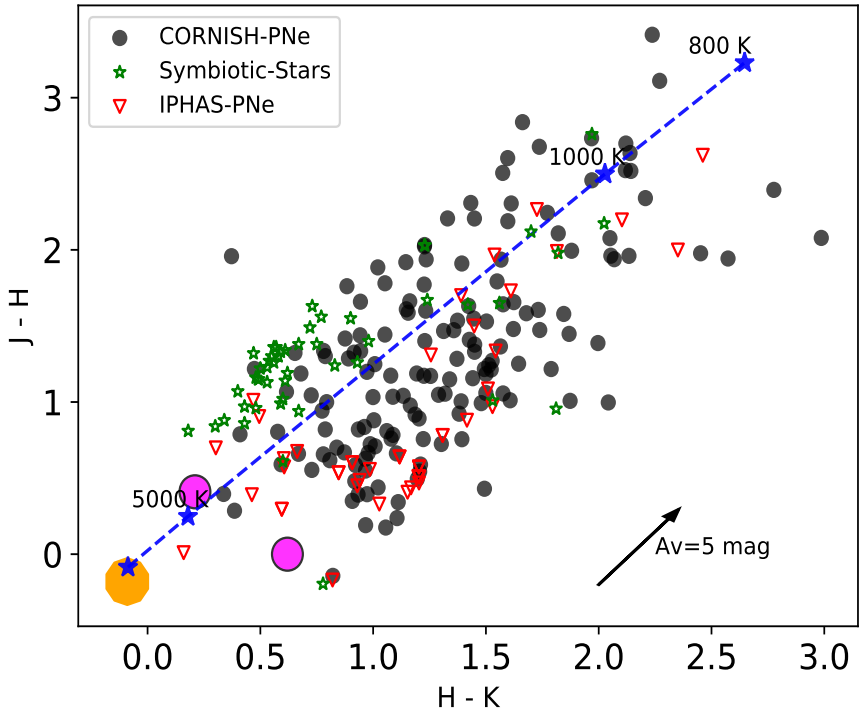

Figure 2.15: J – H *vs.* H – K *colour-colour plot. The IPHAS-PNe are taken from the IPHAS catalogue (Sabin* et al.*, 2014; Viironen* et al.*, 2009b,c); Symbiotic stars samples were taken from Corradi* et al. *2008, 2010; Rodr´iguez-Flores* et al. *2014 and new symbiotic stars from Miszalski* et al. *2013. Modelled intrinsic colours of PNe (NGC 6720 and NGC 7027) shown in magenta (circles) are from Weidmann* et al. *2013. The intrinsic colour of an O9 star (orange) from Ducati* et al. *2001 and blackbodies at different temperatures are also shown.*

is the colour of G035.4719–00.4365 ([r – i] $\sim$ 0.92, [r – Hα] $\sim$ 0.69), where a blend with foreground stars in its photometry could be responsible. The general distribution of the CORNISH-PNe is similar to the distribution of the IPHAS-PNe. Again, PNe (CORNISH-PNe and IPHAS-PNe) show colours similar to symbiotic stars, making it difficult to separate PNe from such contaminants based on optical colour-colour plots alone.

A cross-match of the 23 PNe with the IPHAS catalogue (Sabin *et al.*, 2014; Viironen *et al.*, 2009b) returned 17 counterparts. The 6 PNe not in the IPHAS

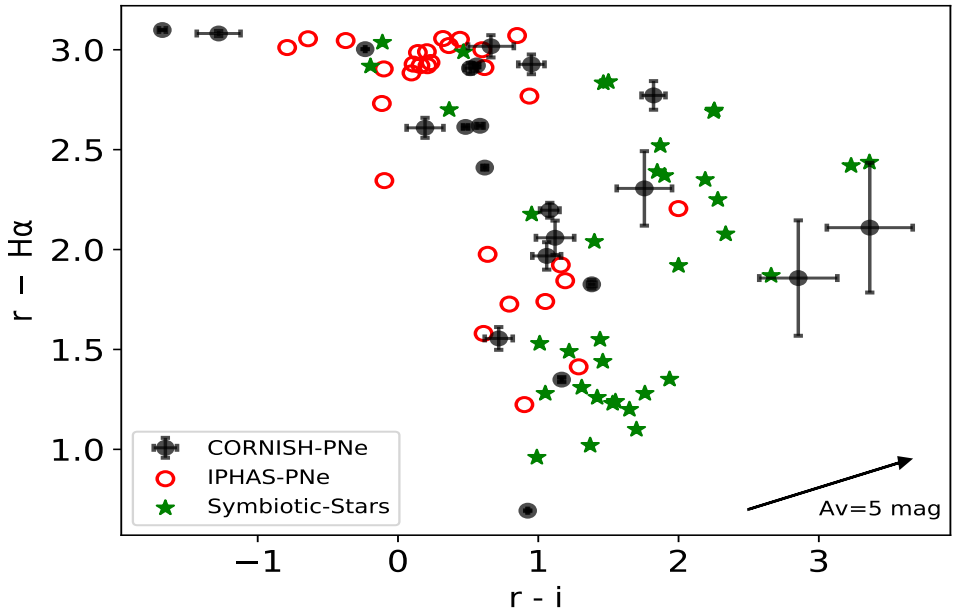

Figure 2.16: *r-Hα vs. r-i colour-colour plane. PNe sample from the IPHAS catalogue (Sabin* et al., *2014; Viironen* et al., *2009b,c) are shown; Symbiotic stars samples from Corradi* et al. *(2008, 2010) and Rodr´ıguez-Flores* et al. *(2014), and new symbiotic stars from Miszalski* et al. *(2013). The reddening vector is from the relationship in Cardelli* et al. *(1989).*

catalogue as PNe or candidate PNe are indicated by the † symbol in Table 2.2 and 2 examples are presented in Figure 2.17. These could have been missed based on the search technique used by the IPHAS team. 10 out of the 17 are catalogued as candidate PNe, 6 are classified as PNe from spectroscopic results and 1 is classified as MASH-II symbiotic star (G050.4802+00.7056) in the IPHAS catalogue (Sabin *et al.*, 2014; Viironen *et al.*, 2009b).

Table 2.2: Hα, *r and i magnitudes and the* Hα *line flux (*erg/cm^2/s*) for the 22 CORNISH-PNe present in the IPHAS survey. These were measured using aperture photometry as discussed in Section 2.4. * indicates PNe that are bipolar in the optical and/or NIR.*

CORNISH Name	Hα (mag)	r (mag)	i (mag)	LogF(Hα) (erg/cm^2/s)
G029.5780–00.2686	16.43 ± 0.01	19.44 ± 0.05	18.78 ± 0.15	–13.38 ± 0.04
G032.5485–00.4739	13.76 ± 0.01	16.68 ± 0.01	16.12 ± 0.02	–12.32 ± 0.01
G032.6136+00.7971†	19.25 ± 0.11	21.11 ± 0.27	18.26 ± 0.08	–14.51 ± 0.40
G033.4543–00.6149	16.30 ± 0.01	18.13 ± 0.02	16.75 ± 0.02	–13.33 ± 0.05
G035.4719–00.4365†	14.38 ± 0.01	15.08 ± 0.01	14.15 ± 0.01	–12.57 ± 0.01
G041.3540+00.5390†	18.08 ± 0.12	20.19 ± 0.30	16.82 ± 0.04	–14.05 ± 0.50
G044.6375+00.4827	16.32 ± 0.01	19.09 ± 0.07	17.27 ± 0.05	–13.34 ± 0.05
G048.5619+00.9029†	16.87 ± 0.03	18.42 ± 0.05	17.71 ± 0.09	–13.56 ± 0.10
G048.7319+00.9305	15.63 ± 0.01	18.24 ± 0.05	18.05 ± 0.12	–13.06 ± 0.04
G050.0405+01.0961	16.42 ± 0.02	18.39 ± 0.06	17.33 ± 0.08	–13.38 ± 0.09
G050.4802+00.7056	16.57 ± 0.01	18.77 ± 0.03	17.69 ± 0.06	–13.44 ± 0.05*
G050.5556+00.0448†	17.29 ± 0.03	19.35 ± 0.08	18.23 ± 0.11	–13.73 ± 0.10
G051.5095+00.16867	14.51 ± 0.01	17.14 ± 0.01	16.47 ± 0.03	–12.61 ± 0.01
G051.8341+00.2838	16.17 ± 0.01	19.10 ± 0.05	18.15 ± 0.08	–13.28 ± 0.04
G055.5070–00.5579	10.12 ± 0.01	13.12 ± 0.01	13.35 ± 0.01	–10.86 ± 0.01
G056.4016–00.9033	14.34 ± 0.01	16.75 ± 0.01	16.13 ± 0.01	–12.55 ± 0.01
G058.6410+00.9196	18.02 ± 0.06	20.33 ± 0.18	18.57 ± 0.09	–14.02 ± 0.20
G059.3987–00.7880†	15.83 ± 0.01	17.18 ± 0.01	16.02 ± 0.01	–13.15 ± 0.02
G059.8236–00.5361	14.90 ± 0.01	17.81 ± 0.03	17.29 ± 0.03	–12.77 ± 0.01
G060.9866–00.5698	14.76 ± 0.01	17.37 ± 0.01	16.79 ± 0.02	–12.71 ± 0.01
G062.4936–00.2699	11.68 ± 0.01	14.78 ± 0.01	16.46 ± 0.02	–11.48 ± 0.01
G062.7551–00.7262	14.10 ± 0.01	17.18 ± 0.01	18.46 ± 0.16	–12.45 ± 0.01*
G063.8893+00.1229	13.79 ± 0.01	16.40 ± 0.01	15.92 ± 0.02	–12.33 ± 0.01*

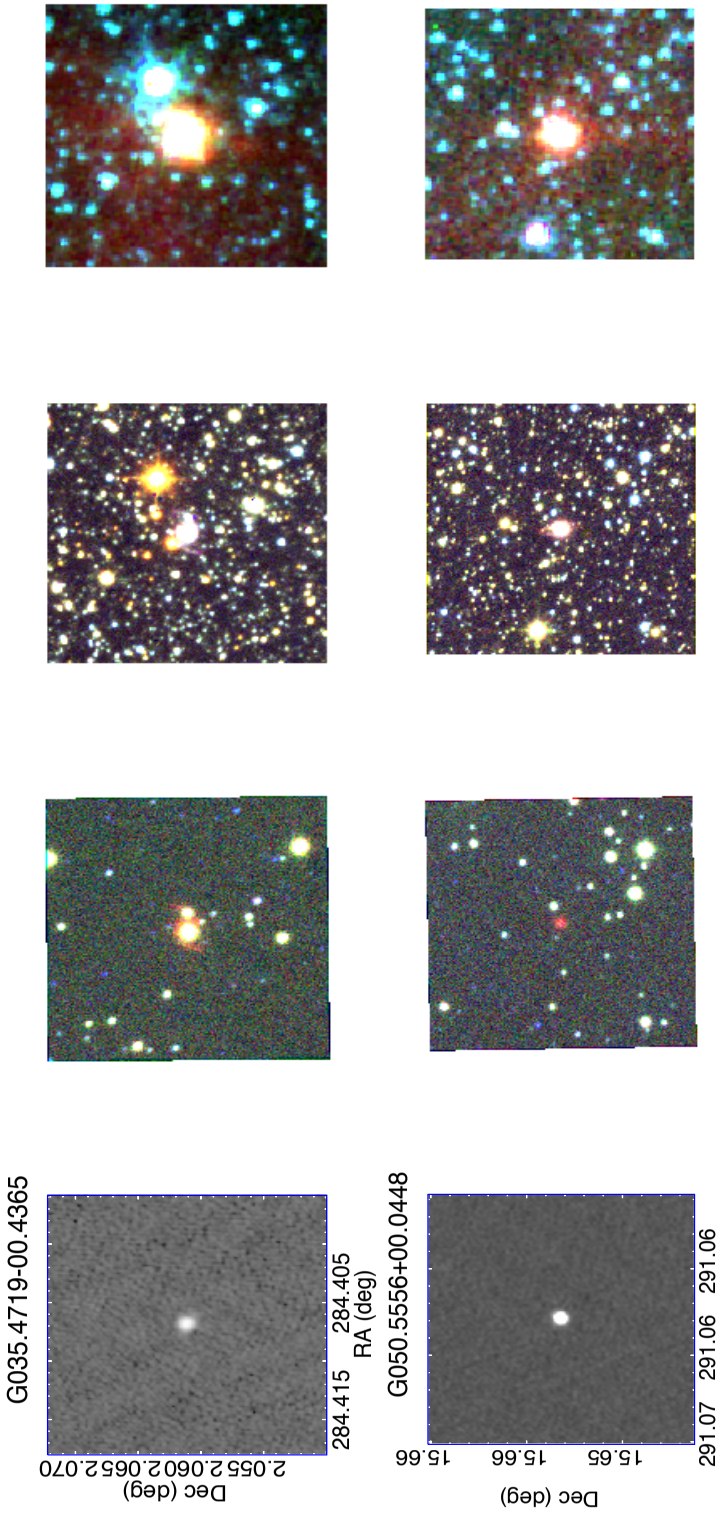

Figure 2.17: *False 3-colour images of PNe detected in the IPHAS survey but not in the IPHAS catalogue. From left to right: CORNISH, IPHAS (Hα=red,r=green and i =blue), NIR (K=red,H=green and J =blue) and MIR (3.6 µm=blue, 4.6 µm=green and 8.0 µm =red). All images are* $80'' \times 80''$.

Table 2.3: *Comparison of the median colours of 160 CORNISH-PNe with PNe samples from Cohen et al. (2011).*

Colour Index	Cohen *et al.* (2011) 107	CORNISH-PNe 160
[3.6] – [4.5]	0.81 ± 0.08	0.84 ± 0.08
[3.6] – [5.8]	1.73 ± 0.10	1.94 ± 0.19
[3.6] – [8.0]	3.70 ± 0.11	3.83 ± 0.37
[4.5] – [5.8]	0.86 ± 0.10	1.08 ± 0.11
[4.5] – [8.0]	2.56 ± 0.11	3.01 ± 0.30
[5.8] – [8.0]	1.86 ± 0.07	1.84 ± 0.18

2.6.3 Mid-Infrared (MIR) Colours

The emission of a PN in the MIR is a summation of dust continuum, free-free, free-bound, atomic lines, molecular lines and PAH emission. All these contribute to the colour of a PN and its position on the MIR colour-colour plot, depending on which is dominant. The work of Cohen *et al.* (2011), using the GLIMPSE data, showed that PNe can be distinguished from HII regions, using their MIR colours.

In Table 2.3, the median MIR colours of the CORNISH-PNe are compared with the median colours of the MASH-PNe sample analysed by Cohen *et al.* (2011). The CORNISH-PNe median colours show good agreement within 2σ. Figure 2.18 shows the colour distribution of the CORNISH-PNe on the [3.6]-[4.5] vs. [5.8]-[8.0] and [3.6]-[5.8] vs [4.5]-[8.0] colour-colour planes. The colours of the PNe sample taken from Cohen *et al.* (2011), colours of the central stars of PNe (Hora *et al.*, 2004), symbiotic stars (Corradi *et al.*, 2008; Miszalski *et al.*, 2013), the mean colour of UCHII regions sample from the CORNISH survey (Kalcheva *et al.*, 2018) and the position of blackbodies at different temperatures are shown in Figure 2.18.

The CORNISH-PNe show the same broad distribution shown as the Cohen *et al.* (2011) PNe sample and they are separated from the S-type symbiotic stars and central stars of PNe, which was not seen in Figure 2.15 and 2.16 (NIR and optical

colour-colour plane). On the [3.6] – [4.5] vs.[5.8] – [8.0] plane, the colours of the CORNISH-PNe, dusty (D-type) stars and UCHII regions seem inseparable. This looks different on the [3.6] – [5.8] vs.[4.5] – [8.0] plane, where the CORNISH-PNe can be distinguished from the mean colour of the CORNISH UCHII regions. This could be as a result of the PAH emission strength in the 8 μm band, compared to bands 3 μm and 5 μm.

Generally, this broad distribution could be a result of different dominant emission mechanisms across the bands (Phillips & Ramos-Larios, 2009). A combination of the evolutionary state and PAH strength across the different bands could also contribute to the wide spread of the CORNISH-PNe colours. Most of the CORNISH-PNe show the red colours typical of PNe, including the ones dominated by dust continuum, H_2 and PAH emission. However, there are a few to the left in Figure 2.18 (both colour-colour planes), where stellar continuum could be contributing to their emission. The colours of such PNe could also be a result of dominant ionized gas emission with little or no dust emission. The measured mid-infrared flux densities using aperture photometry are given in Table A.2.

2.6.4 Far-Infrared (FIR) Colours

The dust content in the circumstellar envelopes of PNe can be better viewed in the FIR, especially when combined with MIR data. This dust, ejected during the AGB phase, has temperatures in the range $\sim 10 \leq T_d \leq 100$ K (van de Steene, 2017; Van de Steene *et al.*, 2015; Villaver *et al.*, 2002).

The heating mechanism of dust grains in PNe is believed to be by direct stellar emission from the central stars, which can extend beyond the ionized region, and by Lyman α radiation within the ionized region (Hoare, 1990; Kwok *et al.*, 1986; Pottasch, 1986; Pottasch *et al.*, 1984; van de Steene, 2017). Following this, compact and younger PNe, where dust grain heating is mainly by direct stellar emission, could show warmer dust temperatures in the range of ~ 110 K $< T_d < 200$ K (Hoare, 1990; Kwok *et al.*, 1986; Pottasch, 1986; Pottasch *et al.*, 1984; van Hoof *et al.*, 1997), and more evolved PNe, where the major source of heating is from Lyman α radiation, would have relatively cooler dust

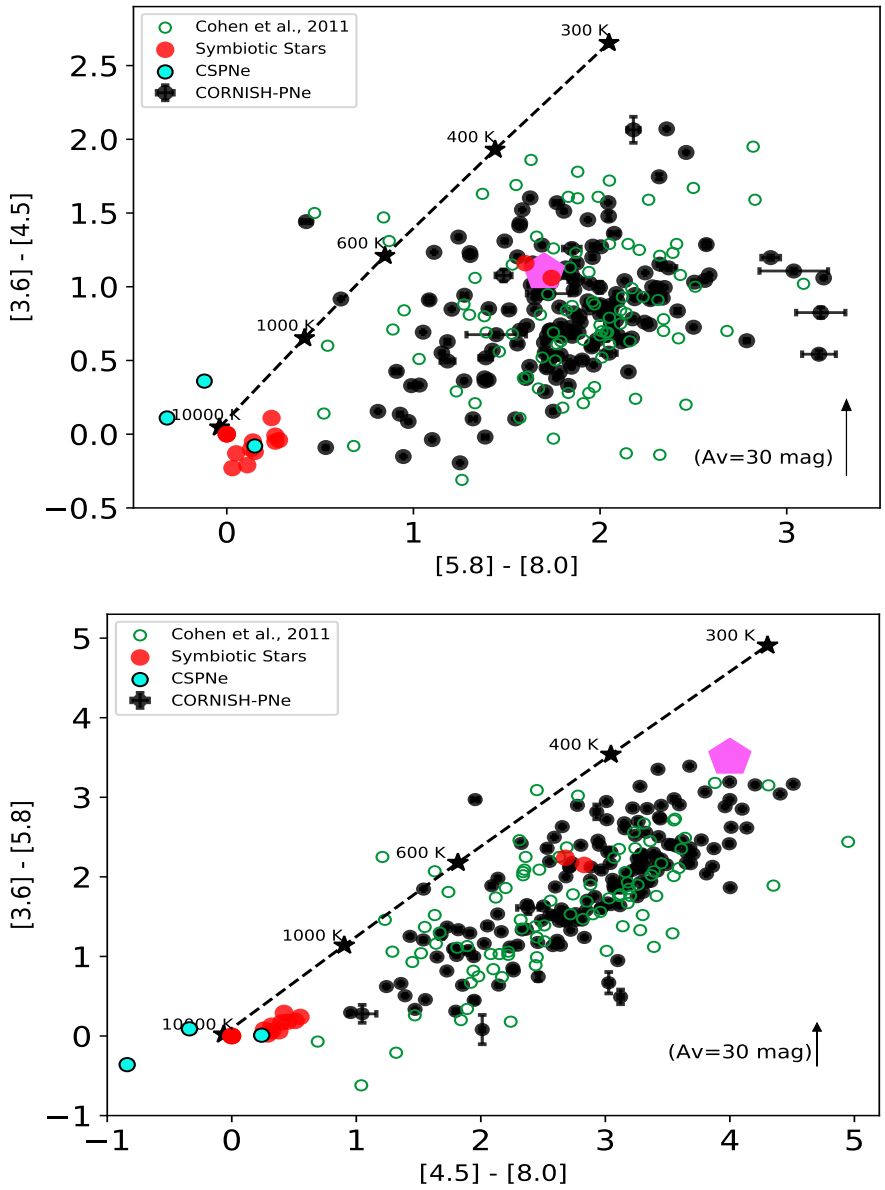

Figure 2.18: *Left panel: [3.6]-[4.5] vs.[5.8]-[8.0]. Right panel: [3.6]-[5.8] vs.[4.5]-[8.0]. The green circles are PNe (GLIMPSE data) taken from Cohen et al. (2011), aqua filled circles are CSPNe (central stars of PNe) taken from Hora et al. (2004) and symbiotic stars from Corradi et al. (2008) and Miszalski et al. (2013) are represented as red filled circles. The purple hexagon shows the mean colours of UCHIIs from the CORNISH survey (Kalcheva et al., 2018). Blackbodies at different temperatures are also shown. The reddening vector is from the average extinction in Indebetouw et al. (2005).*

temperatures in the range of ~ 20 K $\lesssim T_d \lesssim 120$ K (Phillips & Márquez-Lugo, 2011; Van de Steene *et al.*, 2015). The term 'evolved' as used here is relative and according to the analysis of Phillips & Márquez-Lugo (2011), PNe with physical diameters $\lesssim 0.08$ pc show dust temperatures as high as 180 K, whereas PNe with larger physical diameters (more evolved) show a range of dust temperatures (~ 60 K $< T_d < 120$ K).

How bright PNe are in the FIR will be determined by the density and mean temperature of the dust in their circum-stellar envelopes. Young PNe from massive stars will be brighter in the FIR. This is because of their association with cooler dust (outside the ionized region), ejected during the AGB phase (Cox *et al.*, 2011; Hoare, 1989; Hoare *et al.*, 1992; Kwok, 1982) and because they evolve fast to ionized their circum-stellar envelopes, while still dense and compact. This is also the case for bipolar PNe whose progenitors are believed to have experienced strong mass-loss during the AGB phase. Bipolar PNe are also believed to have a torus that remains neutral for a longer time after ionization (Guzman-Ramirez *et al.*, 2014). Furthermore, evolved PNe from massive progenitor stars could have magnetized clouds, such that the dust shells are not easily expelled, as normal PNe would, resulting in large infrared excesses. However, HII regions are brighter in the FIR and at longer wavelengths because of the larger amount of dust they possess and lower mean dust temperatures, which can be as low as ~ 25 K (Anderson *et al.*, 2012).

The use of the Hi-Gal survey together with the MIPSGAL 24 μm, and WISE 12 μm and 22 μm should provide further constraint in identifying HII regions present in the CORNISH-PNe, if there are any. The CORNISH-PNe were cross-matched with the Hi-Gal point source catalogue (individual bands) using a radius of $20''$ and their images were checked to eliminate mis-matches and identifications due to background emission. The CORNISH-PNe were also cross-matched with the WISE 12 μm and 22 μm[7], and MIPSGAL 24 μm point source catalogue (Gutermuth & Heyer, 2015) using the same radius of $20''$.

[7] http://irsa.ipac.caltech.edu/cgi-bin/Gator/nph-scan?submit=Select&projshort=WISE

Table 2.4: *Mean far-infrared colours of the CORNISH-PNe are shown in column 3 and the mean colours in column 2 are from Anderson* et al. *(2012) PNe samples. The error is the standard deviation.*

Colour	Anderson *et al.* (2012)	CORNISH-PNe
$Log_{10}[12/8]$	0.57 ± 0.29	0.45 ± 0.30
$Log_{10}[70/22]$	0.39 ± 0.51	0.34 ± 0.46
$Log_{10}[160/12]$	0.80 ± 0.49	0.77 ± 0.67
$Log_{10}[160/24]$	0.22 ± 0.55	0.02 ± 0.62

In Table 2.4, the mean colours of the CORNISH-PNe are shown, compared to the mean colours of PNe sample analysed by Anderson *et al.* (2012). There is a good agreement of both results within 1σ. Due to the different mean dust temperatures of the PNe and HII regions, they should occupy distinctly different regions on the FIR colour-colour plots. Based on the analysis of Anderson *et al.* (2012) on discriminating between HII regions and PNe (see Table 3 in Anderson *et al.* 2012), the $Log_{10}[F_{160}/F_{24}]$ vs. $Log_{10}[F_{12}/F_8]$ and $Log_{10}[F_{160}/F_{12}]$ vs. $Log_{10}[F_{70}/F_{22}]$ colour-colour planes were chosen. The distributions of the CORNISH-PNe on these colour-colour planes are shown in Figure 2.19. A few of the CORNISH-PNe FIR colours extend into the HII region area. This is likely due to sample selection bias as the Anderson *et al.* (2012) sample is made up of optically detected PNe. At a 3σ significance level, three of the CORNISH-PNe (see Section 2.9.2) are within the HII regions area on both colour-colour planes.

2.7 Extinction

Extinctions were estimated using the Hα line emission, where available, and near-infrared (NIR) magnitudes with the 5 GHz radio integrated flux density. The different methods used are discussed below.

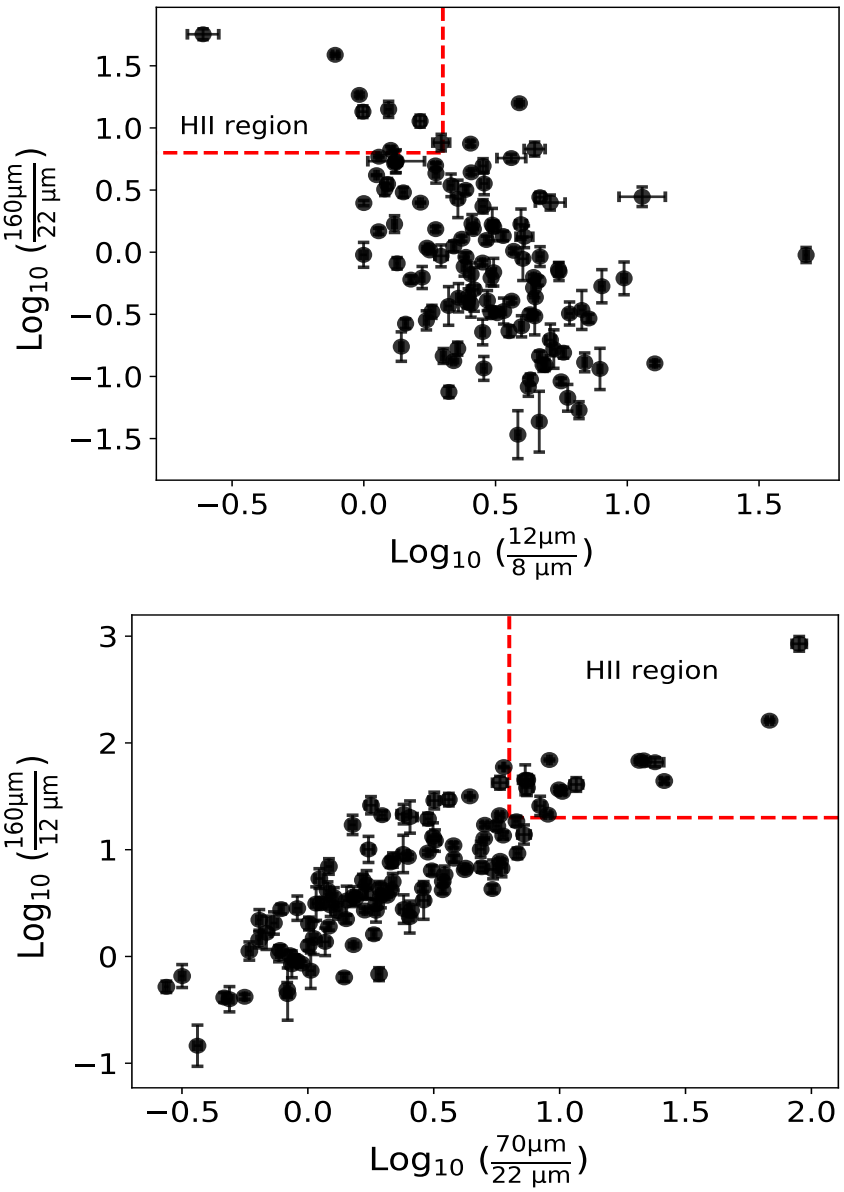

Figure 2.19: *FIR colour-colour planes. Top:* $\mathrm{Log}_{10}[\mathrm{F}_{160}/\mathrm{F}_{24}]$ *vs.* $\mathrm{Log}_{10}[\mathrm{F}_{12}/\mathrm{F}_{8}]$. *Bottom:* $\mathrm{Log}_{10}[\mathrm{F}_{160}/\mathrm{F}_{12}]$ *vs.* $\mathrm{Log}_{10}[\mathrm{F}_{70}/\mathrm{F}_{22}]$. *On both plots the cut-off colours (red dotted lines) from Anderson et al. (2012) are shown for HII regions (see Table 2.4) on the CORNISH-PNe.*

2.7.1 Hα/5GHz Ratio

Both the Hα and 5 GHz emission are assumed to come from the same effective volume of ionized gas, but unlike the hydrogen line emission, the free-free emission at 5 GHz is not affected by interstellar extinction. Following this, the extinction for each PN was estimated by comparing the radio-continuum emission at 5 GHz to the Hα line flux. In estimating the Hα line fluxes (Column 5 in Table 2.2), the continuum contribution was accounted for based on the Sloan filter profile[8], while ignoring the [NII] contribution. Equation 2.12 (see Ruffle *et al.* 2004) was used to estimate the extinction in magnitudes (c_r), which was converted to visual extinction (A_V) using $A_V = 1.2c_r$ (calculated from the Cardelli *et al.* 1989 extinction curve with R = 3.1). The distribution of A_V from this method (for 23 PNe) is shown in Figure 2.20 (upper panel).

$$c_r\ (\mathrm{mag}) = -2.5\log_{10}\left[\frac{F(H_\alpha)(\mathrm{erg/cm^2/s})}{9.20\ \times\ 10^{-13}F_{5GHz}(\mathrm{mJy})}\right] \tag{2.12}$$

2.7.2 K/5GHz and H/5GHz Ratio

The ratio of the NIR to the 5 GHz integrated flux density provides another method in determining extinction. For this method, the intrinsic ratio of the K band flux density on the 5 GHz flux density, determined by Willner *et al.* (1972) ($F_K/F_{5GHz} = 0.3$ and $F_H/F_{5GHz} = 0.26$) was used to determine A_K and A_H in Equation 2.13. The relationship between the NIR extinction (A_K and A_H) and A_V was further calculated from the Cardelli *et al.* (1989) extinction curve for R = 3.1 (see Equation 2.14). This method assumes that emission is due to ionized gas. Thus, in instances where hot dust dominates the emission, which is the case for some very young/dense and compact PNe, A_V will be under-estimated using this method. This will result in negative A_V magnitudes for some PNe. Approximately 38% of the CORNISH-PNe with reliable K band magnitudes have negative A_V (as low as $\sim$ –33 mag) and $\sim$ 23% with reliable H band magnitudes

[8] http://svo2.cab.inta-csic.es/svo/theory/main/

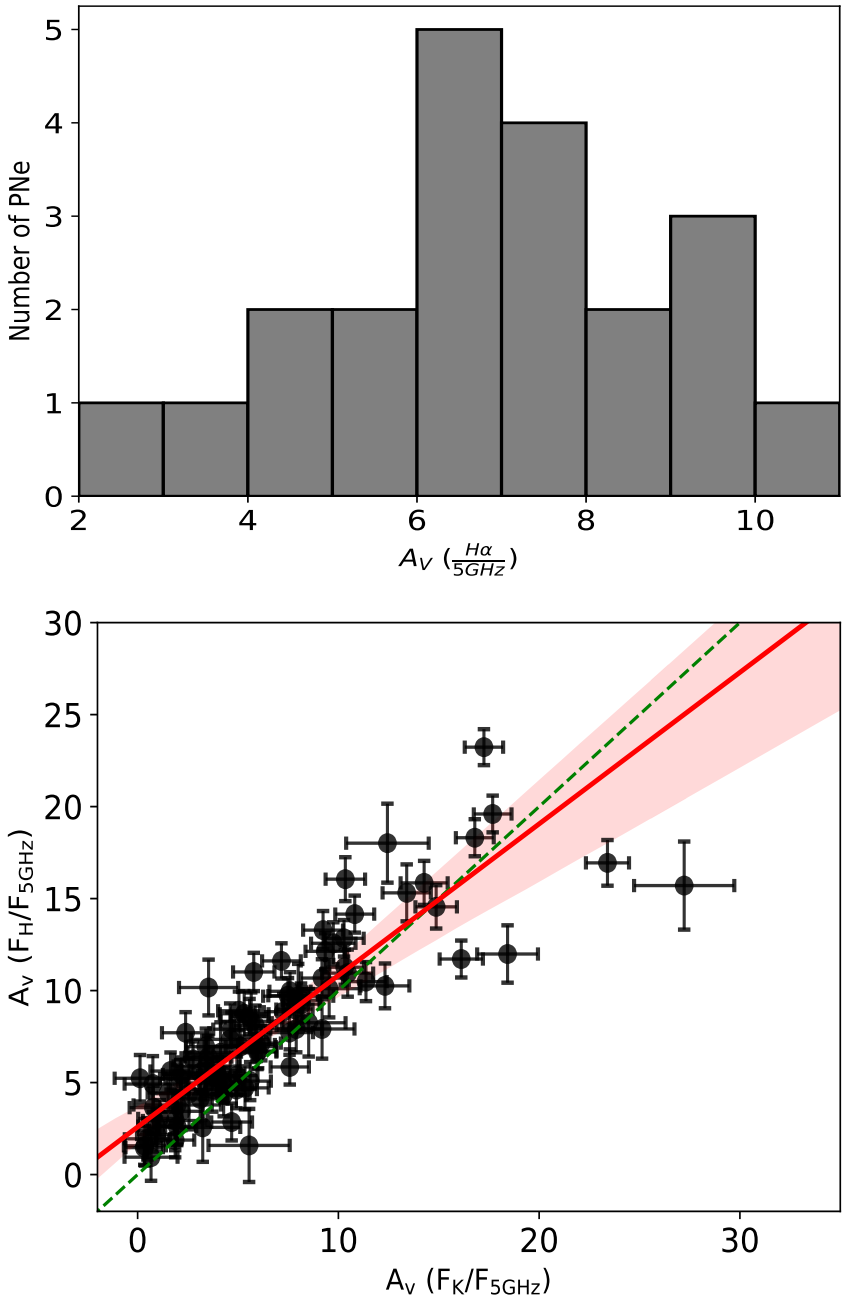

Figure 2.20: *Upper panel:* A_V *from* $H\alpha/F_{5GHz}$ *method for the 23 CORNISH-PNe with IPHAS counterparts. Lower panel:* A_V *from the* F_H/F_{5GHz} *method against* A_V *from the* F_K/F_{5GHz} *method. The regression line is shown in red with a 95% confidence band. Less weight is placed on larger errors and the green line is the one-to-one fit.*

have negative A_V (as low as $\sim$ –18 mag). These sources are not shown on the plot (Figure 2.20), but are given in Table A.3. This could be the effect of hot dust emission, resulting in larger H and K bands flux densities, compared to the level of ionized gas. For such CORNISH-PNe, where the effect is more on the K-band, H/5GHz will give a better estimation. A comparison between K/5GHz and H/5GHz is shown in Figure 2.20 (lower panel). The difference between the regression line and equality line is < 5 mag in A_V.

$$A_K = -1.086 \ln \frac{F_K}{0.3 F_{5GHz}}; A_H = -1.086 \ln \frac{F_H}{0.26 F_{5GHz}} \tag{2.13}$$

$$A_J/A_V = 0.283; A_H/A_V = 0.184; A_K/A_V = 0.113 \tag{2.14}$$

2.7.3 E[H-K] and E[J-H]

Extinction determined from the colour excess method normalizes observed colours to intrinsic or expected colours. Using Equation 2.15 (Kalcheva *et al.*, 2018; Willner *et al.*, 1972), the intrinsic colours of $[H-K]_0 \sim 0.68$ and $[J-H]_0 \sim -0.1$ were determined. These colours agree with the modelled intrinsic colours of NGC 6270 (0.62, 0.0) determined by Weidmann *et al.* (2013) and the average intrinsic colours of $[H-K]_0 \sim 0.65$ and $[J-H]_0 \sim -0.1$ from the Galactic PNe sample analysed by Ramos-Larios & Phillips (2005). Additionally, using the extinction coefficient determined in section 2.7.1, the intrinsic $[H-K]_0$ and $[J-H]_0$ colours of the 23 CORNISH-PNe with Hα emission were determined. Figure 2.21 shows the distribution of these colours, where some extreme intrinsic colours are seen. The mean of the general distribution is $[H-K]_0 \sim 0.7$ and $[J-H]_0 \sim 0.12$, illustrated by the green dotted line. However, if the extreme values are taken out, the mean reduces to $[H-K]_0 \sim 0.65$ and $[J-H]_0 \sim -0.1$, which agrees with the determined colours using equation 2.15.

$$\frac{F_K}{F_{5GHz}} = 0.3; \frac{F_H}{F_{5GHz}} = 0.26; \frac{F_J}{F_{5GHz}} = 0.43; \tag{2.15}$$

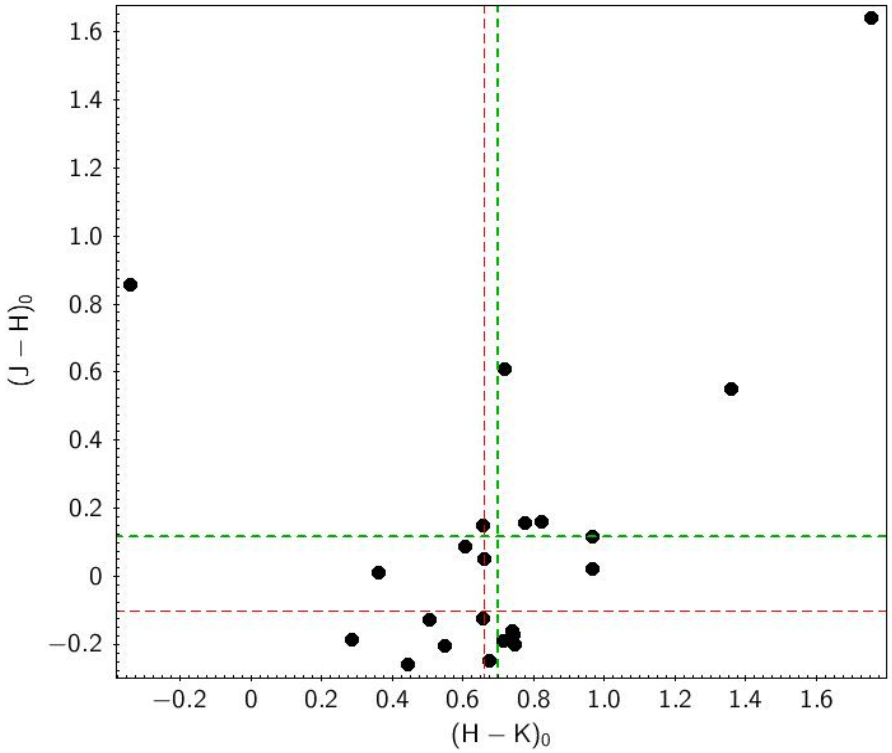

Figure 2.21: *Extinction corrected colours of the 23 CORNISH-PNe with Hα emission. The green shows the mean of all 23 CORNSIH-PNe colours, while the red line shows the mean with the extreme colours excluded.*

The CORNISH-PNe NIR colours were normalized to the mean derived intrinsic colours of $[H-K]_0 \sim 0.68$ and $[J-H]_0 \sim -0.1$ and A_V was determined using the relationships in Equation 2.14. In Figure 2.22, a comparison between A_v obtained using E[J-H] and E[H-K] colour excesses is presented. The effect of hot dust is also seen, which is reflected in the difference between the regression line (red) and the equality line (green).

From the analysis presented in Section 2.6, with the possibility of the CORNISH-PNe being compact and young, some of the CORNISH-PNe are expected to be dominated by hot dust. In addition to hot dust, the large excesses in the H – K and F_K/F_{5GHz} could also result from H_2 emission within the K band. Hence, larger NIR excesses compared to the expected level for thermal ionized gas. For such sources, their intrinsic colours could be higher than 0.68 (H – K). According

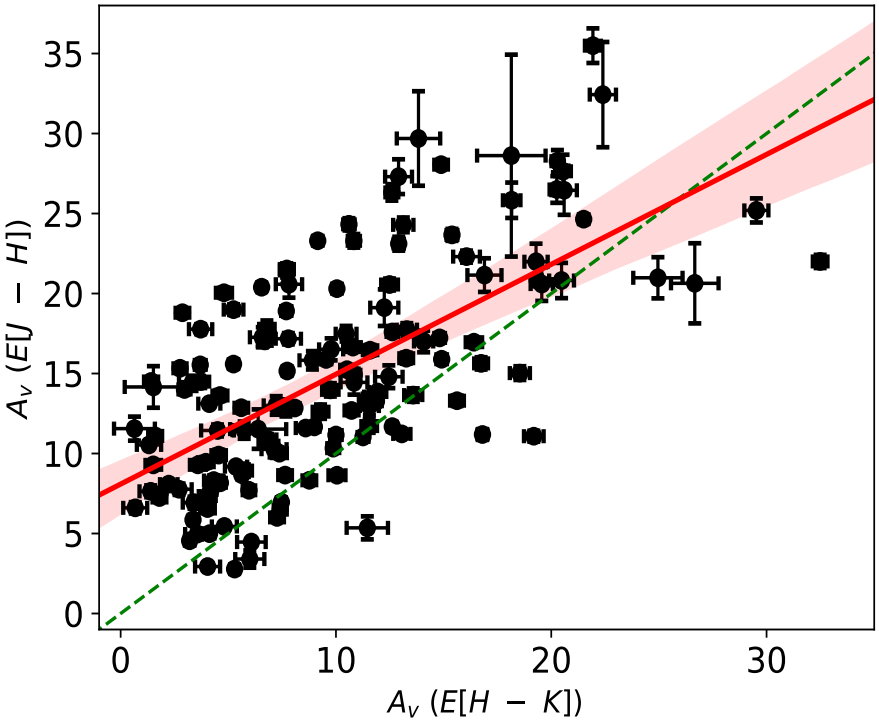

Figure 2.22: *A_V from the colour excess methods, showing A_V from E(J-H) against E(H-K). The regression line is shown in red with a 95% confidence band. The green line is the one-to-one fit. Less weight is placed on larger errors.*

to Pena & Torres-Peimbert (1987), the intrinsic H – K colour for high density and younger PNe could be as high as 0.8. This is also reflected in the range of intrinsic modelled colours for NGC 7027 (0.21, 0.41) and NGC 6720 (0.62, 0.0) by Weidmann *et al.* (2013), shown in Figures 2.15 and the range of intrinsic colours of the 23 CORNISH-PNe in Figure 2.21.

In Table 2.5, A_V from the different methods for a few sources are compared. A literature search for the A_V for a few well known PNe within the CORNISH-PNe sample was carried out. The F_K/F_{5GHz} method appears to underestimate A_V more, compared to other methods. This is reflected in Figure 2.23, where the flux densities of H and K bands are compared. Compared to the H band, the K band flux densities are higher.

No one method can be said to be accurate for all the CORNISH-PNe. However,

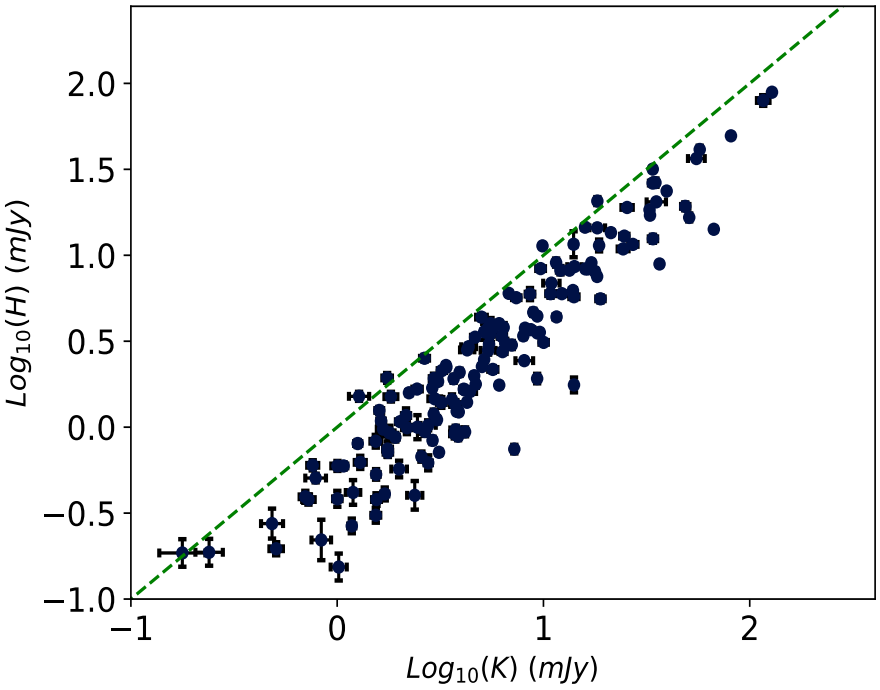

Figure 2.23: *Comparison of the K and H band flux densities. The green line is a one-to-one line.*

there are a few CORNISH-PNe whose A_V from the different methods seems to agree. The varying extinctions from these methods can be attributed to the effect of different dominant emissions mechanism (see Ramos-Larios & Phillips 2005) as observed in Figure 2.15, resulting in the different A_V using the different methods. A_V within lower Galactic latitudes could be as high as ~ 30 mag (see the extinction map of Gonzalez *et al.* 2012; González-Solares *et al.* 2008), which agrees with the maximum estimated A_V for the CORNISH-PNe using the different methods. The estimated A_V from the different methods for the CORNISH-PNe are given in Table A.3.

Table 2.5: *Comparison of the* A_V *from the different methods for some extended sources. Where available, the literature* Hα *or* Hβ *fluxes were used to calculate* A_V*. Where c (extinction constant) is given in the literature, it is converted to* A_V *using* $c/E(B-V) = 1.46$*. * indicates that the* Hα *is from a larger area compared to the radio emission*

Name	Known Name	A_V Hα/radio	A_V E[H – K]	A_V E[J – H]	A_V K/radio	A_V H/radio	A_V Literature
G010.0989+00.7393	NGC 6537	-	3.56 ± 0.56	4.97 ± 0.34	1.96 ± 0.95	2.62 ± 0.95	3.71[1], 3.78[2], 4.3[3]
G035.4719–00.4365	-	8.68 ± 0.29	5.63 ± 0.20	8.68 ± 0.14	4.32 ± 0.95	4.87 ± 0.95	-
G050.5556+00.0448	-	11.60 ± 0.41	11.26 ± 0.25	11.04 ± 0.20	7.25 ± 0.96	8.85 ± 0.97	-
G051.8341+00.2838	-	9.53 ± 0.31	8.76 ± 0.32	8.33 ± 0.15	5.92 ± 0.91	7.07 ± 0.90	-
G055.5070–00.5579	M 1-71	3.45 ± 0.11	4.04 ± 0.58	2.95 ± 0.14	0.96 ± 0.99	2.18 ± 0.93	4.46[4]
G059.8236–00.5361	-	6.81 ± 0.22	7.26 ± 0.32	6.01 ± 0.27	3.94 ± 0.92	5.26 ± 0.91	-
G062.4936–00.2699	M 2-48	2.30 ± 0.08*	6.34 ± 0.35	6.55 ± 0.21	5.61 ± 1.03	5.08 ± 1.03	4.67[4]
G062.7551–00.7262	-	4.95 ± 0.18	5.96 ± 0.29	7.70 ± 0.21	4.95 ± 1.03	5.38 ± 1.04	

[1]Matsuura *et al.* (2005), [2]Pottasch *et al.* (2000), [3]Kaler (1983), [4]Tylenda *et al.* (1992).

2.8 Heliocentric Distances

To better estimate the ionized mass, luminosity and Galactic distribution of PNe, reliable distances are needed. However, only a handful of known PNe have reliable, individually determined distances. Methods used in determining distances to PNe include trigonometric parallax (Harris *et al.*, 2007), expansion parallax (Hajian, 2006; Terzian, 1997), spectroscopic parallax (Ciardullo *et al.*, 1999), reddening (Gathier *et al.*, 1986), and statistical methods (see Cahn *et al.* 1992).

The heliocentric distances to the CORNISH-PNe were estimated based on the optical statistical distance calibration described in Frew (2008) and Frew *et al.* (2016). This method uses the Hα surface brightness-radius (SB-r) relationship and requires the angular diameters and extinction corrected Hα integrated fluxes. The 5 GHz integrated flux density of each CORNISH-PNe was converted to Hα flux density using equation 2.16 and the relationship; F(Hα)/F(Hβ) = 2.85 (Ruffle *et al.*, 2004) and then the corresponding Hα surface brightness was computed using equation 2.17. Physical radii and corresponding distances were then estimated using equation 2.18 (Frew *et al.*, 2016).

$$\frac{S\nu}{F(H\beta)} = 2.51 \times 10^{7} T_{e}^{0.53} \nu^{-0.1} Y \ (\mathrm{Jy\ W^{-1} m^{2}}) \tag{2.16}$$

where ν is radio frequency in GHz and Y ionized ratio of $H_e/H = 1.1$.

$$SH\alpha(\mathrm{erg\ cm^{-2} s^{-1} sr^{-1}}) = \frac{F_{H\alpha}}{4\pi\vartheta^{2}} \tag{2.17}$$

$$\log(SH\alpha) = -3.63(\pm 0.06)\log r - 5.34(\pm 0.05) \tag{2.18}$$

where r (pc) is the physical radius and the distance, (d) is given by:

$$d(\mathrm{pc}) = \frac{206265 r(\mathrm{pc})}{\vartheta_{r}(\mathrm{arcsec})} \tag{2.19}$$

It should be noted that equation 2.18 (Frew *et al.*, 2016) provides a mean distance and optically thin or thick PNe were not treated separately (See Frew *et al.* 2016

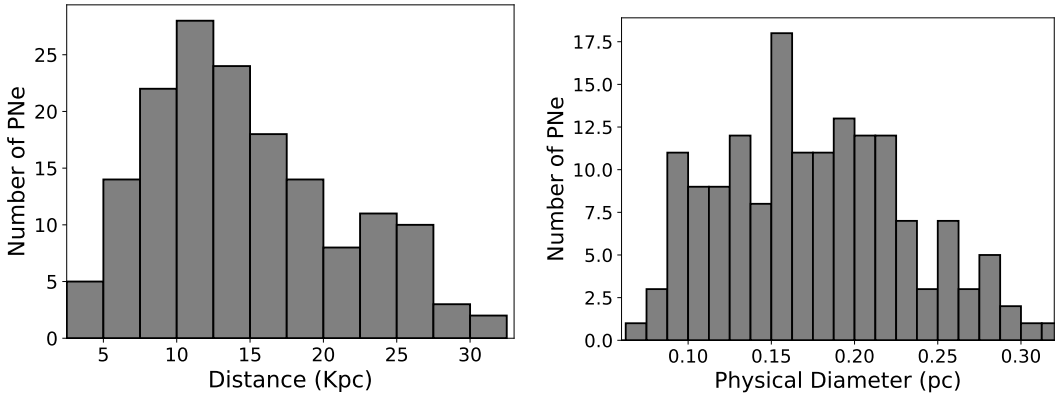

Figure 2.24: *Distribution of the distances in kpc (top) and physical diameters in pc (bottom).*

for review and details). The distributions of the CORNISH-PNe distances and physical sizes are presented in Figure 2.24. The distance distribution shows a peak at $\sim$ 11 kpc and gradually falls off to 32 kpc. 58% of the CORNISH-PNe have distances $\leq$ 15 kpc and 26% have distances $\leq$ 10 kpc. The physical diameter distribution shows a generally compact sample in a range of 0.06 pc to 0.32 pc. 67% have physical diameters lass than 0.2 pc. The mean physical diameter and heliocentric distance are 0.18 ± 0.06 pc and 14 ± 6 kpc, respectively.

Figure 2.25 shows a variation of the distances and physical diameters with angular sizes. CORNISH-PNe with larger angular sizes are closer than $<$ 10 kpc, while CORNISH-PNe with smaller angular sizes are spread over a range of distances. The distances to the angularly small CORNISH-PNe above 15 kpc are possibly over-estimated, given that optically thick PNe were not accounted for separately. This could result in larger errors in the estimated distances. 15% have physical sizes $\leq$ 0.2 pc and closer than 10 kpc. Estimated distances and physical diameters are presented in Table A.4.

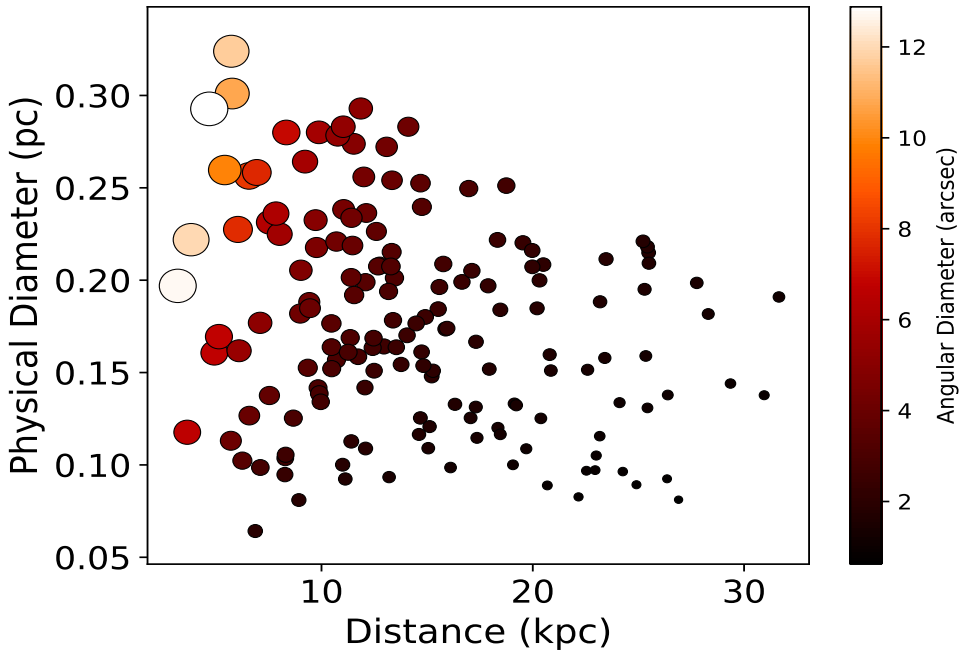

Figure 2.25: *Physical sizes against distances for the CORNISH-PNe, colour coded and scaled with the corresponding angular size.*

2.9 Discussion

2.9.1 Reliability and Completeness

The reliability of this sample has been demonstrated by the quality of the catalogue described in (Purcell *et al.*, 2013), the multi-wavelength visual identification performed by the CORNISH team and the multi-wavelength properties presented in this work. To demonstrate the completeness and depth of the CORNISH survey, the CORNISH-PNe sample is compared with samples of known PNe in the HASH database (Parker *et al.*, 2017). This catalogue includes PNe samples from the Strasbourg-ESO catalogue of Galactic PNe (Acker *et al.*, 1992), catalogue of Galactic PNe by Kohoutek (2001), Macquarie/AAO/Strasbourg Hα planetary Nebula catalogues (MASH I, Parker *et al.* 2006 and MASH II, Miszalski *et al.* 2008) and the IPHAS catalogue (Sabin *et al.*, 2014; Viironen *et al.*, 2009b).

In Figure 2.26, the distribution of the CORNISH-PNe and known PNe is presented. This comparison is restricted within the $10^{\circ} < l < 65^{\circ}$ region for the known PNe in the HASH catalogue. Compared to the CORNISH-PNe, the detection of known PNe drops towards $b = 0^{\circ}$, whereas the CORNISH-PNe clearly peak about $b = 0^{\circ}$. This reflects the extinction bias associated with optically detected PNe and increased reddening in this region (see the extinction map of Gonzalez *et al.* 2012).

The PNe in the HASH database (Parker *et al.*, 2017) have mean and median angular sizes of $44''$ and $15''$, respectively. The median angular size of PNe for both the MASH and IPHAS catalogues is $\sim 22''$ (Parker *et al.*, 2006; Sabin *et al.*, 2014). It can be seen that known PNe, which are optically selected, are biased towards extended and/or more evolved PNe. For the CORNISH-PNe, the mean and median angular sizes are $\sim 3''$ and $\sim 2.5''$, indicating a more compact PNe sample, compared to angular sizes of the known PNe. Hence, the distribution of known PNe in Figure 2.26 (grey shaded region) is dominated by extended PNe. Such extended PNe within the CORNISH survey region may have been completely resolved out, thus, absent in the distribution of the CORNISH-PNe (red shaded region) or only the central regions may have been detected in the CORNISH survey.

If PNe are assumed to be optically thin at physical diameters > 0.12 pc (Zijlstra, 1990), equation 2.20 (Stanghellini *et al.*, 2008) can be used to estimate peak fluxes for a range of angular sizes, at a particular distance. Assuming the CORNISH-PNe are optically thin, the peak flux per CORNISH beam was estimated for phyiscal sizes within the range of 0.12 to 0.9 pc at 10, 15 and 20 kpc.

$$F = \frac{\mu^2}{2.266 \times 10^{-21} D^5 \vartheta^3} \tag{2.20}$$

where F is the flux density in Jy, ϑ is the angular size in arcseconds, D is the distance in pc and μ for optically thin PNe is given as $10^{-0.87}$ (Stanghellini *et al.*, 2008).

Figure 2.27 shows a plot of the peak fluxes versus the angular sizes, indicating the CORNISH detection limits (dotted red lines: 7σ in mJy/beam and beam size

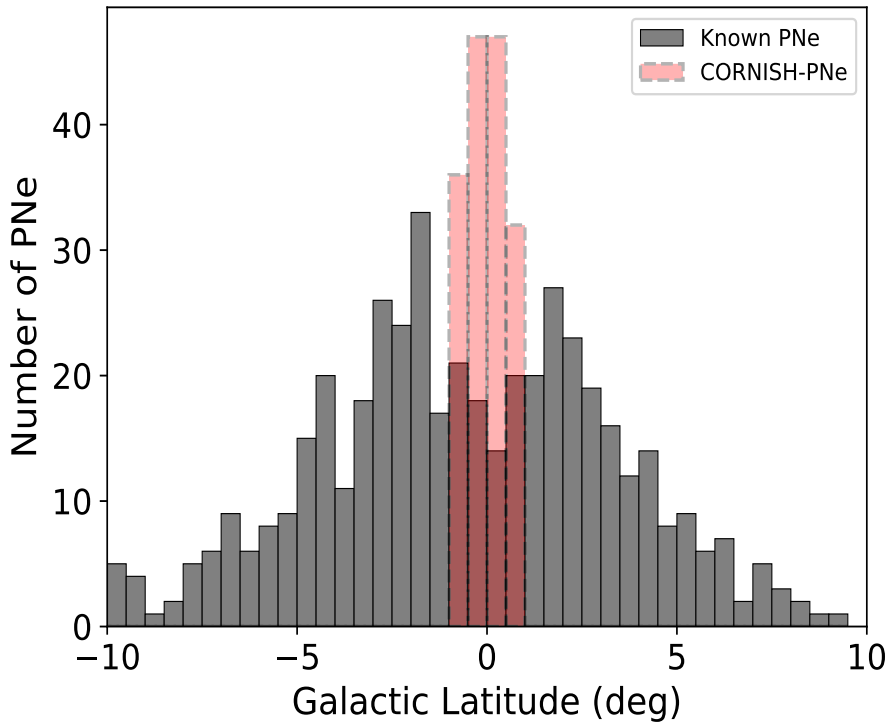

Figure 2.26: *Galactic latitude distribution of the CORNISH-PNe (red) and known PNe (grey). Known PNe samples are from HASH database (Parker et al., 2017) and includes PNe samples from the Strasbourg-ESO Catalogue of Galactic PNe (Acker et al., 1992), Catalogue of Galactic PNe by Kohoutek (2001), Macquarie/AAO/Strasbourg Halpha Planetary Nebula Catalogues (MASH I, Parker et al. 2006 and MASHII, Miszalski et al. 2008) and IPHAS catalogue (Sabin et al., 2014).*

of 1.5″). At 15 kpc, the CORNISH survey would detect PNe with angular sizes $< 2.5''$ and above the CORNISH survey detection limit. At distances closer than 15 kpc, PNe with larger angular sizes will be detected if their peak fluxes are above the detection limit. Unresolved PNe would be detected at distances of 20 kpc and above. This is reflected in Figure 2.25, where CORNISH-PNe with small angular sizes are detected at larger distances.

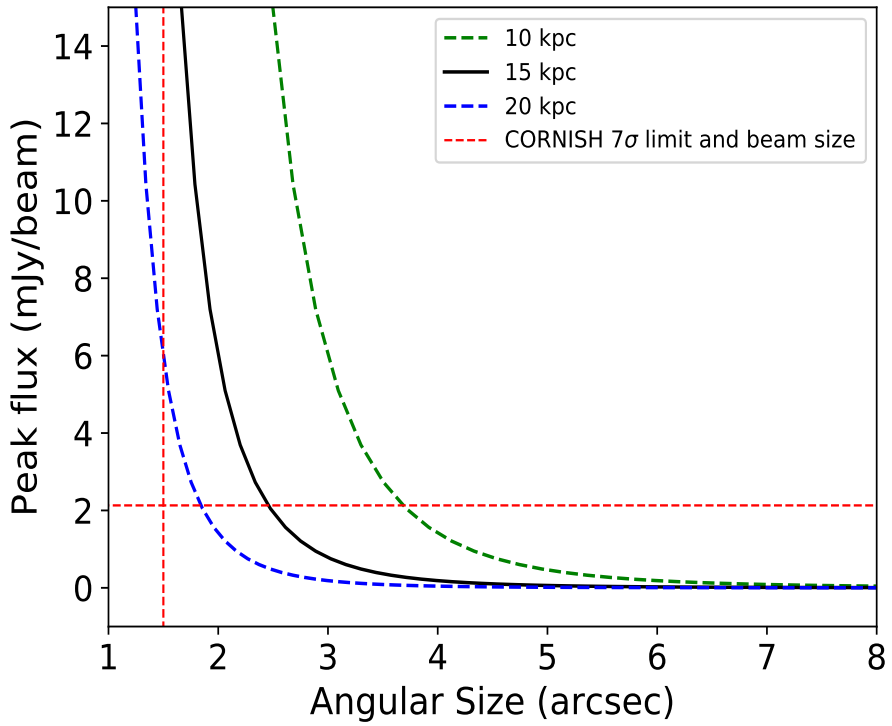

Figure 2.27: *Flux densities at 5 GHz against angular sizes (arcsec) for PNe with physical radii* > 0.12 *pc (optically thin PNe), at a distance of 10, 15 and 20 kpc. The red dotted lines represents the 7σ detection limit (horizontal) and the beam size (vertical) of the CORNISH survey.*

2.9.2 Combined Colour-Colour Plots

The difficulty in spectroscopic confirmation of PNe due to extinction has informed the need for other methods of confirmation. The works of Parker *et al.* (2012a) and Cohen *et al.* (2011), using the MASH PNe have shown that the use of multi-wavelength analysis can be robust in identifying PNe not detected at optical wavelengths, especially when they have reliable MIR and radio emission measurements. Multi-wavelength colour-colour plots, together with the MIR/radio ratio used in this analysis are expected to flag different contaminants. Across the different colour-colour plots, the CORNISH-PNe show colours expected of PNe.

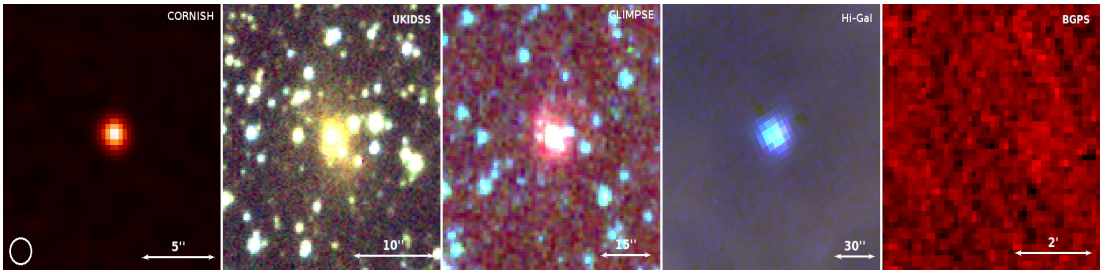

Figure 2.28: *Multi-wavelength images of G052.1498–00.3758. The CORNISH 5 GHz radio image (left), followed by NIR 3-colour images : J band is blue, H is green and K is red; MIR 3-colour image : 3.6* μm *is blue, 4.5* μm *is green and 8.0* μm *is red; FIR 3-colour image (right): 70* μm *is blue, 160* μm *is green and 250* μm *is red and the BGPS 1.1 mm are shown. G052.1498–00.3758 has FIR colours that are similar to HII regions.*

In the NIR colour-colour plot (see Figure 2.15), the CORNISH-PNe show a wide range of colours, which agrees with the range of unreddened PNe colours analysed by Ramos-Larios & Phillips (2005). In the MIR (Figure 2.18), the CORNISH-PNe have colours that separate them from the region occupied by symbiotic stars, except for the D-types (dusty). In the FIR, a few CORNISH-PNe extend into the HII regions area on both colour-colour plots. The three outliers in the FIR colour-colour plots (Figure 2.19) are G019.2356+00.4951, G052.1498–00.3758 and G058.1591–00.5499. G019.2356+00.4951 also has a negative spectral index (discussed in Section 2.9.3). G052.1498–00.3758 has no milimeter dust emission and visual re-inspection of the multi-wavelength images, including the Hi-Gal images, confirms it to be a PN (see Figure 2.28). G058.1591–00.5499 has no millimetre data but, re-inspection of its multi-wavelength images (Figure 2.29), NIR and MIR colours are consistent with PNe colours.

2.9.3 Sources With Negative Spectral Indices

The dominant radio continuum emission in an ionized nebulae is expected to be thermal, although some conditions and processes such as jets and magnetic fields in very young PNe could provide an environment for non-thermal emission.

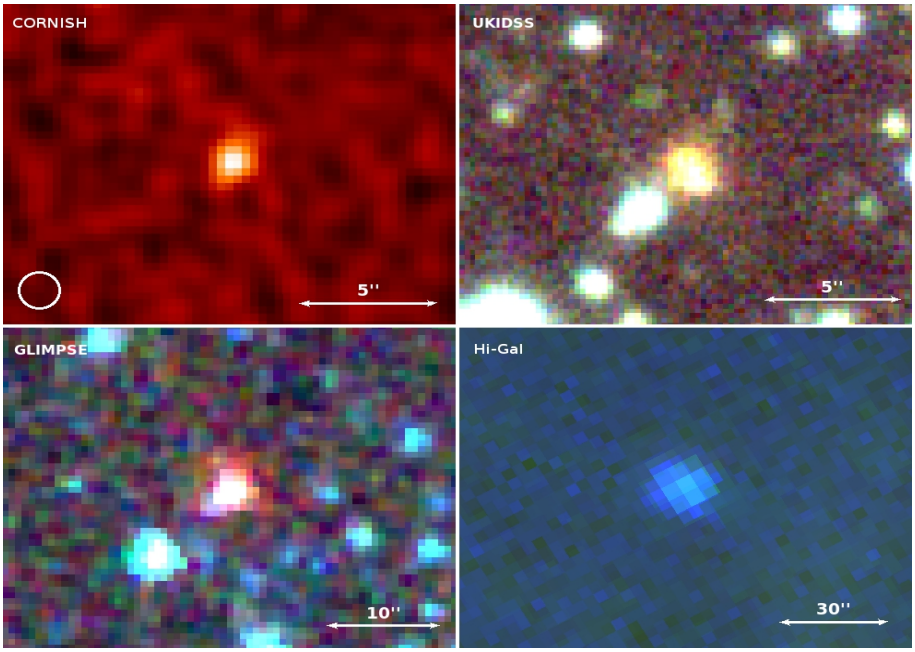

Figure 2.29: *Multi-wavelength images of G058.1591–00.5499. The CORNISH 5 GHz radio image (top left), NIR 3-colour images (top right): J band is blue, H is green and K is red; MIR 3-colour image (bottom left): 3.6* μm *is blue, 4.5* μm *is green and 8.0* μm *is red and FIR 3-colour image (bottom right): 70* μm *is blue, 160* μm *is green and 250* μm *is red are shown. G058.1591–00.5499 has FIR colours that are similar to HII regions.*

The presence of high velocity collimated jets, believed to be the primary shaping mechanism in PNe, could induce shock fronts and accelerate electrons to a relativistic velocity in a magnetic field, which could result in non-thermal emission. Observational evidence of this is seen in a post-AGB source (IRAS 15445 – 5449) with strong magnetic fields, where ionization has not started, but jets are present (Pérez-Sánchez *et al.*, 2013). The two CORNISH-PNe with significant negative spectral indices (see Figure 2.12; middle panel) are discussed below.

G019.2356+00.4951

G019.2356+00.4951 is classified in the SIMBAD database as a radio source (MAGPIS and NVSS surveys). It is associated with X-ray emission (XGPS-I J182416-

115554; 3XMM J182416.7-115558[9] Rosen *et al.* 2016) in the XMM-Newton Galactic Plane Survey (within 4″ search radius), having a hardness ratio of 0.72 (Hands *et al.*, 2004). Although it is isolated in the far-infrared image data (Figure 2.30; top panel), it has FIR colours ($Log_{10}[160/24] \sim 1.28$; $Log_{10}[70/22] \sim 1.32$) expected of HII regions but with no millimetre emission. It can be seen in Figure 2.30 (top panel) that this is an extended source in the MIR and NIR but the CORNISH survey has detected only the bright core.

One of the mechanisms through which X-ray emission is produced in PNe is thought to be related to their shaping mechanisms (wind-wind interaction), resulting in hot bubble formation. Such X-ray emission is observed within the bright innermost shell. The presence of collimated jets and outflows can also result in shocks that emit X-rays. X-ray emission from such processes are thought to be characteristics of young and compact PNe (Chu *et al.*, 2000; Freeman *et al.*, 2014; Kastner, 2007; Kastner *et al.*, 2008).

According to Freeman *et al.* (2014), PNe that emit X-rays from such interactions are mainly elliptical. G019.2356+00.4951 has an elliptical morphology in the radio, NIR and MIR (see multi-wavelength images in Figure 2.30) with a spectral index of -0.66 ± 0.09 that is compatible with synchrotron emission. A distance of $\sim 9 \pm 1$ kpc and a diameter of $\sim 0.18 \pm 0.02$ pc are estimated for this source. This source is classified as a PN and it is likely a young PN, based on the X-ray emission and elliptical morphology in the radio, NIR and MIR. The SED of this source is shown in Figure 2.31 (top panel).

G030.2335–00.1385

This is an unresolved source in the CORNISH survey with T_B close to 10^4 K and a spectral index of -0.55 ± 0.08. This negative spectral index is not due to variability as it has a MAGPIS 6 cm integrated flux density of 348.57 mJy (360 ± 32.91 mJy in the CORNISH). It is not detected in the IPHAS survey. Massive stars are known to evolve fast enough to ionize their circum-stellar envelope while the envelopes are still dense (Kwok, 1993b; Phillips, 2003a). This source was

[9] http://xmm-catalog.irap.omp.eu/source/200519401010016

previously classified as an HII region in Leto *et al.* (2009), but it is isolated in the FIR image, with no millimetre dust emission. It is classified as a PN by Cooper *et al.* (2013) from its NIR spectrum and its multi-wavelength images (Figure 2.30) supports this classification. It is also associated with water (H_2O) maser emission, having a spread of $\sim$ 70 km/s, which supports a young nature. A distance of $\sim 7.0 \pm 0.6$ kpc and a diameter of $\sim$ 0.06 pc are estimated for this source. The SED of this source is shown in Figure 2.31 (lower panel).

Collimated jets have been observed to be traced by H_2O maser components in post-AGB sources. The velocity spread of these masers can be as wide as $\sim$ 500 km/s, as observed towards IRAS 18113 – 2503 (Gómez *et al.*, 2011). The presence of H_2O masers in PNe is indicative of a young nature. A few PNe with negative spectral indices have also been reported in Bojičić *et al.* (2011). The first observational evidence of non-thermal emission in a PN with H_2O maser emission was seen in IRAS 15103 – 5754, with a spectral index of $\simeq -0.54 \pm 0.08$ (Suárez *et al.*, 2015) that is compatible with synchrotron emission. IRAS 15103 – 5754 is presently considered to be the youngest PN ($<$ 100 yr; Gómez *et al.* 2018). G030.2335-00.1385 shares similar characteristics with IRAS 15103 – 5754 and will be a good source to investigate further.

Figure 2.30: *Multi-wavelength images of G019.2356+00.4951 (top) and G030.2335–00.1385 (bottom). The CORNISH 5 GHz radio image (left), followed by NIR 3-colour images : J band is blue, H is green and K is red, MIR 3-colour image : 3.6* μm *is blue, 4.5* μm *is green and 8.0* μm *is red; FIR 3-colour image (right): 70* μm *is blue, 160* μm *is green and 250* μm *is red and, the BGPS 1.1 mm are shown. G030.2335–00.1385 has a negative spectral index of* -0.55 ± 0.08.

Sources with such negative spectral indices could be confused with supernovae remnants (SNRs), having typical spectral indices $\leq$ –0.5 and X-ray emission (Anderson *et al.*, 2017; Bozzetto *et al.*, 2017). However, there is no known detection of the 22 GHz H_2O maser emission towards SNRs (Claussen *et al.*, 1999; Woodall & Gray, 2007), which rules out the possibility of G030.2335–00.1385 being a SNR.

Young SNRs peak at shorter wavelengths (20-50μm) (Williams & Temim, 2016) than PNe, while older or more evolved SNRs have FIR and sub-millimeter emission (Lakićević *et al.*, 2015; Matsuura *et al.*, 2015). The colours (NIR to FIR) of G019.2356+00.4951 are rather consistent with PNe (see Pinheiro Gonçalves *et al.* 2011; Reach *et al.* 2006). If it were a core-collapse SNR or PWNe (pulsar wind nebula), some sub-millimetre emission would be expected or a flatter radio spectrum (see Bietenholz *et al.* 1997; Gaensler & Slane 2006) compared to its steep spectral index of -0.66 ± 0.09.

2.9.4 PNe and Symbiotic Systems

The difficulty in separating some PNe and dusty (D-type) symbiotic stars on the NIR and MIR colour-colour plot is seen on Figures 2.15 and 2.18. Both source classes are heterogeneous and cannot be differentiated using morphology or environment. They both show axisymmetric morphologies (López *et al.*, 2004; Santander-Garc´ıa *et al.*, 2007), making it difficult to separate them using multi-wavelength images or plots. They also share similar observational properties, especially the dusty symbiotic stars (D-type). Additionally, symbiotic systems can also be dominated by free-free emission at radio wavelengths (Mikołajewska & Ivison, 2001). Their positions on the NIR plot is due to dominant stellar and hot dust emission in the NIR (Ivison *et al.*, 1991). Due to their high dust content, D-type symbiotic systems exhibit high intrinsic extinction as well (Phillips, 2007), a property that can also be observed in very young PNe. An example of such difficulty is K 3-22 that was previously classified as a PN but has been re-classified as a symbiotic star from its spectroscopic properties (Corradi *et al.*, 2010). Nonetheless, given the clean separation of the S-types on the MIR colour-

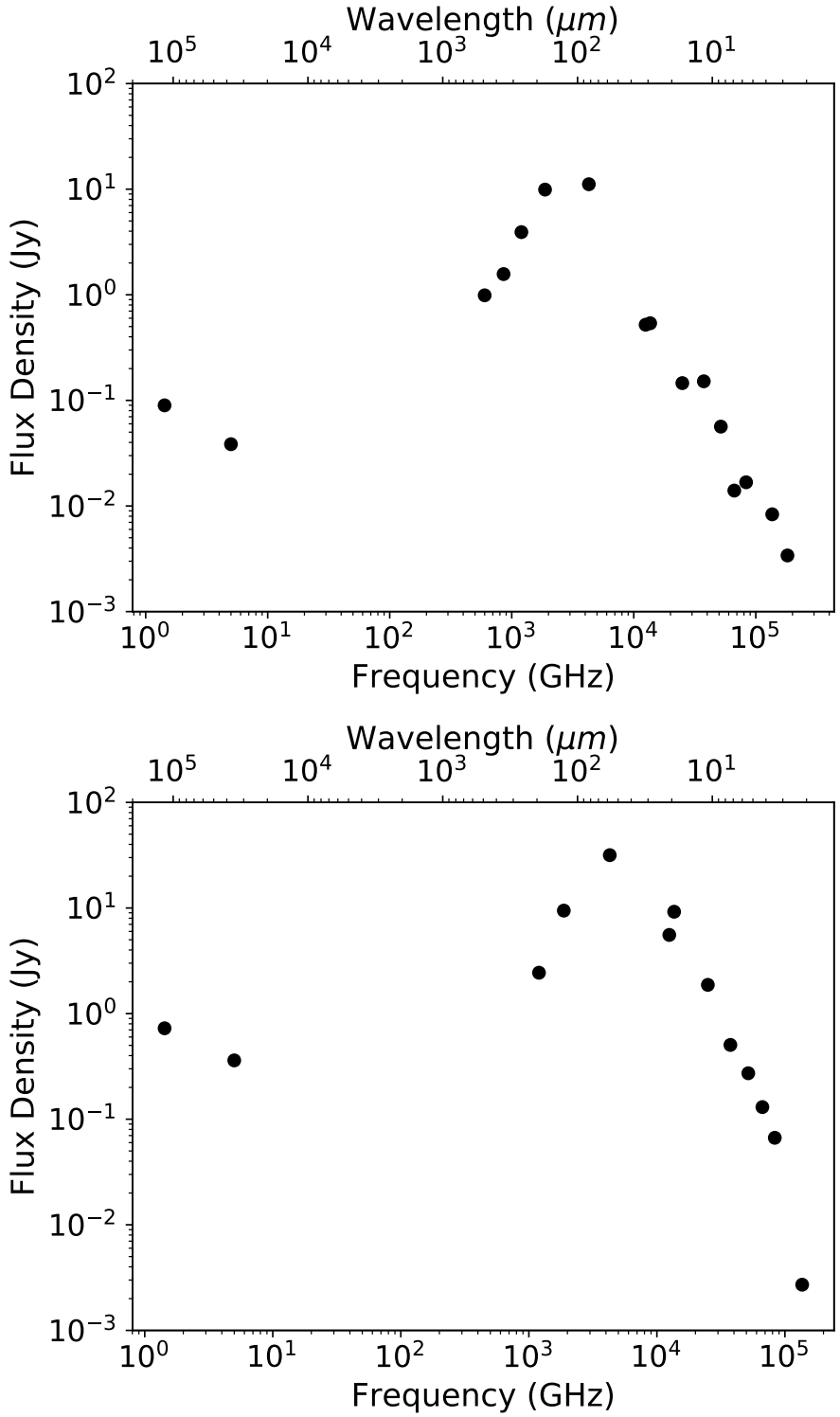

Figure 2.31: *SED (spectral energy distribution) of G019.2356+00.4951 (top) and G030.2335–00.1385 (bottom).*

colour plot, it is expected that D-types would have been flagged out based on the different colour-colour plots.

2.10 CORNISH-PNe Catalogue

The classification of the CORNISH-PNe was done based on the radio properties, MIR/radio ratio, optical colours and infrared colours. In the absence of IPHAS data, the Hα images from the SHS survey (Parker *et al.*, 2005)[10] were used, where available, to aid classification. In cases where a conclusion could not be drawn from this analysis, the PN is tagged as possible PNe with a question mark '?', and where truly in doubt, the PN is tagged 'unknown' or other source type. Sources that meet all requirements for PNe in all considered multi-wavelength analysis and images are classified as PNe. It is indicated if the PNe are newly confirmed, newly classified or newly discovered under the status column. The newly confirmed PNe are sources previously classified as possible PNe in the SIMBAD database, newly classified are sources previously identified as radio sources or YSOs in the SIMBAD database, with no previous classification as PNe, while newly discovered are sources with no astronomical record in the SIMBAD database. The final catalogue is presented in Table 2.7 and the columns are defined as follows: CORNISH name (1), SIMBAD identification (2), Hα detection (3), classification (4), status (5) and comments (6).

A cross-match of the 169 CORNISH-PNe with known PNe (true PNe) from HASH database (Parker *et al.*, 2017) returns 24 matches (Table 2.6), excluding the CORNISH candidates and likely PNe. Figure 2.32 shows the Galactic latitude distribution versus longitude. The known PNe present in the CORNISH-PNe sample are seen, where the red filled circles are enclosed by the black circles. This Figure also shows the spatial distribution of the CORNISH-PNe and known PNe. A further 47 suspected PNe, as classified in the SIMBAD database, are confirmed as such from the analysis here (see Table 2.7 for references). 90 out of the remaining 98 CORNISH-PNe are new PNe (12 newly discovered and 78

[10]http://www-wfau.roe.ac.uk/sss/

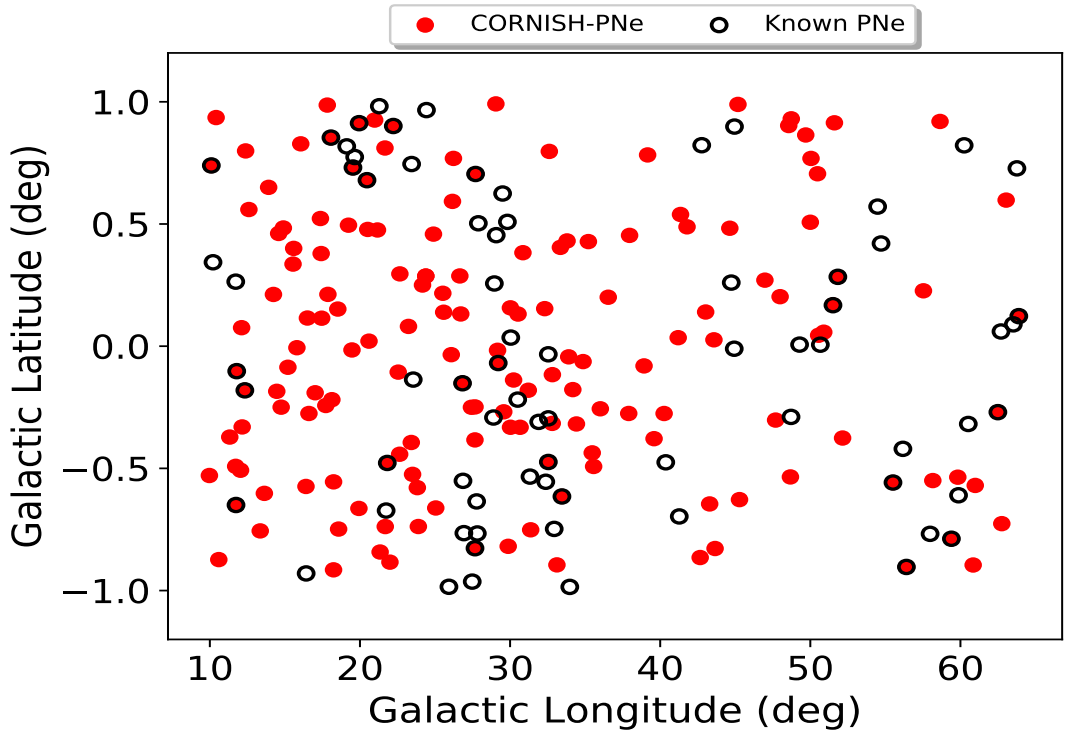

Figure 2.32: *Galactic latitude versus longitude of the CORNISH-PNe and known PNe.*

are newly classified) and the remaining 8 are classified as possible PNe or other source types.

Independently, Fragkou *et al.* (2017) have used visual inspection of the multi-wavelength images on the HASH database (Parker *et al.*, 2017), the MIR/Radio ratio and MIR colours to identify 70 of the sources in CORNISH catalogue as candidate PNe. Some of the intrinsically red sources based on MIR colours from the GLIMPSE surveys that were classified as candidate YSO by Robitaille *et al.* (2008) turn out to be PNe (see Parker *et al.* 2012a).

YSOs are embedded objects with weak radio emission from ionized stellar winds, usually less than a few mJy (Hoare, 2002; Hoare *et al.*, 1994). The 4.8 to 15 GHz radio integrated flux density of the YSO sample from the Red MSX Source Survey (Lumsden *et al.*, 2013) are mostly upper limits (97%). The median MIR/Radio ratio of the Red MSX Source Survey sample is estimated to be of order 10^3,

Table 2.6: *24 known PNe present in the CORNISH–PNe sample.*

CORNISH Name	PNG	Other Names
G010.0989+00.7393	010.1+00.7	NGC 6537
G011.7434–00.6502	011.7–00.6	NGC 6567
G011.7900–00.1022	011.7+00.0	M 1–43
G012.3315–00.1806	012.3–00.1	F2BP 1
G018.0661+00.8535	018.0+00.8	IRAS18179–1249
G019.5326+00.7308	019.5+00.7	GLIPN1823–1133
G019.9448+00.9126	019.9+00.9	M 3–53
G020.4681+00.6793	020.4+00.6	PM 1–231
G021.8201–00.4779	021.8–00.4	M 3–28
G022.2211+00.9009	022.2+00.9	IRAS18257–0908
G026.8327–00.1516	026.8–00.1	MPAJ1840–0529
G027.6635–00.8267	027.6–00.8	PHRJ1844–0503
G027.7016+00.7048	027.7+00.7	M 2–45
G029.2113–00.0689	029.2+00.0	TDC1
G032.5485–00.4739	032.5–00.4	MPAJ1852–0033
G033.4543–00.6149	033.4–00.6	GLMP 844
G050.0405+01.0961	050.0+01.0	IRAS19171+1536
G051.5095+00.1686	051.5+00.2	KLW 1
G051.8341+00.2838	051.8+00.2	IPHASJ192553.5+165331
G055.5070–00.5579	055.5–00.5	M 1–71
G056.4016–00.9033	056.4–00.9	K 3–42
G059.3987–00.7880	059.4–00.7	PM 1–313
G062.4936–00.2699	062.4–00.2	M 2–48
G063.8893+00.1229	063.8+00.1	K 3–48

which is high compared to the MASH PNe (Cohen *et al.*, 2011) and CORNISH-PNe value of 4.7 ± 1.1 and 3.9 ± 0.90, respectively. They are also expected to have FIR colours similar to HII regions as they emit more in the MIR to FIR.

Similarly, 10 out of the 27 high-quality candidate PNe identified by Parker *et al.* (2012a), within the CORNISH survey region, are not in the 7σ catalogue. Parker *et al.* (2012a) classified these as high quality PNe based on the MIR colours of previously known PNe, MIR environment and MIR false-colour images. Inspection of the CORNISH images shows that they are not reliable PNe candidates (see Figure 2.33). Because these sources are compact in the GLIMPSE survey, the possibility that a null detection by the CORNISH survey is due to completely resolved out emission is ruled out. These could possibly be evolved stellar objects or YSOs (Oliveira *et al.*, 2013).

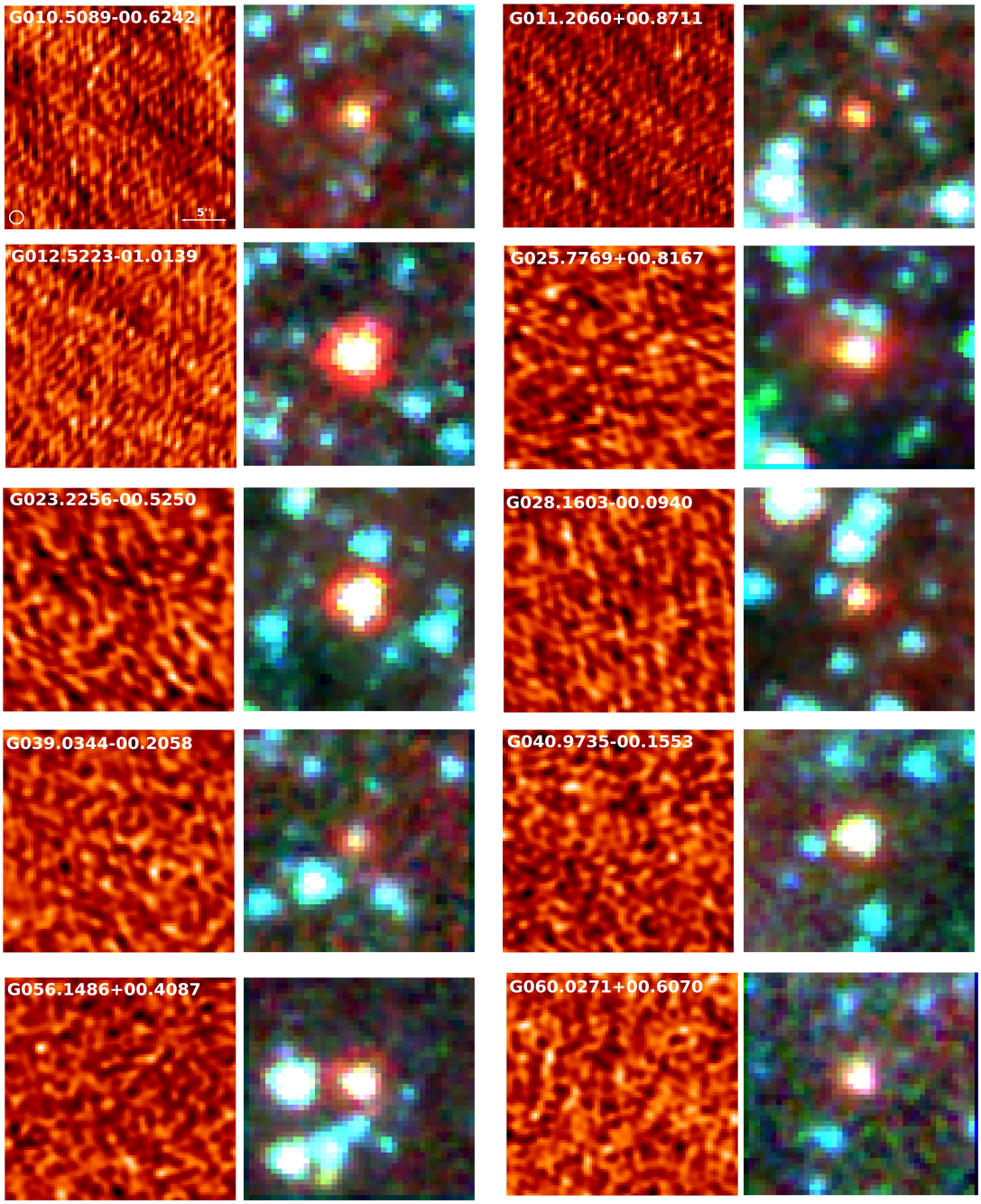

Figure 2.33: *CORNISH 6 cm and 3-colour (3.6* μm *is blue, 5.8* μm *is green and 8.0* μm *is red) GLIMPSE images of the 10 high quality PNe candidates from Parker* et al. *(2012a), within the CORNISH survey region. All images are* $25^{''} \times 25^{''}$ *in size and the CORNISH beam size is shown on the first image.*

2.11 Summary

Following the visual selection of the CORNISH-PNe (169) from the CORNISH survey by the CORNISH team, their multi-wavelength properties were focused on here, including their radio properties, optical to far-infrared colours, extinction and distances. The sensitivity of the CORNISH survey combined with multi-wavelength data, at infrared and millimetre wavelengths, provides an uncontaminated sample of PNe that is free from extinction biases associated with optical based surveys. At 6 cm, the CORNISH survey is more complete within the $|b| < 1^{\circ}$ region and has uncovered 90 new and compact Galactic PNe within 110 deg^2 area. Radio selected samples from such surveys, unaffected by extinction, will be excellent to compare with models of population synthesis. This would contribute to better understanding of the formation and evolution of Galactic PNe. In summary:

- Multi-wavelength properties are used to certify the CORNISH-PNe classification and confirm a clean sample, although optical or NIR spectrum is needed to fully confirm the status of a PN.
- Radio properties show a CORNISH-PNe sample that is compact, with some PNe possessing $T_B > 1000$ K. Spectral indices were estimated for 127 of the CORNISH-PNe (75%). 98% of these have spectral indices that are consistent with thermal free-free emission. The 2% exhibiting non-thermal emission at a 3σ significance level are likely very young PNe.
- 23 out of the 76 CORNISH-PNe within the IPHAS survey region were found to have Hα emitting counterparts. The PNe not detected by IPHAS are likely due to line-of-sight extinction.
- In the MIR, the broad distribution of the CORNISH-PNe colours show a sample dominated by different emission mechanisms across the different IRAC bands. This broad distribution is also observed in NIR colours.
- Some of the CORNISH-PNe, as expected, show higher reddening compared to previous PNe samples studied in the NIR.

- In the FIR, the CORNISH-PNe show a wider range of colours compared to the optically detected PNe studied by Anderson *et al.* (2012).
- Extinction was estimated using the methods in Section 2.7. Extinction variations towards the CORNISH-PNe using the different methods reflect a sample dominated by different emission mechanisms across the near-infrared bands, hence a possible range of intrinsic colours.
- Heliocentric distances were estimated using the Frew *et al.* (2016) calibration. The average distance for the CORNISH-PNe is $\sim$ 15 kpc with a corresponding average physical diameter of 0.18 pc.
- A catalogue of 169 CORNISH-PNe is presented. 90 are classified as new PNe, out of which 12 are newly discovered and 78 are newly classified as PN. A further 47 suspected PNe are confirmed as such from the analysis here and 24 known PNe were detected. Eight sources are classified as possible PNe or other source types.
- The clean sample of PNe, together with the extensive photometry and analysis presented here should form good training sets in using machine learning to build classification/identification models for PNe in future large radio surveys.

Table 2.7: *Final catalogue of the CORNISH–PNe with classifications.*

Name	SIMBAD ID	Hα detection	class	Status	Comments
G009.9702–00.5292	pAG[1] (IRAS 18066–2034)	–	PN	Newly classified	
G010.4168+00.9356	pAG[2] (IRAS 18021–1928)	SHS	PN	Newly classified	
G010.5960–00.8733	star (IRAS 18092–2012)	–	PN	Newly classified	
G011.3266–00.371	YSO?[3]	–	PN	Newly classified	
G011.4290–01.0091	–	–	PN	Newly discovered	
G011.4581+01.0736	pAG[1] (IRAS 18038–1830)	–	PN	Newly classified	
G011.7210–00.4916	-	–	PN?	Newly discovered	FIR colours are upper limits
G012.0438–00.5077	–	–	PN?	Newly discovered	FIR colours are upper limits
G012.1157+00.0757	Radio source[5].	SHS	PN	Newly classified	
G012.1528–00.3304	YSO?(J18132367–1833495)[3]	–	PN	Newly classified	
G012.3830+00.7990	PN?[7] (IRAS 18067–1749)	–	PN	Newly confirmed	
G012.6012+00.5592	YSO?[3] (IRAS 18081–1745)	–	PN	Newly classified	
G013.3565–00.7559	YSO?[3]	–	PN	Newly classified	
G013.6313–00.6023	Radio source[5]	–	PN	Newly classified	
G013.9166+00.6500	PN? [8]	–	PN	Newly confirmed	
G014.2365+00.2117	PN?[9]	SHS	PN	Newly confirmed	
G014.4573–00.1847	Radio source[10]	–	PN	Newly classified	
G014.5851+00.4613	PN?[26]	IPHAS	PN	Newly confirmed	
G014.7503–00.2496	Radio source[10]	-	PN	Newly classified	
G014.8960+00.4837	YSO?[3]	SHS	PN	Newly classified	
G015.1999–00.0863	Radio source[10]	–	PN	Newly classified	
G015.5410+00.3359	Radio source[10]	–	PN	Newly classified	

Continued on next page

Table 2.7 – continued from previous page

Name	SIMBAD ID	Hα detection	class	Status	Comments
G015.5847+00.4002	Radio source[10]	–	PN	Newly classified	
G015.7993–00.0063	PN[9]	–	PN	Newly confirmed	
G016.0550+00.8280	PN[9]	SHS	PN	Newly confirmed	
G016.4034–00.5740	Radio source[5]	–	PN	Newly classified	
G016.4276+01.0072	–	–	PN	Newly discovered	
G016.4999+00.1152	Radio source[5]	–	PN	Newly classified	NIR colours have stellar contamination
G016.6002–00.2754	Radio source[10]	–	PN	Newly classified	
G017.0152–00.1906	Radio source[10]	–	PN	Newly classified	
G017.3669+00.5224	PN?[11]	–	PN	Newly confirmed	
G017.4147+00.3791	Radio source[5]	–	PN	Newly classified	
G017.4487+00.1146	Radio source[10]	–	PN	Newly classified	
G017.7250–00.2427	Radio source[10]	SHS	PN	Newly classified	
G017.8222+00.9866	–	SHS	PN	Newly discovered	
G017.8645+00.2120	YSO?[3] (IRAS 18198–1318)	–	PN	Newly classified	
G018.1286–00.2189	–	–	PN?	Newly discovered	FIR are upper limits
G018.2402–00.9152	PN [9]	IPHAS	PN	Newly confirmed	
G018.2413–00.5552	YSO?[3]	–	PN	Newly classified	Has no FIR colours
G018.5242+00.1519	YSO?[6]	–	PN	Newly classified	
G018.5776–00.7484	–	–	PN	Newly confirmed	
G019.2356+00.4951	Radio source[5]	–	PN	Newly classified	
G019.4676–00.0154	Radio source[10]	–	PN	Newly classified	
G019.9298–00.6639	IR (IRAS 18270–1153)	–	PN	Newly classified	
G020.5176+00.4778	Radio source[5]	SHS	PN	Newly classified	

Continued on next page

Table 2.7 – continued from previous page

Name	SIMBAD ID	Hα detection	class	Status	Comments
G020.6015+00.0206	-	-	PN	Newly discovered	Very resolved in the CORNISH survey compared to the MAGPIS but a clear nebula in the 24 μm. Heavy stellar contamination in the NIR and MIR
G020.9782+00.9253	PN?	SHS	PN	Newly confirmed	
G021.1653+00.4755	PN[9] (IRAS 18252–1016)	SHS	PN	Newly confirmed	
G021.3425–00.8423	PN[9] (IRAS 18303–1043)	–	PN	Newly confirmed	
G021.6657+00.8110	PN[25]	IPHAS	PN	Newly confirmed	
G021.6849–00.7381	Radio source [5]	SHS	PN	Newly confirmed	
G021.9972–00.8838	-	–	PN	Newly discovered	
G022.5477–00.1061	Radio source[10]	–	PN	Newly classified	
G022.6429–00.4422	YSO?[3]	–	PN	Newly classified	
G022.6580+00.2959	Radio source[10]	–	PN	Newly classified	
G023.2321+00.0809	Radio source[10]	–	PN	Newly classified	
G023.4181–00.3940	PN[9] (IRAS 18326–0840)	–	PN	Newly confirmed	
G023.5044–00.5245	Star (IRAS 18332–0839)[5]	–	PN	Newly classified	
G023.8214–00.5788	PN[9]	–	PN	Newly confirmed	
G023.8897–00.7379	PN[13] (IRAS 18347–0825)	–	PN	Newly confirmed	
G024.0943–01.0992	–	–	Radio star?	Newly discovered	Upper limits on FIR colours
G024.1659+00.2502	H II region[14]	–	PN	Newly classified	
G024.3852+00.2869	PN[9]	–	PN	Newly confirmed	
G024.7921–01.0043	IR(IRAS 18373–0744)	SHS	PN	Newly classified	

Continued on next page

Table 2.7 – continued from previous page

Name	SIMBAD ID	Hα detection	class	Status	Comments
G024.8959+00.4586	YSO?[3]	–	PN	Newly classified	
G025.0485–00.6621	PN[8]	–	PN	Newly confirmed	
G025.5190+00.2165	H II region [14]	–	PN	Newly classified	
G025.5769+00.1389	Radio source[10]	–	PN	Newly classified	
G025.8466+01.1718	PN?[13]	–	PN	Newly confirmed	No MIR data but PN colours in NIR and FIR
G026.0823–00.0347	Radio source[10]	–	PN?	Newly classified	Near dark filaments in the MIR but PN colours in the MIR and FIR
G026.1620+00.5926	–	–	PN	Newly discovered	
G026.2268+00.7685	–	–	PN	Newly discovered	
G026.6529+00.2874	Radio source[10]	–	PN	Newly classified	
G026.7145+00.1319	Radio source[10]	–	PN	Newly classified	
G027.4265–00.2499	YSO?[3]	SHS	PN	Newly classified	
G027.6595–00.3835	PN[9] (IRAS 18404–0455)	SHS	PN	Newly confirmed	
G027.6640–00.2485	–	–	PN? Radio star?	Newly classified	
G029.0538+00.9915	YSO?[3]	SHS	PN	Newly classified	
G029.1652–00.0168	Radio source[10]	–	PN	Newly classified	
G029.5780–00.2686	PN[24]	IPHAS	PN	Newly confirmed	
G029.8742–00.8190	PN[9] (IRAS 18461–0309)	–	PN	Newly confirmed	
G030.0226+00.1570	Radio source[10]	–	PN	Newly classified	
G030.0294–00.3318	Radio source[10]	–	PN	Newly classified	
G030.2335–00.1385	PN?[16] (IRAS 18443–0231)	–	PN	Newly confirmed	

Continued on next page

Table 2.7 – continued from previous page

Name	SIMBAD ID	Hα detection	class	Status	Comments
G030.5302+00.1315	Radio source[10]	–	PN?	Newly classified	
G030.6670–00.3319	PN[9] (IRAS 18458–0213)	–	PN	Newly confirmed	
G030.8560+00.3826	Radio source[10]	–	PN	Newly classified	
G031.2131–00.1803	OH & H_2O maser[17]	–	PN	Newly classified	
G031.3724–00.7514	PN? (J18511825–0143487)	–	PN	Newly confirmed	
G032.3076+00.1536	PN[16] (IRAS 18471–0032)	–	PN	Newly confirmed	
G032.6136+00.7971	PN?[9]	IPHAS	PN	Newly confirmed	
G032.8082–00.3159	Radio source[10]	–	PN	Newly classified	
G032.8177–00.1165	–	–	PN	Newly discovered	
G033.1198–00.8949	–	–	PN	Newly discovered	
G033.3526+00.4043	YSO?[3](IRAS 18482+0029)	–	PN	Newly classified	
G033.7952+00.4307	YSO?[3]	–	PN	Newly classified	
G033.9059–00.0436	PN[9]	–	PN	Newly confirmed	
G034.1792–00.1777	Radio source[10]	–	PN	Newly classified	
G034.4200–00.3183	PN[9]	–	PN	Newly confirmed	
G034.8624–00.0630	PN[9]	–	PN	Newly confirmed	
G035.2162+00.4280	Radio source[10]	–	PN	Newly classified	
G035.4719–00.4365	Radio source[10]	IPHAS	PN	Newly classified	
G035.5654–00.4922	PN?[27]	IPHAS	PN	Newly confirmed	
G036.0116–00.2562	Radio source[10]	–	PN	Newly classified	
G036.5393+00.2003	Radio source[10]	–	PN	Newly classified	
G037.9031–00.2754	YSO?[3]	–	PN	Newly classified	
G037.9601+00.4534	PN[9]	–	PN	Newly confirmed	
G038.9237–00.0807	Radio source[10]	–	PN	Newly classified	

Continued on next page

Table 2.7 – continued from previous page

Name	SIMBAD ID	Hα detection	class	Status	Comments
G039.1617+00.7826	PN?[8]	–	PN	Newly confirmed	
G039.5911–00.3785	–	–	PN	Newly discovered	
G040.2606–00.2755	YSO[9] (IRAS 19034+0618)	–	PN	Newly classified	
G040.3359–01.0102	–	–	PN	Newly discovered	
G041.1982+00.0348	YSO?[3] (IRAS 19040+0717)	–	PN	Newly classified	
G041.3540+00.5390	Radio source[5]	IPHAS	PN	Newly classified	
G041.7871+00.4884	YSO?[3]	–	PN	Newly classified	
G042.6629–00.8648	PN?[20,8] (PM 1–288)	–	PN	Newly confirmed	
G043.0281+00.1399	PN[9] (IRAS 19071+0857)	–	PN	Newly confirmed	
G043.2946–00.6455	PN[9]	–	PN	Newly confirmed	
G043.5793+00.0261	PN[16]	–	PN	Newly confirmed	
G043.6554–00.8279	IR (IRAS 19117+0903)	IPHAS	PN	Newly classified	
G044.6375+00.4827	YSO?[3] (IRAS 19089+1032)	IPHAS	PN	Newly classified	
G045.1801+00.9893	Radio source[21]	–	PN	Newly classified	
G045.2830–00.6278	PN[16] (J19163050+1040563)	–	PN	Newly confirmed	
G046.9747+00.2702	YSO?[3] (IRAS 19141+1230)	–	PN	Newly classified	
G047.6884–00.3024	PN[9,1]	–	PN	Newly confirmed	
G047.9875+00.2026	star (IRAS 19163+1322)	–	PN	Newly classified	
G048.5619+00.9029	YSO?[3]	IPHAS	PN	Newly classified	
G048.6748–00.5350	YSO?[3]	–	PN	Newly classified	
G048.7319+00.9305	PN[24]	IPHAS	PN	Newly confirmed	
G049.6948+00.8642	PN?[22] (J19193387+1516421)	–	PN	Newly confirmed	
G050.0003+00.5072	YSO? [3]	–	PN	Newly classified	

Continued on next page

Table 2.7 – continued from previous page

Name	SIMBAD ID	Hα detection	class	Status	Comments
G050.0457+00.7683	PN?[9]	–	HII region?	Newly classified	
G050.4802+00.7056	PN?[24]	IPHAS	PN	Newly confirmed	
G050.5556+00.0448	PN[9]	IPHAS	PN	Newly confirmed	
G050.8950+00.0572	YSO?[3] (J19245196+1557287)	–	PN	Newly classified	
G051.6061+00.9140	YSO?[3] (IRAS 19209+1653)	–	PN	Newly classified	
G052.1498–00.3758	Radio source[5]	–	PN	Newly classified	
G057.5352+00.2266	Radio source[21]	–	PN	Newly classified	
G058.1591–00.5499	Radio source[21]	–	PN	Newly classified	
G058.6410+00.9196	PN[23] – IRAS 19353+2302	IPHAS	PN	Newly confirmed	
G059.8236–00.5361	PN?[16] (IRAS 19434+2320)	IPHAS	PN	Newly confirmed	
G060.8480–00.8954	YSO?[3]	–	PN	Newly classified	
G060.9866–00.5698	Radio source[5]	IPHAS	PN	Newly classified	
G062.7551–00.7262	PN[24]	IPHAS	PN	Newly confirmed	
G063.0455+00.5977	–	–	PN	Newly discovered	

pAG: post–AGB star, SgrS: Super–giant star, IR source: Infrared source. The questionmark (?) in front of some of the source classification indicates 'possible'. e.g. pAG? is a possible post-AGB star

[1](Kohoutek, 2001), [2] (Ratag & Pottasch, 1991),[3] (Robitaille *et al.*, 2008), [4] (Rosolowsky *et al.*, 2010),[5] (Zoonematkermani *et al.*, 1990), [6] (Felli *et al.*, 2002),[7] (Hoare *et al.*, 2012), [8] (Condon *et al.*, 1999), [9] (Urquhart *et al.*, 2009b),[10] (Becker *et al.*, 1994), [11] (Anderson *et al.*, 2011),[12] (Parker *et al.*, 2012a),[13] (Kistiakowsky & Helfand, 1995),[14] (Anderson *et al.*, 2015), [15] (Sewilo *et al.*, 2004),[16] (Kanarek *et al.*, 2015), [17] (Caswell, 2001), [18] (Szczerba *et al.*, 2007), [19] (Suárez *et al.*, 2006a), [20] (Preite-Martinez, 1988), [21] (Taylor *et al.*, 1996), [22] (Phillips & Ramos-Larios, 2008) , [23] (van de Steene & Pottasch, 1995),[24] (Sabin *et al.*, 2014), [25] (van de Steene *et al.*, 1996),[26] (Miszalski *et al.*, 2008),[27] (Parker *et al.*, 2006)

Chapter 3

Planetary Nebulae in the Southern Galactic Plane

3.1 Introduction

The science goals and motivation of the CORNISH survey are described by Hoare *et al.* (2012). Observations of compact ionized regions, such as PNe, at radio frequencies where they are optically thin are particularly important in their search and studies. In the southern Galactic mid-plane, however, there is no existing radio survey that is sufficient for the search and studies of such compact objects. Previous radio surveys in the southern Galactic plane include the MGPS (Green, 1999; Murphy *et al.*, 2007) at 843 MHz with a resolution of $45''$, the 1.4 GHz SGPS covering the $253^\circ < l < 358^\circ$; $|b| < 1^\circ.5$ region, with a resolution of $100''$ and sensitivity of 1 mJy/beam (Haverkorn *et al.*, 2006; McClure-Griffiths *et al.*, 2005) and, the AT20G blind survey, at 20 GHz, covering the southern sky. Subsequent follow-up observations of the AT20G survey were carried out at 5, 8 and 20 GHz, achieving a resolution of 10, 5 and $\sim 11''$, respective, and a flux density limit of 40 mJy. However, the coverage of the follow-up observations at these frequencies (5, 8 and 20 GHz) excluded the $|b| < 1^\circ.5$ region (Massardi *et al.*, 2011; Murphy *et al.*, 2010). These surveys are limited in coverage, resolution and sensitivity

and therefore, insufficient for the studies of compact ionized regions, towards the Galactic mid-plane.

The southern counterpart of the CORNISH survey covers the same region as the GLIMPSE survey, defined by longitude $295^\circ < l < 350^\circ$ and latitude $|b| < 1^\circ$. It is comparable in sensitivity and resolution to multi-wavelength surveys of the southern Galactic plane, at infrared and optical wavelengths. These surveys include the Hi-Gal (Molinari *et al.*, 2010) , GLIMPSE (Carey *et al.*, 2009; Churchwell *et al.*, 2009), VPHAS+ (Drew *et al.*, 2014) and VVV (Minniti *et al.*, 2011) surveys. Availability of comparable radio data to such multi-wavelength data provides a means to properly search for, idenitify and characterize compact ionized regions towards the Galactic mid-plane, while unaffected by extinction.

In this chapter, the calibration and imaging of the CORNISH survey in the southern Galactic plane is presented. Source finding, measured properties of the general catalogue and a catalogue of candidate PNe are also presented.

3.2 Observation Overview

The CORNISH program observed the southern Galactic plane with the ATCA array, using the maximum 2 GHz bandwidth of the CABB (Compact Array Broadband Backend) correlator (Wilson *et al.*, 2011). Observations were carried out for about 450 hours at two different frequency bands (4.5 - 6.5 GHz and 8 - 10 GHz), centred on 5.5 GHz and 9 GHz, simultaneously. The 6A configuration was used and the survey achieved a resolution of $2.5''$. It covered an area of 110 deg^2, defined by the $295^\circ < l < 350^\circ$ and $|b| \leq 1^\circ$ region of the southern Galactic plane. It implemented on-the-fly (OTF) interferometry for scanning, such that the antennas are scanning continuously, while the phase centre is sequentially moved in a traditional mosaic pattern. This resulted in a doubling of the uv-coverage and an elongated primary beam[11].

[11] http://www.narrabri.atnf.csiro.au/observing/users_guide/html/atug.html

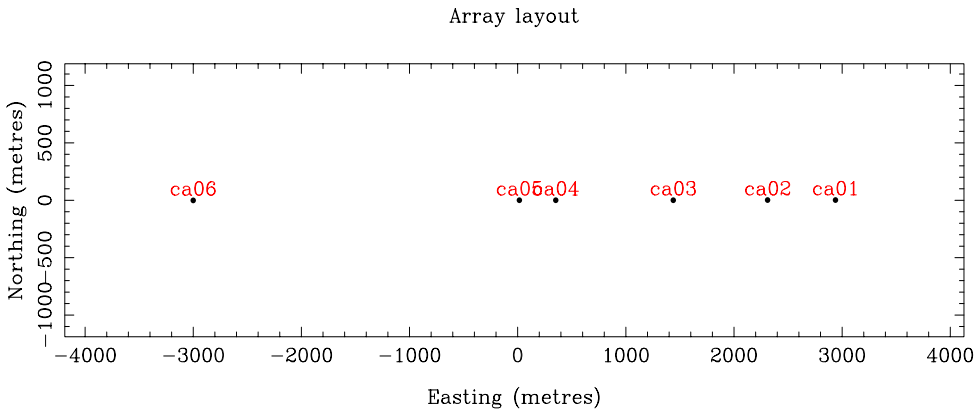

Figure 3.1: *The East-West layout of the ATCA array.*

The mosaic was scanned in Galactic latitude, which required ∼18 pointings to cover the 2° of a row. At a scan rate of 7.4′/10s, each row was completed in 3.2 minutes, including turn around time. A secondary calibrator was then observed for 2 mins after observation of 8 rows for 25 mins. A further 8 rows were observed with a secondary calibration to complete a block of observation for a total of 54 mins. To achieve an optimum uv-coverage, this was repeated 11 times, resulting in 1.8 mins on-source. A total of 12 hours was spent on each block, including flux calibration and set up time. Each 16 row block covers 1.7° and so, 33 of the $1.7° \times 2°$ were required to cover the survey area. The survey achieved a sensitivity of 0.2 mJy/beam at 5.5 GHz.

The 5.5 GHz is spread over a bandwidth of 2048 MHz, consisting of 2048 channels, each of 1 MHz. The position of each antenna in the the ATCA array is shown in Figure 3.1 and observation parameters are summarized in Table 3.1. Observations were carried out with all six antenna between 2010 and 2012 and six secondary calibrators were used to cover the whole survey region (Table 3.2).

3.3 Data Flagging and Calibration

Due to the large dataset and the need for uniform calibration and imaging, a semi-automated pipeline written in python was used to directly interface with

Table 3.1: *Summary of observation parameters.*

Parameters	Values
Number of antennas	6
Number of baselines	15
Observation period	2010 to 2012
Observing frequency	5.5 GHz
Observation region	$295^\circ < l < 350^\circ$; $\lvert b \rvert \leq 1^\circ$
Bandwidth	2048.0 MHz
Channel	2049
Longest baseline	6 km
Size of single dish	22 m
Field of view/Primary beam	$\sim 10^{'}$
Synthesized beam	$2.5^{''}$
Sensitivity	0.2 mJy/beam

the Multichannel Image ReconstructionImage Analysis and Display (MIRIAD) software (Sault *et al.*, 1995) and SQLite database server. The SQLite database was used for book-keeping during the whole process of flagging, calibration, imaging and source cataloguing process. The calibration and imaging pipeline was developed for the CORNISH survey by Purcell, C[12].

Observations for each day or block were labelled in the format of YEAR-MONTH-DAY e.g. 2010-11-01. The full obervation was spread across 33 blocks, each running for 12 hours and can be categorized into two epochs (see Figure 3.2), based on the observation period. Fields that were misssed due to bad weather or correlator problems were repeated at later dates. The data has a total of 104,544 pointings and the typical pointing pattern for a 12 hour observation (i.e a block) is presented in Figure 3.3.

Each day's observation was treated separately. The raw data were converted to a MIRIAD format using the ATLOD task and 5% of the edge channels were flagged out, including self-interference, autocorrelation or cross-correlation data, known bad channels and known RFI. The system variables such as the uv-coverage, seeing monitor versus time, XY-phase versus time and system temperature versus

[12] http://web.science.mq.edu.au/~cpurcell/public/index.php

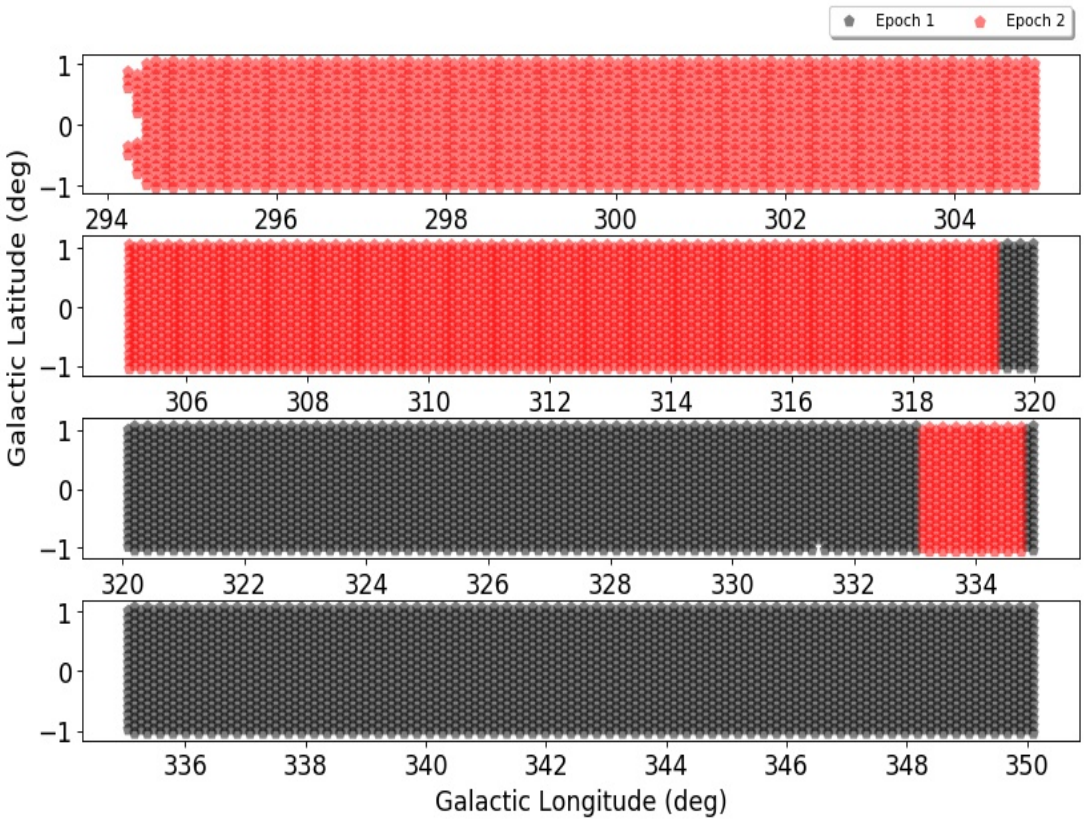

Figure 3.2: *Observation epochs. Epoch 1 (black shaded regions)is defined by block 2010-12-21 to 2011-01-07 and epoch II (red shaded regions) is defined by 2011-12-20 to 2012-01-07. Each pentagon represents a field.*

time (Figures B.1 to B.3) were inspected for each block of observation. These system variables allow quick identification of poor uv-coverage or times with bad visibilities. Additionally, the amplitude and phase variations with time were inspected visually before any flagging or calibration was done. This was to ensure that more data than required were not flagged and that the data are RFI free, which would affect the image fidelity when the data are inverted.

It was realised that the different epochs presented different flagging demands. All XX polarization data of all baselines to antenna ca01 were flagged for the first epoch. For the second epoch, the YY polarization data of all baselines to antenna ca01 were flagged instead. This is due to some ripple effect on the

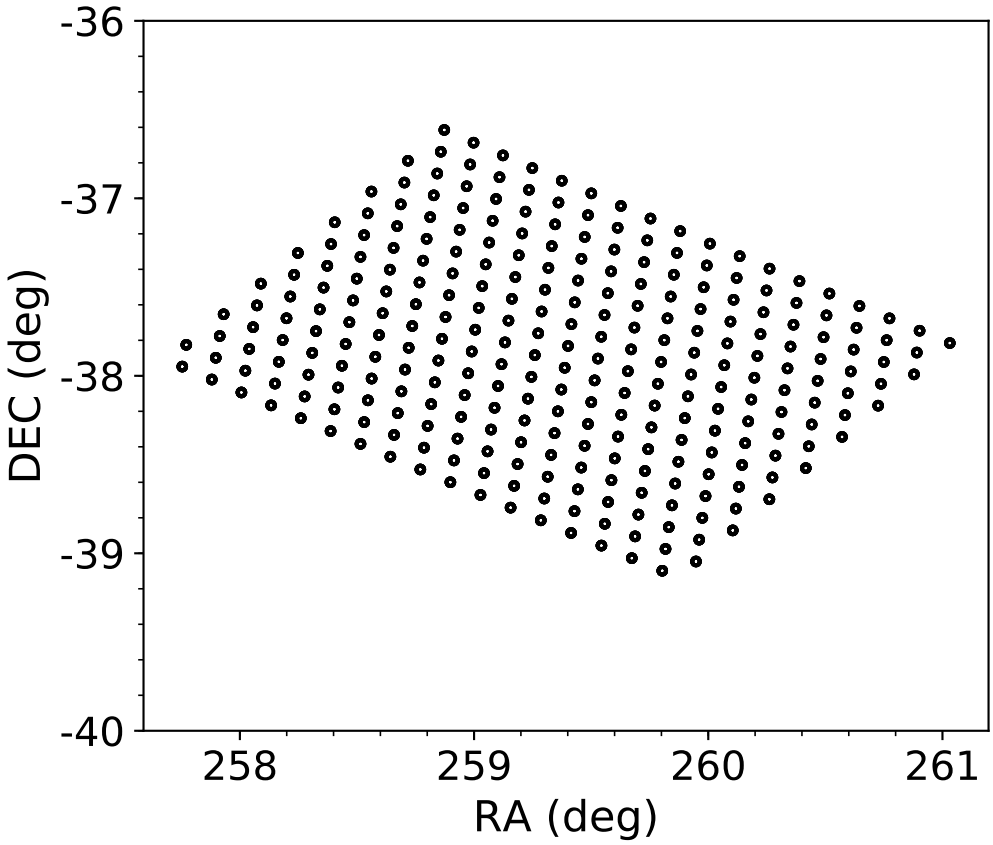

Figure 3.3: *Pointing pattern for a typical 12 hours observation of a block.*

bandpass, which could lead to false structures. The ripple effect is obvious when the bandpass solution is copied over to a strong source, such as the gain calibrator. An illustration of this effect is shown in Figure 3.4, where the ripple effect is not seen on the bandpass but is clearly seen on the test and gain calibrators (See https://atcaforum.atnf.csiro.au/viewtopic.php?f=11&t=184). If not flagged, it can affect the gain solutions as shown in Figure B.4. RFI and bad channels were flagged in both the time and frequency domain.

1934-638 was used as the primary bandpass and flux calibrator. A test calibrator (0823-500) was also observed, at the beginning of each observation, to substitute for bandpass and flux calibration, should the need be, e.g. in cases where 1934-638 could not be observed due to bad weather. When both are observed,

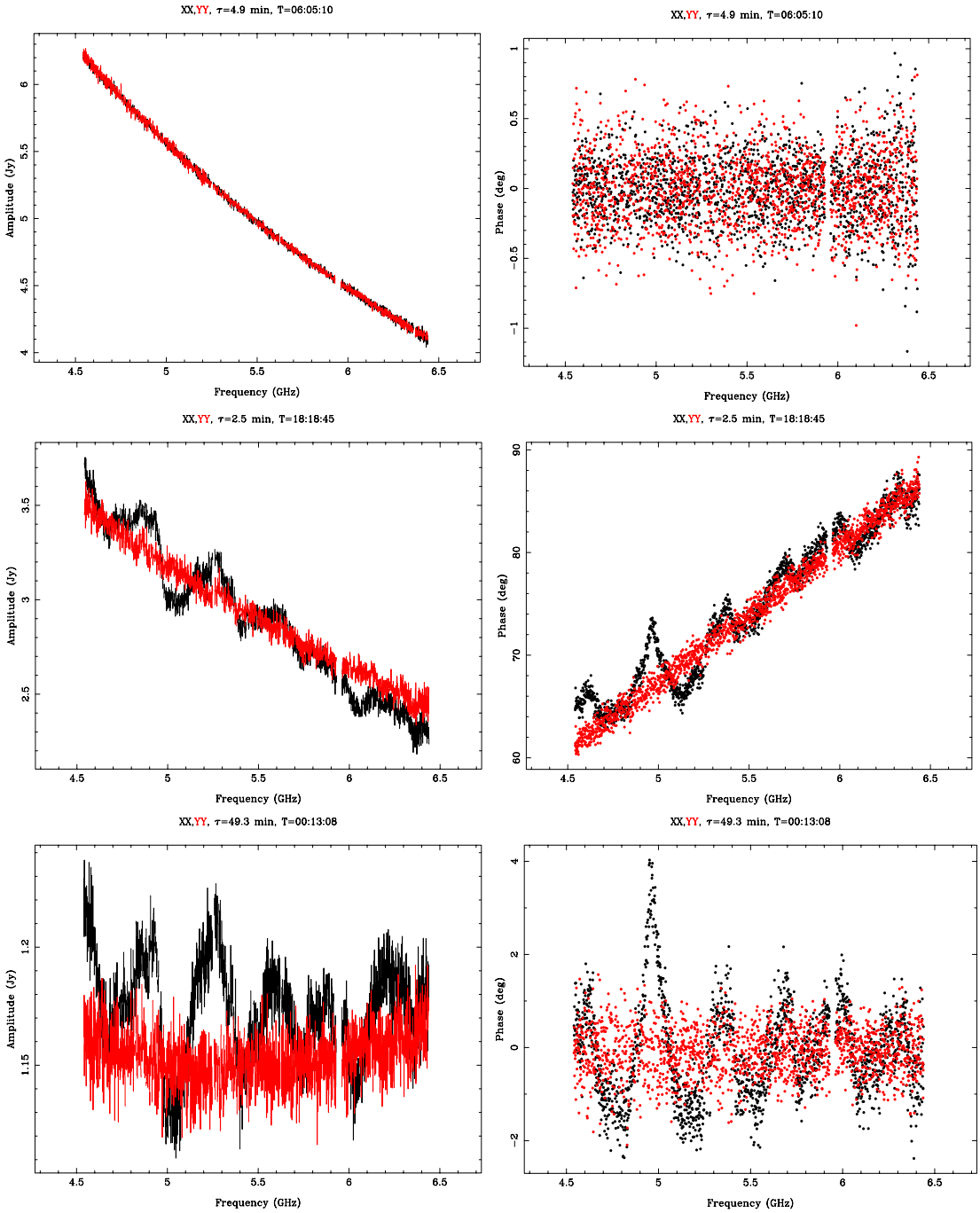

Figure 3.4: *Ripple effect on the bandpass calibrator as seen on the test and secondary calibrators. The top panel is the bandpass calibrator (1934-638), middle panel is the test calibrator (0823-500) and the lower panel is one of the secondary calibrators with the bandpass solution applied. The Y-axis on the left is amplitude and phase on the right panel. The X-axis is frequency.*

Table 3.2: *Secondary calibrators for each block of observations and the longitude range (long.range).*

Obs.Day	Calibrator	long.range	Obs. Day	Calibrator	long.range
2010–12–21	1714–397	348.5 - 350.0	2011–12–21	1511–55	317.8 - 319.4
2010–12–22	1729–37	346.8 - 348.4	2011–12–22	1352–63	304.1 - 305.7
2010–12–23	1729–37	345.1 - 346.7	2011–12–23	1511–55	316.0 - 317.6
2010–12–24	1646–50	343.4 - 345.0	2011–12–24	1352–63,1511–55	314.3 - 315.9
2010–12–25	1646–50	341.7 - 343.3	2011–12–25	1352–63	310.9 - 312.5
2010–12–26	1646–50	340.0 - 341.6	2011–12–26	1352–63	309.2 - 310.8
2010–12–27	1646–50	338.3 - 339.9	2011–12–27	1148–671	297.2 - 298.8
2010–12–28	1646–50	336.5 - 338.2	2011–12–28	1148–671,1511–55	295.5 - 297.1
2010–12–29	1646–50	334.8 - 336.4	2011–12–29	1148–671	299.0 - 304.0
2010–12–30	1646–50	331.4 - 333.0	2011–12–30	1352–63	305.8 - 307.4
2010–12–31	1646–50	329.7 - 331.3	2011–12–31	1148–671	302.4 - 303.9
2011–01–01	1511–55,1646–50	328.0 - 329.6	2012–01–01	1148–671	300.7 - 302.3
2011–01–02	1511–55,1646–50	326.3 - 327.9	2012–01–02	1352–63,1148–671	307.5 - 309.1
2011–01–04	1511–55	324.6 - 326.2	2012–01–03	1148–671,1352–63	294.3 - 295.4
2011–01–05	1511–55	322.9 - 324.5	2012–01–04	1352–63	312.6 - 314.2
2011–01–06	1511–55	321.2 - 322.8	2012–01–05	1148–671,1352–63	301.5 - 326.2
2011–01–07	1511–55	319.5 - 321.1	2012–01–07	1352–63	310.1 - 310.8
2011–12–20	1646–50,1511–55	333.1 - 334.7			

1934-638 was the primary choice for flux calibration because it is brighter. The secondary calibrators for the entire observation are given in Table 3.2, with the corresponding observation block and longitude range. The location of each of these calibrators is also shown in Figure 3.6. For the days with two secondary calibrators, calibration was done separately and the solutions combined. Figures B.11 and B.12 show typical gain solutions in amplitude and phase, after flagging and calibration. Figures B.5 to B.14 show example plots of the visiblities before and after flagging and calibration of typical bandpass, gain calibrators and observed visibilities data.

All flagging and calibration parameters were determined manually for each block. Determined parameters were then put into a configuration file, such that the parameters were automatically applied when the pipeline was run. The work flow for the calibration process that is implemented in the pipeline is presented in Figure 3.5. This is adapted from the calibration of the CORNISH north dataset using AIPS (see Purcell *et al.* 2013).

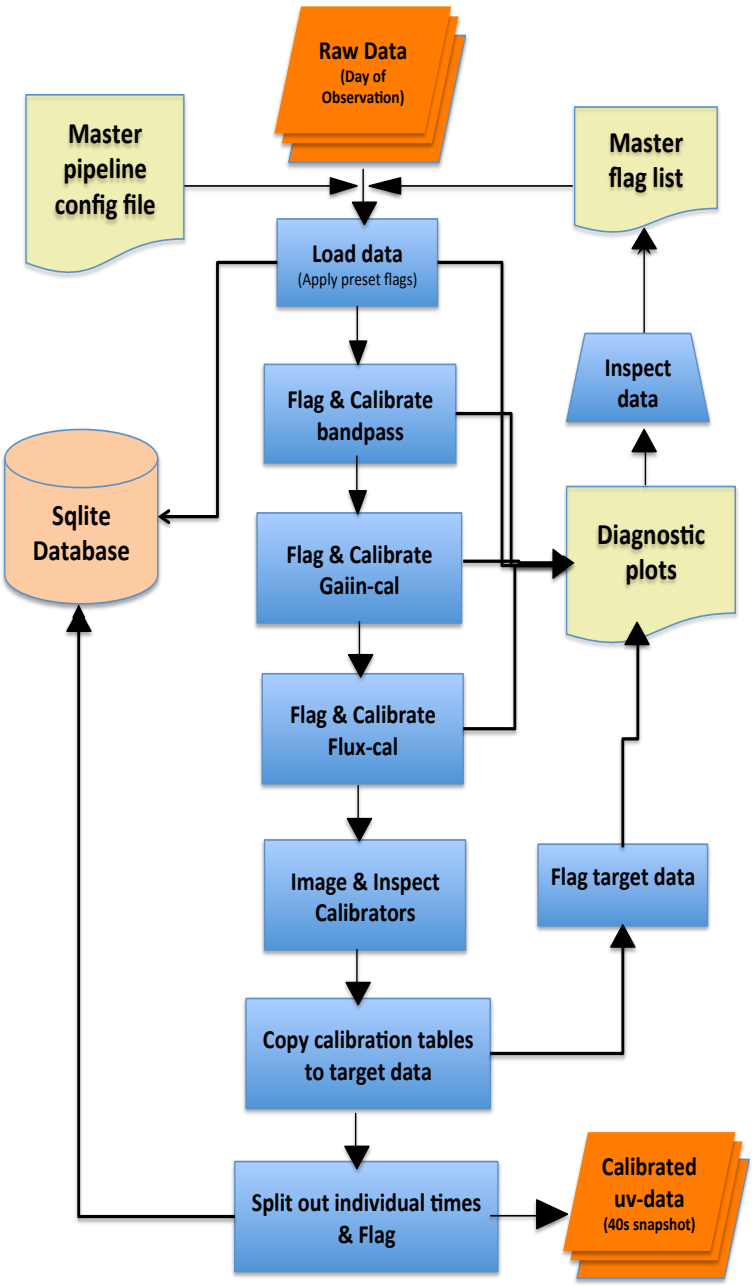

Figure 3.5: *Work flow of the calibration pipeline. This flow is adapted from the CORNISH north calibration pipeline by Purcell et al. (2013).*

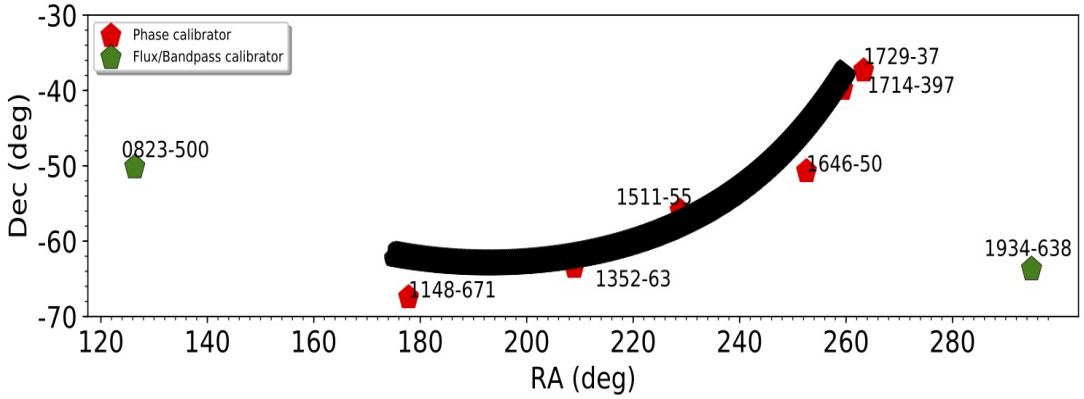

Figure 3.6: *Positions of the six secondary and two bandpass/flux calibrators within the survey region.*

3.4 Imaging

A brief theory behind imaging an interferomtric dataset is presented in Section 1.7.2. The imaging process was executed through an automated pipeline that is driven by a configuration file. The configuration file holds parameters that have been pre-defined (see Table 3.3). Images of the calibrators (Figure 3.7) were first inspected and they showed no jets or extended emission. For this reason, self calibration was not performed on the secondary calibrators. The calibrated visibilities were imaged using multi-frequency synthesis in MIRIAD (Sault & Conway, 1999). Multi-frequency synthesis accounts for the spectral index variation across the observation bandwidth of 2 GHz during the deconvolution process, using the MFCLEAN task in MIRIAD.

Each day's or block of observation is made up of 280 fields and each field is defined by $\sim$ 11 overlapping pointings. The fields were imaged separately by combining the uv-data of the overlapping pointings under a given field. Individual fields were imaged by iteratively cleaning down to a defined cut-off of 1.5 times the rms noise level in Stokes V map (mJy/beam). The rms was determined by first imaging a portion of the field in Stokes V, without cleaning. Stokes V maps usually have no sources or very few sources, since there are few circularly polarized sources at 5.5 GHz (Homan & Lister, 2006; Roberts *et al.*, 1975), hence is dominated by

thermal noise.

The dirty images were created using the robust weighting scheme (Briggs, 1995) of 0.5 robustness. The robust weighting scheme provides a trade-off between uniform and natural weighting schemes, which is a trade-off between resolution and sensitivity. The choice of 0.5 provides an improved sensitivity without sacrificing the resolution. A restoring Gaussian beam of $2.5''$ was defined for restoring the clean components. This value was determined from initial imaging of the individual fields, without constraining the beam. Figure 3.8 shows the distribution of the intrinsic major and minor axes of the dirty beam. The median of the major axis distribution is determined to be $2.5''$, which was then used as the restoring beam for uniformity across the survey region. This results in the super-resolution distribution presented in Figure 3.9 with a peak about 1.1 and maximum value that is less than 2.5.

3.4.1 Mosaicking

Individually imaged fields were linearly mosaicked onto overlapping $(60'') \sim 20' \times \sim 20'$ grid tiles, using LINMOS, a MIRIAD task[13]. The tiles are arranged in equatorial coordinates (J2000) and 1825 tiles were required to cover the survey region. LINMOS combines the overlapping region in a tile by minimizing the rms noise. Wide-band primary beam correction is performed by LINMOS for each field before linearly mosaicking.

To properly account for the geometry and avoid interpolation problems during mosaicking, the overlaping fields to be mosaicked should be on the same pixel grid. In order to do this, the option '*mosaic*' was used in INVERT and the coordinate of the pointing that is closest to the centre of each tile was used as a reference, using the '*offset*' key. If this is not done, the position of sources would be altered from one tile to another because LINMOS did not account for the geometric correction properly.

[13] https://www.atnf.csiro.au/computing/software/miriad/doc/linmos.html

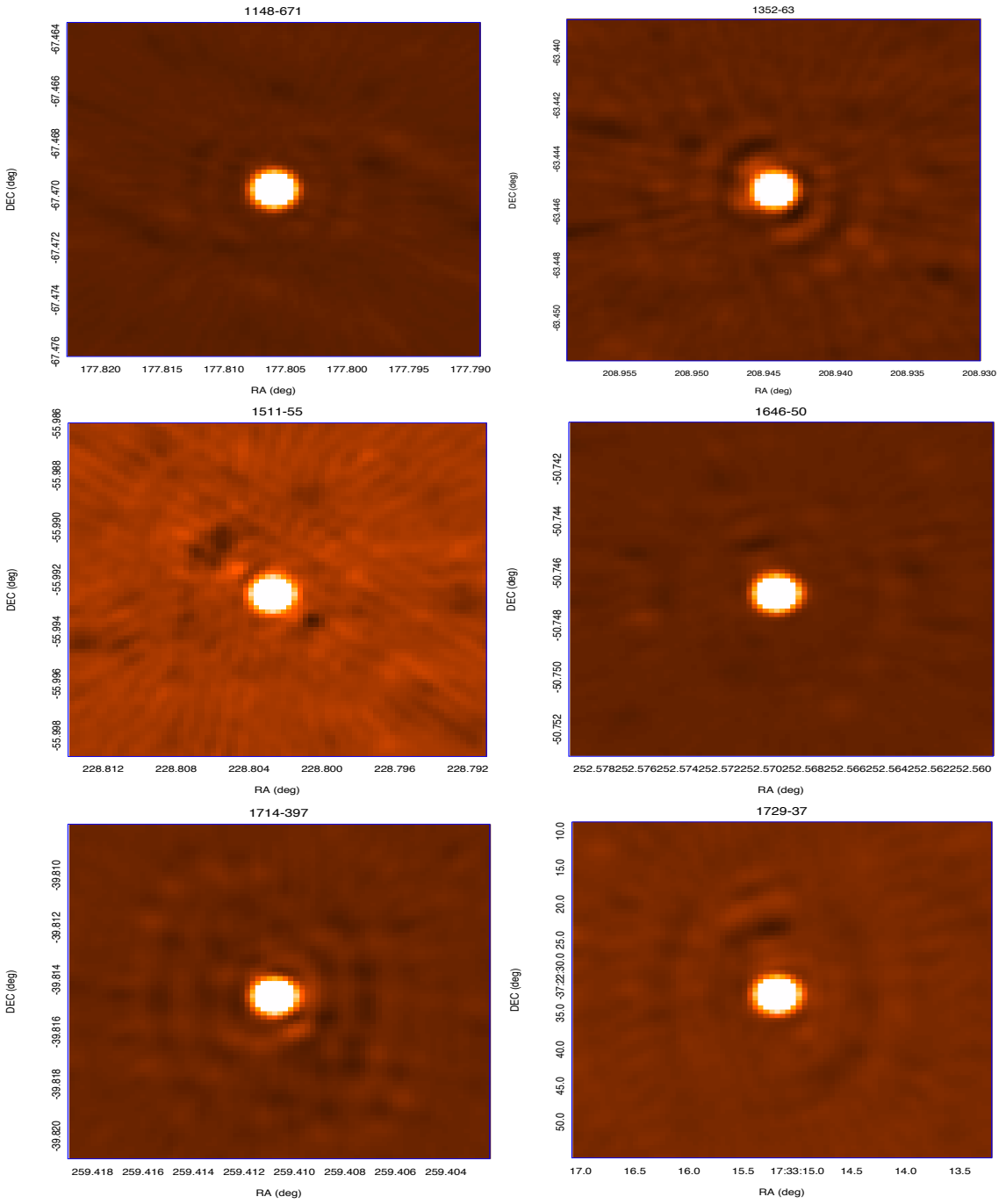

Figure 3.7: *Images of the secondary calibrators used for the entire survey region.*

Table 3.3: *Imaging parameters.*

Parameters	Values
Cell size	$0.6''$
Restoring Beam	$2.5''$, $2.5''$, $0''$
Field size	$\sim 10'$
RMS multiplier	1.5

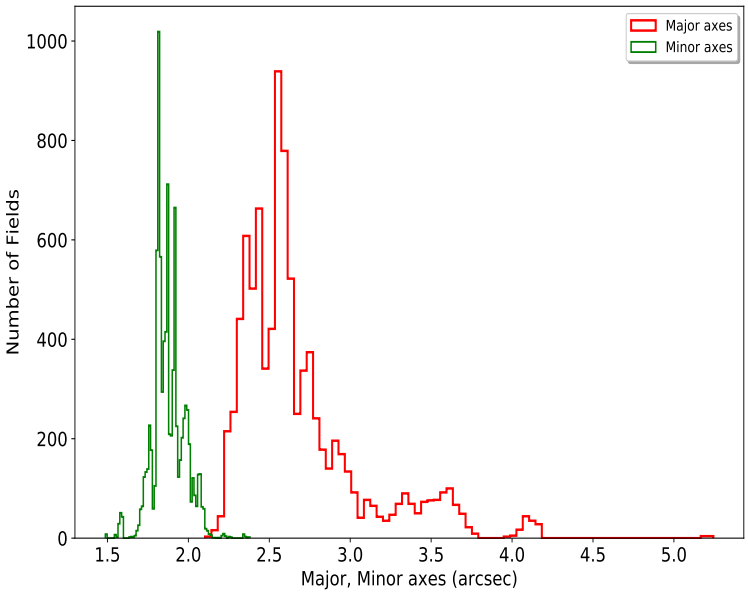

Figure 3.8: *Major and minor axes distribution of the imaged fields with a median major axis of $2.5''$.*

3.4.2 Synthesized Beam

The distributions of the beam major and minor axis are shown in Figure 3.8. The distribution of the major axis has a median of $2.5''$ and extends up to $5.5''$ with two peaks seen around 2.4 and $2.6''$. The minor axis shows a narrower distribution with a larger peak about $1.8''$. The elongation of the synthesized beam, the ratio of the major to the minor axis, is shown in Figure 3.10 with a peak less than 1.5. 96% of the fields have elongation $< 2''$. This means that there are a few fields where the major axis is 2 to 3.5 times the minor axis. The variation of the beam's major axis across the survey region is shown in Figure 3.11. The

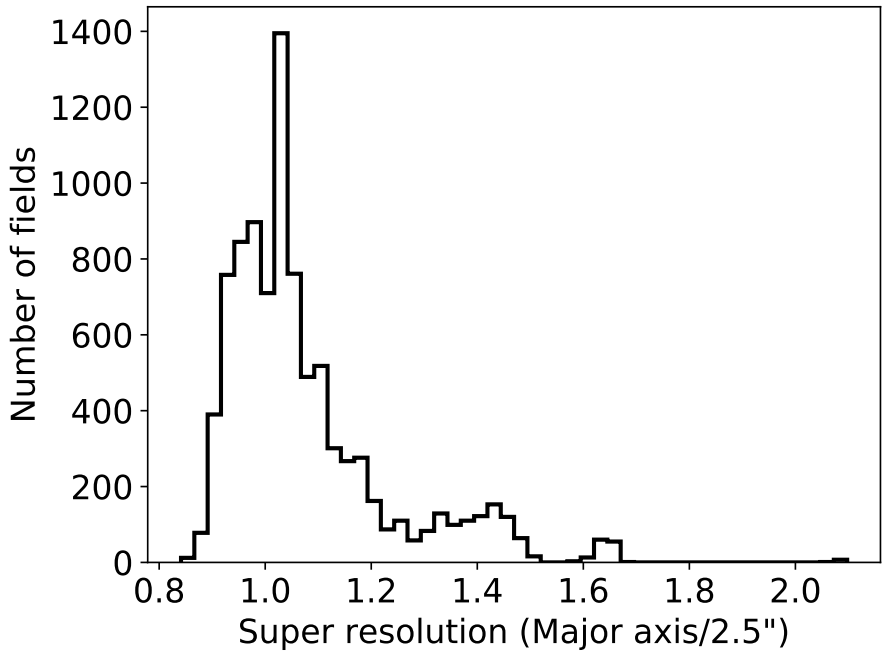

Figure 3.9: *Beam super-resolution distribution achieved with a restoring beam of 2.5″.*

fields with higher major axes in Figure 3.8 are also seen in Figure 3.11 within the longitude 333° to 335° region. There are also a few fields with high major axis seen from the longitude 344°. Figure 3.12 shows a scatter plot of the major axis against the minor axis, colour coded by the epoch. The second epoch shows a less elongated beam, with major axes lower than 3″ for 93% of the fields. The fields with higher major axes within the longitude 333° to 335° region are seen to come from the second epoch. This is due to scans that were not repeated during observation of the block (2011-12-20) covering the region. This results in a poor uv-coverage, due to fewer than the typical 11 pointings for each field. However, only a few fields were affected, making up about 6% of the second epoch data.

3.4.3 RMS Noise Level

The noise level achieved across the survey region in CLEANed Stokes I (see Figure B.15 for unCLEANed Stokes V map) is shown in Figure 3.13, which is

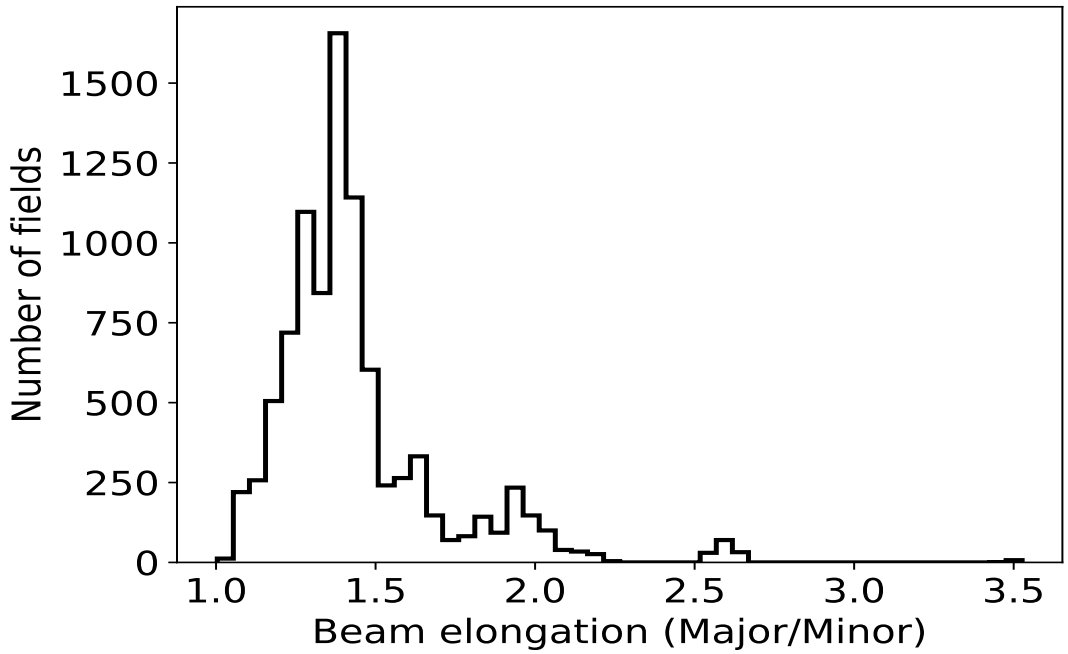

Figure 3.10: *Beam elongation across the survey region.*

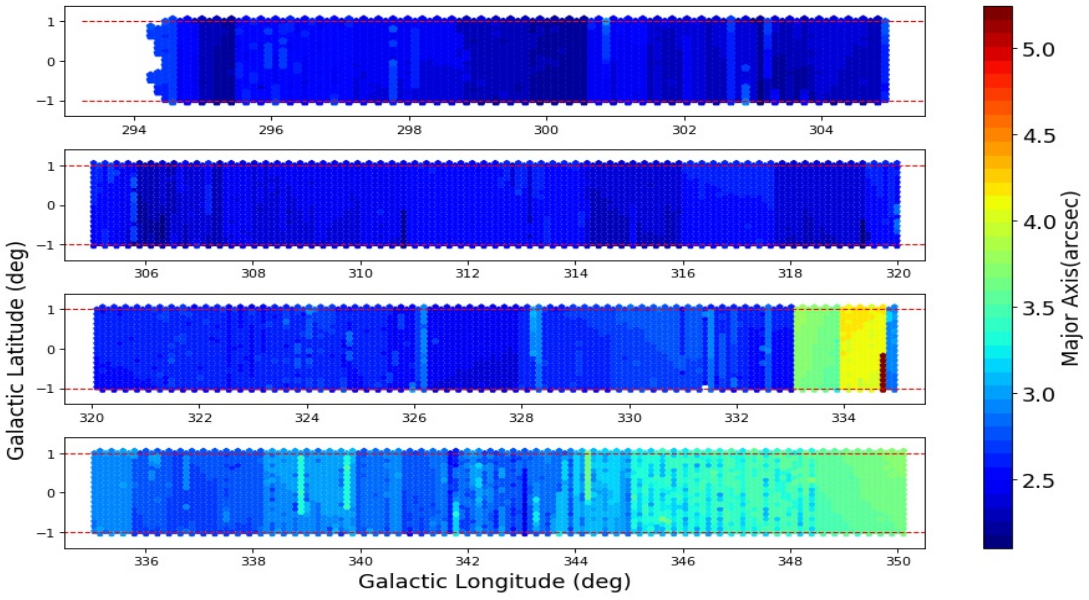

Figure 3.11: *The variation of the major axis of the synthesized beam across the survey region.*

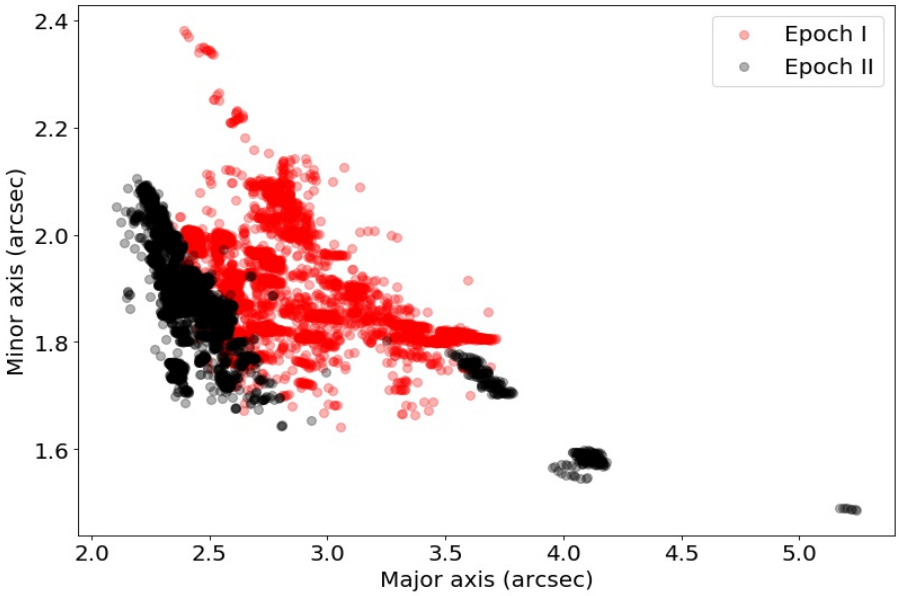

Figure 3.12: *Major axis versus minor axis of the synthesized beam across the survey, colour coded by the epoch.*

fairly uniform, having a mean of 0.1 mJy/beam. The noise level for the second epoch is better compared to the first epoch, except for the same region within the longitude 333° to 335° region. This is also observed in the major axis distribution. The noise level around a few very bright sources is particularly high.

In Figure 3.14, a plot of the noise level in Stokes I against Stokes V is shown (color coded by the two epochs). The noise level in Stokes V (mean of 0.2 mJy/beam) is higher compared to Stokes I but, it gives a better estimation of the expected theoretical rms noise of 0.2 mJy/beam. The noise level in Stokes V is higher because it is estimated from unCLEANed images and the noise has not been smoothed out by forcing a restoring beam, compared to the Stokes I images. A few fields are also observed in the second epoch to have higher noise levels, corresponding to the same fields with elongation $> 2''$.

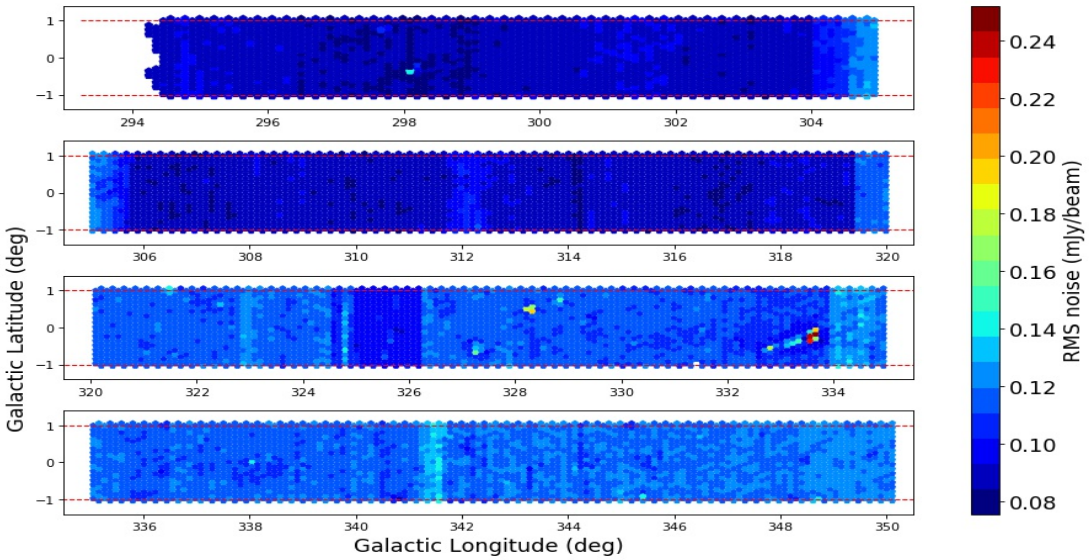

Figure 3.13: *The variation of the rms noise in Stokes I across the survey region.*

3.5 Catalogue

3.5.1 Source Finding

Source finding, measurement of source properties and cataloguing of sources were done using AEGEAN, an algorithm implemented in *python* by Hancock *et al.* (2012, 2018). AEGEAN uses the flood-fill algorithm, where two thresholds are defined (σ_f: flooding threshold, σ_s: seeding threshold), such that the seeding threshold is greater than the flooding threshold. The flooding threshold is used to grow an island and the seeding threshold is used to seed the island, such that all detected sources have signal-to-noise (SNR) $> \sigma_s$ (see Hancock *et al.* 2012). The AEGEAN algorithm detect sources by finding pixels above a defined flux threshold (σ_s), after subtracting the background, and then groups them into contigous islands.

In order to characterize the detected sources, AEGEAN assumes the sources are compact and can be described by Gaussians. With this assumption, each island is fitted with one or more overlapping Gaussians (see Figures 3.18, 3.19 and 3.20: left panel). This results in single islands having a single or multiple Gaussian

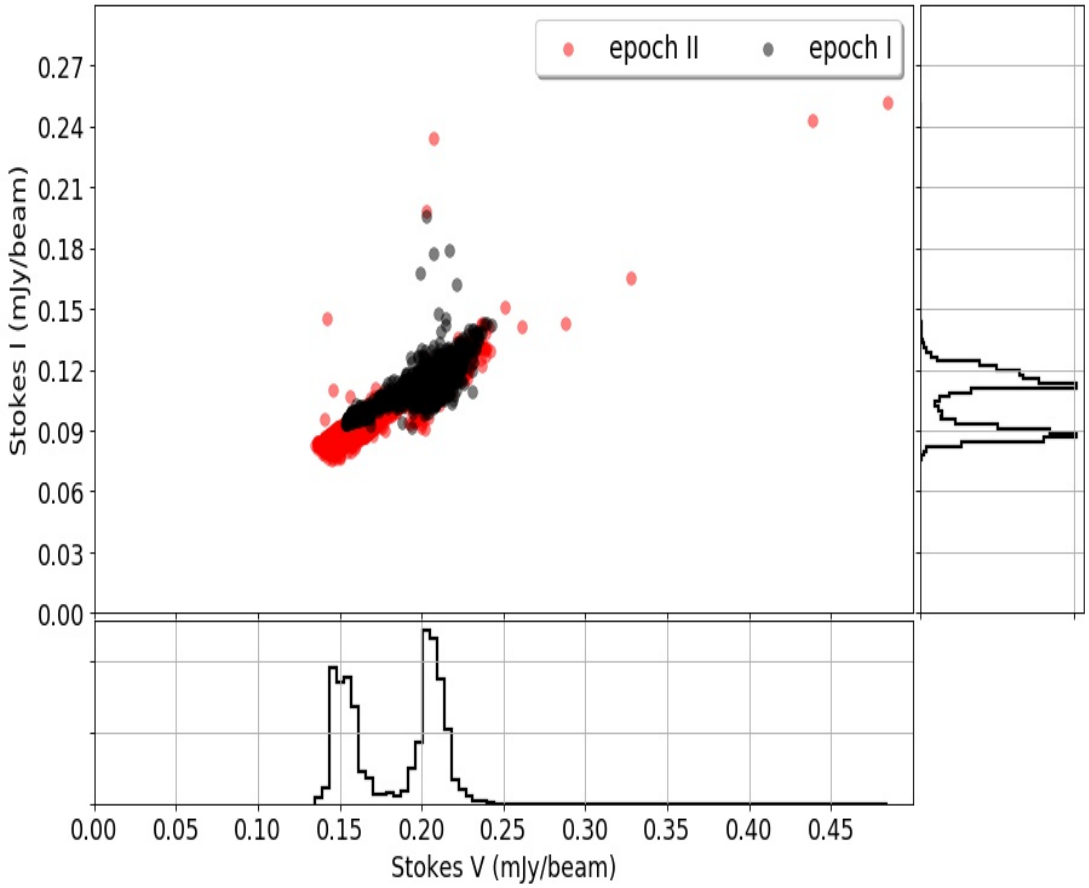

Figure 3.14: *Distribution of the rms noise in Stokes V and I images.*

fits. For a uniform catalogue, the source detection and characterization were automated, making full use of AEGEAN.

The background and noise estimation function (BANE) in AEGEAN was used to compute background and rms noise images for each tile. BANE estimates the background and rms by estimating the median and standard deviation of an image on a sparse grid of pixels, which is then interpolated to create the background and rms images. Because radio images do not have very complicated backgrounds, the noise properties across a $20^{'} \times 20^{'}$ tile may not change much. However, in high noise or complex regions, tracing HII regions, an appropriate grid size is needed to better estimate the background level and rms noise. Following this, a grid size that is 4 $\times$ beamsize ($10^{''} \times 10^{''}$) was used to estimate the background

and rms noise. Over this grid, the background would not be expected to change much and also bearing in mind that the smaller the size of the grid, the longer time it takes to compute the background and rms images.

3.5.2 Quality Control

Elimination of Spurious Sources

The choice of a cut-off threshold for a catalogue is a trade-off between completeness and reliability. A low threshold e.g. 3σ, will result in more sources but with many unreal sources, while a high threshold will result in a highly reliable catalogue but miss real sources with low surface brightness. In order to determine an appropriate cut-off threshold for a reliable catalogue, the number of spurious sources was estimated. Based on the analysis in Purcell *et al.* (2013), 15 tiles were selected to represent all 1825 tiles. These tiles were chosen such that there were no sources with very bright side lobes, contained point sources and fairly extended sources.

To estimate the number of spurious sources as a function of SNR (signal to noise ratio), the tiles were inverted by multiplying the pixel values in the tiles by -1. A detection threshold of 4.5 σ was used to search for sources on both set of tiles (normal and inverted tiles). To account for the number of detections across the survey region, the detections from the 15 tiles were multiplied by 122 (1825/15) to scale up the number of sources. Figure 3.15 shows a cumulative histogram of the detected sources before and after inversion, as a function of SNR. Detections below 5σ are dominated by spurious sources ($> 90\%$) as indicated by the grey shaded region. Spurious detections fall off steeply compared to real sources above 5σ and then shows a sharp fall to zero above 6σ.

Again, following the analysis in Purcell *et al.* (2013), if the source population is assumed to be governed by Gaussian statistics, the fraction, $f(\sigma)$, of the source population that falls within a given detection threshold is given by $f(\sigma) = 1 - \mathrm{erf}(\sigma/\sqrt{2})$ ($\mathrm{erf}(\sigma)$ is the Gaussian error function, given by equation 3.1). $f(\sigma)$ is plotted in Figure 3.15, assuming the total number of possible detections equals the

number of beams within the CORNISH survey region (2.02×10^8 beams). With this assumption, the total number of spurious sources is underestimated (blue dashed line). However, the number of sources can be used as a free parameter, resulting in a fit represented by the black line. The black line appears to predict the number of spurious sources at 4.5σ but falls off rather too steeply, compared to the number of spurious sources. Fitting f(σ) to bins higher than 5σ and adjusting the width of the Gaussian ($\sigma = 0.8\sigma_{\rm gauss}$) results in a better fit (green dashed line) and predicts the number of spurious sources to be less than 10 at 7σ. The number of spurious sources, however, decreases to 1 at 7.3σ.

Based on this analysis, the cut-off threshold for a reliable catalogue is accepted to be 7σ. A cut-off threshold of 5σ was initially used to search for sources and then aperture photometry (see Section 2.4) was used to remove sources below 7σ. This was done to account for the SNR ($S_{\rm peak}$/rms) of extended sources (see the next section). Based on Figure 3.15, a lower limit of ~ 3000 sources above 7σ are expected in the final catalogue.

$$\mathrm{erf}(\sigma) = \frac{1}{\sqrt{\pi}} \int_{-\sigma}^{\sigma} \mathrm{e}^{-\mathrm{t}^2} \mathrm{dt} = \frac{2}{\sqrt{\pi}} \int_{0}^{\sigma} \mathrm{e}^{-\mathrm{t}^2} \mathrm{dt} \tag{3.1}$$

Extended sources

Extended sources were automatically detected by searching for islands with more than one fitted Gaussian that are overlapping. A single optimal polygon was then defined to trace the outline of the island, enclosing the emission. In order to compute the polygon automatically, the following steps were carried out:

- The individual Gaussian fits were discretized by generating a polygon that approximates an ellipse, using the individual Gaussian Major, minor, positional angle and centres in equation 3.2. This is illustrated in Figure 3.16 (left) e.g. a Gaussian can be discretized into 10 points or 20 points.
- A convex hull was then computed that optimally surrounds all the generated points. A convert hull or envelope is the smallest polygon determined that encloses a set of points. To implement this, the position of the farthest

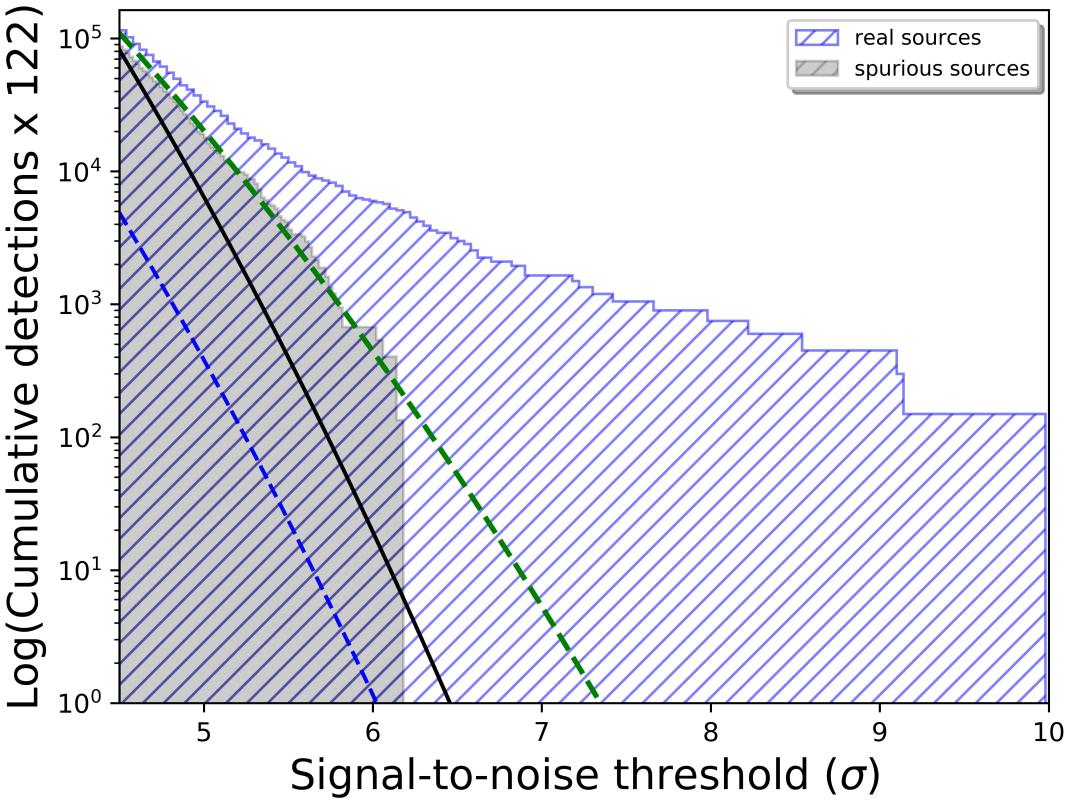

Figure 3.15: *Number of sources found as a function of signal-to-noise ratio for 15 real and inverted tiles. The hatched grey region represents spurious sources, while the hatched blue region represents real sources. The blue-dashed line represents the fit to the distribution of spurious sources, assuming the total number of possible detections equals the number of beams within the survey region. The black line represents the same fit but with the number of sources used as a free parameter, while the green-dashed line is the same fit as the black line but with* $\sigma = 0.8\sigma_{\rm gauss}$. *See section 3.5.2 for details.*

point on the left is determined (minimum x value) and, moving clockwise, the next farthest point is then determined, using the initial point as a pivot. This finally creates an envelope around the points as illustrated in Figure 3.16 (right).

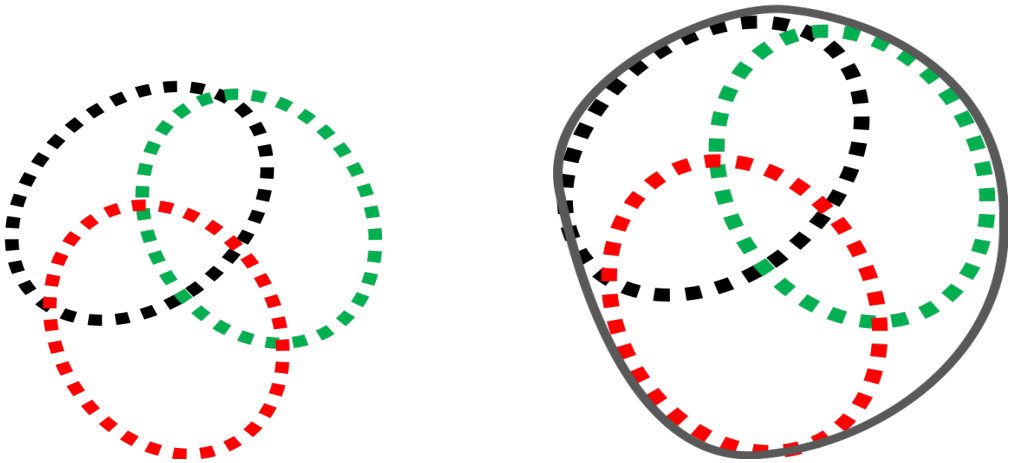

Figure 3.16: *Illustration on how the polygon is created for extended sources. The blue, green and black are polygons approximating three different Gaussians.*

$$\begin{aligned} \mathrm{x} &= \mathrm{xCen} + \mathrm{minAx}\ \cos(\mathrm{t})\cos(\mathrm{pa}) - \mathrm{majAx}\ \sin(\mathrm{t})\sin(\mathrm{pa}) \\ \mathrm{y} &= \mathrm{yCen} + \mathrm{minAx}\ \cos(\mathrm{t})\sin(\mathrm{pa}) + \mathrm{majAx}\ \sin(\mathrm{t})\cos(\mathrm{pa}) \end{aligned} \tag{3.2}$$

where $\mathrm{t} = 2\pi/\mathrm{npt}$ and npt is the number of points, xCen and yCen are the centre positions of the individual Gaussians, pa is the positional angle in radians, majAx and minAx are the major and minor axes.

Given the new generated polygons, new intensity weighted centres and diameters were determined for each extended source. The diameter was determined by the geometric mean of the distances between each point on the polygon and the intensity weighted centre (see Figure 3.17). The extent of the generated polygon is strongly affected by the extent of the individual Gaussians. Thus, before generating the polygons, there was the need to remove side-lobes and multiple sources (see next section), otherwise the generated polygon may be over-estimated. For extended sources that were not properly imaged, manual intervention may still be needed. Figures 3.18, 3.19 and 3.20 show the multiple fitted Gaussians and the generated polygons on different extended sources. The Gaussians fits are shown as green (left panel), while the defined polygon is shown as white (right panel).

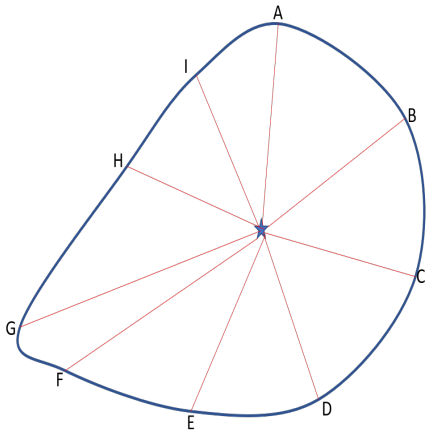

Figure 3.17: *Illustration on how the geometric mean diameter from polygon is created for extended sources.*

Elimination of Side-lobes and Multiple Sources

Because the tiles have a $60''$ overlap, sources closer to the edge of the tiles were detected more than once. To eliminate such duplicated sources, sources with similar positions ($< 1.5''$) and peak flux ($\mathrm{Peak_{min}}/\mathrm{Peak_{max}} > 0.7$) were searched for. Using both conditions, the source closer to the centre of a tile was retained, over the ones closer to the edges.

Having removed duplicate sources, visual inspection was then used to eliminate spurious sources and side-lobes close to bright sources. Figure 3.21 shows a histogram of detections, binned by the tiles, before and after visual inspection. After these eliminations, the final catalogue has a total of 5013 sources above 7σ. There is still the possibility of spurious sources that could come from noisy regions or very extended sources that were not properly imaged (see Figure 3.22 for an example). Further elimination would need the aid of other radio and/or infrared data, especially for some tiles between 1200 and 1500 (Figure 3.21).

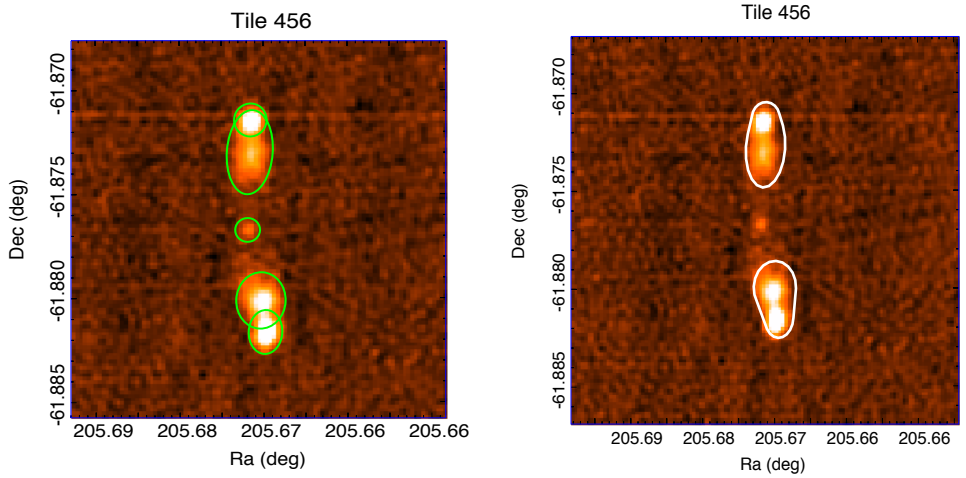

Figure 3.18: *Examples showing the original Gaussian fits (green) and the new automated polygon (white).*

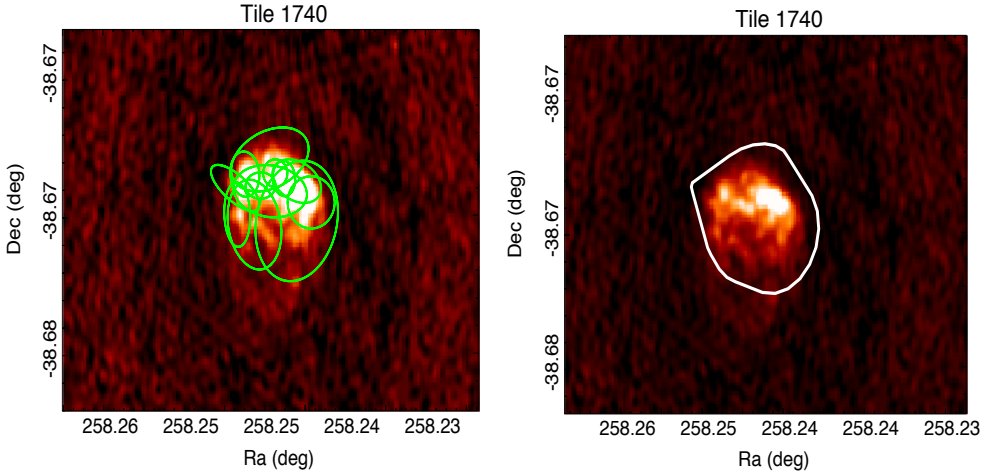

Figure 3.19: *Same illustration as in Figure 3.18.*

3.5.3 Catalogued Properties

In order to create a uniform CORNISH catalogue, the associated errors of the measured properties were estimated using the same equations given in Purcell *et al.* (2013) for the northern half of the CORNISH survey (see Condon 1997). For the simple and unresolved sources, defined by a single Gaussian fit, the Gaussian properties were preferred over the measurements from aperture photometry. The

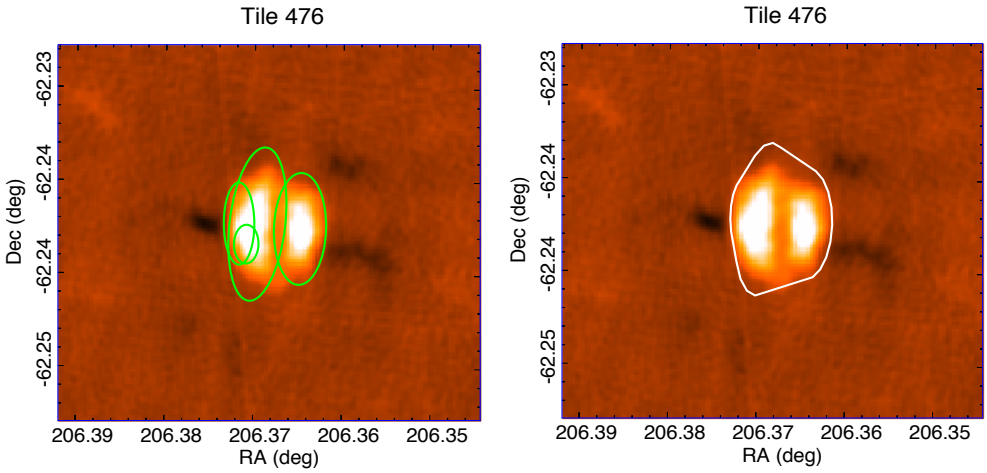

Figure 3.20: *Same illustration as in Figure 3.18.*

catalogued size is the geometric mean (see equation 3.3 and 3.4) of the major and minor axes.

The properties of the extended sources were re-measured under the defined polygons, using aperture photometry (see Section 2.4 and Purcell *et al.* 2013). The new positions are the intensity-weighted positions, using the polygons. For the northern half of the CORNISH survey, intensity-weighted diameters, given by equation 3.5 (Purcell *et al.*, 2013), were used as the sizes for the extended sources. However, it was realised that the intensity-weighted diameters under-estimated the sizes by $\geq$50%. Figure 3.23 (left) shows a comparison of the intensity-weighted diameters and the geometric mean diameters in section 3.5.2. The intensity-weighted diameters are consistently smaller compared to the geometric mean. This effect is further shown in Figure 3.23 (right) for an example source, with the intensity-weighted diameter and geometric mean diameter overlaid. Based on this, the geometric mean diameters are catalogued for extended sources.

$$\vartheta_{\rm mean} = \sqrt{\vartheta_{\rm maj}\vartheta_{\rm min}} \tag{3.3}$$

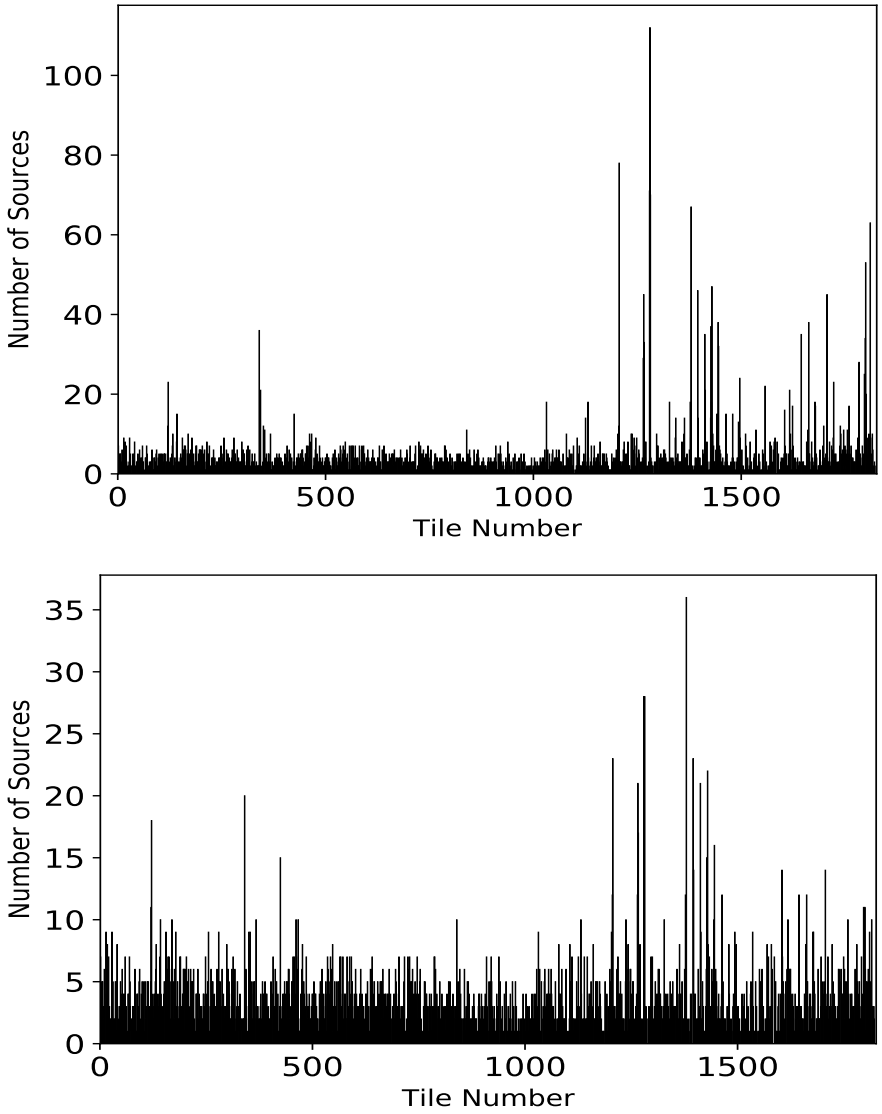

Figure 3.21: *Histogram showing number of sources per tile before (top) and after (bottom) elimination of spurious sources and sidelobes. The x-axis shows the tile number.*

$$\sigma(\vartheta_{\text{mean}}) = \frac{\vartheta_{\text{mean}}}{2}\sqrt{\frac{\sigma^2(\vartheta_{\text{maj}})}{\vartheta^2_{\text{maj}}} + \frac{\sigma^2(\vartheta_{\text{min}})}{\vartheta^2_{\text{min}}}} \tag{3.4}$$

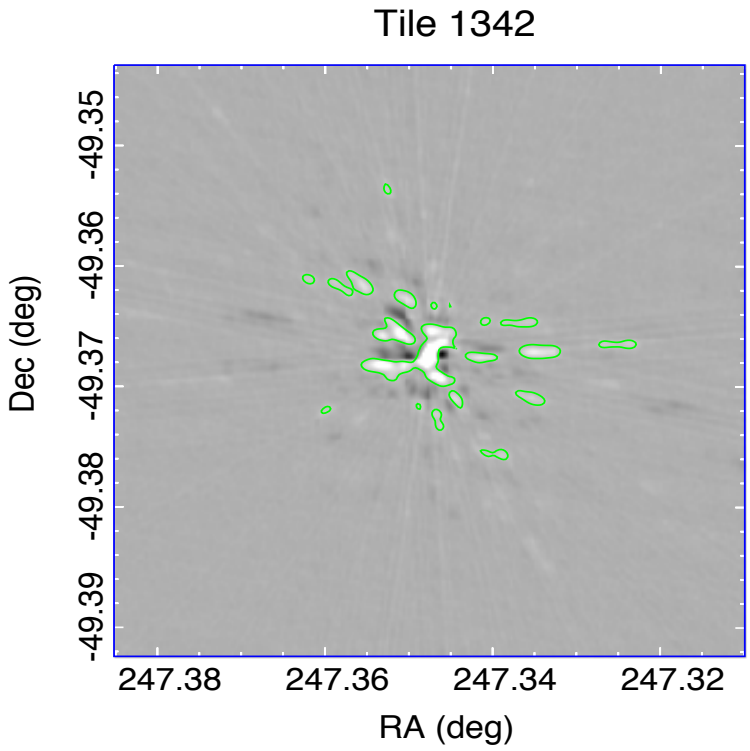

Figure 3.22: *Example of a source that is not properly imaged. Contour is at a 7σ level.*

$$d_w = \sum_{i=1}^{N_{src}} r_i A_i \Big/ \sum_{i=1}^{N_{src}} A_i \tag{3.5}$$

where d_w is the intensity-weighted diameter, $\sum_{i=1}^{Nsrc} A_i$ is the sum of the flux within the defined source aperture and N_{src} is the number of pixels in the source aperture.

The 7σ catalogue contains 5013 sources and non-Gaussian sources (extended sources) make up 16%. The measured properties of the 7σ catalogue are summarized in Figure 3.24 and an excerpt of the catalogue is presented in section B (Table B.3). The final version of the full table will be made available on the CORNISH website (`http://cornish.leeds.ac.uk/public/index.php`). As with interferometric observations, the observation will not properly image very extended emission due to missing information on large scale structures, limited by the small-

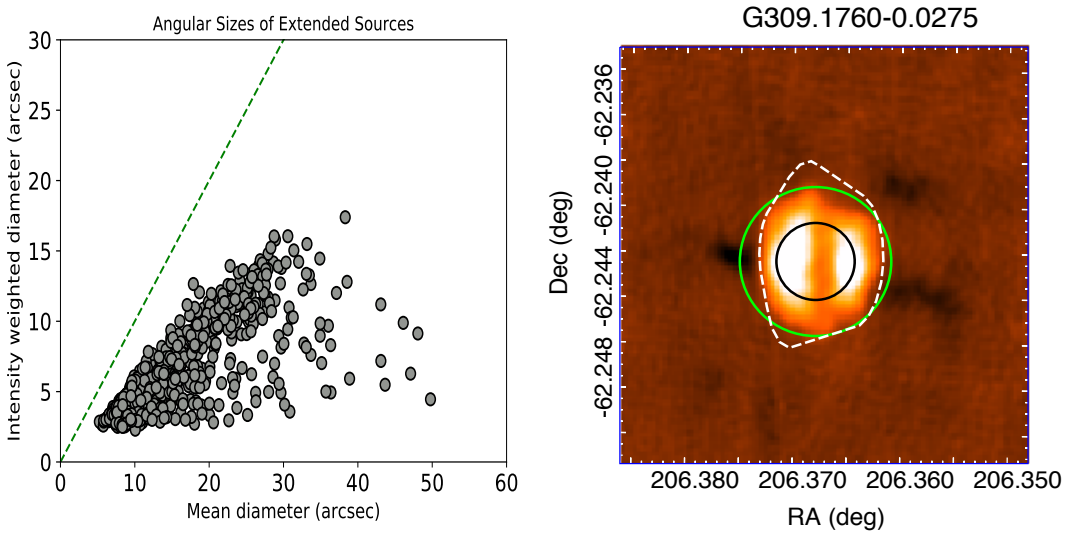

Figure 3.23: *Left: A plot of the intensity-weighted diameter against the geometric mean diameter from the polygons. Right: A comparison of the intensity-weighted diameter (black) and the new geometric mean diameter green) on an extended source. The dashed circle is the defined polygon. The intensity weighted centre and the radius is used to create the circles.*

est baseline of the array (~ 30.0 m). For this reason, caution should be applied in interpreting the radio properties of very extended sources. The mean positional accuracy of the gain calibrators (Table 3.4) with median offset of $0.1''$ is adopted as the systematic positional uncertainty for this catalogue.

Based on the mean error of the angular sizes, which is $0.2''$ and the size of the restoring beam ($2.5''$), resolved sources are defined as sources with angular sizes $> 2.8''$ for the CORNISH-South catalogue. The angular size distribution (Figure 3.24; bottom right) is dominated by unresolved sources and accounts for the peak at $\sim 3''$. Resolved sources account for 39% of the catalogue (1947), of which 41% are non-Gaussians (803). The non-Gaussian sources (polygon), dominates the distribution of angular sizes above $10''$ and extends up to $50''$.

The Galactic latitude and longitude distributions are similar to the distributions of the CORNISH-North catalogue (Purcell *et al.*, 2013), showing the broad peak attributed to resolved sources in latitude (rose-red shaded histogram). Resolved

Table 3.4: *Secondary calibrators positional accuracies taken from* *http://www.narrabri.atnf.csiro.au/calibrators/*

Calibrator	positonal accuracy
1714–397	$0.002 < \sigma < 0.01$ arcsec
1646–50	$0.10 < \sigma < 0.25$ arcsec
1511–55	$0.10 < \sigma < 0.25$ arcsec
1352–63	$0.10 < \sigma < 0.25$ arcsec
1148–671	$0 < \sigma < 0.02$ arcsec

Galactic sources are be dominated by PNe and HII regions. The flux density distribution shows a few sources with flux density above 1Jy (0.7%).

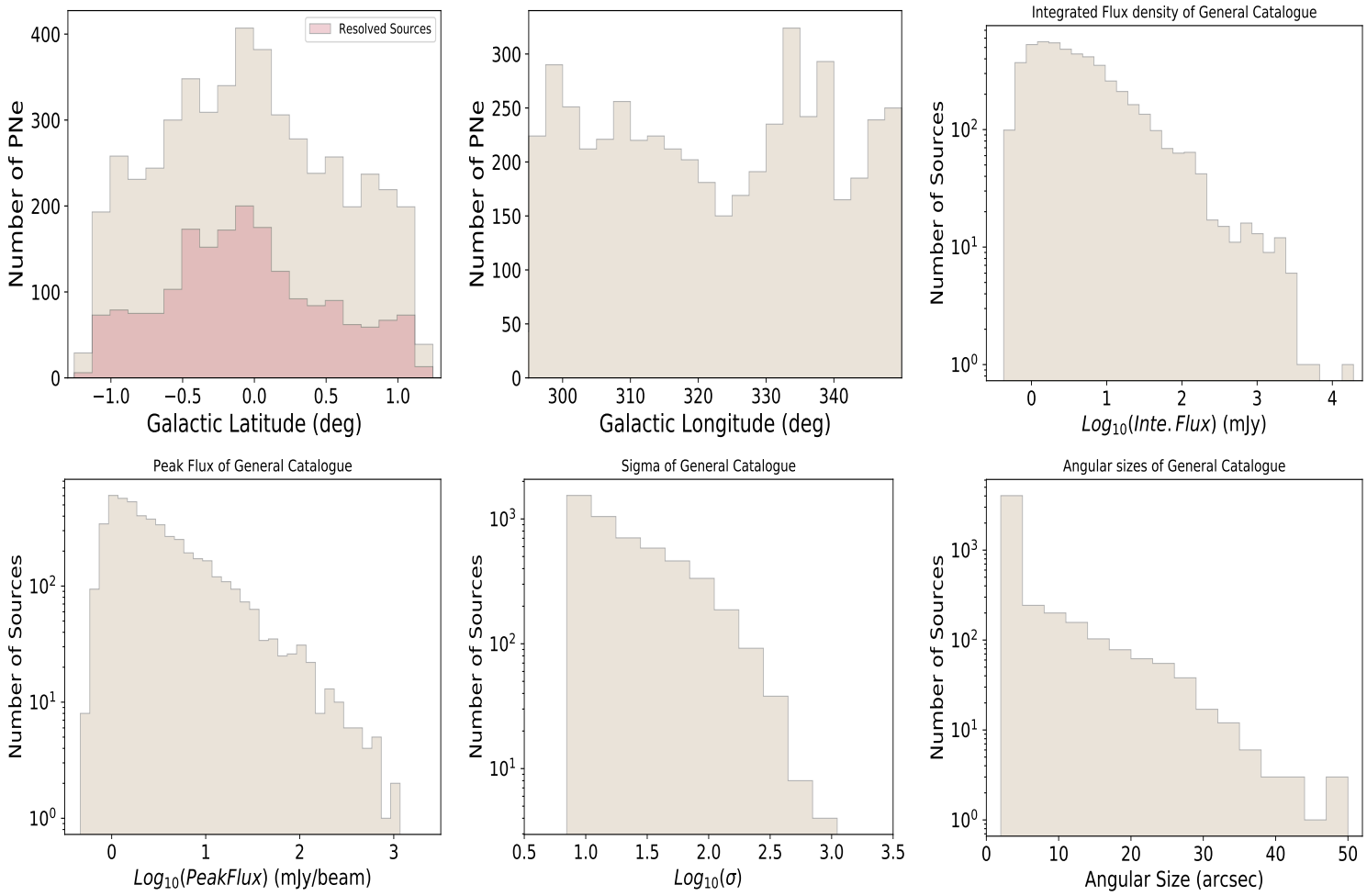

Figure 3.24: *Histograms of the latitude (top left), longitude (top middle), integrated flux density (top right), peak flux (lower left), signal-to-noise ratio (lower middle) and angular size (lower right) distributions for the CORNISH south catalogue.*

3.6 PNe Sample Selection

Because there is no comparable radio survey covering the CORNISH region in the southern Galactic plane (coverage and resolution), infrared colours and visual inspection were used for PNe sample selection. The radio flux densities of PNe at 5.5 GHz are usually a few mJy. According to Hoare *et al.* (2012), PNe having flux densities between 5 - 50 mJy, at typical distances, are expected within the CORNISH survey. Based on this, Fragkou *et al.* (2017) used a cut-off of 110 mJy in their search for PNe, using the CORNISH north data at 5 GHz. Ionized regions with higher flux densities would be considered to be HII regions. However, in the CORNISH north, there were a few PNe (9%) with flux densities between 100 mJy and 500 mJy, and so no cut was placed on the radio flux density in the selection.

3.6.1 RMS Catalogue Conterparts

A cross-match of the CORNISH catalogue of 5013 sources with the RMS (Red MSX Source) catalogue (Lumsden *et al.*, 2013), within a radius of 20″, returned 440 matches. Out of the 440 matches, 328 were classified as HII region (including 24 classified as possible HII regions), 21 as YSOs, 38 as PNe (including 15 possible PNe), 6 as evolved stars and 36 rejected in the RMS catalogue (see Figure 3.25). The rejected sources in the RMS catalogue were due to extended background emissions or artefacts (see Lumsden *et al.* (2013) for details of source classifications). Figure 3.25 summarizes the proportion of cross-matched sources that were classified in the RMS catalogue. PNe make up 9.7% of the cross-matched sources.

3.6.2 Multi-Wavelength Counterparts

MIR and FIR Counterparts: GLIMPSE, WISE, MIPSGAL and Hi-Gal

The GLIMPSE survey in the southern plane covers the longitude $295° < l < 350°$; $284°$ and latitude $|b| < 1°$ region (see section 2.2.2). Uniform cutouts were made

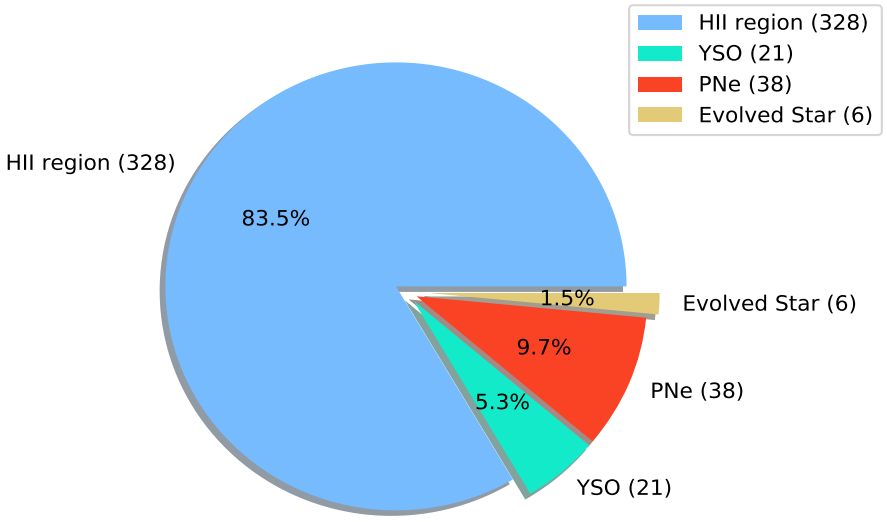

Figure 3.25: *Proportion of the CORNISH-RMS sources with classifications in the RMS catalogue (Lumsden et al., 2013). The CORNISH-RMS cross-match resulted in 440 matches.*

from large tiles[15] using the CORNISH positions and aperture photometry was performed to obtain integrated flux densities in the 3.6 μm, 4.5 μm, 5.8 μm and 8.0 μm bands. Sources with measured flux densities $< 3\sigma$ were rejected as non-detections. The WISE, MIPSGAL and Hi-Gal surveys were introduced in section 2.2.2. The CORNISH catalogue was cross-matched with the WISE, MIPSGAL (24 μm) and Hi-Gal catalogues with a cross-match radius of $20''$. The cross-match radius is based on the resolution of the individual surveys and the CORNISH survey.

PNe and HII regions are usually good infrared emitters and so, non-detections across all the four IRAC bands or WISE bands were attributed to extragalactic sources or radio stars. Figure 3.26 shows the distribution of the sources with MIR measurements on the MIR colour-colour planes. The distribution of the CORNISH-north PNe, CSPNe, symbiotic stars and the colours of HII regions from the CORNISH-RMS cross-match (see section 3.6.1) are also shown in Figure

[15] https://irsa.ipac.caltech.edu/data/SPITZER/GLIMPSE/catalogs/GLMI/

3.26. On both colour-colour planes in Figure 3.26 ([3.6] – [4.5] vs.[5.8] – [8.0] and [3.6] – [5.8] vs. [4.5] – [8.0]), the MIR detections are dominated by PNe and HII regions. Sources with [5.8] – [8.0]s > 0.5 are dominated by PNe and HII regions, while sources with [5.8] – [8.0] < 0.5 are dominated by stellar emissions e.g. radio stars. On the [3.6] – [5.8] vs. [4.5] – [8.0] colour-colour plane, the CORNISH-RMS HII regions (cyan) have redder colours.

On the [4.5] – [12] vs.[3.6] – [5.8] colour-colour plane (Figure 3.27), PNe and HII regions dominate sources with colours in the range of 3 < [4.5] – [12] < 12. The cluster of sources enclosed within the black-dashed box is dominated by sources with bluer colours. These could be radio stars, extragalactic sources or photometry contamination from background sources across the IRAC bands. On the FIR colour-colour planes in Figure 3.28 ($\log_{10}$[12μm/8μm] vs $\log_{10}$[160μm/22μm] and $\log_{10}$[70μm/22μm] vs. $\log_{10}$[160μm/12μm]), the colours of the CORNISH south sources classified as HII regions in the RMS catalogue (cyan filled circles) overlap with colours of the CORNISH north PNe. This makes it difficult to place a colour cut. However, as noted by Anderson *et al.* (2012), the region enclosed by the red-dashed rectangle is dominated by HII regions on both colour planes.

NIR Counterparts: VVV survey

The VVV is an ESO NIR survey. It mapped the Galactic bulge and the southern Galactic plane region, defined by longitude 294.7° < l < 350° and latitude 2.25° < b < +2.25° in the Z, Y, J, H and K filters (Minniti *et al.*, 2011; Saito *et al.*, 2012). Image resolution is between ∼ 0.9″ and 1.0″. Large tiles covering the CORNISH survey region were downloaded, using the ESO query form (phase 3 data,)[14]. Photometry was then performed on uniform cutouts made from large tiles, to obtain J, H and K magnitudes (see section 2.4).

The NIR colour-colour plane ([H-K]-[J-H]) is presented in Figure 3.29. The colours of PNe from the northern CORNISH survey, intrinsic colours of PNe (Weidmann *et al.*, 2013), and the intrinsic colour of an O9 star (Ducati *et al.*, 2001)

[14] http://archive.eso.org/wdb/wdb/adp/phase3_main/form?phase3_collection=VVV&release_tag=6

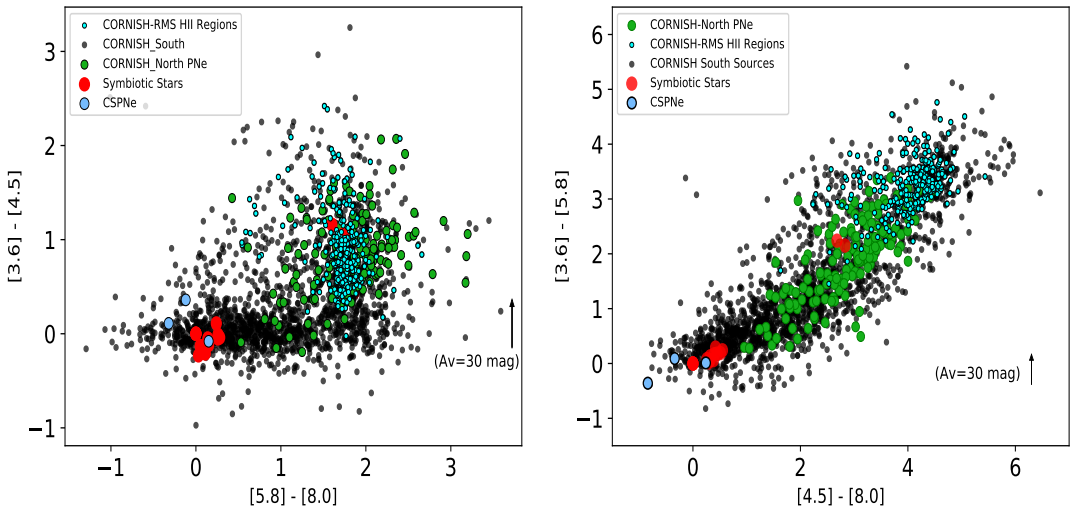

Figure 3.26: *Left panel:* [3.6] – [4.5] *vs.* [5.8] – [8.0]. *Right panel:* [3.6] – [5.8] *vs.* [4.5] – [8.0]. *The green circles are the CORNISH north PNe, blue filled circles are CSPNe (central stars of PNe) taken from (Hora* et al., *2004), symbiotic stars from Corradi* et al. *(2008) and Miszalski* et al. *(2013) are represented as red filled circles. The cyan filled circles show CORNISH sources classified as HII regions in the RMS catalogue (Lumsden* et al., *2013). The reddening vector is from the average extinction in Indebetouw* et al. *(2005).*

are also shown in Figure 3.29 (left). Again, based on the distribution of the CORNISH north PNe, there are sources with bluer colours ([H-K] <0.5). From visual inspection, these sources are from stars, which could be radio stars. Combining the NIR and MIR colours, as shown in Figure 3.29 (right), shows a distribution that is similar to Figure 3.27. According to colour analysis of different Galactic sources by Akras *et al.* (2019), the region enclosed by the red-dashed rectangle is dominated by symbiotic stars (S- and D-type), while the region defined by $7 < [3.4] - [22] < 14$ is dominated by PNe. The distribution of the CORNISH-North PNe is also seen to dominate the colours within the $7 < [3.4] - [22] < 14$ region. However, as noted in the FIR colour-colour planes, it is dangerous to place a direct colour cut based on the distribution of sources in the colour-colour planes. This is due to the overlapping regions on these colour-colour planes, although there are regions dominated by different sources.

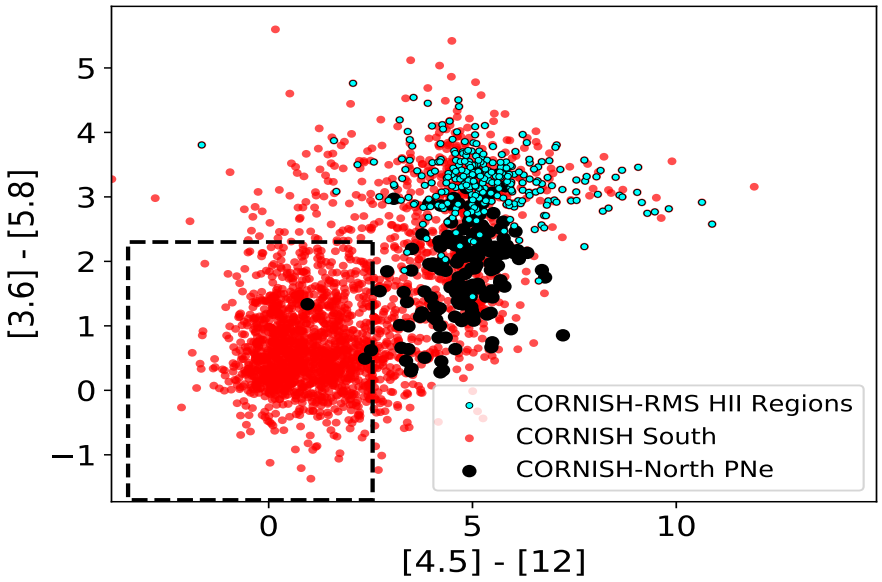

Figure 3.27: [4.5] – [12] *vs.* [3.6] – [5.8] *colour-colour plane. The black filled circles are the CORNISH north PNe, the red filled circles represent the CORNISH south colours and the cyan filled circles show CORNISH sources classified as HII regions in the RMS catalogue (Lumsden* et al., *2013). The region enclosed within the black-dashed box defines a region possibly dominated by radio stars or extragalactic sources. The 12* μm *magitudes are from the WISE catalogue.*

ATLASGAL: Sub-mm Identifications

ATLASGAL (APEX Telescope Large Area Survey of the Galaxy) is a sub-mm continuum survey at 870 μm (Schuller *et al.*, 2009). The Galactic region defined by longitude –60° < l < 60° and latitude |b|< 1.5 was mapped with the APEX telescope. At this wavelength, cool dust emission in molecular clouds that host massive star formation are traced. Only a few PNe have been identified so far at 870 μm (see Urquhart *et al.* 2013), hence sources with ATLASGAL counterparts are more likely to be HII regions. A cross-match of the CORNISH south sources with the ATLASGAL catalogue returned 436 matches. 238 of these were classified as HII regions in the CORNISH-RMS cross-matched sources.

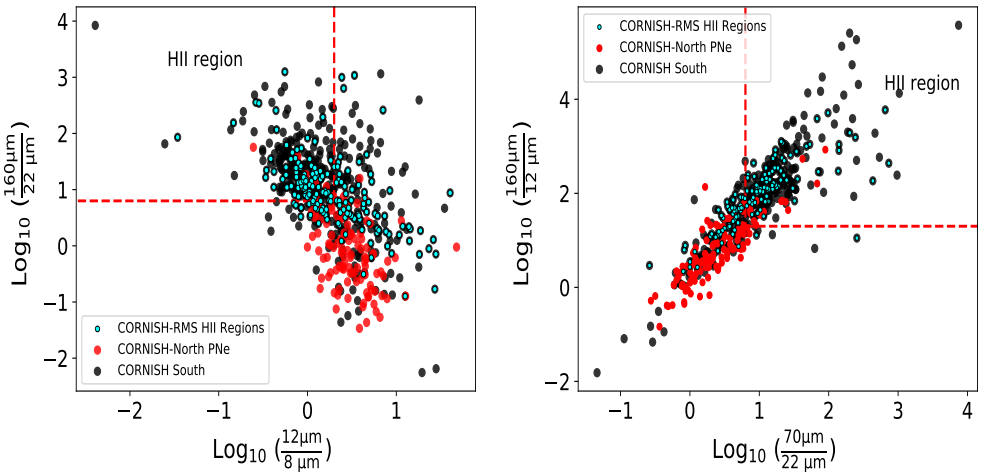

Figure 3.28: *FIR colours of the CORNISH south sources on the* $\log_{10}(12\mu m/8\mu m)$ *versus* $\log_{10}(160\mu m/22\mu m)$ *and* $\log_{10}(70\mu m/22\mu m)$ *versus* $\log_{10}(160\mu m/12\mu m)$ *colour-colour planes. The black filled circles are the FIR colours of the CORNISH south sources, red filled circles are the CORNISH-North PNe and cyan filled circles show CORNISH sources classified as HII regions in the RMS catalogue (Lumsden et al., 2013). The region enclosed by the red-dashed line indicates a region dominated by HII regions, according to Anderson et al. (2012).*

3.7 PNe Candidates

The colour distributions of the CORNISH south data across different colour-colour planes with colours of the CORNISH north PNe, symbiotic stars and HII regions overlaid are presented in section 3.6.2. There were regions dominated by PNe, however, there were also overlapping colours of HII regions in the MIR and FIR. This makes it difficult to use colour cuts alone in the selection of PNe candidates. The colours of a PN across the different wavelengths are affected by the age of the PN and the different dominant emission mechanisms. Thus, visual inspection of the multi-wavelengths images, aided by the position of sources on the colour-colour planes, was used to select candidate PNe from the CORNISH south survey. It should be noted that there were some sources at the edge of the CORNISH survey area without infrared counterparts i.e. they have only radio data, hence could not be classified.

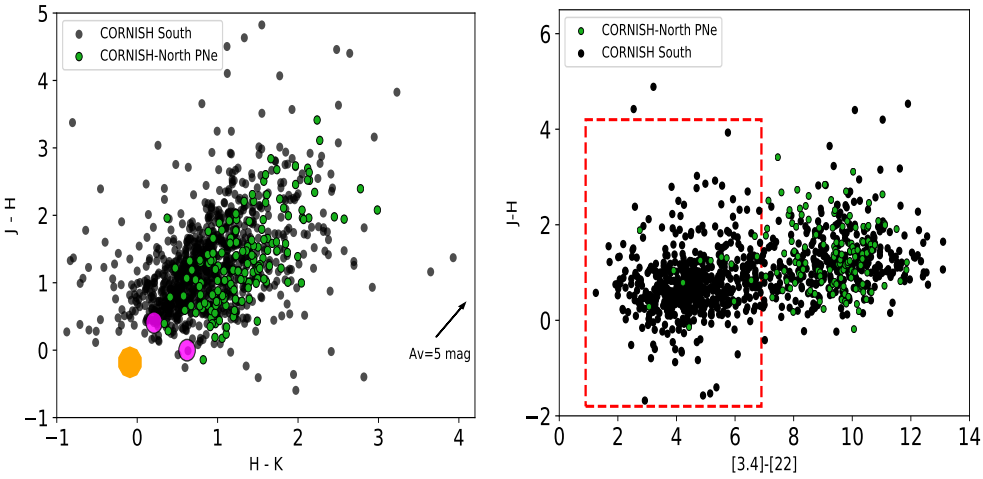

Figure 3.29: *Left:* [H] – [K] *vs.* [J] – [H] *colour-colour plane showing the distribution of the CORNISH-South sources (black) and the CORNISH-North PNe (green). The intrinsic colour of an O9 star (orange) from Ducati* et al. *(2001) and intrinsic colours of PNe (magenta) from Weidmann* et al. *(2013) are also shown. Right:* [3.4] – [22] *vs.* [J] – [H] *colour-colour plane showing the distribution of the CORNISH-South sources (black) and the CORNISH-North PNe (green). The region enclosed by the red-dashed box defines a region possibly dominated by stars and extragalactic sources, as observed in Figure 3.27. The 3.4 and 22* μm *magitudes are from the WISE catalogue.*

Multi-wavelength images used include the MIR (GLIMPSE) 8μm or false 3-colour images, NIR (VVV) K band or false 3-colour images, the 24 μm (MIPSGAL) images, the 70, 160, 250 and 500 μm images (HI-GAL) and the ATLASGAL 850 μm images, where available. Additionally, 2-colour (Hα and r continuum) images from the SHS survey (Parker *et al.*, 2005) were also used, where available. The criteria outlined in section 2.3 were used in the visual selection of PNe and Figures 3.30 to 3.33 show examples of sources rejected as HII regions, YSOs, radio stars and radio galaxies, across the different wavelengths. Based on the infrared colours and visual inspection, 184 sources in the 7σ catalogue were classified as PNe and 3 as possible PNe due to insufficient data. Seven out of the 436 CORNISH-South-ATLASGAL matches are classified as PNe. The PNe with ATLASGAL counterparts are presented in Table 3.5.

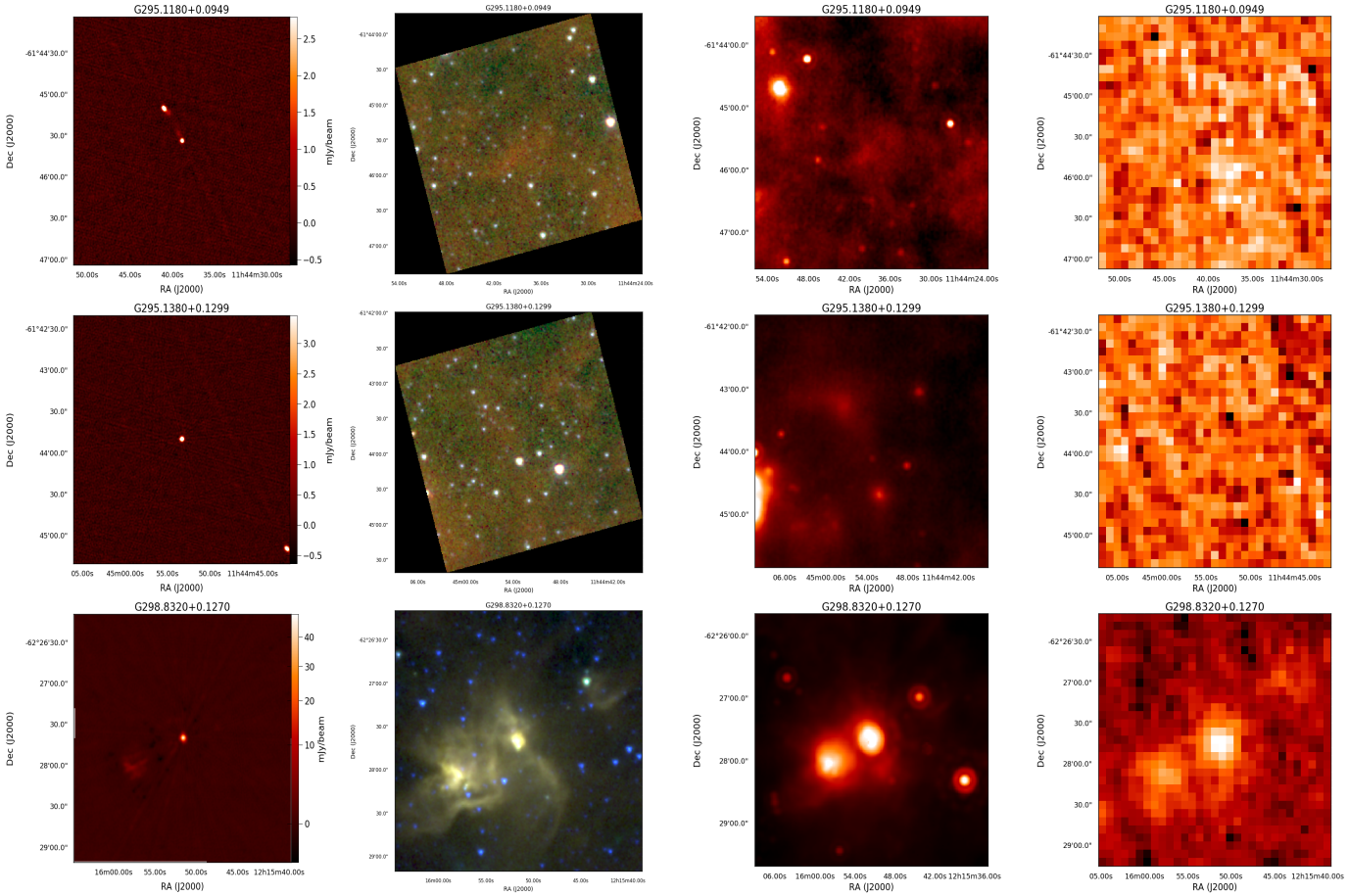

Figure 3.30: *Sources rejected as other source types in the mulit-wavelength visual inspection of the CORNISH-South sources. From left to right: Radio (5.5 GHz), 3-colour GLIMPSE images (3.6* μm*=ble, 5.8* μm*=green and 8.0* μm*=red), 24* μm *MIPSGAL image and 850* μm *ATLASGAL image.*

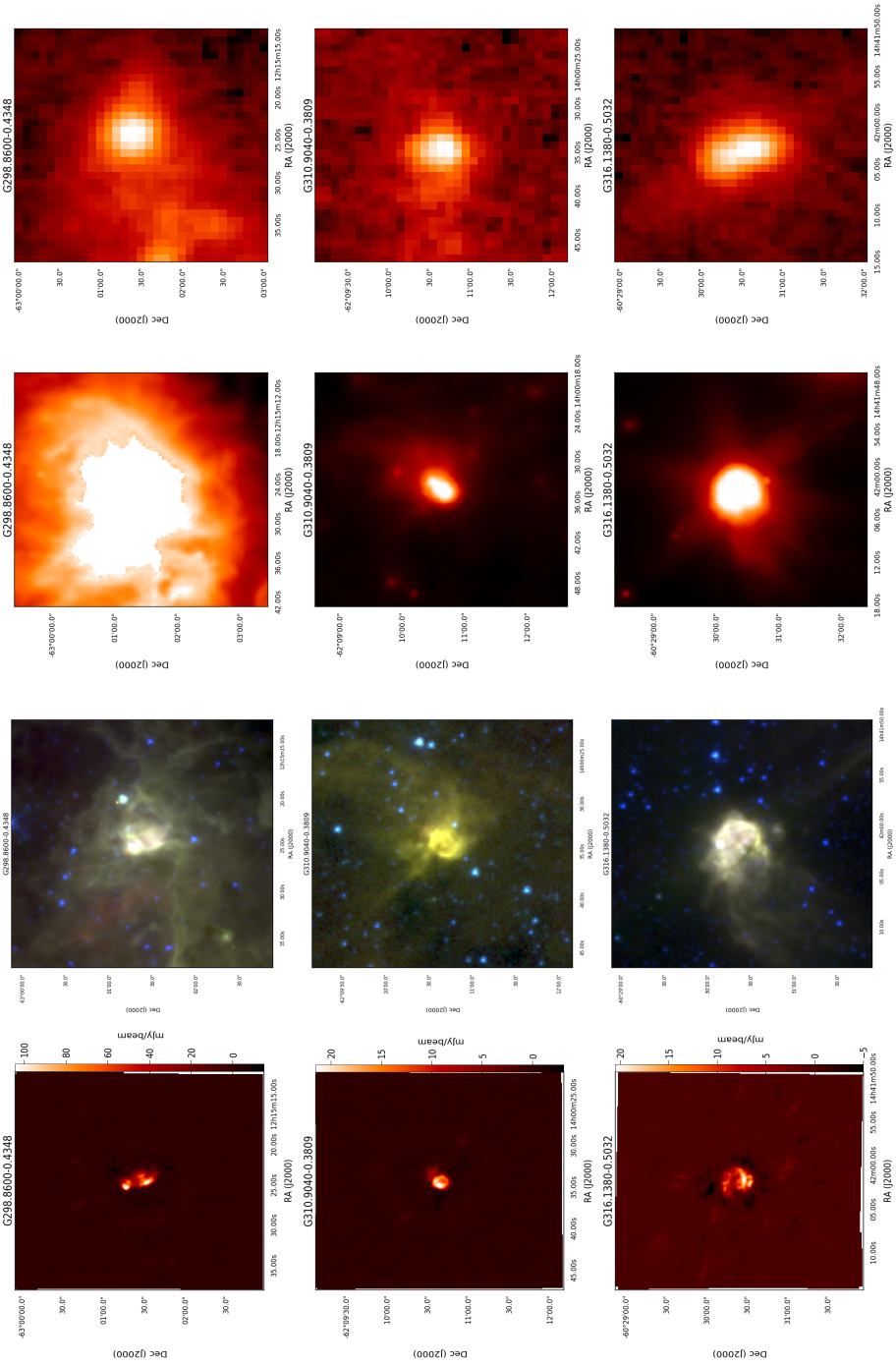

Figure 3.31: *Continued from Figure 3.30.*

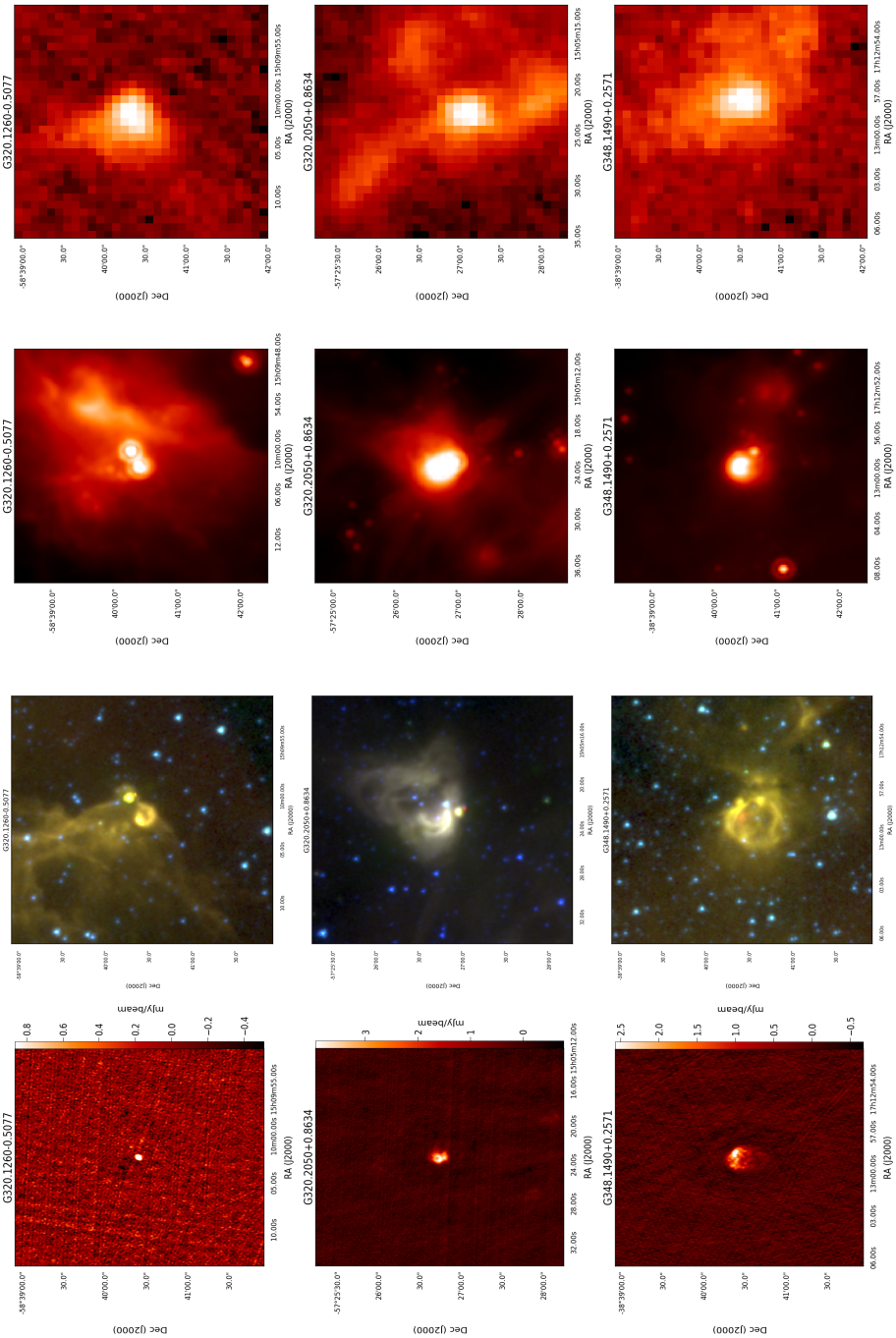

Figure 3.32: *Continued from Figure 3.31.*

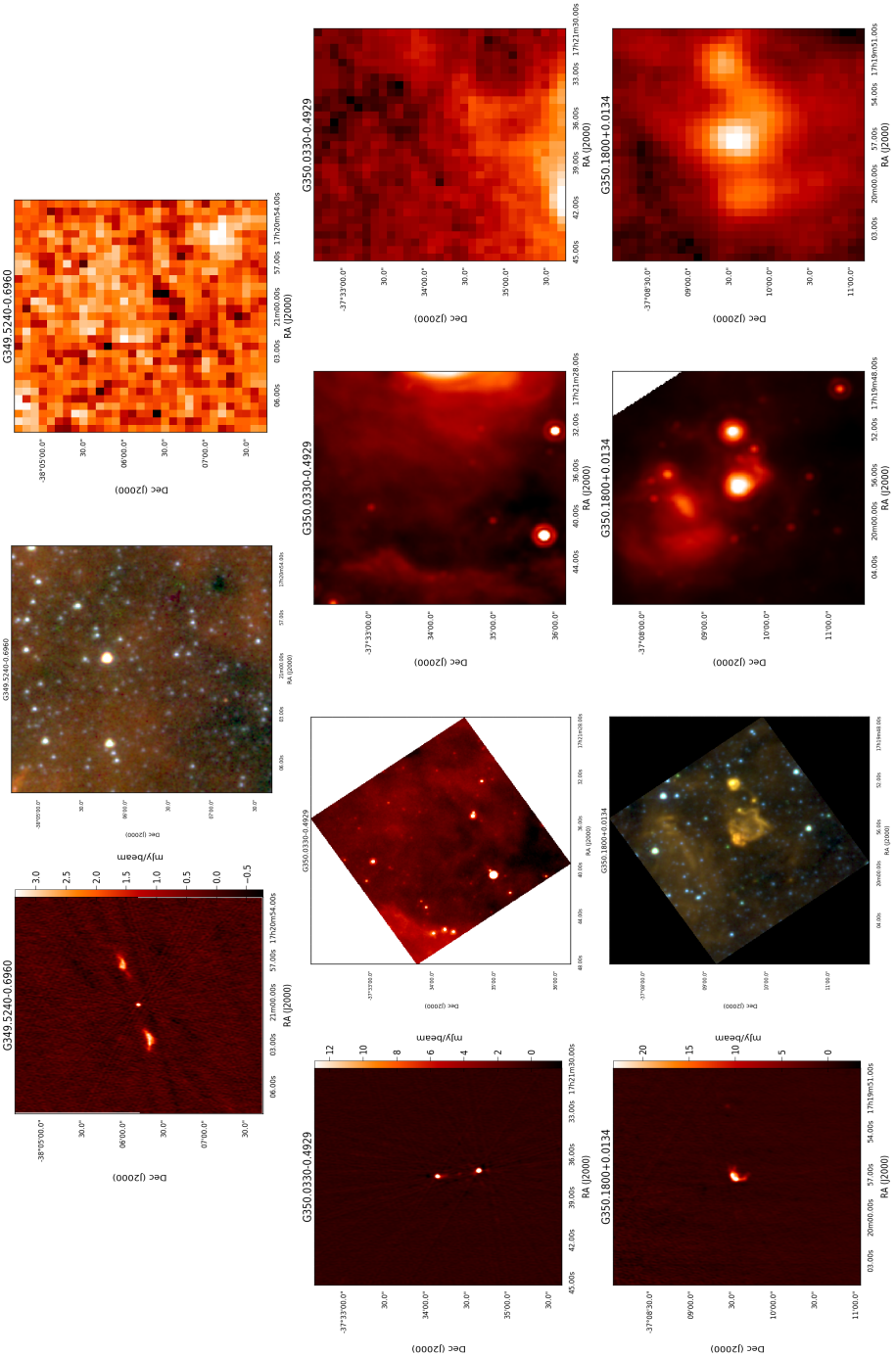

Figure 3.33: *Continued from Figure 3.32.*

Table 3.5: *CORNISH-South-ATLASGAL counterparts. The integrated flux density at 850* μm *and 5.5 GHz are shown in columns 2 and 5.*

sourceName	S_{int} mJy	maj arcsec	min arcsec	S_{int}(radio) mJy	dS_{int}(radio) mJy
G303.9978+0.2804	750	28	19	35.00	0.33
G328.4240–0.0892	1060	35	22	25.13	5.03
G334.4740–0.1495	680	29	23	5.00	1.06
G336.6440–0.6956	420	23	19	35.83	2.52
G346.1960+0.0402	710	32	22	6.72	1.42
G349.3510–0.2113	400	22	19	44.16	2.04
G349.5090+1.0558	4140	29	23	2719.67	23.22

3.7.1 Radio Properties of the CORNISH South PNe

The radio properties of the identified PNe are given in Figures 3.34 and 3.35. The latitude distribution (Figure 3.34, left panel) shows a distribution that is fairly uniform and a longitude distribution (Figure 3.34: right panel) that is similar to the CORNISH-North PNe. The mean angular size is 4.3″ with a distribution that extends up to 23″. Extended PNe whose sizes were determined by means of polygons make up 16% of the identified PNe. These extended PNe have angular sizes between 7″ and 24″ (see Figure 3.35: left panel). An example is G318.9310+0.6956, a known PN (see Table 3.7), with a radio diameter of 20″.

The mean integrated flux density is ∼38 mJy. Compared to the integrated flux density distribution of the CORNISH-North PNe, the CORNISH-South PNe show a broader distribution and extend to lower values (Figure 3.35; right panel). This is due to the sensitivity of the CORNISH south survey (0.2 mJy/beam) that is twice better than the northern counterpart. The PN with the highest flux density of 2.7 Jy is G349.5090+1.0558 (NGC 6302), a known PNe. The distribution of the $F_{8.0\mu m}/F_{5GHz}$ for the CORNISH-South PNe (Figure 3.36) is similar to the northern counterpart (red histogram in Figure 3.36). The resulting median is 4.3 ± 1.2, which is in good agreement within 1σ with the CORNISH-North PNe of 3.9 ± 0.90.

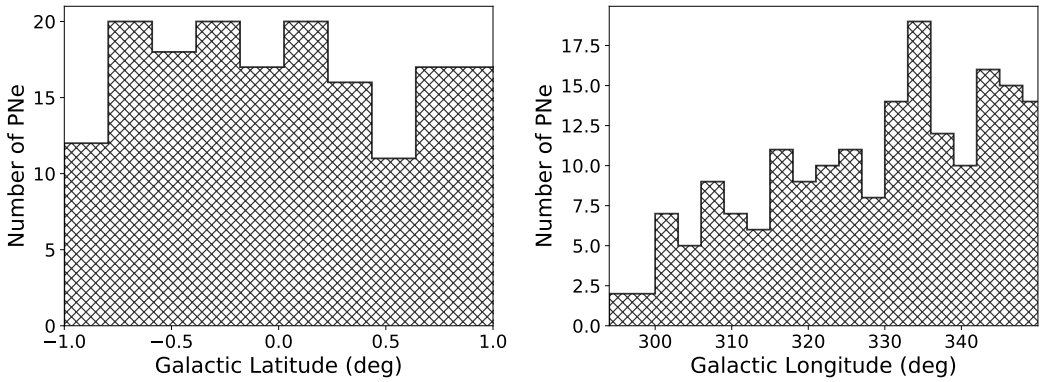

Figure 3.34: *Galactic latitude (left panel) and longitude (right panel) distribution of the CORNISH-South PNe.*

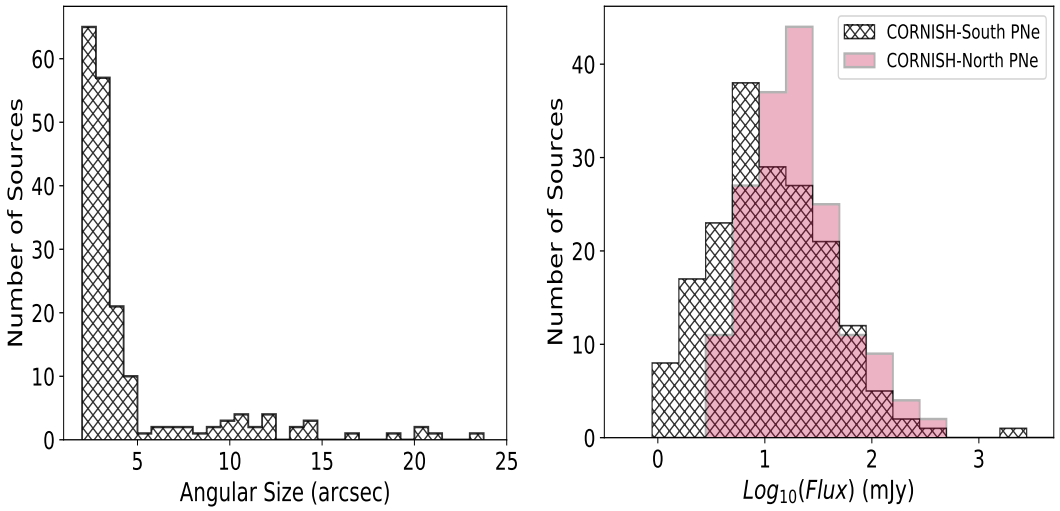

Figure 3.35: *Angular size (left panel) and integrated flux density (right panel) distribution of the CORNISH-South PNe. The integrated flux density distribution of the CORNISH-North PNe is also shown (rose red).*

3.7.2 Multi-Wavelength Colours

The MIR, NIR and FIR colours of the 184 PNe are shown in Figures 3.37 and 3.38 with the CORNISH-North PNe colours overlaid. The southern and northern CORNISH PNe show similar colour distributions in all three colour-colour planes. Compared to the CORNISH-South PNe, however, some of the CORNISH-North

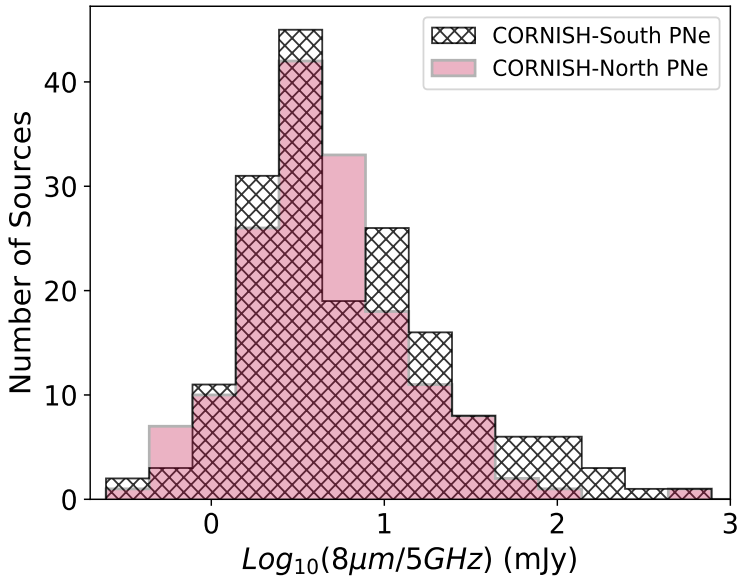

Figure 3.36: $\log_{10}(F_{8\mu m}/F_{5GHz})$ *distribution of the CORNISH-South PNe. The red histogram shows the distribution of the CORNISH-North PNe.*

PNe have higher reddening ($\sim$ 5 mag in Av). On the FIR colour-colour plane, there are more CORNISH-South PNe within the HII region area compared to the CORNISH-North PNe. Table 3.6 presents the MIR and FIR colours of the CORNISH-North and South PNe. These mean FIR and median MIR colours show good agreement within 1σ.

3.7.3 CORNISH-South PNe Catalogue

A cross-match of the CORNISH-South PNe candidates with the HASH catalogue (Parker *et al.*, 2017) returned 29 matches of true PNe (see Table 3.7) with 13 likely PNe and possible PNe matches. The true PNe are those whose status have been confirmed through spectroscopy. In Figure 3.39 (upper panel) the latitude distribution of the CORNISH-South PNe candidates from this study is compared with the distribution of known PNe in the HASH catalogue. The CORNISH-South PNe were restricted to the $|b|< 1^{\circ}$ region, where the CORNISH survey is complete and the known PNe were restricted by longitude to the CORNISH

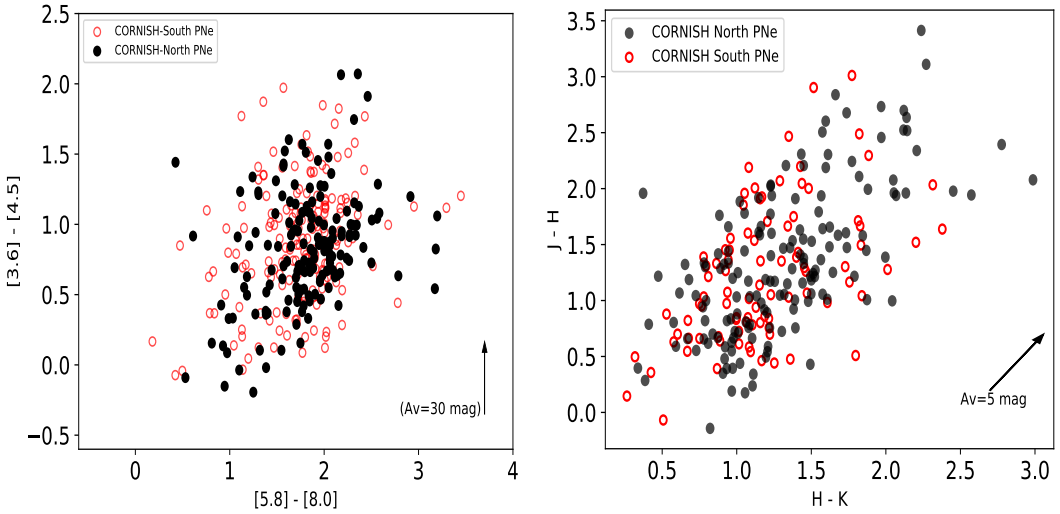

Figure 3.37: *Left panel: [3.6]-[4.5] vs. [5.8]-[8.0] colour-colour plane. Right panel: [H-K] vs. [J-H] colour-colour plane. The black filled circles are the CORNISH-North PNe and the red circles are the CORNISH-South PNe.*

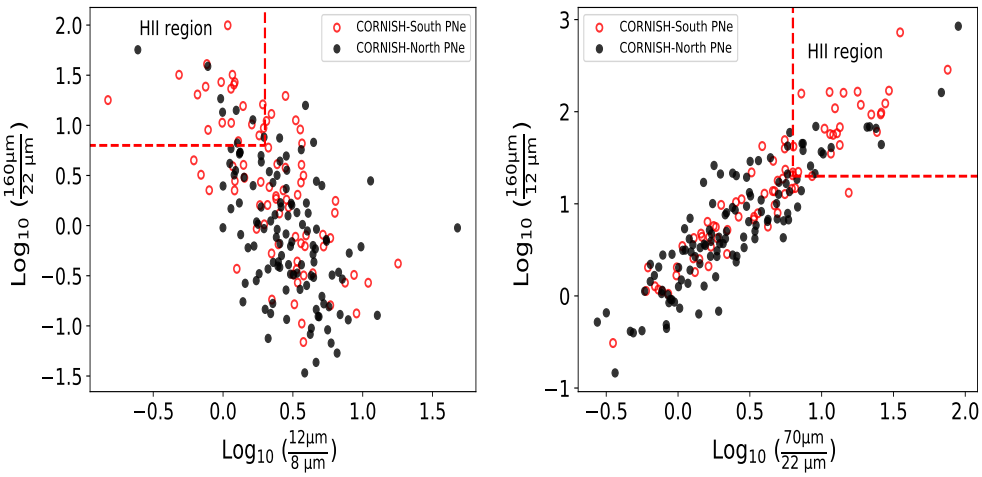

Figure 3.38: *FIR colours of the CORNISH-South PNe (red) with colours of the CORNISH-North PNe (black filled circles) overlaid. The region enclosed by the red-dashed rectangle represents the area dominated by HII regions.*

survey region but extended out to latitude |b|= 10°. Similar to the CORNISH north survey, more PNe are detected within the |b|< 1° region (see Figure 3.39: lower panel).

Table 3.6: *Comparison of the mean and median colours of 160 CORNISH north PNe with the 184 southern PNe. Columns 2 and 3 show the median colours of the CORNISH-South and CORNISH-North PNe, respectively. The mean FIR colours of PNe from the CORNISH-North catalogue are shown in column 6 and the mean colours in column 5 are the colours of the southern PNe. The errors on the MIR colours are the standard error on the median and standard deviation is quoted as the errors on the FIR colours.*

Colour Index	South 184	North 160	Colour	South	North
[3.6] – [4.5]	0.86 ± 0.04	0.84 ± 0.08	Log_{10}[12/8]	0.43 ± 0.36	0.45 ± 0.30
[3.6] – [5.8]	1.77 ± 0.07	1.94 ± 0.19	Log_{10}[70/22]	0.44 ± 0.53	0.34 ± 0.46
[4.5] – [8.0]	2.70 ± 0.07	3.01 ± 0.30	Log_{10}[160/12]	1.20 ± 0.77	0.77 ± 0.67
[5.8] – [8.0]	1.79 ± 0.04	1.84 ± 0.18	Log_{10}[160/24]	0.70 ± 0.85	0.02 ± 0.62

A cross-match of the 184 PNe with the SIMBAD database, within a 60″ search radius, returned 132 matches. The main classifications of the matched sources in the SIMBAD database are shown in Figure 3.40. Only 1.6% of the matched sources is classified as HII regions. These sources (G332.1880–0.0898 and G326.3150+0.7034) are, however, not detected in the ATLASGAL survey and their MIR colours and images correspond to PNe (see multi-wavelength images in Section B). YSO classification (17%) is also ruled out based on the $F_{8\mu m}/F_{5GHz}$ distribution (see Figure 3.36) and visual inspection. The remaining 54 of the CORNISH-South PNe have no astronomical records in the SIMBAD database. Thus, they are classified as new detections and indicated with the $*$ symbol in Table 3.8.

3.8 Conclusion

The calibration and imaging of data from the CORNISH south survey is presented. The resolution of 2.5″ and noise level of 0.2 mJy/beam of the CORNISH survey presents a matching radio data to the GLIMPSE and VVV survey of the southern Galactic plane. The CORNISH-South survey achieved a better sensitivity compared to the CORNISH-North survey, despite the smaller number of dishes of the ATCA array, due to the 'on-the-fly' method and the multi-frequency

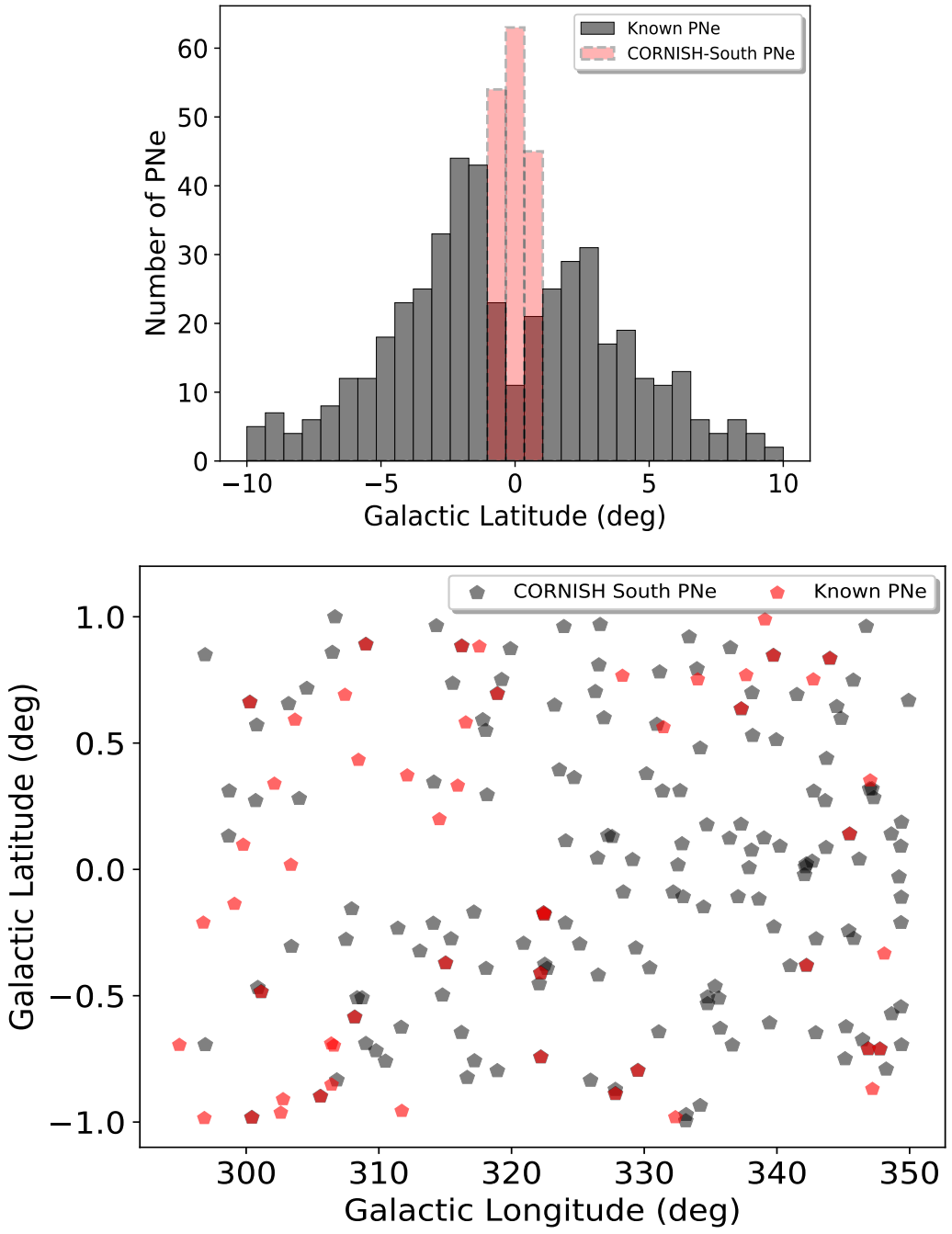

Figure 3.39: *Comparison of the CORNISH-South PNe and known PNe from the HASH catalogue (Parker* et al., *2017).*

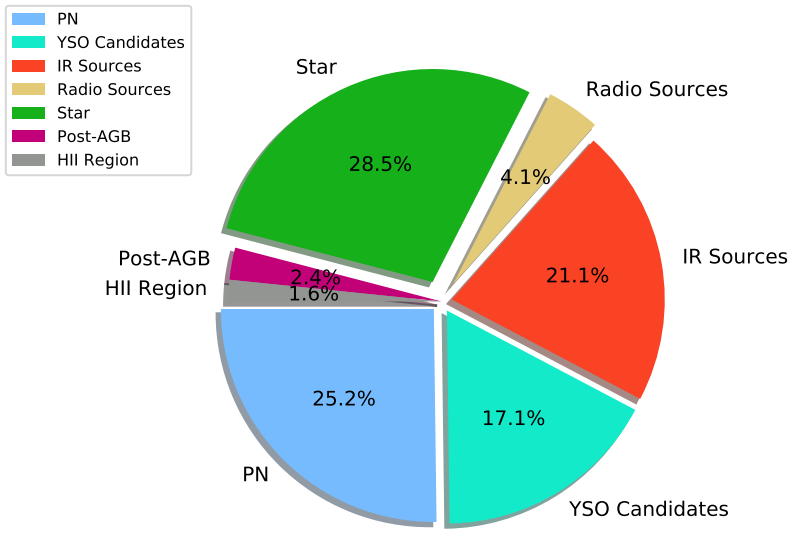

Figure 3.40: *A pie chart showing the percentage of the different source types in the CORNISH-South PNe catalogue and SIMBAD database cross-match. The classification is according to the SIMBAD database. Other source type makes up 6.8%.*

synthesis implemented. This doubled the uv-coverage compared to the traditional mosaicing used for the CORNISH-North survey (VLA; Purcell *et al.* 2013). This CORNISH-South data is particularly important in the characterization of compact ionized sources, such as PNe, towards the Galactic mid-plane, as no radio survey has previously covered the southern Galactic plane in such resolution and sensitivity. The general catalogue presented here contains 5013 sources at a 7σ threshold. However, direct interpretation of very extended images should be done with caution. This is because some very extended sources were not properly imaged and some regions would have done better with manual CLEANing. Visual inspection will still be needed to provide a more reliable catalogue by eliminating spurious sources from regions that were not properly imaged. Data products, images and catalogues of individual source classes, will be made available on the CORNISH Web site `http://cornish.leeds.ac.uk`. The measured properties show similar distributions compared to CORNISH-North catalogue presented in Purcell *et al.* (2013).

The focus of this study was, however, on PNe. Based on multi-wavelength properties and visual inspection of multi-wavelength images, which included the use of infrared, sub-mm and optical data. 184 of the 7σ sources are classified as PNe and 3 are classified as possible PNe due to insufficient data (see Figure B.78). With the sensitivity of the CORNISH south survey that is two times better than the CORNISH north counterpart, PNe with lower radio flux densities were detected. The CORNISH-South PNe show similar NIR and MIR colours compared to the CORNISH-North PNe. In the FIR colour-colour planes, the CORNISH-South PNe show a few more PNe within the region dominated by HII regions, compared to the distribution of the CORNISH-North PNe. A mean $F_{8.0\mu m}/F_{5GHz}$ of 4.3 ± 1.2 was estimated, which agrees within 1σ with the CORNISH-North PNe value of 3.9 ± 0.90.

29 previously known PNe were recovered and 54 have no astronomical records in the SIMBAD database, within a $60''$ search radius. The CORNISH survey has detected more PNe in the southern Galactic plane compared to previously known PNe within the $|b| < 1^\circ$ region. This demonstrates that the search for PNe at radio wavelengths is a strong tool in finding new PNe. The radio properties of the CORNISH south PNe are presented in Table 3.8 and the infrared colours are presented in Tables B.1 and B.2. The image catalogue of all the sources classified as PNe is presented in section B.

Table 3.7: *Known true PNe detected in the CORNISH south survey. Columns 4 and 5 are diameters as reported in the HASH database (Parker et al., 2017), column 6 is the radio diameter determined in this work and the last column shows if it is an extended source (P) or a Gaussian (G) in the CORNISH survey.*

CORNISH Name	PNG	Other name	MajDiam arcsec	MinDiam arcsec	$\vartheta_{\rm radio}$ arcsec	mtype
G300.2780+0.6616	300.2+00.6	Hen 2-83	4.7	4.5	4.73	G
G300.4290–0.9820	300.4-00.9	Hen 2-84	35.8	23.7	4.05	G
G300.5890–1.1087	300.5-01.1	Hen 2-85	9.2	7.9	6.88	G
G301.1270–0.4848	301.1-00.4	MPA J1235-6318	7.0	5.0	4.49	G
G305.5990–0.8984	305.6-00.9	MPA J1315-6338	6.0	6.0	5.11	G
G308.1820–0.5848	308.1-00.5	MPA J1337-6258	8.0	7.0	5.78	G
G309.0210+0.8907	309.0+00.8	Hen 2-96	2.8	2.8	3.82	G
G313.3010+1.1335	313.3+01.1	WRAY 17-66	4.5		2.6	G
G315.0310–0.3694	315.0-00.3	Hen 2-111	29.4	14.5	15.76	P
G315.7820–1.1441	315.7-01.1	MPA J1441-6114	7.0	6.0	4.21	G
G316.2470+0.8837	316.2+00.8	GLMP 387	6.0	6.0	7.19	P
G318.9310+0.6956	318.9+00.7	PHR J1457-5812	27.8		20.11	P
G322.1980–0.4107	322.2-00.4	BMP J1522-5729	13.0	11.0	4.48	G
G322.2070–0.7429	322.2-00.7	PM 1-90	7.0	7.0	4.17	G
G322.4180–0.1721	322.4-00.1a	MPA J1523-5710	35.0	6.5	6.56	G
G322.4690–0.1779	322.4-00.1	Pe 2-8	2.5		6.88	P
G327.8290–0.8881	327.8-00.8	PM 1-104	8.0		5.02	G
G329.5230–0.7963	329.5-00.8	MPA J1605-5319	8.0	6.0	7.58	P
G331.0310+1.2055	331.0+01.2	IRAS 16005-5041	2.7		2.8	G
G333.4290+1.1869	333.4+01.1	Pe 1-5	9.3	8.0	5.0	G
G335.4920–1.1031	335.4-01.1	Hen 2-169	33.0	19.0	5.17	G
G337.3140+0.6350	337.3+00.6	PHR J1633-4650	13.9		3.91	G
G339.7360+0.8469	339.7+00.8	GLIPN1642-4453			4.54	G
G342.2260–0.3801	342.2-00.3	PM 1-119	4.7		5.08	G
G343.9920+0.8350	343.9+00.8	H 1-5	5.2		5.91	G
G345.4790+0.1392	345.4+00.1	IC 4637	18.9	13.5	8.0	P
G346.8830–0.7106	346.8-00.7	MPA J1713-4015	7.0	5.0	3.75	G
G347.7630–0.7109	347.7-00.7	RPZM 8			3.91	G
G349.5090+1.0558	349.5+01.0	NGC 6302	90	35.0	6.3	G

Table 3.8: *Radio properties of the PNe detected in the CORNISH survey of the southern Galactic plane at 5.5 GHz. The Type column indicates if the properties of the source is measured under a 2D Gaussian or a polygon. Sources marked with 'a' are possible PNe (3) with insufficient data to draw a conclusion. ∗ indicates PNe with no match in the SIMBAD database.*

sourceName	RA2000	DEC2000	S_{int} mJy	dS_{int} mJy	Peak mJy/beam	dpeak mJy/beam	ϑ arcsec	$d\vartheta$ arcsec	Type
G296.9040+0.8494	12:00:42.67	-61:25:38.4	0.81	0.07	1.08	0.1	2.17	0.01	G[a]
G296.9180–0.6942∗	11:58:10.55	-62:56:32.4	1.05	0.09	1.31	0.1	2.23	0.04	G
G298.7140+0.3104	12:15:04.05	-62:15:47.4	19.32	0.12	18.71	0.12	2.54	0.0	G
G299.1520+0.0088	12:18:28.63	-62:37:16.1	18.83	1.82	2.23	0.44	12.45	0.34	P
G300.2780+0.6616	12:28:43.97	-62:05:35.2	67.09	0.35	37.63	0.17	3.34	0.0	G
G300.4290–0.9820	12:28:46.82	-63:44:36.9	8.43	0.14	6.49	0.1	2.85	0.01	G
G300.5890–1.1087	12:30:07.54	-63:53:00.7	79.84	0.66	21.18	0.15	4.85	0.01	G
G300.7130+0.2719∗	12:32:11.15	-62:31:00.9	0.81	0.09	0.97	0.11	2.29	0.0	G[a]
G300.7950+0.5707∗	12:33:04.78	-62:13:29.4	10.82	0.19	4.91	0.09	3.71	0.0	G
G300.8780–0.4677	12:33:09.66	-63:15:59.7	5.56	0.15	4.22	0.1	2.87	0.02	G
G301.1270–0.4848	12:35:21.45	-63:18:00.6	1.88	0.15	1.24	0.1	3.08	0.02	G
G303.1960+0.6558	12:53:42.15	-62:12:53.3	1.13	0.09	1.26	0.1	2.37	0.01	G
G303.4090–0.3055	12:55:40.03	-63:10:23.9	1.06	0.1	1.3	0.1	2.26	0.05	G
G304.5710+0.7160	13:05:27.86	-62:06:39.7	41.3	0.37	30.92	0.24	2.89	0.01	G
G305.5990–0.8984	13:15:30.39	-63:38:43.6	7.54	0.21	3.61	0.1	3.61	0.0	G
G306.1250–1.1375	13:20:27.22	-63:49:45.2	8.31	0.32	8.3	0.27	2.5	0.02	G
G306.4970+0.8585∗	13:21:41.07	-61:48:13.1	2.81	0.2	1.44	0.09	3.49	0.06	G
G306.6950+0.9993∗	13:23:12.08	-61:38:24.6	1.74	0.1	1.68	0.1	2.54	0.0	G
G306.8350–0.8337∗	13:26:27.51	-63:26:23.3	1.74	0.12	1.56	0.09	2.64	0.05	G

Continued on next page

Table 3.8 – continued from previous page

sourceName	RA2000	DEC2000	S_{int} mJy	dS_{int} mJy	Peak mJy/beam	dpeak mJy/beam	ϑ arcsec	$d\vartheta$ arcsec	Type
G307.5240–0.2775	13:31:46.31	-62:47:20.7	45.76	1.78	38.58	0.18	6.14	0.1	P
G307.9500–0.1567∗	13:35:15.95	-62:36:02.3	9.92	0.26	3.07	0.07	4.5	0.03	G
G308.1820–0.5848	13:37:54.92	-62:58:54.5	2.48	0.27	0.94	0.08	4.07	0.13	G
G308.3650–0.5085	13:39:22.52	-62:52:24.4	1.68	0.08	2.28	0.1	2.15	0.03	G
G308.7340–0.5086	13:42:33.10	-62:48:10.7	34.29	2.36	8.82	0.18	22.96	0.1	P
G309.0200–0.6894	13:45:19.56	-62:55:20.7	4.67	0.13	3.89	0.09	2.74	0.02	G
G309.0210+0.8907	13:42:36.17	-61:22:28.9	75.75	0.2	64.86	0.17	2.7	0.0	G
G309.7840–0.7181	13:51:55.17	-62:46:56.7	6.04	0.14	4.25	0.1	2.98	0.0	G
G310.5000–0.7593	13:58:03.96	-62:38:52.5	32.43	0.25	18.99	0.12	3.27	0.01	G
G311.4310–0.2333∗	14:04:34.06	-61:53:32.4	9.05	0.12	7.05	0.09	2.83	0.0	G
G311.6840–0.6255	14:07:35.38	-62:11:46.4	62.62	0.17	48.84	0.13	2.83	0.0	G
G311.8200–1.0601	14:09:48.64	-62:34:18.1	7.88	0.18	6.2	0.14	2.82	0.0	G
G313.0900–0.3236∗	14:18:07.82	-61:28:25.2	4.49	0.32	1.29	0.08	4.67	0.1	G
G313.3010+1.1335	14:15:53.31	-60:01:37.7	56.44	0.55	51.54	0.43	2.62	0.01	G
G314.1020–0.2136	14:25:43.49	-61:01:25.6	2.1	0.15	1.15	0.08	3.39	0.01	G
G314.1460+0.3451	14:24:26.35	-60:29:09.3	23.63	0.17	11.63	0.08	3.56	0.0	G
G314.3340+0.9639	14:24:06.44	-59:50:26.0	20.15	0.17	17.86	0.13	2.66	0.01	G
G314.7930–0.4976	14:31:53.67	-61:02:04.4	4.07	0.38	0.86	0.07	5.43	0.1	G
G315.0310–0.3694	14:33:17.96	-60:49:38.0	17.52	3.34	1.89	0.48	24.34	0.14	P
G315.1680–1.0001∗	14:36:22.26	-61:21:13.7	1.42	0.13	1.03	0.1	2.94	0.0	G
G315.4370–0.2749	14:36:03.73	-60:34:52.2	12.23	0.15	11.28	0.12	2.6	0.01	G
G315.5620+0.7363∗	14:33:50.12	-59:36:02.7	2.32	0.15	1.47	0.09	3.13	0.01	G
G315.7820–1.1441	14:41:32.17	-61:14:18.1	26.3	0.95	18.57	0.58	2.98	0.03	G
G316.2270–0.6457	14:43:09.87	-60:36:02.9	34.84	3.97	30.24	0.33	5.63	0.11	P

Continued on next page

Table 3.8 – continued from previous page

sourceName	RA2000	DEC2000	S_{int} mJy	dS_{int} mJy	Peak mJy/beam	dpeak mJy/beam	ϑ arcsec	$d\vartheta$ arcsec	Type
G316.2470+0.8837	14:38:19.97	-59:11:46.5	63.42	3.9	48.56	0.95	7.19	0.11	P
G316.6570–0.8240∗	14:46:57.44	-60:34:47.8	1.7	0.11	1.4	0.09	2.76	0.0	G
G317.1650–0.1697	14:48:22.16	-59:46:11.6	27.19	1.77	5.26	0.23	9.55	0.16	P
G317.2040–0.7580	14:50:42.74	-60:16:55.3	26.57	0.16	23.71	0.14	2.65	0.0	G
G317.8340+0.5920∗	14:50:27.54	-58:47:34.1	2.86	0.17	1.52	0.09	3.43	0.0	G
G318.0520+0.5496	14:52:06.63	-58:44:02.0	18.47	0.26	7.98	0.1	3.8	0.01	G
G318.0800–0.3924∗	14:55:38.31	-59:33:38.5	14.21	0.19	8.85	0.1	3.17	0.01	G
G318.1590+0.2944∗	14:53:44.37	-58:54:48.4	5.23	0.12	4.27	0.1	2.77	0.0	G
G318.9290–0.7972∗	15:03:03.21	-59:31:02.7	29.68	2.53	28.02	0.28	5.93	0.11	P
G318.9310+0.6956	14:57:35.47	-58:12:06.9	51.7	2.67	3.12	1.62	20.63	0.13	P
G319.2560+0.7512	14:59:33.44	-58:00:04.7	1.38	0.09	1.68	0.1	2.26	0.0	G
G319.9150+0.8732	15:03:27.87	-57:34:43.3	13.34	0.21	11.98	0.16	2.64	0.01	G
G320.3670–1.0613	15:13:49.51	-59:01:33.7	7.35	2.17	2.16	1.27	10.56	2.7	P
G320.9060–0.2928	15:14:18.37	-58:05:20.8	49.92	0.32	43.38	0.24	2.68	0.0	G
G322.0860–0.4532	15:22:27.05	-57:35:49.6	8.44	0.15	9.05	0.14	2.41	0.01	G
G322.1980–0.4107	15:22:58.94	-57:29:59.4	25.53	0.25	15.92	0.14	3.17	0.01	G
G322.2070–0.7429	15:24:24.04	-57:46:21.5	48.18	0.3	34.65	0.19	2.95	0.0	G
G322.4180–0.1721	15:23:22.54	-57:10:48.9	8.7	0.35	2.72	0.11	4.47	0.02	G
G322.4690–0.1779	15:23:42.86	-57:09:25.2	155.05	10.46	130.9	0.73	6.88	0.1	P
G322.5030–0.3761	15:24:43.89	-57:18:13.0	30.26	0.23	27.15	0.18	2.64	0.0	G
G322.6850–0.3924	15:25:55.03	-57:12:59.9	3.49	0.25	1.96	0.12	3.34	0.06	G
G323.2460+0.6498	15:25:06.66	-56:02:17.9	1.79	0.1	2.4	0.14	2.16	0.0	G
G323.6010+0.3936	15:28:14.73	-56:03:10.1	25.88	0.25	17.98	0.15	3.0	0.01	G
G323.9470+0.9607	15:28:00.73	-55:23:22.1	0.88	0.1	1.04	0.12	2.3	0.02	G

Continued on next page

Table 3.8 – continued from previous page

sourceName	RA2000	DEC2000	S_{int} mJy	dS_{int} mJy	Peak mJy/beam	dpeak mJy/beam	ϑ arcsec	$d\vartheta$ arcsec	Type
G324.0610–0.2125	15:33:26.68	-56:17:17.9	43.02	0.27	30.34	0.19	2.98	0.0	G
G324.0810+0.1125∗	15:32:13.07	-56:00:40.0	1.33	0.12	1.45	0.13	2.39	0.01	G
G324.7230+0.3628	15:34:54.43	-55:26:08.7	10.26	0.2	7.02	0.14	3.02	0.0	G
G325.1370–0.2960	15:40:01.39	-55:43:25.0	30.29	4.27	14.56	0.24	12.77	0.1	P
G325.9530–0.8350∗	15:46:56.94	-55:39:22.4	6.46	0.22	2.47	0.09	4.04	0.01	G
G326.3150+0.7034	15:42:24.52	-54:12:58.2	20.42	2.79	3.78	0.56	8.47	0.17	P
G326.4820+0.0448∗	15:46:04.46	-54:38:14.6	7.59	0.21	6.04	0.14	2.8	0.02	G
G326.5300–0.4188	15:48:19.39	-54:58:20.8	19.85	0.27	15.5	0.18	2.83	0.01	G
G326.5800+0.8090	15:43:24.39	-53:58:20.7	32.83	3.98	30.37	0.36	5.41	0.1	P
G326.6780+0.9689	15:43:16.70	-53:47:08.5	21.42	0.24	14.3	0.16	3.06	0.0	G
G326.9680+0.5997∗	15:46:21.75	-53:54:04.3	3.03	0.37	1.17	0.12	4.03	0.15	G
G327.2660+0.1339∗	15:49:55.17	-54:04:53.2	8.92	0.18	9.04	0.16	2.48	0.01	G
G327.5840+0.1301	15:51:37.39	-53:53:06.3	17.84	2.41	4.24	0.16	9.84	0.13	P
G327.8260–0.8712	15:57:15.53	-54:30:08.0	17.21	2.4	13.77	0.3	6.59	0.1	P
G327.8290–0.8881	15:57:21.08	-54:30:46.5	65.74	0.47	32.8	0.23	3.54	0.0	G
G328.4240–0.0892	15:56:56.32	-53:31:09.5	25.13	5.03	7.27	0.25	14.86	0.15	P
G329.1200+0.0385	15:59:55.59	-52:58:14.4	6.18	0.24	4.14	0.14	3.05	0.03	G
G329.3620–0.3111	16:02:40.22	-53:04:31.0	3.05	0.2	2.18	0.12	2.96	0.05	G
G329.5230–0.7963	16:05:37.35	-53:19:53.9	10.29	1.7	6.07	0.2	7.58	0.13	P
G330.1680+0.3779∗	16:03:39.07	-52:01:34.3	2.56	0.24	1.21	0.12	3.64	0.01	G
G330.4100–0.3900	16:08:10.69	-52:26:09.5	5.77	0.28	2.98	0.12	3.48	0.04	G
G330.9510+0.5738	16:06:34.96	-51:21:30.3	32.48	0.29	23.8	0.18	2.92	0.01	G
G331.0310+1.2055	16:04:16.70	-50:50:04.1	51.99	5.6	40.82	4.33	2.82	0.03	G
G331.0970–0.6435	16:12:36.06	-52:09:20.4	37.58	0.32	15.68	0.12	3.87	0.01	G

Continued on next page

Table 3.8 – continued from previous page

sourceName	RA2000	DEC2000	S_{int} mJy	dS_{int} mJy	Peak mJy/beam	dpeak mJy/beam	ϑ arcsec	$d\vartheta$ arcsec	Type
G331.1580+0.7811	16:06:40.63	-51:03:57.3	3.03	0.15	2.91	0.13	2.55	0.03	G
G331.3720+0.3100	16:09:42.64	-51:16:11.3	29.69	0.23	27.64	0.19	2.59	0.01	G
G331.7280–1.0097	16:17:13.32	-51:59:04.8	252.28	12.59	33.31	2.63	18.72	0.11	P
G332.1280–1.0061	16:19:03.37	-51:42:09.4	5.58	0.24	2.55	0.11	3.7	0.0	G
G332.1880–0.0898	16:15:14.82	-51:00:11.0	19.54	0.23	16.39	0.17	2.73	0.01	G
G332.5450+0.0174∗	16:16:24.63	-50:40:41.1	13.67	0.27	7.03	0.12	3.49	0.02	G
G332.6990+0.3108∗	16:15:49.43	-50:21:36.1	4.28	2.05	1.28	0.54	8.53	0.12	P
G332.8470+0.1009	16:17:24.60	-50:24:29.9	2.86	0.15	3.04	0.14	2.42	0.03	G
G332.9300–0.1090	16:18:42.11	-50:30:03.5	4.41	0.45	1.11	0.09	4.98	0.16	G
G333.1310–0.9954	16:23:33.24	-50:59:15.5	20.9	0.16	19.93	0.13	2.56	0.0	G
G333.1600–0.9705	16:23:34.62	-50:56:57.3	53.81	2.87	6.49	0.19	13.04	0.16	P
G333.3830+0.9199	16:16:16.09	-49:26:49.5	55.53	3.2	12.44	0.37	9.24	0.1	P
G333.4290+1.1869	16:15:20.04	-49:13:21.7	132.96	2.37	33.37	0.59	4.99	0.0	G
G333.8770–1.0078	16:26:54.33	-50:27:46.3	6.1	0.14	6.42	0.12	2.44	0.01	G
G333.9730+0.7937	16:19:23.81	-49:07:34.3	21.03	0.16	20.0	0.15	2.56	0.0	G
G334.1310+1.0148	16:19:08.52	-48:51:26.1	13.42	0.17	13.6	0.17	2.48	0.0	G
G334.2150+0.4794∗	16:21:48.22	-49:10:42.0	16.97	3.04	4.14	0.14	11.68	0.1	P
G334.2180–0.9350∗	16:28:03.49	-50:10:01.2	23.81	0.26	17.3	0.16	2.93	0.01	G
G334.4740–0.1495	16:25:39.75	-49:26:12.4	5.0	0.15	4.8	0.15	2.55	0.0	G
G334.7200+0.1763	16:25:17.32	-49:01:58.4	9.58	0.18	8.88	0.15	2.6	0.01	G
G334.7640–0.5319	16:28:35.92	-49:29:35.9	3.45	0.12	3.71	0.12	2.41	0.0	G
G334.7680–1.0420∗	16:30:54.07	-49:50:30.1	13.79	0.21	10.35	0.14	2.89	0.01	G
G334.7730–0.5050	16:28:31.03	-49:28:05.2	4.88	0.13	5.37	0.14	2.38	0.0	G
G334.8320+1.0014∗	16:22:12.54	-48:22:23.5	2.03	0.21	1.13	0.12	3.35	0.02	G

Continued on next page

Table 3.8 – continued from previous page

sourceName	RA2000	DEC2000	S_{int} mJy	dS_{int} mJy	Peak mJy/beam	dpeak mJy/beam	ϑ arcsec	$d\vartheta$ arcsec	Type
G335.3370–0.4632	16:30:42.68	-49:01:50.1	7.41	0.18	6.57	0.14	2.65	0.02	G
G335.4920–1.1031	16:34:13.40	-49:21:12.1	8.91	1.15	4.36	0.46	3.57	0.13	G
G335.6160–0.5101	16:32:04.86	-48:51:34.8	5.14	0.2	3.27	0.13	3.13	0.0	G
G335.7200–0.6294	16:33:02.51	-48:51:54.0	6.25	0.16	5.43	0.13	2.68	0.0	G
G336.4230+0.1230∗	16:32:36.66	-47:50:14.4	9.6	0.22	5.91	0.12	3.19	0.02	G
G336.4910+0.8775	16:29:37.65	-47:16:16.8	10.98	0.38	3.67	0.11	4.33	0.04	G
G336.6440–0.6956	16:37:06.60	-48:13:42.8	35.83	2.52	26.98	0.25	7.13	0.11	P
G337.0640–1.1730	16:40:55.80	-48:13:59.7	16.96	1.3	15.86	1.04	2.58	0.05	G
G337.0700–0.1085∗	16:36:13.57	-47:31:06.1	11.78	0.22	9.04	0.17	2.85	0.0	G
G337.2910+0.1782	16:35:51.29	-47:09:42.2	5.53	0.21	2.79	0.1	3.52	0.0	G
G337.3140+0.6350	16:33:58.30	-46:50:09.3	38.55	0.24	31.62	0.17	2.76	0.0	G
G337.9010+0.0063	16:39:00.00	-46:49:27.8	2.05	0.26	1.16	0.12	3.32	0.12	G
G338.0840+0.0757	16:39:24.48	-46:38:30.6	6.53	0.12	6.77	0.13	2.45	0.0	G
G338.1210+0.6991∗	16:36:51.64	-46:11:51.9	7.65	0.17	6.3	0.12	2.75	0.01	G
G338.1700+0.5297∗	16:37:46.66	-46:16:29.6	5.91	0.15	5.81	0.13	2.52	0.02	G
G338.6430–0.1176∗	16:42:23.98	-46:21:04.2	14.15	2.55	7.01	0.19	9.21	0.11	P
G339.0280+0.1243	16:42:48.69	-45:54:06.2	28.29	0.26	20.69	0.16	2.92	0.01	G
G339.4050+1.0302∗	16:40:21.14	-45:01:12.3	14.9	0.27	8.37	0.13	3.34	0.02	G
G339.4430–0.6081∗	16:47:34.01	-46:03:51.1	11.57	0.19	7.57	0.12	3.09	0.0	G
G339.7360+0.8469	16:42:21.99	-44:53:34.4	2.29	0.18	1.4	0.11	3.2	0.01	G
G339.7730–0.2274∗	16:47:07.36	-45:34:00.6	6.13	0.14	6.58	0.13	2.41	0.01	G
G339.9510+0.5127	16:44:35.30	-44:56:58.8	1.47	0.17	1.12	0.13	2.87	0.01	G
G340.2290+0.0915∗	16:47:25.02	-45:00:45.6	3.66	0.52	1.07	0.11	4.62	0.22	G
G340.9940–0.3820	16:52:14.23	-44:43:43.9	8.72	0.24	5.43	0.15	3.17	0.01	G

Continued on next page

Table 3.8 – continued from previous page

sourceName	RA2000	DEC2000	S_{int} mJy	dS_{int} mJy	Peak mJy/beam	dpeak mJy/beam	ϑ arcsec	$d\vartheta$ arcsec	Type
G341.3620–1.0363	16:56:24.57	-44:51:18.5	4.19	0.2	3.78	0.15	2.63	0.03	G
G341.5040+0.6919∗	16:49:26.52	-43:39:03.1	12.29	0.27	10.9	0.21	2.66	0.01	G
G342.0820–0.0220∗	16:54:31.22	-43:39:31.1	5.33	0.17	4.92	0.14	2.6	0.02	G
G342.1470+0.0101	16:54:36.62	-43:35:15.2	37.46	0.24	34.56	0.22	2.6	0.0	G
G342.2140+0.0213∗	16:54:47.68	-43:31:42.8	5.8	0.13	6.0	0.14	2.46	0.0	G
G342.2260–0.3801	16:56:33.97	-43:46:14.6	199.49	0.99	97.19	0.48	3.58	0.0	G
G342.6560+0.0320	16:56:16.57	-43:10:38.3	10.26	0.36	3.11	0.09	4.54	0.04	G
G342.7770+0.3094∗	16:55:30.46	-42:54:33.8	7.9	0.18	5.93	0.13	2.89	0.0	G
G342.9260–0.6469	17:00:07.15	-43:23:17.2	9.88	1.07	1.05	0.08	7.67	0.31	G
G342.9550–0.2750∗	16:58:36.89	-43:08:04.8	28.28	0.23	24.08	0.17	2.71	0.01	G
G343.6380+0.2717∗	16:58:35.14	-42:15:37.2	2.12	0.15	2.33	0.14	2.38	0.04	G
G343.7020+0.0862	16:59:35.24	-42:19:29.9	13.21	0.15	11.82	0.13	2.64	0.0	G
G343.7380+0.4392∗	16:58:12.81	-42:04:41.2	3.39	1.82	1.34	0.19	6.62	0.13	P
G343.7430–1.0878∗	17:04:46.42	-43:00:40.7	6.29	0.36	2.97	0.17	3.64	0.01	G
G343.9920+0.8350	16:57:23.76	-41:37:58.4	328.78	0.95	117.74	0.29	4.18	0.0	G
G344.0600+1.0054	16:56:54.63	-41:28:24.7	8.32	0.29	3.3	0.11	3.97	0.01	G
G344.5090+0.6443	16:59:54.56	-41:20:42.5	18.88	0.28	11.68	0.15	3.18	0.01	G
G344.8350+0.5975∗	17:01:10.26	-41:07:03.8	6.2	0.36	2.01	0.1	4.39	0.07	G
G345.1350–0.7500	17:07:51.38	-41:41:46.5	4.06	0.32	1.75	0.12	3.81	0.08	G
G345.2060–0.6231∗	17:07:32.42	-41:33:48.6	6.94	0.15	6.94	0.15	2.5	0.0	G
G345.4050–0.2440	17:06:33.61	-41:10:38.1	2.39	0.12	2.97	0.14	2.24	0.03	G
G345.4790+0.1392	17:05:10.60	-40:53:10.3	131.98	6.12	12.64	0.17	22.37	0.12	P
G345.7570+0.7486∗	17:03:30.96	-40:17:45.1	9.54	0.25	5.3	0.12	3.35	0.02	G
G345.7960–0.2738	17:07:56.02	-40:52:55.0	2.52	0.15	2.68	0.14	2.42	0.04	G

Continued on next page

Table 3.8 – continued from previous page

sourceName	RA2000	DEC2000	S_{int} mJy	dS_{int} mJy	Peak mJy/beam	dpeak mJy/beam	ϑ arcsec	$d\vartheta$ arcsec	Type
G346.1960+0.0402	17:07:52.27	-40:22:25.1	6.72	0.16	5.3	0.13	2.81	0.0	G
G346.4200–1.0610∗	17:13:14.48	-40:50:48.6	2.89	0.22	2.86	0.18	2.51	0.05	G
G346.4560–0.6739∗	17:11:42.21	-40:35:24.5	2.96	2.27	1.02	0.34	10.41	0.37	P
G346.7300+0.9617	17:05:42.40	-39:23:35.3	5.8	0.26	3.0	0.11	3.47	0.04	G
G346.8830–0.7106	17:13:10.82	-40:15:56.8	21.42	0.2	19.07	0.16	2.65	0.01	G
G346.9840+0.3185	17:09:09.91	-39:34:32.2	12.98	0.27	5.39	0.11	3.88	0.0	G
G347.1660+0.3190∗	17:09:43.38	-39:25:46.0	2.39	0.22	1.69	0.13	2.97	0.07	G
G347.2970+0.2832	17:10:16.62	-39:20:41.5	10.12	0.15	10.16	0.15	2.49	0.0	G
G347.7630–0.7109	17:15:51.61	-39:33:08.5	27.09	0.22	22.17	0.18	2.76	0.0	G
G348.2330–0.7909∗	17:17:36.53	-39:12:53.5	3.22	0.13	3.82	0.15	2.3	0.0	G
G348.6210+0.1399	17:14:52.40	-38:21:32.7	7.4	0.15	6.98	0.14	2.57	0.0	G
G348.6420–0.5720∗	17:17:54.13	-38:45:17.3	8.47	0.3	3.12	0.11	4.12	0.0	G
G349.1970–0.0301∗	17:17:16.83	-37:59:19.7	5.97	0.28	3.23	0.13	3.4	0.04	G
G349.3340+0.0915	17:17:10.71	-37:48:24.7	1.12	0.13	1.25	0.14	2.36	0.0	G[a]
G349.3480–0.5442	17:19:51.46	-38:09:40.6	17.91	0.16	16.01	0.15	2.64	0.0	G
G349.3510–0.2113	17:18:28.99	-37:58:02.1	44.16	0.21	43.53	0.18	2.52	0.0	G
G349.3700–0.1105	17:18:07.25	-37:53:37.3	22.41	0.25	9.93	0.11	3.75	0.0	G
G349.3870+0.1862∗	17:16:56.50	-37:42:31.5	3.14	1.62	1.95	0.42	5.13	0.17	P
G349.3890–0.6949	17:20:36.39	-38:12:49.6	4.0	0.13	4.83	0.14	2.27	0.02	G
G349.5090+1.0558	17:13:44.48	-37:06:11.2	2719.7	6.01	433.37	0.82	6.26	0.0	G
G349.9210+0.6682	17:16:31.30	-36:59:40.3	13.92	0.15	13.16	0.15	2.57	0.0	G
G350.0920+0.2309	17:18:48.43	-37:06:25.3	104.1	10.25	84.99	0.54	7.08	0.1	P
G350.1930–0.2232	17:20:57.96	-37:17:04.0	131.97	8.2	141.98	3.29	5.27	0.1	P

Chapter 4

PN Population Synthesis in Comparison to the CORNISH Survey

4.1 Introduction

A better understanding of stellar evolution, from the AGB phase up to PNe formation and further evolution, will require comparison of observational properties to predictions from population synthesis models. Using a population synthesis method, Moe & De Marco (2006) estimated a Galactic PNe population of 46000 ± 13000 PNe (with radii < 0.9 pc), assuming single and binary stellar systems result in PNe, and 8100 ± 2300 (Moe & De Marco, 2012), assuming only binary interactions result in observable PNe. The known population of PNe is biased towards angularly large PNe that are evolved or nearby and, optically visible PNe. However, the concern, in an attempt to understand these objects, will be to arrive at a statistically representative sample that is appropriate to compare with population synthesis model, a sample that is not biased by extinction. Such comparison provides the means to predict the properties of PNe and also test current evolution models.

Several authors (e.g. Marigo *et al.* 2001; Stanghellini & Renzini 2000a; Stasińska *et al.* 1998) have created synthetic population models of PNe with certain approximations e.g. morphology, density, expansion velocity, distance, nebulae mass that allow comparison of model predictions with specific observed properties of PNe. This is usually done in an attempt to understand specific properties of PN evolution and formation.

In this chapter the PNe sample from chapters 2 and 3 were used to test the population synthesis model. Observed properties such as Galactic latitude distribution, integrated flux densities, angular sizes and number of PNe are compared to population synthesis predictions within the CORNISH survey region.

4.2 Formulation of the Model

The observed properties of a PN are strongly tied to the evolution and ionizing spectrum of the central star (Kwok, 1993b, 1994; Rauch, 2003), hence modelling of PNe observables at radio wavelengths will be strongly affected by the ionizing spectrum and the mass loss history. The mass loss history determines the final mass of the central star and the mass available to form a PN. The progenitor mass, however, determines how quickly the PN evolves and fades away into the ISM i.e. its lifetime (Bloecker & Schoenberner, 1990). In order to compare the CORNISH survey to a population synthesis prediction, a synthetic population constrained by population synthesis parameters and by the CORNISH selection criteria, is created. In this work, the population synthesis model by Moe & De Marco (2006) is adopted. The basic structure of the model is presented in Figure 4.1. To create the synthetic population, the following assumptions are made:

- The Galactic disk population was considered, given that the CORNISH survey covers longitude, $l > 10^\circ$ and $l < 60^\circ$ in the northern Galactic plane and $l > 295^\circ$ and $l < 350^\circ$ in the southern Galactic plane.
- The central star emits as a blackbody. This is usually a fair approximation, however, there are indications that such approximation could overestimate the flux for CSPNe with temperatures < 40000 K (Marigo *et al.*, 2001).

Table 4.1: *Scale heights from the literature for the thin and thick disks.*

	Thin disk (pc)	Thick disk (pc)	Data/Description
Gilmore & Reid (1983)	~ 300	~ 1350	Stellar luminosity function from absolute magnitudes using photometric parallax of 12500 stars.
de Jong *et al.* (2010)		750 ± 70	By fitting colour-magnitude diagrams to photometric data from the Sloan Extension for Galactic Understanding and Exploration survey (SEGUE).
Chen *et al.* (2017)	~ 322	~ 794	Based on photometric data from the Xuyi Schmidt Telescope Photometry Survey and the Sloan Sky Survey (SDSS).
Chang *et al.* (2011)	360 ± 10	1020 ± 30	Using the K's band differential star count from the 2MASS survey for latitudes $\|b\| > 30$
Jurić *et al.* (2008)	300	900	Using 3D number density distribution in the Galaxy from distances (photometric parallax method) obtained for 48 million stars in the SDSS survey

- The nebula is a homogenous sphere of gas with uniform density.
- Constant electron temperature of 10000 K.

4.2.1 Distribution of PNe in the Galaxy

The Galactic disk is traditionally divided into the thin and thick disks. The thin disk accounts for $\sim 90\%$ of the stars close to the Sun (Zijlstra & Pottasch, 1991) and is sometimes characterized by the young and old disk or intermediate disk, where the young disk is closer to the Galactic plane (see Figure 4.2 for illustration). Different, but comparable scale heights have been proposed for the thin and thick disks by different authors (see Table 4.1), using different objects and methods.

Scale Height of PNe

From the work of Quireza *et al.* (2007), based on the initial work of Peimbert (1978), PNe are classified into four groups (see also Peimbert & Serrano 1980;

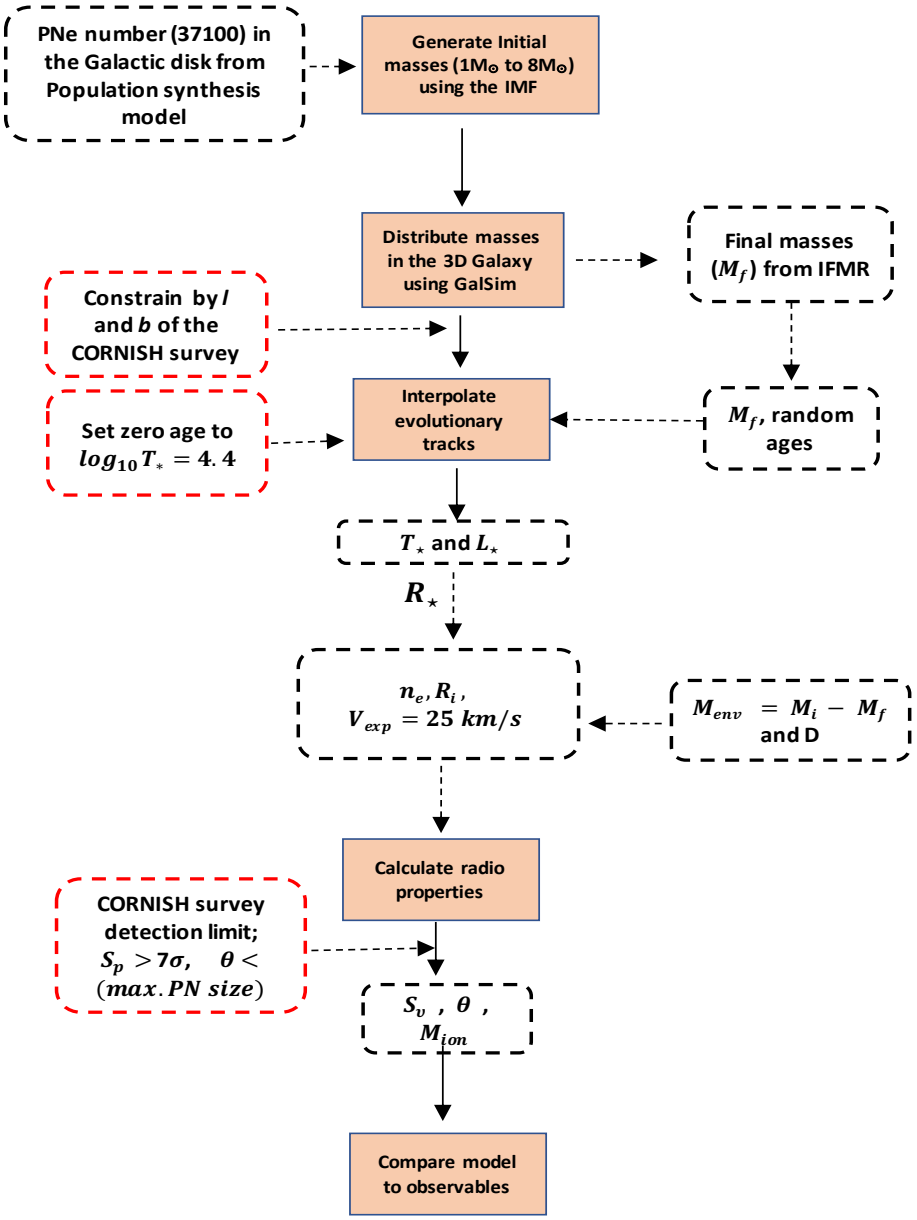

Figure 4.1: *Flow chart of the model.* M_f *is the final mass,* M_i *is the initial mass,* S_p *is the peak flux, D is the distance,* M_{env} *is the envelope mass,* ϑ *is the angular size,* n_e *is the electron density,* 7σ *is the detection limit of the CORNISH catalogue,* S_ν *is the flux density,* T_* *is the temperature of the central star,* L_* *is the luminosity of the central star and* R_* *is the radius of the central star.*

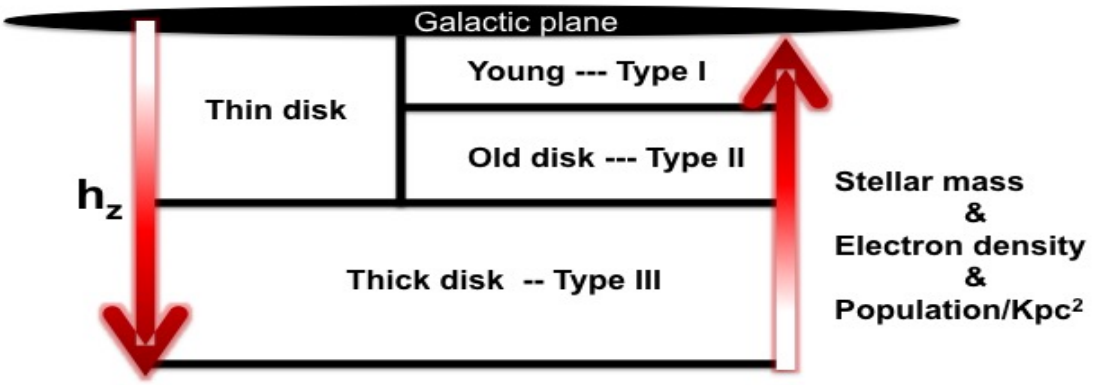

Figure 4.2: *The Galactic disk structure, showing how the population density and masses of PNe vary with height above the mid-plane. The types are defined by Peimbert (1978), excluding the bulge defined by type V PNe and halo PNe defined by type IV.*

Peimbert & Torres-Peimbert 1983 and Maciel & Dutra 1992). These are type I, II, III and IV, having progenitor mass stratification. PNe from the most massive progenitors (usually $> 0.6 M_{\odot}$; Quireza *et al.* 2007) are type I, found in the young disk that is closer to the Galactic mid-plane. Type II dominates the disk population of PNe, which is part of the intermediate disk, also referred to as the old disk (Zijlstra & Pottasch, 1991). Type III are PNe from old stars, found in the thick disk (> 10 Gyr; Hayden *et al.* 2017) and type IV are PNe in the Galactic halo. Figure 4.2 shows a simple stratification of the disks and the direction in which population and masses vary according to Peimbert (1978).

Scale heights of PNe have been discussed by different authors, based on samples of PNe, including Corradi & Schwarz (1995a); Frew (2008); Phillips (2003b, 2004); Zijlstra & Pottasch (1991) and Stanghellini *et al.* (2002). Assuming an exponential disk, Zijlstra & Pottasch (1991) estimated the scale height of local PNe to be 250 ± 50 pc or 190 ± 40 pc, assuming an isothermal disk. Stanghellini *et al.* (2002) estimated the scale of PNe based on statistical distances and they obtained different scale heights for the different morphological types. The highest scale height of 730 pc was estimated for round PNe and 200 pc for bipolar. The

scale height for round PNe agrees with the work of Manchado *et al.* (2000), who estimated a scale height of 753 pc for round PNe as well. Other estimates are 216 ± 24 pc (Frew, 2008), 325 for elliptical PNe and 259 pc for all PNe analyzed by (Corradi & Schwarz, 1995b). Using hydrogen-rich white dwarfs in the thin disk, Vennes *et al.* (2002) estimated a scale height of 220 - 300 pc. With better distance estimates for proto-Planetary nebulae (pPNe) by Vickers *et al.* (2015), Bobylev & Bajkova (2017) estimated a scale height of 146 ± 15 pc for thin disk pPNe having luminosities higher than $5000 L_{\odot}$ and 568 ± 42 pc for pPNe with luminosity lower than $5000 L_{\odot}$, excluding the bulge objects.

Initial Mass Distribution

The Kroupa (2001) multi-part law was used to generate stars with initial masses between 0.9 and $8 M_{\odot}$ for the assumed population. A lower mass limit of $0.9 M_{\odot}$ is set according to Moe & De Marco (2006) and the higher mass limit was set to $120 M_{\odot}$. The higher mass limit is, however, not important since the interest was just in stars within a mass range of 0.9 and $8 M_{\odot}$. The Kroupa (2001) IMF for the Galactic disk population is given by Equation 4.1 for different mass ranges in the form $\xi(m) \propto m^{-\alpha_i}$, such that $\xi(m)dm$ represents the number of stars in the mass interval between m to $m + dm$ and $\xi(m)$ is the initial mass function.

$$\xi(m) \propto m^{-\alpha_2 = +2.3 \pm 0.3}, \; 0.50 \leqslant m/M_{\odot} \leqslant 120 \tag{4.1}$$

Figure 4.3 shows the initial mass distribution obtained for a total population of 37100 (thin and thick disks). The mean and median values are shown on Table 4.2, along side the mean and median values obtained by Moe & De Marco (2006). Assuming 8.5 kpc (IAU standard) as the Galactocentric distance of the Sun (also see Chen *et al.* 2018; Eisenhauer *et al.* 2003; Qin *et al.* 2018 and Malkin 2013 and references therein), the estimated initial masses were then distributed in the thin and thick disks and the number density per kpc^2 for each of the disks is shown in Figure 4.5.

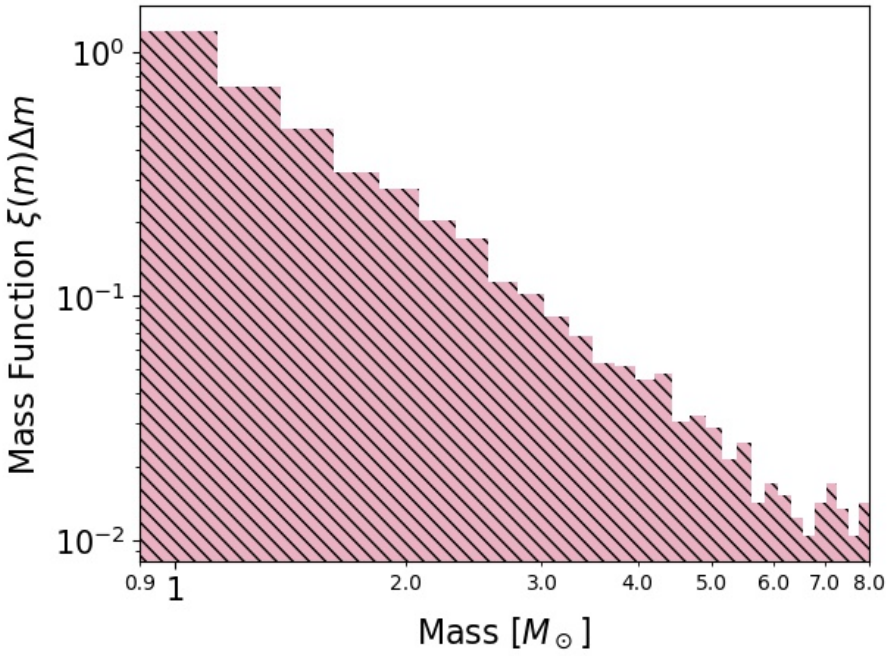

Figure 4.3: *Initial mass distribution of the generated populated according to Kroupa (2001).*

To determine a Galactic position for each star in the defined population, an algorithm developed by Davies *et al.* (2011) and Steggles (2016) was used. The density of the neutral gas in the Galaxy is assumed to be the same as the density structure of the Galactic free electrons according to Cordes & Lazio (2002); Taylor & Cordes (1993) (also see Yao *et al.* 2017). Each star is then inserted into the Galaxy following the Schmidt-Kennicutt law (Kennicutt, 1998), given by equation 4.2. The density of the thin and thick disks were treated separately, using the model parameters (NE2001) defined in Cordes & Lazio (2002) and the density map of the thin and thick disks are shown in Figure 4.4 (slice through Z=0). With the density of the thin and thick disks, an average constant SFR (star formation rate) of $1.5 M_\odot yr^{-1}$ is assumed in contrary to a smoothly varying SFR used by Moe & De Marco (2006).

$$\mathrm{SFR} \propto \sum \mathrm{N}_{\mathrm{dens}} \tag{4.2}$$

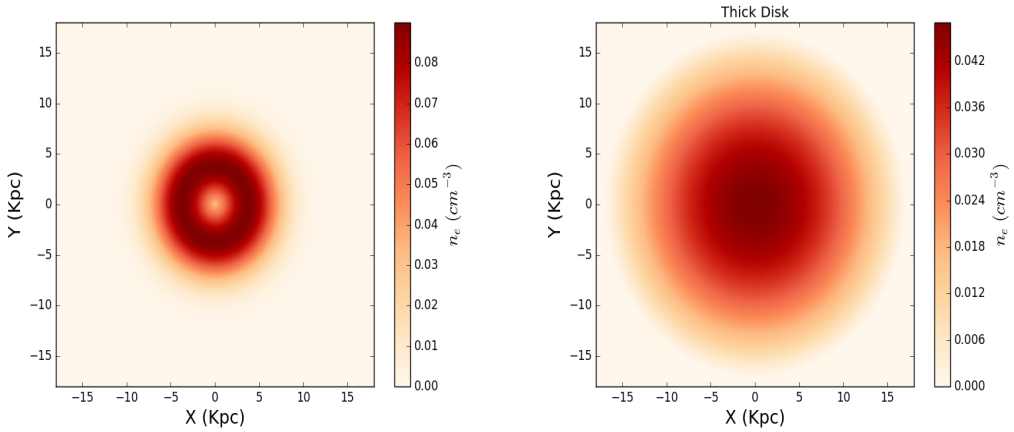

Figure 4.4: *A slice through Z=0 of the electron number density map for the thin (left) and thick (right) disk according to Cordes & Lazio (2002).*

where $\sum_{\text{dens}}$ is the surface density of the neutral gas and is assumed to be proportional to the neutral gas density ($\rho \propto \sum_{\text{dens}}$). N is taken as 1.4 (Davies *et al.*, 2011; Steggles, 2016).

Based on the estimated scale heights in the literature, given in previous section, the PNe population estimated from population synthesis (Moe & De Marco, 2006), for masses between 0.9 and $8M_{\odot}$, were distributed in the thin (36000 ± 1100) and thick disks (1100 ± 320). Figure 4.5 shows the number density of the distributed sources in the disks.

4.2.2 Final Mass Distribution

Based on the mass-loss history adopted, the final mass i.e. CSPNe (central star of PNe) can be estimated, given the initial mass of the star on the main sequence, by means of the IFMR (initial-to-final mass ratio). Moe & De Marco (2006) used the average IFMR from the evolutionary tracks of Vassiliadis & Wood (1994), Bloecker (1995) and Schoenberner (1983) to derive the CSPNe of their defined population. It should be noted that the Vassiliadis & Wood (1994) evolutionary tracks predicts larger CSPNe masses compared to the Bloecker (1995) tracks, hence shorter visibility time for higher masses (Moe & De Marco, 2006; Zijlstra

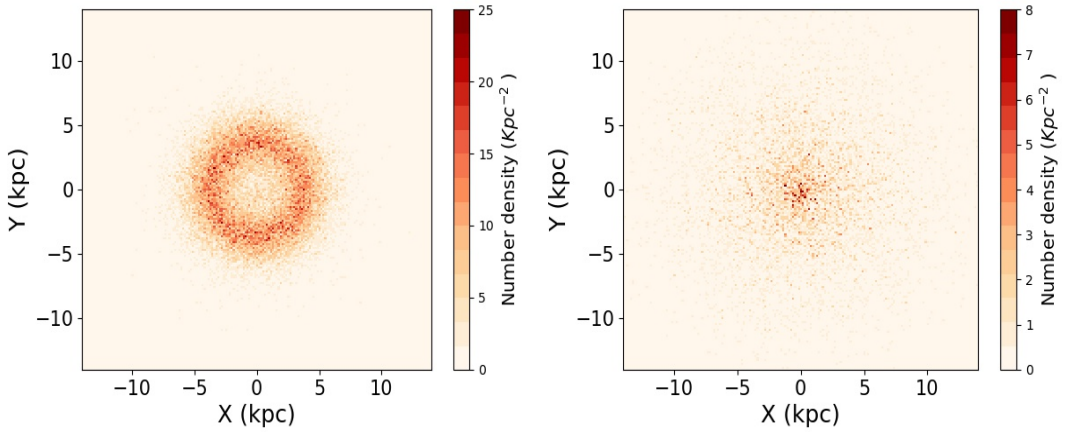

Figure 4.5: *Number density map (kpc^{-2}) of the thin (left:* 36000*) and thick (right:* 1100*) disks. X and Y are the cartesian coordinates and this view is a slice through Z=0.*

et al., 2008b). More recent evolutionary tracks (Miller Bertolami, 2016), however, predict CSPNe with lower masses (as low as $0.528M_{\odot}$) and faster evolution than previous tracks. The need for faster evolution tracks was previously demonstrated by Gesicki *et al.* (2014) who compared the distribution of CSPNe masses using the Bloecker (1995) tracks to the distribution of white dwarfs masses and asteroseismological masses.

To derive a comparable distribution of CSPNe masses compared to the Moe & De Marco (2006) distribution, the CSPNe were estimated using the average IFMR from the evolutionary tracks of Vassiliadis & Wood (1994) and Bloecker (1995), complemented at lower masses by Schoenberner (1983) $0.546M_{\odot}$ track for initial masses $< 1M_{\odot}$. Separately, the recent evolutionary tracks by (Miller Bertolami, 2016) were used to obtain the CSPNe masses as well. Vassiliadis & Wood (1994) defined an IFMR for initial masses in the range of $1 \lesssim M_i/M_{\odot} \lesssim 5$. These correspond to CSPNe between $0.569M_{\odot}$ and $0.9M_{\odot}$, depending on the metallicity chosen. The Bloecker (1995) tracks predict final masses within the range of 0.53 to $0.94M_{\odot}$ for initial masses between 1 and $7M_{\odot}$. The IFMR of Miller Bertolami (2016) provides final masses between $0.528M_{\odot}$ and $0.9M_{\odot}$ for corresponding initial masses between $1M_{\odot}$ and $5M_{\odot}$. The last track of $0.9M_{\odot}$

(initial mass of $5M_{\odot}$) is not part of the published tracks but was obtained through private communications from Miller Bertolami (2016).

Figure 4.6 (top) shows the plots of the IFMR for the first set of tracks (Bloecker 1995; Vassiliadis & Wood 1994 and Schoenberner 1983: top right) and the recent tracks by Miller Bertolami (2016) (top left). The extrapolated regions are shown as dashed continuing lines and the average of the Vassiliadis & Wood (1994) and Bloecker (1995) tracks for initial masses $> 1M_{\odot}$ is represented by the red dashed lines (Figure 4.6: top right). The corresponding distributions of the final masses are shown in the same Figure 4.6 (bottom).

The final mass distribution using the IFMR of Miller Bertolami (2016) peaks at $\sim 0.58M_{\odot}$ (Figure 4.6; bottom left), with a median of $0.58M_{\odot}$. This corresponds to the CSPNe peak value ($\sim 0.58M_{\odot}$) obtained by Gesicki & Zijlstra (2007); Gesicki *et al.* (2014) from accelerating the post-AGB evolution of the Bloecker (1995) tracks. The final mass distribution using the average IFMR of Bloecker (1995); Schoenberner (1983); Vassiliadis & Wood (1994) shows a distribution that is comparable to the CSPNe distribution of Moe & De Marco (2006).

In Table 4.2, the mean and median masses are compared to the values in Moe & De Marco (2006). Both the initial and final mass compare well with the values reported by Moe & De Marco (2006) within 2σ, especially the estimates from BVS with a standard deviation of $0.1M_{\odot}$. The difference of $0.08M_{\odot}$ in the mean and median initial mass is attributed to how the IMF was treated. Moe & De Marco (2006) averaged over the Kroupa (2001) and Chabrier (2003) IMF, while this work made use of the Kroupa (2001) IMF only.

4.2.3 Interpolation of Evolutionary Tracks

In order to estimate the ionizing photons given by equation 4.3, the radii (equation 4.4) of the final masses are needed. Estimating the radii, however, requires the temperatures and luminosities. The sets of evolution tracks provided by Vassiliadis & Wood (1994) , and the recent tracks by Miller Bertolami (2016) were

Table 4.2: *Summary of the initial and final masses given by Moe & De Marco (2006)=MD 2006, compared to the values estimated in this work: BVS=Bloecker (1995); Schoenberner (1983); Vassiliadis & Wood (1994) and MB2016=Miller Bertolami (2016).*

	$M_{initial}(M_\odot)$ (Mean)	$M_{initial}(M_\odot)$ (Median)	$M_{final}(M_\odot)$ (Mean)	$M_{final}(M_\odot)$ (Median)
MD 2006	1.7 ± 0.3	1.2 ± 0.2	0.61 ± 0.02	0.57 ± 0.01
BVS (this work)	1.78	1.28	0.61	0.57
MB2016 (this work)	1.78	1.28	0.61	0.58

both interpolated to obtain two sets of temperatures and luminosities. For simplicity the tracks will be referred to as VW-Tracks and MB-Tracks, respectively. Only the H-burning tracks were interpolated as He burners make up a small fraction (Schoenberner, 1988). According to the visibility time for PNe defined by Moe & De Marco (2006), ages in the range of 0 and 35,000 yrs were uniformly distributed. The zero age is forced to begin at $\log_{10}T_{eff} = 4.4$, where ionization would have been initiated.

$$q_i = \int_0^{\lambda_{lim}} \frac{\pi\lambda B_\lambda(T)}{hc} d\lambda \ cm^{-2}s^{-1} \tag{4.3}$$

$$R_*^2 = \frac{L_*}{4\pi\sigma T_{eff}^4} \tag{4.4}$$

where q_i is the ionizing flux, R_* is the radius of the stars, L_* is the stellar luminosity and the Stefan-Boltzmann constant, $\sigma = 5.7 \times 10^{-8}$ $Wm^{-2}K^{-4}$.

With the ages and final masses, the VW-Tracks and MB-Tracks tracks were interpolated following the procedures described in Stanghellini & Renzini (2000b). This involves dividing the tracks into phases of hydrogen burning, quenching, cooling and white dwarf phases, and normalizing the ages of the different phases (see Stanghellini & Renzini 2000b for details). For the VW-Tracks, final masses lower than $0.569M_\odot$ were forced to use the $0.569M_\odot$ track and masses higher than $0.9M_\odot$ were forced to use the $0.9M_\odot$ track. The same rule is applied to the

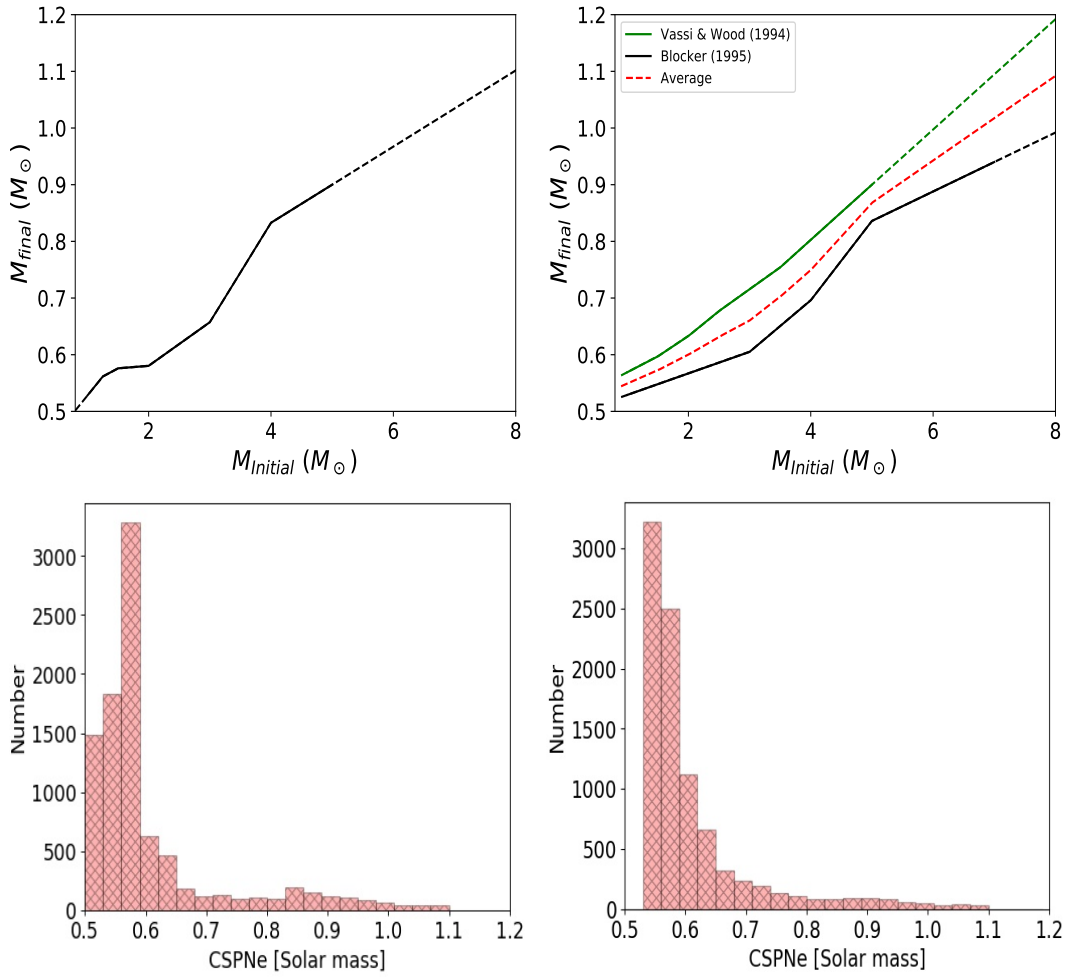

Figure 4.6: *Top: Plot of the initial mass vs final mass from the IFMR Miller Bertolami (2016) tracks (left) and from the average IFMR given by Bloecker (1995); Vassiliadis & Wood (1994) and Schoenberner (1983) (right). The dashed regions of the lines show the extrapolated regions. The red dash line shows the average between the Bloecker (1995) and Vassiliadis & Wood (1994) tracks. Below* $< 1M_\odot$*, the 0.546*$M_\odot$ *track by Schoenberner (1983) track is used (corresponds to initial mass of 0.8*$M_\odot$*). Bottom: Distribution of the corresponding CSPNe masses within* $|b| < 1°$; $9.9° < l < 65°$ *and for a scale height of 350 pc.*

MB-Tracks with an extra track obtained from Miller Bertolami (2016) ($0.9M_\odot$ track through private communication). The extra track was used to extrapolate higher masses.

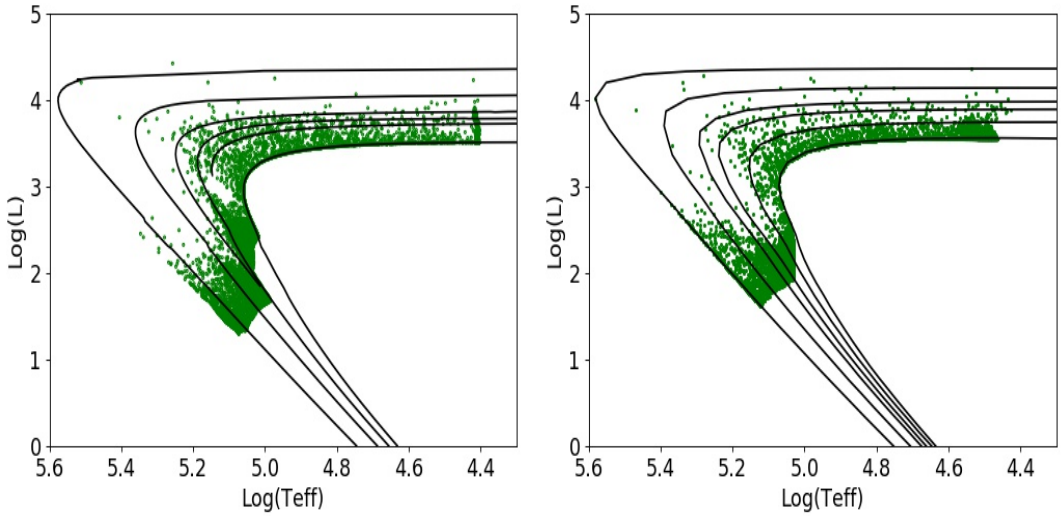

Figure 4.7: *Interpolated MB-Tracks (left) and VW-Tracks (right) within* |b|< 1°; 9.9° < l < 65° *and for a scale height of 350 pc and 9414 final masses. For the VW-Tracks tracks the tracks shown are the 0.569*$M_\odot$*, 0.597*$M_\odot$*, 0.633*$M_\odot$*, 0.677*$M_\odot$*, 0.754*$M_\odot$ *and 0.9*$M_\odot$*. For the MB-Tracks the tracks shown are the 0.528*$M_\odot$*,0.561*$M_\odot$*, 0.576*$M_\odot$*, 0.58*$M_\odot$*, 0.657*$M_\odot$ *and 0.833*$M_\odot$*.*

The interpolated MB-Tracks and VW-Tracks are shown in Figure 4.7 with the final masses overlaid. Higher masses are clustered around low luminosity, while lower masses show higher luminosities. Both tracks show similar distribution of final masses, however, the MB-Tracks show cluster around lower luminosities for higher masses, compared to the VW-Tracks. This reflects the faster evolution of the MB-Tracks. The corresponding luminosity distributions for both tracks are shown in Figure 4.8. The double peaks shown by the luminosity distribution in Moe & De Marco (2006) ($Log_{10}(L/L_\odot) = 2.5$ and 3.5) is seen in Figure 4.8 for using the VW-Tracks. However, the luminosity distribution using the MB-Tracks shows three peaks, with a consistent peak at $Log_{10}(L/L_\odot) = 3.5$ and two other peaks at $Log_{10}(L/L_\odot) = 1.7$ and $Log_{10}(L/L_\odot) = 2.3$.

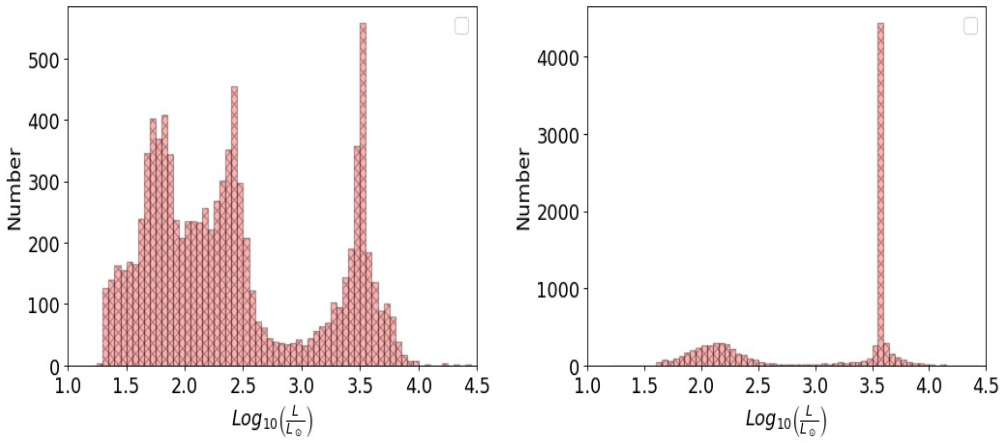

Figure 4.8: *Interpolated luminosity distribution of the MB-Tracks (left) and VW-Tracks (right).*

4.3 Radio Properties

To calculate the observed properties of the synthetic population, such as the radio flux densities and angular sizes, the central star was assumed to emit as a blackbody, where the radiation depends on the temperature. Equation 4.3 was used to calculate the ionizing flux, where B_ν is given by equation 1.6. The luminosities and temperature gotten from the interpolating the evolution tracks were then used to estimate the radii of the final masses using equation 4.4. The radius of the ionized region (Strömgren radius) for each object was estimated using equation 4.5 and 4.6, where the density, n_e is given by equation 4.8. This radius is dependent on the ionizing flux of the central star and the nebula density as shown in equation 4.6.

Assuming an average expansion velocity of 25 km/s, the outer radii of the PNe were then estimated using equation 4.7. To estimate the density, the mass of the each nebula was calculated by subtracting the final mass from the initial mass, assuming all the mass lost through the AGB forms the nebula and no mass is lost to the ISM. Equation 4.10 was further used to define the radius of each PN

i.e. R_i.

$$Q = 4\pi R_*^2 q_i(T_*) \text{ photons}^{-1} \tag{4.5}$$

where Q is the ionizing photons per second and T_* is the stellar temperature.

$$R_s(pc) = \left(\frac{3Q}{4\pi n_e^2 \alpha_\beta} \right)^{1/3} \tag{4.6}$$

where R_s is the stromgren radius, n_e is the electron density (cm^{-3}) and α_β is the recombination rate coefficient in $cm^3 s^{-1}$.

$$R_{out}(pc) = tV_r \tag{4.7}$$

where t is the kinematic age, R_{out} is the outer radius, which could extend beyond the stromgren radius (R_s) and V_r is the expansion velocity.

$$n_e = n_H = \frac{3M_{env}}{4\pi R_{out}^3 m_H} \tag{4.8}$$

where the mass of the envelope, M_{env} is given by equation 4.9.

$$M_{env} = f(M_i - M_f) \tag{4.9}$$

where f is a scaling parameter.

$$R_i = \begin{cases} R_{out}, & R_s > R_{out} \\ R_s, & R_s < R_{out} \end{cases} \tag{4.10}$$

where R_i is the radius of the PN.

Finally, the flux densities were estimated using equation 4.11. The brightness temperatures and peak fluxes were also estimated using $T_B = T_e(1 - e^{-\tau})$ and

equation 1.7. For sources with angular sizes smaller than the beam size of the CORNISH survey, the beam dilution was accounted for (multiply by $\Omega_{source}/\Omega_{beam}$).

$$S_\nu = \frac{2k\nu^2}{c^2\vartheta_i^2} T_e(1 - e^{-\tau}) \tag{4.11}$$

where the angular size, $\vartheta_i = R_i/D$, T_e is the electron temperature, ν is the frequency and τ is the optical depth.

4.4 Results and Discussion

The parameters of interest that are likely to affect the model predictions, in number and distribution, are the scale height of PNe in the thin disk, and mass of the envelope (equation 4.9). Based on the uniform random distribution of the ages, a Monte-Carlo approach was used to arrive at a best-fitting model by averaging the results over many runs. The northern (Chapter 2) and southern (Chapter 3) PNe from the CORNISH survey were treated separately.

4.4.1 CORNISH North PNe

The CORNISH survey in the northern Galactic plane was described in Chapter 2 (see Purcell *et al.* 2013). The initial geometric cut was applied before interpolating the evolutionary tracks (see green region in Figure 4.1), resulting in a total of 9414 sources out of 37000 for both disks. Applying the final detection cut (see Figure 4.1) required two properties, which are the angular size and the peak flux limits.

Firstly, because of the rms noise variation across the CORNISH survey region (see Figure 10 in Purcell *et al.* 2013), two peak flux limits, at 7σ, were defined. For the region defined by $49^\circ < l < 65^\circ$, an average peak flux limit of $S_p = 7 \times 0.25 = 1.75$ mJy/beam was used and for the remaining region, $S_p = 7 \times 0.35 = 2.45$ mJy/beam was used. Secondly, based on the maximum angular size of the CORNISH-North PNe ($12''$) and the optimum angular size detectable by the CORNISH-North survey (see Purcell *et al.* 2013), the angular size limit was

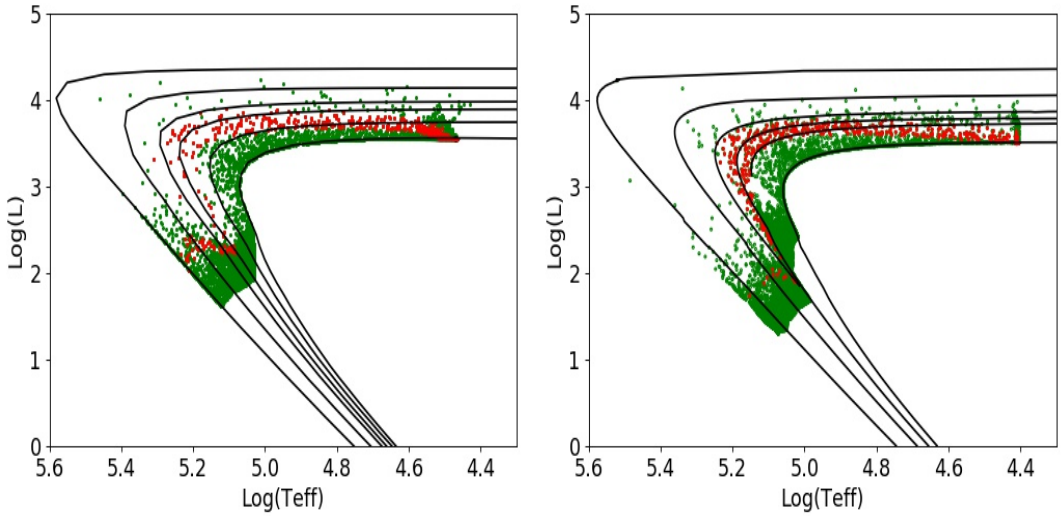

Figure 4.9: *Interpolated VW-Tracks (left) and MB-Tracks(right) showing the position of the CSPNe that fall within the survey region of the CORNISH-North survey (green dots) and the CSPNe that detected by the CORNISH survey, after the final cut (red dots). This is within* $|b| < 1^{\circ}$; $9.9^{\circ} < l < 65^{\circ}$ *and for a scale height of 350 pc. For the VW-Tracks tracks the tracks shown are the 0.569*$M_{\odot}$, *0.597*$M_{\odot}$, *0.633*$M_{\odot}$, *0.677*$M_{\odot}$, *0.754*$M_{\odot}$ *and 0.9*$M_{\odot}$. *For the MB-Tracks the tracks shown are the 0.528*$M_{\odot}$,*0.561*$M_{\odot}$, *0.576*$M_{\odot}$, *0.58*$M_{\odot}$, *0.657*$M_{\odot}$ *and 0.833*$M_{\odot}$.

set to $14''$. Figure 4.9 shows the distribution of the central stars (CSs) on the interpolated tracks (green dots), after the geometry cut and the distribution of the central stars (CSs) on the interpolated tracks after the final cut (red dots).

The PNe not making it through to the final cut either have low mass CS that result in PNe that are below the detection limit or high mass CS that evolve too fast and are on cooling tracks with low luminostiy (Log(L) < 2). For both tracks, the synthesized population within the detection of the CORNISH-North survey have average CS masses between 0.57$M_{\odot}$ and 0.6$M_{\odot}$.

Scale Heights and Galactic Latitude Distribution

The scale height of the Galactic PNe from population synthesis was not stated by Moe & De Marco (2006). Thus, the scale height was investigated to find a best fitting scale height to the CORNISH-North PNe latitude distribution. The scale height of the thick disk was kept constant (contributes $\sim 3\%$ of the PNe population in the Galaxy from population synthesis model; Moe & De Marco 2006), while that of the thin disk was varied from 200 pc to 700 pc (Bovy *et al.*, 2016), assuming the thin disk PNe population is concentrated in the old/intermediate disk. With this assumption, the random distribution of the ages was seeded and f in equation 4.9 was set to 1.

The expansion velocity and visibility time both play an important role in the number count of PNe population, as also noted by Moe & De Marco (2006). The thick disk PNe have been suggested to show higher average expansion velocity compared to PNe closer to the Galactic plane (Phillips, 2002). However, a constant average expansion velocity of 25 km/s was assumed, according to Moe & De Marco (2006).

The visibility time of a PN depends on the time evolution of the CS and the nebula. For high mass CS ($> 0.6 M_{\odot}$), they may evolve too fast such that the visibility time is very short. Low mass CS ($< 0.6 M_{\odot}$) may evolve too slow that before the right temperature is attained, the envelope has become too dispersed, such that even if it becomes ionized, it may not be detectable. From interpolation of the VW-Tracks and Bloecker (1995) tracks, Moe & De Marco (2006) suggested an average expansion velocity of 25 km/s, resulting in a visibility time of 35,000 years, for a maximum physical size of 0.9 pc. This visibility time of 35,000 yrs is stated by Moe & De Marco (2006) as flexible, such that it allowed them compare their predicted population to observation. It is, however, suggested that the average visibility time of PNe is actually shorter than predictions from previous evolution tracks, following the fact that low mass stars could actually result in observable PNe (Gesicki & Zijlstra, 2007; Miller Bertolami, 2016). Jacob *et al.* (2013) estimated an average expansion velocity of 42 km/s with corresponding age of $21,000 \pm 5000$ years for a maximum radius of 0.9 pc. By equating the birth

rate of PNe to white dwarfs, Zijlstra & Pottasch (1991) suggested a visibility time of 50,000 years. However, because the predicted population is for Galactic PNe with radius < 0.9 pc, the visibility time of 35,000 yrs from Moe & De Marco (2006) was not changed in order to keep the comparison with the model constant. These parameters (see Table 4.3 were used to run the model using the VW-Tracks and MB-Tracks.

For the analysis of the results, the reduced chi-square (χ^2) statistics given by equation 4.12 was used to estimate the goodness-of-fit of the latitude distribution of the model to the CORNISH-north PNe. The best model would be the model with the minimum reduced χ^2 ($\tilde{\chi}^2$).

$$\tilde{\chi}^2 = \frac{1}{K}\sum_{i}^{N}\left(\frac{x_i - \mu_i}{\sigma_i}\right)^2 \tag{4.12}$$

where K is the number of degrees of freedom, the CORNISH binned data is $x_i \pm \sigma_i$ and the binned model data is μ_i.

Figure 4.10 shows a plot of the $\tilde{\chi}^2$ versus scale heights using the VW-Tracks and the MB-Tracks. Scale heights of 200 and 250 pc show $\tilde{\chi}^2$ value above 1, which is considered a bad fit and scale heights from 350 to 700 pc show $\tilde{\chi}^2$ values below 1. These can be considered good fits (Andrae *et al.*, 2010), however, it was also important to see the actual fit. Figure 4.11 shows the modelled latitude distribution compared to the latitude distribution of the CORNISH-North PNe, for scale heights of 350 pc (red dashed line) and 550 pc (blue dashed line). Based on these plots, a scale height of 550 pc, which has the minimum $\tilde{\chi}^2$, was considered a best fit. A scale height of 550 pc appears in the extreme of estimated thin disk values, but it agrees with the scale height of pPNe obtained by Bobylev & Bajkova (2017), indicative of intermediate disk PNe sample (Bovy *et al.*, 2016) or even a mixed disk sample of PNe. Figures 4.10 and 4.11 were obtained by averaging over multiple runs.

The initial parameters on Table 4.3 and a scale height of 550 pc predicts a population of ~ 750 with the VW-Tracks and ~ 500 with the MB-Tracks, which is about 5 and 3 times more PNe within the CORNISH-North survey region (see

Table 4.3: *Initial model parameters according to the population predicted by Moe & De Marco 2006.*

Parameter	Values
Thin disk population	36000
Thick disk population	1100
Expansion velocity	25 km/s
Lifetime	35000 yrs
Envelope Mass	$(M_i - M_f)$
Scale height of thick disk	1200 pc
Scale height of thin disk	200 to 700 pc

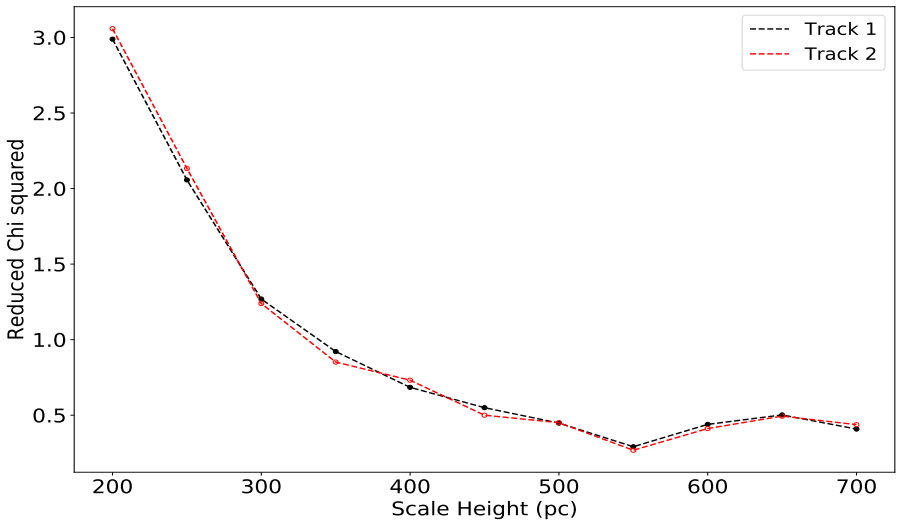

Figure 4.10: *Reduced χ^2 versus scale heights using the VW-Tracks and MB-Tracks.*

Figure 4.14). Figure 4.12 shows the physical sizes for all the PNe within the CORNISH-North survey region (maximum size of 0.9 pc) and the distribution of the PNe after applying the CORNISH detection cuts (red shaded region). The model predicts PNe with physical radii less than 0.3 pc for both sets of tracks. The corresponding ages predict ages that lie in the range of 1 kyrs to 9 kyrs as shown in Figure 4.13, for both set of tracks. The MB-Tracks, however, predict a younger population with a maximum of $\sim$ 6 kyrs. The predicted ages and sizes agree with the distribution of the CSs in Figure 4.9. PNe with radii larger than

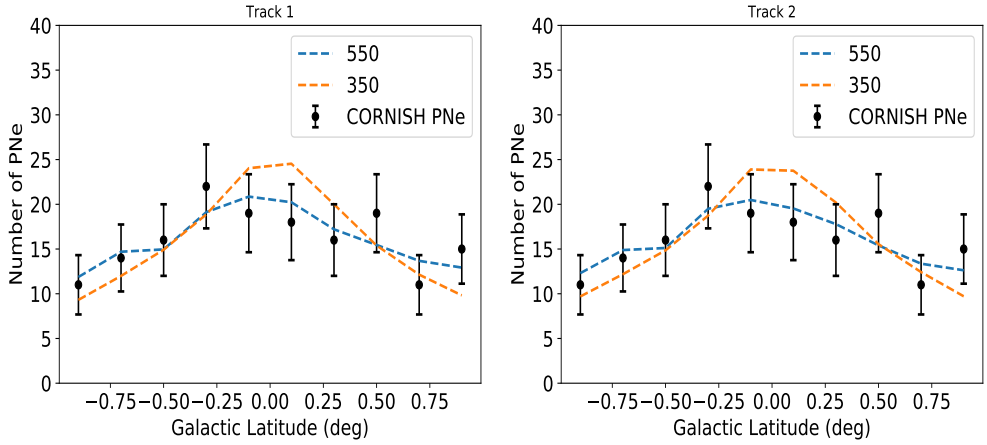

Figure 4.11: *Comparison of modelled Galactic latitude distribution to observed latitude distribution for the CORNISH-North PNe. This is for a scale height of 550 pc (left panel) and comparison of the scale height of 350 pc and 550 pc (right panel). The bin size used is 0.2 deg.*

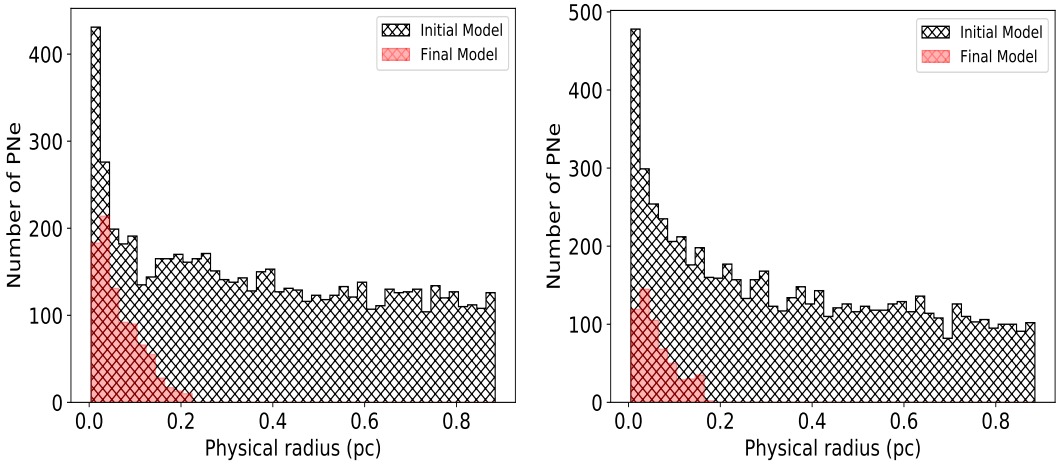

Figure 4.12: *Comparison of the distribution of modelled physical sizes with the first geometric cut applied and the modelled physical sizes after the detection cut (final cut) for the VW-Tracks (left) and MB-Tracks (right). This is for a scale height of 550 pc.*

0.3 pc and older would have become too faint and below the peak detection of the CORNISH-North survey.

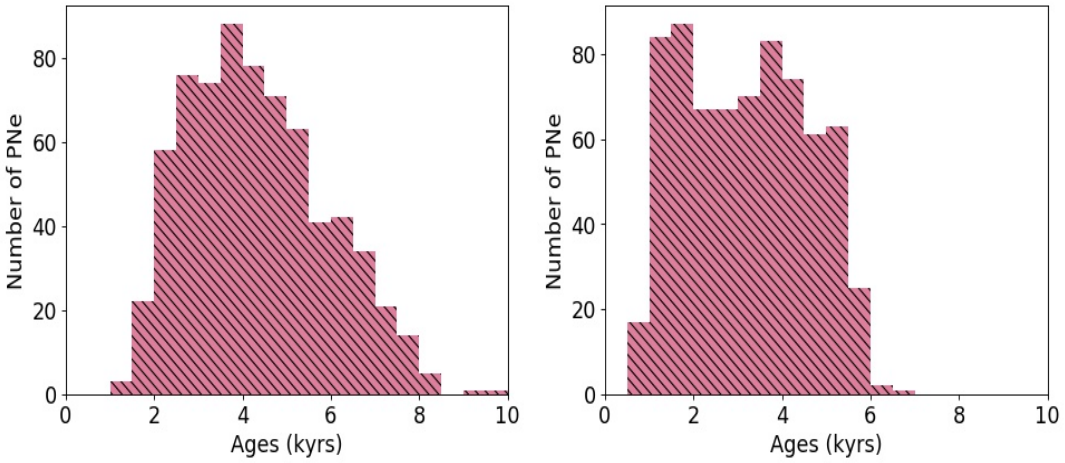

Figure 4.13: *Modelled ages distribution using the VW-Tracks (left) and MB-Tracks (right) after the final cuts (geometry and detection limit of the CORNISH-North survey.*

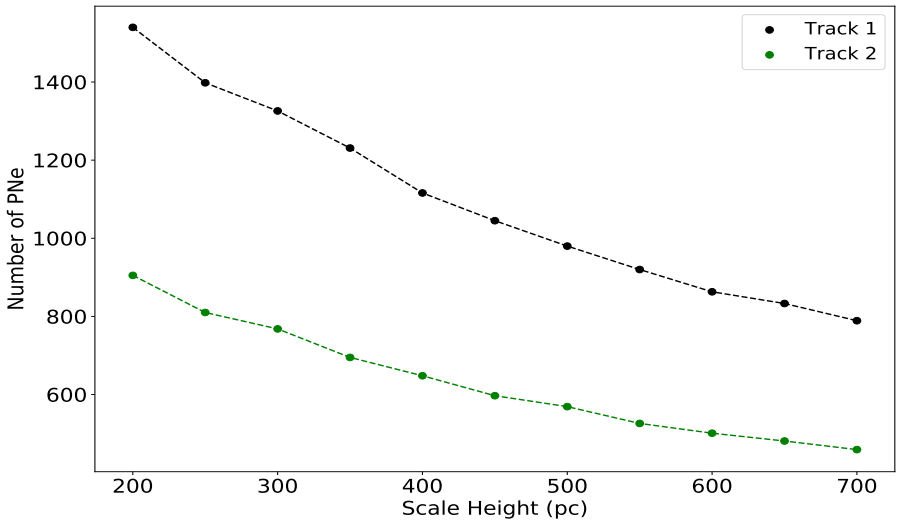

Figure 4.14: *Number of predicted population versus scale height for the CORNISH-North PNe for the VW-Tracks and MB-Tracks.*

Flux Density and Angular size

Figure 4.15 (top) shows a kernel density estimation (kde) plot of the modelled angular size and flux density with the CORNISH-North data overlaid. 16% of the

data lie outside the high density region. The modelled kde shows a good match with the distribution of the CORNISH-North angular sizes and flux densities. Using the VW-Tracks resulted in angular size distribution that extends up to $10''$, while using the MB-Tracks resulted in a maximum of $8''$. The flux density distribution (lower panel) of the model (scaled to the number of the CORNISH-North PNe) shows a peak at a higher flux density compared to the peak of the CORNISH-North PNe. This could be due to the assumed envelope mass that results in higher flux density in the model.

Envelope Mass

The initial model runs assumed all the mass lost during the RGB and AGB phase form the nebula, such that f is 1 in equation 4.9. With the initial envelope mass used, Figure 4.16 shows the distribution of the envelope mass (top) and corresponding ionized mass (bottom) before and after applying the CORNISH detection limit for both sets of tracks. The final envelope mass distribution peaks about $0.5M_{\odot}$ and extends up to $\sim 4M_{\odot}$. For f=1, the final ionized mass (after final detection cut) extends up to $0.6M_{\odot}$ for the MB-Tracks and $1M_{\odot}$ for the VW-Tracks. Figure 4.17 shows the distribution of ionized mass estimated by Zhang (1995) for a sample of Galactic PNe, assuming they are optically thin and based on individually determined distances estimated by Zhang & Kwok (1993) (based ojn stellar parameters) for $\varepsilon = 0.6$. The modelled ionized mass shows a similar distribution with ionized mass distribution in Figure 4.17, considering the assumptions made.

There is, however, mass-loss during the AGB phase that is not accounted for in the final nebula mass (Kwok, 1994). According to Wareing *et al.* (2007), up to 90% of the envelope mass, during the AGB phase, could be lost through interaction with the ISM. The envelope mass is usually less than $1M_{\odot}$, which is a summation of the molecular/neutral and ionized gas (Huggins *et al.*, 1996; Kimura *et al.*, 2012; Natta & Hollenbach, 1998). The ionized mass is usually less than $1M_{\odot}$ as well (Mendez *et al.*, 1992; Ueta *et al.*, 2014), depending if the nebula is fully ionized or

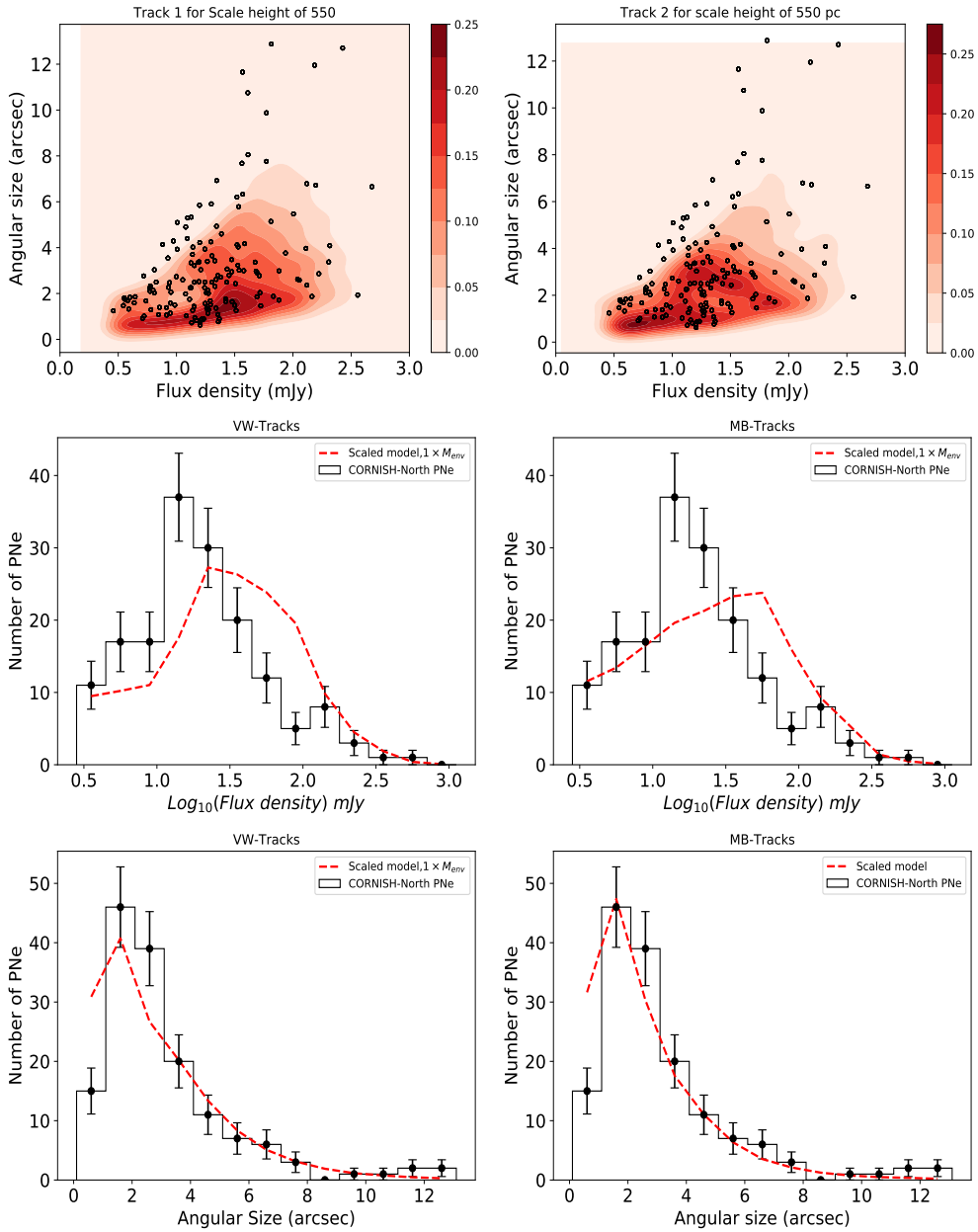

Figure 4.15: *Top: Angular size and flux density kernel density estimation plot with the CORNISH-North PNe angular sizes overlaid for the VW-Tracks and MB-Tracks. Middle: Comparison of the modeled flux density distribution and the CORNISH-North PNe for VW-Tracks (left) and MB-Tracks (right). Bottom: Comparison of the modelled angular size distribution and the CORNISH-North PNe for VW-Tracks (left) and MB-Tracks (right). All the plots are scaled to the sample size of the CORNISH-North PNe.*

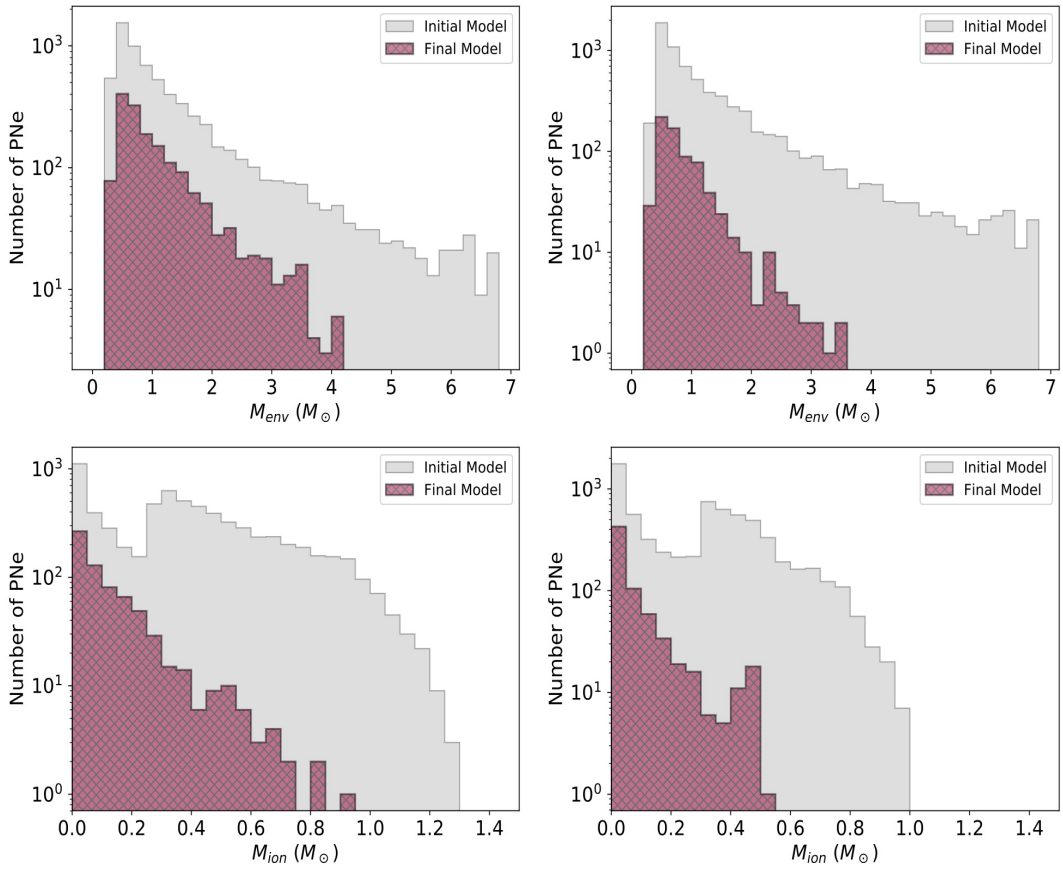

Figure 4.16: *Initial envelope mass (top) and ionized mass (bottom) of the modelled population using the VW-Tracks (left) and the MB-Tracks (right). This is for f=1 in equation 4.9 and a scale height of 550 pc.*

not. Through the modelling of the SEDs of a sample of PNe, an average ionized mass of $0.1M_\odot$ was determined (Planck Collaboration *et al.*, 2015).

In order to see how the envelope mass would affect the number of predicted population and flux density distribution, the envelope mass was scaled to account for mass-loss during the evolution through the AGB phase that is not reflected in the nebula that forms the PN. Scale factors, f between 1 and 1/5 were defined. The plot of the scale factor versus the predicted population, using both tracks is shown in Figure 4.18. Scaling the envelope by a factor of 1/4 brings the population to 482 and 342 for the VW-Tracks and MB-Tracks, respectively. This

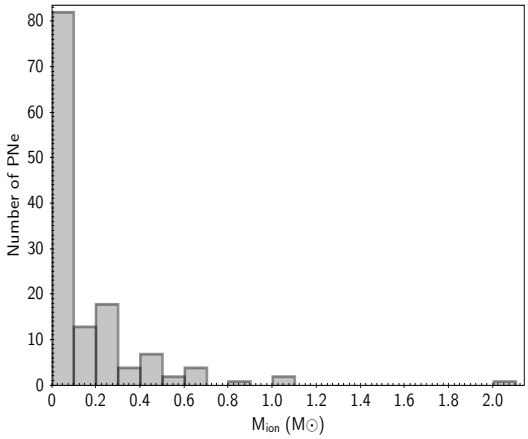

Figure 4.17: *Ionized mass distribution of 134 Galactic PNe from Zhang (1995).*

is still 3 and 2 times higher than the CORNISH population. Figure 4.19 shows the influence of scaling the envelope mass on the flux density and angular size distribution for both tracks. The scaled envelope results in a shift of the flux density peak, which improved the fit of the model to the CORNISH-North PNe flux density when the envelope mass is scaled by 1/4.

From Figure 4 in Bloecker (1995), Gesicki *et al.* (2014) found that the envelope mass at maximum temperature i.e. when the CS attains maximum temperature on the evolutionary track, is 1/4 the mass of the envelope at the end of the post-AGB phase. This may not represent the case for all the synthetic PN population modelled. On the average, however, it shows an improved fit to the flux density distribution. The corresponding ionized mass distributions shown in Figure 4.20 shows that scaling the envelope mass shifts the maximum value of the predicted ionized mass as well for the CORNISH-North PNe towards lower values with a mean ionized mass of $0.1 M_{\odot}$ for f = 1/4.

Figure 4.21 shows the modelled distributions of optical depth (τ_{ν}), peak flux and brightness temperature (T_B) compared to the estimated optical depth and T_B for the CORNISH-North PNe. The model shows a good fit to the observed distributions. The optical depth, however, is sensitive to the electron temperature, T_e. Figure 2.13 in Chapter 2 shows that some of the CORNISH-North PNe are best fitted with T_e of 5000 K and of 15000 K. For the model, a constant T_e

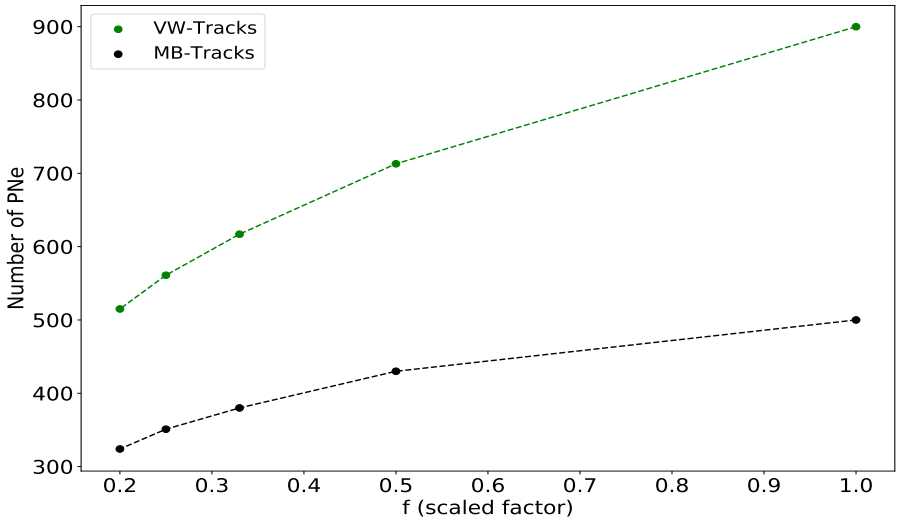

Figure 4.18: *Number of predicted population versus scaled envelope mass. Modelled population is normalized to the number of the CORNISH-PNe.*

of 10000 K was used. The low end of the CORNISH-North PNe T_B could not be fitted by the model. In order to fit lower T_B, Hajduk *et al.* (2018) suggested using a prolate ellipsoid defined by inner and outer ellipsoids instead of a homogenous sphere model. Siódmiak & Tylenda (2001) also suggested a two component model defined by two different optical thicknesses. These are considerations for subsequent updates of the model.

Distances

The model that fits the angular sizes and flux density distribution, show a distance distribution that peaks at $\sim$ 10 kpc. Figure 4.22 shows the comparison of the modelled and estimated distances for the CORNISH-North PNe. The modelled distance peaks about the same distance with the CORNISH-North PNe distances, however, the CORNISH-North PNe distances, based on statistical distance scale, predict larger distances. As discussed in Chapter 2, the distances of optically thick PNe will be over-estimated by the method used, resulting in larger distances (the mean of the distance scale was used). For angular sizes less than the beam size,

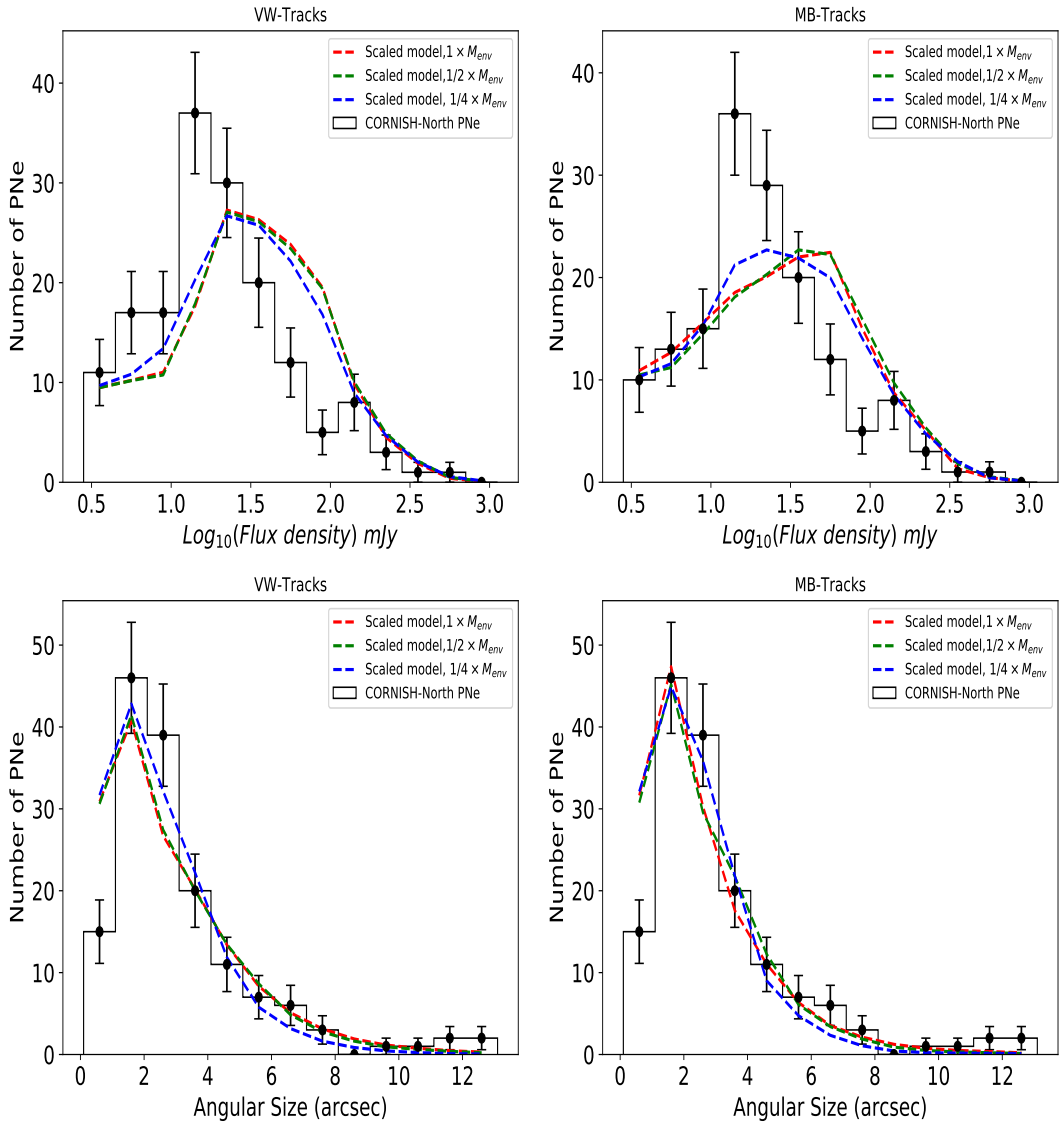

Figure 4.19: *Flux density (top) and angular size distribution (bottom) for VW-Tracks and MB-Tracks for envelope mass scaled by 1/2 and 1/4. Modelled population is normalized to the number of the CORNISH-PNe.*

the distances could also be in larger errors as well. The model predicts distances less than 20 kpc for the CORNISH-North PNe.

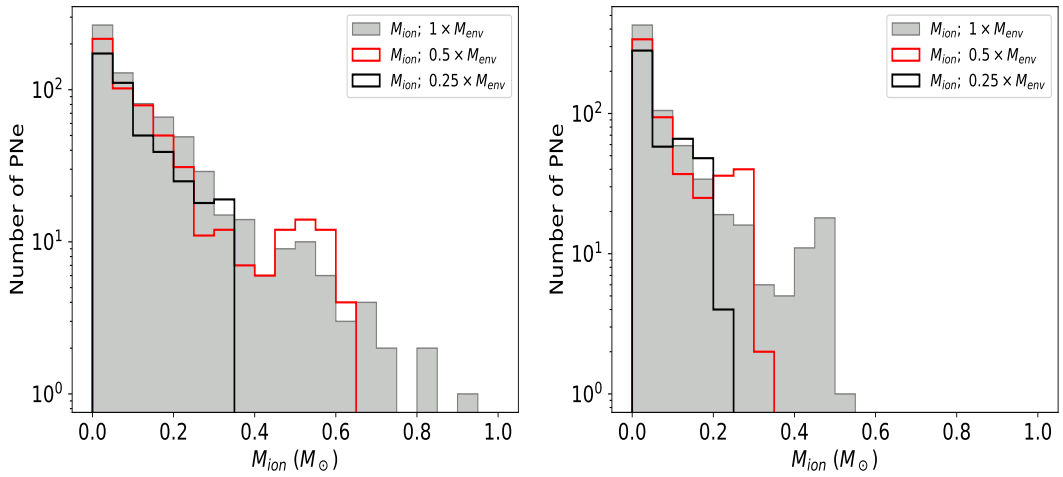

Figure 4.20: *Ionized mass distribution for scaled envelope mass. Modelled population is normalized to the number of the CORNISH-PNe.*

Binary Population Synthesis

To test the binary population synthesis prediction, the model was run with a binary population according to Moe & De Marco (2012). Based on binary interactions, Moe & De Marco (2012) predicted a population of 8100 ± 2300 in the Galaxy. This population was distributed in the thin and thick disk based on the ratio of the single stars synthesis. The synthesized binary population show the same fit parameters (Figure 4.23) as with the synthesized single population in previous section. However, the model predicted a population of 137 and 87 for the VW-Tracks and the MB-Tracks, respectively. This accounts for the equivalent of 84% and 54% of the CORNISH-North PNe within the b $< |1°|$ region (162). Scaling the envelope mass by 1/2 resulted in 70% and 44% and scaling by 1/4 results in 53% and 37% for the respective sets of tracks (see Table 4.4).

The synthesized binary model results in a comparable number of 84% (envelope mass scaled by 1), using the VW-Tracks, of the CORNISH-North PNe (see Figure 4.23). The best fit model is, however, the model with envelope mass scaled by 1/4 that is consistent with the synthesized single model and accounts for 53% and 37% of the CORNISH-North PNe using the VW-Tracks and MB-Tracks, respectively.

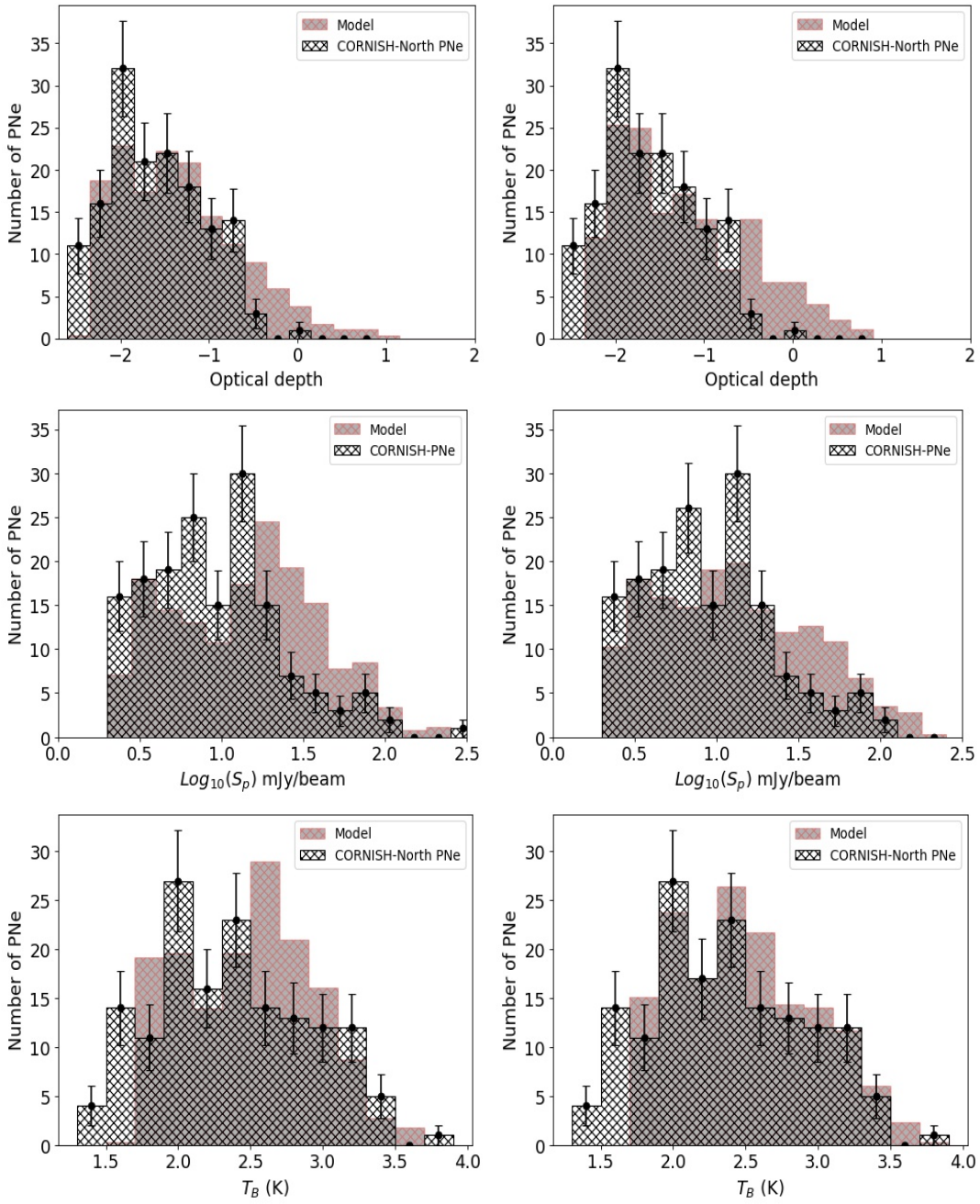

Figure 4.21: *Modelled optical depth (τ_ν) and brightness temperature (T_B) compared to the CORNISH-North PNe for envelope mass scaled by 1/4. Modelled population is normalized to the CORNISH-North PNe number.*

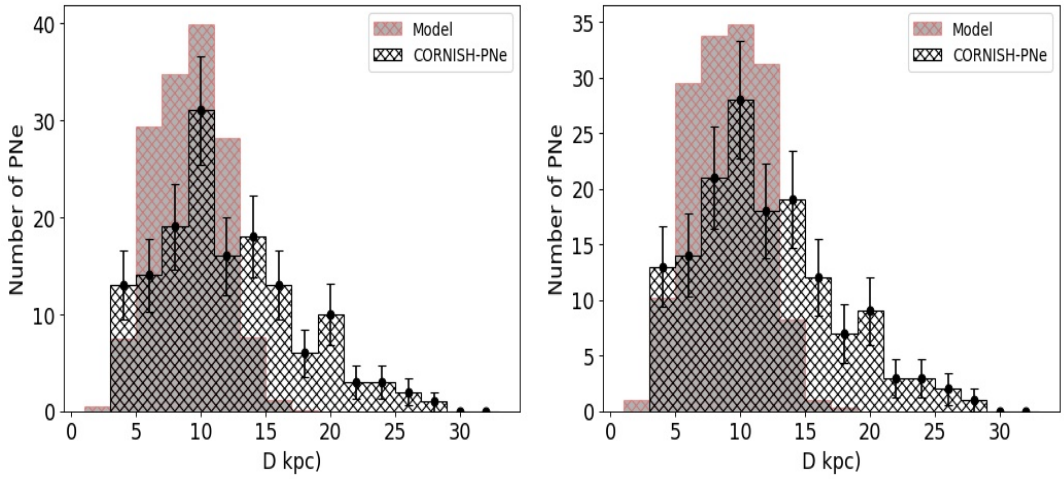

Figure 4.22: *Modelled distance distribution compared to the CORNISH-North PNe distribution for the best fit model. The model distribution is scaled to the CORNISH-North PNe.*

4.4.2 CORNISH South PNe

The CORNISH survey in the southern Galactic plane was described in Chapter 3. Two peak flux limits, at 7σ, were defined as in the CORNISH-North. For the region defined by $295^{\circ} < l < 320^{\circ}$, an average peak flux limit of $S_p = 7 \times 0.09 = 0.63$ mJy/beam was used and for the remaining region, $S_p = 7 \times 0.12 = 0.84$ mJy/beam was used. Based on the maximum angular size of the CORNISH-South PNe, the angular size limit was set to $25''$. Figure 4.24 shows the positions of the synthesized population after applying the selection criteria for both sets of tracks. Based on the positions of the synthesized population, more older PNe with lower luminosities are predicted, compared to the synthesized population positions of the CORNISH-North PNe in Figure 4.9.

The same procedures applied to the CORNISH-North PNe in section 4.4.1 were further applied to the CORNISH-South PNe. Figure 4.25 shows the $\tilde{\chi}^2$ versus scale height (top panel) and the fit of the modelled Galactic latitude distribution to the CORNISH-South PNe (lower panel). Based on the statistical fit, a scale height of 600 pc, with a minimum $\tilde{\chi}^2$ was chosen as the best fit scale height. For a scale height of 600 pc, the VW-Tracks predicts a population of 1307 and

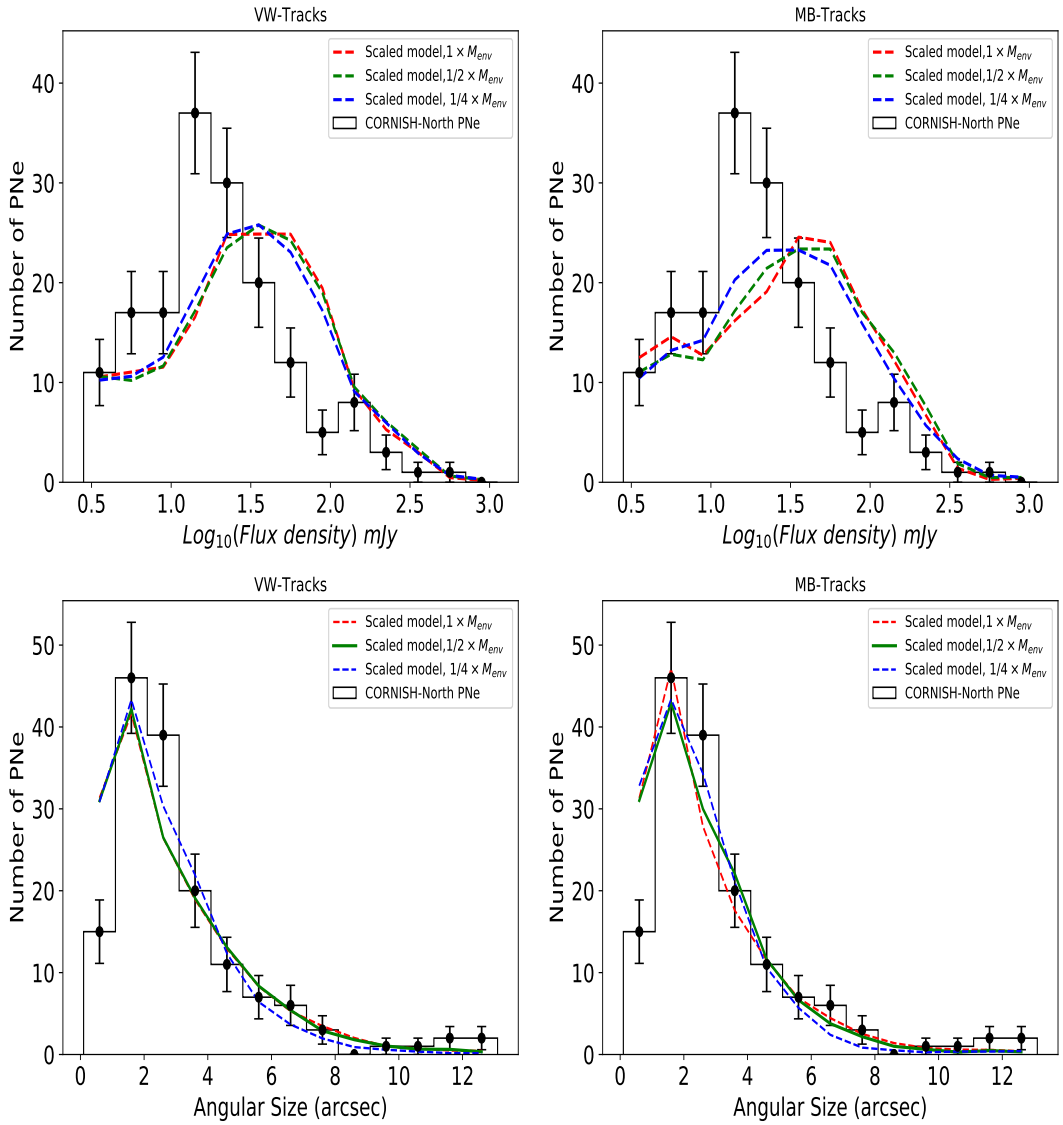

Figure 4.23: *Flux density (top) and angular size distribution (bottom) for the synthesized binary model using the VW-Tracks and MB-Tracks for envelope mass scaled by 1/2 and 1/4. Modelled population is normalized to the CORNISH-PNe number.*

the MB-Tracks predicts a population of 956 within the b $< |1°|$ region of the CORNISH-South survey.

Again, scaling the envelope mass by 1/4 results in an improved fit to the flux

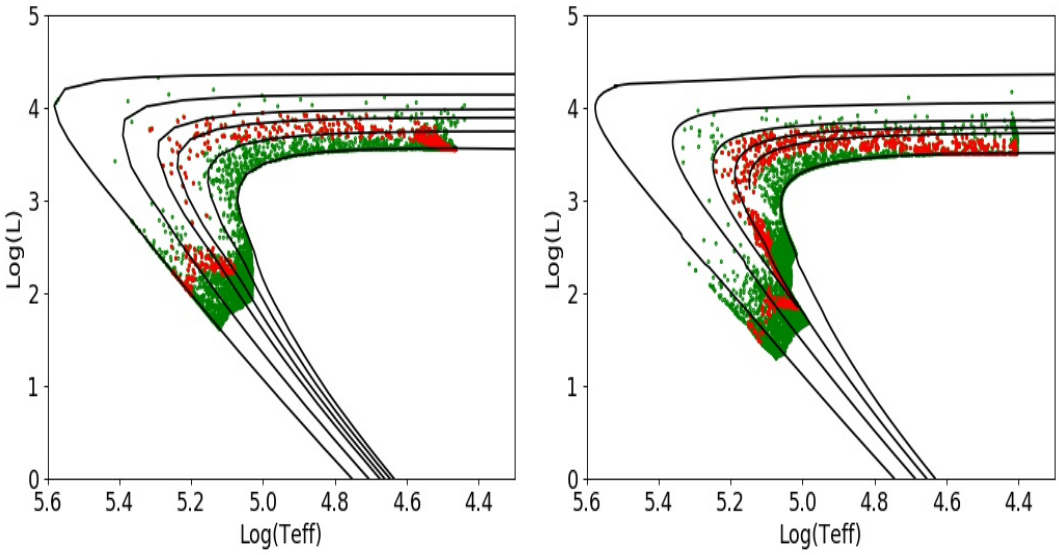

Figure 4.24: *Interpolated VW-Tracks (left) and MB-Tracks(right) showing the position of the PNe that fall within the detection range of the CORNISH-South survey. This is within* $|b| < 1^{\circ}$*;* $295^{\circ} < l < 350^{\circ}$ *and for a scale height of 600 pc. For the VW-Tracks tracks the tracks shown are the 0.569*$M_{\odot}$*, 0.597*$M_{\odot}$*, 0.633*$M_{\odot}$*, 0.677*$M_{\odot}$*, 0.754*$M_{\odot}$ *and 0.9*$M_{\odot}$*. For the MB-Tracks the tracks shown are the 0.528*$M_{\odot}$*,0.561*$M_{\odot}$*, 0.576*$M_{\odot}$*, 0.58*$M_{\odot}$*, 0.657*$M_{\odot}$ *and 0.833*$M_{\odot}$*.*

density distribution (Figure 4.26; top panel). This resulted in 822 and 619 synthesized PNe using the VW-Tracks and MB-Tracks, respectively. This is about 5 and 4 times the number of observed CORNISH-South PNe from the respective sets of tracks. The model fit to the observed angular sizes is also shown in Figure 4.26 (middle panel). For the PNe whose sizes were measured by means of a polygon in Chapter 3, their angular sizes were retained and for the PNe whose angular sizes were measured by means of a 2D Gaussian, the deconvolved sizes were used. The resulting kde plot for the scaled envelope (1/4) is also shown in Figure 4.26 (lower panel) for both tracks. The kde plots show a good match with the distribution of the observed CORNISH-South PNe and extends to larger angular sizes compared to the CORNISH-North PNe as also noted in Figure 4.24.

The distribution of the ionized mass is shown in Figure 4.27 for both sets of tracks. Using the VW-Tracks shows a distribution of ionized mass that extends

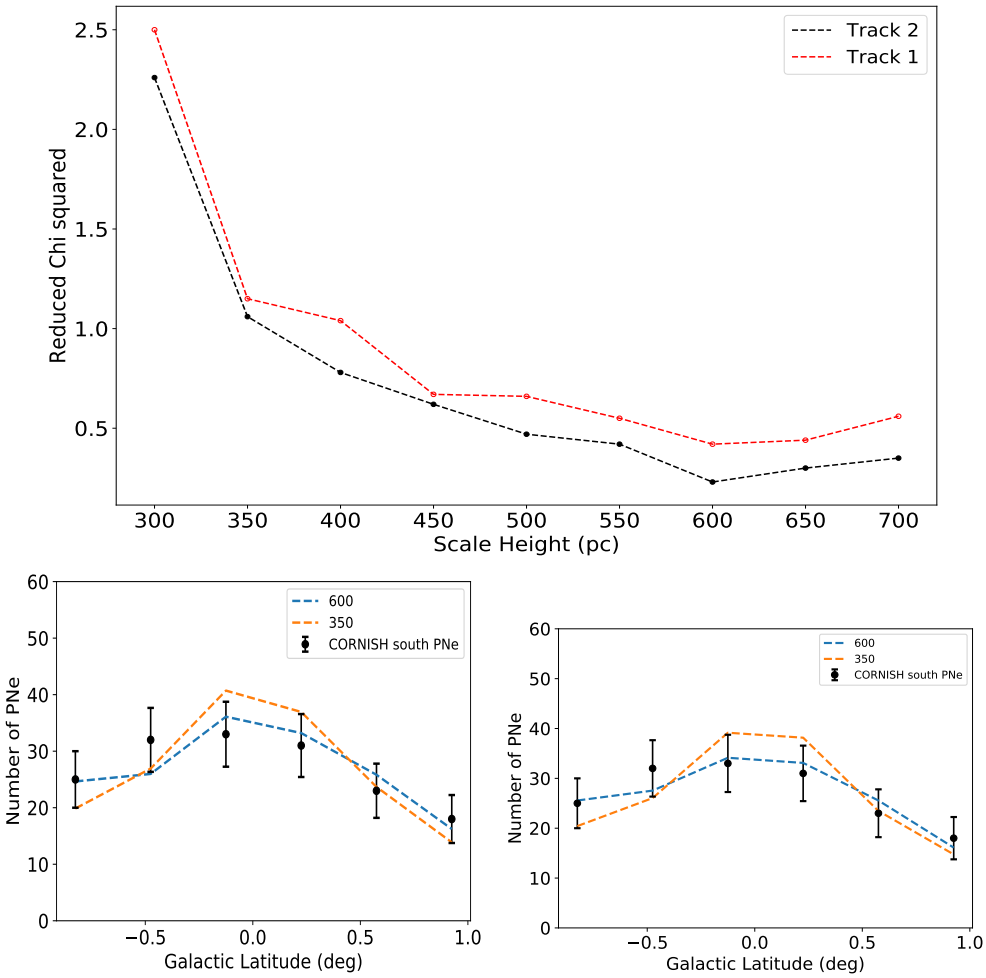

Figure 4.25: *Top: Reduced chi-squared and corresponding scale heights for the CORNISH-South PNe, using the VW-Tracks (left) and MB-Tracks (right). Lower: Comparison of the latitude distribution of the model for scale heights of 350 and 600 pc to the CORNISH-South PNe using the VW-Tracks (left) and MB-Tracks (right). Modelled population is normalized to the number of the CORNISH-PNe.*

to larger values compared to using the MB-Tracks. Compared to the CORNISH-North PNe, the model predicts a distribution of ionized mass that extends to larger values in general.

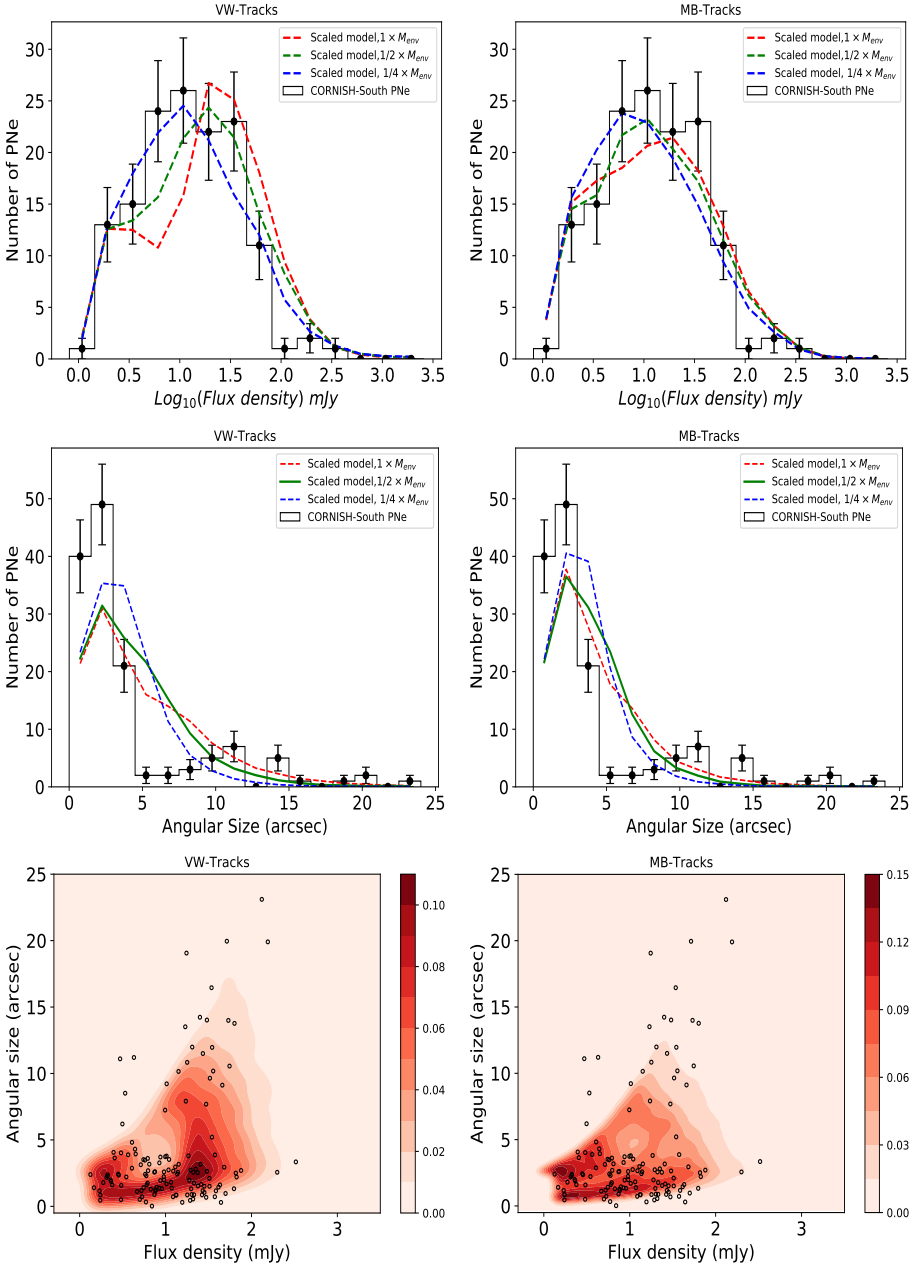

Figure 4.26: *Top: Comparison of the flux density distribution of the CORNISH-South PNe and modelled distribution for different scaled envelope masses. Middle: Comparison of the angular size distribution of the CORNISH-South PNe and modelled distribution for different scaled envelope masses. Bottom: Comparison of the modelled KDE to the distribution of the CORNISH-South PNe flux density versus angular size for VW-Tracks (left) and MB-Tracks (right). Modelled population is normalized to the CORNISH-South PNe number.*

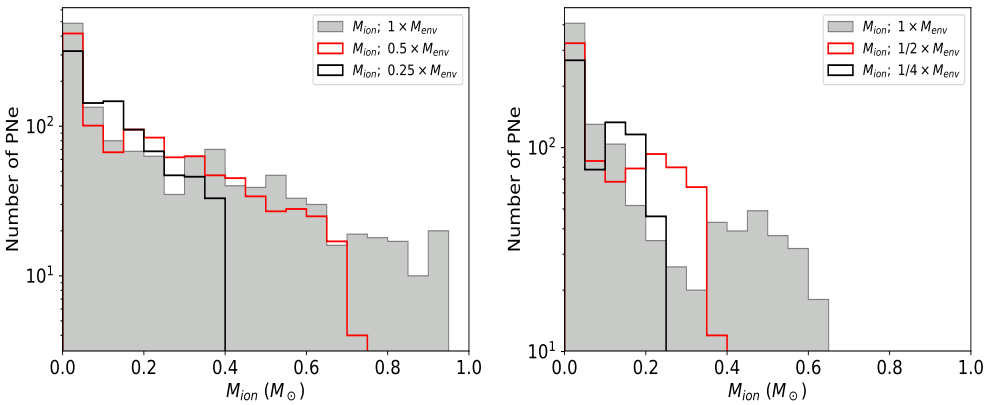

Figure 4.27: *Ionized mass distribution of the modelled CORNISH-South PNe for different scaled envelope mass using the VW-Tracks and MB-Tracks. Modelled population is normalized to the CORNISH-South PNe number.*

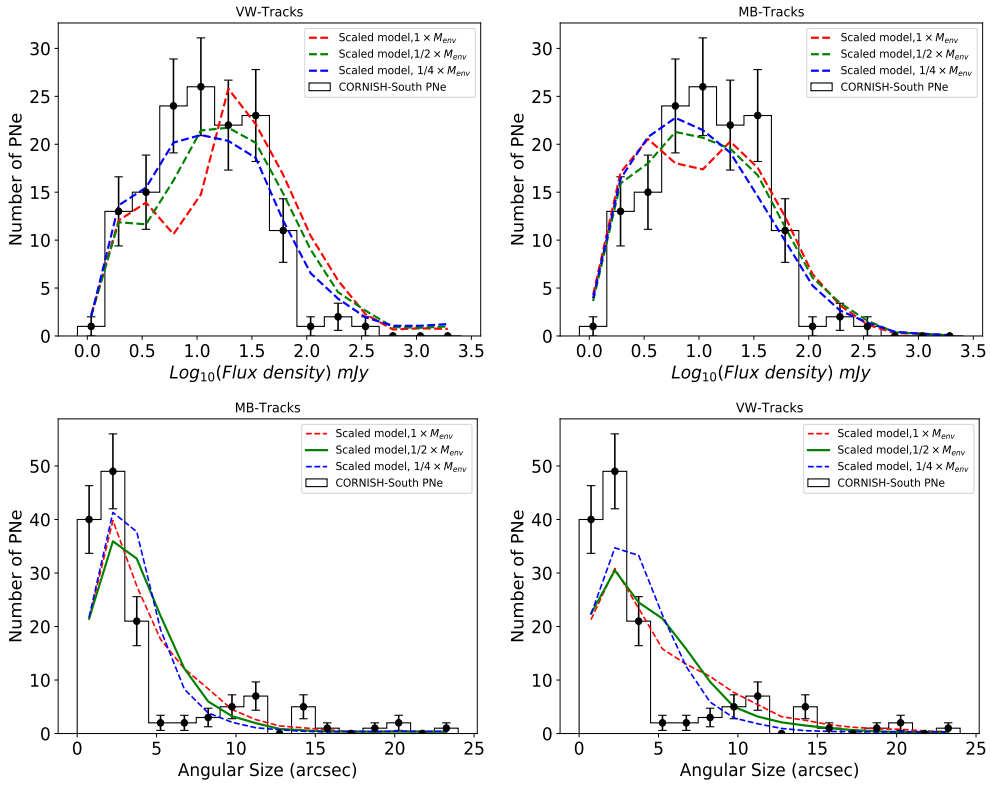

Figure 4.28: *Comparison of the modelled flux density (top) and angular size (lower) distribution for different scaled envelope mass for the synthesized binary model for the CORNISH-South PNe, using the VW-Tracks (left) and MB-Tracks (right). Modelled population is normalized to the CORNISH-South PNe number.*

Binary Population Synthesis

Considering a synthesized binary model, the flux density and angular size fit to the CORNISH-South PNe is shown in Figure 4.28. Consistently, scaling the envelope mass by a factor of 1/4 results in an improved fit to the flux density distribution, using both tracks. Scaling by a factor of 1/4 results in a synthesized PNe population of 149 (92%), and 109 (67%) using the VW-Tracks and MB-Tracks, respectively.

4.4.3 Best-Fit Model

Table 4.4 presents the summary of the results in scale height and number of synthesized PNe population using the VW-Tracks and MB-Tracks. Using the single and binary synthesized model results in a similar fit to the observed data. The synthesized binary model, however, results in a population of PNe that is comparable to the observed number of PNe within the $|b|< 1^{\circ}$ region. The assumed expansion velocity of 25 km/s is one parameter that affects the synthesized population, such that increasing the expansion results in a lower number of the synthesized population. Given the best fit scale height of 500 pc and 600 pc and the indication that expansion velocity increases with increasing scale height (e.g. Phillips 2002), it is possible that given an appropriate average expansion velocity, the population synthesis model would predict lower number of Galactic PNe for single stellar system. Thus, the synthesized single model could predict the number of observed CORNISH PNe.

Based on the model fit to the CORNISH-PNe flux density distribution, scaling the envelope mass, $M_{env}M_{\odot}$ results in an improved fit, although not significant. This is reflected in a shift in the peak of the modelled flux density distribution. Based on the assumption of a homogeneous sphere, this parameter need not be over-interpreted. The comparison of the model to the observed distribution of the flux density, however, infers an improved fit to observed flux density distribution for a scaled $M_{env}M_{\odot}$.

Within the limits of the assumptions made in building the model, assumed constants and predicted number from population synthesis of Galactic PNe, the synthesized binary population results in a better prediction of the observed CORNISH-PNe population and scaling the envelope mass by 1/4 consistently resulted in an improved fit to the flux density distribution for the northern and southern CORNISH-PNe.

Table 4.5 presents the mean of the observed properties distributions for the best fit model, based on a synthesized binary population and an envelope mass scaled by 1/4. This model predicts central star masses in the range of $0.57M_{\odot}$ to $0.62M_{\odot}$, mean distance of 8.5 kpc and an ionized mass of $0.12M_{\odot}$. This is similar to

Table 4.4: *Summary of the numbers of PNe predicted by the model by scaling the envelope mass,* M_{env}*. The percentages in bracket show the comparison of the model prediction to the CORNISH-PNe in the northern and southern Galactic planes. There are 162 PNe within the* $|b| < 1^{\circ}$ *region in the north and in the south.*

	CORNISH North PNe			
	Single		Binary	
Parameters	VW-Tracks	MB-Tracks	VW-Tracks	MB-Tracks
Scale height	550 (pc)		550 (pc)	
$M_{env} = 1(M_i - M_f)$	754 (465%)	507 (300%)	137 (84%)	87 (54%)
$M_{env} = 1/2(M_i - M_f)$	614 (380%)	421 (260%)	113 (70%)	72 (44%)
$M_{env} = 1/4(M_i - M_f)$	482 (297%)	342 (210%)	90 (56%)	60 (37%)
	CORNISH South PNe			
Scale height	600 (pc)		600 (pc)	
$M_{env} = 1(M_i - M_f)$	1307 (806%)	956 (590%)	237 (146%)	165 (100%)
$M_{env} = 1/2(M_i - M_f)$	1063 (656%)	773 (477%)	186 (115%)	134 (83%)
$M_{env} = 1/4(M_i - M_f)$	822 (507%)	619 (382%)	149 (92%)	109 (67%)

mean ionized mass of $0.12M_{\odot}$ obtained for 134 Galactic PNe by Zhang (1995) (see Figure 4.17). From a similar studies, where the synthesized radio properties were compared to observed properties, Stasińska & Tylenda (1994) obtained a mean ionized mass of $0.10M_{\odot}$ to $0.12M_{\odot}$ for the Galactic bulge PNe for constant $M_{env}M_{\odot}$.

The VW-Tracks and MB-Tracks resulted in similar distributions of the modelled properties. The VW-Tracks tracks, however, predict more PNe within the CORNISH survey region and larger CS masses. This is expected since the MB-Tracks predict faster evolution and lower final masses (see Section 4.2.2). To investigate and understand the effect of the MB-Tracks tracks on the predicted population would require integration into the population synthesis code.

Table 4.5: *Mean values of observed properties from the best-fit model results for the CORNISH-PNe in the northern and southern Galactic plane.*

	CORNISH North PNe		**CORNISH South PNe**	
Parameters	VW-Tracks	MB-Tracks	VW-Tracks	MB-Tracks
M_{ion}	$0.12M_{\odot}$	$0.10M_{\odot}$	$0.13M_{\odot}$	$0.10M_{\odot}$
CS mass	$0.60M_{\odot}$	$0.57M_{\odot}$	$0.62M_{\odot}$	$0.58M_{\odot}$
Age	3.0 kyrs	2.5 kyrs	4.0 kyrs	3.7 kyrs
Physical size	0.10 pc	0.10 pc	0.15 pc	0.14
Distance	8.5 kpc	9.0 kpc	9.0 kpc	8.3 kpc

4.5 Conclusions

This chapter presented a comparison of a synthesized population to the observed CORNISH-PNe in the Galactic plane. The synthesized population were generated by assuming Galactic PNe population from population synthesis by Moe & De Marco (2006) and interpolating on the previous evolution tracks (Vassiliadis & Wood, 1994) and the more recent evolution tracks (Miller Bertolami, 2016) (see Figure 4.1). The population synthesis prediction from single and binary stellar systems were investigated. The CORNISH survey detection limit in peak flux and angular size, and the survey regions were used to constrain the synthesized population. The comparison of the synthesized PNe and observed CORNISH-PNe was further restrained within the region where the CORNISH survey is complete[16] ($|b|< 1^{\circ}$). Within this region there are 162 PNe in the CORNISH-North and 162 in the CORNISH-South region. Properties investigated are the scale height, number of PNe within the CORNISH survey region, distribution of the flux densities and angular sizes, and the envelope mass.

The scale height of the CORNISH-PNe was investigated by comparing the synthesized latitude distribution to the observed latitude distribution. The $\tilde{\chi}^2$ statistics was used to analyse the comparison and a best fitting scale height of 550 pc was found to fit the CORNISH-North PNe latitude distribution. For the southern PNe counterparts, the best fitting scale height was found to be 600 pc. These

[16]the CORNISH survey extends more than the $|b|< 1^{\circ}$ region, making up the 169 in the north and 184 in the south

scale heights are on the high side, given the estimated values in the literature. This is, however, indicative of a mixed population of PNe, in terms of PNe types and their scale heights (Peimbert, 1978; Quireza *et al.*, 2007). From the $\tilde{\chi}^2$ analysis (see Figures 4.10 and 4.25 (top panel)) 350 pc was also a fit, but the choice of 550 pc and 600 pc were arrived at based on the minimum reduced $\tilde{\chi}^2$ and Figures 4.11 and 4.25.

Assuming a homogenous sphere of constant density and an average expansion velocity of 25 km/s, the radio properties of the synthesized population were modelled. Within the limits of the assumptions made in building the model, the model shows a good fit to the observed angular size, peak flux, brightness temperature, flux density distribution and the optical depth. The angular size and flux density kde plot of the model was found to show a good match with the observed distribution. An improved fit to the flux density distribution was found to be an initial envelope mass (M_{env} $M_{\odot}$) scaled by a factor of 1/4 i.e. $1/4(M_i - M_f)$, for both the northern and southern CORNISH-PNe.

The two evolutionary tracks (MB-Tracks and VW-Tracks) that were interpolated to obtain the temperatures and luminosities of the central stars resulted in similar distributions of the modelled properties. The MB-Tracks, however, predicted a younger CORNISH-PNe and a population that is consistently smaller compared to the VW-Tracks as summarized in Table 4.4. This is due to the fact that the more recent evolutionary tracks (MB-Tracks) are faster than previous tracks by (Vassiliadis & Wood, 1994) and Bloecker (1995). An indepth investigation of the effects of these tracks would require the use of both in the population synthesis model.

The modelled distances did not fit the distribution of the estimated distances, at distances above 15 kpc, for the CORNISH-North PNe (Chapter 2). The modelled and estimated distances, however, peak about the same distance. Based on the statistical methods used, the estimated distances would result in larger distances for the PNe that are optically thick and PNe with angular sizes that are smaller than the beam of the CORNISH survey. This would put such CORNISH-PNe at larger distances.

Based on the fit to the observed distribution and the predicted number of PNe, the synthesized binary stellar model for an envelope mass of $1/4(M_i – M_f)$ is considered the best fit model to the observed properties of the CORNISH-PNe (see Table 4.4). This resulted in a mean central star mass of $0.58M_\odot$ for the CORNISH-North PNe and $0.6M_\odot$ for the CORNISH-South PNe. The VW-Tracks predicts a wider range of ionized mass compared to the MB-Tracks. Table 4.5 shows a summary of the average parameters for the North and South PNe.

Previous works that have compared modelled predictons to observations by means of a synthetic population include Stasińska & Tylenda (1994), Stanghellini & Renzini (2000a) and Marigo *et al.* (2001). This is, however, the first model of its kind that investigates the scale height of observed PNe and compares modelled radio properties to population synthesis predictions. Within the limits of the model, it shows a good fit to the observed radio properties. More work still needs to be done in order to improve the model and make more detailed investigations.

Chapter 5

Conclusion and Future work

5.1 Conclusion

Understanding the formation processes and evolution of PNe provides a means to understand the late phase evolution of intermediate-mass stars ($0.8M_{\odot} \rightarrow 8M_{\odot}$) in our Galaxy, including their mass-loss history. To understand the formation and evolution of PNe, however, requires a sample that represents the PNe in our Galaxy, in a statistical sense. Observed PNe exhibit different evolutionary ages, morphologies, central star masses, ionization structures and are formed in different environments. Thus, a representative sample should reflect this range of PNe, including PNe that are old, middle aged and the very young PNe, where the physical processes associated with formation and shaping may still be active.

Presently, 3500 PNe are known (Parker *et al.*, 2017), while predictions from population synthesis (Moe & De Marco, 2006, 2012) and other estimates from column density (Zijlstra & Pottasch, 1991) indicate a hidden population. Part of this missing population are the PNe close to the Galactic mid-plane. This population include PNe from massive progenitors that could ionize their envelopes, while they are still dense. Dust extinction close to the Galactic mid-plane is, however, at a maximum. Thus, the search for such PNe population is limited in the optical regime. The known PNe population is mainly from optical observa-

tions (Strasbourg-ESO catalogue: Acker *et al.* 1992; MASH: Miszalski *et al.* 2008; Parker *et al.* 2006; IPHAS: Sabin *et al.* 2014) and not only biased by extinction, but also towards middle aged and angularly large or extended PNe that are either close by or evolved. To overcome dust extinction and incompleteness associated with the optical regime, it was necessary to search for PNe at longer wavelengths, where extinction is negligible.

By taking advantage of the almost transparent intersteller medium at radio wavelengths, the CORNISH survey was used as the primary dataset to search for PNe close to the Galactic mid-plane. The CORNISH survey is a radio continuum survey that mapped the inner Galactic plane defined by $10^\circ < l < 65^\circ$; $295^\circ < l < 350^\circ$ and $|b| < 1^\circ$. Data processing and measurements of the properties of the northern half data was performed by Purcell *et al.* (2013) and the calibration and imaging of the southern half are presented in this work. At a 7σ detection limit, 5013 sources were catalogued and the distributions of the measured properties are presented, which are similar to the northern counterpart.

The properties of non-Gaussian extended sources were measured by means of automated polygons that are drawn to enclose all the emission from the sources. 16% of the catalogued 7σ sources were described by such polygons, while the properties of the remaining sources were measured with 2D Gaussians. The general properties of the detected sources and step by step quality control processes of the catalogue are also presented. The radio properties of the CORNISH-South survey are particularly important in the characterization of compact ionized sources, including HII regions, towards the Galactic mid-plane. This is because no radio survey has previously mapped the southern Galactic mid-plane at such resolution ($2.5''$) and sensitivity of 0.2 mJy/beam. Hence, the importance of the CORNISH-South catalogue is not only in the studies of PNe, but also extends to HII regions, radio galaxies, YSO and radio stars. Examples of these are presented in Chapter 3.

169 PNe candidates, above a 7σ detection limit, were identified in the northern half of the survey (CORNISH-North PNe). Due to dust extinction, not all PNe detected by the CORNISH survey would have optical counterparts, hence cannot be identified using spectroscopy. For this reason, detailed multi-wavelength

investigations, including visual inspection, the radio spectral index (6 cm and 20 cm), MIR-to-radio ratio, infrared colours and optical colours, were used in this work to confirm their PNe nature. Based on visual inspection and the use of multi-wavelength colours, including NIR, MIR and FIR colours, 184 PNe were identified in the 7σ catalogue of the southern Galactic plane (CORNISH-South PNe). The image catalogue of all the sources classified as PNe across multiple wavelength is also presented in section B. The use of the ATLASGAL, Hi-Gal survey and RMS database were very useful in the elimination of HII regions and YSOs.

A mean MIR-to-radio (8μm/5GHz) ratio of 3.9±0.9 was found for the CORNISH-North PNe and 4.3 ± 1.2 for the CORNISH-South PNe. At a 3σ significant level, 3 of the CORNISH-North PNe have spectral indices < -1, which is inidicative of non-thermal emission. The youngest PNe from the CORNISH survey have brightness temperatures > 1000 K and closer than 6 kpc. The MIR and NIR colours of the CORNISH PNe show a broad distribution. This broad distribution is interpreted as a result of different dominant mechanisms across the different bands and wide range of intrinsic colours. In the FIR, the CORNISH PNe show a wider range of colours compared to the optically detected PNe that were studied by Anderson *et al.* (2012).

A total of 353 PNe were identified. Fifty three previously known PNe were recovered and 175 were newly classified as PNe. The newly classified are sources that were previously classified as either stars, infrared sources, radio sources or YSOs in the SIMBAD database. A further 51 sources that were previously classified as probable PNe were confirmed as such from the analysis presented. Eight of the candidate PNe in the CORNISH-North survey were classified as possible PNe or other source types. 66 PNe were detected for the first time. Table 5.1 shows a summary of the detected PNe in the CORNISH survey. There were more newly detected in the southern half of the survey because the southern Galactic plane is less explored.

In order to test the single and binary synthesis model by Moe & De Marco (2006, 2012), the observed properties of the CORNISH PNe were compared to the radio

Table 5.1: *Summary of detected PNe in the CORNISH survey. Newly detected PNe are PNe with no astronomical records in the SIMBAD database, within a 60″ search radius. Newly classified are sources that were previously classified as either candidate stars, infrared sources, radio sources or YSOs in the SIMBAD database.*

CORNISH PNe					
	Previously Known	Newly Classified	Newly Detected	Previously probable	Total
North PNe	24	78	12	47	169*
South PNe	29	97	54	4	184
	53	**175**	**66**	**51**	**353**

*8 sources were classified as probable or other source type based on insufficient data.

properties of a synthesized population. The synthesized population were generated by assuming a Galactic PNe population from the population synthesis model by Moe & De Marco (2006, 2012) and interpolating on the previous evolution tracks by Vassiliadis & Wood (1994) and the more recent evolution tracks by Miller Bertolami (2016). The CORNISH detection limit in peak flux and angular size, and the survey regions were used to constrain the synthesized population. Properties investigated are the scale height, number of PNe within the CORNISH survey region, and distribution of the flux densities and angular sizes.

The scale height of the CORNISH PNe was investigated by comparing the synthesized latitude distribution to the observed latitude distribution. The χ^2 statistics was used to derive the goodness-of-fit by means of the reduced $\tilde{\chi}^2$. A best fit scale height of 550 pc was found to fit the CORNISH-North PNe latitude distribution. For the southern PNe counterparts, the best fit scale height was found to be 600 pc. This is interpretated as an indication of a mixed population of PNe, in terms of PNe types and their scale heights (Peimbert, 1978; Quireza *et al.*, 2007). From the $\tilde{\chi}^2$ analysis (see Figures 4.10 and 4.25 (top panel)) 350 pc was also an acceptable fit, however, the choice of 550 pc and 600 pc were arrived at based on the minimum reduced $\tilde{\chi}^2$ and Figures 4.11 and 4.25.

The radio properties of the synthesized population were further modelled, assuming a constant density homogenous sphere and electron temperature, T_e of

10^4 K. Within the limits of the assumptions made in building the model, the model resulted in a good fit to the observed latitude distribution, angular size, brightness temperature (T_B), flux density distribution and the optical depth (τ_ν) for a scaled envelope mass. Based on the assumptions and predicted Galactic PNe population from population synthesis, the modelled parameters that fit the angular size, flux density distributions and observed number of PNe support the formation of observable PNe through binary interactions. This is not a claim that observed PNe are all necessarily from binary interactions as a more in-depth investigation still needs to be done. Using the model with the best fit parameters, a mean central star mass of $0.58M_\odot$ was derived for the CORNISH-North PNe and $0.60M_\odot$ for the CORNISH-South PNe. Table 4.5 shows the mean of derived properties from the model for the North and South PNe based on the best fit model.

The modelled distances of the synthesized population were less than 20 kpc and did not fit the distribution of the estimated distances for the CORNISH-North PNe (Chapter 2) at distances larger than 15 kpc. The modelled and estimated distances, however, peak about the same distance. Based on the statistical methods used, the distances to optically thick PNe and PNe with angular sizes less than the CORNISH beam size would be over-estimated, resulting in larger distances. The comparison of the modelled distances and estimated distances, however, indicate that the CORNISH-North PNe are concentrated at a distance of 10 kpc.

The more recent evolutionary tracks by Miller Bertolami (2016), consistently, predicted lower CSPNe masses and number of PNe, compared to the tracks by Vassiliadis & Wood (1994). This is due to the faster evolution of the (Miller Bertolami, 2016) tracks. An in-depth investigation of the effects of these tracks would require the use of the new tracks in the population synthesis model. This is the first model of its kind in terms of its formulation and approach and forms a basis for future investigations that compares observed radio properties directly with predictions from population synthesis. Within the limits of the model, it shows a good fit to the observed radio properties. More work still needs to be done in order to improve the model and make more detailed investigations that

would improve existing population synthesis models, hence the evolution models of PNe.

5.2 Future Work

5.2.1 CORNISH South Data and Upcoming Surveys

The 9 GHz (8-10 GHz) radio continuum dataset that was obtained simultaneously with the 5.5 GHz (4.5 - 6.5 GHz) data is yet to be processed. It is expected to be sensitive to sources above 0.3 to 1 mJy/beam. The calibration and imaging of this data will allow the spectral indices estimation for the CORNISH-South PNe. Although PNe are usually optically thin about 5 GHz, this data will enable the exploration of the very dense PNe population that may be optically thick at 5 - 5.5 GHz, hence not detected. In addition to the continuum data, RRLs (H112α and H87α) were also observed.

The CORNISH survey in the southern Galactic plane, at 5.5 GHz, provides a new dataset with which to explore radio sources in the southern Galactic plane. In addition to the studies of PNe, these data will be useful in the exploration of HII regions, especially, UCHII regions in the southern Galactic plane. Kalcheva *et al.* (2018) used data from the northern counterpart to explore the UCHII populations of the northern Galactic plane. From the 5.5 GHz data, a few cometary shaped UCHII regions have also been identified (see Figure 5.1). Exploration of the 5.5 GHz and 9 GHz data should reveal more new radio data for such UCHII regions.

Additionally, the CORNISH south data will complement surveys such as the MeerGAL survey that will map the same region ($280^\circ < l < 350^\circ, |b| < 1^\circ$) at 2 cm, with a resolution of $0.8''$ and sensitivity of 60 μJy (Thompson *et al.*, 2016) in the studies of compact ionized regions. It will also be interesting to see the CORNISH survey in the context of the on-going VLA sky survey (VLASS) with the same resolution ($2.5''$) but better sensitivity to larger structures using the S-band (2 - 4 GHz). VLASS (Lacy *et al.*, 2016; Villarreal Hernández & Andernach,

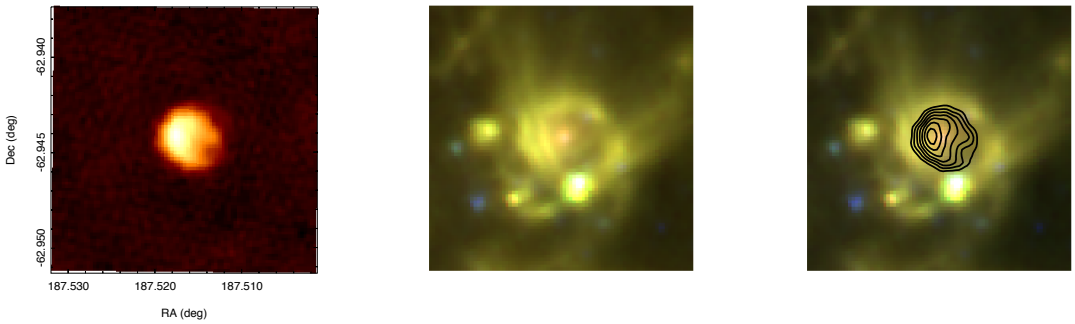

Figure 5.1: *Cometary shaped UCHII region from the CORNISH-South survey. Left: 5.5 GHz (CORNISH) data, middle: 3-colour image from the GLIMPSE survey, right: 3-colour image from the GLIMPSE survey showing the contour of the CORNISH data.*

2018) will cover the sky north of declination -40 deg (33885 deg^2) with a sensitivity of 69 μJy at 1σ level.

Other upcoming survey radio surveys of the Galactic plane with better sensitivity include:

- The KuGARS (Ku-band Galactic Reconnaissance Survey). The KuGARs is a proposed 14-18 GHz radio continuum survey of the Galactic plane with a sensitivity of 0.11 mJy, using the Jansky Very Large Array (JVLA). It is proposed to map the $10^\circ \leqslant l \leqslant 65^\circ$ and $|b| \leqslant 1$ region of the northern Galactic plane (Thompson *et al.*, 2016).
- GLOSTAR (Global view of star formation in the Galaxy). It is a JVLA survey with a sensitivity of 40 μJy, observing the Galactic plane ($-2^\circ < l < 85^\circ$ and $|b| < 1$ region) at 5 GHz and 8 GHz using the B and D configurations. This survey will also deliver RRLs with sensitivity of 5 mJy (Medina *et al.*, 2019).

Previous surveys of the southern Galactic plane, before the CORNISH survey, were limited in resolution and coverage, especially the $|b| < 1^\circ$ region, hence not suitable for the studies of compact ionized regions. The CORNISH data, together with these on-going and upcoming surveys will enable the studies of PNe

at multiple radio wavelengths. This will allow exploration of a new population of PNe that are very dense and the extended population at radio wavelengths. Future projects can then build a more suitable population of PNe that can be compared with population synthesis models.

5.2.2 Explore 5σ Sources in the CORNISH Survey

The 5σ catalogue would be dominated by unreal sources, compared to the 7σ counterpart, as described in Purcell *et al.* (2013) and Chapter 3 of this work. However, it can be explored through a multi-wavelength analysis. Multi-wavelength exploration of the 5σ catalogue may reveal more PNe within the CORNISH survey region than presented in this work. This will be one interesting work that should be considered as it may also reveal other sources, aside from PNe, with peak flux $< 7\sigma$.

5.2.3 Updating the Model

The model presented in this work is still a bit crude, based on the simplified assumptions. In order to arrive at a more robust and realistic model, the following improvements can be considered:

- **Brightness temprature**: The model could not fit the low end of the CORNISH PNe T_B disribution. To achieve a better fit with the brightness temperature, a more realistic model is needed. According to Hajduk *et al.* (2018), a homogenous sphere model cannot fit the observed temperature brightness of PNe. They suggested a prolate ellipsoid defined by inner and outer ellipsoids. Siódmiak & Tylenda (2001) also suggested a two component defined by two different optical thickness.
- **Two-winds or three-winds models**: Instead of a sphere, two-winds or three-winds models should be considered (Kahn, 1989; Marigo *et al.*, 2001; Marten & Schoenberner, 1991). The modelling of the dynamic evolution of the nebula itself, which takes into consideration the expansion of the

ionized envelope by radiation pressure should also be considered (Marigo *et al.*, 2001; Marten & Schoenberner, 1991; Mellema & Frank, 1995; Volk & Kwok, 1985).

– **Envelope mass**: Instead of scaling the envelope mass by an average factor, a more deterministic approach should be employed. One method could be interpolating the evolutionary tracks to obtain an estimated envelope mass for each PN at a particular age, luminosity and temperature. Another method could consider the dynamic evolution from the AGB through to the PN phase in order to account for individual mass loss of each object. This will also account for individual visibility times as well.

– **Expansion velocity**: Given that there is some indication in the literature about increasing expansion velocity with scale height (e.g Phillips 2002) and the range of average expansion velocity in the literature (e.g 20 - 50 km/s Bloecker 1995; Choi *et al.* 2008; Jacob *et al.* 2013; Schönberner *et al.* 2014), the expansion velocity of each CORNISH PNe could be estimated, using the RRL data. This would give an informed average expansion velocity considering that the model predicts a scale height of 500 pc and 600 pc, which is higher than scale heights of PNe in the literature.

  The population synthesis model may also take into consideration the increasing expansion velocity with scale height and the effect of metalicity on the expansion velocity, instead of predicting the Galactic PNe population based on an average value. This is one parameter that the predicted population is sensitive to. According to Schönberner *et al.* (2010), based on hydrodynamical models, the expansion velocity of PNe is influenced by their metal content and this decreases with scale height from the Galactic mid-plane. This would inprove the estimation of the predicted population.

– To improve the comparison of the data with the model, the radio images of the PNe can be simulated and put through the interferometric uv coverage of the CORNISH survey. This will also allow consistency in the comparison of angular sizes as well.

Based on these suggestions, a better and more robust model could be designed to compare with observed radio properties of the CORNISH PNe. Comparisons of this kind can also be extended to larger and deeper radio surveys, which will improve our understanding on the formation and evolution of PNe.

5.2.4 Archival Data Search for PNe

The analysis presented in this work can be applied to archival data to search for PNe e.g. using the NVSS and MAGPIS surveys. An example is the 5 sources found by searching the IPHAS images using the CORNISH positions. It is possible that there are more of such PNe that have been missed and still in archives. Based on the multi-wavelength investigations from this study, published catalogues from wide area surveys such as WISE, Hi-Gal and GLIMPSE can also be reviewed to search for candidate PNe. This can be done by building a data pipeline that will automatically scrape through databases and create clusters of possible different objects using their colours or available properties. The properties of the clusters can then be analysed to search for candidate PNe. A similar work was done by Stenborg (2017) to recover more than 300 PNe candidates in the Galactic bulge by reviewing [OIII] data.

5.2.5 PNe Study in the SKA Era

With the SKA era ushering in deeper and larger radio surveys, it is undeniable that the search for new PNe will be very active, given that radio emission is a strong indicator of PN formation. To efficiently explore such surveys e.g. EMU (Norris *et al.*, 2011b) in the future, manual intervention will be limited. A future project should look at developing machine learning algorithms using the CORNISH PNe sample to build training sets that will automatically identify PNe.

Machine learning involves providing a system or systems the ability to automatically learn and improve from past experience without being programmed explicitly. The use of machine learning has been successfully applied in astronomy (Ball *et al.*, 2006; Banerji *et al.*, 2010; Fadely *et al.*, 2012; Kamdar *et al.*, 2015;

Kim & Brunner, 2017; Sevilla-Noarbe & Etayo-Sotos, 2015). However, for machine learning to be successful, a diverse source of example datasets are needed. This allows the algorithm to draw many patterns, relationships, and clusters to broaden and extend its pattern matching and correlations.

This work has provided extensive photometry and uniform cut-outs of multi-wavelength images which can serve as good initial training sets. The sample can then be extended to include diverse PNe samples from already existing databases, such as the HASH database (Parker *et al.*, 2017) and on-going and up-coming radio surveys (section 5.2.1). This will provide a robust algorithm that can be used to automatically identify PNe in a more efficient and unbiased manner.

5.3 Final Remarks

Towards the Galactic mid-plane, where dust extinction is at a maximum, it is important that PNe are searched for and identified using alternative methods. The analysis presented in this thesis demonstrates that the search for PNe at radio wavelengths is a strong tool in finding new PNe. This study also demonstrated the pitfalls associated with the use of infrared colours alone in the identification of PNe, as they could readily be confused with YSOs. This is demonstrated in Chapter 2. At 5.45 cm (southern plane) and 6 cm (northern plane), the CORNISH survey is more complete within the $|b| < 1^{\circ}$ region and has uncovered 66 PNe that are detected for the first time within 220 deg^2 area of the Galactic plane. The sample of PNe presented in this work will complement PNe from the NVSS survey, at the compact and young end of the PNe population detected at radio wavelengths. The extensive NIR and MIR photometry presented in this work will provide a new colour selection criteria for PNe in the NIR and MIR colour-colour planes for future PNe search.

Appendix A

Additional Figures and Tables for Chapter 2

Photometric Errors Versus Magnitude

Tables

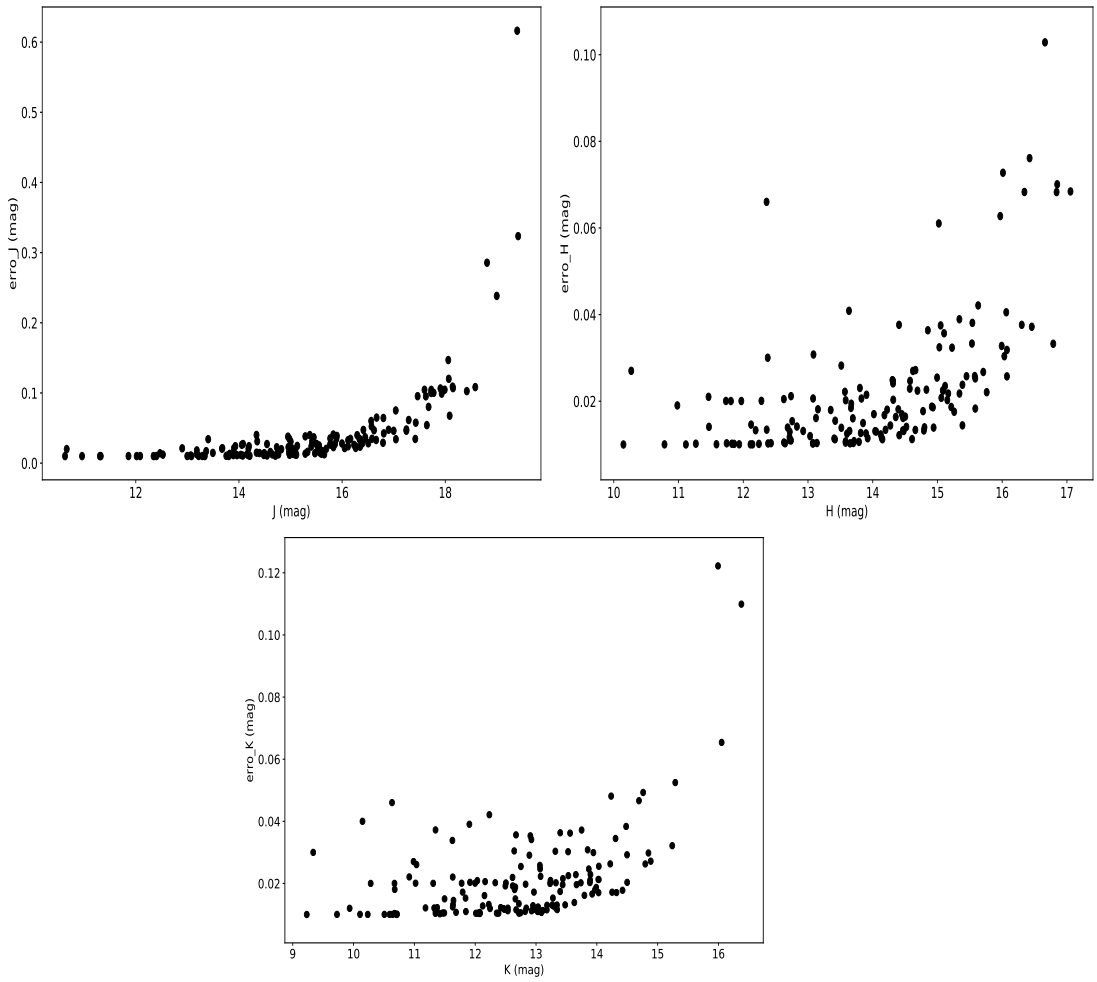

Figure A.1: *Measured magnitudes versus errors from aperture photometry across the J, H and K band. The errors are observed to increase with PNe that are fainter.*

Table A.1: *Radio properties of the CORNISH–PNe. For the angular sizes of sources whose deconvolved sizes could not be determined, upper limits of 3σ are propagated and they are preceded by '<'. Column 6 shows measured (aperture photometry) 1.4 GHz flux densities (MAGPIS) not present in the point source catalogue.*

Name	RA	DEC	F_{5GHz}	dF_{5GHz}	$F_{1.4GHz}$	$dF_{1.4GHz}$	Size	dSize	Tb	dTb	α	dα
	J2000	J2000	mJy	mJy	mJy	mJy	arcsec	arcsec	K	K		
G009.9702–00.5292	18:09:40.54	–20:34:21.7	12.6	1.6	11.55	0.65	2.45	0.25	154	29	0.070	0.11
G010.0989+00.7393	18:05:13.13	–19:50:35.2	476.0	43.6			6.66	0.01	784	72	0.20	0.10
G010.4168+00.9356	18:05:09.17	–19:28:11.3	14.4	1.5			0.94	0.27	1182	489	–	
G010.5960–00.8733	18:12:14.95	–20:11:24.7	34.5	3.8			3.02	0.05	276	31	0.010	0.10
G011.3266–00.3718	18:11:52.34	–19:18:31.0	13.8	2.4	11.63	0.84	4.02	0.11	62	11	0.14	0.15
G011.4290–01.0091	18:14:27.14	–19:31:26.8	14.6	2.0			3.08	0.31	112	22	–0.40	0.14
G011.4581+01.0736	18:06:47.64	–18:29:37.7	7.4	1.2			1.89	0.37	152	48	–	
G011.7210–00.4916	18:13:07.15	–19:01:12.4	5.9	1.1	8.06	0.48	2.1	0.48	98	37	–0.24	0.16
G011.7434–00.6502	18:13:45.22	–19:04:35.4	156.9	15.0			6.72	0.01	253	24	0.00	0.09
G011.7900–00.1022	18:11:48.89	–18:46:21.4	41.2	6.9	49.1	1.13	8.05	0.08	46	8	–0.14	0.13
G012.0438–00.5077	18:13:49.94	–18:44:39.8	13.5	1.4	4.81	1.03	0.72	0.31	1880	1160	0.81	0.19
G012.1157+00.0757	18:11:49.08	–18:24:05.4	47.4	4.4			3.37	0.11	305	32	0.16	0.17
G012.1528–00.3304	18:13:23.74	–18:33:50.0	12.0	1.4			1.99	0.24	222	46	–	
G012.3315–00.1806	18:13:12.12	–18:20:07.1	33.7	3.3	28.95	1.6	3.22	0.14	236	27	0.12	0.10
G012.3830+00.7990	18:09:41.62	–17:49:06.6	19.6	2.0			1.52	0.17	621	118	0.43	0.21
G012.6012+00.5592	18:11:01.10	–17:44:35.5	17.1	1.7	5.03	0.41	0.89	0.24	1590	636	0.96	0.10
G013.3565–00.7559	18:17:23.11	–17:42:31.3	9.7	1.3	10.95	0.73	1.49	0.32	316	106	–0.10	0.12
G013.6313–00.6023	18:17:21.89	–17:23:38.4	19.9	3.3			5.91	0.67	42	10	–	
G013.9166+00.6500	18:13:19.85	–16:32:45.6	27.0	2.6			2.49	0.13	317	39	0.45	0.11
G014.2365+00.2117	18:15:34.46	–16:28:27.8	24.3	2.9			4.6	0.31	84	13	–0.42	0.10
G014.4573–00.1847	18:17:28.03	–16:28:07.3	48.3	4.5			2.97	0.1	399	41	0.67	0.10

Continued on next page

Table A.1 – continued from previous page

Name	RA	DEC	F_{5GHz}	dF_{5GHz}	$F_{1.4GHz}$	$dF_{1.4GHz}$	Size	dSize	Tb	dTb	α	dα
	J2000	J2000	mJy	mJy	mJy	mJy	arcsec	arcsec	K	K		
G014.5851+00.4613	18:15:21.17	–16:02:56.8	22.1	3.5			4.93	0.08	66	11	–0.13	0.14
G014.7503–00.2496	18:18:17.06	–16:14:29.4	19.8	2.6	18.26	0.4	4.26	0.34	80	14	0.060	0.10
G014.8960+00.4837	18:15:53.23	–15:45:54.0	8.8	1.2			1.14	0.4	493	254	–	
G015.1999–00.0863	18:18:34.30	–15:46:05.5	10.0	1.6	12.4	0.46	2.73	0.39	98	25	–0.17	0.13
G015.5410+00.3359	18:17:41.95	–15:16:03.7	21.9	3.2	12.84	0.34	2.61	0.08	234	36	0.42	0.12
G015.5847+00.4002	18:17:33.02	–15:11:55.7	21.9	2.1	9.2	0.42	1.36	0.16	862	168	0.68	0.10
G015.7993–00.0063	18:19:27.34	–15:12:08.3	49.2	4.5	39.03	2.2	1.86	0.1	1039	122	0.18	0.10
G016.0550+00.8280	18:16:54.96	–14:34:54.5	14.1	1.4			1.44	0.18	500	102	0.37	0.27
G016.4034–00.5740	18:22:42.53	–14:56:11.8	37.0	5.3			6.33	0.06	67	10	–0.18	0.13
G016.4276+01.0072	18:16:59.74	–14:10:07.7	16.4	2.7			4.45	0.51	61	14	0.020	0.14
G016.4999+00.1152	18:20:22.87	–14:31:38.3	15.8	2.3	16.54	0.55	5.85	0.54	34	7	–0.040	0.12
G016.6002–00.2754	18:22:00.02	–14:37:21.7	22.2	4.3	20.14	0.7	6.93	0.11	34	7	0.080	0.16
G017.0152–00.1906	18:22:29.81	–14:12:59.0	13.3	2.3	14.23	0.5	3.33	0.11	88	16	–0.050	0.14
G017.3669+00.5224	18:20:35.14	–13:34:14.5	18.4	1.9			3.4	0.18	117	15	0.28	0.14
G017.4147+00.3791	18:21:11.93	–13:35:46.0	41.0	5.1			10.75	0.06	26	3	–	
G017.4487+00.1146	18:22:13.54	–13:41:25.4	9.4	1.7	8.3	0.38	4.29	0.59	37	10	0.10	0.15
G017.7250–00.2427	18:24:03.46	–13:36:50.4	59.1	6.0	67.96	3.7	7.76	0.31	72	8	–0.11	0.10
G017.8222+00.9866	18:19:47.16	–12:57:01.1	15.4	1.8			3.36	0.23	99	15	0.21	0.15
G017.8645+00.2120	18:22:40.49	–13:16:39.4	23.4	2.2	6.34	0.44	0.89	0.18	2170	668	1.0	0.10
G018.0661+00.8535	18:20:44.35	–12:47:52.8	33.2	3.2			4.12	0.16	143	16	0.39	0.13
G018.1286–00.2189	18:24:44.86	–13:14:46.0	8.5	1.7	7.14	0.41	2.27	0.51	121	45	0.14	0.16
G018.2402–00.9152	18:27:29.64	–13:28:19.6	65.2	8.3			12.88	0.05	29	4	–	
G018.2413–00.5552	18:26:11.16	–13:18:12.6	8.2	0.9	1.14	0.21	<0.30	–			1.6	0.17
G018.5242+00.1519	18:24:09.72	–12:43:22.8	3.7	0.8	0.8	0.22	1.74	0.58	88	45	1.2	0.28

Continued on next page

Table A.1 – continued from previous page

Name	RA	DEC	F_{5GHz}	dF_{5GHz}	$F_{1.4GHz}$	$dF_{1.4GHz}$	Size	dSize	Tb	dTb	α	dα
	J2000	J2000	mJy	mJy	mJy	mJy	arcsec	arcsec	K	K		
G018.5776–00.7484	18:27:31.92	–13:05:44.9	7.6	1.5	4.9	0.52	4.14	0.63	32	9	0.34	0.18
G019.2356+00.4951	18:24:16.99	–11:56:01.3	38.5	4.4			4.17	0.04	161	19	–0.67	0.10
G019.4676–00.0154	18:26:34.34	–11:58:00.8	18.8	1.9	20.59	1.0	2.01	0.14	341	48	–0.070	0.10
G019.5326+00.7308	18:24:00.00	–11:33:39.2	6.0	1.1	4.71	0.76	2.33	0.47	81	28	0.19	0.19
G019.9298–00.6639	18:29:47.86	–11:51:33.1	14.1	1.4	6.95	0.45	<0.2	–			0.56	0.10
G019.9448+00.9126	18:24:07.90	–11:06:42.1	29.8	3.1			3.48	0.17	180	22	0.090	0.12
G020.4681+00.6793	18:25:58.08	–10:45:28.8	86.4	8.7			3.77	0.02	445	45	0.34	0.10
G020.5176+00.4778	18:26:47.26	–10:48:29.2	15.6	1.9			3.38	0.25	100	16	0.060	0.13
G020.6015+00.0206	18:28:35.69	–10:56:47.4	3.6	0.9			1.77	0.69	84	50	–	
G020.9782+00.9253	18:26:03.00	–10:11:31.6	13.7	1.9			3.71	0.34	73	14	0.21	0.20
G021.1653+00.4755	18:28:01.32	–10:14:09.2	131.7	12.4			2.36	0.01	1720	163	0.79	0.10
G021.3425–00.8423	18:33:06.41	–10:41:20.8	17.6	2.7			2.5	0.36	205	53	–	
G021.6657+00.8110	18:27:45.65	–09:38:12.8	52.9	4.8			1.46	0.11	1814	249	1.1	0.20
G021.6849–00.7381	18:33:22.39	–10:20:14.3	36.5	6.0	33.8	0.53	7.68	0.08	45	7	0.06	0.13
G021.8201–00.4779	18:32:41.30	–10:05:50.3	34.2	3.9	44.63	0.74	5.78	0.34	75	11	–0.21	0.10
G021.9972–00.8838	18:34:29.02	–10:07:38.3	14.2	1.7			2.49	0.22	167	28	–	
G022.2211+00.9009	18:28:29.04	–09:06:12.2	21.4	2.4			3.43	0.22	133	19	0.32	0.13
G022.5477–00.1061	18:32:42.82	–09:16:48.7	32.1	3.0			2.43	0.11	398	46	0.20	0.12
G022.6429–00.4422	18:34:06.00	–09:21:02.9	6.3	1.2	3.92	0.28	2.14	0.46	100	36	0.37	0.16
G022.6580+00.2959	18:31:28.54	–08:59:47.8	14.2	1.4			1.42	0.18	512	104	–0.01	0.17
G023.2321+00.0809	18:33:19.25	–08:35:12.5	24.0	2.4	21.19	0.31	2.71	0.14	238	29	0.10	0.10
G023.4181–00.3940	18:35:22.37	–08:38:25.8	26.5	2.5			1.76	0.12	622	83	0.49	0.15
G023.5044–00.5245	18:36:00.12	–08:37:26.0	27.2	2.7			3.07	0.14	211	25	–0.020	0.10
G023.8214–00.5788	18:36:47.18	–08:22:02.6	52.1	4.7			2.04	0.09	916	101	0.82	0.13

Continued on next page

Table A.1 – continued from previous page

Name	RA	DEC	F_{5GHz}	dF_{5GHz}	$F_{1.4GHz}$	$dF_{1.4GHz}$	Size	dSize	Tb	dTb	α	dα
	J2000	J2000	mJy	mJy	mJy	mJy	arcsec	arcsec	K	K		
G023.8897–00.7379	18:37:29.09	–08:22:46.9	113.4	10.7			2.58	0.01	1243	118	0.70	0.10
G024.0943–01.0992	18:39:09.74	–08:21:49.0	16.4	1.6			<0.2	–			0.51	0.13
G024.1659+00.2502	18:34:27.19	–07:40:48.4	37.0	6.8	29.46	2.1	11.66	0.12	20	4	0.18	0.14
G024.3852+00.2869	18:34:43.78	–07:28:06.6	6.5	1.5			3.03	0.66	51	20	–	
G024.7921–01.0043	18:40:06.72	–07:41:59.6	9.7	1.4			2.47	0.32	116	27	0.11	0.16
G024.8959+00.4586	18:35:03.79	–06:56:10.3	13.3	2.0	6.93	0.33	2.26	0.1	191	30	0.51	0.12
G025.0485–00.6621	18:39:21.50	–07:18:55.1	30.1	2.8			1.64	0.11	813	108	0.56	0.13
G025.5190+00.2165	18:37:04.97	–06:29:39.1	267.3	24.9			12.7	0.01	121	11	–	
G025.5769+00.1389	18:37:28.03	–06:28:41.9	13.8	1.4	13.76	0.29	1.27	0.18	626	142	0.00	0.08
G025.8466+01.1718	18:34:16.58	–05:45:50.0	31.3	4.4			4.69	0.41	104	19	0.10	0.13
G026.0823–00.0347	18:39:01.27	–06:06:32.4	14.2	1.9	24.14	0.48	3.22	0.3	100	19	–0.42	0.11
G026.1620+00.5926	18:36:55.63	–05:45:00.7	12.4	2.2			4.4	0.56	47	12	–0.20	0.18
G026.2268+00.7685	18:36:25.15	–05:36:42.8	6.5	1.0	8.39	0.8	2.03	0.37	115	34	–0.21	0.14
G026.6529+00.2874	18:38:55.34	–05:27:15.1	6.7	1.3	9.39	0.38	2.5	0.48	79	26	–0.27	0.15
G026.7145+00.1319	18:39:35.50	–05:28:14.5	13.2	1.5	14.69	0.45	2.25	0.21	190	34	–0.090	0.10
G026.8327–00.1516	18:40:49.30	–05:29:44.2	8.5	1.8	11.12	0.29	3.55	0.15	49	11	–0.22	0.17
G027.4265–00.2499	18:42:15.86	–05:00:45.0	5.5	1.0	6.22	0.42	1.68	0.48	142	63	–0.10	0.15
G027.6595–00.3835	18:43:10.13	–04:51:59.0	11.2	1.2	3.35	0.35	< 0.23				0.95	0.12
G027.6635–00.8267	18:44:45.55	–05:03:55.1	8.2	1.0			1.38	0.26	313	91	–	
G027.6640–00.2485	18:42:41.69	–04:48:02.2	5.1	0.8	8.2	0.32	<0.5	–			–0.38	0.13
G027.7016+00.7048	18:39:21.79	–04:19:50.9	131.8	13.1			6.79	0.02	209	21	–0.080	0.10
G029.0538+00.9915	18:40:49.39	–02:59:51.7	5.1	0.9			0.92	0.64	443	444	–	
G029.1652–00.0168	18:44:37.18	–03:21:34.2	11.3	1.3			2.6	0.2	122	19	–0.41	0.10
G029.2113–00.0689	18:44:53.38	–03:20:32.3	101.2	9.9			5.47	0.02	247	24	–0.020	0.10

Continued on next page

Table A.1 – continued from previous page

Name	RA	DEC	F_{5GHz}	dF_{5GHz}	$F_{1.4GHz}$	$dF_{1.4GHz}$	Size	dSize	Tb	dTb	α	dα
	J2000	J2000	mJy	mJy	mJy	mJy	arcsec	arcsec	K	K		
G029.5780–00.2686	18:46:16.32	–03:06:25.9	6.2	1.0	1.9	0.32	<0.5	–			0.93	0.18
G029.8742–00.8190	18:48:46.54	–03:05:40.9	167.2	16.1			2.86	0.01	1490	144	0.69	0.10
G030.0226+00.1570	18:45:34.13	–02:31:02.6	8.7	1.4	11.87	0.41	2.47	0.38	104	28	–0.24	0.13
G030.0294–00.3318	18:47:19.34	–02:44:03.8	13.0	1.6	12.79	0.35	1.75	0.25	311	73	0.010	0.10
G030.2335–00.1385	18:47:00.38	–02:27:52.6	360.4	32.9			1.93	0.01	7070	647	–0.55	0.10
G030.5302+00.1315	18:46:35.23	–02:04:38.6	10.2	2.3			5.09	0.15	29	7	–	
G030.6670–00.3319	18:48:29.23	–02:10:01.6	145.9	13.9			1.87	0.01	3043	291	1.2	0.10
G030.8560+00.3826	18:46:17.28	–01:40:22.4	49.5	4.6			2.89	0.1	433	45	0.47	0.10
G031.2131–00.1803	18:48:56.64	–01:36:42.8	3.0	0.7			<0.8	–	–			
G031.3724–00.7514	18:51:16.13	–01:43:50.2	22.7	2.3			2.79	0.15	212	27	0.22	0.12
G032.3076+00.1536	18:49:45.14	–00:29:07.8	17.7	1.9	13.76	0.47	1.57	0.21	526	115	0.20	0.10
G032.5485–00.4739	18:52:25.56	–00:33:26.3	51.5	4.7	40.39	0.54	2.78	0.09	487	50	0.19	0.10
G032.6136+00.7971	18:48:01.18	+00:04:48.7	3.5	0.8			1.48	0.67	117	80	–	–
G032.8082–00.3159	18:52:20.21	–00:15:15.1	15.9	2.4	16.18	0.45	4.22	0.08	65	10	–0.020	0.12
G032.8177–00.1165	18:51:38.66	–00:09:17.3	4.4	0.9	2.98	0.3	1.86	0.57	93	45	0.31	0.18
G033.1198–00.8949	18:54:57.98	–00:14:27.2	18.6	1.8	16.7	1.89	<0.20	–	–	–	0.080	0.12
G033.3526+00.4043	18:50:45.94	+00:33:31.7	14.9	1.5	7.75	0.49	0.82	0.25	1617	709	0.51	0.10
G033.4543–00.6149	18:54:34.80	+00:11:04.2	75.8	6.8			1.71	0.09	1887	223	1.1	0.10
G033.7952+00.4307	18:51:28.75	+00:57:52.9	8.9	1.1	5.22	0.46	1.58	0.26	259	68	0.42	0.12
G033.9059–00.0436	18:53:22.20	+00:50:49.2	16.0	1.5	1.75	0.49	0.62	0.27	3019	1863	1.7	0.23
G034.1792–00.1777	18:54:20.74	+01:01:44.4	10.1	1.8	11.45	0.47	3.93	0.52	48	12	–0.10	0.14
G034.4200–00.3183	18:55:17.14	+01:10:45.1	12.1	1.3	4.45	0.31	1.03	0.28	837	334	0.79	0.10
G034.8624–00.0630	18:55:11.06	+01:41:21.5	64.7	7.3			5.14	0.03	178	20	0.43	0.10
G035.2162+00.4280	18:54:04.90	+02:13:41.2	12.0	2.6	13.31	0.75	4.9	0.8	37	11	–0.080	0.17

Continued on next page

Table A.1 – continued from previous page

Name	RA	DEC	F_{5GHz}	dF_{5GHz}	$F_{1.4GHz}$	$dF_{1.4GHz}$	Size	dSize	Tb	dTb	α	dα
	J2000	J2000	mJy	mJy	mJy	mJy	arcsec	arcsec	K	K		
G035.4719–00.4365	18:57:37.68	+02:03:40.3	207.1	19.6			4.08	0.01	906	86	0.30	0.10
G035.5654–00.4922	18:57:59.83	+02:07:08.0	59.3	7.0			9.88	0.05	44	5	–	
G036.0116–00.2562	18:57:58.32	+02:37:25.3	18.2	1.7	9.47	0.45	1.35	0.14	729	125	0.51	0.10
G036.5393+00.2003	18:57:18.62	+03:18:05.4	13.4	2.6	16.88	2.31	5.33	0.12	34	7	–0.18	0.15
G037.9031–00.2754	19:01:30.31	+04:17:49.9	32.5	3.0	14.49	0.32	1.26	0.14	1491	266	0.64	0.10
G037.9601+00.4534	18:59:00.58	+04:40:52.0	22.7	2.1	8.55	0.42	1.08	0.16	1412	319	0.77	0.10
G038.9237–00.0807	19:02:41.18	+05:17:37.0	12.4	2.5	11.89	0.57	5.29	0.8	32	10	0.040	0.16
G039.1617+00.7826	19:00:02.33	+05:54:01.1	28.3	2.8			2.79	0.13	266	31	–0.16	0.10
G039.5911–00.3785	19:04:58.78	+05:45:00.7	4.3	1.0	3.29	0.45	1.59	0.66	125	79	0.22	0.21
G040.2606–00.2755	19:05:50.88	+06:23:32.3	7.0	1.0	1.4	0.19	<0.4	–			1.3	0.16
G040.3359–01.0102	19:08:36.74	+06:07:16.3	9.1	1.5			3.35	0.42	59	14	–0.31	0.15
G041.1982+00.0348	19:06:28.42	+07:22:03.0	37.9	4.4			2.99	0.04	309	36	0.20	0.10
G041.3540+00.5390	19:04:57.34	+07:44:15.0	33.9	3.5			4.03	0.18	152	18	0.16	0.10
G041.7871+00.4884	19:05:56.40	+08:05:56.4	8.2	1.0			1.06	0.35	533	260	2.3	0.21
G042.6629–00.8648	19:12:25.46	+08:15:07.2	17.5	2.2			3.93	0.3	83	14	–	
G043.0281+00.1399	19:09:30.14	+09:02:25.1	109.6	9.8	56.78	3.22	2.62	0.08	1166	116	0.52	0.10
G043.2946–00.6455	19:12:49.30	+08:54:48.6	68.1	6.1			1.88	0.09	1410	161	0.74	0.10
G043.5793+00.0261	19:10:56.59	+09:28:36.1	16.0	1.5	9.22	0.46	0.74	0.24	2137	1012	0.43	0.10
G043.6554–00.8279	19:14:09.24	+09:08:54.6	20.2	2.1			2.49	0.16	237	32	–	
G044.6375+00.4827	19:11:17.14	+10:37:34.0	17.5	1.9			2.26	0.18	250	40	0.43	0.14
G045.1801+00.9893	19:10:28.58	+11:20:28.7	5.5	0.8			<0.4	–	–			
G045.2830–00.6278	19:16:30.50	+10:40:55.9	21.4	2.2			2.31	0.16	293	42	0.57	0.21
G046.9747+00.2702	19:16:29.09	+12:35:51.0	18.1	1.9	16.49	0.91	2.04	0.18	317	52	0.070	0.10
G047.6884–00.3024	19:19:55.78	+12:57:38.2	16.4	1.6			0.87	0.25	1571	646	–	

Continued on next page

Table A.1 – continued from previous page

Name	RA	DEC	F_{5GHz}	dF_{5GHz}	$F_{1.4GHz}$	$dF_{1.4GHz}$	Size	dSize	Tb	dTb	α	dα
	J2000	J2000	mJy	mJy	mJy	mJy	arcsec	arcsec	K	K		
G047.9875+00.2026	19:18:40.34	+13:27:41.0	6.0	0.9	6.88	0.7	1.29	0.43	263	129	–0.10	0.14
G048.5619+00.9029	19:17:13.66	+14:17:47.4	3.6	0.7			1.81	0.48	80	33	–	
G048.6748–00.5350	19:22:40.85	+13:43:17.8	5.9	1.1			2.23	0.45	86	29	–	
G048.7319+00.9305	19:17:27.26	+14:27:34.9	18.6	1.9			2.14	0.14	297	41	–	
G049.6948+00.8642	19:19:33.60	+15:16:46.9	26.6	2.4			1.65	0.11	714	95	–	
G050.0003+00.5072	19:21:27.77	+15:22:54.1	19.5	1.9			1.68	0.13	505	74	–	
G050.0405+01.0961	19:19:22.92	+15:41:37.3	17.9	1.8			2.75	0.15	173	22	–	
G050.0457+00.7683	19:20:35.69	+15:32:40.6	15.6	1.6			2.52	0.14	180	23	–	
G050.4802+00.7056	19:21:40.42	+15:53:54.6	7.0	0.8			1.08	0.31	441	187	–	
G050.5556+00.0448	19:24:14.57	+15:39:11.2	129.4	12.4			3.97	0.01	600	57	0.32	0.10
G050.8950+00.0572	19:24:51.94	+15:57:28.4	9.0	1.1			2.06	0.24	155	32	0.11	0.17
G051.5095+00.1686	19:25:40.30	+16:33:06.5	153.4	14.2			11.95	0.01	78	7	–	
G051.6061+00.9140	19:23:07.18	+16:59:22.9	18.9	1.8			1.3	0.14	811	146	–	
G051.8341+00.2838	19:25:53.54	+16:53:31.6	76.0	6.8			2.98	0.08	624	61	0.26	0.10
G052.1498–00.3758	19:28:56.71	+16:51:18.4	22.9	2.1			0.77	0.19	2822	1009	–0.36	0.10
G055.5070–00.5579	19:36:26.93	+19:42:24.1	203.1	18.7			3.37	0.01	1303	120	0.64	0.10
G056.4016–00.9033	19:39:35.78	+20:19:01.9	18.6	1.7			1.14	0.15	1044	217	–	
G057.5352+00.2266	19:37:45.72	+21:51:34.2	3.9	0.7			1.32	0.5	162	91	–	
G058.1591–00.5499	19:42:00.10	+22:01:11.3	3.8	0.7			1.69	0.48	97	43	–	
G058.6410+00.9196	19:37:29.33	+23:09:46.4	5.3	0.7			1.01	0.39	376	209	–	
G059.3987–00.7880	19:45:34.22	+22:58:32.5	29.9	2.8			2.95	0.11	251	27	–	
G059.8236–00.5361	19:45:32.88	+23:28:10.6	31.6	2.9			1.49	0.11	1033	142	0.65	0.12
G060.8480–00.8954	19:49:09.77	+24:10:23.2	2.9	0.6			1.24	0.7	135	111	–	
G060.9866–00.5698	19:48:14.28	+24:27:27.0	7.2	0.8	3.83	0.47	1.39	0.25	270	75	0.49	0.13

Continued on next page

Table A.1 – continued from previous page

Name	RA	DEC	F_{5GHz}	dF_{5GHz}	$F_{1.4GHz}$	$dF_{1.4GHz}$	Size	dSize	Tb	dTb	α	dα
	J2000	J2000	mJy	mJy	mJy	mJy	arcsec	arcsec	K	K		
G062.4936–00.2699	19:50:28.51	+25:54:29.9	20.3	2.1			3.64	0.17	111	14	0.23	0.14
G062.7551–00.7262	19:52:48.82	+25:53:59.3	16.2	1.7			3.04	0.16	128	16	–	
G063.0455+00.5977	19:48:23.28	+26:49:26.8	5.2	1.0			2.76	0.51	50	16	–	
G063.8893+00.1229	19:52:09.14	+27:18:31.7	33.0	3.9			6.21	0.04	63	7	0.18	0.11

Table A.2: *Measured NIR magnitudes and MIR flux densities of the CORNISH–PNe. These are measured using aperture photometry as described in Section 2.4. In the NIR, some of the CORNISH-PNe were not detected in one or more bands. For such sources, the corresponding columns are left blank. For non-detections in one or more of the bands and where the measured flux density is less than 3σ in the MIR, an upper limit of 3σ, preceeded by '<'. Full table is also available online as Table A2.*

Name	J	dJ	H	dH	K	dK	$F_{3.6}$	$dF_{3.6}$	$F_{4.5}$	$dF_{4.5}$	$F_{5.8}$	$dF_{5.8}$	$F_{8.0}$	$dF_{8.0}$
	mag	mag	mag	mag	mag	mag	mJy	mJy	mJy	mJy	mJy	mJy	mJy	mJy
G009.9702-00.5292	16.35	0.03	14.69	0.02	13.07	0.02	8.6	0.18	10.15	0.14	15.32	0.22	41.53	0.47
G010.0989+00.7393	10.66	0.02	10.27	0.03	9.34	0.03	228.81	0.18	621.73	0.16	1105.25	0.43	4046.75	0.82
G010.4168+00.9356	14.18	0.02	13.51	0.03	12.64	0.03	8.06	0.09	9.25	0.07	7.9	0.16	57.35	0.16
G010.5960–00.8733	16.16	0.03	14.05	0.01	12.23	0.04	48.09	0.09	46.99	0.07	98.96	0.21	245.86	0.3
G011.3266–00.3718	16.58	0.03	14.27	0.01	12.84	0.01	12.44	0.12	13.22	0.09	20.91	0.23	33.71	0.34
G011.4290–01.0091	11.32	0.01	11.46	0.02	10.64	0.01	27.49	0.11	23.82	0.08	14.76	0.24	20.47	0.32
G011.4581+01.0736	15.56	0.02	14.12	0.01	13.18	0.01	<0.15		9.46	0.08	<0.48		47.58	0.21
G011.7210–00.4916	–	–	–				<0.3		0.91	0.09	<0.63		<1.08	
G011.7434–00.6502	10.96	0.01	10.78	0.01	9.73	0.01	157.13	0.18	175.46	0.15	536.58	0.34	1814.38	0.58
G011.7900–00.1022	11.86	0.01	11.27	0.01	10.68	0.01	25.03	0.31	28.5	0.23	13.65	0.64	53.31	1.68

Continued on next page

Table A.2 – continued from previous page

Name	J	dJ	H	dH	K	dK	$F_{3.6}$	$dF_{3.6}$	$F_{4.5}$	$dF_{4.5}$	$F_{5.8}$	$dF_{5.8}$	$F_{8.0}$	$dF_{8.0}$
	mag	mag	mag	mag	mag	mag	mJy	mJy	mJy	mJy	mJy	mJy	mJy	mJy
G012.0438–00.5077	17.77	0.1	16.34	0.07	15.99	0.12	<0.39		<0.33		1.47	0.2	3.62	0.24
G012.1157+00.0757	13.91	0.01	12.36	0.01	10.92	0.02	34.64	0.24	43.16	0.17	39.72	0.44	120.58	0.39
G012.1528–00.3304	15.61	0.02	13.4	0.01	12.07	0.01	16.1	0.13	11.88	0.1	20.61	0.25	57.55	0.36
G012.3315–00.1806	13.68	0.02	12.76	0.02	11.38	0.01	41.44	0.19	62.09	0.13	95.26	0.32	242.65	0.75
G012.3830+00.7990	16.33	0.03	15.08	0.02	13.44	0.02	5.06	0.1	7.79	0.08	14.66	0.2	55.9	0.22
G012.6012+00.5592	–	–	16.43	0.15			4.1	0.1	8.5	0.09	21.11	0.27	71.66	0.88
G013.3565–00.7559	–	–	14.65	0.04			2.16	0.11	3.4	0.09	6.04	0.19	18.67	0.28
G013.6313–00.6023	12.47	0.01	11.47	0.01	10.68	0.02	42.21	0.2	29.24	0.15	27.54	0.32	37.6	0.47
G013.9166+00.6500	16.12	0.03	14.18	0.02	12.61	0.02	28.02	0.18	25.01	0.11	24.35	0.22	43.8	0.25
G014.2365+00.2117	14.06	0.03	13.08	0.02	11.91	0.02	37.93	0.33	75.44	0.29	340.35	1.28	629.81	1.09
G014.4573–00.1847	–	–	–				4.92	0.11	11.88	0.1	31.1	0.57	25.66	1.61
G014.5851+00.4613	14.54	0.03	13.66	0.02	12.66	0.02	8.18	0.18	15.78	0.11	23.67	0.23	80.25	0.38
G014.7503–00.2496	–		16.01	0.07	13.7	0.03	17.81	0.16	19.26	0.14	24.39	0.35	50.46	0.55
G014.8960+00.4837	15.45	0.04	15.02	0.06	13.53	0.03	4.14	0.26	10.34	0.14	20.32	0.26	74.6	0.23
G015.1999–00.0863	14.96	0.02	13.63	0.04	12.72	0.01	4.71	0.27	9.84	0.19	11.09	0.49	65.94	0.79
G015.5410+00.3359	10.63	0.01	10.15	0.01	9.23	0.01	91.38	0.11	56.52	0.08	50.91	0.28	78.24	0.36
G015.5847+00.4002	13.78	0.01	11.86	0.01	10.71	0.01	112.46	0.17	62.57	0.12	70.17	0.24	93.52	0.25
G015.7993–00.0063	14.18	0.01	12.74	0.01	11.69	0.01	68.72	0.16	62.5	0.11	95.99	0.23	191	0.31
G016.0550+00.8280	14.07	0.01	12.74	0.02	11.79	0.02	77.35	0.15	41.38	0.1	67.28	0.21	118.6	0.27
G016.4034–00.5740	14.65	0.01	11.97	0.02	10.23	0.01	66.41	0.11	57.74	0.09	49.93	0.31	72.04	0.64
G016.4276+01.0072	16.29	0.04	14.66	0.03	13.24	0.02	11.25	0.13	12.65	0.1	11.55	0.39	27.03	0.94
G016.4999+00.1152	15.37	0.04	13.35	0.02	12.12	0.01	5.29	0.39	7.23	0.27	4.01	1.21	41.96	1.61
G016.6002–00.2754	16	0.03	14.47	0.02	12.97	0.02	5.68	0.25	8.74	0.18	10.24	1.78	27.89	5.52
G017.0152–00.1906	–		17.69	0.14	15.69	0.08	0.78	0.16	3.35	0.11	4.28	0.31	17.76	0.38

Continued on next page

Table A.2 – continued from previous page

Name	J	dJ	H	dH	K	dK	$F_{3.6}$	$dF_{3.6}$	$F_{4.5}$	$dF_{4.5}$	$F_{5.8}$	$dF_{5.8}$	$F_{8.0}$	$dF_{8.0}$
	mag	mag	mag	mag	mag	mag	mJy	mJy	mJy	mJy	mJy	mJy	mJy	mJy
G017.3669+00.5224	17.62	0.1	15.63	0.04	13.75	0.04	4.5	0.11	6.25	0.1	6.58	0.28	14.78	0.48
G017.4147+00.3791	15.5	0.03	13.9	0.02	12.67	0.04	21.59	0.27	24.83	0.22	15.93	0.5	63.78	0.89
G017.4487+00.1146	–	–	–				2.85	0.25	4.91	0.16	3.77	0.32	8.23	0.39
G017.7250–00.2427	13.49	0.01	12.69	0.01	11.62	0.03	22.6	0.31	29.71	0.23	42.34	0.54	174.94	0.83
G017.8222+00.9866	15.04	0.02	14.31	0.02	13.33	0.02	3.38	0.19	5.18	0.12	< 1.17		15.84	0.49
G017.8645+00.2120	17.99	0.1	16.01	0.07	13.56	0.04	4.96	0.11	9.17	0.09	16.06	0.21	75.86	0.26
G018.0661+00.8535	12.53	0.01	11.83	0.01	10.99	0.03	30.25	0.19	29.8	0.13	65.4	0.26	222.84	0.24
G018.1286–00.2189	15.1	0.02	13.9	0.01	12.92	0.03	5.45	0.23	5.54	0.15	13.22	0.69	42.55	1.36
G018.2402–00.9152	13.06	0.01	12.12	0.01	11.35	0.04	20.2	0.26	43.18	0.21	26.2	0.39	57.59	0.44
G018.2413–00.5552	–		16.28	0.04	13.94	0.04	5.71	0.11	7.23	0.08	42.74	0.18	123.73	0.36
G018.5242+00.1519	16.8	0.06	14.41	0.04	11.63	0.01	243.22	0.16	484.6	0.14	1437.61	0.39	2229.56	0.73
G018.5776–00.7484	14.97	0.02	14.57	0.02	14.23	0.05	2.94	0.14	2.85	0.11	6.67	0.31	18.04	0.6
G019.2356+00.4951	15.9	0.04	13.69	0.02	12.24	0.01	16.78	0.19	14	0.13	56.45	0.31	151.54	0.31
G019.4676–00.0154	18.81	0.29	15.97	0.06	14.31	0.03	5.05	0.21	16.13	0.16	32.24	0.29	151.79	0.43
G019.5326+00.7308	14.82	0.02	14.02	0.02	13.44	0.02	2.47	0.19	2.93	0.11	4.45	0.21	16.1	0.26
G019.9298–00.6639	16.79	0.03	15.76	0.02	14.76	0.05	4.41	0.12	6.22	0.1	17.35	0.22	62.01	0.47
G019.9448+00.9126	13.67	0.02	13.09	0.03	12.16	0.02	16.82	0.11	19.99	0.09	41.25	0.2	158.16	0.17
G020.4681+00.6793	13.22	0.01	12.63	0.01	11.42	0.01	24.07	0.11	36.14	0.08	45.98	0.2	207.76	0.19
G020.5176+00.4778	13.96	0.01	12.63	0.02	11.85	0.01	14.97	0.27	13.34	0.21	21.11	0.36	42.07	0.35
G020.6015+00.0206	–	–	–				–	–	–	–				
G020.9782+00.9253	14.35	0.03	13.57	0.02	12.48	0.01	9.91	0.11	13.96	0.08	16.35	0.21	54.65	0.23
G021.1653+00.4755	13.08	0.01	11.81	0.02	10.28	0.02	145.56	0.1	189.52	0.1	526.67	0.26	2003.64	0.36
G021.3425–00.8423	15.4	0.02	13.81	0.01	12.66	0.02	8.78	0.12	11.24	0.1	34.78	0.22	129.32	0.34
G021.6657+00.8110	14.98	0.01	13.83	0.02	12.38	0.01	30.25	0.07	54.69	0.06	180.06	0.16	534.61	0.28

Continued on next page

Table A.2 – continued from previous page

Name	J	dJ	H	dH	K	dK	$F_{3.6}$	$dF_{3.6}$	$F_{4.5}$	$dF_{4.5}$	$F_{5.8}$	$dF_{5.8}$	$F_{8.0}$	$dF_{8.0}$
	mag	mag	mag	mag	mag	mag	mJy	mJy	mJy	mJy	mJy	mJy	mJy	mJy
G021.6849–00.7381	14.49	0.01	12.72	0.01	11.49	0.01	155.42	0.2	114.66	0.15	158.83	0.32	186.74	0.69
G021.8201–00.4779	14.04	0.01	13.03	0.01	11.64	0.01	17.28	0.23	19.08	0.25	30.89	0.49	104.31	0.82
G021.9972–00.8838	15.29	0.01	14.47	0.01	13.53	0.02	2.63	0.08	4.4	0.07	2.89	0.22	9.03	0.41
G022.2211+00.9009	14.18	0.01	13.52	0.01	12.54	0.01	9.42	0.13	12.13	0.1	17.43	0.22	76.43	0.21
G022.5477–00.1061	16.81	0.04	14.5	0.02	12.89	0.03	15.74	0.2	19.32	0.15	99.51	0.32	274.5	0.5
G022.6429–00.4422	15.51	0.03	13.85	0.01	12.91	0.04	4.93	0.11	5.08	0.1	9.08	0.38	18.18	1.21
G022.6580+00.2959	17	0.05	15.53	0.03	14.22	0.03	4.75	0.12	8.87	0.09	27.08	0.21	68.33	0.43
G023.2321+00.0809	17.6	0.1	14.99	0.03	13.4	0.04	4.36	0.23	6.45	0.18	15.67	0.4	23.72	0.99
G023.4181–00.3940	16.45	0.04	15.06	0.02	13.06	0.03	25.4	0.13	35.36	0.11	196.94	0.37	501.64	0.79
G023.5044–00.5245	14.08	0.03	13.42	0.02	12.75	0.03	10.58	0.12	12.46	0.1	28.29	0.37	82.35	0.91
G023.8214–00.5788	15.83	0.04	13.64	0.01	12.04	0.01	24.56	0.13	29.26	0.11	92.46	0.36	263.97	0.46
G023.8897–00.7379	15.06	0.01	13.42	0.01	11.84	0.02	32.56	0.15	79.51	0.12	128.52	0.35	425.76	0.72
G024.0943–01.0992	15.81	0.03	14.52	0.01	13.63	0.01	1.64	0.08	–		1.16	0.16		
G024.1659+00.2502	12.4	0.01	10.98	0.02	10.11	0.01	55.14	0.34	38.83	0.23	40.63	1.03	76.36	2.16
G024.3852+00.2869	17.73	0.1	15.09	0.02	12.95	0.01	9.19	0.13	15.19	0.13	27.86	0.39	156.14	1.18
G024.7921–01.0043	13.4	0.03	12.36	0.07	11.63	0.01	16.7	0.1	17.46	0.07	37.72	0.16	105.54	0.3
G024.8959+00.4586	18.06	0.15	15.54	0.04	13.4	0.02	14.17	0.18	31.06	0.11	53.89	0.4	94.32	0.53
G025.0485–00.6621	14.95	0.04	13.8	0.02	12.46	0.01	17.71	0.14	22.32	0.12	53.35	0.27	130.75	0.59
G025.5190+00.2165	13.73	0.01	12.29	0.01	–		66.46	0.34	115.03	0.25	136.45	0.86	822.77	1.29
G025.5769+00.1389	16.67	0.07	–	–			10.24	0.28	11.68	0.19	38.12	0.54	63.15	0.6
G025.8466+01.1718	14.16	0.01	12.38	0.03	11.33	0.01	–	–	–	–				
G026.0823–00.0347	15.53	0.02	14.36	0.02	13.28	0.02	20.03	0.18	20.4	0.15	33.81	0.6	92.56	1.51
G026.1620+00.5926	16.56	0.06	15.03	0.03	13.65	0.02	5.63	0.14	13.25	0.11	14.32	0.25	33.86	0.43
G026.2268+00.7685	15.47	0.01	13.71	0.01	12.83	0.02	13.53	0.11	9.81	0.08	14.08	0.21	18.46	0.32

Continued on next page

Table A.2 – continued from previous page

Name	J	dJ	H	dH	K	dK	$F_{3.6}$	$dF_{3.6}$	$F_{4.5}$	$dF_{4.5}$	$F_{5.8}$	$dF_{5.8}$	$F_{8.0}$	$dF_{8.0}$
	mag	mag	mag	mag	mag	mag	mJy	mJy	mJy	mJy	mJy	mJy	mJy	mJy
G026.6529+00.2874	16.41	0.05	15.23	0.03	14.03	0.03	5.29	0.17	6.48	0.12	17.22	0.41	47.24	0.75
G026.7145+00.1319	17.04	0.08	15.1	0.04	13.87	0.02	3.25	0.27	5.21	0.15	10.96	0.45	38.49	0.83
G026.8327–00.1516	13.9	0.02	12.71	0.01	12.03	0.02	8.74	0.34	9.28	0.21	5.41	0.41	19.88	1.14
G027.4265–00.2499	15.13	0.02	14.58	0.02	13.85	0.03	2.99	0.18	4.29	0.12	9.42	0.31	32.4	0.46
G027.6595–00.3835	15.77	0.04	14.85	0.04	13.67	0.02	15.68	0.12	37.42	0.09	115.48	0.2	273.48	0.35
G027.6635–00.8267	15.29	0.04	15.05	0.04	13.94	0.03	3.74	0.13	6.97	0.08	18.91	0.19	59.2	0.23
G027.6640–00.2485	15.55	0.03	13.67	0.02	12.65	0.02	50	0.25	29.43	0.16	36.27	0.25	32.96	0.43
G027.7016+00.7048	12.09	0.01	11.74	0.01	10.63	0.05	38.04	0.16	61.09	0.12	45.99	0.25	209.6	0.39
G029.0538+00.9915	15.77	0.03	14.93	0.02	13.97	0.02	4.26	0.06	3.86	0.06	13.51	0.14	32.96	0.14
G029.1652–00.0168	19.39	0.62	16.66	0.1	14.69	0.05	4.52	0.13	5.38	0.1	2.39	0.62	5.04	1.32
G029.2113–00.0689	13.18	0.02	12.43	0.01	11.03	0.03	38.95	0.25	62.3	0.24	94.64	0.97	457.53	2.24
G029.5780–00.2686	15	0.03	13.79	0.01	12	0.02	46.27	0.11	65.51	0.09	115.15	0.25	331.67	0.42
G029.8742–00.8190	14.73	0.02	13.15	0.02	11.31	0.02	42.39	0.09	74.28	0.07	122.3	0.27	537.64	0.85
G030.0226+00.1570	16.62	0.05	15.58	0.03	14.5	0.03	3.46	0.12	6.25	0.1	5.34	0.44	26.36	1.25
G030.0294–00.3318	17.25	0.05	15.58	0.02	14.42	0.02	4.79	0.09	4.84	0.07	5.38	0.33	8.91	0.54
G030.2335–00.1385	–	–	–				66.66	0.15	130.19	0.12	272.3	0.66	504.93	1.53
G030.5302+00.1315	18.07	0.12	16.85	0.07	16.38	0.11	0.77	0.08	2.35	0.08	1.61	0.42	14.49	1.19
G030.6670–00.3319	17.42	0.03	15.34	0.02	12.35	0.01	47.38	0.09	204.11	0.1	440.68	0.43	2153.76	0.91
G030.8560+00.3826	–	–	14.82	0.04			3.58	0.09	9.73	0.07	8.35	0.29	23.76	0.63
G031.2131–00.1803	18.08	0.07	15.39	0.01	13.27	0.01	10.02	0.1	14.04	0.09	30.49	0.3	61.95	0.47
G031.3724–00.7514	16.11	0.02	15.12	0.02	13.08	0.02	5.67	0.1	8.49	0.08	7.02	0.26	33.62	0.34
G032.3076+00.1536	15.42	0.03	14.41	0.01	12.54	0.01	11.72	0.15	14.63	0.09	34.9	0.37	130.05	0.89
G032.5485–00.4739	12.9	0.02	12.19	0.01	11.18	0.01	29.67	0.11	34.19	0.08	82.04	0.23	283.86	0.39
G032.6136+00.7971	14.71	0.01	13.65	0.01	12.07	0.01	9.34	0.07	8.82	0.05	27.23	0.16	110.22	0.2

Continued on next page

Table A.2 – continued from previous page

Name	J	dJ	H	dH	K	dK	$F_{3.6}$	$dF_{3.6}$	$F_{4.5}$	$dF_{4.5}$	$F_{5.8}$	$dF_{5.8}$	$F_{8.0}$	$dF_{8.0}$
	mag	mag	mag	mag	mag	mag	mJy	mJy	mJy	mJy	mJy	mJy	mJy	mJy
G032.8082–00.3159	16.67	0.06	15.34	0.04	13.89	0.02	2.81	0.1	4.98	0.07	1.24	0.52	11.33	0.37
G032.8177–00.1165	15.09	0.02	14.3	0.02	13.89	0.02	4.54	0.12	4.08	0.1	7.55	0.27	15.31	0.31
G033.1198–00.8949	17.46	0.1	16.42	0.08	15.29	0.05	2.58	0.07	2.44	0.05	3.61	0.13	4.65	0.15
G033.3526+00.4043	17.93	0.1	15.99	0.03	13.92	0.02	6.05	0.09	15.57	0.06	30.26	0.17	89.07	0.23
G033.4543–00.6149	13.29	0.01	12.28	0.02	10.67	0.02	101.39	0.14	128.59	0.09	461.38	0.26	2070.51	0.35
G033.7952+00.4307	16.26	0.02	14.66	0.01	12.93	0.01	19.55	0.08	32.22	0.07	67.23	0.18	185.51	0.26
G033.9059–00.0436	15.86	0.03	14.62	0.03	13.11	0.01	18.07	0.16	21.07	0.12	64.72	0.29	266.14	0.33
G034.1792–00.1777	–		17.87	0.2	14.95	0.05	2.1	0.11	5.37	0.09	2.41	0.35	<1.68	
G034.4200–00.3183	16.05	0.02	14.14	0.01	12.75	0.01	8.38	0.07	10.45	0.06	22.39	0.18	124.95	0.19
G034.8624–00.0630	14.61	0.02	12.65	0.01	10.59	0.01	194.19	0.13	277.87	0.12	452.2	0.68	1673.05	2.21
G035.2162+00.4280	17.73	0.1	14.31	0.02	12.08	0.01	38.99	0.14	54.45	0.11	120.44	0.36	203.86	0.44
G035.4719–00.4365	12.35	0.01	11.59	0.01	10.51	0.01	144.14	0.14	222.01	0.12	601.22	0.41	1566.85	0.74
G035.5654–00.4922	13.89	0.01	12.72	0.01	11.46	0.01	29.3	0.19	40	0.16	45.63	0.41	140.88	0.46
G036.0116–00.2562	16.39	0.03	14.91	0.02	13.29	0.01	12.21	0.12	12.84	0.08	69.05	0.22	199.72	0.18
G036.5393+00.2003	16.9	0.05	14.4	0.02	12.82	0.01	11.13	0.08	17.26	0.07	38.31	0.21	101.74	0.21
G037.9031–00.2754	19.41	0.32	16.3	0.04	14.03	0.02	7.22	0.06	20.21	0.06	33.36	0.21	83.14	0.55
G037.9601+00.4534	18.42	0.1	16.46	0.04	14.32	0.02	9.53	0.07	19.66	0.06	65.81	0.18	232.47	0.19
G038.9237–00.0807	19	0.24	17.05	0.07	14.48	0.04	7.27	0.11	7.73	0.1	8.51	0.3	22.84	0.55
G039.1617+00.7826	16.66	0.03	15.21	0.02	13.34	0.01	8.96	0.05	11.99	0.06	30.52	0.16	96.93	0.16
G039.5911–00.3785	14.4	0.01	13.07	0.01	12.42	0.01	5.57	0.05	4.83	0.04	6.51	0.12	19.6	0.17
G040.2606–00.2755	–		17.33	0.08	14.28	0.02	10.75	0.05	27.95	0.05	66.43	0.17	159.22	0.36
G040.3359–01.0102	16.45	0.03	15.17	0.02	13.8	0.02	2.12	0.06	4.08	0.06	1.72	0.2	14.05	0.15
G041.1982+00.0348	17.91	0.11	15.45	0.03	13.48	0.01	9.59	0.06	35.64	0.06	56.64	0.18	304.81	0.34
G041.3540+00.5390	14.34	0.01	12.38	0.01	12.01	0.01	65.14	0.09	45.86	0.07	75.92	0.17	175.99	0.15

Continued on next page

Table A.2 – continued from previous page

Name	J	dJ	H	dH	K	dK	$F_{3.6}$	$dF_{3.6}$	$F_{4.5}$	$dF_{4.5}$	$F_{5.8}$	$dF_{5.8}$	$F_{8.0}$	$dF_{8.0}$
	mag	mag	mag	mag	mag	mag	mJy	mJy	mJy	mJy	mJy	mJy	mJy	mJy
G041.7871+00.4884	17.04	0.03	14.8	0.01	13.03	0.01	23.56	0.06	43.25	0.05	106.17	0.14	282.61	0.23
G042.6629–00.8648	16.57	0.05	15.39	0.02	13.89	0.02	2.95	0.05	6.61	0.06	3.27	0.18	12.32	0.17
G043.0281+00.1399	14.34	0.04	13.12	0.02	11.63	0.02	30.38	0.06	46.51	0.05	69.37	0.17	289.8	0.18
G043.2946–00.6455	14.98	0.03	13.6	0.01	12.15	0.02	20.64	0.05	33.87	0.05	84.98	0.18	284.08	0.44
G043.5793+00.0261	18.15	0.11	16.07	0.03	14.02	0.02	5.7	0.06	9.88	0.05	24.64	0.15	75.32	0.21
G043.6554–00.8279	15.09	0.01	14.04	0.01	12.72	0.01	16.41	0.05	14.88	0.05	75.25	0.16	213.43	0.16
G044.6375+00.4827	13.34	0.01	11.94	0.01	10.71	0.01	69.6	0.06	84.21	0.06	100.55	0.15	147.73	0.22
G045.1801+00.9893	18.14	0.11	16.84	0.07	16.05	0.07	<0.2		<0.2		<0.42		<0.39	
G045.2830–00.6278	16.26	0.02	14.79	0.01	13.05	0.01	7.87	0.06	13.15	0.05	19.76	0.15	78.46	0.13
G046.9747+00.2702	15.89	0.03	14.83	0.02	13.33	0.01	7.63	0.08	10.69	0.05	21.37	0.2	79.45	0.26
G047.6884–00.3024	15.69	0.02	14.48	0.01	12.96	0.01	6.87	0.07	11.65	0.05	15.65	0.14	166.01	0.13
G047.9875+00.2026	17.43	0.06	16.06	0.04	14.5	0.02	2.6	0.06	3.07	0.05	9.57	0.17	29.36	0.25
G048.5619+00.9029	16.23	0.03	15.58	0.03	14.8	0.03	1.02	0.05	1.45	0.04	3.83	0.13	13.38	0.13
G048.6748–00.5350	17.25	0.05	16.07	0.03	14.85	0.03	1.28	0.08	2.61	0.06	3.7	0.3	11.33	0.82
G048.7319+00.9305	14.77	0.01	14.22	0.02	13.02	0.01	5.01	0.07	8.01	0.06	7.82	0.15	36.51	0.12
G049.6948+00.8642	15.33	0.02	13.92	0.01	12.5	0.02	38.76	0.08	39	0.06	292.67	0.25	885.6	0.44
G050.0003+00.5072	13.18	0.01	12.11	0.01	11.5	0.02	13.13	0.06	12.77	0.04	18.29	0.16	55.89	0.27
G050.0405+01.0961	14.75	0.01	14.2	0.01	13.23	0.02	3.87	0.06	6.28	0.05	5.21	0.15	13.04	0.14
G050.0457+00.7683	15.05	0.01	13.58	0.01	12.22	0.01	41.66	0.08	39.22	0.06	280.87	0.24	808.45	0.41
G050.4802+00.7056	14.48	0.01	12.14	0.01	9.94	0.01	363.38	0.06	540.9	0.08	814.49	0.27	797.59	0.23
G050.5556+00.0448	13.82	0.01	12.83	0.01	11.35	0.01	37.5	0.07	48.25	0.06	104.34	0.19	333.13	0.22
G050.8950+00.0572	17.29	0.06	15.71	0.03	14.03	0.02	4.79	0.06	8.33	0.05	12.37	0.19	35.19	0.22
G051.5095+00.1686	13	0.01	12.24	0.01	11.02	0.02	45.77	0.1	61.83	0.09	107	0.26	377.15	0.27
G051.6061+00.9140	15.66	0.01	14.61	0.01	13.32	0.03	6.08	0.04	8.56	0.04	11.97	0.12	42.35	0.15

Continued on next page

Table A.2 – continued from previous page

Name	J	dJ	H	dH	K	dK	$F_{3.6}$	$dF_{3.6}$	$F_{4.5}$	$dF_{4.5}$	$F_{5.8}$	$dF_{5.8}$	$F_{8.0}$	$dF_{8.0}$
	mag	mag	mag	mag	mag	mag	mJy	mJy	mJy	mJy	mJy	mJy	mJy	mJy
G051.8341+00.2838	13.8	0.01	13.08	0.01	11.78	0.02	18.32	0.1	26.9	0.07	28.29	0.22	108.27	0.3
G052.1498–00.3758	16.35	0.02	14.32	0.02	13.09	0.01	5.21	0.04	5.9	0.04	30.31	0.13	80.96	0.11
G055.5070–00.5579	11.3	0.01	11.11	0.01	10.15	0.04	74.84	0.07	111.58	0.06	216.88	0.18	904.88	0.25
G056.4016–00.9033	13.93	0.02	13.58	0.01	12.67	0.01	6.74	0.04	8.93	0.04	11.81	0.11	43.82	0.09
G057.5352+00.2266	18.58	0.11	16.79	0.03	15.24	0.03	2.16	0.04	4.19	0.03	12.39	0.14	28.99	0.16
G058.1591–00.5499	16.51	0.03	15.26	0.02	14.25	0.02	0.88	0.04	0.93	0.03	0.57	0.12	5.86	0.09
G058.6410+00.9196	15.83	0.02	14.94	0.01	13.74	0.02	4.59	0.04	6.75	0.03	14.6	0.12	48.35	0.09
G059.3987–00.7880	13.76	0.01	13.14	0.01	12.33	0.02	10.06	0.05	12.32	0.04	12.01	0.14	28.45	0.11
G059.8236–00.5361	14.19	0.02	13.7	0.01	12.5	0.02	10.98	0.05	15.77	0.04	18.73	0.13	65.94	0.13
G060.8480–00.8954	17.64	0.05	16.03	0.03	14.89	0.03	1.22	0.03	1.68	0.03	4.62	0.1	23.82	0.09
G060.9866–00.5698	14.21	0.01	13.58	0.02	12.62	0.02	10.67	0.04	12.88	0.03	26.76	0.09	84.55	0.1
G062.4936–00.2699	14.54	0.01	14.15	0.01	13.18	0.01	4.76	0.05	8.35	0.05	8.91	0.15	26.42	0.12
G062.7551–00.7262	15.11	0.01	14.45	0.02	13.35	0.01	4.58	0.04	9.55	0.04	17.06	0.14	45.04	0.11
G063.0455+00.5977	15.6	0.01	14.78	0.02	13.99	0.02	3.16	0.04	4.81	0.04	3.93	0.12	7.08	0.11
G063.8893+00.1229	13.36	0.02	12.93	0.01	11.9	0.04	12.97	0.07	19.23	0.06	20.31	0.18	91.54	0.1

Table A.3: *Extinction table showing* A_V *from the different methods in Section 2.7 for the CORNISH-PNe. Sources whose* Hα *emission area is larger than radio are indicated using *. Full table is also available online as Table A3.*

Name	$H\alpha_{5GHz}$	$dH\alpha_{5GHz}$	E(H-K)	dE(H-K)	E(J-H)	dE(J-H)	F_H/F_{5GHz}	dF_H/F_{5GHz}	F_K/F_{5GHz}	dF_K/F_{5GHz}
	mag	mag	mag	mag	mag	mag	mag	mag	mag	mag
G009.9702-00.5292	-		13.29	0.47	17.74	0.4	5.24	1.26	0.12	1.26
G010.0989+00.7393	-		3.56	0.57	4.97	0.34	2.62	0.96	1.97	0.96
G010.4168+00.9356	–		2.71	0.58	7.77	0.35	–0.4	1.09	–2.39	1.09

Continued on next page

Table A.3 – continued from previous page

Name	$H\alpha_{5GHz}$	$dH\alpha_{5GHz}$	E(H-K)	dE(H-K)	E(J-H)	dE(J-H)	F_H/F_{5GHz}	dF_H/F_{5GHz}	F_K/F_{5GHz}	dF_K/F_{5GHz}
	mag	mag	mag	mag	mag	mag	mag	mag	mag	mag
G010.5960–00.8733	–		16.07	0.62	22.31	0.37	7.71	1.12	2.39	1.18
G011.3266–00.3718	–		10.6	0.26	24.32	0.38	3.49	1.75	–1.03	1.75
G011.4290–01.0091	–		1.99	0.33	–0.43	0.24	–11.49	1.39	–19.89	1.37
G011.4581+01.0736	–		3.7	0.25	15.54	0.2	–0.99	1.55	–3.96	1.55
G011.7210–00.4916	–		–	–	–	–				
G011.7434–00.6502	–		5.29	0.2	2.78	0.14	–1.15	0.96	–5.21	0.96
G011.7900–00.1022	–		–1.24	0.2	6.98	0.14	–6.42	1.67	–9.66	1.67
G012.0438–00.5077	–		–4.63	1.97	15.46	1.23	14.62	1.24	26.55	1.52
G012.1157+00.0757	–		10.79	0.36	16.65	0.2	0.37	0.94	–6.19	0.95
G012.1528–00.3304	–		9.15	0.22	23.3	0.21	–2.09	1.19	–9.15	1.19
G012.3315–00.1806	–		9.88	0.28	10.34	0.26	0.49	0.99	–5.42	0.99
G012.3830+00.7990	–		13.59	0.42	13.65	0.42	9.96	1.04	7.59	1.03
G012.6012+00.5592	–		–	–	–		32.69	1.73		
G013.3565–00.7559	–		–	–	–		11.53	1.39		
G013.6313–00.6023	–		1.6	0.32	11.1	0.2	–9.61	1.65	–16.61	1.66
G013.9166+00.6500	–		12.49	0.39	20.56	0.37	6.95	0.99	3.4	0.99
G014.2365+00.2117	–		6.83	0.41	10.88	0.34	0.34	1.22	–3.77	1.21
G014.4573–00.1847	–		–	–	–	–				
G014.5851+00.4613	–		4.55	0.34	9.9	0.33	2.94	1.62	1.87	1.61
G014.7503–00.2496	–		22.95	0.99	56.87	47.18	15.04	1.47	9.96	1.32
G014.8960+00.4837	–		11.46	0.96	5.35	0.72	4.92	1.52	0.76	1.41
G015.1999–00.0863	–		3.32	0.61	14.39	0.47	–1.9	1.67	–5.2	1.62
G015.5410+00.3359	–		3.36	0.2	5.85	0.14	–16.24	1.47	–28.44	1.47
G015.5847+00.4002	–		6.55	0.2	20.39	0.15	–6.93	0.98	–15.36	0.98

Continued on next page

Table A.3 – continued from previous page

Name	$H\alpha_{5GHz}$	$dH\alpha_{5GHz}$	E(H-K)	dE(H-K)	E(J-H)	dE(J-H)	F_H/F_{5GHz}	dF_H/F_{5GHz}	F_K/F_{5GHz}	dF_K/F_{5GHz}
	mag	mag	mag	mag	mag	mag	mag	mag	mag	mag
G015.7993–00.0063	–		5.24	0.22	15.59	0.16	2.63	0.91	0.94	0.91
G016.0550+00.8280	–		3.73	0.38	14.49	0.24	–4.73	1.04	–10.04	1.02
G016.4034–00.5740	–		14.88	0.32	28.05	0.24	–3.23	1.45	–14.58	1.44
G016.4276+01.0072	–		10.47	0.48	17.49	0.49	6.62	1.66	4.13	1.64
G016.4999+00.1152	–		7.71	0.31	21.44	0.44	–0.75	1.47	–6.07	1.46
G016.6002–00.2754	–		11.58	0.33	16.46	0.33	7.35	1.96	4.61	1.96
G017.0152–00.1906	–		18.53	2.32	–		21.86	2.29	23.76	1.89
G017.3669+00.5224	–		16.9	0.79	21.15	1.05	12.57	1.14	9.75	1.11
G017.4147+00.3791	–		7.79	0.59	17.17	0.35	7.91	1.27	7.9	1.29
G017.4487+00.1146	–		–	–	–	–				
G017.7250–00.2427	–		5.36	0.52	9.18	0.2	3.44	1.02	2.18	1.06
G017.8222+00.9866	–		4.32	0.45	8.31	0.33	4.34	1.17	4.29	1.16
G017.8645+00.2120	–		24.95	1.14	20.98	1.29	16.06	1.19	10.35	0.98
G018.0661+00.8535	–		2.24	0.41	8.08	0.16	–4.66	0.98	–8.99	1.01
G018.1286–00.2189	–		4.12	0.51	13.12	0.2	–1.4	1.99	–4.89	2.02
G018.2402–00.9152	–		1.32	0.56	10.54	0.18	0.95	1.28	0.67	1.32
G018.2413–00.5552	–		23.3	0.74	–		11.35	1.18	3.75	1.15
G018.5242+00.1519	–		29.53	0.56	25.19	0.75	–3.65	2.17	–24.45	2.14
G018.5776–00.7484	–		–4.83	0.75	5.01	0.28	1.58	1.99	5.55	2.02
G019.2356+00.4951	–		10.83	0.28	23.29	0.42	6.38	1.16	3.52	1.15
G019.4676–00.0154	–		13.83	1.01	29.69	2.95	14.55	1.18	14.88	1.03
G019.5326+00.7308	–		–1.45	0.39	9.13	0.26	–2.86	1.88	–3.76	1.89
G019.9298–00.6639	–		4.5	0.76	11.44	0.37	11.72	1.0	16.13	1.08
G019.9448+00.9126	–		3.41	0.52	6.93	0.37	1.56	1.08	0.36	1.05

Continued on next page

Table A.3 – continued from previous page

Name	$H\alpha_{5GHz}$	$dH\alpha_{5GHz}$	E(H-K)	dE(H-K)	E(J-H)	dE(J-H)	F_H/F_{5GHz}	dF_H/F_{5GHz}	F_K/F_{5GHz}	dF_K/F_{5GHz}
	mag	mag	mag	mag	mag	mag	mag	mag	mag	mag
G020.4681+00.6793	–		7.46	0.21	6.96	0.15	5.38	1.01	4	1.01
G020.5176+00.4778	–		1.41	0.33	14.5	0.24	–4.75	1.22	–8.61	1.21
G020.6015+00.0206	–		–4.15	0.32	3.89	0.23	–18.33	2.47	–27.13	2.46
G020.9782+00.9253	–		5.75	0.35	8.93	0.39	–0.38	1.39	–4.25	1.37
G021.1653+00.4755	–		11.94	0.4	13.84	0.23	3.4	0.96	–2	0.96
G021.3425–00.8423	–		6.69	0.32	17.04	0.27	2.42	1.55	–0.31	1.56
G021.6657+00.8110	–		10.73	0.33	12.69	0.24	8.99	0.92	7.81	0.9
G021.6849–00.7381	–		7.69	0.23	18.91	0.19	0.77	1.66	–3.61	1.65
G021.8201–00.4779	–		10	0.27	11.16	0.17	2.1	1.16	–2.9	1.16
G021.9972–00.8838	–		3.58	0.37	9.29	0.19	4.71	1.17	5.35	1.18
G022.2211+00.9009	–		4.2	0.26	7.73	0.18	1.94	1.13	0.48	1.12
G022.5477–00.1061	–		13.13	0.47	24.29	0.46	9.72	0.96	7.49	0.98
G022.6429–00.4422	–		3.71	0.54	17.77	0.31	–3.45	1.85	–7.96	1.87
G022.6580+00.2959	–		8.91	0.6	15.83	0.57	10.49	1.06	11.38	1.03
G023.2321+00.0809	–		12.91	0.62	27.3	1.09	10.68	1.02	9.19	1.04
G023.4181–00.3940	–		18.54	0.47	15.03	0.43	11.62	0.96	7.17	0.96
G023.5044–00.5245	–		–0.16	0.42	7.67	0.32	2.86	1.0	4.69	1.02
G023.8214–00.5788	–		12.92	0.24	23.11	0.43	7.9	0.91	4.68	0.91
G023.8897–00.7379	–		12.62	0.27	17.6	0.18	11.27	0.95	10.32	0.96
G024.0943–01.0992	–		2.97	0.28	14	0.29	5.85	0.96	7.58	0.95
G024.1659+00.2502	–		2.76	0.3	15.33	0.22	–8.61	1.84	–15.71	1.83
G024.3852+00.2869	–		20.55	0.36	27.64	1.04	3.43	2.37	–7.35	2.36
G024.7921–01.0043	–		0.64	0.95	11.56	0.75	–9.02	1.59	–15.05	1.44
G024.8959+00.4586	–		20.6	0.59	26.45	1.53	10.17	1.52	3.54	1.47

Continued on next page

Table A.3 – continued from previous page

Name	$H\alpha_{5GHz}$	$dH\alpha_{5GHz}$	E(H-K)	dE(H-K)	E(J-H)	dE(J-H)	F_H/F_{5GHz}	dF_H/F_{5GHz}	F_K/F_{5GHz}	dF_K/F_{5GHz}
	mag	mag	mag	mag	mag	mag	mag	mag	mag	mag
G025.0485–00.6621	–		9.28	0.37	12.61	0.45	5.53	0.94	3.11	0.92
G025.5190+00.2165	–		–		15.6	0.2	10.2	0.94	–	
G025.5769+00.1389	–		–	–	–	–				
G025.8466+01.1718	–		5.25	0.46	18.99	0.33	–1.99	1.42	–6.54	1.39
G026.0823–00.0347	–		5.6	0.32	12.86	0.26	4.11	1.35	3.12	1.34
G026.1620+00.5926	–		9.78	0.56	16.51	0.69	6.96	1.79	5.11	1.77
G026.2268+00.7685	–		2.87	0.32	18.8	0.18	–4.06	1.57	–8.41	1.57
G026.6529+00.2874	–		7.23	0.58	13	0.58	4.4	1.94	2.56	1.92
G026.7145+00.1319	–		7.82	0.61	20.58	0.84	7.72	1.21	7.57	1.17
G026.8327–00.1516	–		0	0.34	13	0.24	–7.9	2.12	–12.84	2.13
G027.4265–00.2499	–		0.68	0.56	6.6	0.35	–0.33	1.83	–1	1.83
G027.6595–00.3835	–		7.13	0.58	10.27	0.51	5.39	1.1	4.23	1.04
G027.6635–00.8267	–		6	0.68	3.4	0.54	4.64	1.22	3.72	1.19
G027.6640–00.2485	–		4.8	0.37	20.05	0.32	–5.75	1.56	–12.36	1.55
G027.7016+00.7048	–		6.07	0.66	4.47	0.15	3.05	1.0	1.1	1.08
G029.0538+00.9915	–		3.96	0.36	9.45	0.33	1.19	1.71	–0.6	1.71
G029.1652–00.0168	–		18.15	1.59	28.62	6.31	15.31	1.55	13.41	1.2
G029.2113–00.0689	–		10.05	0.39	8.64	0.21	5.22	0.98	2.12	1.01
G029.5780–00.2686	6.52	0.37	15.62	0.32	13.3	0.33	–3.87	1.61	–16.1	1.62
G029.8742–00.8190	–		16.41	0.38	16.96	0.29	12.14	0.98	9.35	0.98
G030.0226+00.1570	–		5.74	0.54	11.46	0.54	7.92	1.61	9.19	1.61
G030.0294–00.3318	–		6.79	0.36	17.8	0.52	10.26	1.22	12.33	1.21
G030.2335–00.1385	–		–	–	–	–				
G030.5302+00.1315	–		–2.91	1.84	13.31	1.4	15.71	2.39	27.23	2.5

Continued on next page

Table A.3 – continued from previous page

Name	$H\alpha_{5GHz}$	$dH\alpha_{5GHz}$	E(H-K)	dE(H-K)	E(J-H)	dE(J-H)	F_H/F_{5GHz}	dF_H/F_{5GHz}	F_K/F_{5GHz}	dF_K/F_{5GHz}
	mag	mag	mag	mag	mag	mag	mag	mag	mag	mag
G030.6670–00.3319	–		32.49	0.34	22	0.41	23.24	0.98	17.26	0.96
G030.8560+00.3826	–		–	–	–				28.69	0.98
G031.2131–00.1803	–		20.29	0.27	28.27	0.7	0.46	2.26	–11.99	2.26
G031.3724–00.7514	–		19.19	0.46	11.08	0.34	11.01	1.04	5.79	1.03
G032.3076+00.1536	–		16.8	0.23	11.19	0.33	5.69	1.09	–1.35	1.09
G032.5485–00.4739	6.07	0.2	4.63	0.25	8.17	0.25	–0.07	0.93	–3.05	0.92
G032.6136+00.7971	9.22	0.81	12.62	0.21	11.68	0.15	–8.02	2.26	–20.93	2.26
G032.8082–00.3159	–		10.84	0.62	14.45	0.76	10.11	1.56	9.54	1.52
G032.8177–00.1165	–		–3.81	0.48	8.97	0.32	–3.08	2.14	–2.64	2.14
G033.1198–00.8949	–		6.39	1.3	11.52	1.23	16.94	1.24	23.41	1.07
G033.3526+00.4043	–		19.56	0.52	20.59	1.05	13.29	1.04	9.24	0.99
G033.4543–00.6149	9.69	0.31	13.06	0.4	11.23	0.23	2.71	0.92	–3.83	0.91
G033.7952+00.4307	–		14.82	0.25	17.23	0.27	2.98	1.22	–4.48	1.22
G033.9059–00.0436	–		11.73	0.41	13.56	0.39	6.26	0.98	2.76	0.94
G034.1792–00.1777	–		31.61	2.83	–		21.26	2.7	14.6	1.82
G034.4200–00.3183	–		10.04	0.22	20.31	0.25	1.99	1.1	–3.1	1.1
G034.8624–00.0630	–		19.35	0.2	20.82	0.19	3.76	1.13	–6.06	1.12
G035.2162+00.4280	–		21.93	0.37	35.49	1.08	2.89	2.14	–9.09	2.13
G035.4719–00.4365	8.68	0.29	5.63	0.2	8.68	0.14	4.87	0.95	4.32	0.95
G035.5654–00.4922	–		8.09	0.21	12.84	0.16	3.64	1.19	0.79	1.19
G036.0116–00.2562	–		13.26	0.32	15.96	0.34	8.59	0.96	5.58	0.94
G036.5393+00.2003	–		12.6	0.3	26.32	0.51	3.97	1.91	–1.49	1.91
G037.9031–00.2754	–		22.4	0.61	32.43	3.29	19.6	1.0	17.69	0.94
G037.9601+00.4534	–		20.48	0.58	20.81	1.1	18.31	1.01	16.8	0.94

Continued on next page

Table A.3 – continued from previous page

Name	$H\alpha_{5GHz}$	$dH\alpha_{5GHz}$	E(H-K)	dE(H-K)	E(J-H)	dE(J-H)	F_H/F_{5GHz}	dF_H/F_{5GHz}	F_K/F_{5GHz}	dF_K/F_{5GHz}
	mag	mag	mag	mag	mag	mag	mag	mag	mag	mag
G038.9237–00.0807	–		26.67	1.1	20.64	2.5	18.02	2.15	12.45	2.06
G039.1617+00.7826	–		16.74	0.32	15.63	0.38	12.84	0.99	10.28	0.98
G039.5911–00.3785	–		–0.38	0.22	14.37	0.18	–9.88	2.28	–15.81	2.28
G040.2606–00.2755	–		33.51	1.19	–		16.17	1.65	5.16	1.42
G040.3359–01.0102	–		9.74	0.38	13.98	0.42	5.9	1.64	3.42	1.63
G041.1982+00.0348	–		18.16	0.41	25.83	1.11	15.86	1.2	14.28	1.17
G041.3540+00.5390	10.79	0.57	–4.34	0.21	20.79	0.18	–1.49	1.02	0.26	1.02
G041.7871+00.4884	–		15.39	0.25	23.67	0.37	3.29	1.25	–4.34	1.24
G042.6629–00.8648	–		11.55	0.44	12.97	0.58	10.95	1.28	10.47	1.27
G043.0281+00.1399	–		11.45	0.38	13.3	0.44	9.48	0.91	8.14	0.92
G043.2946–00.6455	–		10.85	0.29	14.93	0.37	9.27	0.91	8.18	0.91
G043.5793+00.0261	–		19.29	0.54	21.99	1.13	14.16	1.01	10.82	0.97
G043.6554–00.8279	–		9	0.24	11.66	0.18	4.44	1.03	1.52	1.02
G044.6375+00.4827	7.76	0.3	7.73	0.2	15.16	0.14	–7.85	1.09	–17.59	1.09
G045.1801+00.9893	–		1.52	1.33	14.16	1.3	11.99	1.56	18.43	1.51
G045.2830–00.6278	–		14.91	0.24	15.89	0.26	8.9	1.04	5.05	1.04
G046.9747+00.2702	–		11.54	0.36	11.72	0.42	8.1	1.08	5.86	1.06
G047.6884–00.3024	–		11.88	0.25	13.27	0.24	5.63	1.01	1.64	1.01
G047.9875+00.2026	–		12.46	0.64	14.8	0.71	8.33	1.57	5.66	1.52
G048.5619+00.9029	6.33	0.42	1.4	0.52	7.64	0.37	2.57	1.87	3.24	1.87
G048.6748–00.5350	–		7.68	0.55	12.85	0.53	8.25	1.84	8.52	1.84
G048.7319+00.9305	7.01	0.25	7.41	0.3	6.49	0.22	4.98	1.01	3.39	1.0
G049.6948+00.8642	–		10.51	0.31	15.24	0.2	5.44	0.93	2.19	0.94
G050.0003+00.5072	–		–0.9	0.25	11.79	0.17	–6.24	0.95	–9.58	0.96

Continued on next page

Table A.3 – continued from previous page

Name	$H\alpha_{5GHz}$	$dH\alpha_{5GHz}$	E(H-K)	dE(H-K)	E(J-H)	dE(J-H)	F_H/F_{5GHz}	dF_H/F_{5GHz}	F_K/F_{5GHz}	dF_K/F_{5GHz}
	mag	mag	mag	mag	mag	mag	mag	mag	mag	mag
G050.0405+01.0961	7.92	0.29	4.03	0.34	6.56	0.19	4.62	1.01	4.92	1.02
G050.0457+00.7683	–		9.54	0.24	15.88	0.17	0.43	1.0	–5.32	1.0
G050.4802+00.7056	6.86	0.29	21.51	0.22	24.65	0.16	–12.11	1.17	–33.13	1.17
G050.5556+00.0448	11.6	0.41	11.26	0.25	11.04	0.2	8.85	0.97	7.25	0.96
G050.8950+00.0572	–		14.07	0.45	17	0.68	8.74	1.24	5.31	1.22
G051.5095+00.1686	–		7.64	0.32	8.65	0.14	6.66	0.93	5.97	0.94
G051.6061+00.9140	–		8.59	0.46	11.59	0.17	7.15	0.94	6.16	0.97
G051.8341+00.2838	9.53	0.31	8.76	0.32	8.33	0.15	7.07	0.9	5.92	0.91
G052.1498–00.3758	–		7.72	0.32	21.53	0.31	6.71	0.93	6	0.91
G055.5070–00.5579	3.45	0.11	4.04	0.58	2.94	0.14	2.18	0.93	0.96	0.99
G056.4016–00.9033	5.42	0.18	3.21	0.22	4.55	0.27	1.47	0.93	0.33	0.93
G057.5352+00.2266	–		12.24	0.65	19.12	1.15	9.7	1.76	8	1.75
G058.1591–00.5499	–		4.61	0.35	13.63	0.34	1.24	1.85	–0.92	1.84
G058.6410+00.9196	8.25	0.41	7.37	0.35	10.02	0.27	1.44	1.28	–2.33	1.28
G059.3987–00.7880	7.89	0.26	1.8	0.32	7.25	0.15	1.88	0.94	1.87	0.95
G059.8236–00.5361	6.81	0.22	7.26	0.32	6.01	0.27	5.26	0.91	3.94	0.92
G060.8480–00.8954	–		6.58	0.57	17.26	0.63	3.78	2.18	1.97	2.17
G060.9866–00.5698	4.67	0.19	4.02	0.39	7.34	0.23	–4.16	1.15	–9.3	1.15
G062.4936–00.2699	2.3	0.08 *	4.13	0.23	4.99	0.16	5.08	1.03	5.61	1.03
G062.7551–00.7262	4.95	0.18	5.96	0.29	7.7	0.21	5.38	1.04	4.95	1.03
G063.0455+00.5977	–		1.52	0.36	9.29	0.22	0.49	1.96	–0.19	1.96
G063.8893+00.1229	5.52	0.23	4.82	0.58	5.44	0.22	1.31	1.2	–0.93	1.25

Table A.4: *Distances and physical diameters estimated for the CORNISH-PNe. For the angular sizes whose deconvolved sizes could not be determined, upper limits (<) and lower limits (>) are stated for the distances and physical diameters, respectively. Full table is also available online as Table A4.*

Name	$Log_{10}R$ pc	$dLog_{10}R$ pc	Dist kpc	dDist kpc
G009.9702–00.5292	–0.73	0.06	15.52	2.29
G010.0989+00.7393	–0.93	0.04	3.65	0.33
G010.4168+00.9356	–0.98	0.05	23	2.65
G010.5960–00.8733	–0.8	0.05	10.71	1.2
G011.3266–00.3718	–0.63	0.08	12.12	2.15
G011.4290–01.0091	–0.7	0.07	13.45	2.29
G011.4581+01.0736	–0.73	0.08	20.2	3.79
G011.7210–00.4916	–0.68	0.1	20.5	4.9
G011.7434–00.6502	–0.79	0.04	4.93	0.47
G011.7900–00.1022	–0.59	0.07	6.57	1.1
G012.0438–00.5077	–1.03	0.05	26.36	2.93
G012.1157+00.0757	–0.82	0.04	9.35	0.93
G012.1528–00.3304	–0.78	0.06	17.31	2.38
G012.3315–00.1806	–0.79	0.05	10.47	1.13
G012.3830+00.7990	–0.9	0.05	17.06	1.88
G012.6012+00.5592	–1.01	0.05	22.54	2.42
G013.3565–00.7559	–0.82	0.06	20.85	3.26
G013.6313–00.6023	–0.58	0.09	9.22	2.16
G013.9166+00.6500	–0.82	0.04	12.49	1.31
G014.2365+00.2117	–0.66	0.06	9.77	1.45
G014.4573–00.1847	–0.85	0.04	9.84	0.96
G014.5851+00.4613	–0.63	0.07	9.72	1.58
G014.7503–00.2496	–0.66	0.07	10.71	1.76
G014.8960+00.4837	–0.87	0.07	24.11	3.89
G015.1999–00.0863	–0.68	0.08	15.76	3.22
G015.5410+00.3359	–0.78	0.06	12.95	1.93
G015.5847+00.4002	–0.94	0.04	17.36	1.82
G015.7993–00.0063	–0.96	0.04	12.08	1.14
G016.0550+00.8280	–0.88	0.05	19.13	2.11
G016.4034–00.5740	–0.64	0.06	7.54	1.09
G016.4276+01.0072	–0.62	0.09	11.05	2.44
G016.4999+00.1152	–0.55	0.08	9.88	1.97

Continued on next page

Table A.4 – continued from previous page

Name	$Log_{10}R$ pc	$dLog_{10}R$ pc	Dist kpc	dDist kpc
G016.6002–00.2754	–0.55	0.09	8.34	1.64
G017.0152–00.1906	–0.67	0.08	13.32	2.35
G017.3669+00.5224	–0.7	0.05	12.08	1.46
G017.4147+00.3791	–0.52	0.05	5.78	0.72
G017.4487+00.1146	–0.57	0.1	13.08	3.33
G017.7250–00.2427	–0.64	0.05	6.05	0.72
G017.8222+00.9866	–0.68	0.06	12.76	1.73
G017.8645+00.2120	–1.05	0.04	20.69	2.02
G018.0661+00.8535	–0.73	0.05	9.42	1.02
G018.1286–00.2189	–0.71	0.1	17.89	4.54
G018.2402–00.9152	–0.53	0.06	4.69	0.6
G018.2413–00.5552	> -1.05		<33.85	
G018.5242+00.1519	–0.67	0.11	25.48	6.8
G018.5776–00.7484	–0.55	0.11	14.11	3.86
G019.2356+00.4951	–0.74	0.05	8.99	1.04
G019.4676–00.0154	–0.83	0.05	15.22	1.63
G019.5326+00.7308	–0.66	0.1	19.53	4.66
G019.9298–00.6639	> -1.18		<34.06	
G019.9448+00.9126	–0.75	0.05	10.47	1.22
G020.4681+00.6793	–0.86	0.04	7.53	0.76
G020.5176+00.4778	–0.68	0.06	12.68	1.84
G020.6015+00.0206	–0.66	0.13	25.43	7.94
G020.9782+00.9253	–0.65	0.07	12.6	2.18
G021.1653+00.4755	–1.02	0.04	8.27	0.78
G021.3425–00.8423	–0.77	0.08	14.05	2.71
G021.6657+00.8110	–1.03	0.04	13.2	1.24
G021.6849–00.7381	–0.59	0.07	6.94	1.15
G021.8201–00.4779	–0.65	0.06	8.02	1.14
G021.9972–00.8838	–0.74	0.06	14.91	2.01
G022.2211+00.9009	–0.72	0.05	11.54	1.52
G022.5477–00.1061	–0.85	0.04	12.06	1.22
G022.6429–00.4422	–0.68	0.09	19.98	4.61
G022.6580+00.2959	–0.88	0.05	19.22	2.1
G023.2321+00.0809	–0.79	0.05	12.42	1.35
G023.4181–00.3940	–0.9	0.04	14.68	1.45
G023.5044–00.5245	–0.77	0.05	11.36	1.24

Continued on next page

Table A.4 – continued from previous page

Name	$Log_{10}R$ pc	$dLog_{10}R$ pc	Dist kpc	dDist kpc
G023.8214–00.5788	–0.95	0.04	11.41	1.08
G023.8897–00.7379	–0.98	0.04	8.29	0.78
G024.0943–01.0992	> –1.24		<35.11	
G024.1659+00.2502	–0.49	0.08	5.73	1.05
G024.3852+00.2869	–0.6	0.13	16.97	5.39
G024.7921–01.0043	–0.7	0.07	16.65	2.93
G024.8959+00.4586	–0.76	0.06	15.88	2.37
G025.0485–00.6621	–0.93	0.04	14.62	1.4
G025.5190+00.2165	–0.71	0.04	3.2	0.3
G025.5769+00.1389	–0.9	0.05	20.38	2.19
G025.8466+01.1718	–0.69	0.07	9.02	1.64
G026.0823–00.0347	–0.68	0.07	13.28	2.2
G026.1620+00.5926	–0.59	0.1	12	2.89
G026.2268+00.7685	–0.7	0.08	20.32	3.88
G026.6529+00.2874	–0.65	0.1	18.33	4.49
G026.7145+00.1319	–0.76	0.06	15.95	2.11
G026.8327–00.1516	–0.6	0.09	14.69	3.18
G027.4265–00.2499	–0.73	0.09	23.18	5.17
G027.6595–00.3835	> –1.12		<33.77	
G027.6635–00.8267	–0.82	0.05	22.59	2.97
G027.6640–00.2485	> –0.85		<30.66	
G027.7016+00.7048	–0.77	0.04	5.15	0.51
G029.0538+00.9915	–0.86	0.08	30.95	6.29
G029.1652–00.0168	–0.71	0.05	15.58	2.02
G029.2113–00.0689	–0.79	0.04	6.1	0.6
G029.5780–00.2686	> –0.86		<28.19	
G029.8742–00.8190	–1.01	0.04	7.11	0.69
G030.0226+00.1570	–0.69	0.08	17.12	3.4
G030.0294–00.3318	–0.82	0.06	17.94	2.48
G030.2335–00.1385	–1.19	0.04	6.87	0.63
G030.5302+00.1315	–0.53	0.1	11.86	2.75
G030.6670–00.3319	–1.09	0.04	8.93	0.85
G030.8560+00.3826	–0.86	0.04	9.9	0.96
G031.2131–00.1803	> –0.66		<27.93	
G031.3724–00.7514	–0.77	0.05	12.46	1.4
G032.3076+00.1536	–0.88	0.05	17.3	2.1

Continued on next page

Table A.4 – continued from previous page

Name	$Log_{10}R$ pc	$dLog_{10}R$ pc	Dist kpc	dDist kpc
G032.5485–00.4739	–0.87	0.04	9.96	0.96
G032.6136+00.7971	–0.7	0.11	27.76	7.81
G032.8082–00.3159	–0.63	0.07	11.42	1.74
G032.8177–00.1165	–0.67	0.11	23.47	6.28
G033.1198–00.8949	> –1.23		<32.92	
G033.3526+00.4043	–1.02	0.04	24.26	2.56
G033.4543–00.6149	–1.03	0.04	11.13	1.03
G033.7952+00.4307	–0.8	0.06	20.8	2.9
G033.9059–00.0436	–1.09	0.04	26.9	2.67
G034.1792–00.1777	–0.6	0.1	13.34	3.2
G034.4200–00.3183	–0.94	0.05	23.17	2.82
G034.8624–00.0630	–0.75	0.05	7.09	0.8
G035.2162+00.4280	–0.56	0.12	11.53	3.54
G035.4719–00.4365	–0.95	0.04	5.71	0.54
G035.5654–00.4922	–0.59	0.05	5.42	0.64
G036.0116–00.2562	–0.92	0.04	18.35	1.82
G036.5393+00.2003	–0.56	0.08	10.77	2.08
G037.9031–00.2754	–1.01	0.04	16.11	1.56
G037.9601+00.4534	–1	0.04	19.06	1.87
G038.9237–00.0807	–0.55	0.12	11.03	3.25
G039.1617+00.7826	–0.8	0.04	11.73	1.24
G039.5911–00.3785	–0.71	0.12	25.29	7.24
G040.2606–00.2755	> –0.92		<29.50	
G040.3359–01.0102	–0.62	0.09	14.75	3.11
G041.1982+00.0348	–0.82	0.05	10.48	1.23
G041.3540+00.5390	–0.73	0.05	9.46	1.1
G041.7871+00.4884	–0.88	0.06	25.43	3.61
G042.6629–00.8648	–0.66	0.06	11.47	1.79
G043.0281+00.1399	–0.98	0.04	8.3	0.77
G043.2946–00.6455	–1	0.04	11	1.03
G043.5793+00.0261	–1.05	0.04	24.91	2.52
G043.6554–00.8279	–0.79	0.05	13.54	1.53
G044.6375+00.4827	–0.79	0.05	14.74	1.8
G045.1801+00.9893	> –0.89		<32.00	
G045.2830–00.6278	–0.81	0.05	13.77	1.59
G046.9747+00.2702	–0.82	0.05	15.28	1.81

Continued on next page

Table A.4 – continued from previous page

Name	$Log_{10}R$ pc	$dLog_{10}R$ pc	Dist kpc	dDist kpc
G047.6884–00.3024	–1.01	0.05	22.95	2.48
G047.9875+00.2026	–0.8	0.07	25.35	4.56
G048.5619+00.9029	–0.66	0.09	25.22	5.8
G048.6748–00.5350	–0.67	0.09	19.97	4.56
G048.7319+00.9305	–0.81	0.05	14.82	1.61
G049.6948+00.8642	–0.92	0.04	15.12	1.46
G050.0003+00.5072	–0.88	0.04	16.32	1.65
G050.0405+01.0961	–0.75	0.05	13.38	1.49
G050.0457+00.7683	–0.75	0.05	14.48	1.59
G050.4802+00.7056	–0.86	0.06	26.39	3.49
G050.5556+00.0448	–0.9	0.04	6.58	0.63
G050.8950+00.0572	–0.74	0.06	18.46	2.59
G051.5095+00.1686	–0.65	0.04	3.83	0.35
G051.6061+00.9140	–0.93	0.04	18.46	1.83
G051.8341+00.2838	–0.9	0.04	8.67	0.81
G052.1498–00.3758	–1.08	0.04	22.16	2.11
G055.5070–00.5579	–0.99	0.04	6.26	0.58
G056.4016–00.9033	–0.96	0.04	19.69	1.92
G057.5352+00.2266	–0.74	0.09	28.3	5.88
G058.1591–00.5499	–0.68	0.09	25.5	5.76
G058.6410+00.9196	–0.84	0.06	29.36	4.3
G059.3987–00.7880	–0.79	0.04	11.26	1.12
G059.8236–00.5361	–0.96	0.04	15.05	1.42
G060.8480–00.8954	–0.72	0.11	31.65	8.41
G060.9866–00.5698	–0.8	0.05	23.41	3.0
G062.4936–00.2699	–0.7	0.05	11.4	1.33
G062.7551–00.7262	–0.71	0.05	13.17	1.5
G063.0455+00.5977	–0.6	0.1	18.75	4.76
G063.8893+00.1229	–0.63	0.05	7.85	0.94

Appendix B

Additional Figures and Tables for Chapter 3

Calibration and Imaging

System Variables and Gains Calibration Solution Without Flagging XX polarization to Ca01

The system variable allows a quick check for poor UV coverage, missing data or bad weather.

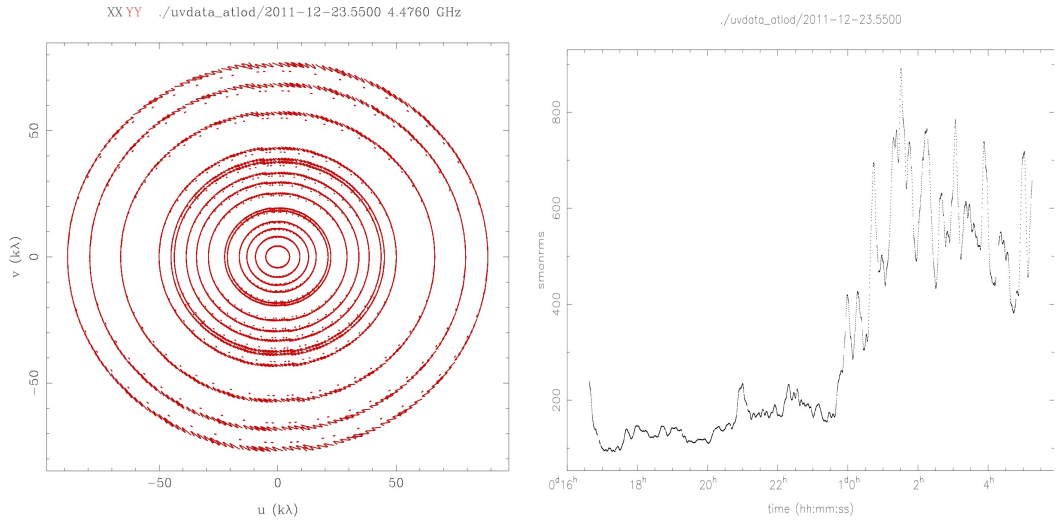

Figure B.1: *System variables showing the UV coverage and System monitor of a typical observation day (2011-12-23) at 5.5 GHz.*

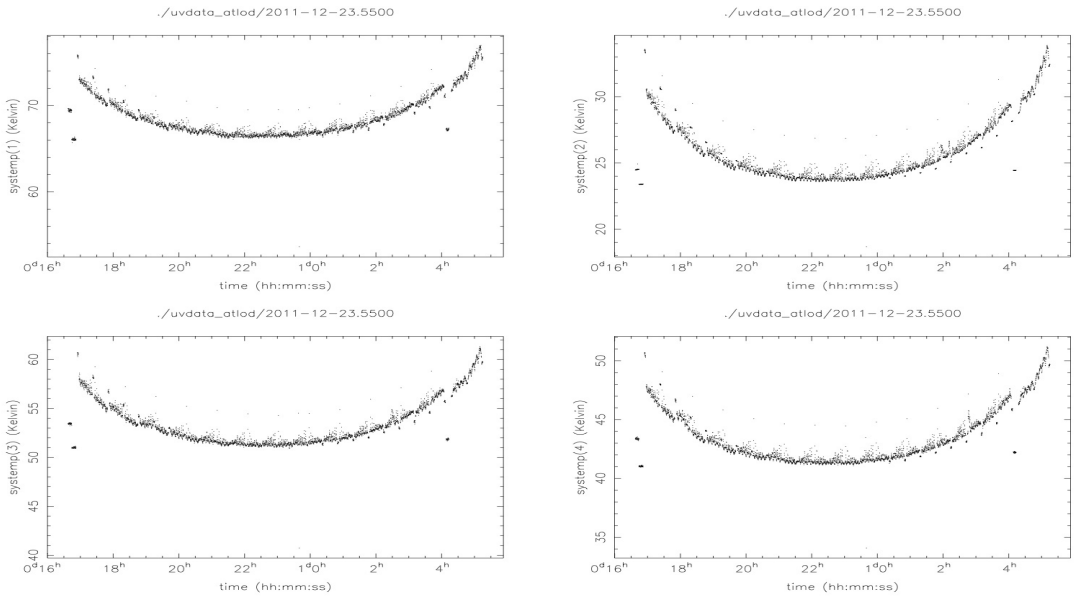

Figure B.2: *System temperature of a typical observation day (2011-12-23) at 5.5 GHz. Four baselines are shown.*

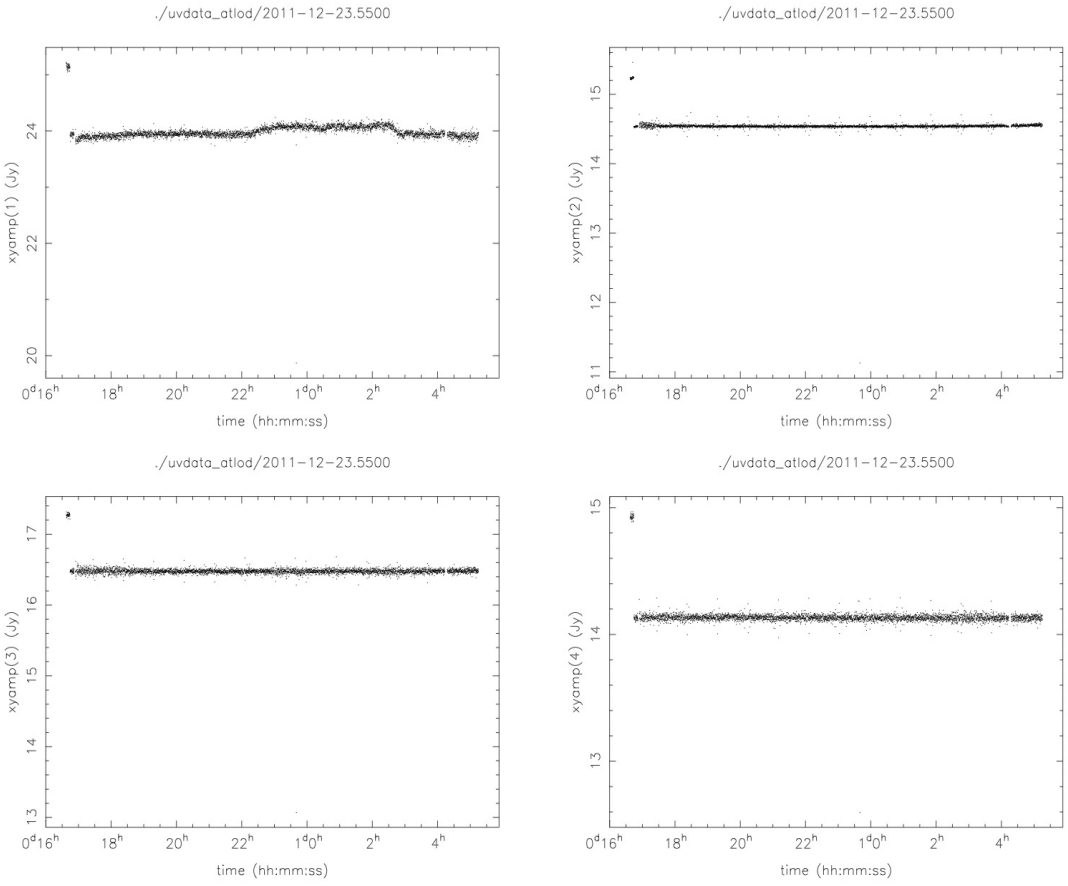

Figure B.3: *XY Amplitude of a typical observation day (2011-12-23) at 5.5 GHz. Four baselines are shown.*

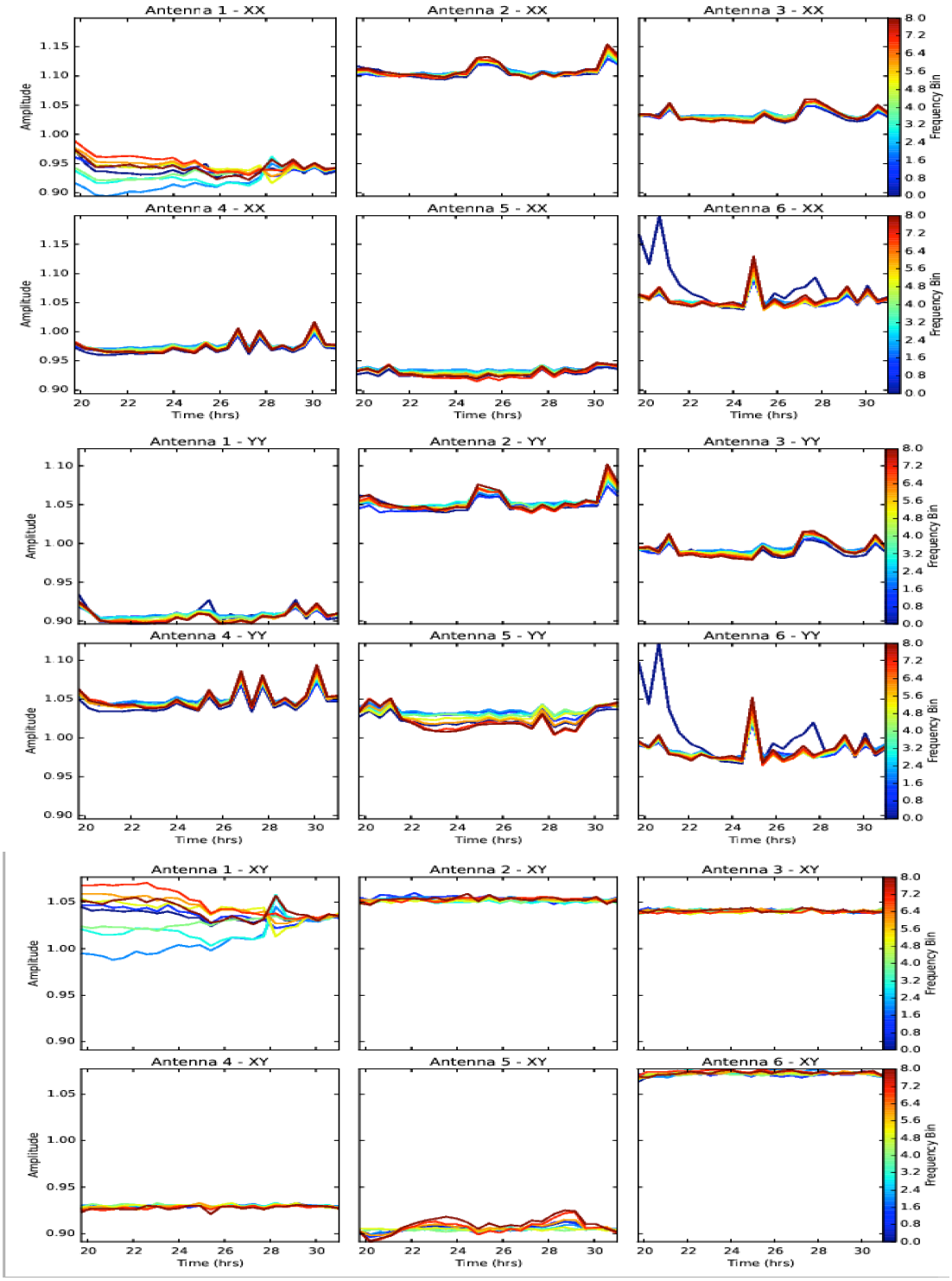

Figure B.4: *The gains solution for each baseline without flagging the xx polarization of all baselines to ant 1 (Ca01).*

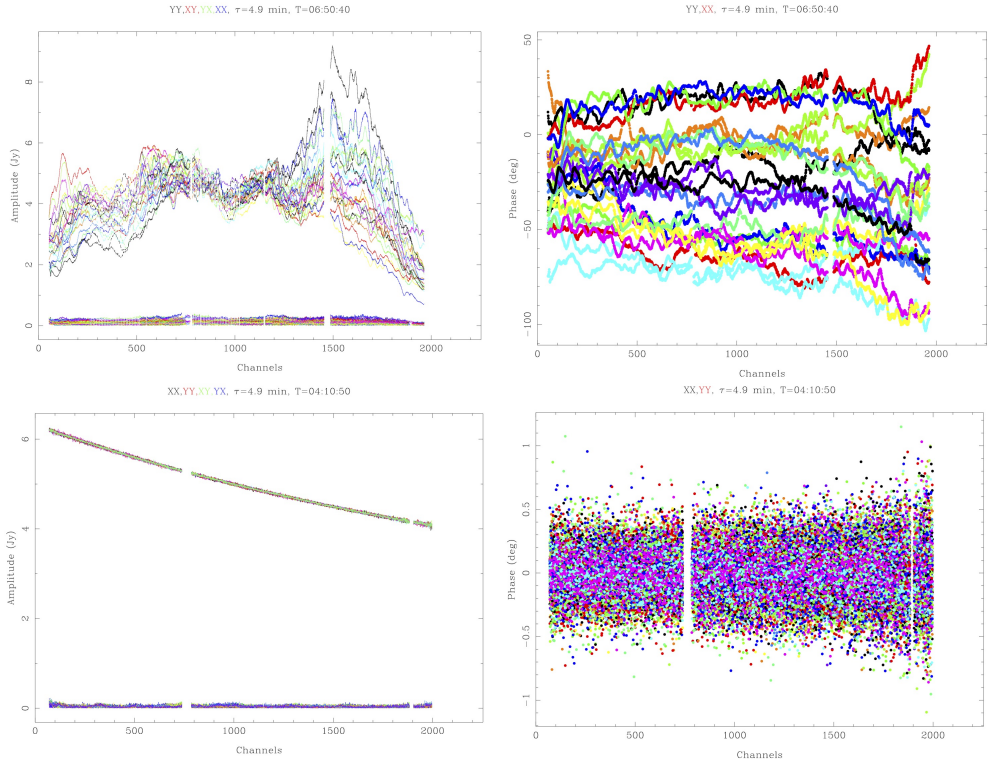

Figure B.5: *Amplitude (left) and phase (right) spectrum of the bandpass calibrator before and after calibration.*

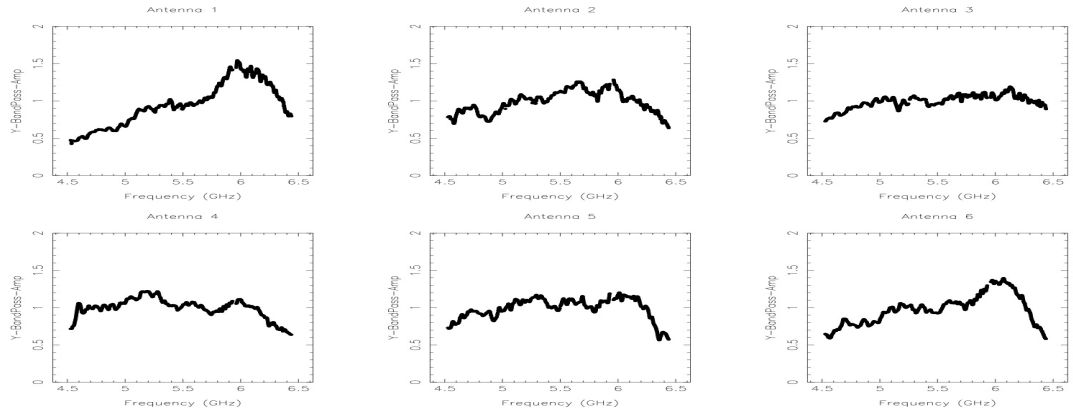

Figure B.6: *Typical bandpass amplitude solutions in Y.*

Example Calibration plots for observation block 2011-12-23

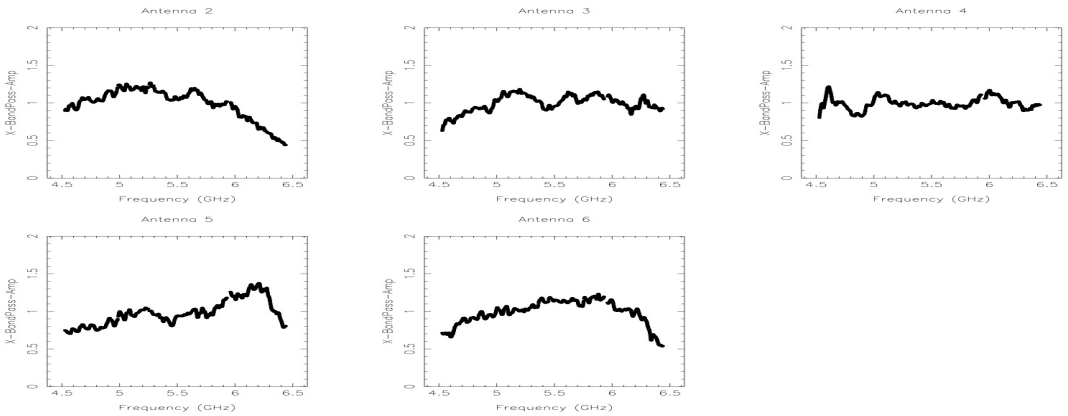

Figure B.7: *Typical bandpass amplitude solutions in X.*

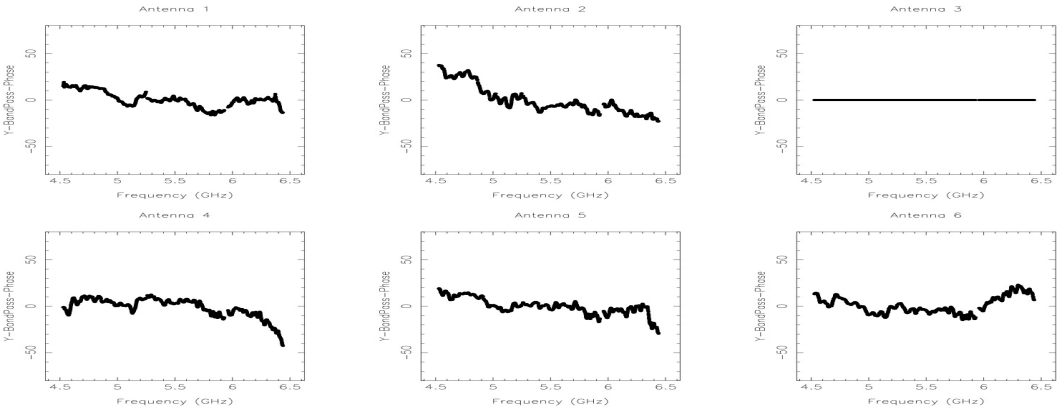

Figure B.8: *Typical bandpass phase in solutions in Y.*

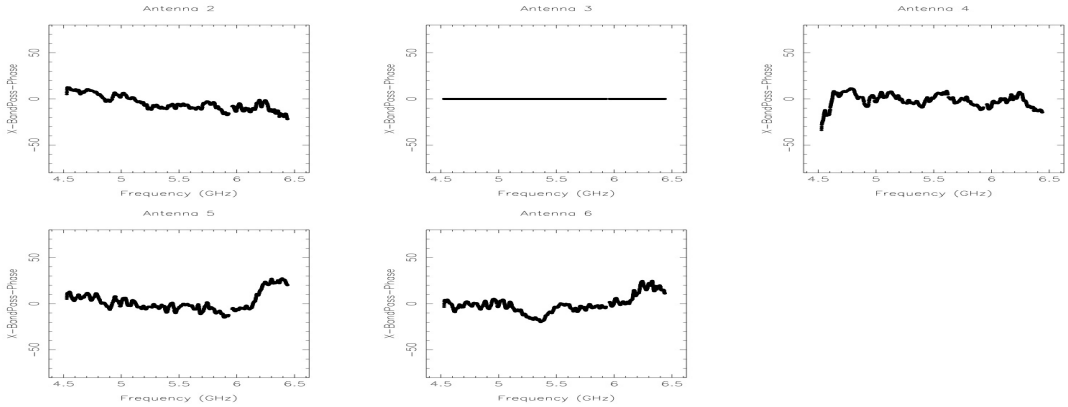

Figure B.9: *Typical bandpass phase solutions in X.*

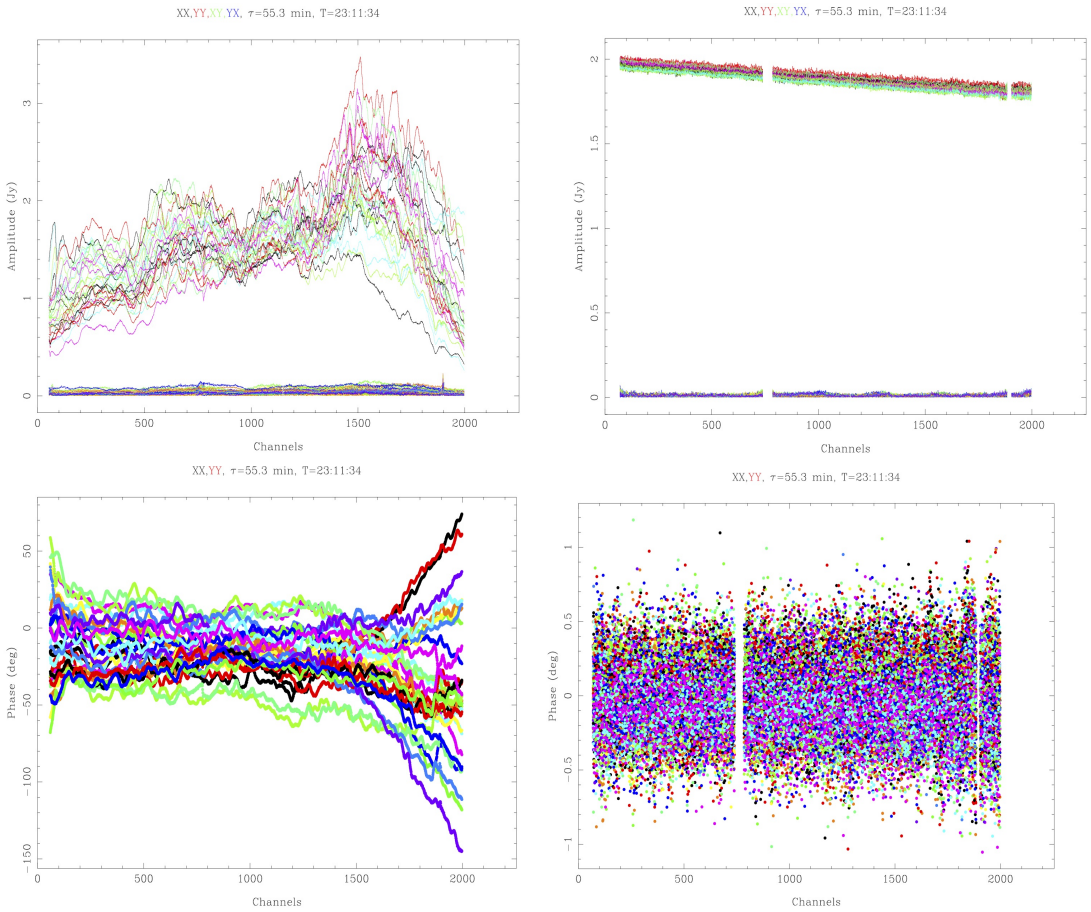

Figure B.10: *Before and after calibration of the secondary calibrator before and ater calibration.*

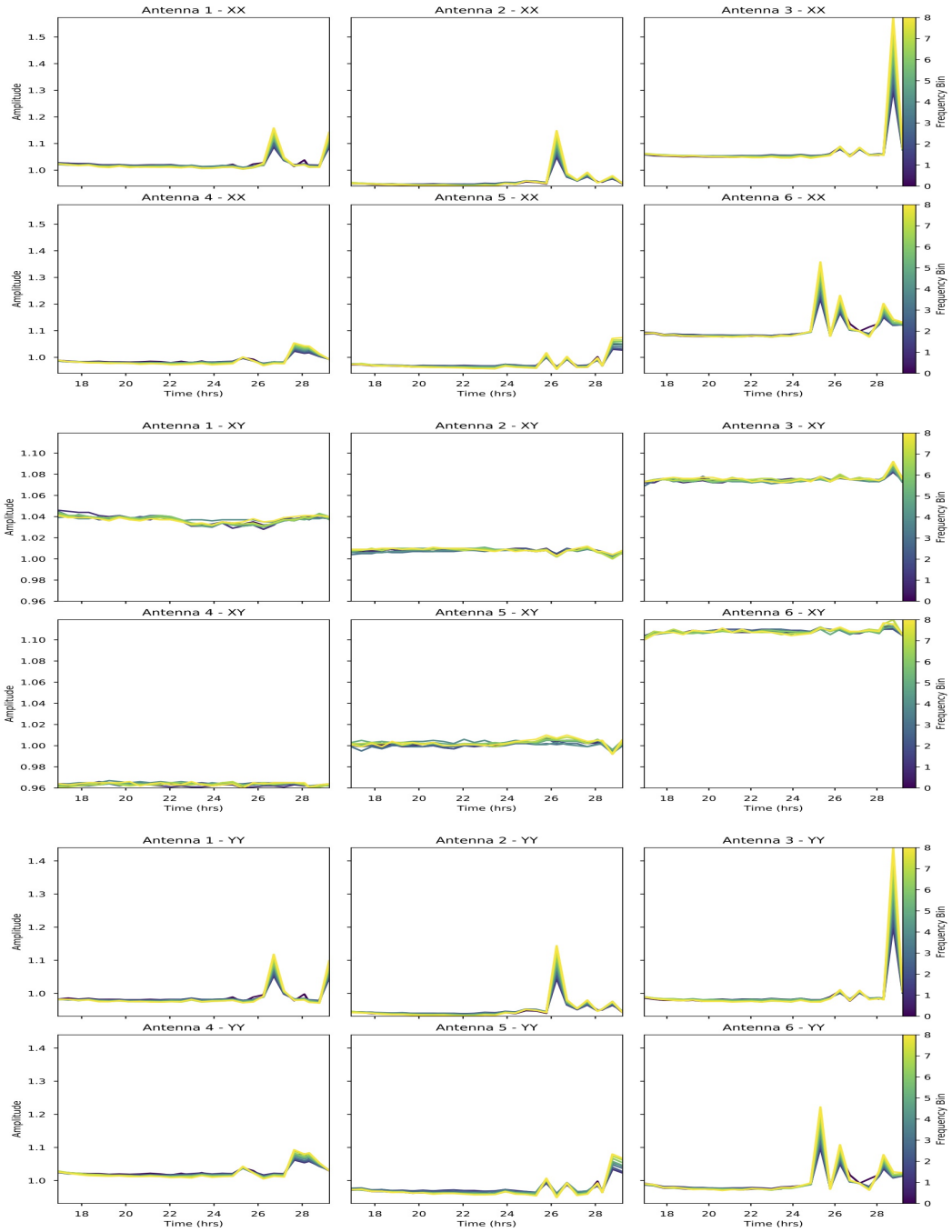

Figure B.11: *Gain solutions in amplitude. Colour coded in frequency bins.*

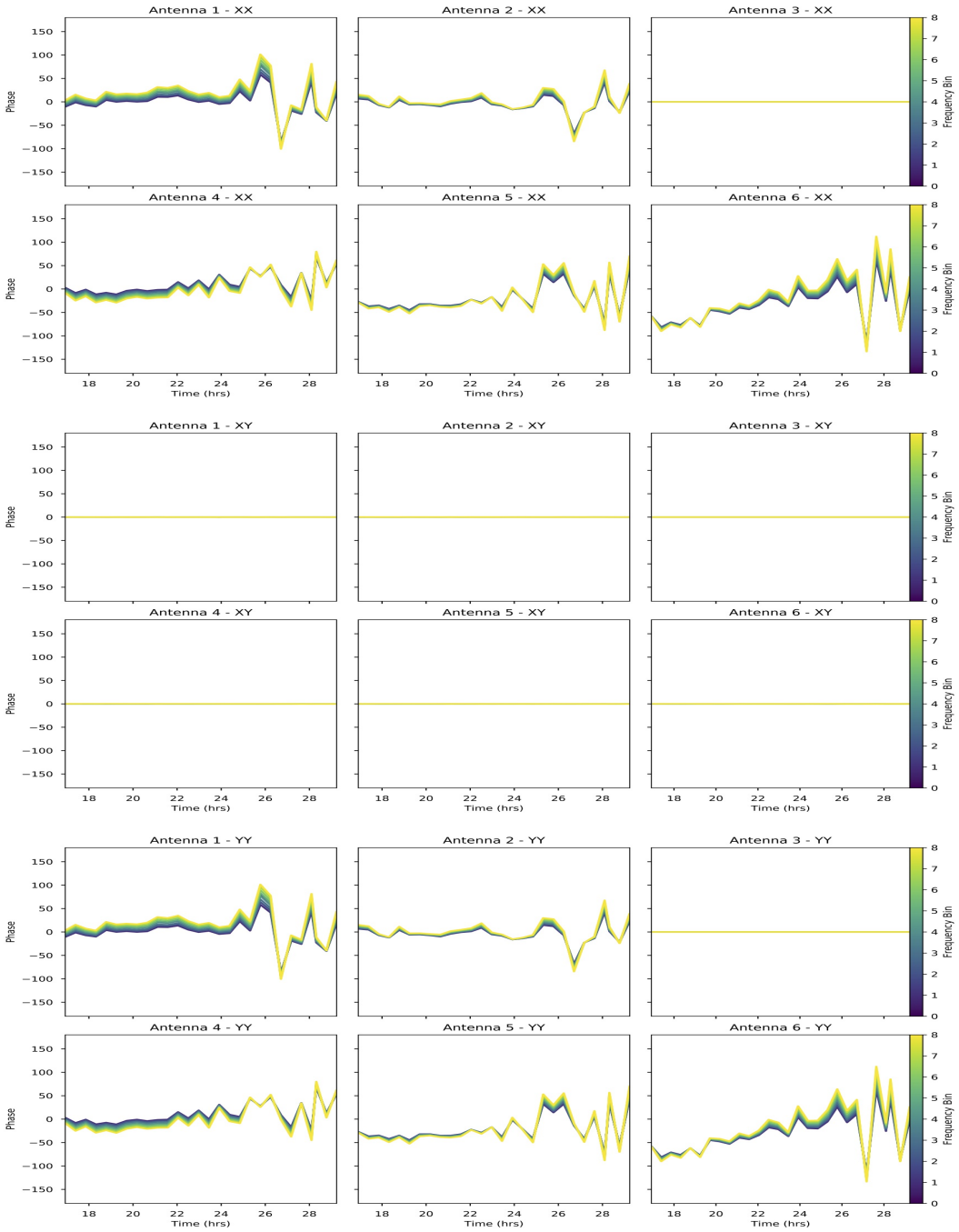

Figure B.12: *Gain solutions in phase. Colour coded in frequency bins.*

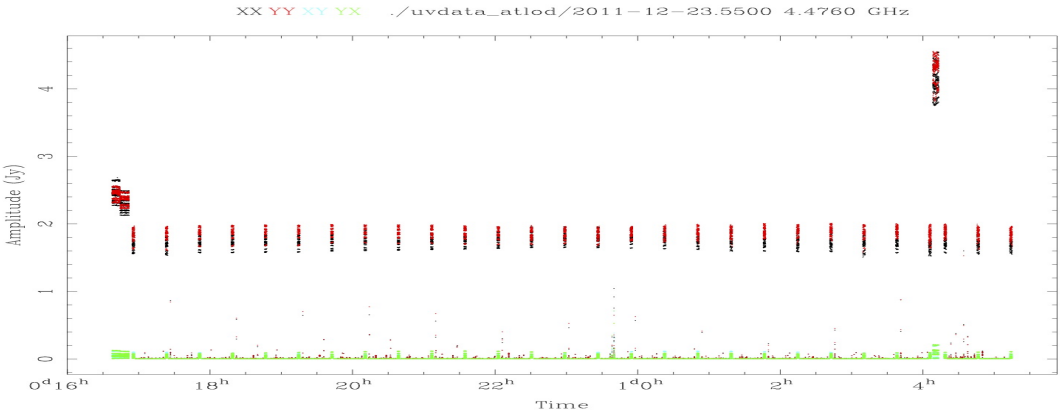

Figure B.13: *Amplitude versus time plot for the observed data.*

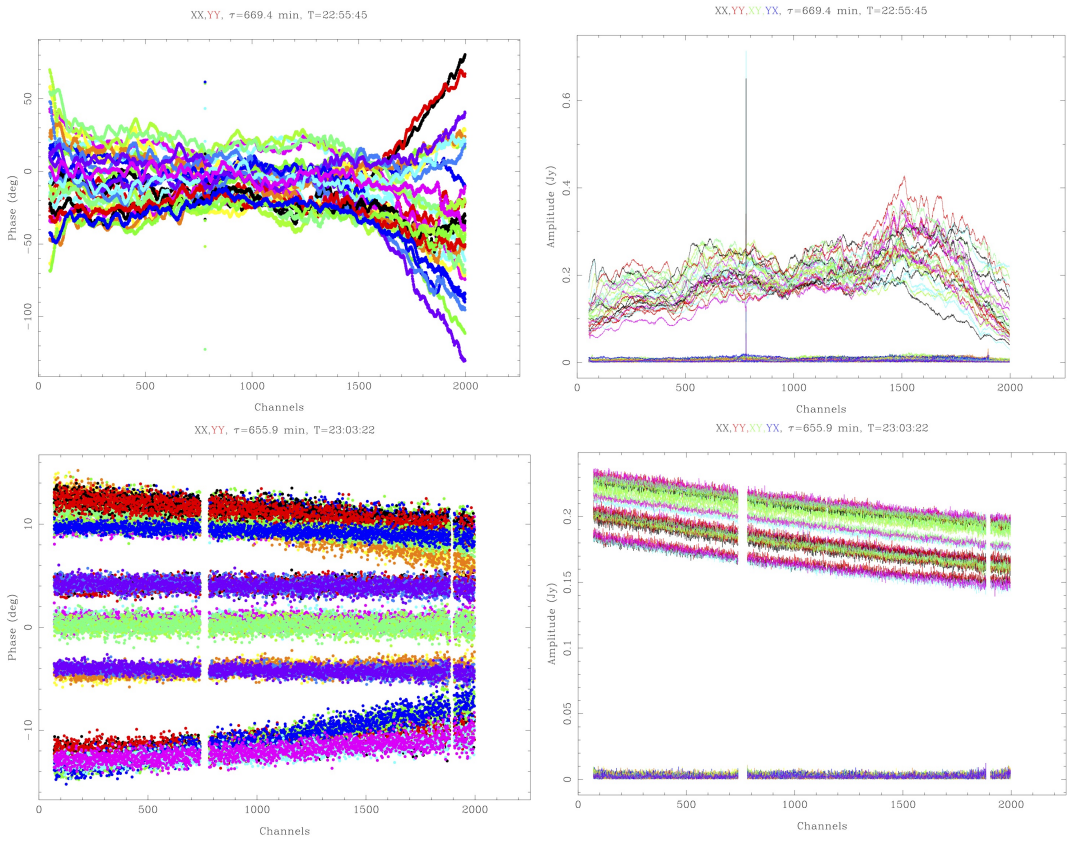

Figure B.14: *Before and after flagging and calibration of the observed data in phase (left) and amplitude (right) versus time.*

Variation of the rms noise in Stokes V across the survey region.

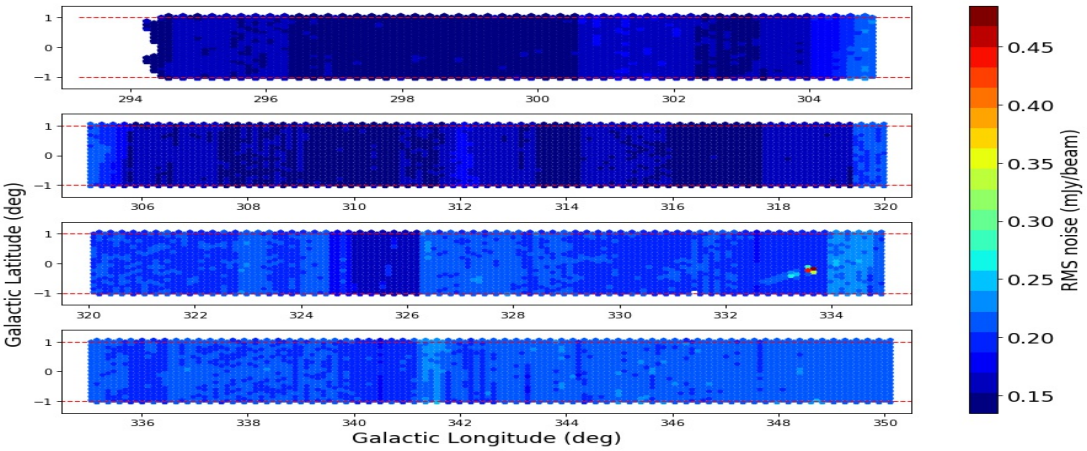

Figure B.15: *Variation of the rms noise in stokes V across the survey region.*

CORNISH South PNe

Mulit-wavelength Images of the CORNISH South PNe

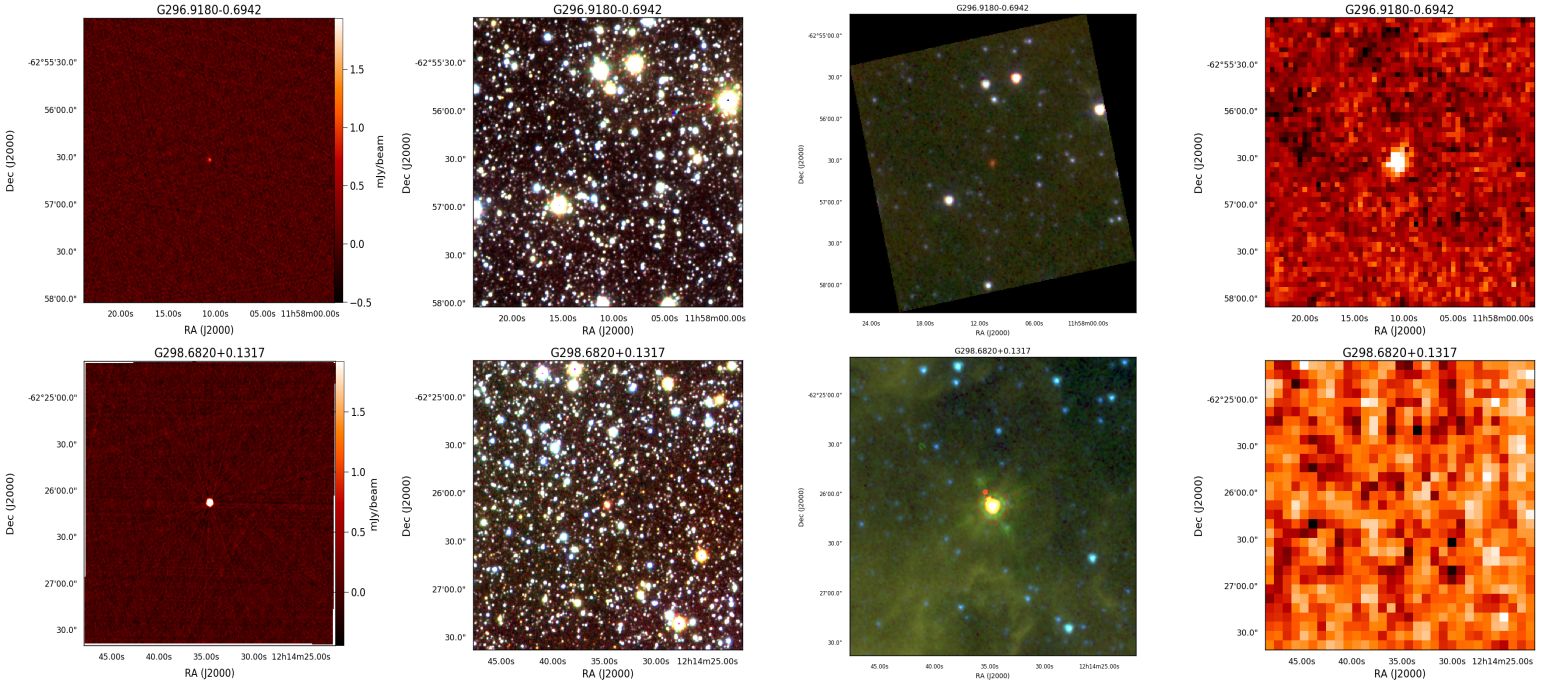

Figure B.16: *Image catalogue of CORNISH south PNe across different wavelengths. Images from four different surveys are preferably shown, otherwise, available data are shown. From left to right: Radio, SHS or VVV, GLIMPSE and 70* μm *image from Hi-Gal or 500* μm *from Hi-Gal or 850* μm *from ATLASGAL.*

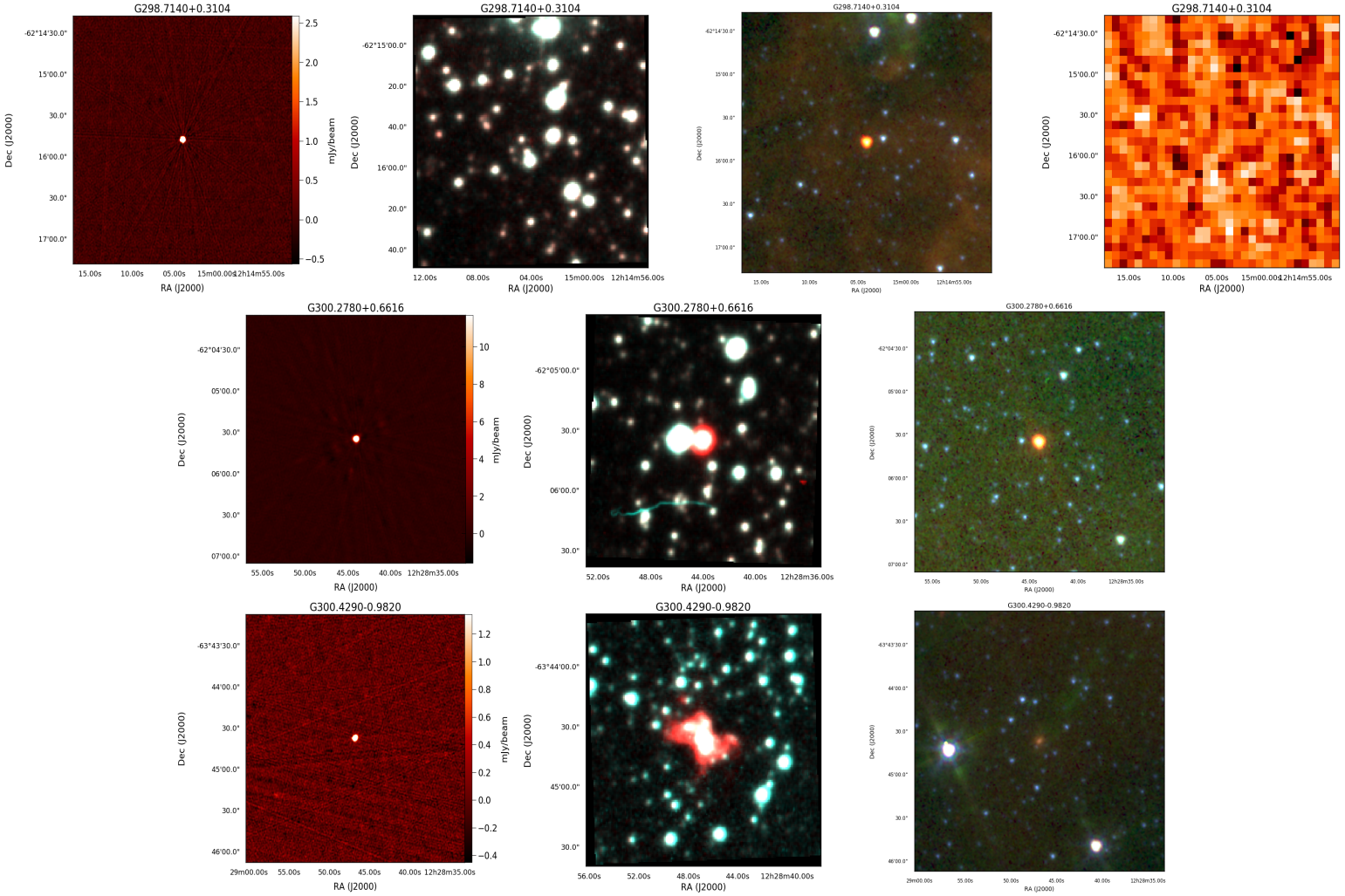

Figure B.17: *Continuation from previous Figure.*

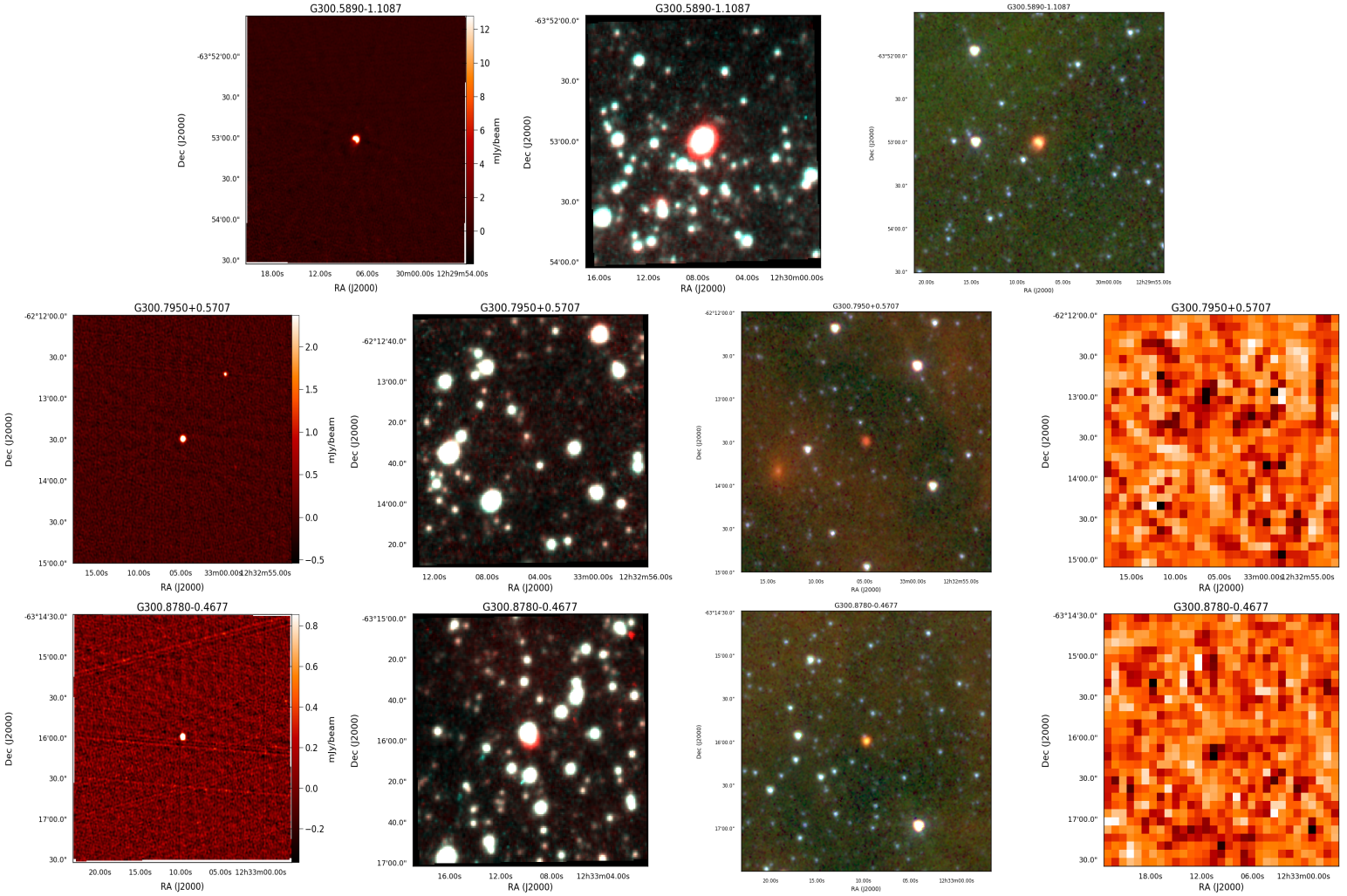

Figure B.18: *Continuation from previous Figure.*

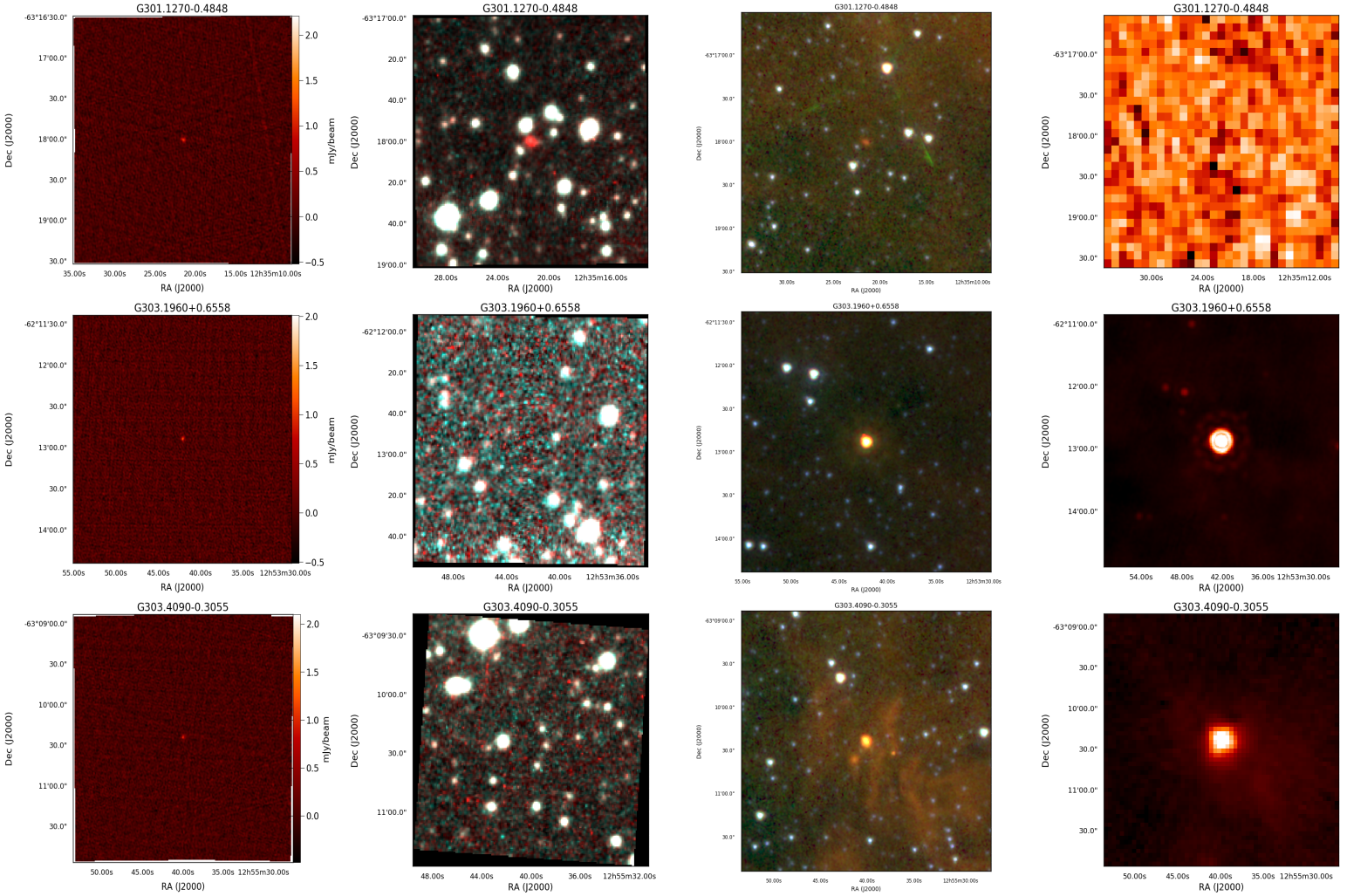

Figure B.19: *Continuation from previous Figure.*

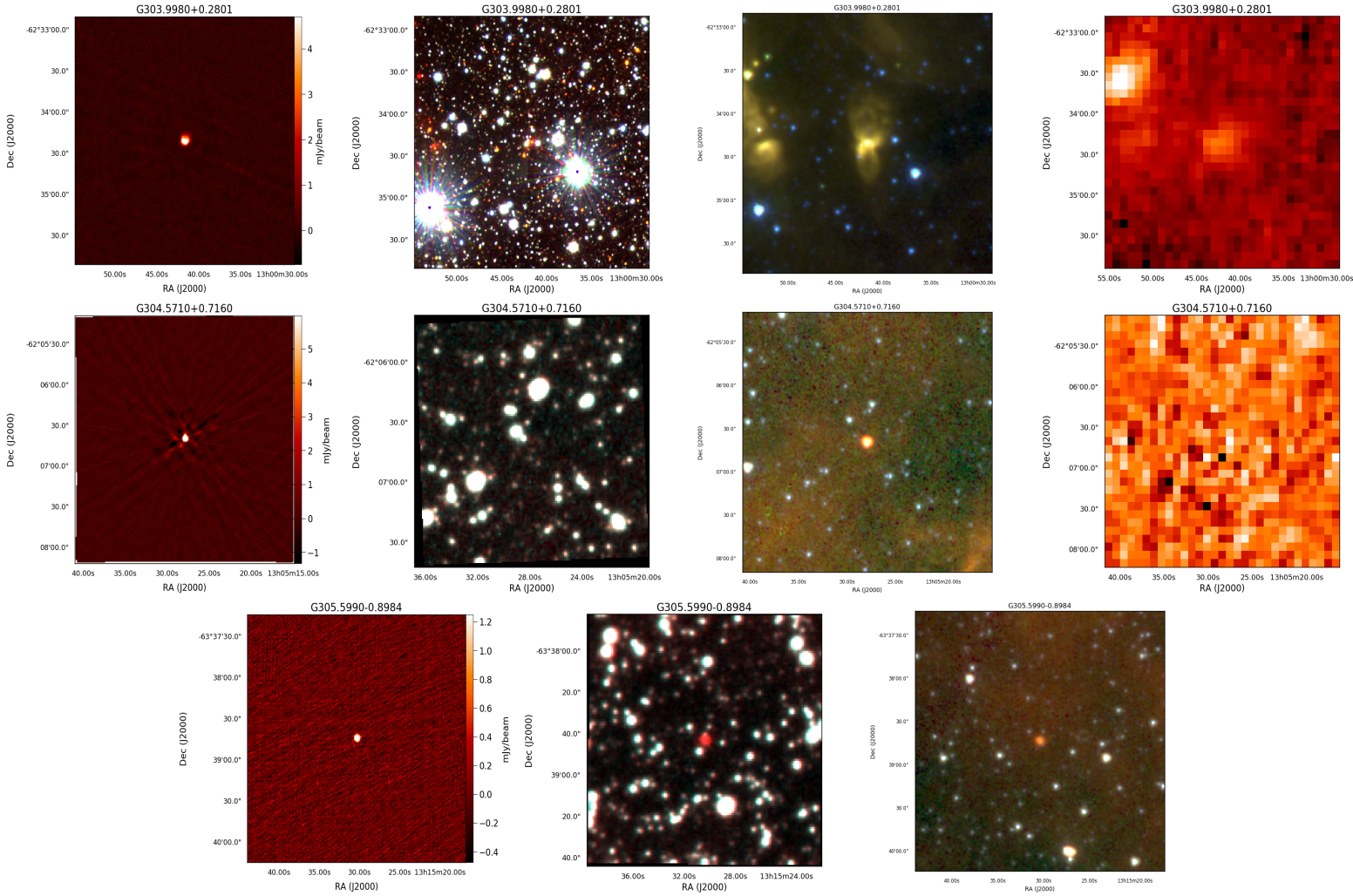

Figure B.20: *Continuation from previous Figure.*

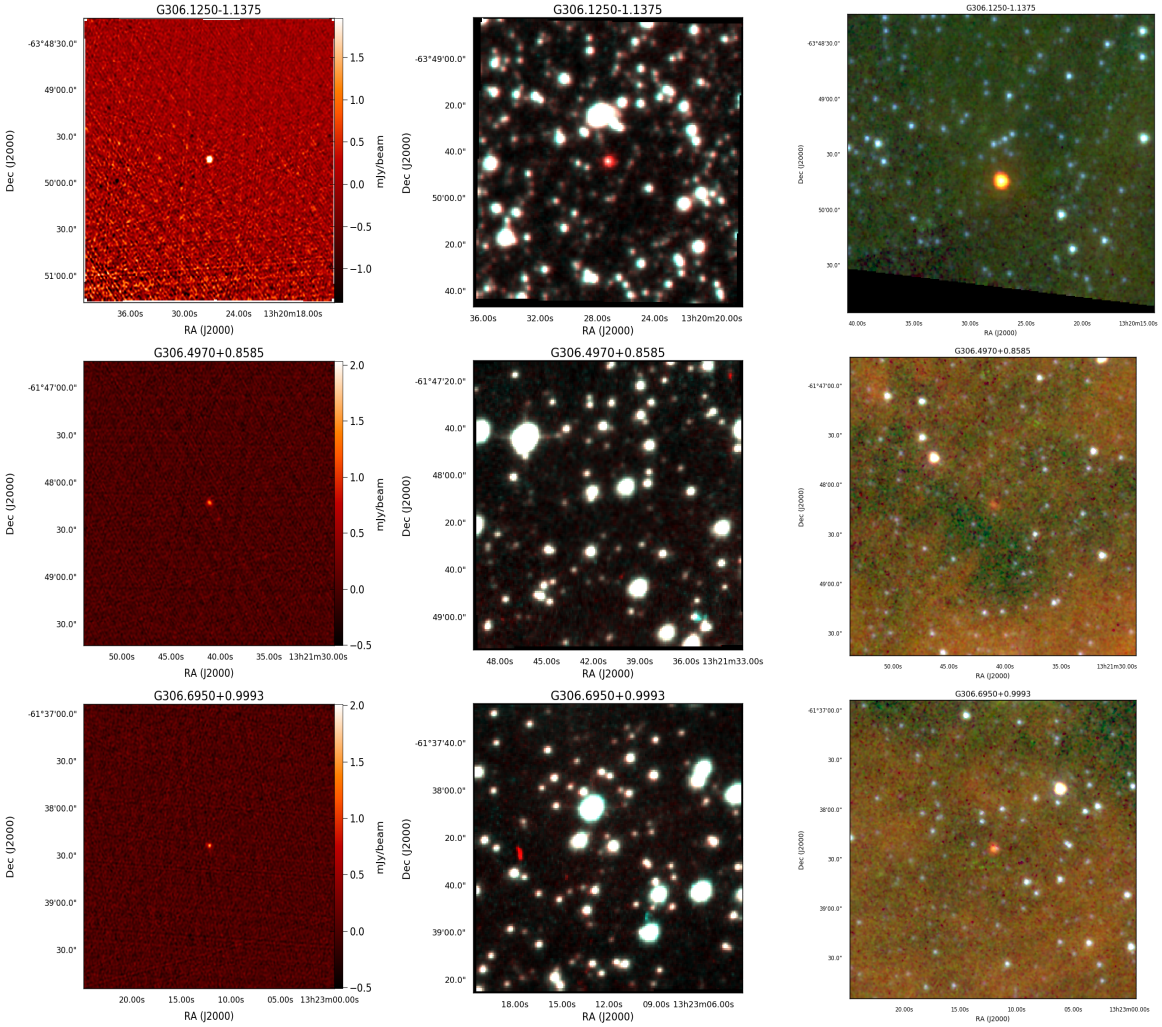

Figure B.21: *Continuation from previous Figure.*

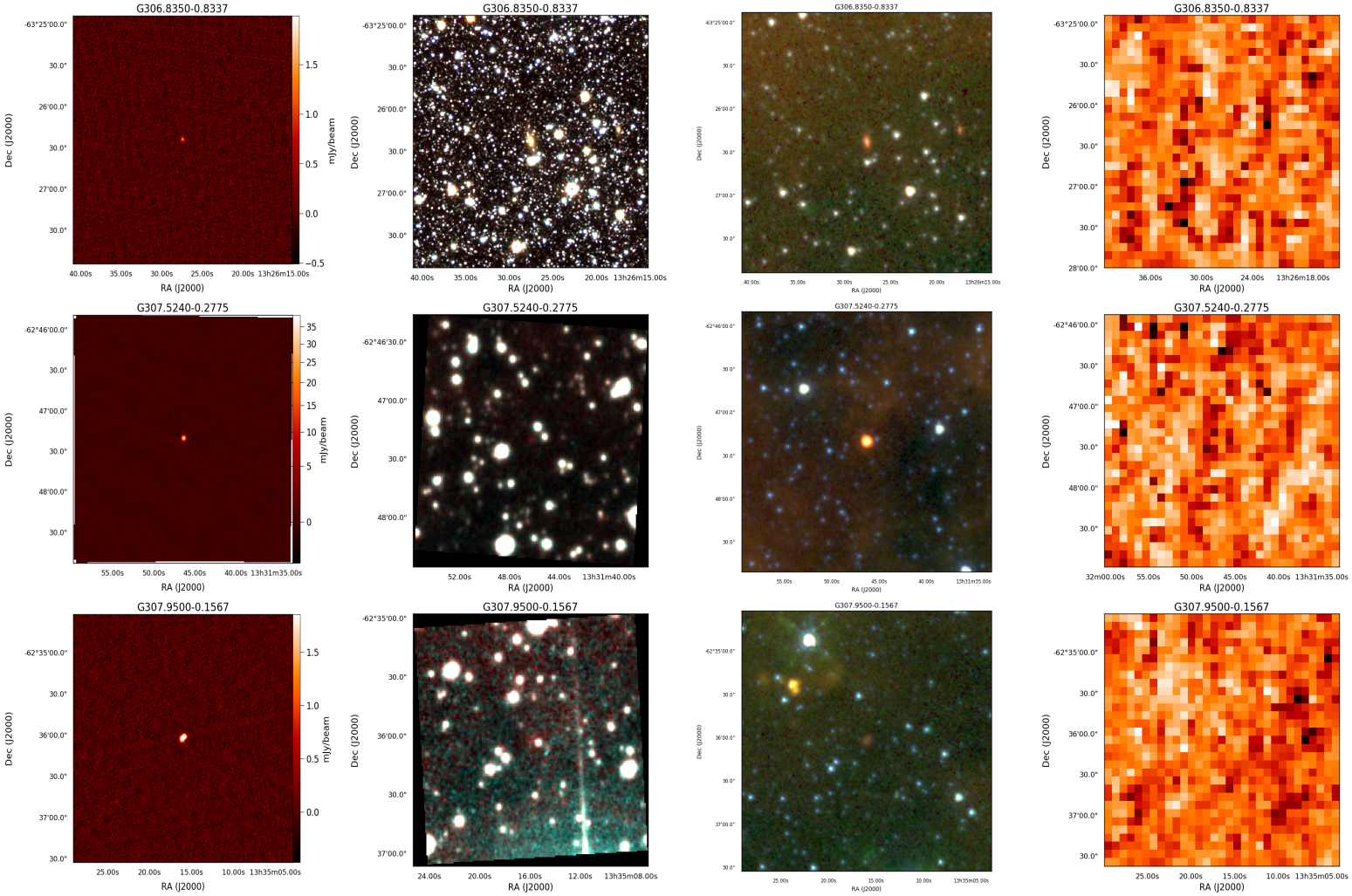

Figure B.22: *Continuation from previous Figure.*

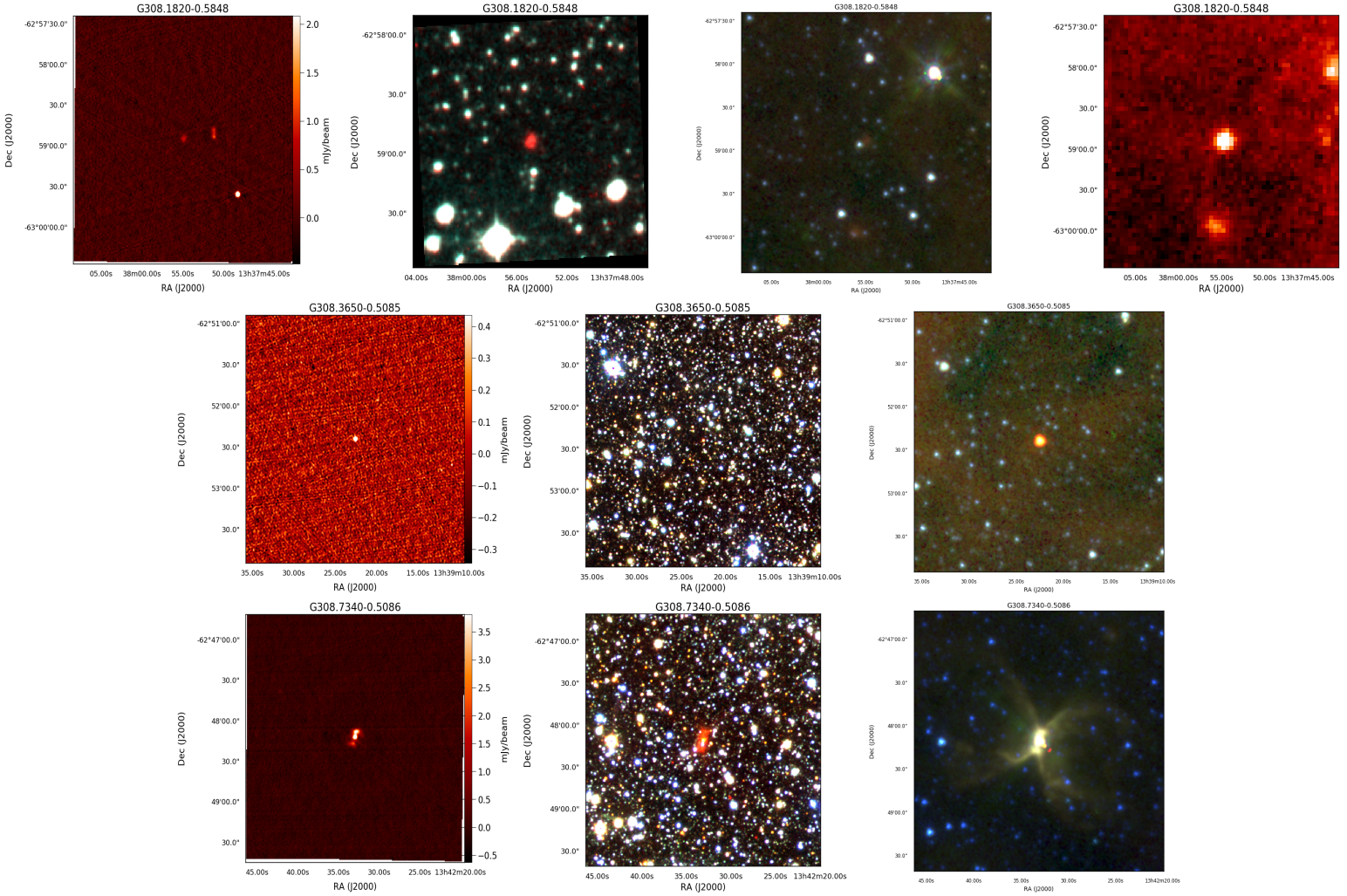

Figure B.23: *Continuation from previous Figure.*

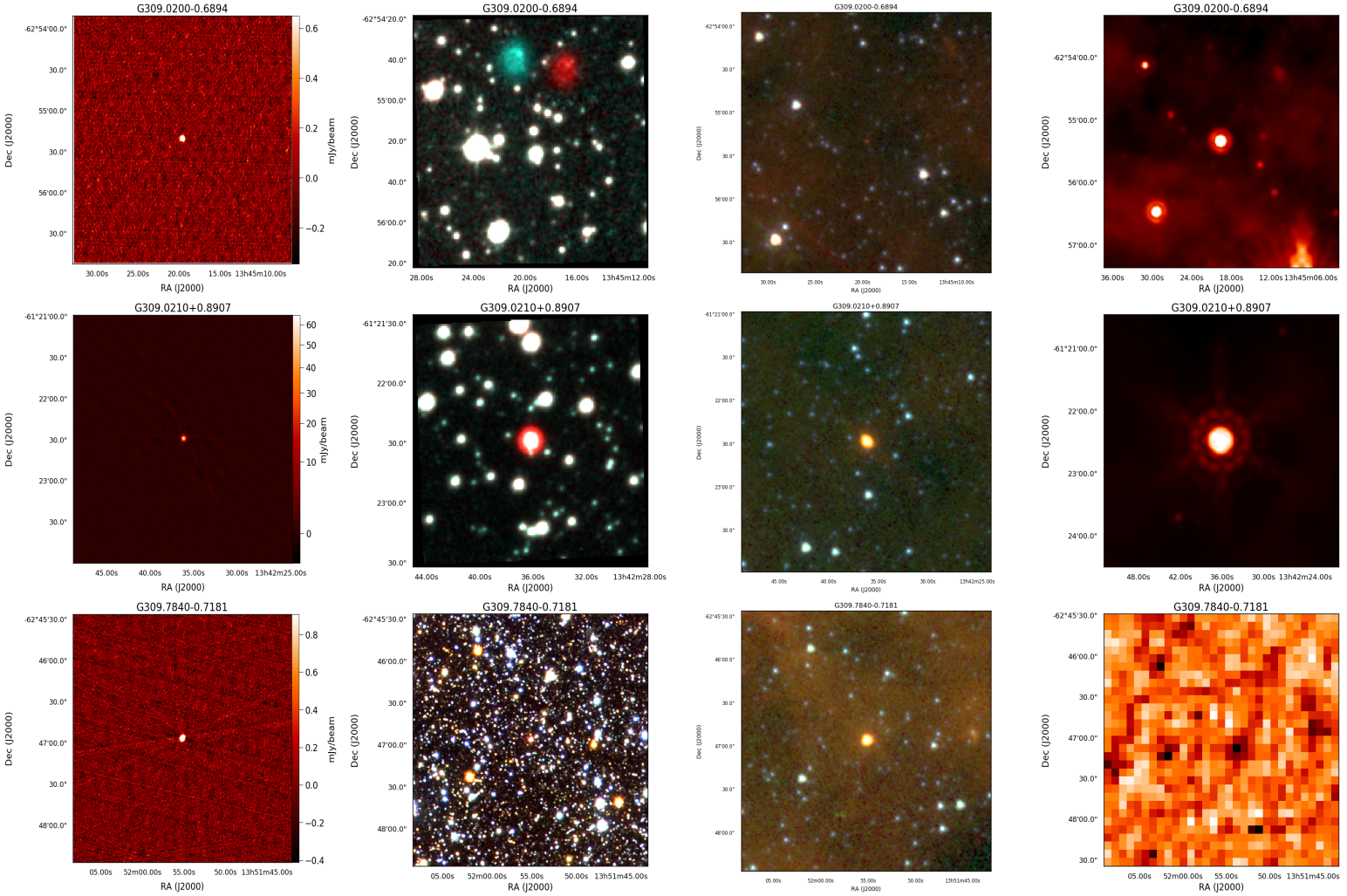

Figure B.24: *Continuation from previous Figure.*

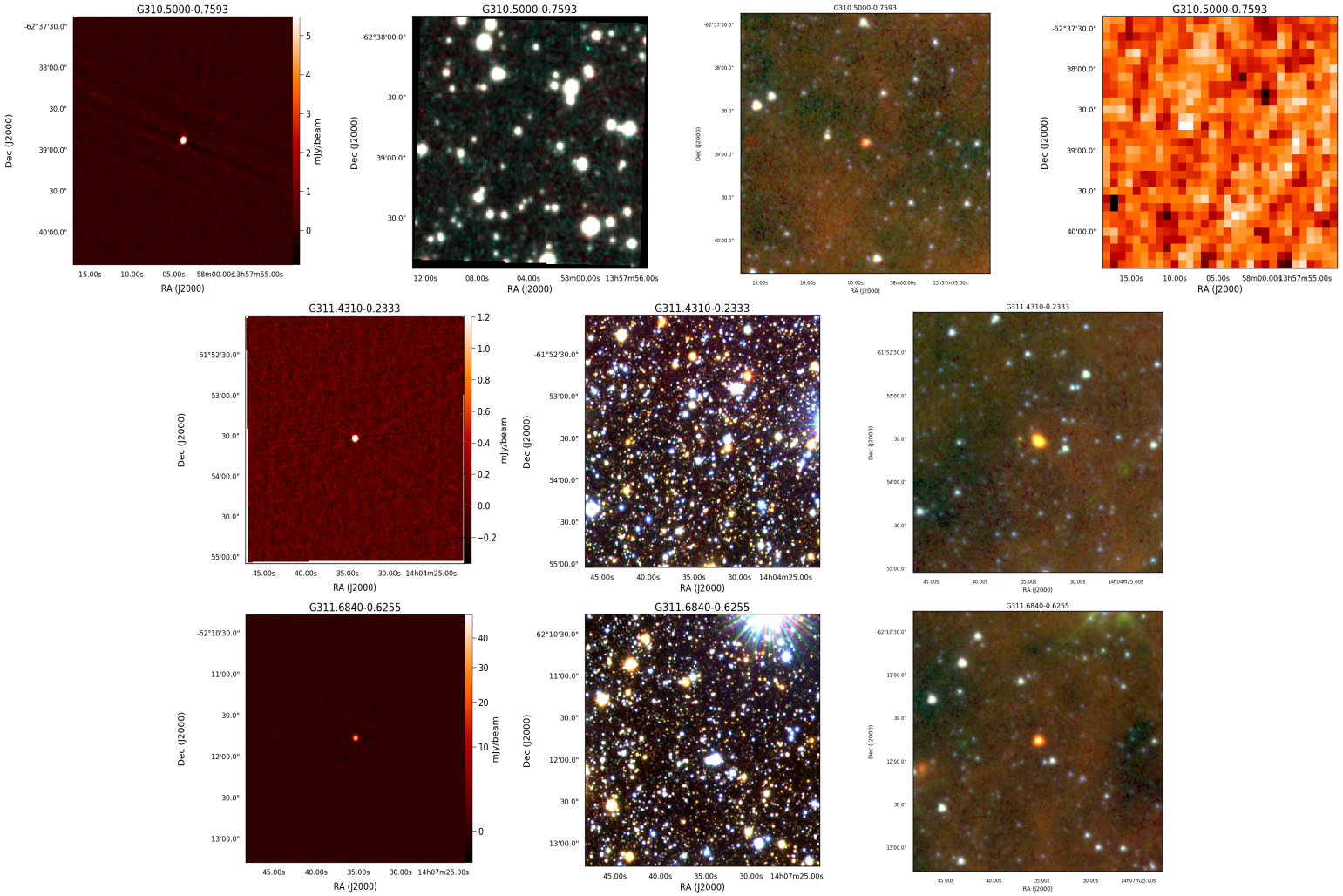

Figure B.25: *Continuation from previous Figure.*

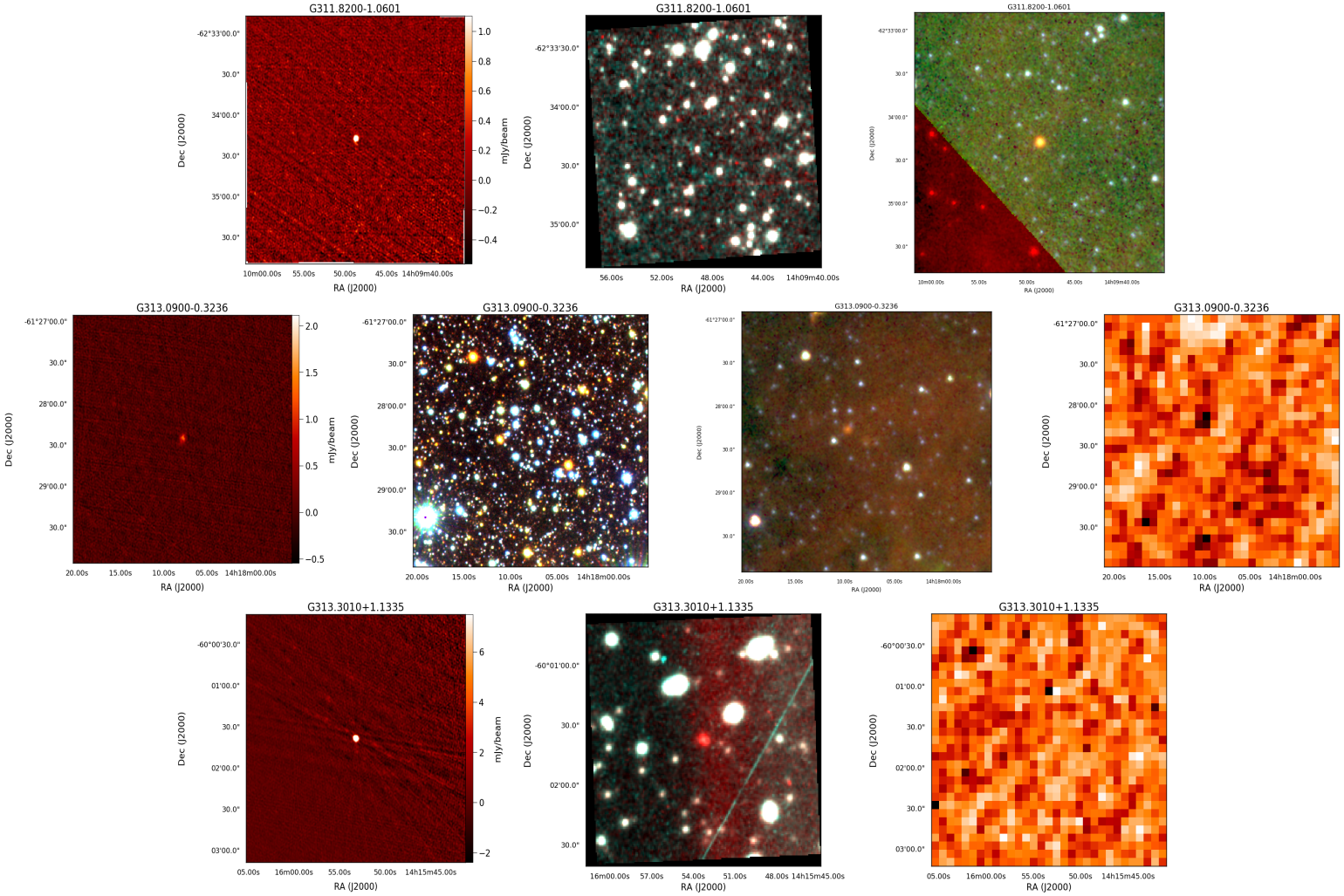

Figure B.26: *Continuation from previous Figure.*

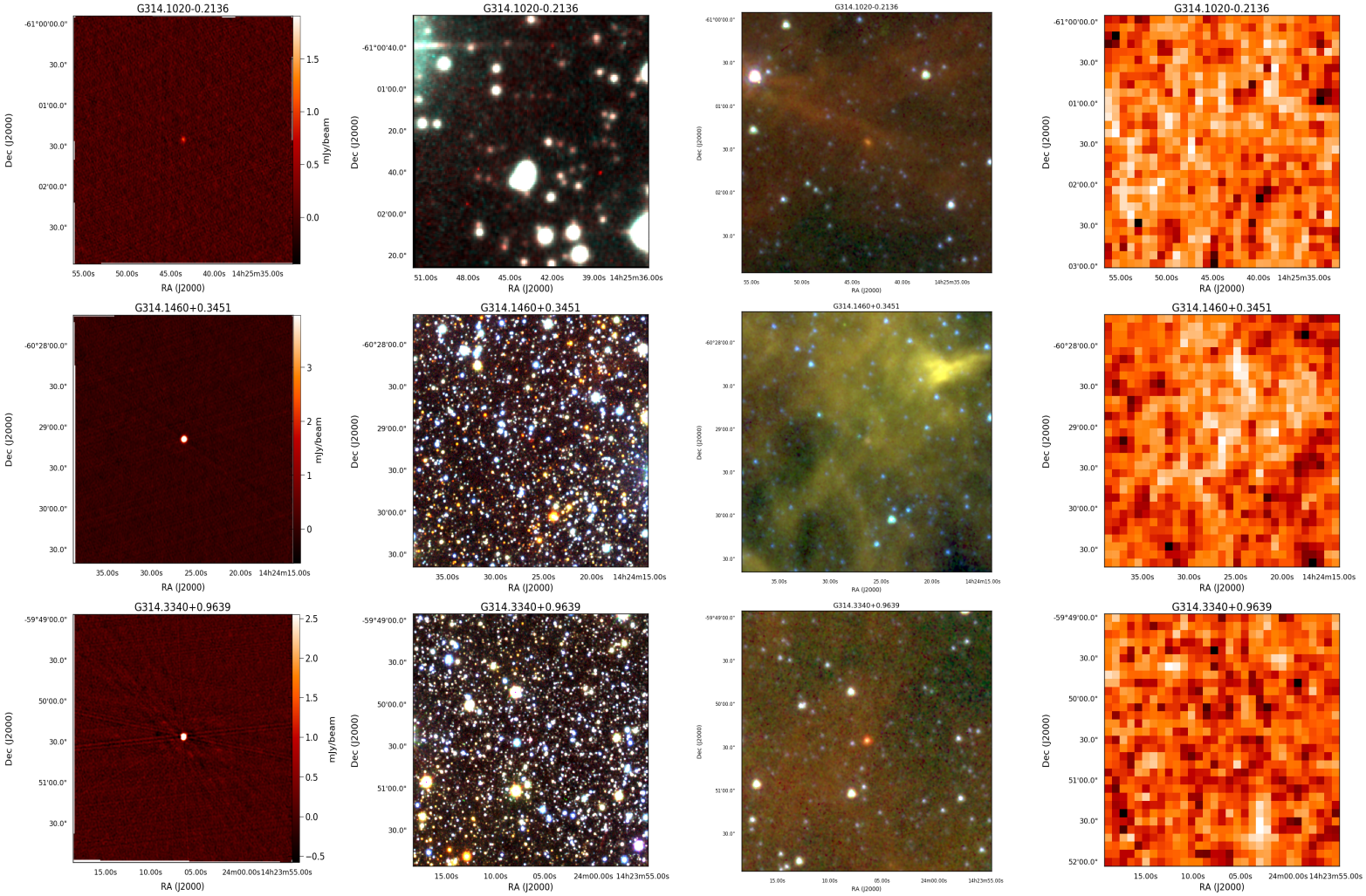

Figure B.27: *Continuation from previous Figure.*

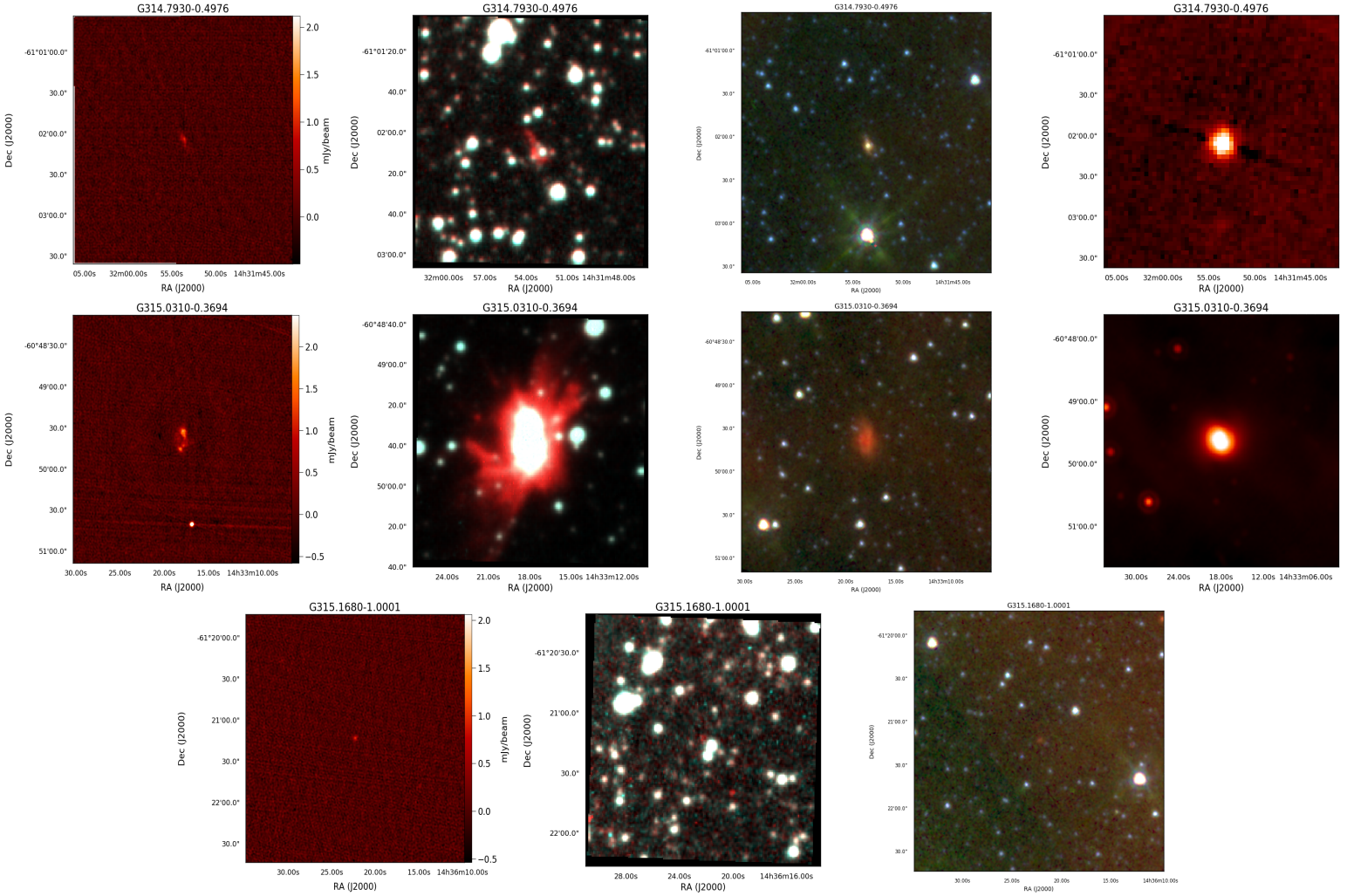

Figure B.28: *Continuation from previous Figure.*

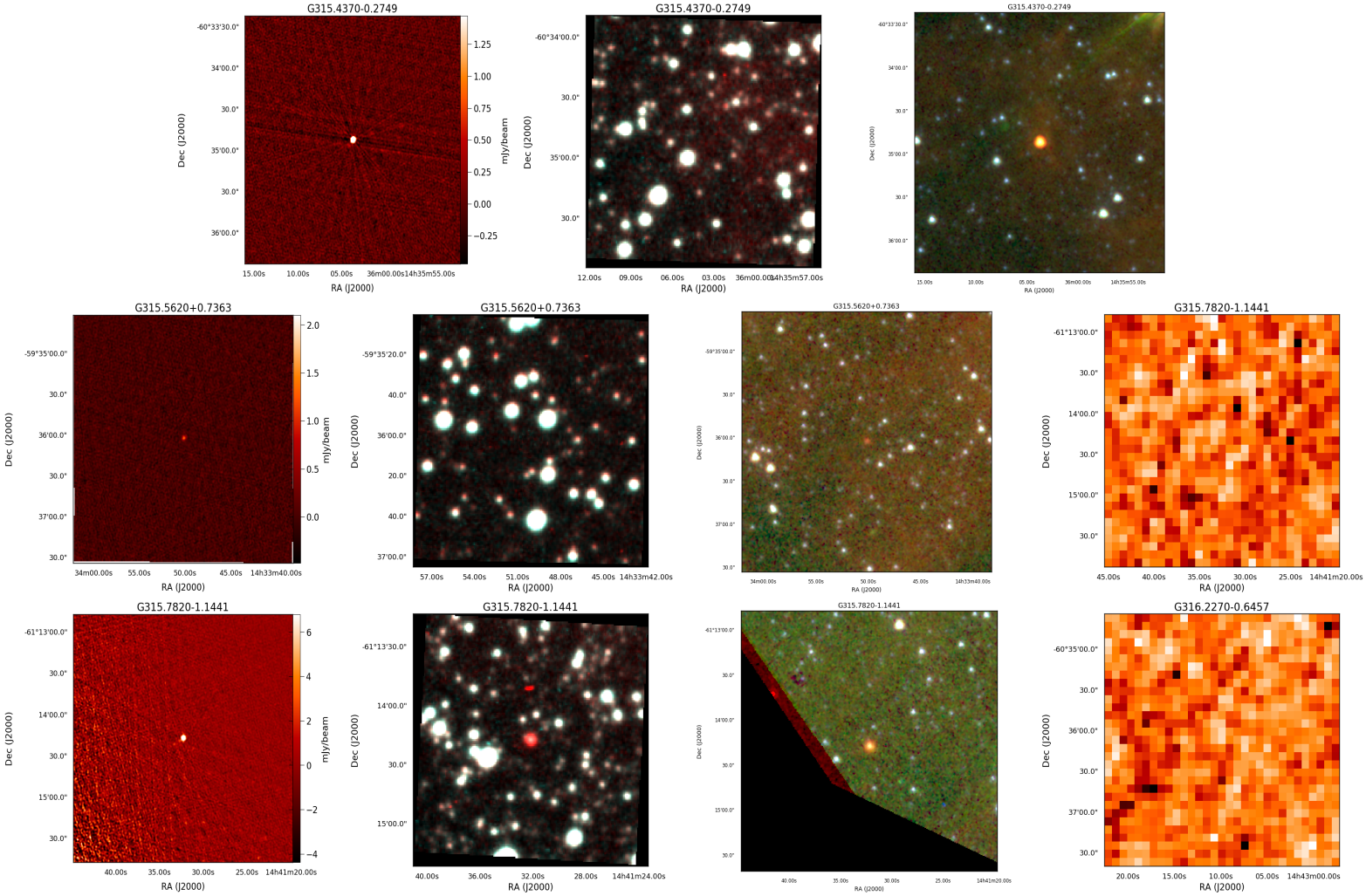

Figure B.29: *Continuation from previous Figure.*

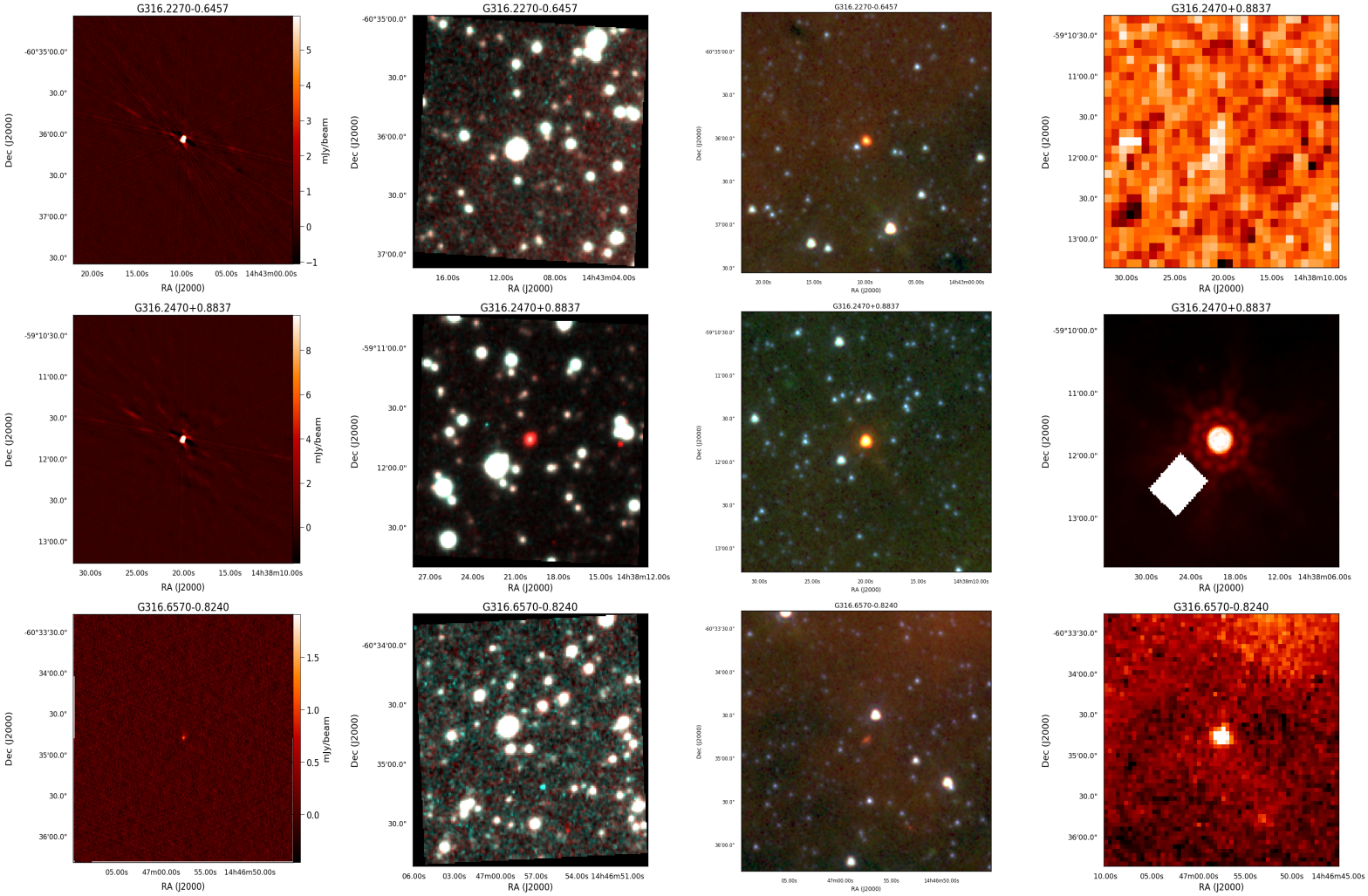

Figure B.30: *Continuation from previous Figure.*

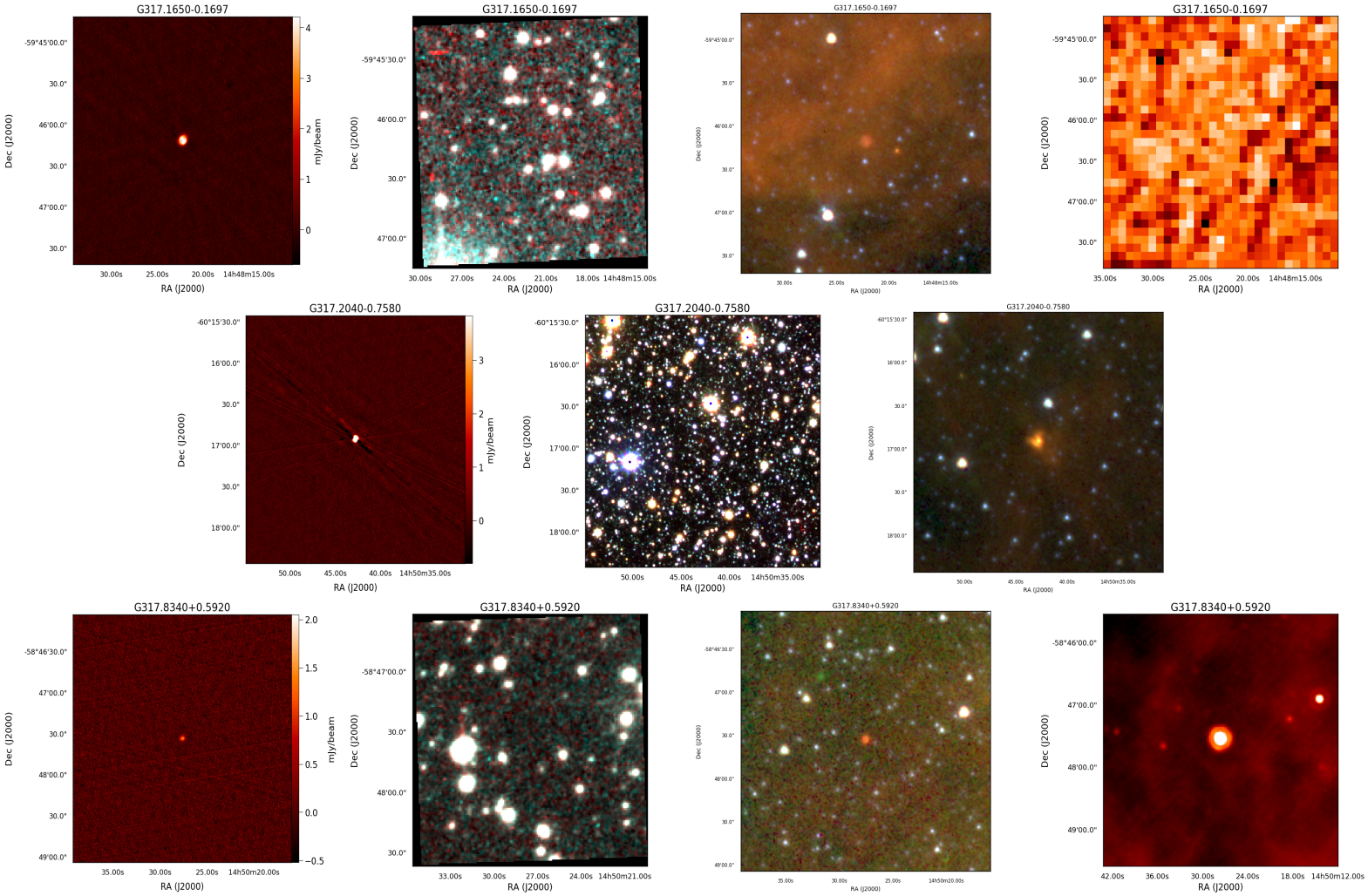

Figure B.31: *Continuation from previous Figure.*

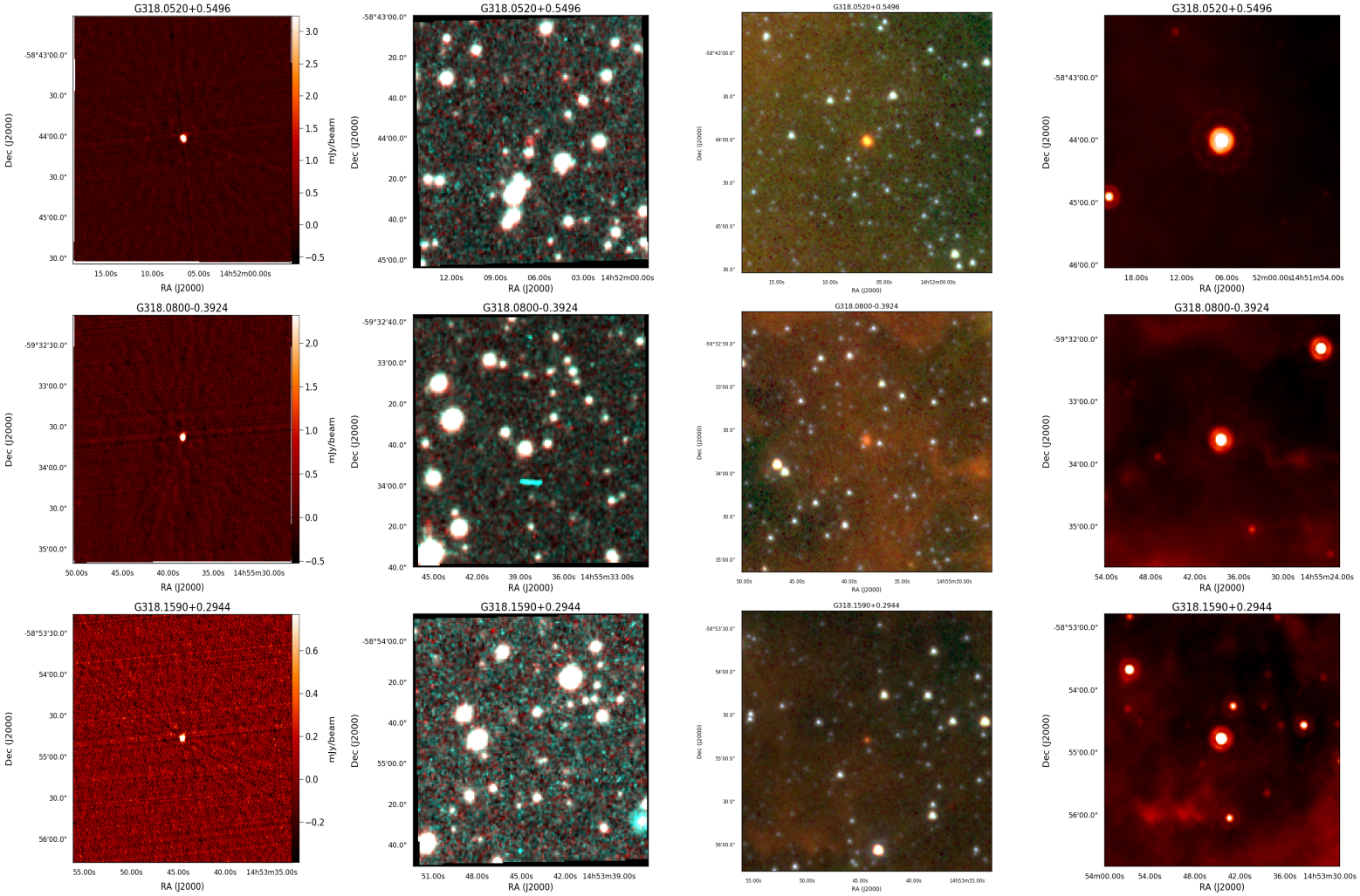

Figure B.32: *Continuation from previous Figure.*

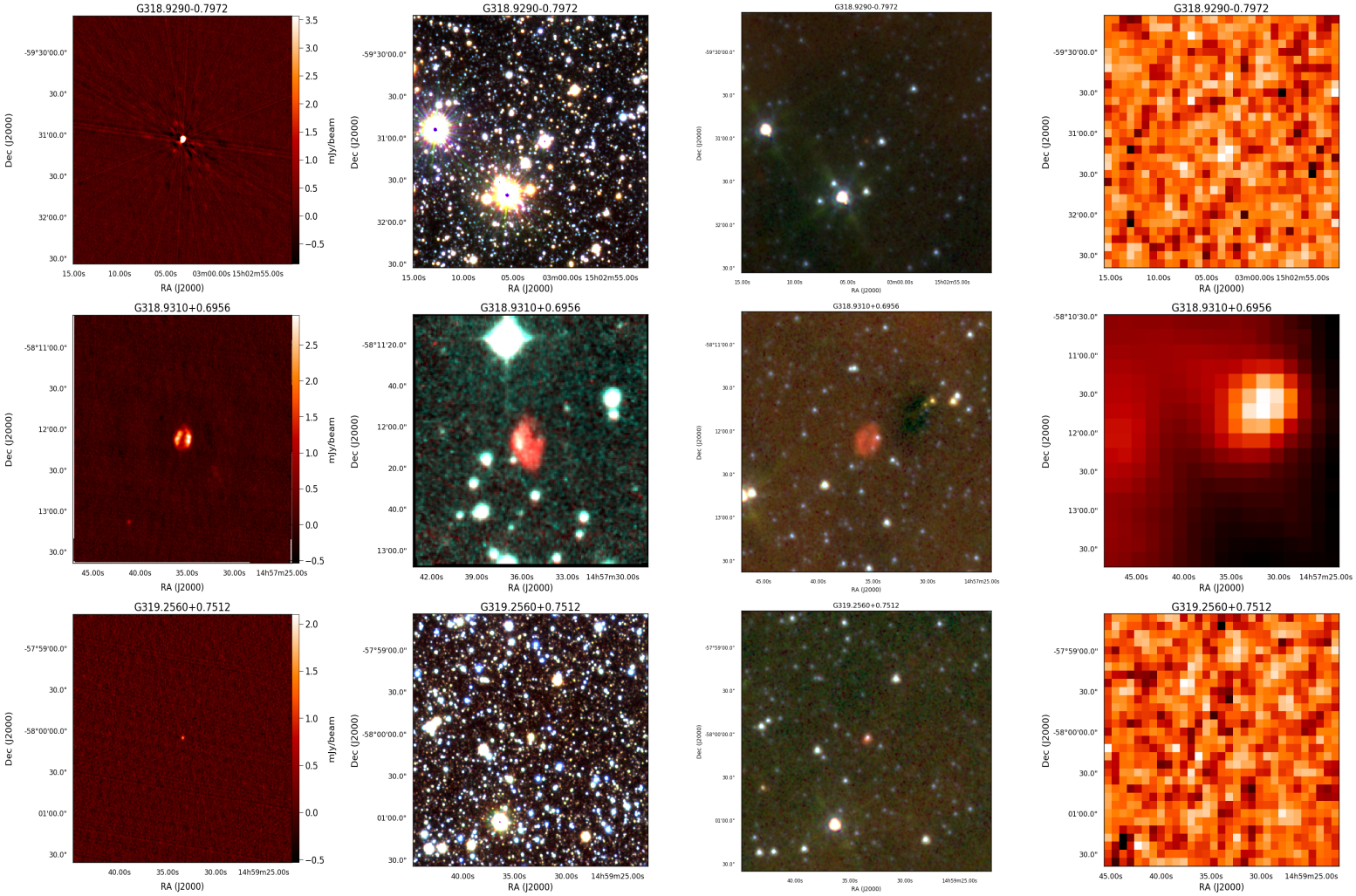

Figure B.33: *Continuation from previous Figure.*

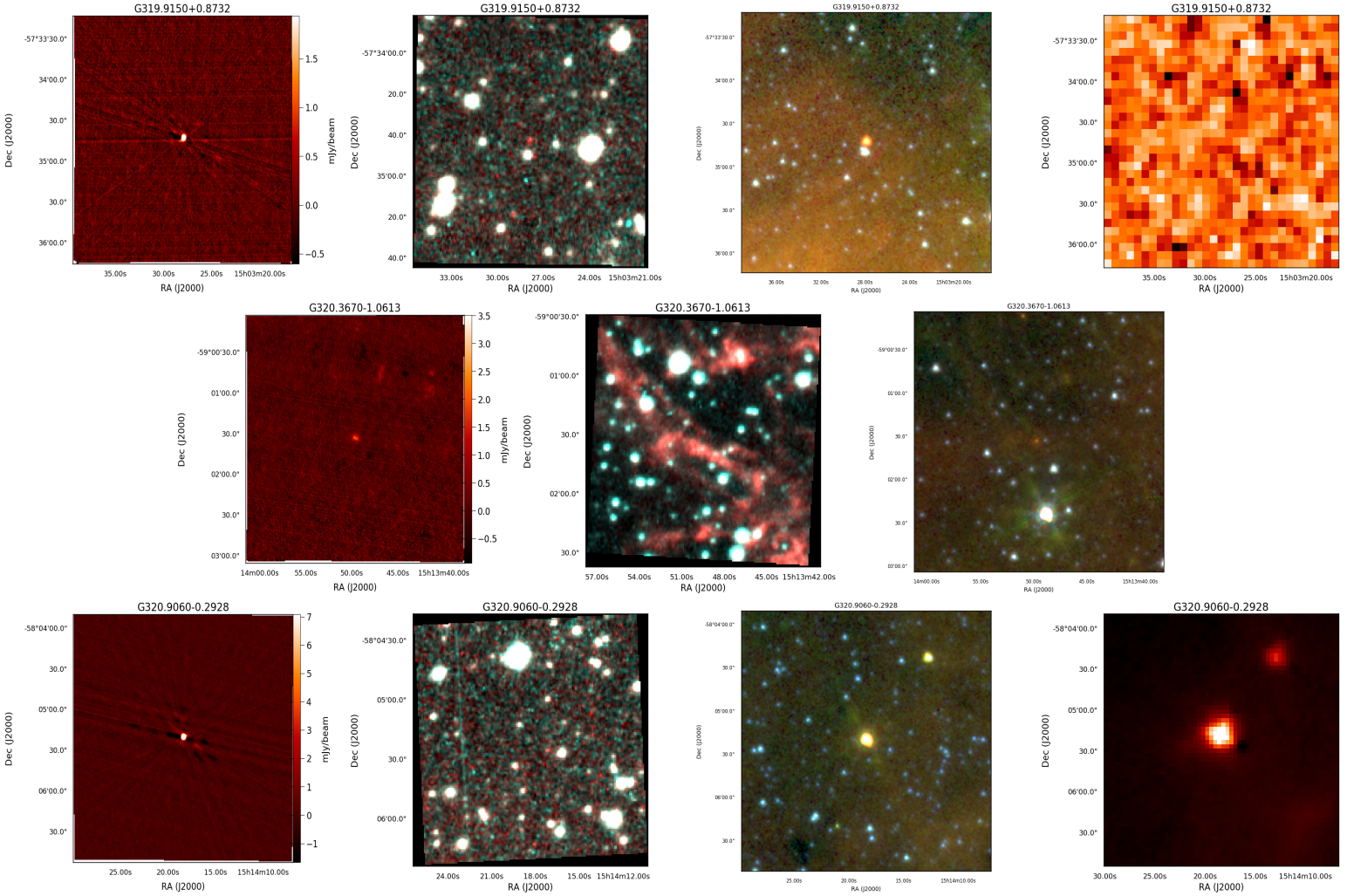

Figure B.34: *Continuation from previous Figure.*

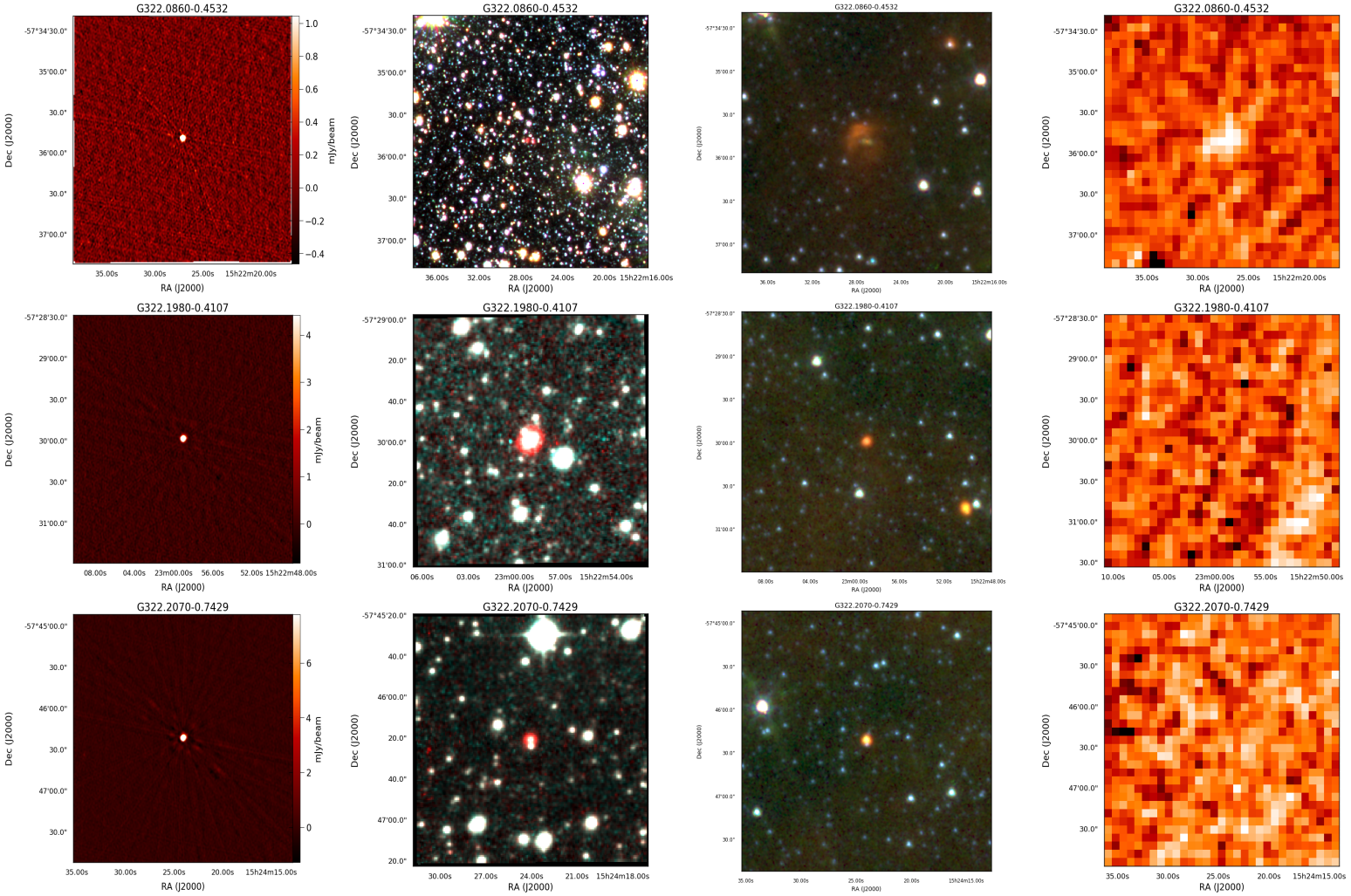

Figure B.35: *Continuation from previous Figure.*

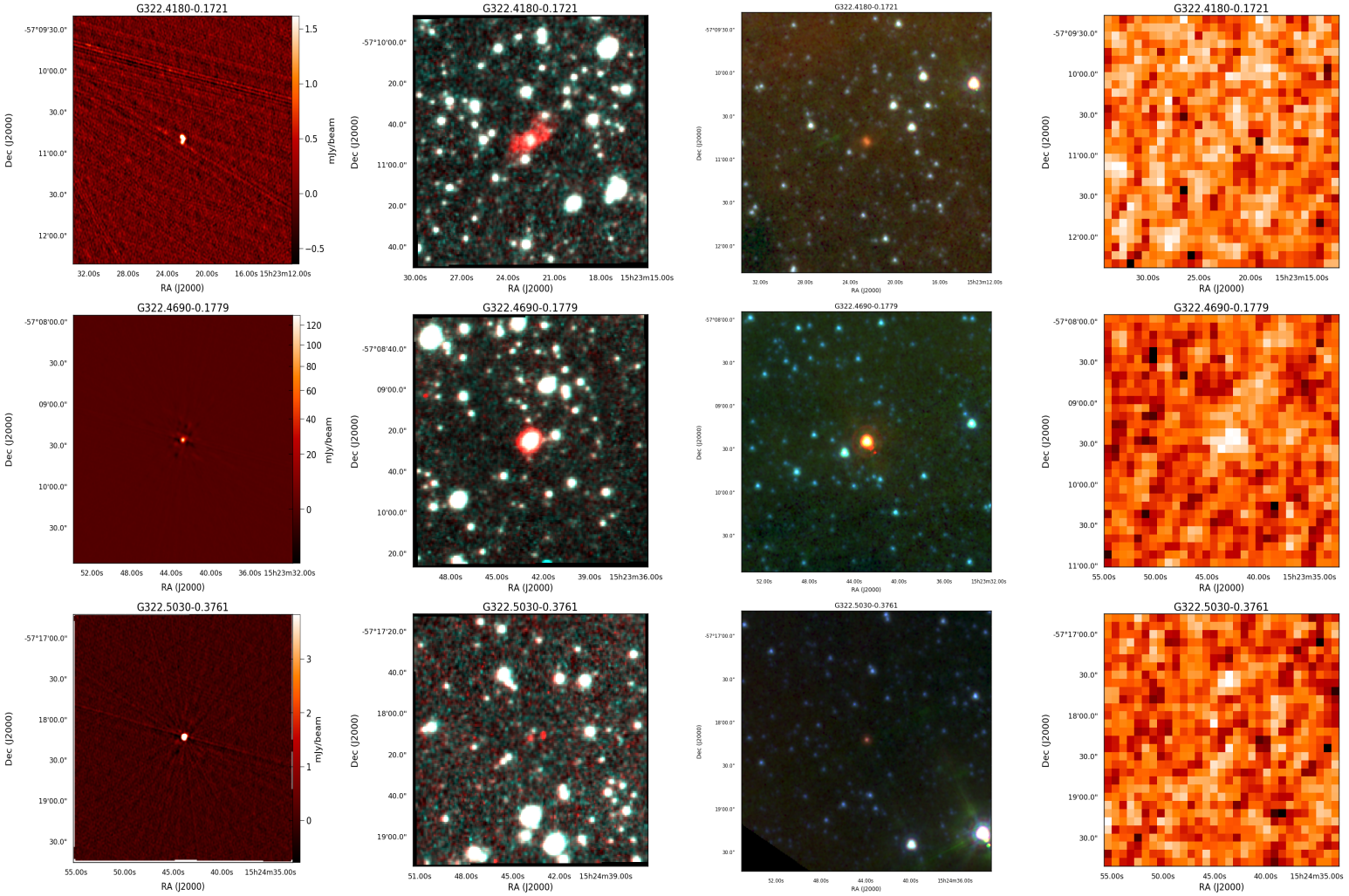

Figure B.36: *Continuation from previous Figure.*

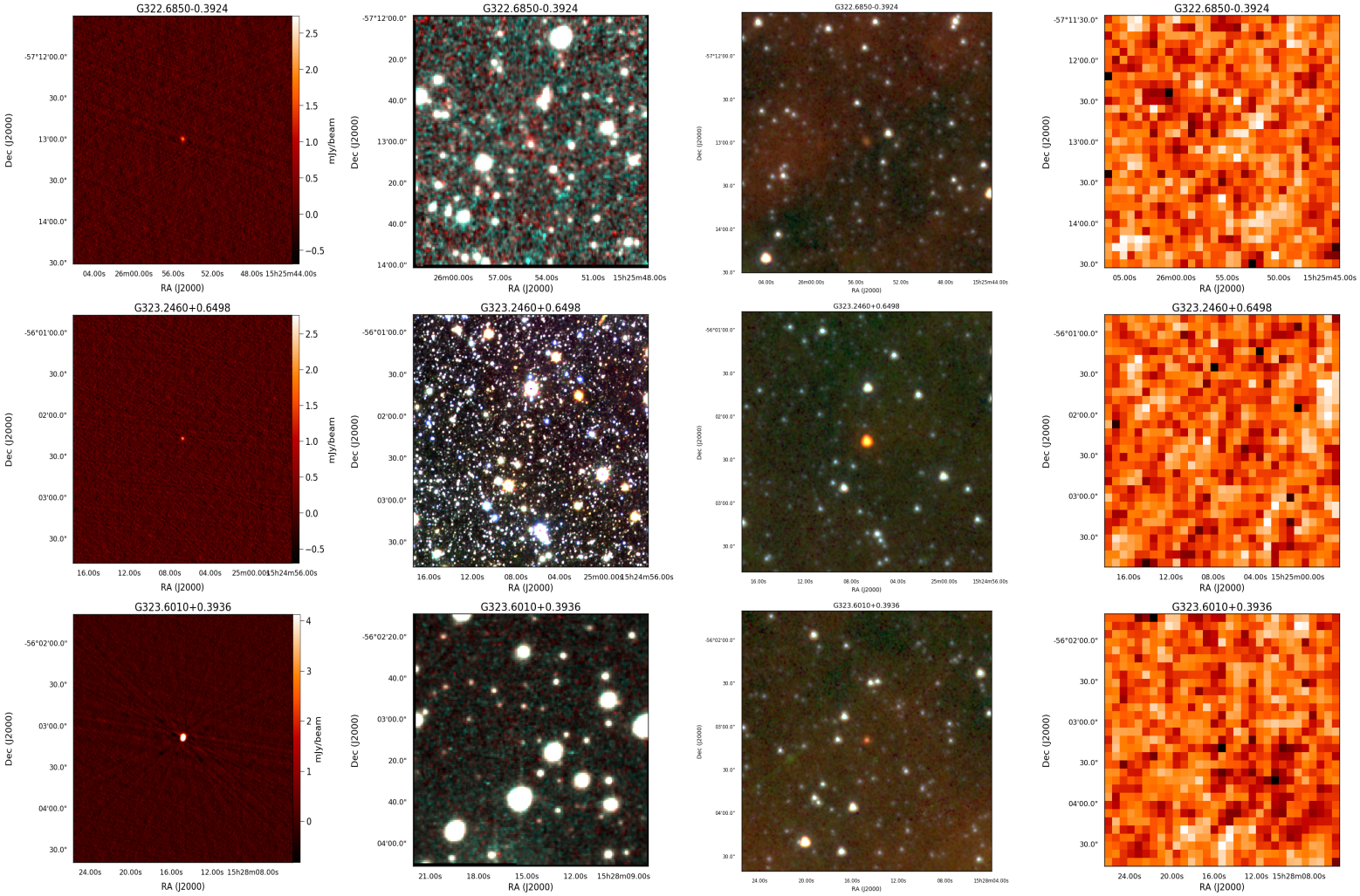

Figure B.37: *Continuation from previous Figure.*

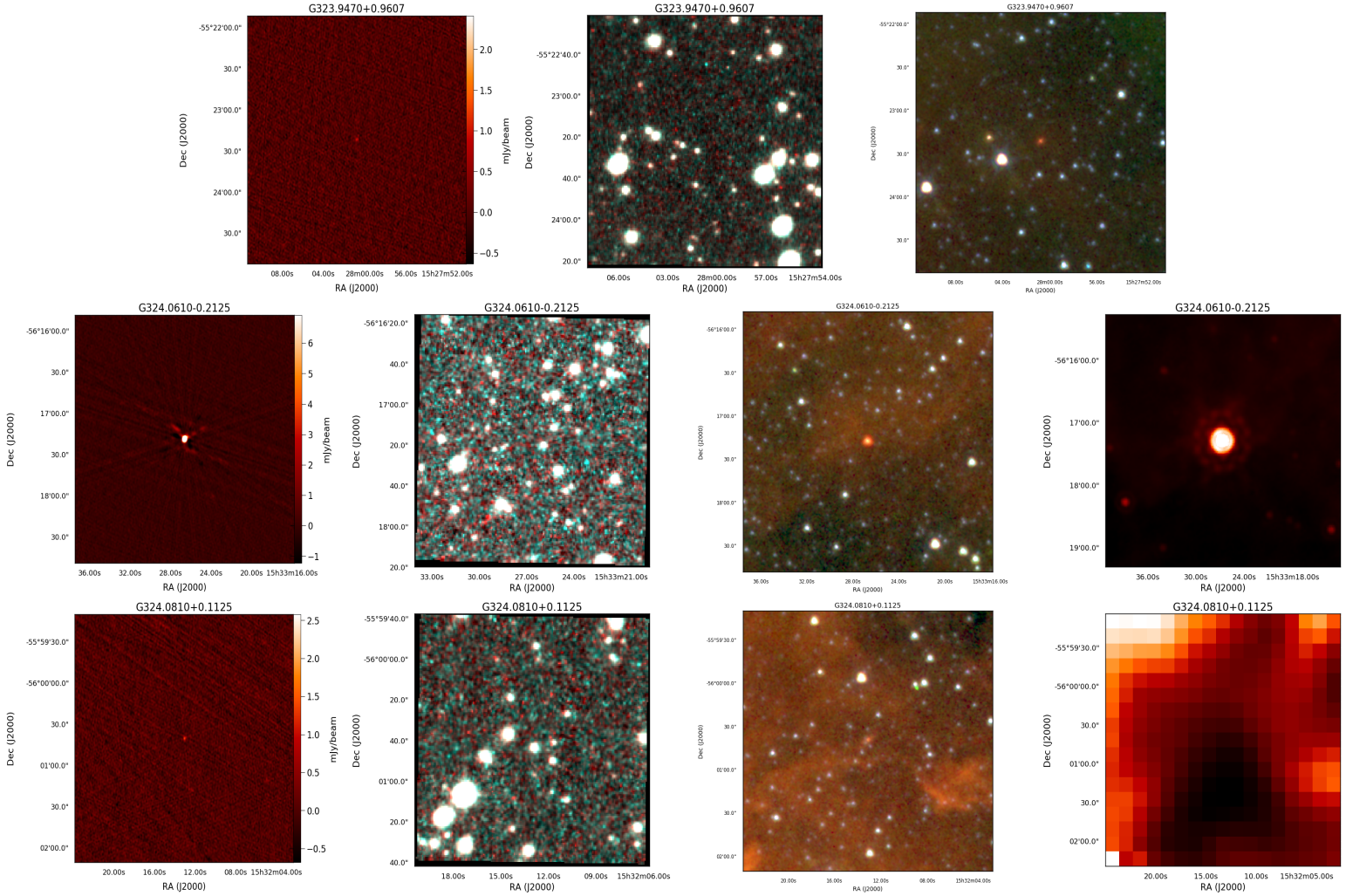

Figure B.38: *Continuation from previous Figure.*

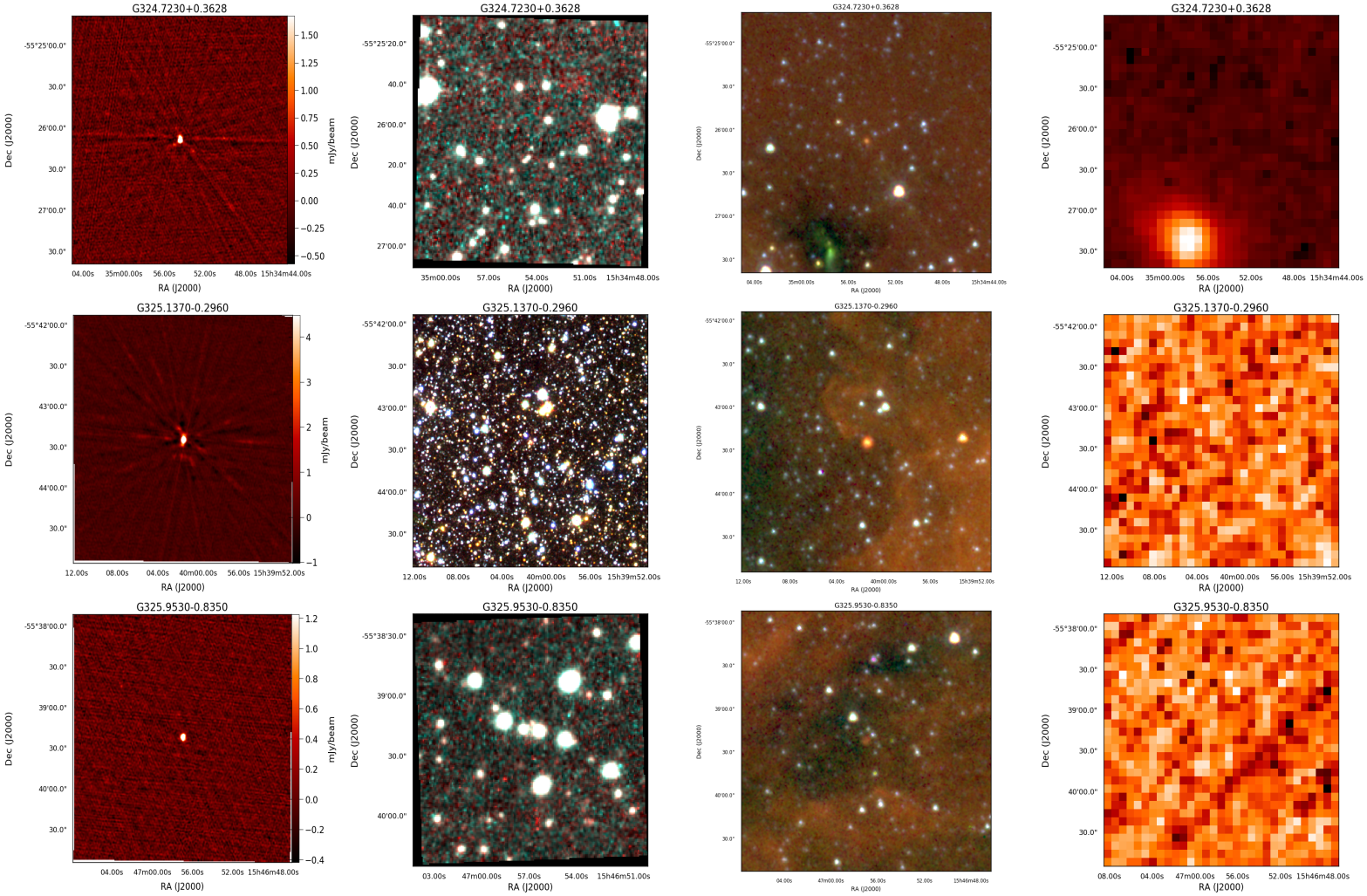

Figure B.39: *Continuation from previous Figure.*

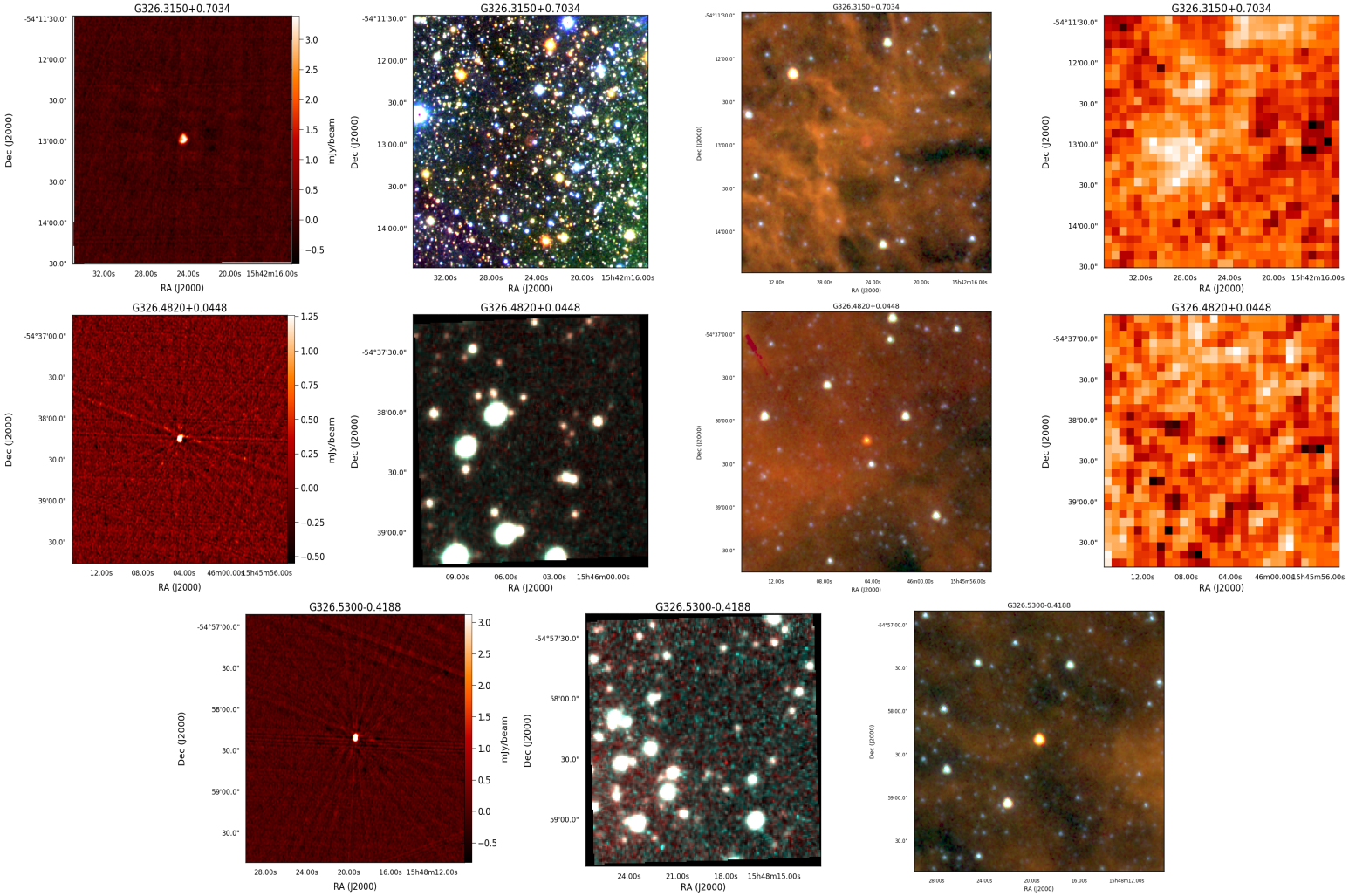

Figure B.40: *Continuation from previous Figure.*

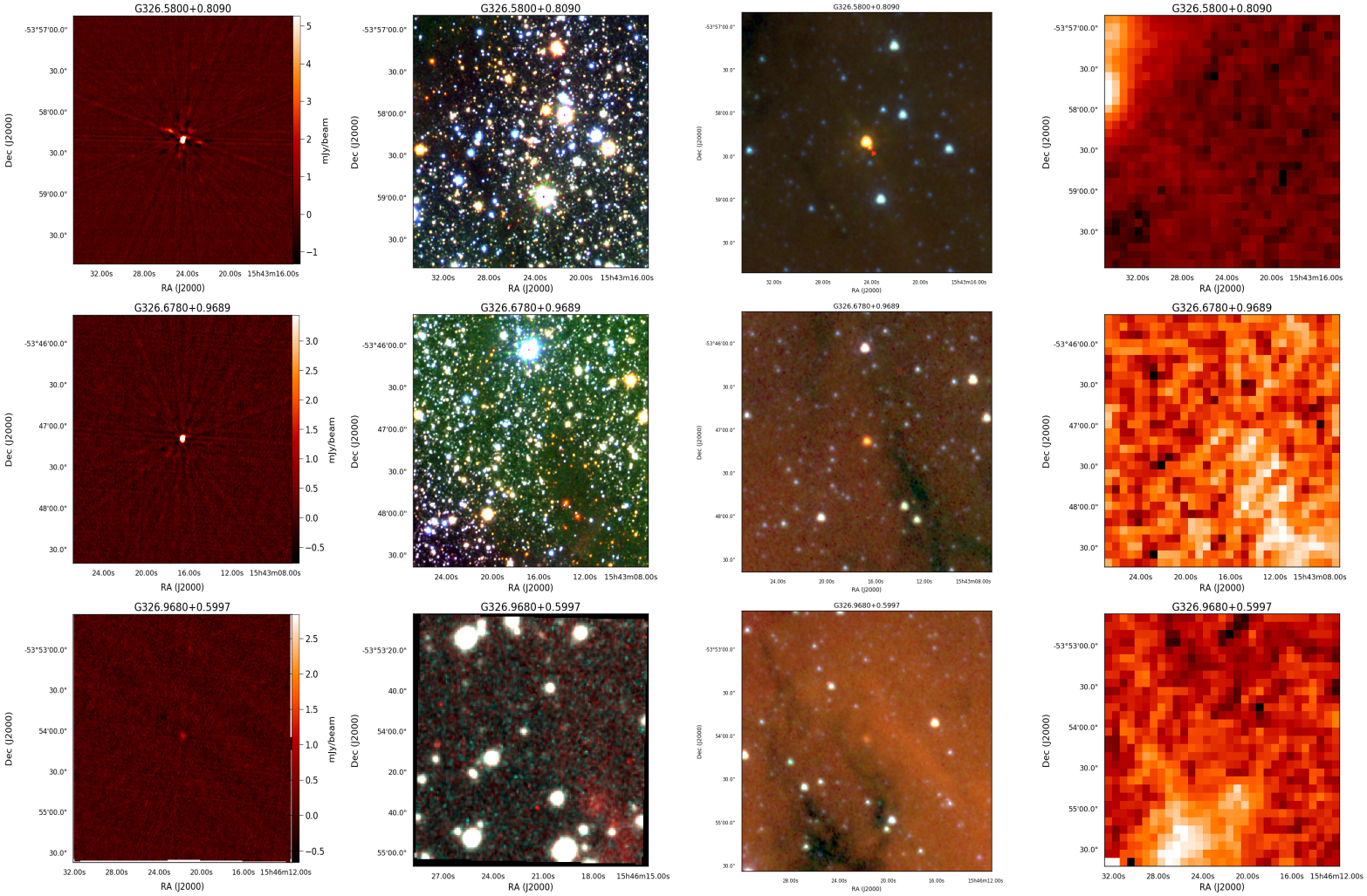

Figure B.41: *Continuation from previous Figure.*

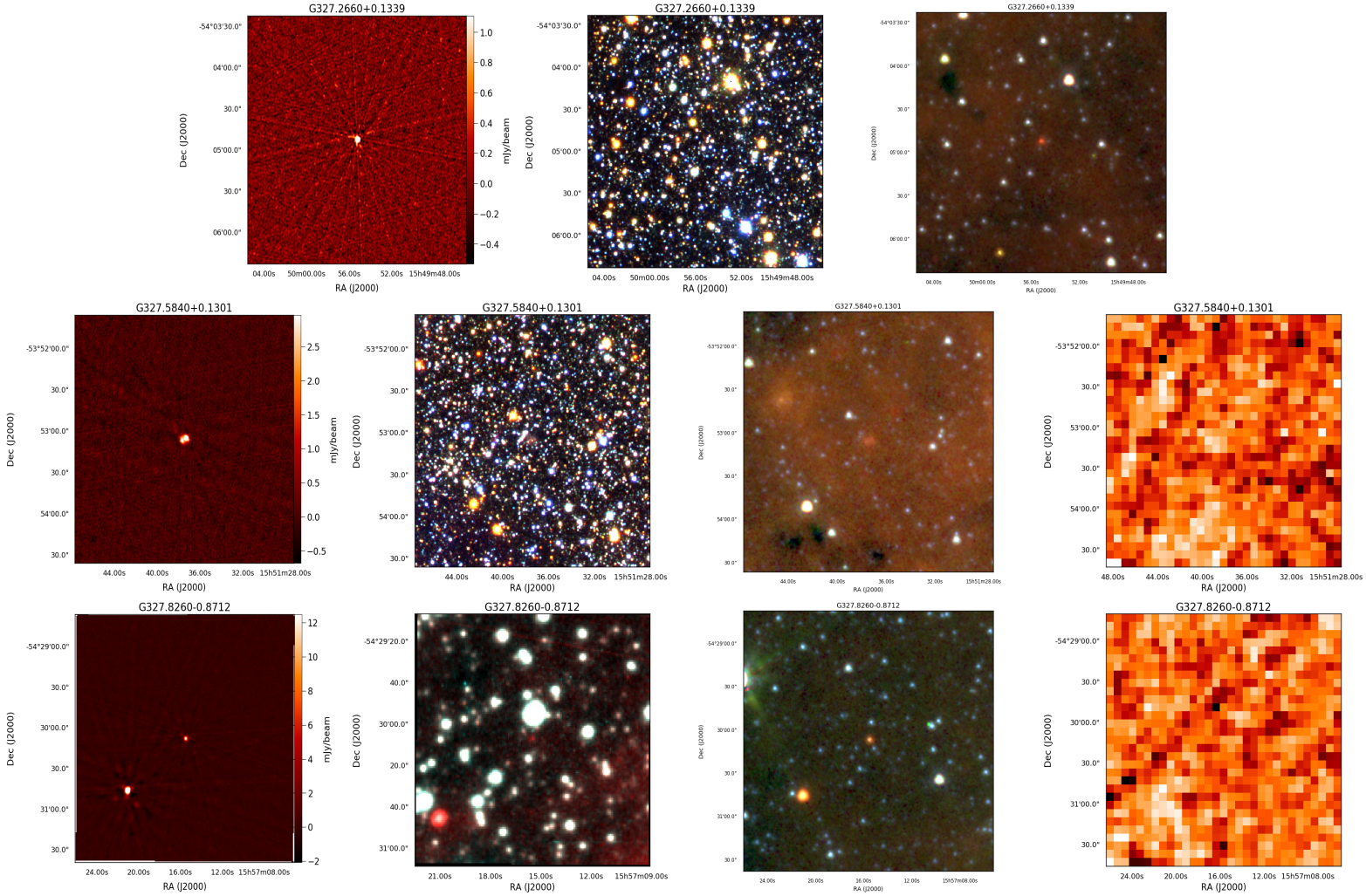

Figure B.42: *Continuation from previous Figure.*

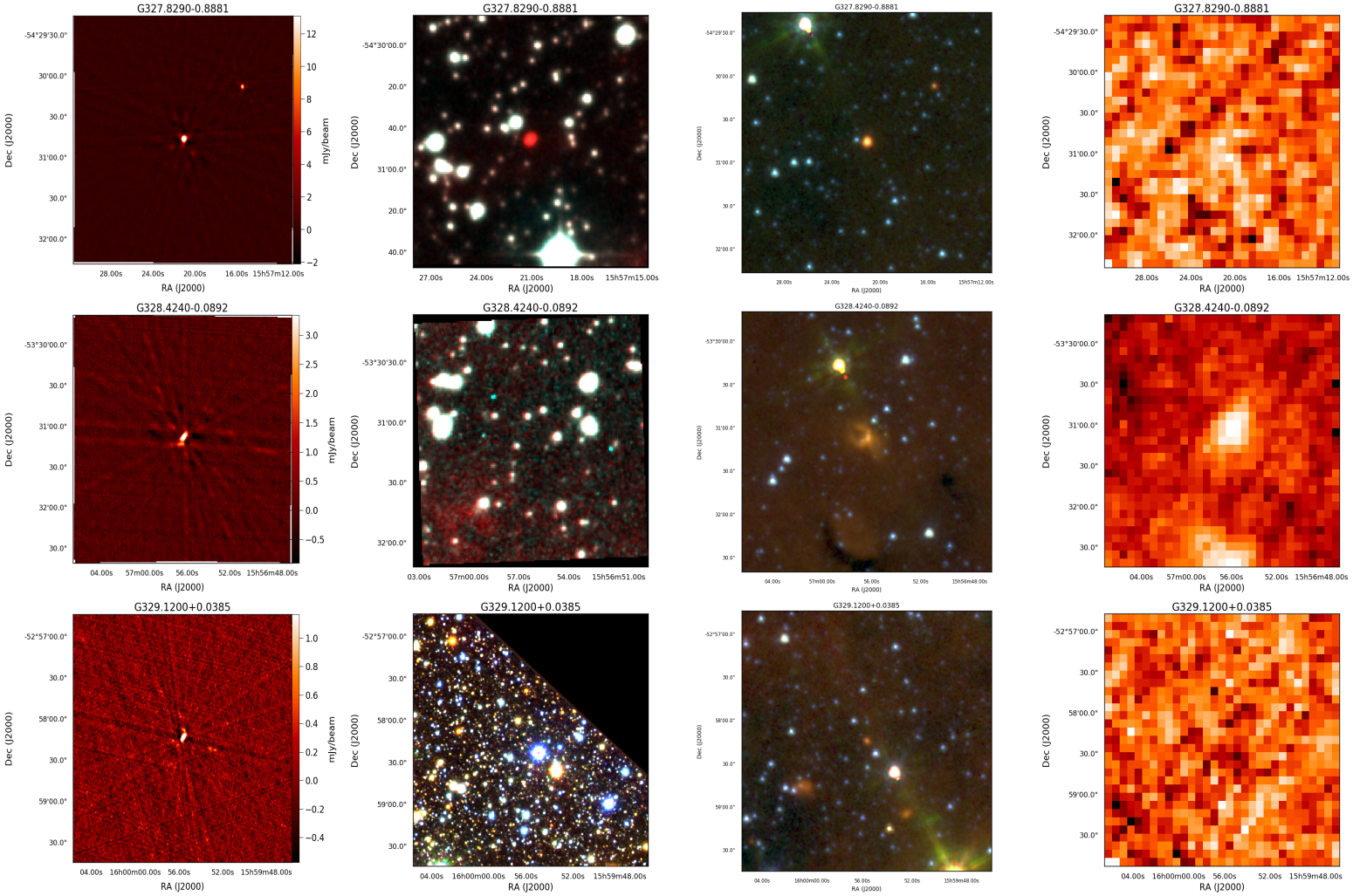

Figure B.43: *Continuation from previous Figure.*

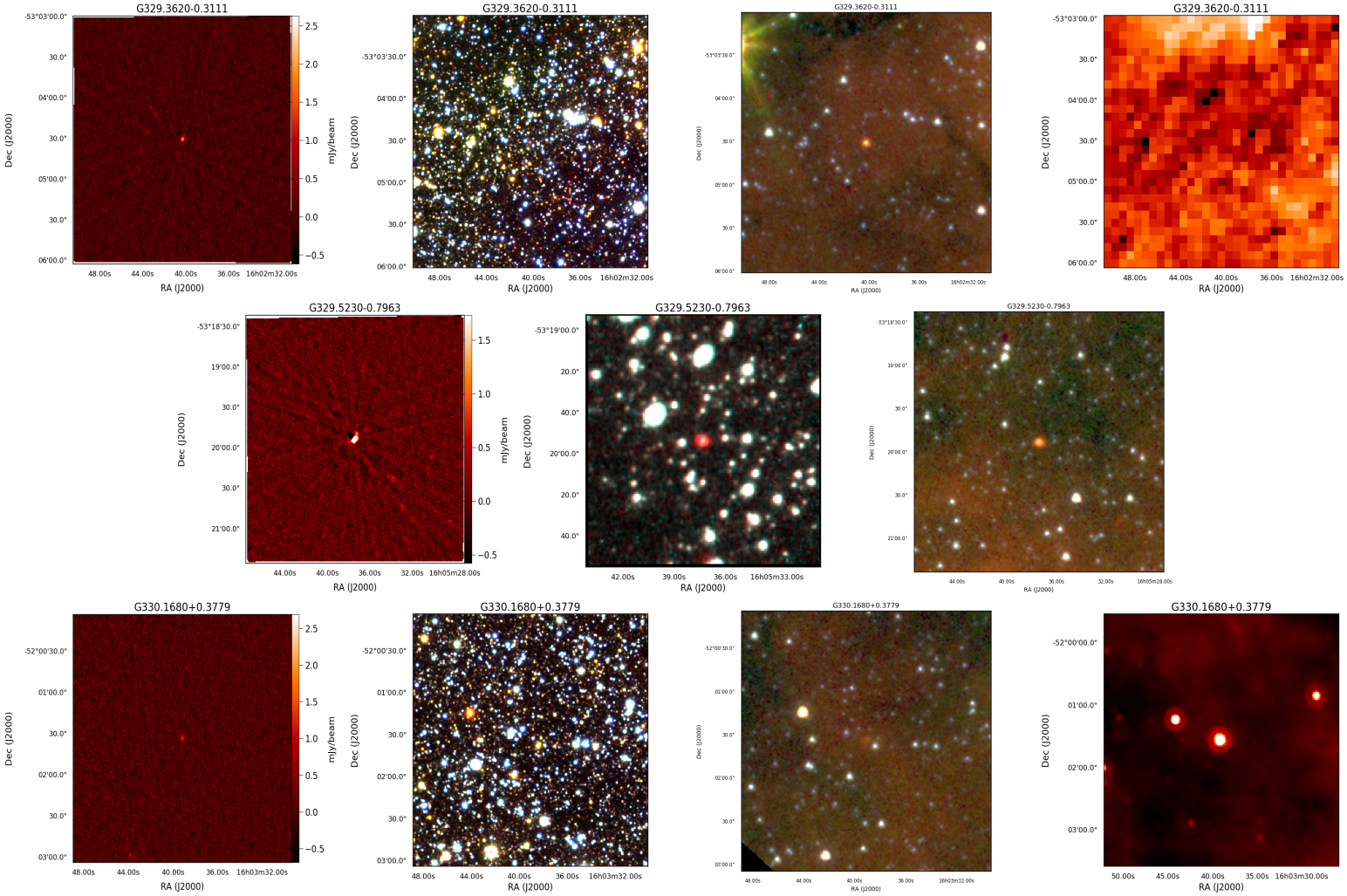

Figure B.44: *Continuation from previous Figure.*

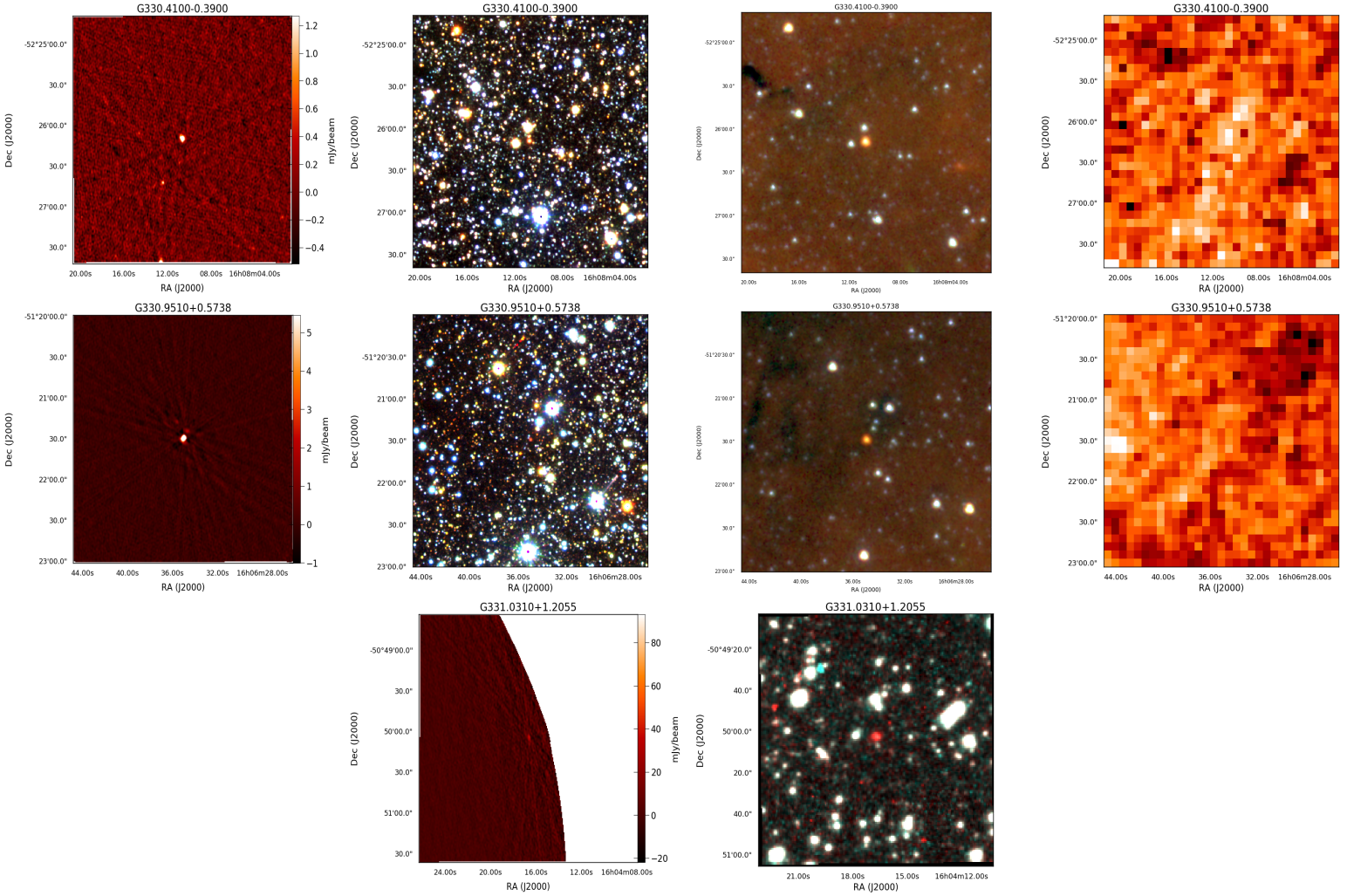

Figure B.45: *Continuation from previous Figure.*

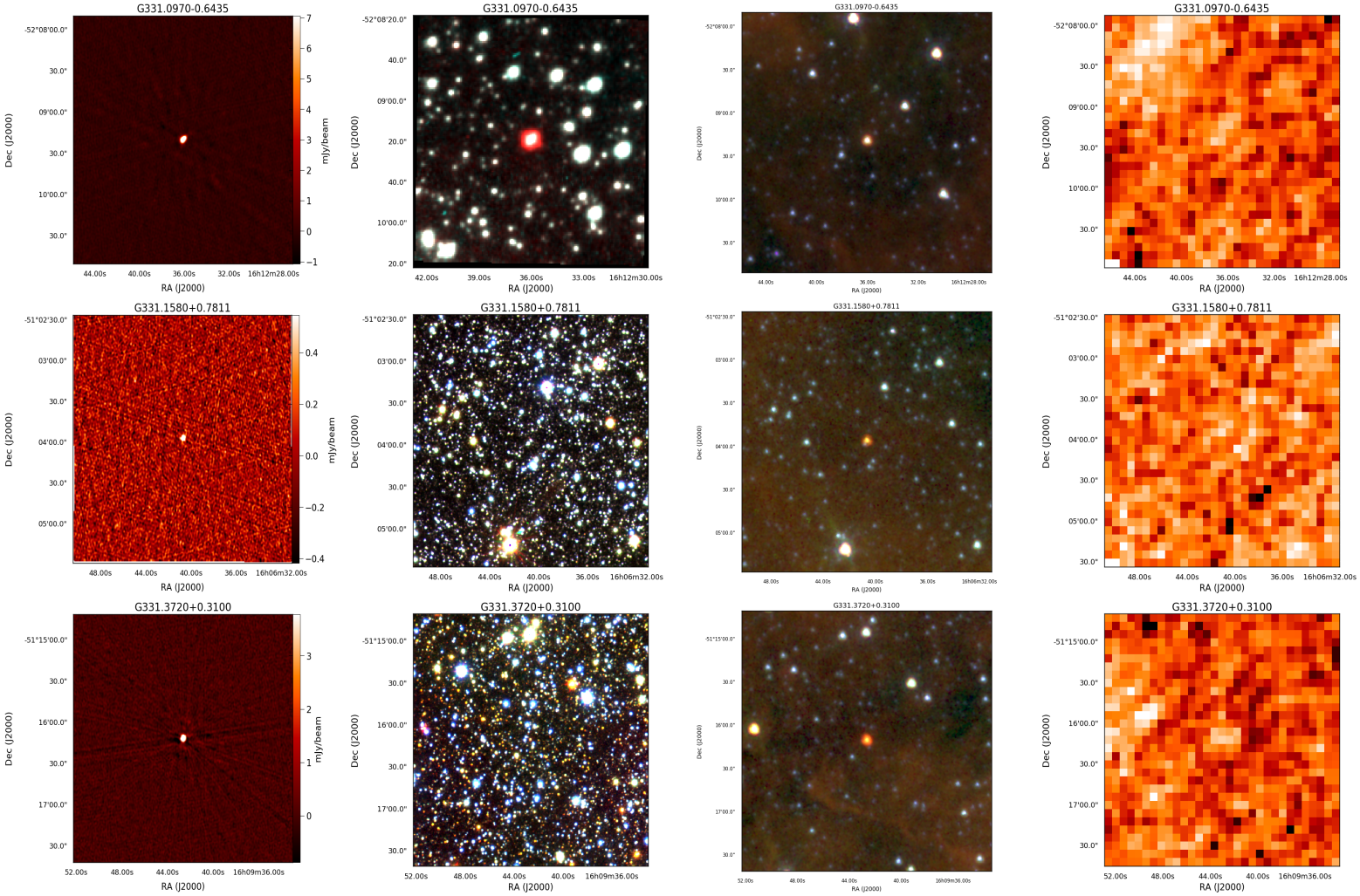

Figure B.46: *Continuation from previous Figure.*

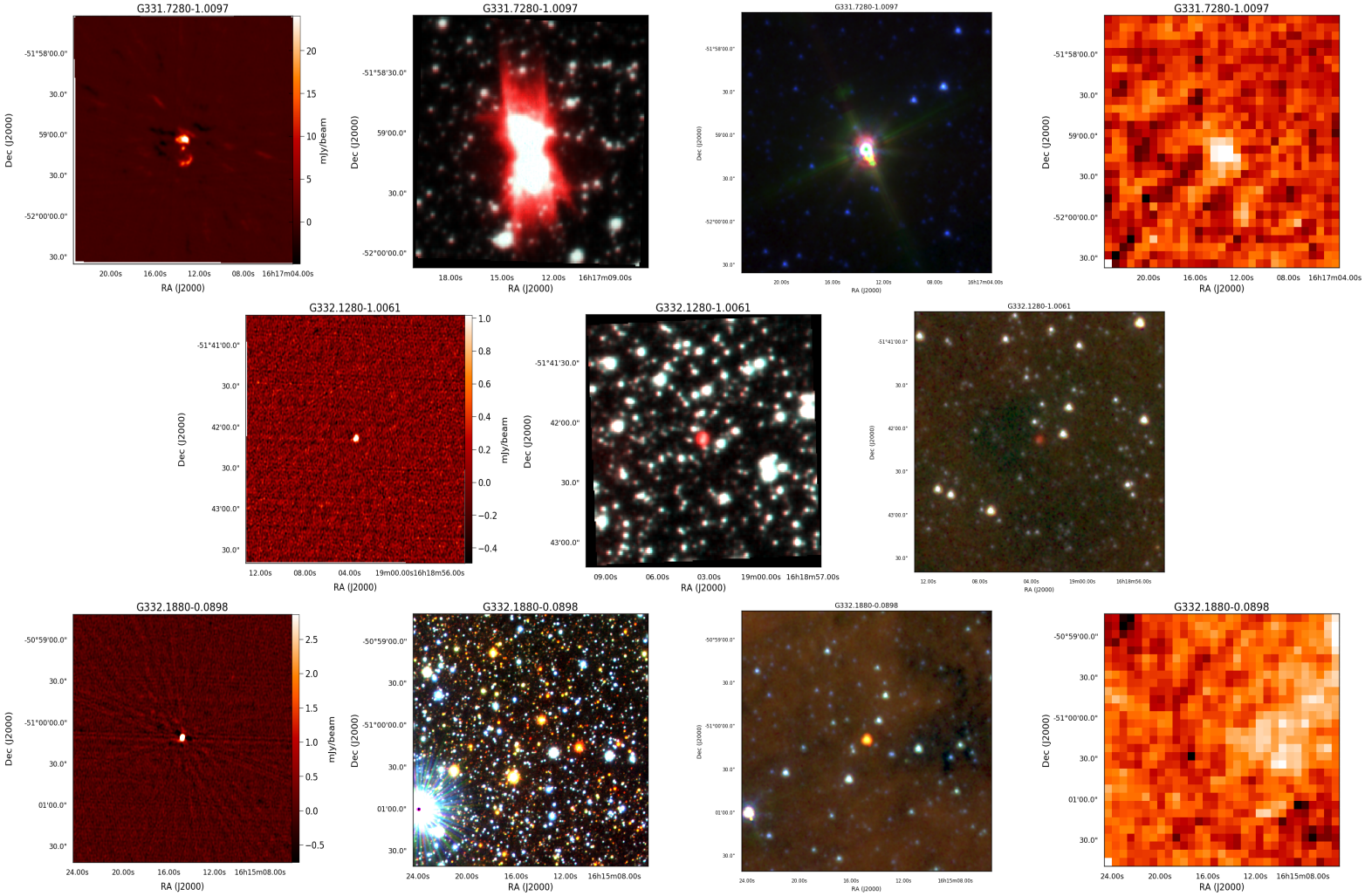

Figure B.47: *Continuation from previous Figure.*

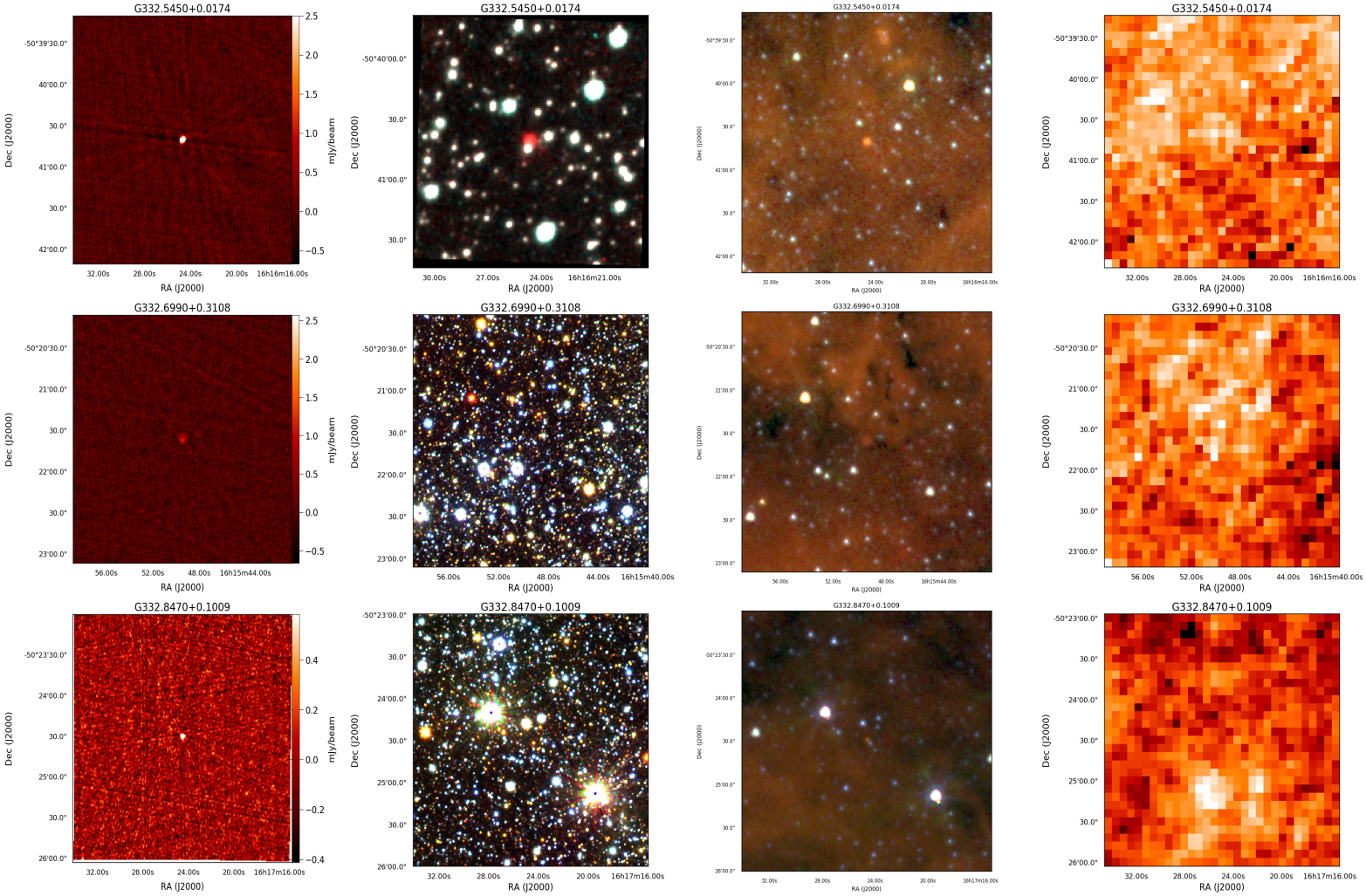

Figure B.48: *Continuation from previous Figure.*

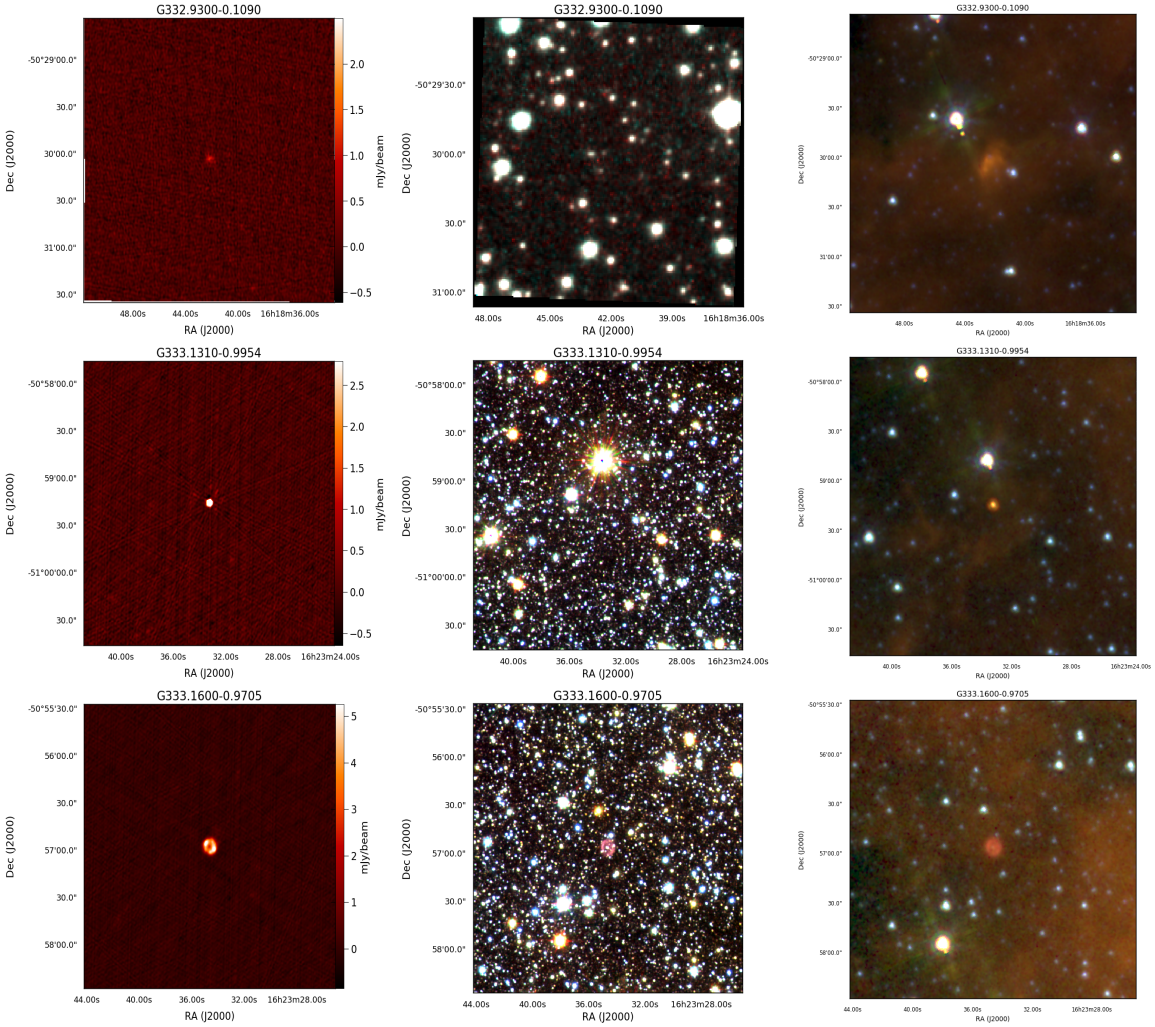

Figure B.49: *Continuation from previous Figure.*

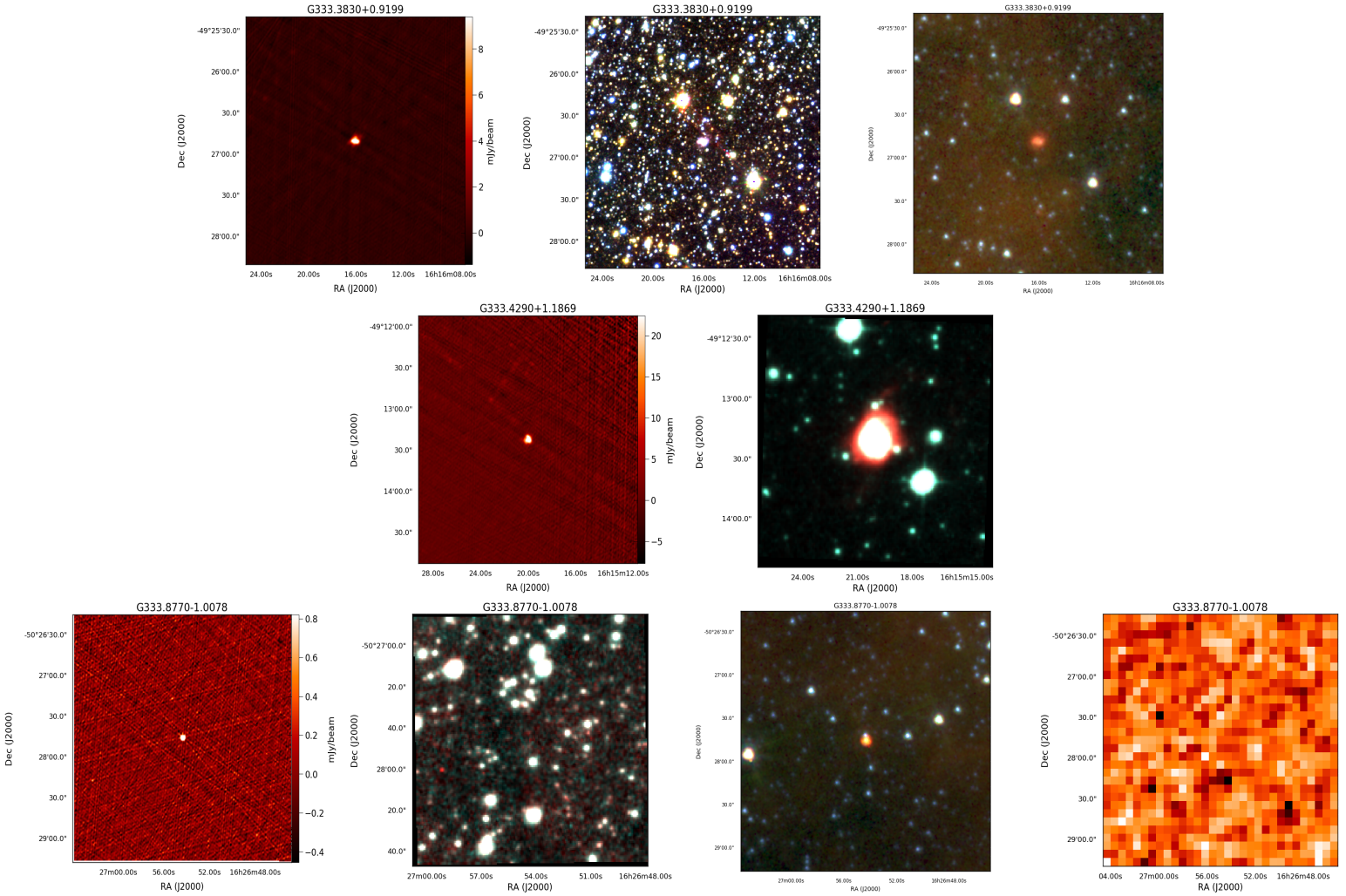

Figure B.50: *Continuation from previous Figure.*

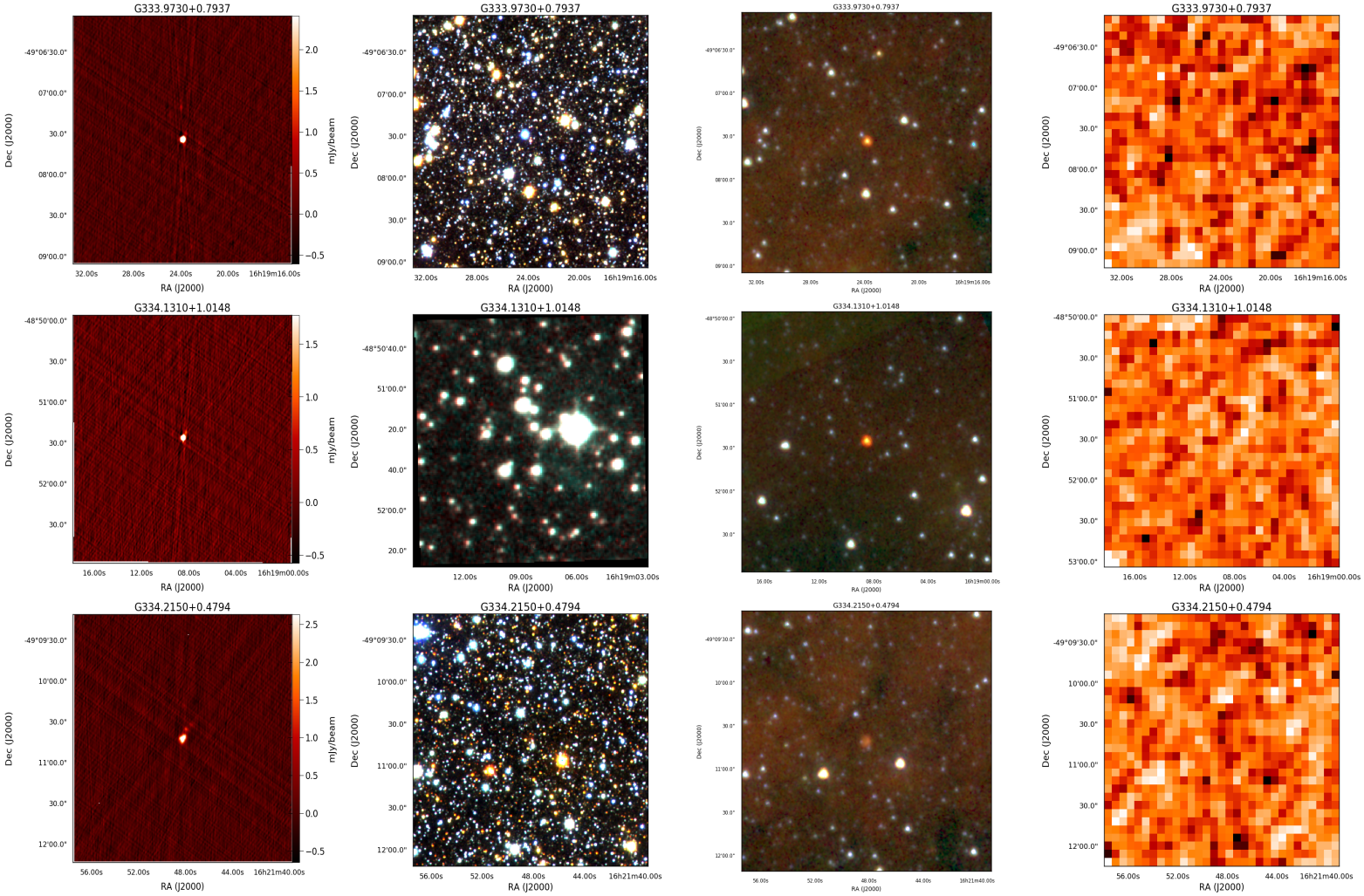

Figure B.51: *Continuation from previous Figure.*

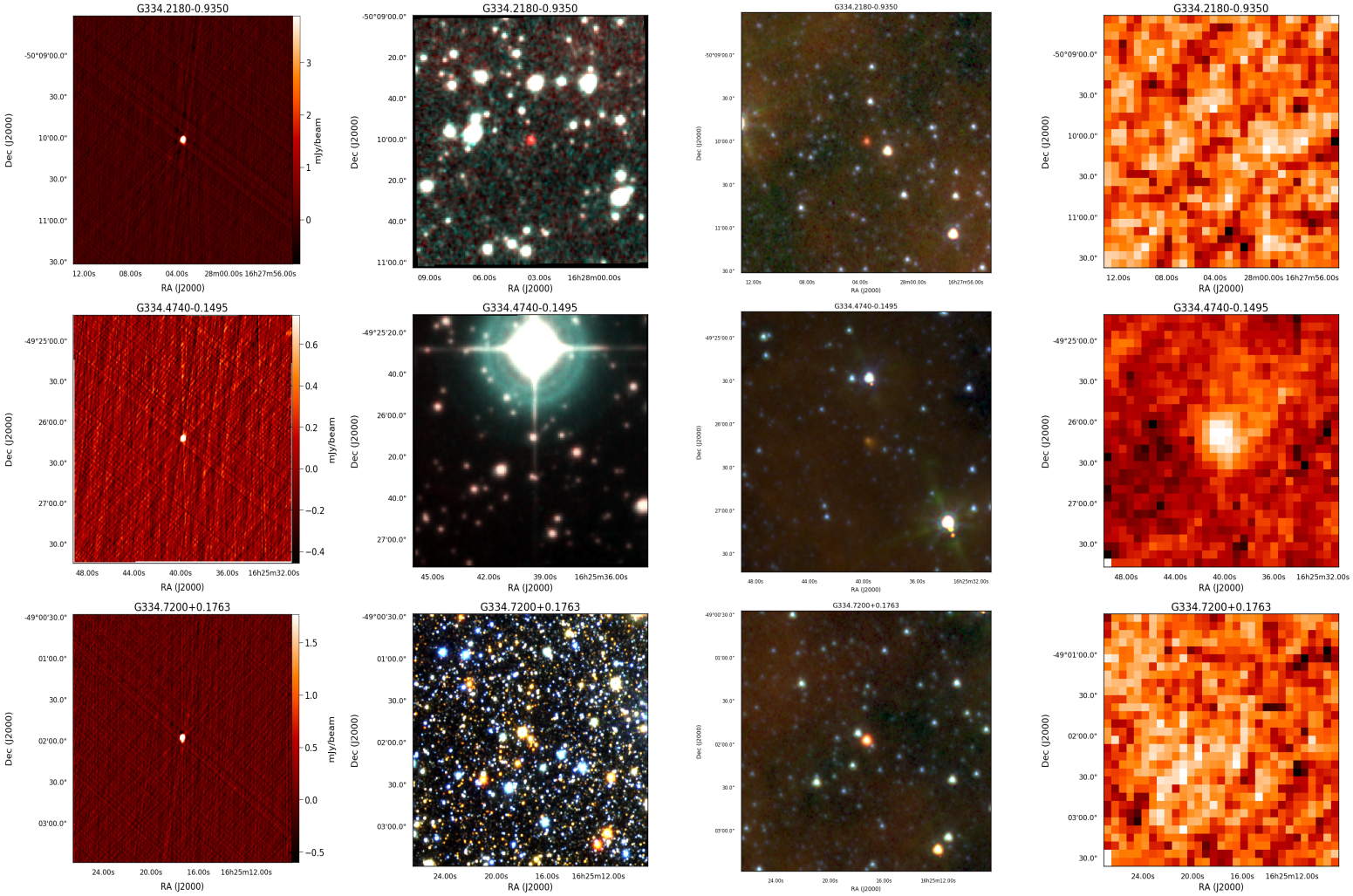

Figure B.52: *Continuation from previous Figure.*

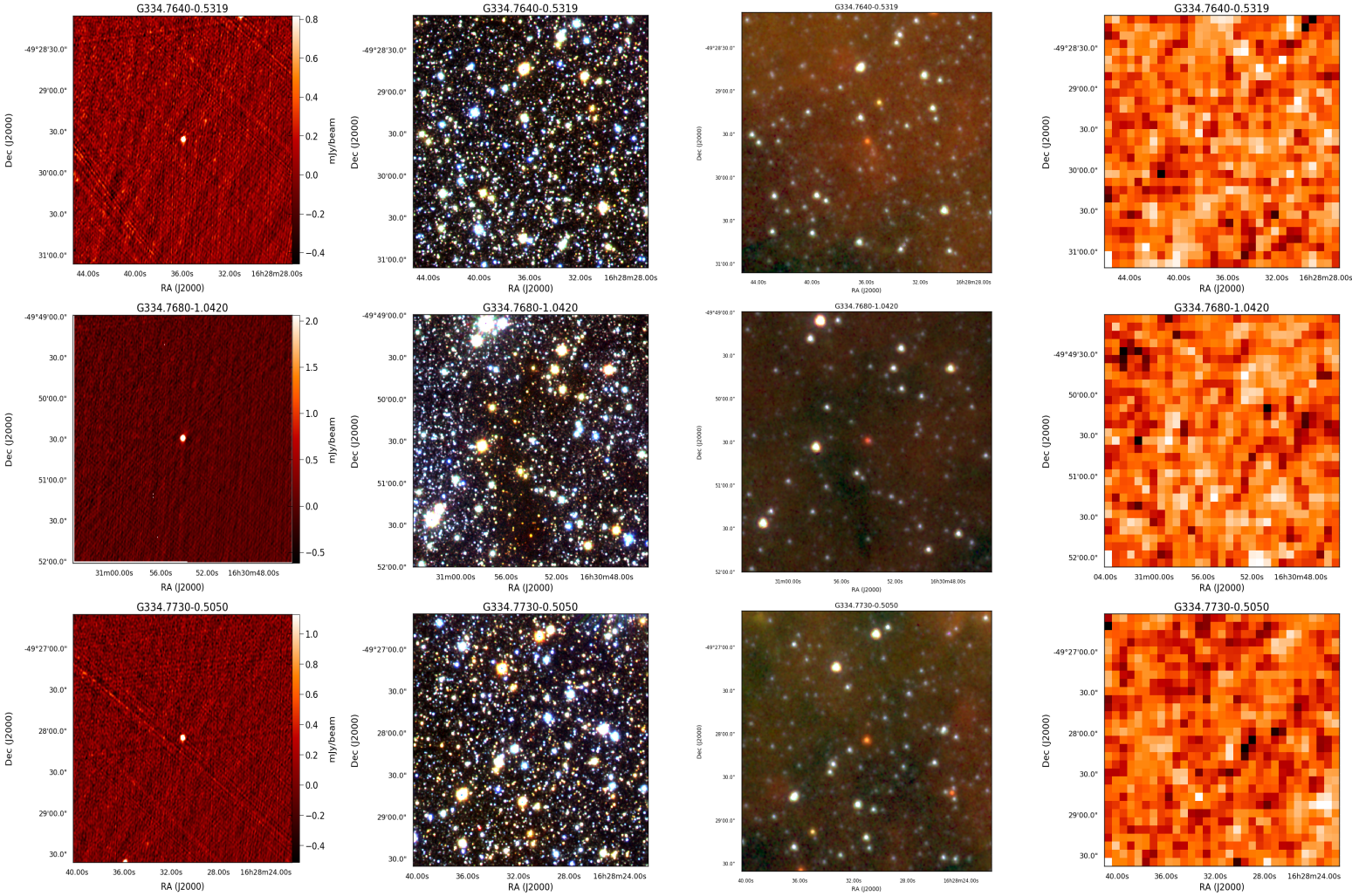

Figure B.53: *Continuation from previous Figure.*

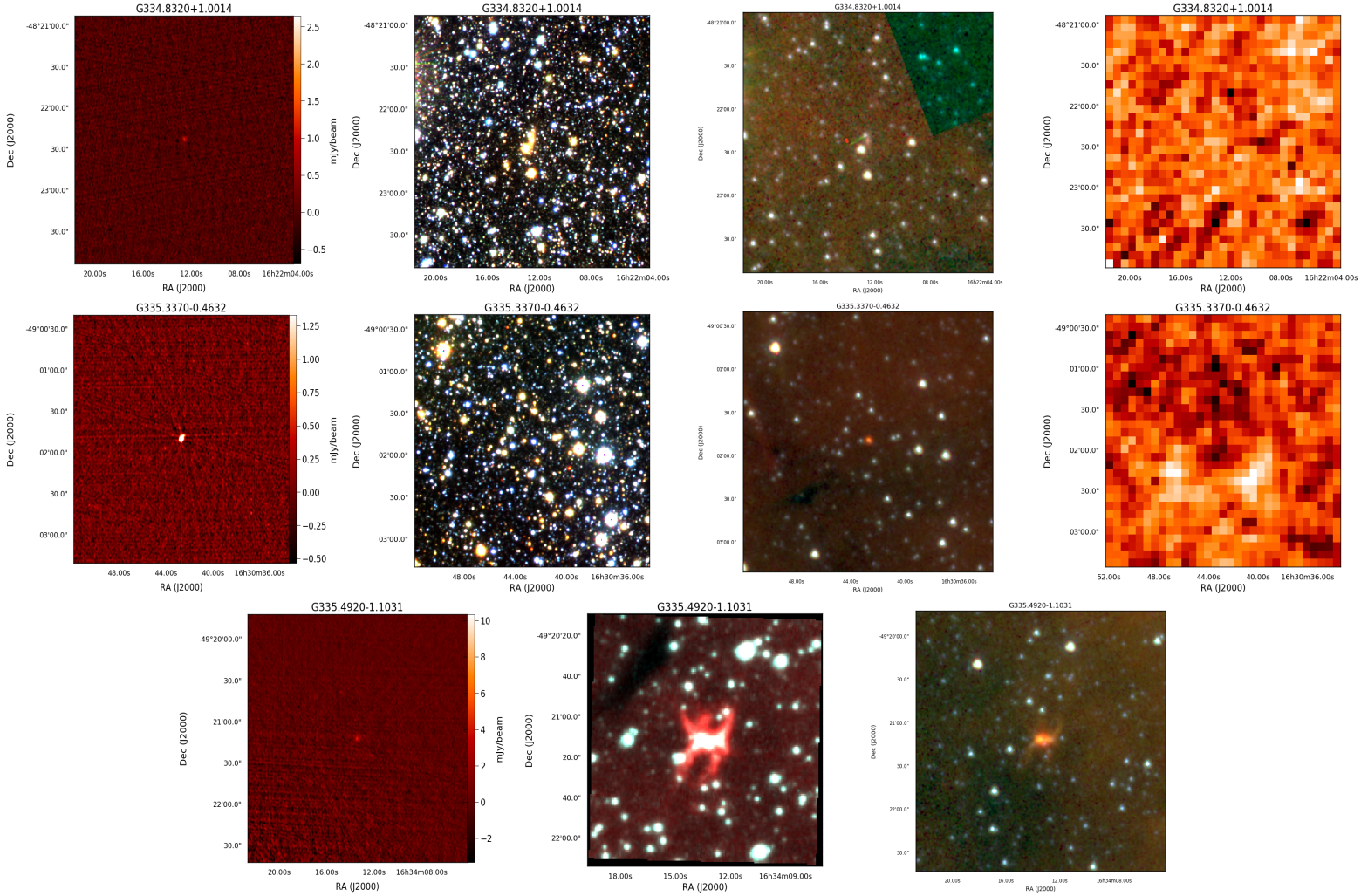

Figure B.54: *Continuation from previous Figure.*

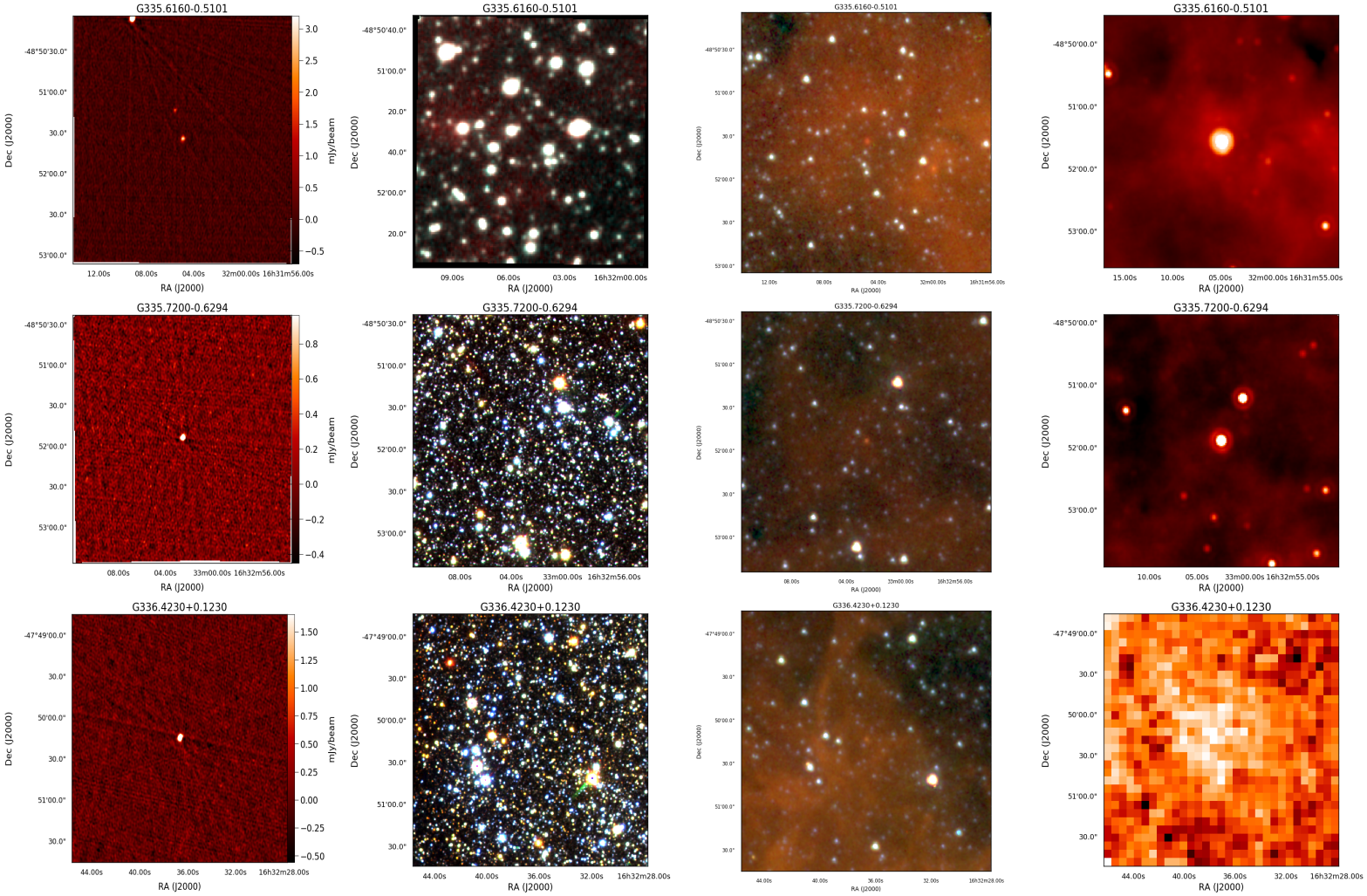

Figure B.55: *Continuation from previous Figure.*

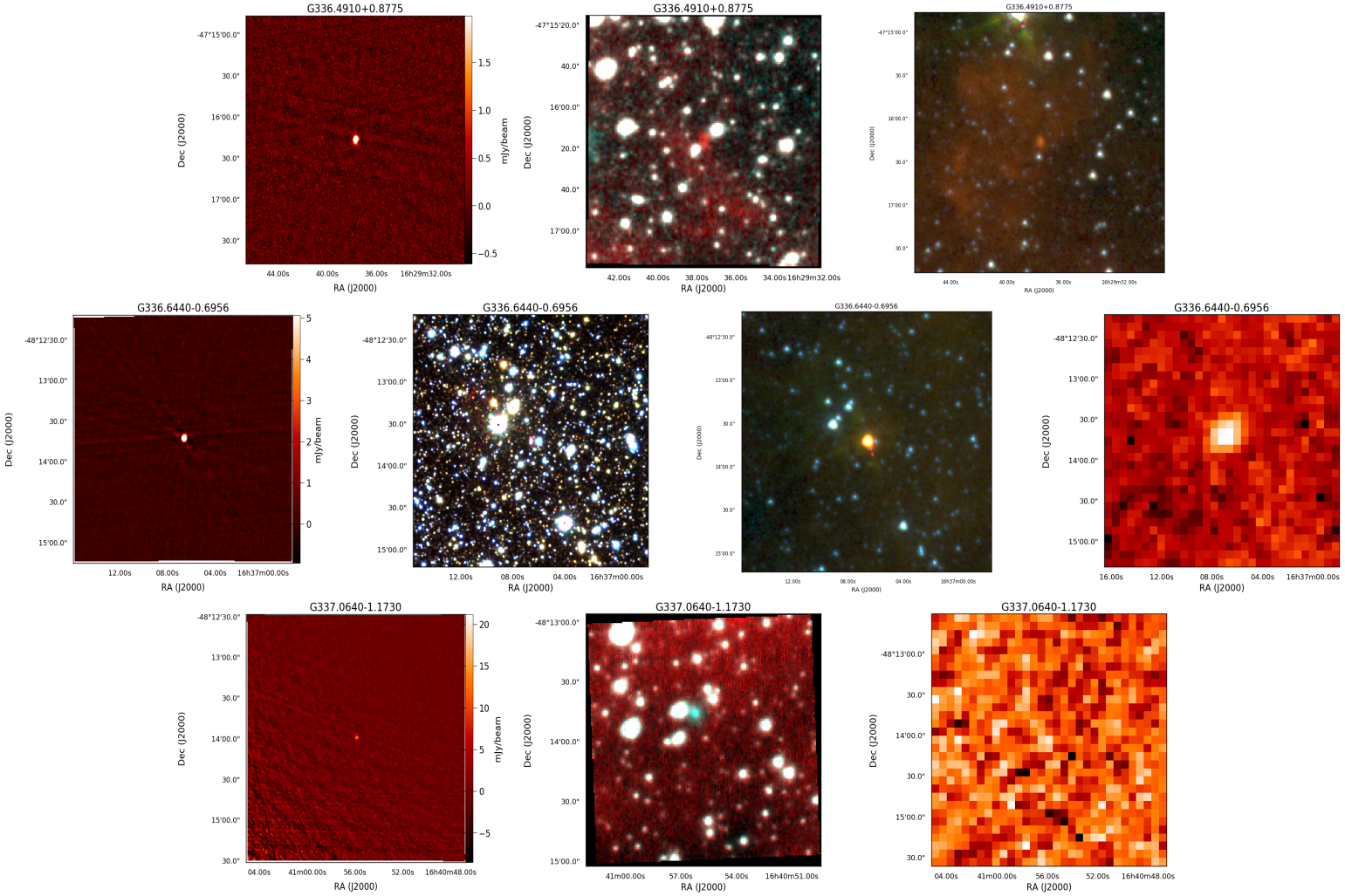

Figure B.56: *Continuation from previous Figure.*

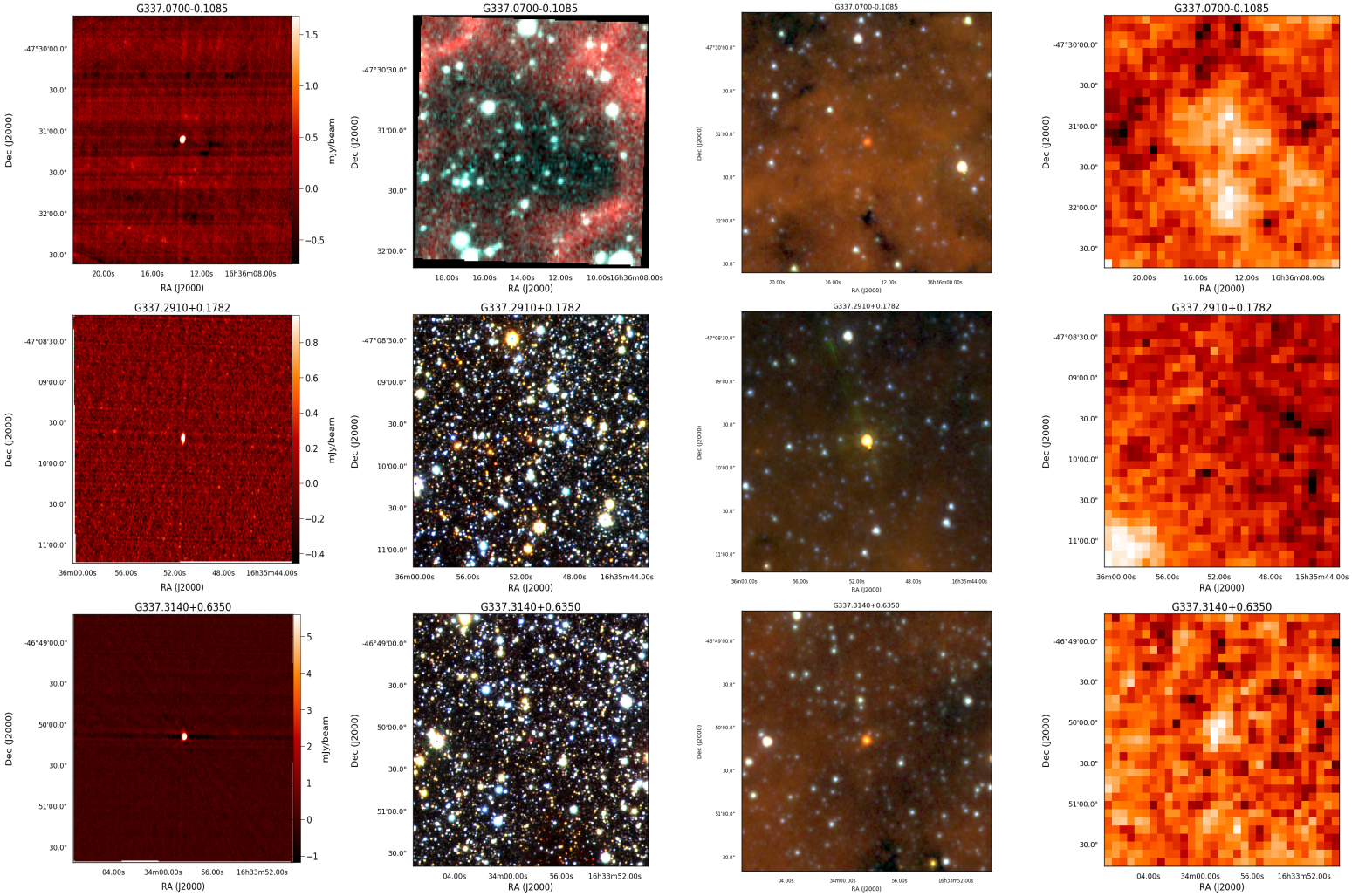

Figure B.57: *Continuation from previous Figure.*

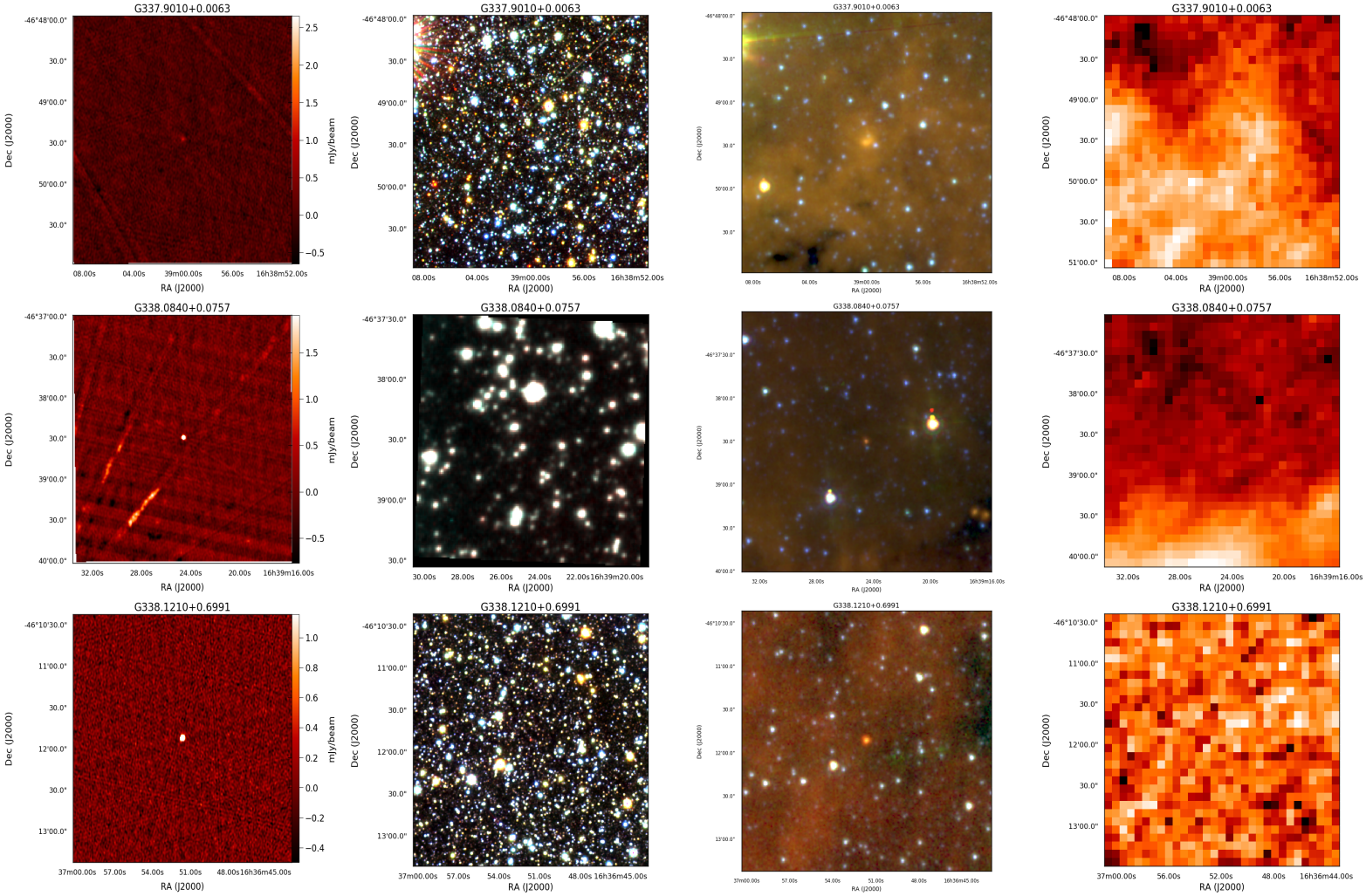

Figure B.58: *Continuation from previous Figure.*

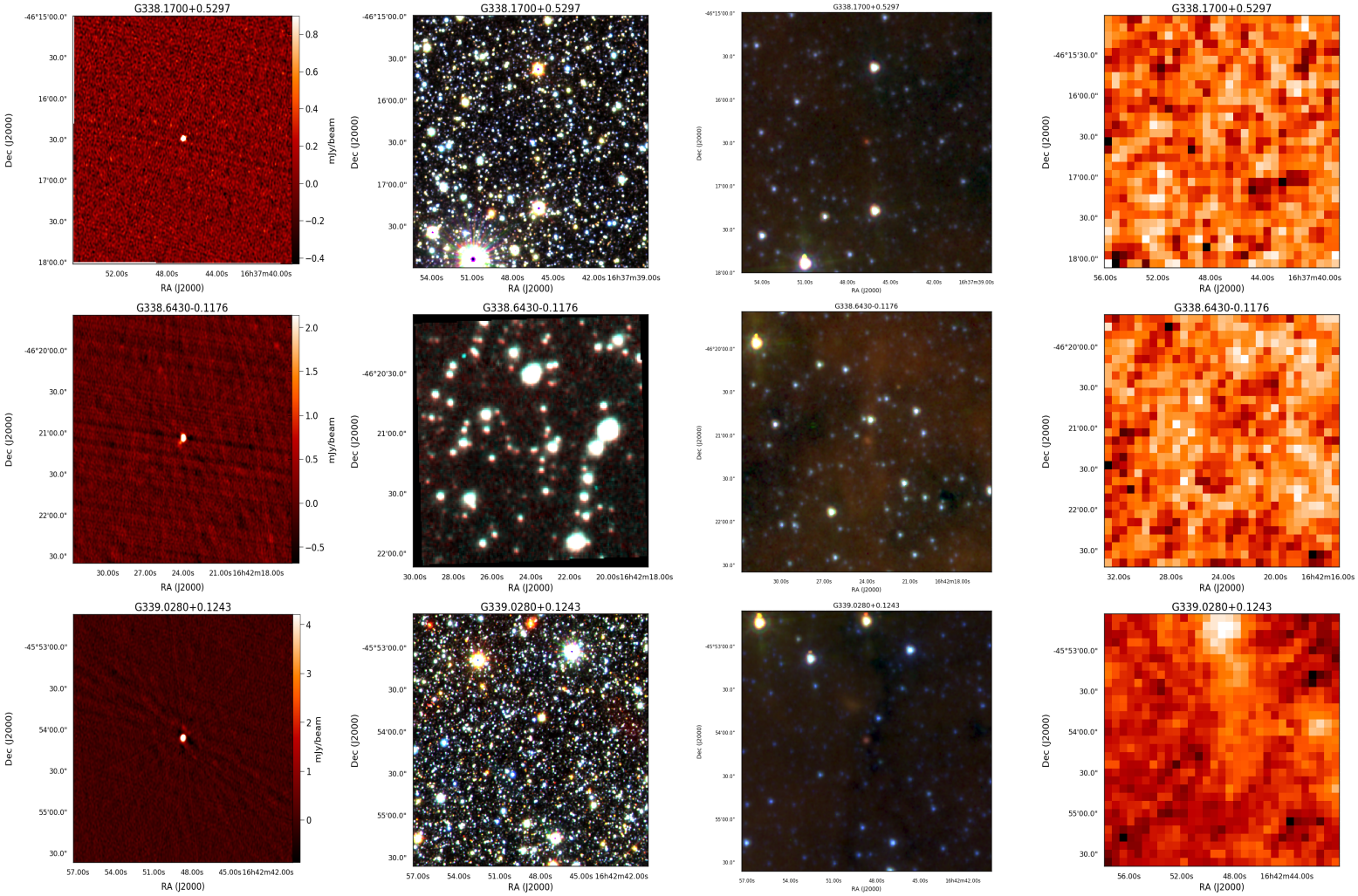

Figure B.59: *Continuation from previous Figure.*

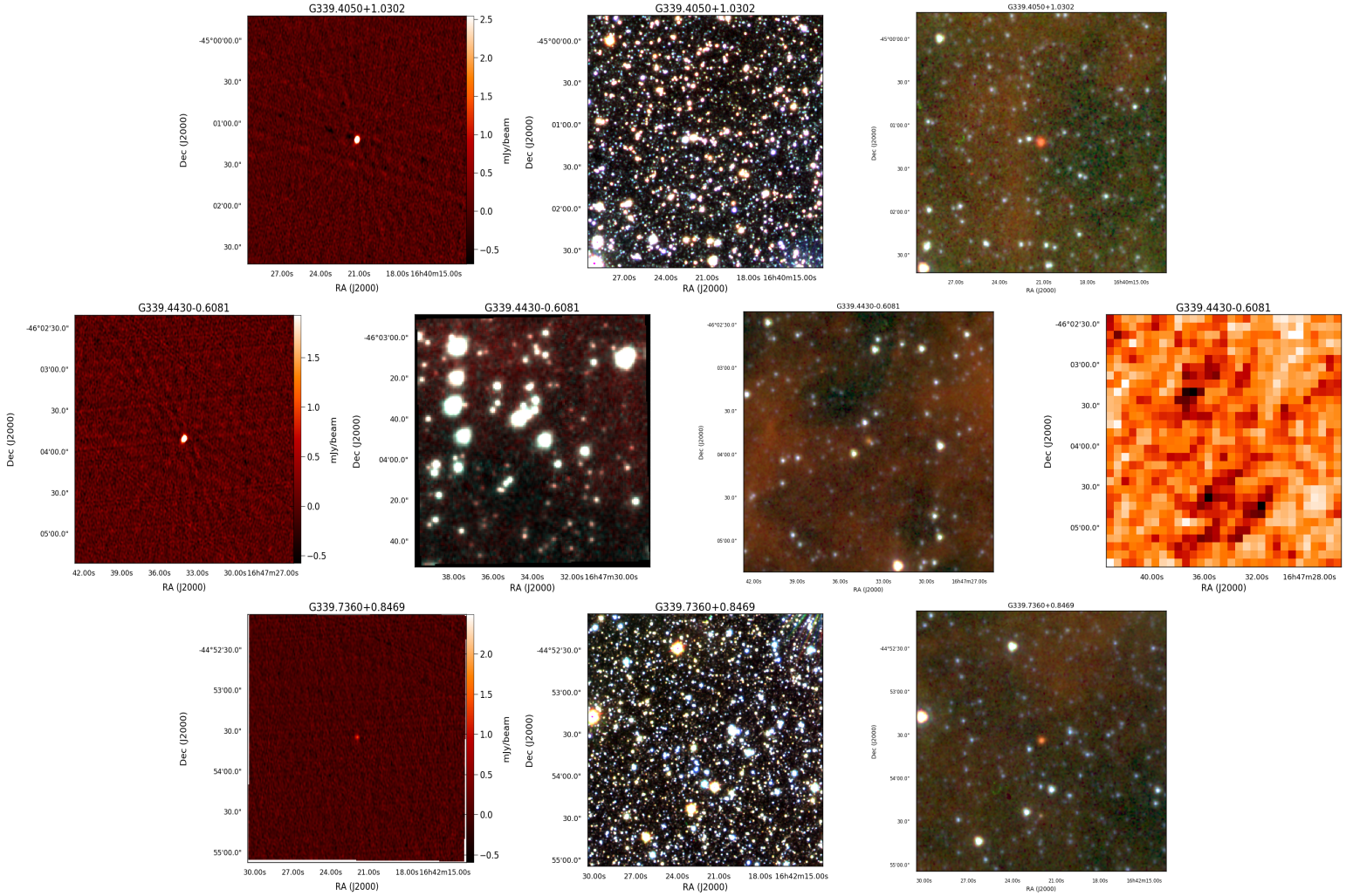

Figure B.60: *Continuation from previous Figure.*

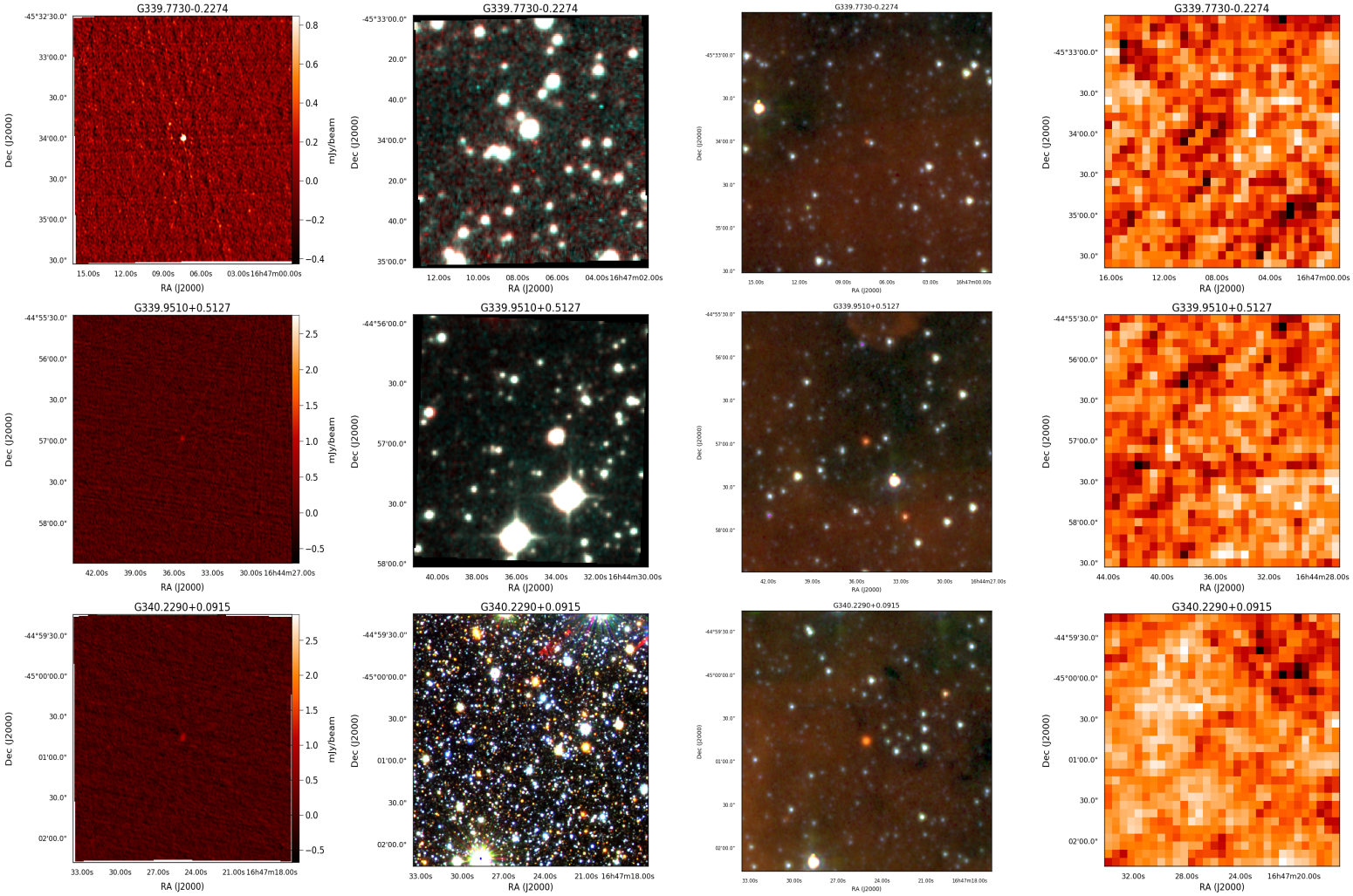

Figure B.61: *Continuation from previous Figure.*

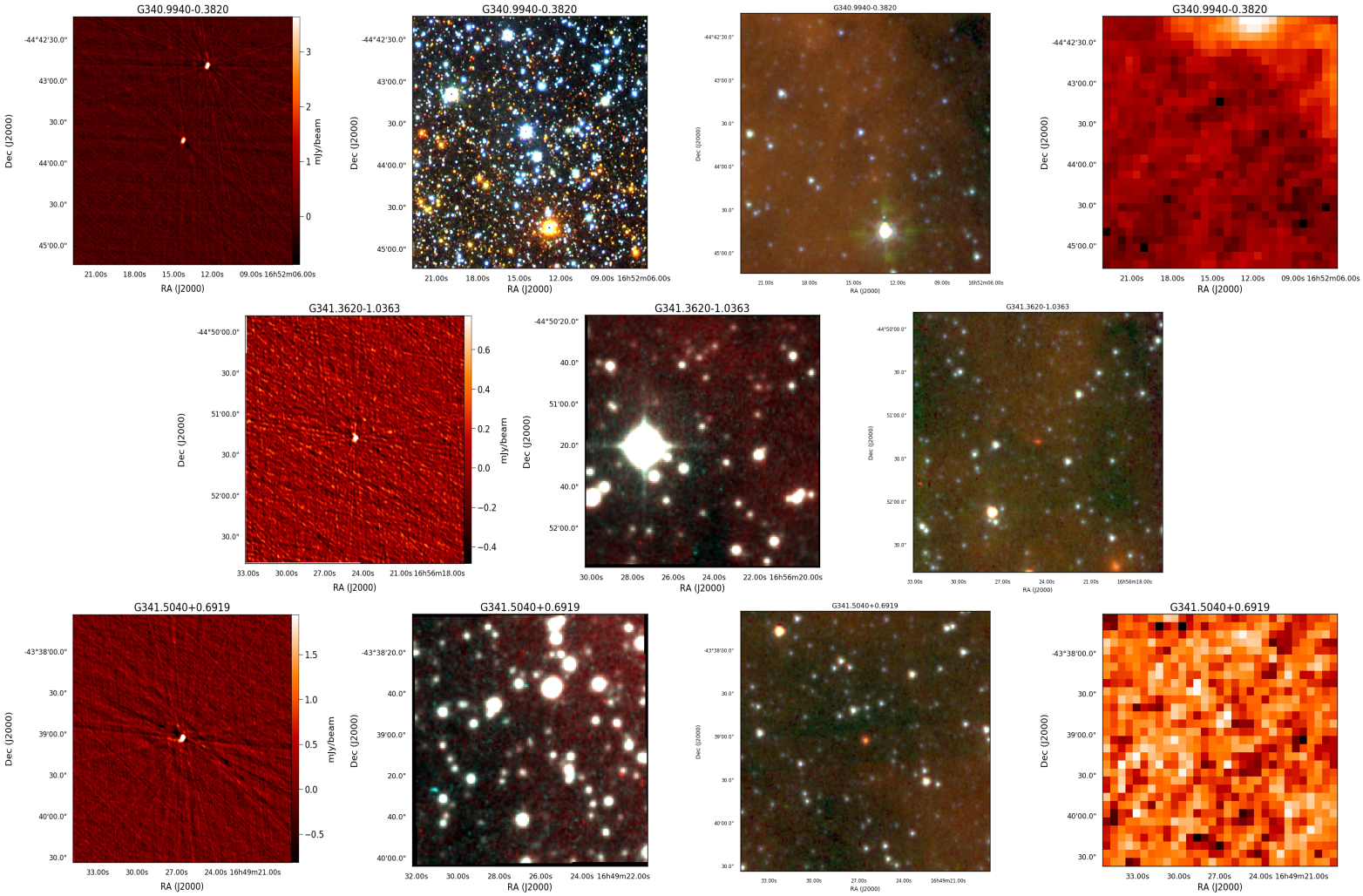

Figure B.62: *Continuation from previous Figure.*

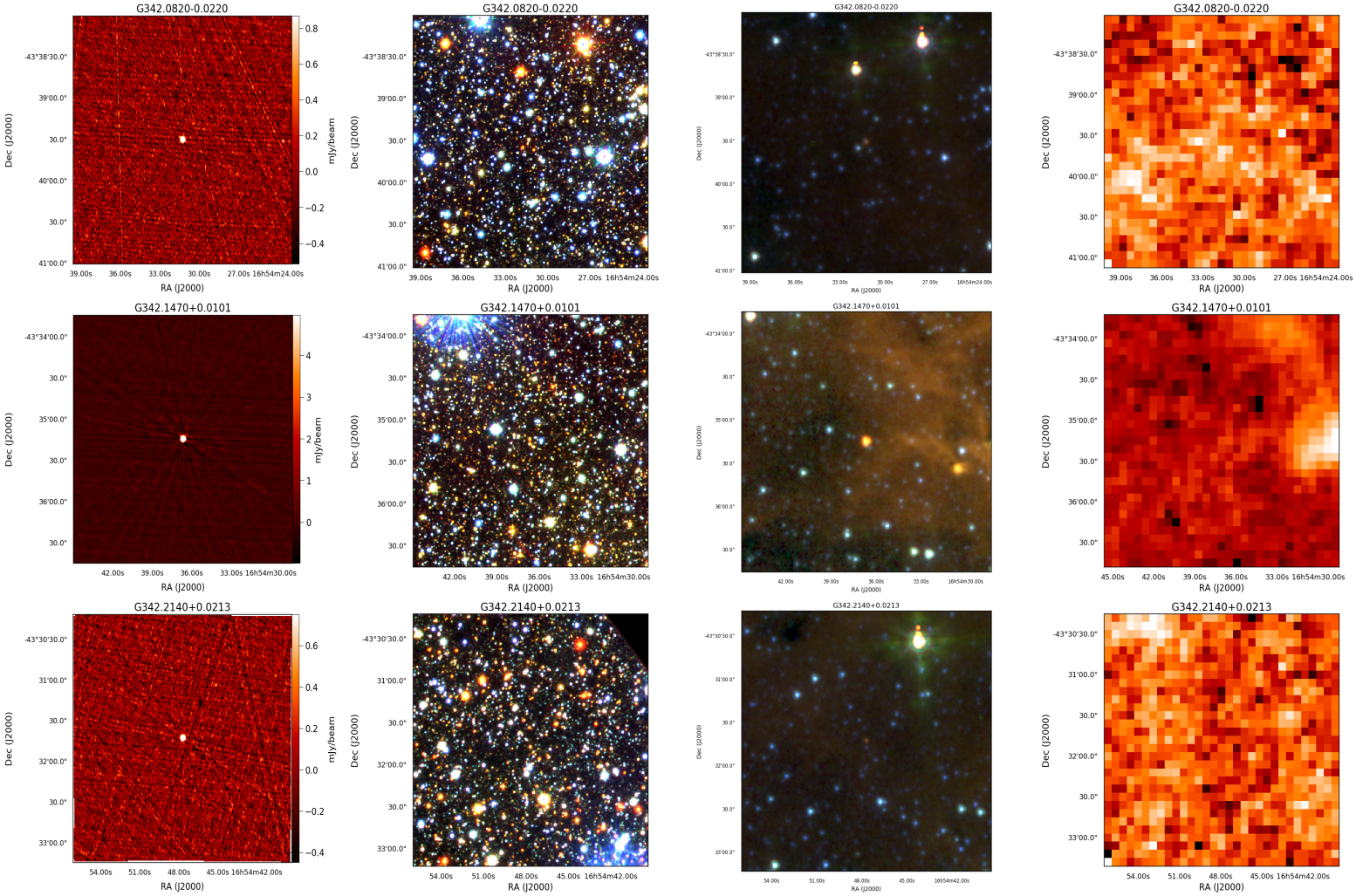

Figure B.63: *Continuation from previous Figure.*

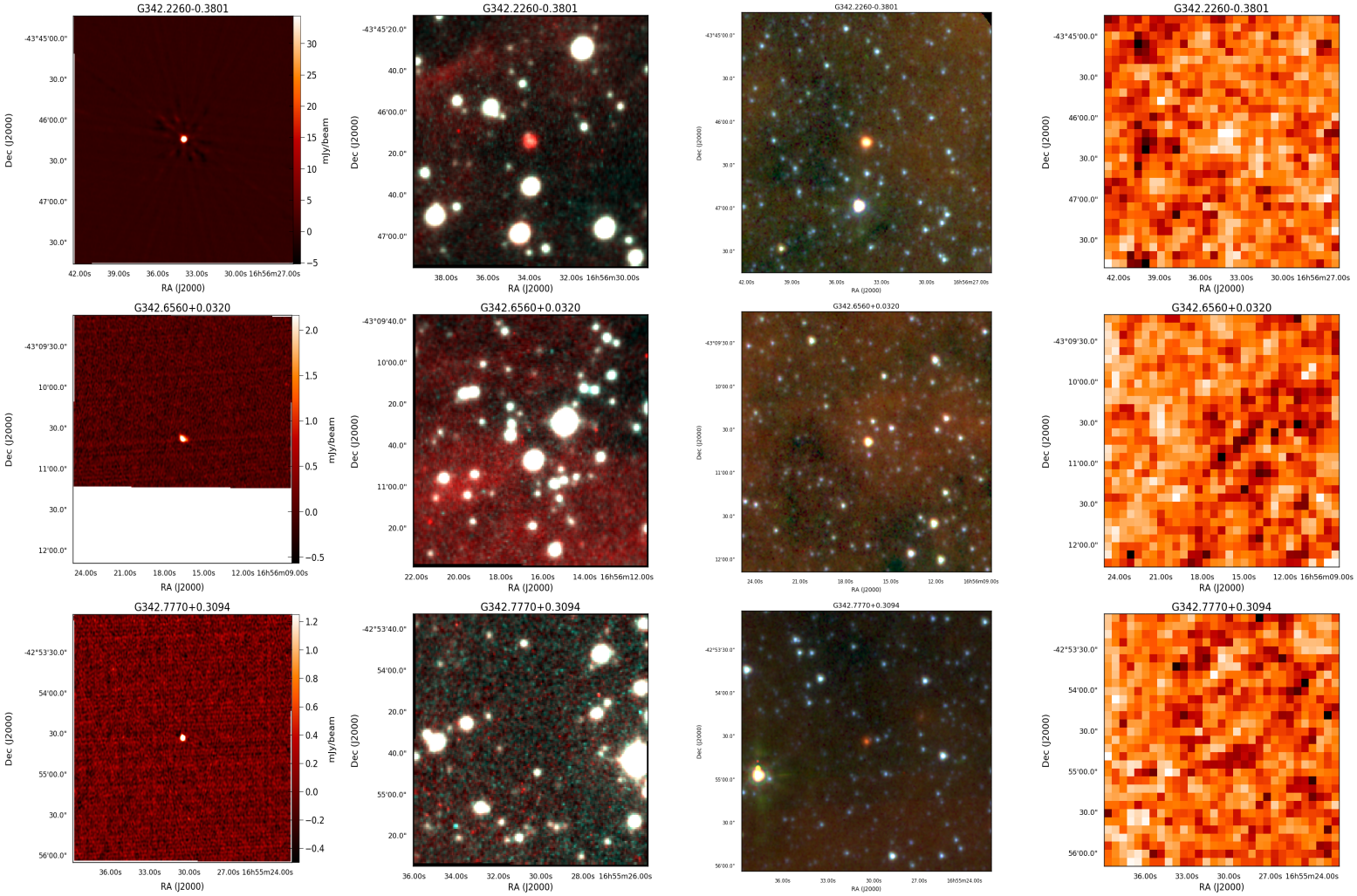

Figure B.64: *Continuation from previous Figure.*

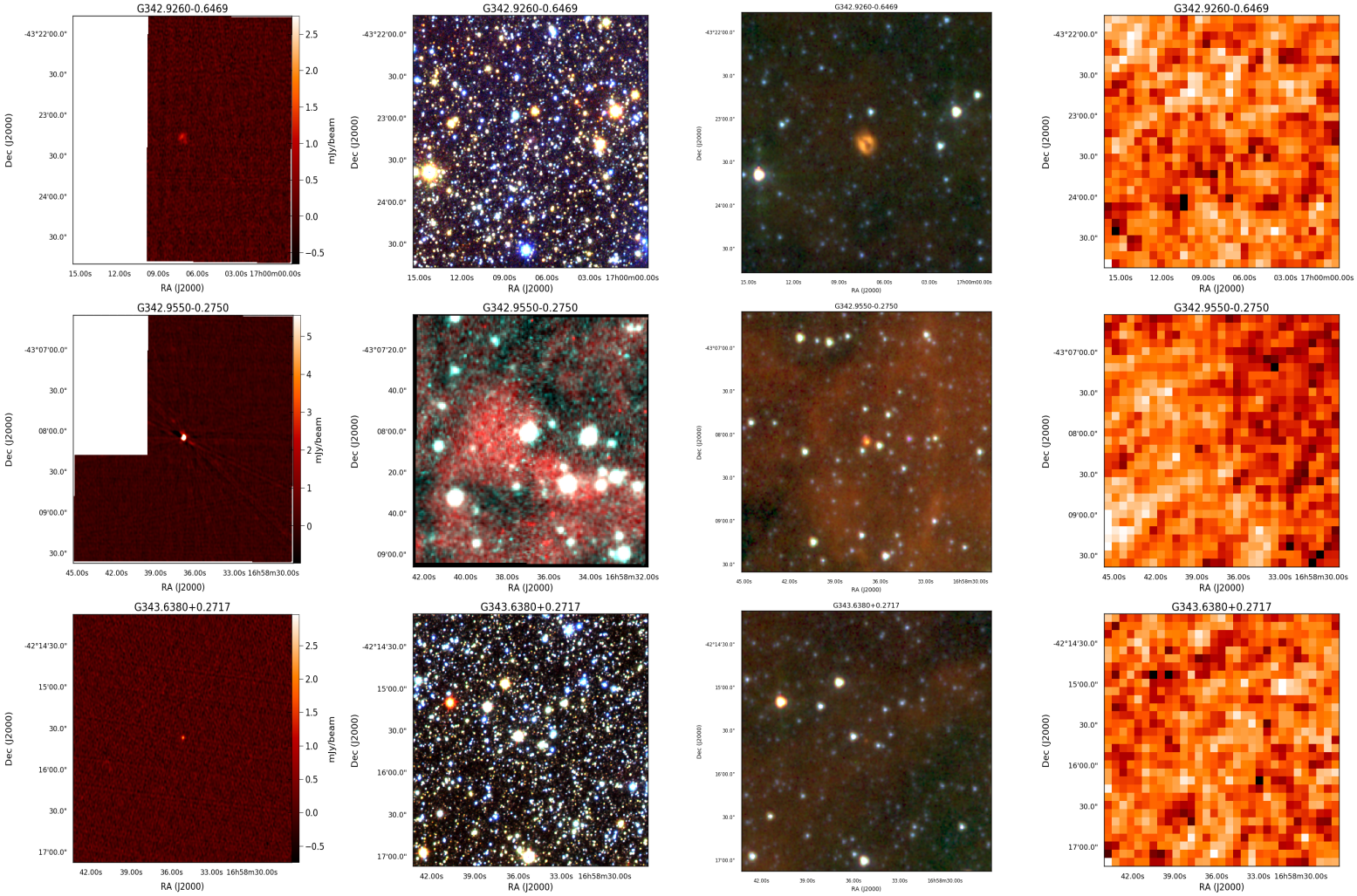

Figure B.65: *Continuation from previous Figure.*

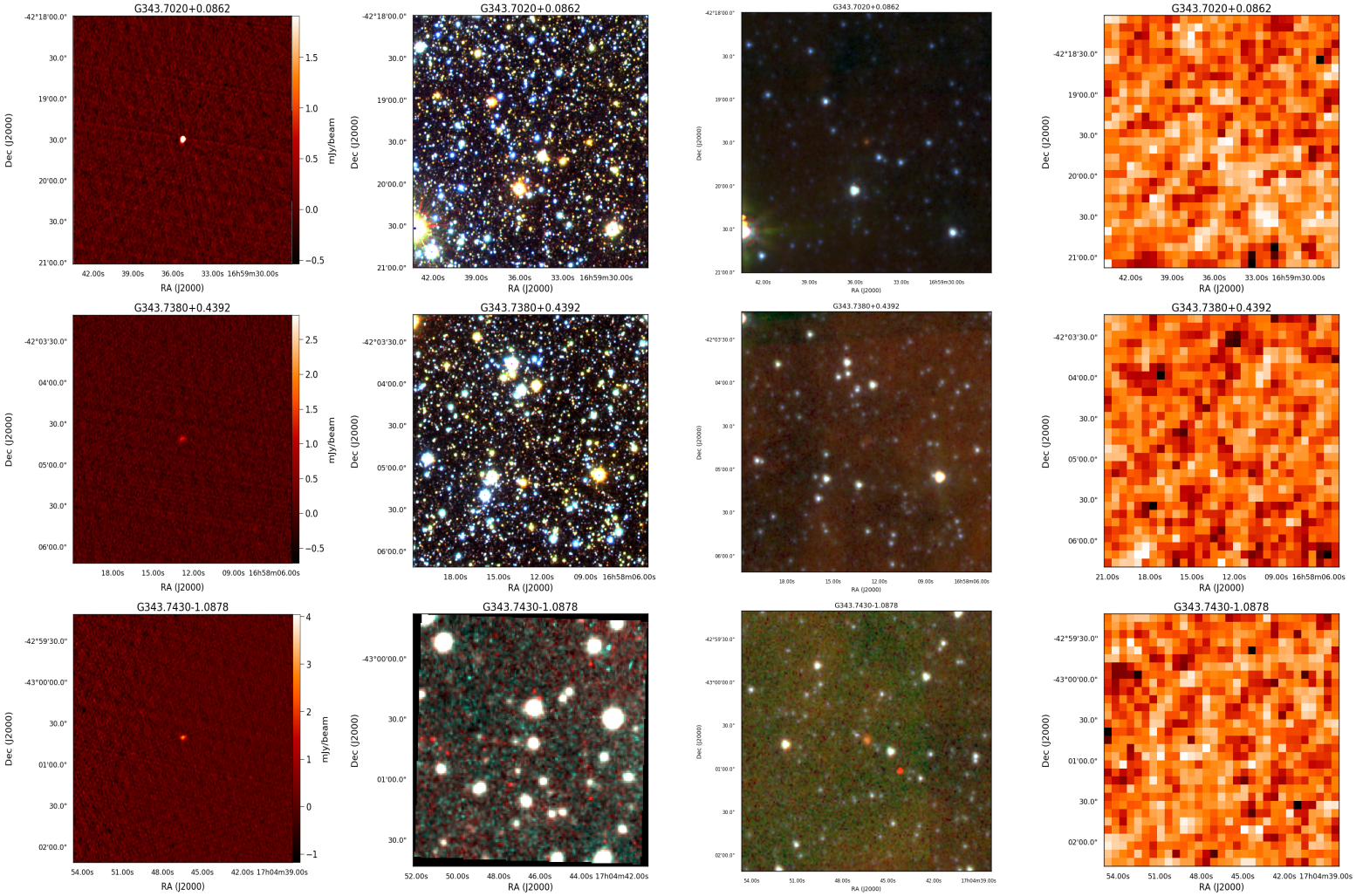

Figure B.66: *Continuation from previous Figure.*

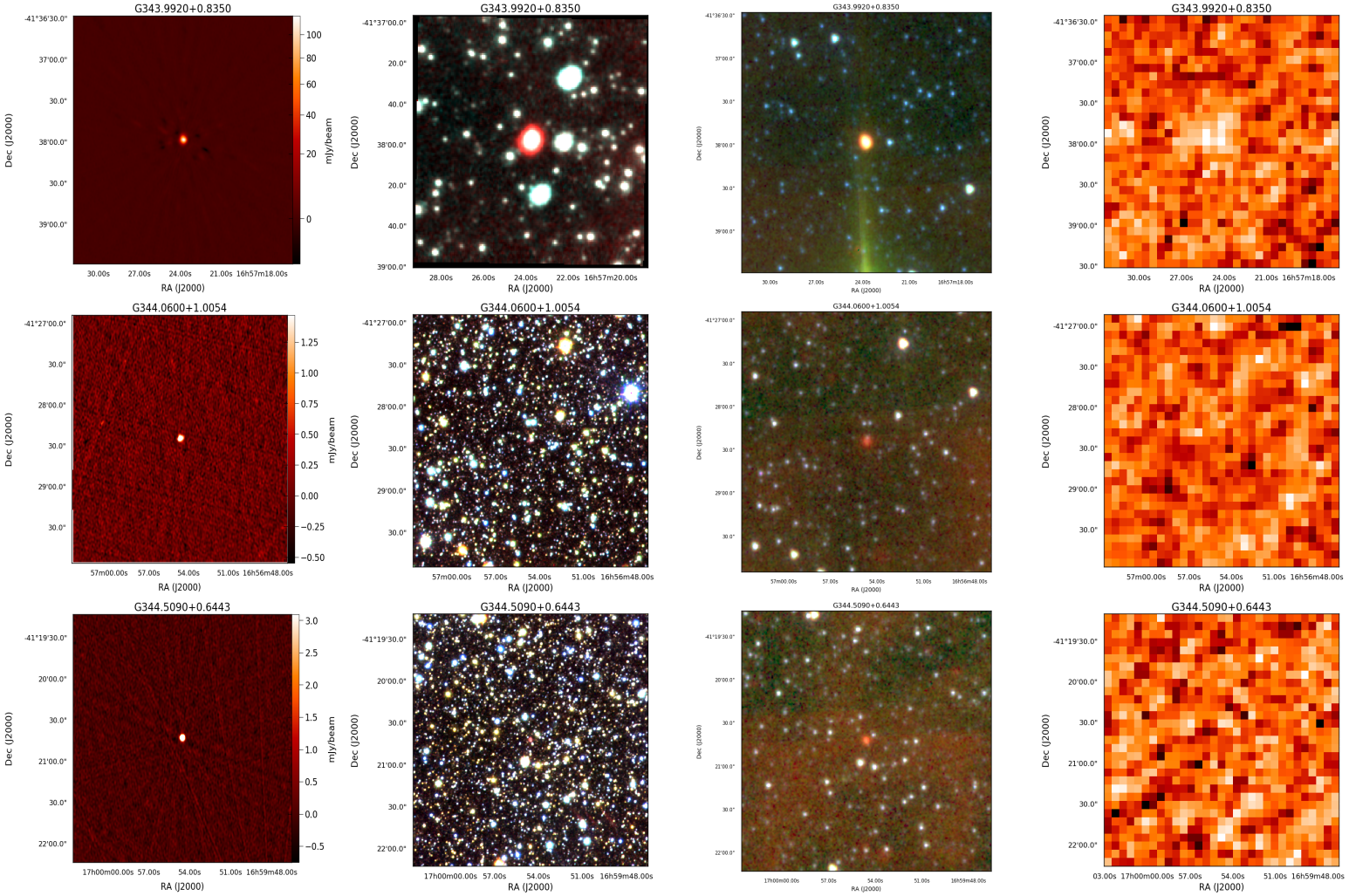

Figure B.67: *Continuation from previous Figure.*

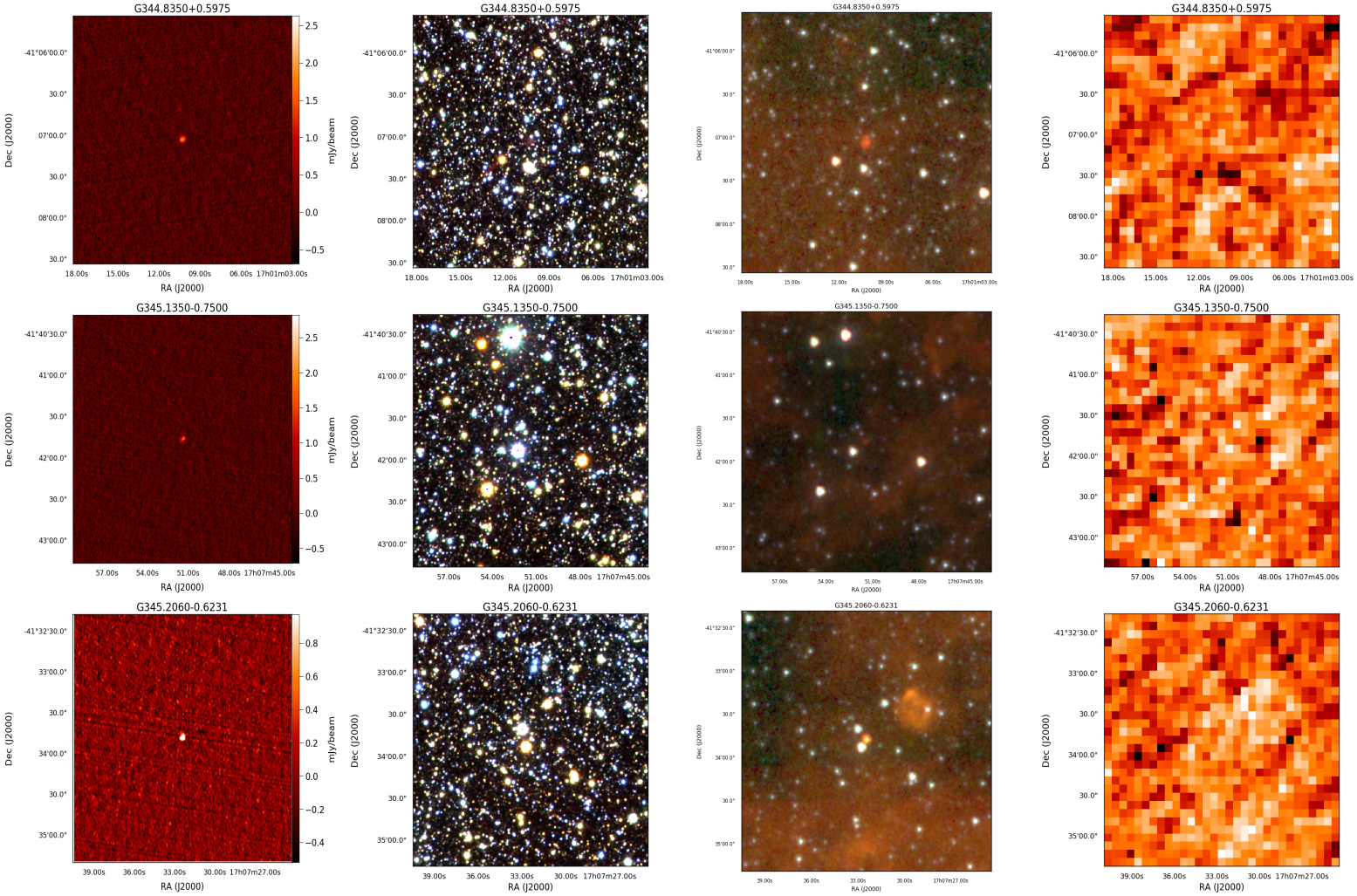

Figure B.68: *Continuation from previous Figure.*

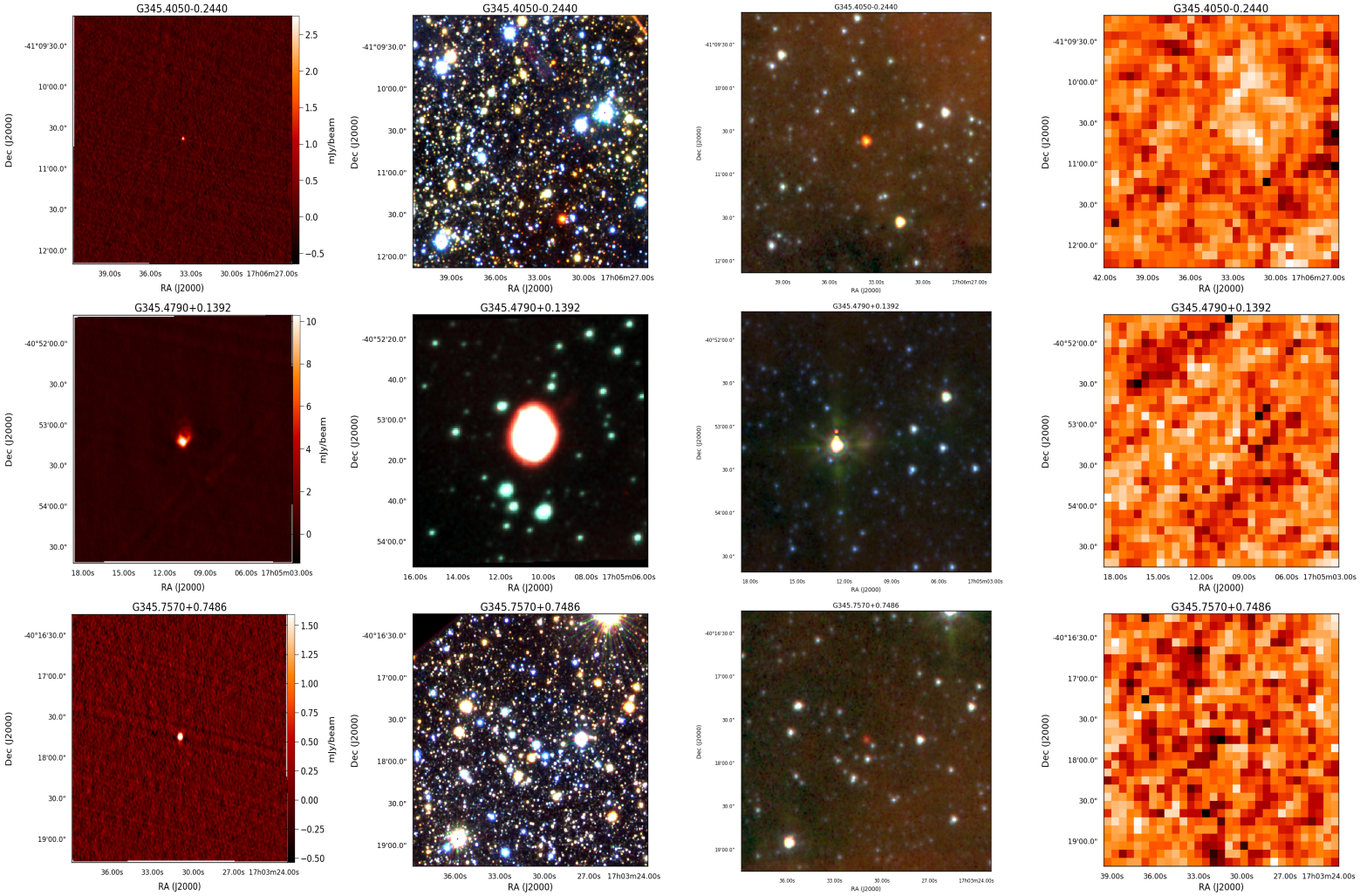

Figure B.69: *Continuation from previous Figure.*

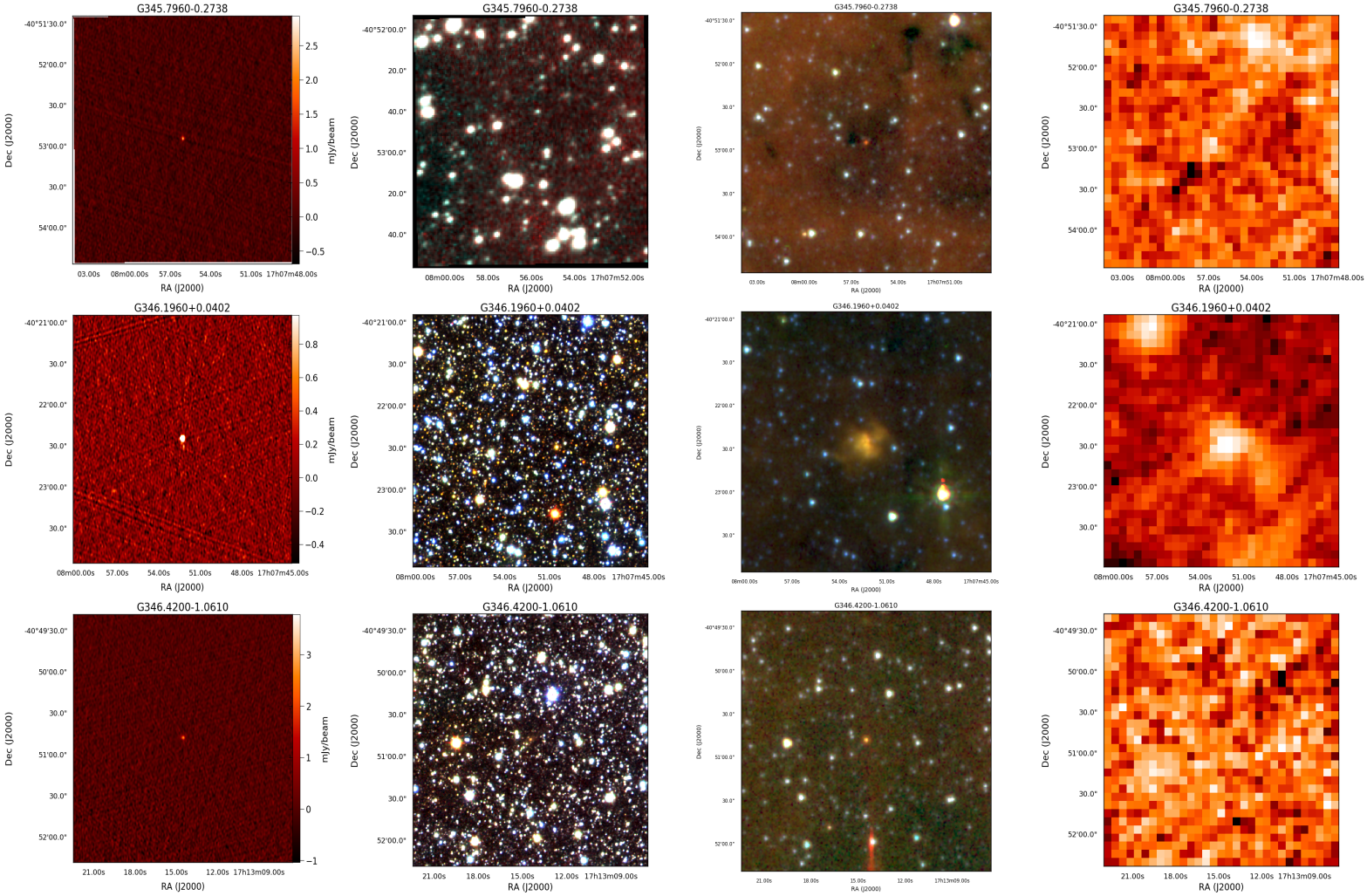

Figure B.70: *Continuation from previous Figure.*

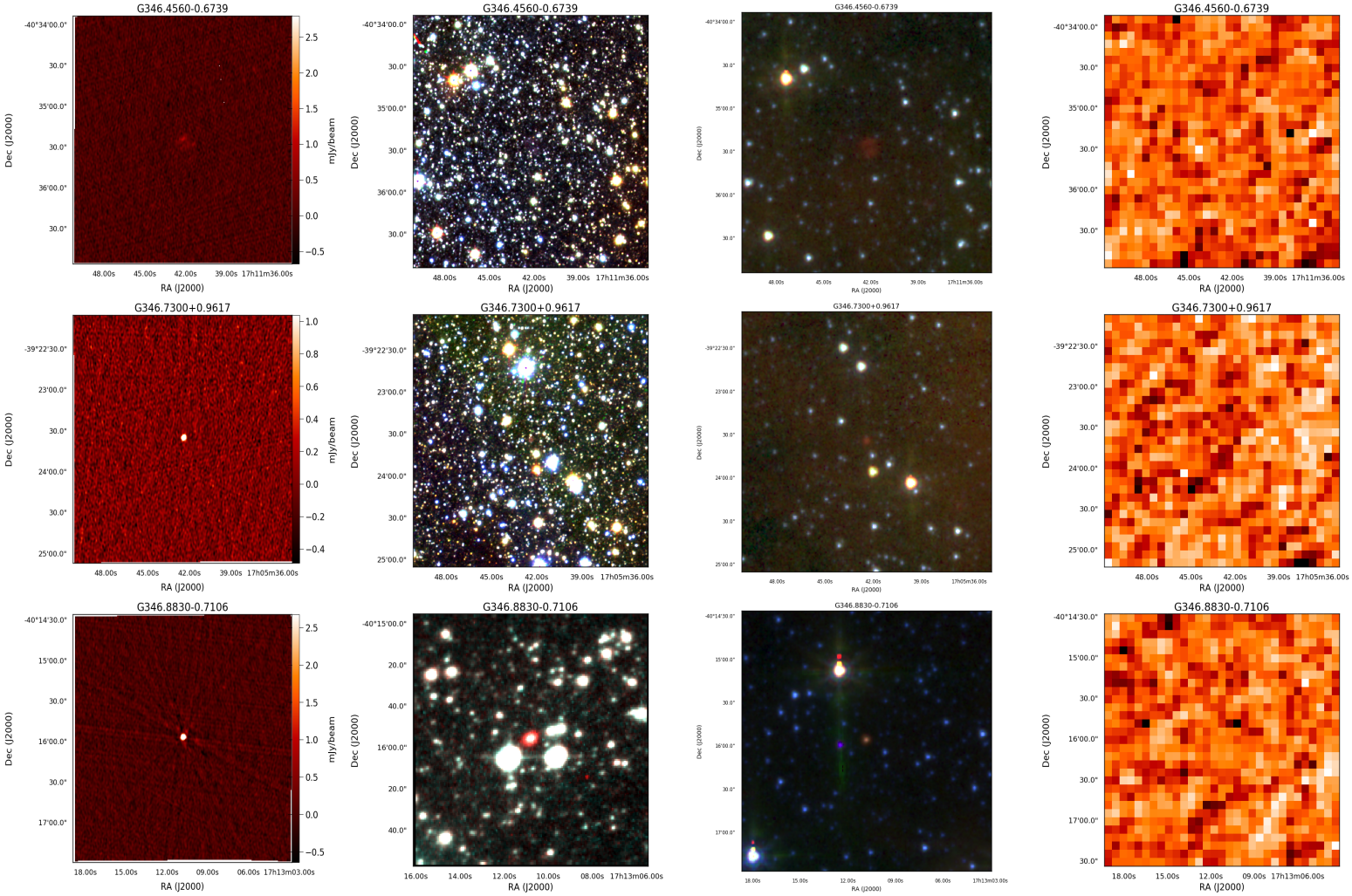

Figure B.71: *Continuation from previous Figure.*

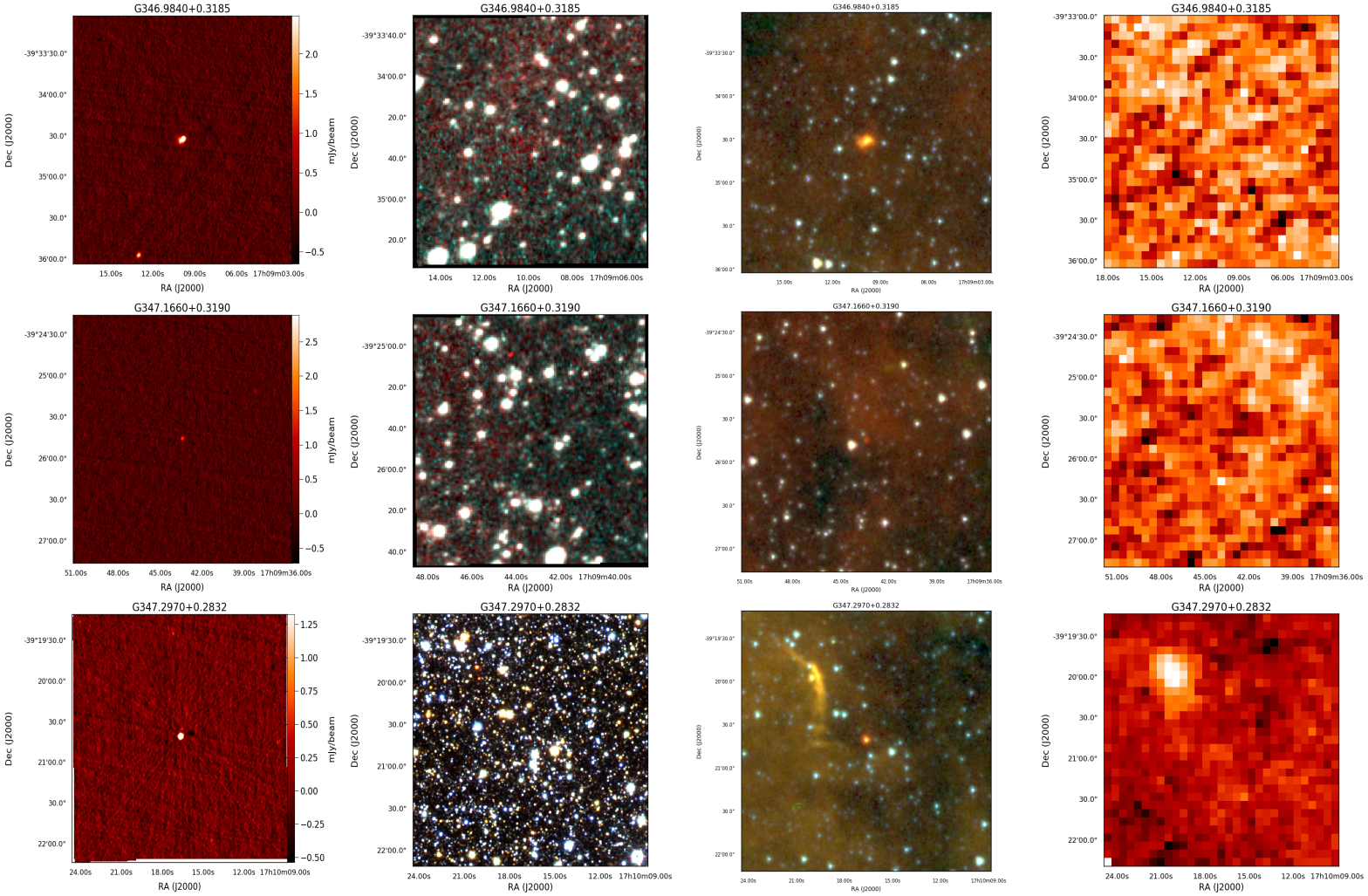

Figure B.72: *Continuation from previous Figure.*

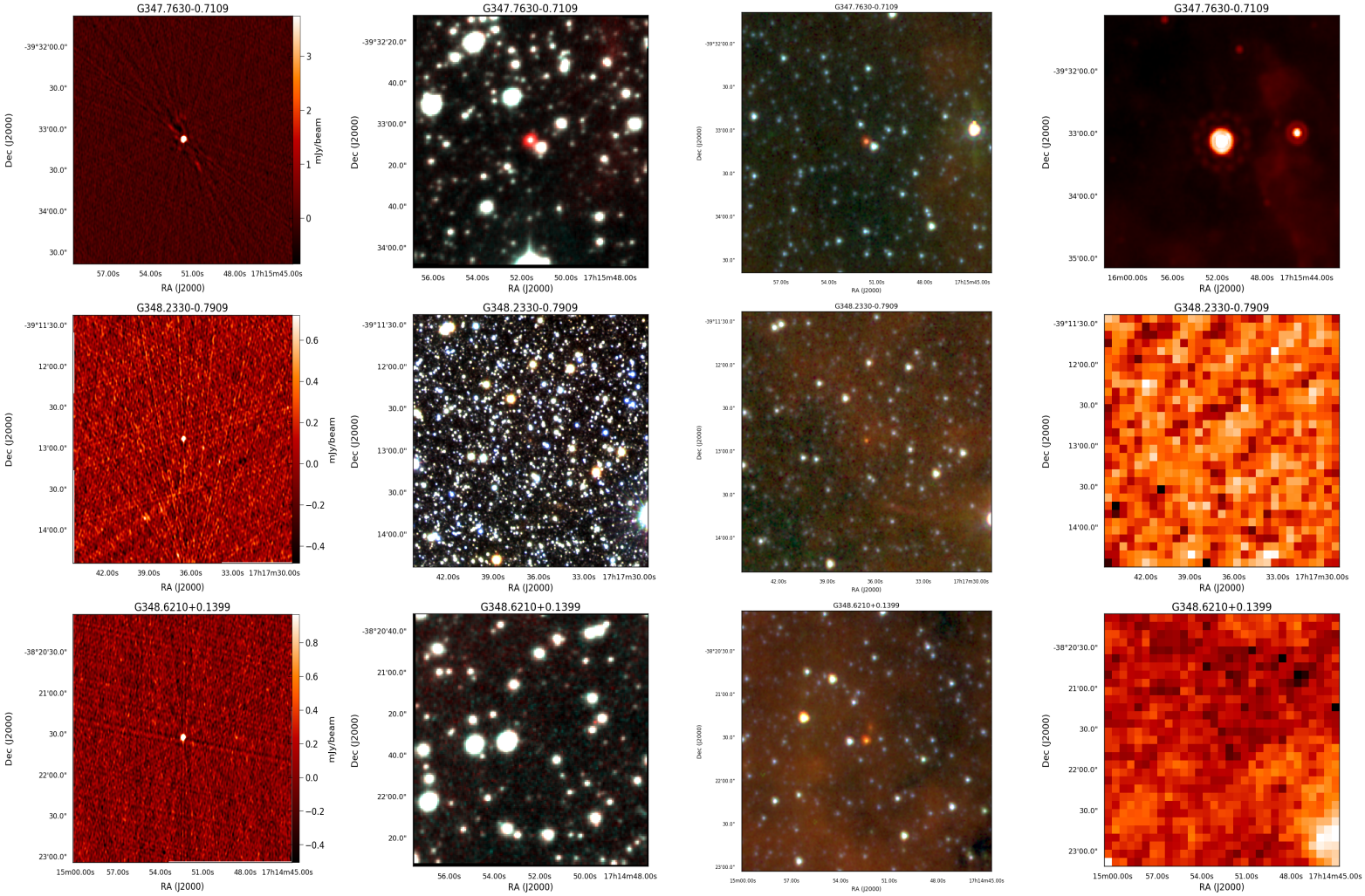

Figure B.73: *Continuation from previous Figure.*

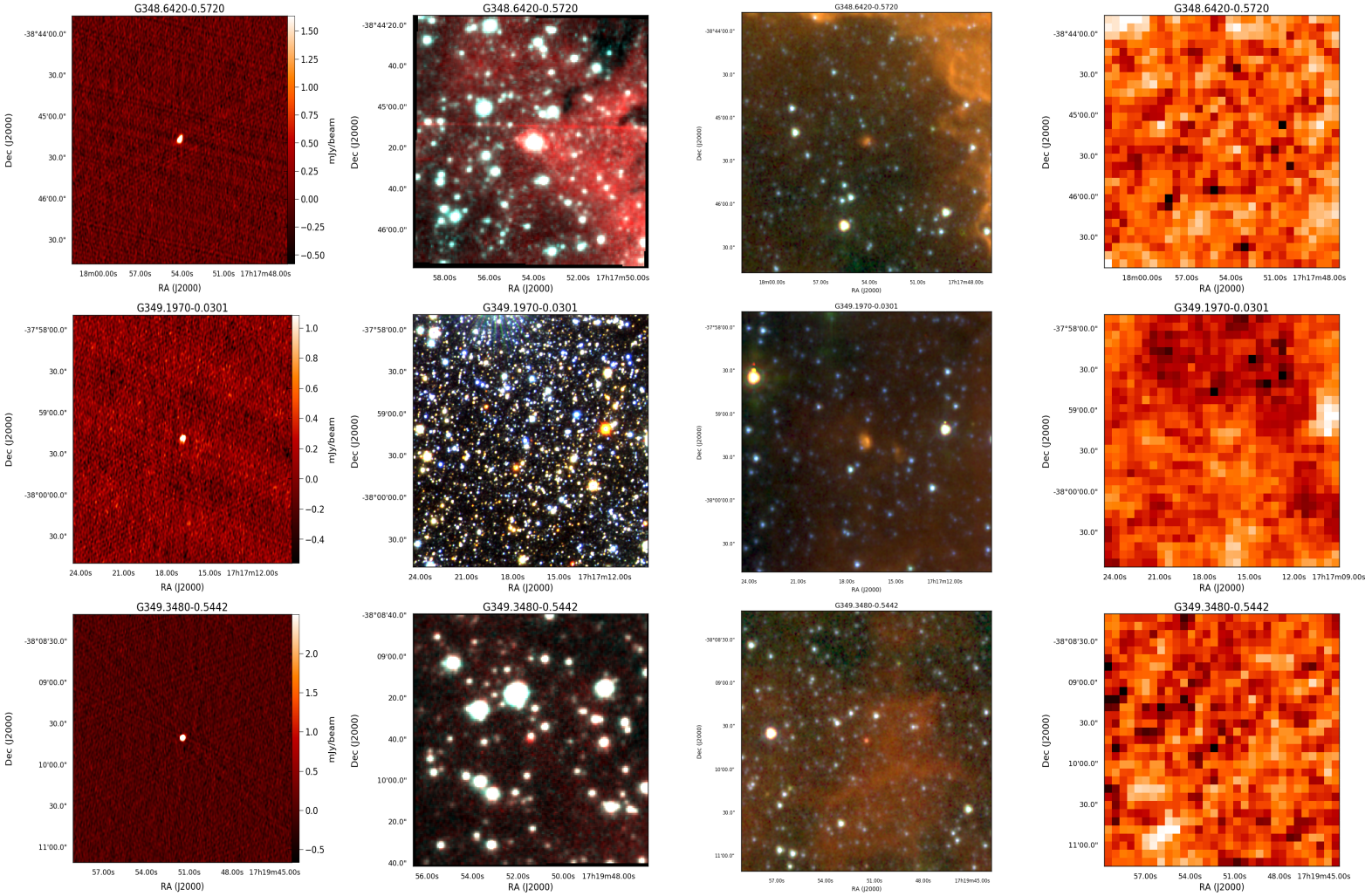

Figure B.74: *Continuation from previous Figure.*

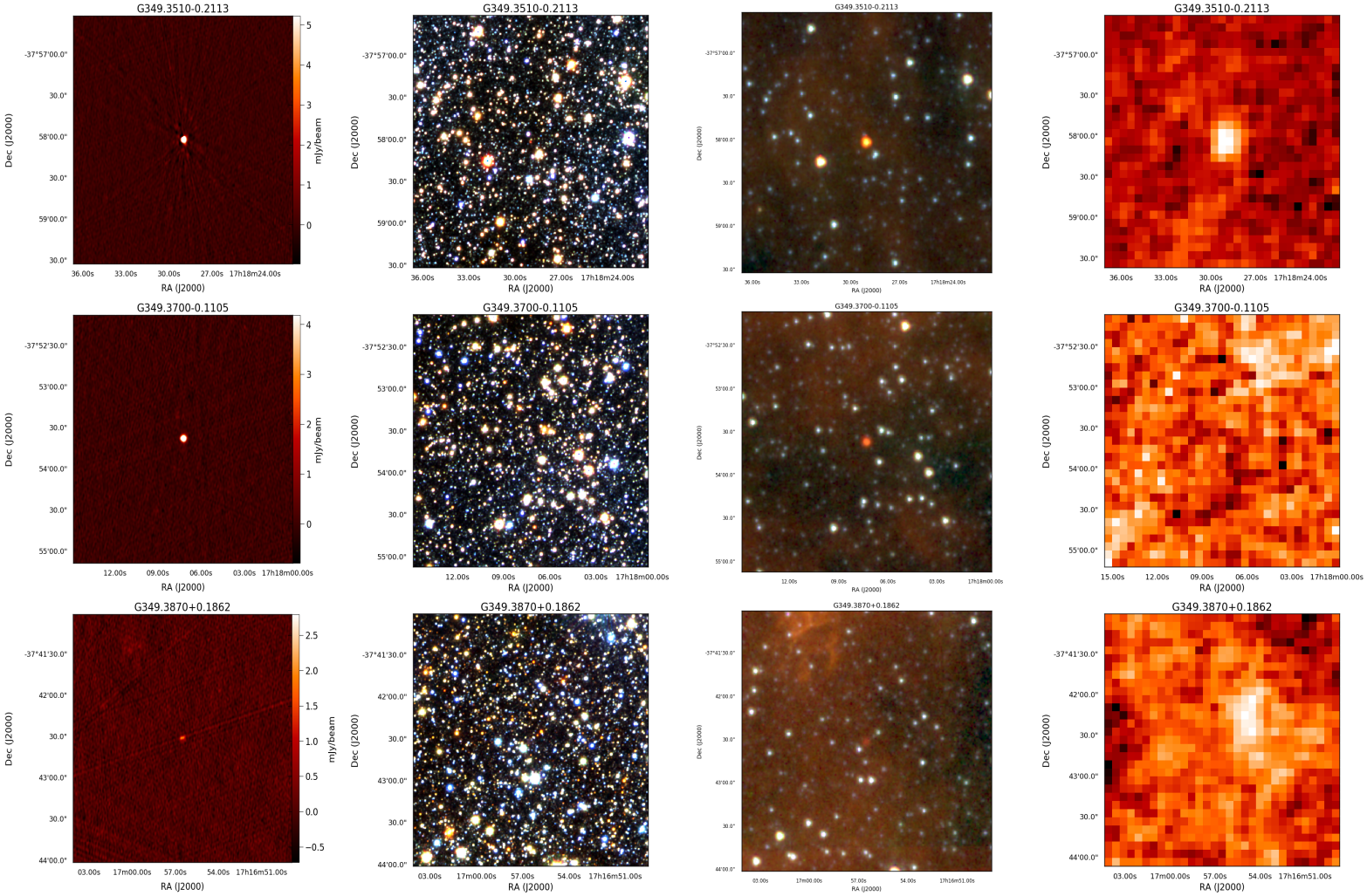

Figure B.75: *Continuation from previous Figure.*

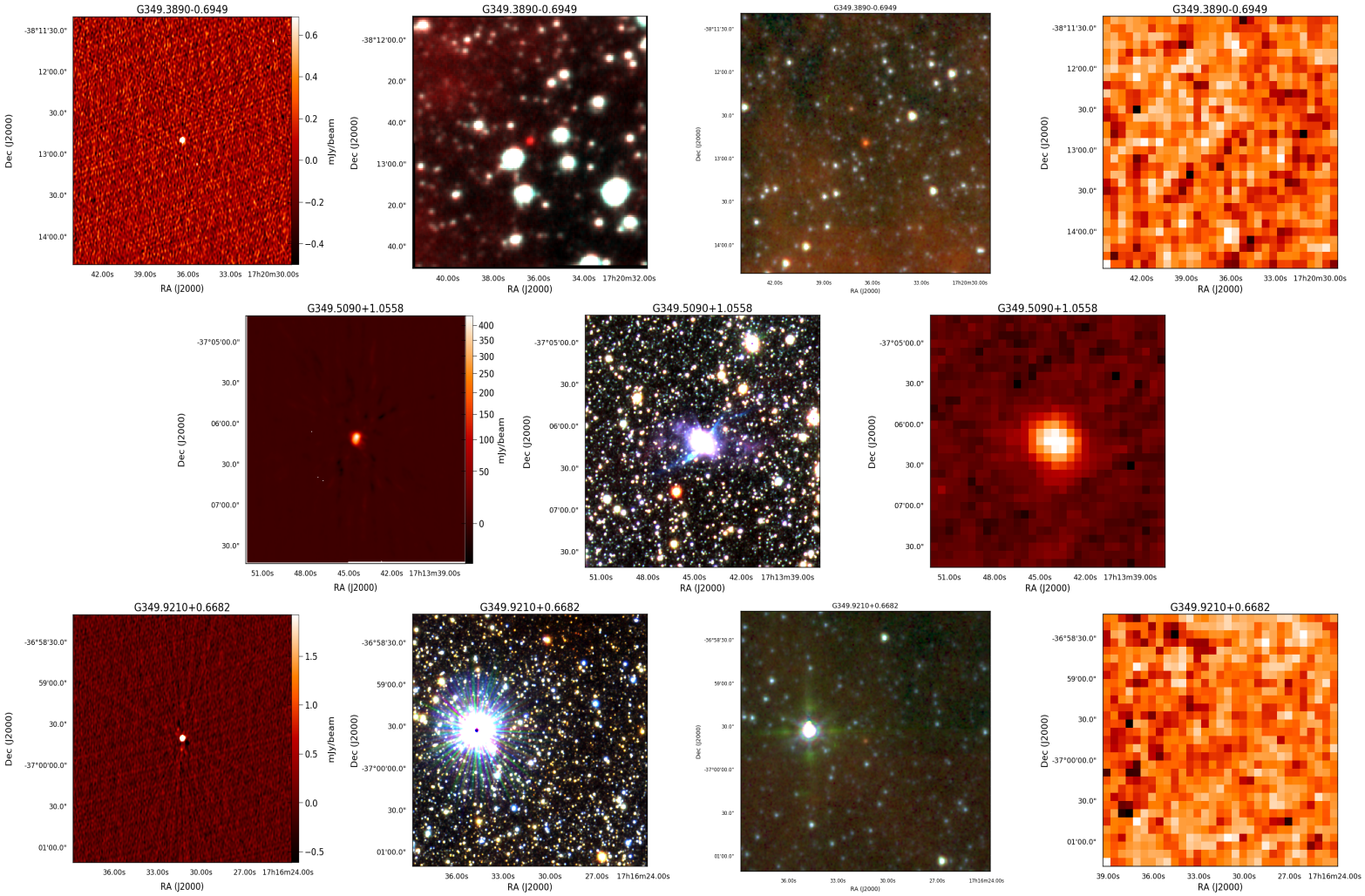

Figure B.76: *Continuation from previous Figure.*

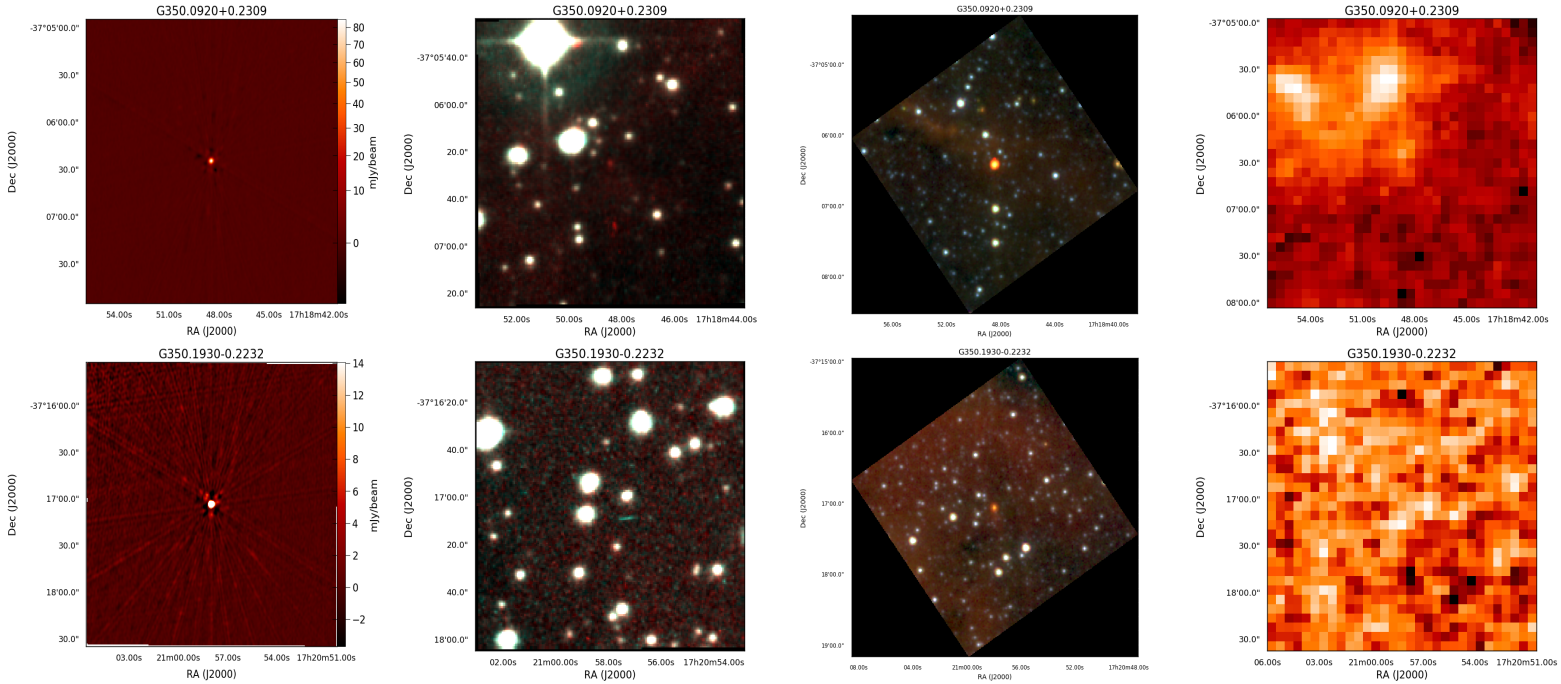

Figure B.77: *Continuation from previous Figure.*

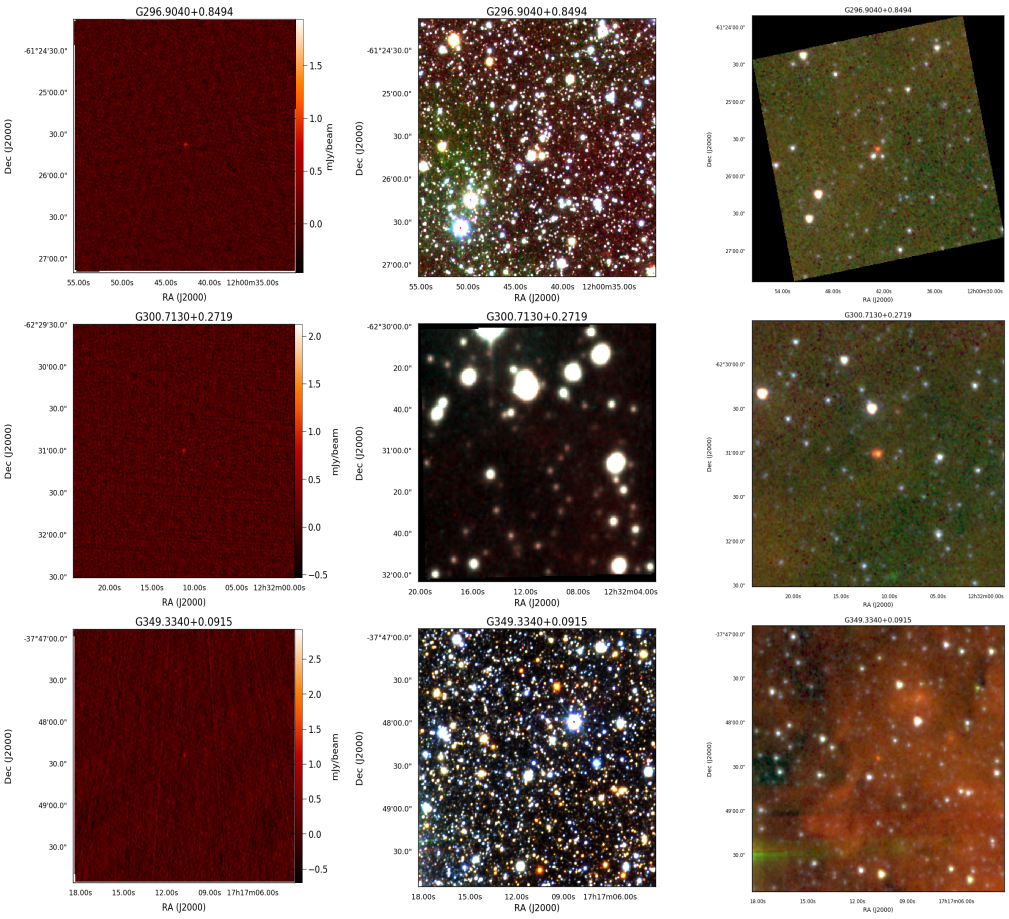

Figure B.78: *Possible PNe based on insufficient data.*

MIR and NIR colours of the CORNISH South PNe

Table B.1: *MIR colours of the PNe detected in the CORNISH survey of the southern Galactic plane.*

SourceName	$F_{3.6}$ mJy	$dF_{3.6}$ mJy	$F_{4.5}$ mJy	$dF_{4.5}$ mJy	$F_{5.8}$ mJy	$dF_{5.8}$ mJy	$F_{8.0}$ mJy	$dF_{8.0}$ mJy
G296.9040+0.8494	1.49	0.05	1.15	0.04	2.08	0.09	7.43	0.06
G296.9180-0.6942	0.8	0.02	0.91	0.01	2.06	0.08	6.94	0.05
G298.1910+0.3398	1.24	0.03	1.08	0.03	1.75	0.11	9.97	0.27
G298.7140+0.3104	22.97	0.04	37.83	0.05	108.73	0.11	337.67	0.22
G299.1520+0.0088	218.14	0.85	216.33	0.68	1265.37	6.21	3453.72	15.95
G300.2780+0.6616	26.04	0.05	37.24	0.05	62.92	0.12	279.96	0.22
G300.4290-0.9820	3.66	0.04	4.64	0.04	8.54	0.12	22.2	0.12
G300.5890-1.1087	18.23	0.06	52.51	0.07	26.32	0.12	78.02	0.14
G300.7130+0.2719	2.82	0.03	2.01	0.03	5.92	0.08	21.01	0.09
G300.7950+0.5707	3.51	0.04	6.68	0.04	5.03	0.11	19.12	0.16
G300.8780-0.4677	7.21	0.03	5.53	0.04	15.74	0.09	46.0	0.13
G301.1270-0.4848	1.05	0.05	1.66	0.04	2.0	0.1	6.58	0.09
G302.9570+0.7802	2.09	0.03	1.62	0.03	1.07	0.07	1.26	0.05
G303.1960+0.6558	111.62	0.05	201.95	0.08	340.68	0.1	538.2	0.14
G303.4090-0.3055	6.38	0.05	9.25	0.04	42.77	0.17	113.9	0.35
G303.4840-0.4601	86.82	0.21	76.47	0.2	639.26	1.22	1898.7	1.91
G303.9980+0.2801	78.43	0.15	107.36	0.16	492.6	1.11	1195.31	2.97
G304.1840-0.9917	447.57	0.19	381.56	0.18	311.05	0.16	237.39	0.17
G304.5710+0.7160	20.28	0.05	26.78	0.04	46.36	0.11	149.46	0.13
G305.5990-0.8984	5.94	0.04	7.44	0.03	11.6	0.09	27.08	0.17
G306.1250-1.1375	14.58	0.02	20.56	0.03	61.38	0.1	209.87	0.18
G306.6950+0.9993	2.87	0.03	2.39	0.04	2.85	0.1	11.96	0.11
G306.8350-0.8337	9.38	0.07	6.72	0.05	10.47	0.1	19.41	0.07
G307.3950-0.5845	89.67	0.09	238.79	0.14	553.71	0.42	842.36	0.97
G307.5240-0.2775	37.46	0.06	44.58	0.06	187.53	0.19	648.04	0.54
G307.7360-0.5944	27.46	0.07	28.98	0.05	208.46	0.1	570.17	0.19
G307.9500-0.1567	2.82	0.06	5.37	0.06	3.44	0.15	14.93	0.19
G307.9560+0.0169	26.84	0.13	32.76	0.14	267.49	1.15	743.04	2.89
G308.1820-0.5848	7.03	0.09	6.57	0.08	10.29	0.2	15.84	0.15
G308.3650-0.5085	19.27	0.04	33.57	0.04	79.43	0.13	263.6	0.17
G308.6510-0.5086	23.34	0.2	29.58	0.2	222.96	1.18	585.54	2.88
G309.0210+0.8907	46.4	0.05	48.99	0.05	183.91	0.15	634.26	0.3
G309.7840-0.7181	61.08	0.07	76.97	0.07	147.2	0.18	301.57	0.38

Continued on next page

Table B.1 – continued from previous page

SourceName	$F_{3.6}$ mJy	$dF_{3.6}$ mJy	$F_{4.5}$ mJy	$dF_{4.5}$ mJy	$F_{5.8}$ mJy	$dF_{5.8}$ mJy	$F_{8.0}$ mJy	$dF_{8.0}$ mJy
G310.5000-0.7593	9.22	0.05	20.46	0.05	13.56	0.13	26.33	0.15
G311.4310-0.2333	12.38	0.05	19.53	0.06	115.83	0.16	297.71	0.28
G311.5960-0.3984	11.55	0.05	35.48	0.06	99.41	0.19	223.61	0.27
G311.6840-0.6255	16.32	0.06	23.85	0.06	50.49	0.14	199.06	0.19
G311.8200-1.0601	3.4	0.05	5.41	0.04	15.31	0.15	38.57	0.1
G312.5010-0.0845	29.54	0.45	43.09	0.42	334.34	2.32	930.98	2.03
G314.1020-0.2136	1.97	0.05	2.28	0.04	9.78	0.22	26.63	0.39
G314.3340+0.9639	4.2	0.04	7.48	0.04	6.01	0.11	21.38	0.11
G315.0310-0.3694	19.58	0.14	37.9	0.14	43.85	0.37	208.69	0.51
G315.4370-0.2749	24.43	0.05	32.78	0.04	101.36	0.16	293.49	0.3
G315.7820-1.1441	6.79	0.05	10.61	0.05	9.72	0.15	26.67	0.11
G316.2270-0.6457	12.84	0.1	18.54	0.08	44.58	0.27	178.12	0.61
G316.2470+0.8837	50.6	0.14	71.1	0.12	193.12	0.27	764.06	0.38
G316.6570-0.8240	3.32	0.07	2.63	0.05	3.71	0.16	13.36	0.14
G317.1650-0.1697	5.66	0.11	17.57	0.11	14.22	0.4	55.48	1.01
G317.1880+0.3106	613.75	0.29	649.16	0.35	609.54	0.33	441.87	0.65
G317.2040-0.7580	10.1	0.09	17.13	0.08	87.61	0.23	278.3	0.28
G317.4000-0.1254	49.41	0.08	80.14	0.07	109.11	0.22	129.54	0.35
G317.8340+0.5920	1.27	0.06	2.21	0.05	2.73	0.12	11.26	0.1
G318.0520+0.5496	7.03	0.06	15.85	0.06	25.89	0.15	80.17	0.16
G318.0800-0.3924	10.35	0.07	14.32	0.06	14.62	0.17	36.84	0.19
G318.1590+0.2944	3.36	0.05	3.35	0.04	5.47	0.12	15.82	0.23
G318.9310+0.6956	40.84	0.16	49.51	0.14	37.35	0.4	152.46	0.44
G319.2560+0.7512	22.35	0.04	13.86	0.03	12.58	0.1	20.0	0.1
G319.9150+0.8732	18.86	0.07	15.1	0.05	38.7	0.13	88.08	0.23
G320.6750+0.2454	167.66	0.13	154.87	0.16	1253.93	0.72	3413.48	1.89
G320.9060-0.2928	190.49	0.09	368.82	0.18	599.73	0.25	1201.12	0.43
G321.1250-0.2653	121.9	0.23	295.72	0.3	751.27	1.04	1254.38	2.47
G322.0860-0.4532	6.68	0.06	21.81	0.07	20.08	0.22	31.52	0.38
G322.1980-0.4107	8.91	0.07	16.79	0.06	23.35	0.15	97.04	0.19
G322.2070-0.7429	33.16	0.07	46.63	0.06	66.94	0.14	184.81	0.2
G322.4180-0.1721	4.49	0.13	8.22	0.11	12.28	0.22	37.79	0.21
G322.4690-0.1779	116.03	0.19	207.82	0.17	322.14	0.37	3736.73	1.48
G322.6850-0.3924	2.28	0.07	8.19	0.06	4.05	0.13	7.87	0.19
G323.2460+0.6498	11.69	0.05	11.11	0.04	77.76	0.12	254.37	0.15
G323.6010+0.3936	4.06	0.08	8.21	0.06	5.31	0.15	14.65	0.12
G323.7500+0.4379	88.32	0.34	89.31	0.32	616.31	3.37	1666.99	9.16

Continued on next page

Table B.1 – continued from previous page

SourceName	$F_{3.6}$ mJy	$dF_{3.6}$ mJy	$F_{4.5}$ mJy	$dF_{4.5}$ mJy	$F_{5.8}$ mJy	$dF_{5.8}$ mJy	$F_{8.0}$ mJy	$dF_{8.0}$ mJy
G324.0610-0.2125	8.62	0.07	15.39	0.06	14.77	0.21	60.83	0.43
G324.7230+0.3628	3.82	0.07	8.47	0.07	7.44	0.17	14.54	0.2
G325.1370-0.2960	16.23	0.16	23.74	0.13	28.83	0.44	86.16	1.14
G325.9530-0.8350	7.54	0.09	8.89	0.07	8.43	0.21	10.05	0.28
G326.3150+0.7034	6.47	0.15	11.68	0.11	7.45	0.71	62.97	1.53
G326.4820+0.0448	5.53	0.07	7.1	0.06	24.59	0.24	73.31	0.57
G326.5300-0.4188	89.55	0.06	193.03	0.1	217.12	0.21	402.6	0.52
G326.5800+0.8090	169.26	0.21	333.82	0.21	1045.12	0.57	3105.45	1.13
G326.6780+0.9689	6.92	0.05	16.15	0.05	24.74	0.13	57.88	0.2
G326.9680+0.5997	3.32	0.07	5.19	0.06	5.16	0.26	7.0	1.17
G326.9790-0.0954	6.8	0.14	15.64	0.12	40.43	0.76	150.46	2.05
G327.5840+0.1301	5.92	0.13	11.46	0.11	10.05	0.27	33.04	0.36
G327.8260-0.8712	5.35	0.11	8.15	0.09	10.94	0.18	38.69	0.17
G327.8290-0.8881	27.62	0.09	34.3	0.07	85.75	0.16	310.91	0.2
G327.8480+0.0179	78.84	0.12	146.07	0.13	718.11	0.65	1634.88	1.73
G328.0620+0.0778	53.88	0.13	89.88	0.11	137.27	0.34	393.06	0.85
G328.4240-0.0892	28.21	0.38	39.68	0.35	193.77	1.22	522.41	1.92
G329.1200+0.0385	2.13	0.19	5.52	0.14	12.47	0.35	26.73	0.51
G329.3620-0.3111	7.54	0.09	13.72	0.06	22.07	0.17	56.24	0.24
G329.5230-0.7963	5.19	0.08	6.47	0.07	14.33	0.18	45.1	0.29
G329.6480-0.2375	37.95	0.26	51.76	0.19	84.74	0.32	156.87	0.41
G330.4100-0.3900	40.85	0.12	50.4	0.09	72.48	0.24	118.66	0.32
G330.9510+0.5738	4.56	0.11	17.94	0.1	30.15	0.18	71.28	0.44
G331.0970-0.6435	161.66	0.15	184.14	0.12	169.4	0.3	193.54	0.46
G331.1580+0.7811	12.31	0.09	20.7	0.06	32.75	0.17	84.63	0.19
G331.3720+0.3100	8.16	0.07	28.0	0.06	48.63	0.2	197.33	0.27
G331.6030-0.1075	130.34	0.16	161.42	0.18	1199.03	0.91	3355.18	3.02
G332.1280-1.0061	4.31	0.17	5.28	0.11	2.89	0.22	16.33	0.2
G332.1880-0.0898	14.72	0.13	26.95	0.1	176.48	0.26	545.32	0.69
G332.3560-0.2525	9.84	0.09	14.35	0.06	13.61	0.22	116.73	0.47
G332.5450+0.0174	5.61	0.13	14.07	0.1	16.64	0.29	51.07	0.48
G332.6990+0.3108	2.01	0.2	2.77	0.17			11.39	1.21
G332.7100-0.2127	11.44	0.17	16.56	0.14	28.77	0.41	95.6	0.83
G332.7870-0.2397	39.79	0.36	45.86	0.25	203.31	1.36	550.14	3.58
G332.9300-0.1090	21.74	0.24	21.86	0.31	169.57	1.44	488.97	2.88
G333.1310-0.9954	7.19	0.06	16.35	0.07	41.97	0.28	129.05	0.45
G333.1600-0.9705	19.55	0.13	28.71	0.11	19.33	0.28	89.85	0.56

Continued on next page

Table B.1 – continued from previous page

SourceName	$F_{3.6}$ mJy	$dF_{3.6}$ mJy	$F_{4.5}$ mJy	$dF_{4.5}$ mJy	$F_{5.8}$ mJy	$dF_{5.8}$ mJy	$F_{8.0}$ mJy	$dF_{8.0}$ mJy
G333.3830+0.9199	19.01	0.08	47.49	0.09	24.25	0.26	97.43	0.25
G333.3870+0.0318	12.3	0.09	19.55	0.09	127.58	0.25	303.13	0.52
G333.6530-0.9493	4.03	0.06	6.6	0.05	4.59	0.14	16.77	0.26
G333.8770-1.0078	77.47	0.1	53.69	0.08	137.08	0.19	390.27	0.37
G333.9730+0.7937	10.53	0.07	17.68	0.06	29.57	0.15	66.91	0.17
G334.1310+1.0148	7.61	0.07	17.24	0.06	50.6	0.15	161.1	0.19
G334.2150+0.4794	13.48	0.14	15.83	0.1	15.07	0.34	30.7	0.33
G334.2180-0.9350	5.54	0.1	9.58	0.07	7.36	0.18	26.0	0.21
G334.2440-0.1067	246.57	0.15	229.7	0.12	480.51	0.32	815.07	0.52
G334.3420+0.0483	70.06	0.87	95.2	0.98	700.01	8.76	1952.38	22.53
G334.4740-0.1495	5.95	0.11	6.63	0.09	34.95	0.24	87.52	0.38
G334.7200+0.1763	134.01	0.12	171.0	0.13	201.39	0.28	485.48	0.52
G334.7680-1.0420	11.13	0.06	10.94	0.05	7.9	0.13	26.83	0.21
G335.3900-0.2905	21.16	0.22	46.43	0.18	83.2	0.27	97.08	0.3
G335.4920-1.1031	14.16	0.12	32.52	0.12	39.8	0.3	206.77	0.57
G335.5780-0.2072	111.12	0.83	146.44	0.69	551.07	4.67	1935.17	12.18
G336.4910+0.8775	8.82	0.12	13.95	0.09	19.11	0.32	39.34	0.6
G336.6440-0.6956	171.39	0.25	311.4	0.25	824.37	0.45	2930.19	1.08
G336.9830-0.1832	664.71	0.44	1222.8	0.77	4617.11	3.32	6596.31	9.58
G337.0700-0.1085	9.11	0.11	23.38	0.1	29.25	0.47	130.13	1.82
G337.1890-0.1194	17.81	0.12	57.28	0.15	137.21	0.68	410.91	1.65
G337.2910+0.1782	431.57	0.28	760.15	0.39	1501.06	0.73	1680.62	0.81
G337.3140+0.6350	8.28	0.09	14.86	0.06	34.78	0.14	97.61	0.25
G337.9010+0.0063	15.32	0.19	26.54	0.15	97.76	0.59	259.9	1.52
G338.1210+0.6991	1.87	0.08	6.57	0.08	13.7	0.21	47.55	0.42
G338.3740-0.1516	463.68	0.77	368.75	0.62	723.28	3.05	1351.61	4.97
G338.4890+0.0448	52.76	0.28	71.15	0.28	518.15	2.02	1197.62	7.11
G338.6800-0.1313	9.68	0.28	16.01	0.23	110.87	0.77	313.85	1.09
G338.6810-0.0843	199.6	0.3	302.26	0.29	875.68	1.1	1782.17	2.6
G339.0280+0.1243	10.91	0.12	14.92	0.11	14.05	0.38	49.75	1.09
G339.3310+0.0967	135.45	0.23	174.77	0.19	436.02	0.62	854.59	2.15
G339.4050+1.0302	6.09	0.07	9.54	0.07	6.46	0.15	29.76	0.22
G339.4430-0.6081	18.44	0.16	16.56	0.12	17.98	0.21	20.72	0.33
G339.5660-0.0863	21.18	0.1	34.88	0.1	262.66	0.56	675.11	1.49
G339.7360+0.8469	2.94	0.1	2.95	0.08	6.6	0.18	21.15	0.2
G339.9320+0.3654	795.4	0.32	1208.57	0.51	3217.14	0.97	3510.43	1.12
G339.9510+0.5127	12.2	0.15	15.46	0.1	21.26	0.22	56.71	0.2

Continued on next page

Table B.1 – continued from previous page

SourceName	$F_{3.6}$ mJy	$dF_{3.6}$ mJy	$F_{4.5}$ mJy	$dF_{4.5}$ mJy	$F_{5.8}$ mJy	$dF_{5.8}$ mJy	$F_{8.0}$ mJy	$dF_{8.0}$ mJy
G340.2290+0.0915	6.39	0.19	12.1	0.15	39.32	0.4	139.74	0.67
G340.2490-0.0461	291.07	0.18	562.61	0.27	1680.47	1.3	3547.03	3.17
G340.3600+0.1283	13.44	0.1	17.34	0.08	125.46	0.33	327.18	0.7
G341.3130+0.1913	47.0	0.23	61.75	0.22	421.87	1.68	1036.25	5.35
G341.5040+0.6919	8.14	0.09	14.43	0.06	12.99	0.15	31.67	0.18
G341.9620-0.4534	25.73	0.15	24.67	0.11	190.33	0.52	510.42	1.12
G342.1470+0.0101	21.9	0.08	51.57	0.08	115.86	0.36	306.06	1.31
G342.2260-0.3801	48.41	0.11	95.54	0.11	76.63	0.2	206.77	0.38
G342.6560+0.0320	204.34	0.22	152.4	0.2	148.75	0.33	97.99	0.49
G342.7770+0.3094	5.56	0.13	10.28	0.09	13.96	0.26	61.63	0.33
G342.9260-0.6469	25.75	0.2	22.17	0.18	133.4	0.39	359.09	0.35
G342.9550-0.2750	13.42	0.13	18.29	0.12	28.23	0.26	71.13	0.28
G343.6380+0.2717	0.94	0.14	1.12	0.1	2.78	0.17	6.02	0.22
G343.7020+0.0862	1.84	0.21	4.76	0.16	9.99	0.35	30.01	0.36
G343.7430-1.0878	4.94	0.09	8.51	0.08	7.55	0.26	15.91	0.22
G343.9920+0.8350	89.01	0.15	137.0	0.11	184.73	0.36	759.06	0.53
G344.0600+1.0054	7.79	0.08	8.58	0.07	6.27	0.22	24.81	0.2
G344.5090+0.6443	5.39	0.11	8.45	0.08	6.11	0.2	21.33	0.25
G344.7720-0.6862	23.74	0.14	35.34	0.11	48.77	0.3	55.44	0.31
G344.8350+0.5975	8.38	0.18	8.1	0.15	10.83	0.25	31.19	0.24
G345.1980-0.0301	7.64	0.05	16.08	0.07	56.5	0.19	127.04	0.39
G345.2060-0.6231	35.69	0.18	23.8	0.14	72.99	0.23	122.53	0.27
G345.4050-0.2440	8.07	0.07	19.12	0.07	53.36	0.18	184.43	0.18
G345.4790+0.1392	79.95	0.56	105.95	0.52	148.1	1.04	220.9	0.76
G345.7570+0.7486	10.9	0.14	9.83	0.1	8.45	0.24	18.72	0.26
G345.7960-0.2738	3.54	0.09	3.83	0.06	4.27	0.16	9.99	0.31
G345.8040+0.0480	88.05	0.46	101.92	0.41	721.49	1.77	1857.87	3.11
G346.1960+0.0402	15.45	0.19	20.33	0.19	195.21	1.07	575.63	3.03
G346.4560-0.6739	3.11	0.13	6.02	0.1	2.29	0.24	30.57	0.33
G346.8830-0.7106	9.58	0.12	11.34	0.1	31.87	0.21	111.44	0.17
G346.9840+0.3185	16.4	0.13	23.99	0.11	94.22	0.31	269.55	0.45
G347.1660+0.3190	10.16	0.13	7.38	0.11	7.17	0.35	10.45	1.17
G347.2120-0.0958	25.71	0.12	31.31	0.12	195.84	0.41	486.76	0.93
G347.2940+0.1317	26.05	0.13	35.4	0.13	253.33	0.48	636.48	1.25
G347.2970+0.2832	7.25	0.15	11.61	0.1	21.05	0.39	138.35	0.97
G347.3050+0.0148	27.52	0.17	53.0	0.16	218.13	1.1	491.17	4.09
G347.7630-0.7109	43.21	0.17	30.97	0.12	46.29	0.19	99.78	0.16

Continued on next page

Table B.1 – continued from previous page

SourceName	$F_{3.6}$ mJy	$dF_{3.6}$ mJy	$F_{4.5}$ mJy	$dF_{4.5}$ mJy	$F_{5.8}$ mJy	$dF_{5.8}$ mJy	$F_{8.0}$ mJy	$dF_{8.0}$ mJy
G347.8940-0.1708	87.2	0.29	211.14	0.22	360.37	0.91	508.35	2.47
G348.5500-0.3386	21.29	0.22	24.1	0.13	124.51	0.44	342.62	0.96
G348.6210+0.1399	4.39	0.27	6.17	0.18	31.7	0.32	108.94	0.41
G348.6420-0.5720	10.33	0.17	17.82	0.12	16.64	0.28	46.47	0.45
G349.1970-0.0301	37.48	0.19	29.09	0.15	125.4	0.37	307.24	0.84
G349.3510-0.2113	29.98	0.19	81.33	0.14	168.9	0.25	475.63	0.46
G349.3700-0.1105	14.63	0.25	16.35	0.2	26.18	0.29	92.72	0.38
G350.0920+0.2309	178.49	0.71	143.03	0.5	322.0	1.34	1025.54	1.78
G350.1930-0.2232	5.16	0.31	8.38	0.21	23.38	0.33	48.82	0.46

Table B.2: *NIR colours of the PNe detected in the CORNISH survey of the southern Galactic plane.*

sourceName	J mag	dJ mag	H mag	dH mag	K mag	dK mag
G296.9040+0.8494	16.12	0.02	15.17	0.01	14.4	0.02
G296.9180-0.6942	18.52	0.07	18.01	0.08	16.21	0.05
G298.1910+0.3398	17.67	0.04	15.98	0.02	14.94	0.02
G301.1270-0.4848	16.9	0.03	16.29	0.05	15.28	0.04
G302.9570+0.7802	16.26	0.01	14.81	0.01	14.09	0.03
G303.9980+0.2801	14.9	0.01	13.78	0.01	12.24	0.01
G305.5990-0.8984	14.96	0.01	14.29	0.01		
G306.8350-0.8337	14.39	0.01	13.0	0.01	12.23	0.01
G308.3650-0.5085	17.39	0.02	15.09	0.01	13.21	0.01
G308.6510-0.5086	19.01	0.22	16.66	0.08	14.24	0.02
G309.7840-0.7181	14.85	0.01	13.18	0.01	11.35	0.01
G311.4310-0.2333	17.37	0.03	15.7	0.02	14.36	0.02
G311.5960-0.3984	19.03	0.16	16.36	0.04	14.69	0.02
G311.6840-0.6255	14.96	0.01	13.89	0.01	12.42	0.01
G312.5010-0.0845	17.77	0.11	16.5	0.08		
G314.3340+0.9639	15.42	0.01	14.59	0.01	13.37	0.01
G315.7820-1.1441	14.5	0.01	13.95	0.02	12.86	0.09
G316.2470+0.8837	13.2	0.02	12.39	0.01	11.33	0.09
G317.2040-0.7580	18.03	0.08	16.73	0.07	15.28	0.05
G317.4000-0.1254	16.55	0.01	15.3	0.01	12.6	0.01
G318.9310+0.6956	13.18	0.01	11.64	0.01	10.52	0.01

Continued on next page

Table B.2 – continued from previous page

sourceName	J	dJ	H	dH	K	dK
	mag	mag	mag	mag	mag	mag
G322.0860-0.4532	16.79	0.03	15.74	0.03	13.91	0.02
G323.2460+0.6498	16.63	0.02	14.88	0.01	13.5	0.01
G324.7230+0.3628	15.15	0.01	14.06	0.01		
G325.1370-0.2960	13.11	0.01	12.41	0.01	11.81	0.01
G325.9530-0.8350	16.28	0.03	15.36	0.05		
G326.3150+0.7034	14.69	0.01	13.86	0.01	12.87	0.01
G326.4820+0.0448	16.19	0.01	14.59	0.01		
G326.5300-0.4188	15.47	0.01	12.83	0.01		
G326.5800+0.8090	13.66	0.01	12.23	0.01	10.82	0.01
G326.6780+0.9689	16.38	0.02	14.99	0.02	13.59	0.01
G327.5840+0.1301	16.46	0.03	14.76	0.02	13.55	0.02
G327.8480+0.0179	17.17	0.05	14.93	0.02	13.03	0.01
G329.1200+0.0385	16.34	0.03	15.9	0.06	14.65	0.05
G329.3620-0.3111	17.06	0.03	16.08	0.04	14.47	0.02
G329.6480-0.2375	15.04	0.02	13.88	0.03	12.39	0.02
G330.4100-0.3900	15.86	0.02	13.37	0.01	11.55	0.01
G330.9510+0.5738	17.02	0.04	15.86	0.03	14.1	0.02
G331.1580+0.7811	14.73	0.01	13.51	0.01	12.7	0.01
G331.3720+0.3100	17.4	0.03	15.9	0.03	14.07	0.02
G332.1880-0.0898					14.7	0.03
G332.3560-0.2525	16.76	0.02	14.35	0.01	12.56	0.01
G332.6990+0.3108	14.62	0.01	13.99	0.02	13.42	0.02
G333.1310-0.9954	15.71	0.01	14.66	0.02	13.43	0.01
G333.1600-0.9705	13.21	0.01	12.37	0.01	11.29	0.01
G333.3830+0.9199	13.0	0.01	12.34	0.01	11.59	0.01
G333.3870+0.0318	18.76	0.14	16.93	0.08	14.68	0.03
G333.9730+0.7937	16.01	0.02	14.74	0.02	13.28	0.01
G334.2150+0.4794	13.8	0.01	12.49	0.01	11.7	0.01
G334.2180-0.9350	14.99	0.01	14.29	0.02	13.06	0.01
G334.3420+0.0483	15.06	0.01	14.09	0.02	12.39	0.01
G334.7200+0.1763	14.57	0.01	12.11	0.01	10.76	0.01
G334.7680-1.0420	14.09	0.01	12.72	0.01	11.78	0.01
G335.3900-0.2905	17.82	0.05	15.06	0.02	13.19	0.01
G336.4910+0.8775	15.47	0.03	14.67	0.04	13.51	0.02
G336.6440-0.6956	14.51	0.02	13.23	0.02	11.22	0.01
G337.2910+0.1782	15.19	0.02	13.16	0.01	10.84	0.01

Continued on next page

Table B.2 – continued from previous page

sourceName	J	dJ	H	dH	K	dK
	mag	mag	mag	mag	mag	mag
G337.3140+0.6350	15.64	0.02	14.78	0.03	13.59	0.02
G337.9010+0.0063	15.69	0.03	15.05	0.05	14.17	0.04
G338.1210+0.6991	17.73	0.12	16.42	0.1	14.7	0.04
G338.3740-0.1516	12.34	0.01	10.46	0.01	9.04	0.01
G339.0280+0.1243	14.61	0.01	13.59	0.01	12.51	0.01
G339.3310+0.0967	15.56	0.02	13.84	0.02	11.76	0.01
G339.4050+1.0302	14.65	0.01	13.97	0.02	13.09	0.01
G339.4430-0.6081	16.31	0.02	13.67	0.01		
G339.7360+0.8469	15.28	0.02	14.3	0.03	13.56	0.02
G339.9320+0.3654	14.38	0.01	11.97	0.02	9.54	0.01
G340.2290+0.0915	15.07	0.02	14.24	0.03	13.57	0.03
G340.2490-0.0461	14.87	0.01	13.05	0.02	10.73	0.01
G340.3600+0.1283	17.98	0.08	15.89	0.04	14.04	0.02
G341.9620-0.4534	16.48	0.03	14.42	0.02	12.99	0.02
G342.1470+0.0101	17.28	0.03	14.27	0.01	12.49	0.01
G342.2260-0.3801	12.68	0.01	11.89	0.01	10.79	0.01
G342.9260-0.6469	15.28	0.02	13.36	0.01	12.19	0.01
G343.6380+0.2717		1.81	17.78	0.41	17.5	0.66
G343.7020+0.0862	18.71	0.11	17.19	0.12	14.99	0.05
G343.9920+0.8350	11.62	0.01	11.16	0.01	9.99	0.01
G344.0600+1.0054	14.53	0.01	13.08	0.01	12.13	0.01
G344.5090+0.6443	15.85	0.02	14.49	0.02	13.19	0.02
G344.7720-0.6862	16.71	0.04	14.89	0.03	12.72	0.01
G344.8350+0.5975	14.38	0.01	13.35	0.01	12.57	0.02
G345.1980-0.0301	17.29	0.03	15.63	0.02	14.13	0.02
G345.2060-0.6231	14.93	0.01	13.38	0.01	12.42	0.01
G345.4050-0.2440	17.11	0.02	14.91	0.01	13.48	0.01
G345.7570+0.7486	16.46	0.02	15.11	0.03	13.95	0.03
G345.8040+0.0480	13.44	0.01				
G346.4560-0.6739	16.04	0.02	14.9	0.03	13.75	0.03
G346.6120-0.7649	15.15	0.02	14.43	0.03	13.78	0.03
G346.8830-0.7106	14.49	0.02	13.9	0.02	12.82	0.01
G346.9840+0.3185	15.33	0.02			12.77	0.01
G347.2970+0.2832	15.41	0.02	14.47	0.02	13.35	0.02
G347.7630-0.7109	13.69	0.01	12.97	0.02	11.96	0.01
G347.8940-0.1708	12.39	0.01	12.05	0.01	10.96	0.01

Continued on next page

Table B.2 – continued from previous page

sourceName	J	dJ	H	dH	K	dK
	mag	mag	mag	mag	mag	mag
G348.5500-0.3386	15.35	0.03	13.86	0.02	13.0	0.02
G348.6420-0.5720	12.53	0.01	12.17	0.01	11.75	0.01
G349.1970-0.0301	14.5	0.01	14.11	0.03	13.24	0.03
G349.3510-0.2113	17.03	0.06	15.03	0.04	13.55	0.02
G349.3700-0.1105	14.43	0.01	12.98	0.02	12.05	0.01

CORNISH South Catalogue

Table B.3: *A sample of the radio properties of the 7σ CORNISH South Catalogue.*

Source Name	RA J2000	σ_{ra} $''$	DEC J2000	σ_{dec} $''$	Peak mJy/bm	σ_{peak} mJy/bm	S mJy	σ_S mJy	ϑ $''$	σ_ϑ $''$	SNR	rms mJy/bm	Type	Tile
G294.5600+0.3739	11:40:44.64	0.07	–61:20:36.7	0.09	1.29	0.1	1.0	0.08	2.21	0.024	11.34	0.11	G	6
G294.5740+0.5171	11:41:10.70	0.04	–61:12:34.0	0.05	2.68	0.09	3.37	0.13	2.804	0.01	27.58	0.1	G	5
G294.5990+0.2792	11:40:50.58	0.09	–61:26:42.6	0.08	1.34	0.1	1.31	0.11	2.471	0.027	13.18	0.1	G	6
G294.6060+0.3159	11:40:58.91	0.06	–61:24:42.1	0.06	1.66	0.1	1.32	0.08	2.227	0.013	16.84	0.1	G	6
G294.6080+0.6004	11:41:37.90	0.04	–61:08:17.2	0.04	2.64	0.1	2.41	0.09	2.39	0.008	24.52	0.11	G	5
G294.6200–0.9135	11:38:13.28	0.05	–62:35:51.9	0.07	1.8	0.11	1.46	0.1	2.247	0.017	15.07	0.12	G	2
G294.6210+0.2443	11:40:56.20	0.1	–61:29:04.4	0.11	0.98	0.11	0.65	0.08	2.04	0.028	8.94	0.11	G	6
G294.6250–0.9089	11:38:16.49	0.05	–62:35:41.1	0.05	2.68	0.1	3.1	0.14	2.69	0.012	22.37	0.11	G	2
G294.6300+0.6949	11:42:00.87	0.01	–61:03:10.1	0.01	17.49	0.11	18.14	0.11	2.547	0.002	126.35	0.14	G	5
G294.6320–0.5125	11:39:17.07	0.04	–62:12:57.3	0.03	4.1	0.09	8.42	0.19	3.583	0.013	34.9	0.12	G	1
G294.6350–0.5129	11:39:18.20	0.01	–62:13:01.1	0.01	10.24	0.11	10.57	0.11	2.539	0.003	76.69	0.13	G	1
G294.6370–0.5133	11:39:19.48	0.07	–62:13:05.0	0.04	2.77	0.09	6.32	0.2	3.779	0.028	25.24	0.11	G	1
G294.6460–0.7176	11:38:54.44	0.1	–62:25:00.2	0.11	1.19	0.11	1.14	0.11	2.444	0.03	11.04	0.1	G	1
G294.6470–0.5707	11:39:15.88	0.08	–62:16:32.8	0.08	1.58	0.1	1.82	0.12	2.683	0.031	14.11	0.12	G	1
G294.6810+0.2503	11:41:26.27	0.04	–61:29:41.8	0.03	3.21	0.1	2.91	0.11	2.379	0.006	30.85	0.1	G	6
G294.7010+0.5552	11:42:16.40	0.14	–61:12:23.6	0.18	1.42	0.04	2.41	1.42	7.949	0.263	11.37	0.12	P	5
G294.7010+0.5583	11:42:16.86	0.12	–61:12:11.2	0.14	1.73	0.05	3.99	1.63	8.608	0.189	13.99	0.12	P	5
G294.7170+0.1680	11:41:32.51	0.08	–61:35:01.9	0.08	1.42	0.11	1.09	0.09	2.191	0.014	14.22	0.09	G	7
G294.7380–0.6364	11:39:51.93	0.08	–62:21:50.6	0.08	1.69	0.11	2.03	0.15	2.736	0.028	15.35	0.11	G	1
G294.7470+0.9178	11:43:25.77	0.07	–60:52:07.0	0.1	1.41	0.11	1.27	0.11	2.376	0.028	13.68	0.11	G	14
G294.7530+0.9698	11:43:35.41	0.11	–60:49:12.3	0.14	0.93	0.11	0.7	0.09	2.171	0.048	7.91	0.12	G	14

Continued on next page

Table B.3 – continued from previous page

sSource Name	RA J2000	σ_{ra} $''$	DEC J2000	σ_{dec} $''$	Peak mJy/bm	σ_{peak} mJy/bm	S mJy	σ_S mJy	ϑ $''$	σ_ϑ $''$	SNR	rms mJy/bm	Type	Tile
G294.7600+0.8676	11:43:25.65	0.1	–60:55:14.1	0.11	1.16	0.1	1.24	0.13	2.583	0.045	10.76	0.11	G	14
G294.7700+0.8480	11:43:27.76	0.05	–60:56:31.1	0.06	2.1	0.11	1.83	0.11	2.336	0.012	19.34	0.11	G	14
G294.7740–0.7080	11:39:59.88	0.0	–62:26:34.3	0.0	37.48	0.15	38.19	0.15	2.523	0.002	192.57	0.18	G	2
G294.7790–0.6222	11:40:14.25	0.06	–62:21:41.4	0.08	1.78	0.11	1.51	0.11	2.302	0.018	14.96	0.12	G	1
G294.8030–0.9058	11:39:46.32	0.04	–62:38:28.0	0.05	2.89	0.11	2.43	0.11	2.291	0.009	21.43	0.13	G	2
G294.8120–0.3655	11:41:06.60	0.12	–62:07:24.4	0.12	1.02	0.11	0.93	0.12	2.382	0.036	9.62	0.1	G	8
G294.8520–1.0214	11:39:54.20	0.04	–62:45:55.8	0.06	3.18	0.11	4.0	0.14	2.802	0.014	23.16	0.13	G	3
G294.8590–0.9084	11:40:13.79	0.01	–62:39:31.2	0.01	21.27	0.13	20.94	0.15	2.48	0.002	109.64	0.19	G	2
G294.8670–0.1207	11:42:07.00	0.07	–61:54:07.8	0.06	1.73	0.1	1.34	0.08	2.196	0.012	15.66	0.1	G	8
G294.8960+0.6687	11:44:04.94	0.02	–61:08:51.9	0.02	5.48	0.1	5.19	0.1	2.433	0.003	47.2	0.11	G	15
G294.8960+1.0351	11:44:51.27	0.02	–60:47:36.8	0.03	5.17	0.11	7.43	0.15	2.999	0.006	46.67	0.11	G	14
G294.9210–0.2548	11:42:15.58	0.05	–62:02:45.1	0.06	2.09	0.1	1.74	0.1	2.278	0.009	20.03	0.1	G	8
G294.9260+0.9436	11:44:54.13	0.0	–60:53:22.9	0.0	67.16	0.18	70.61	0.22	2.564	0.002	209.61	0.32	G	14
G294.9400–0.5829	11:41:39.77	0.14	–62:22:01.3	0.18	0.84	0.11	0.85	0.12	2.52	0.109	7.13	0.11	G	9
G294.9490–0.7021	11:41:27.87	0.08	–62:29:03.6	0.11	1.15	0.11	0.86	0.08	2.165	0.032	10.12	0.12	G	10
G294.9650+0.7143	11:44:43.80	0.1	–61:07:16.6	0.05	2.22	0.08	7.1	0.25	4.468	0.049	24.86	0.1	G	15
G294.9670+0.7171	11:44:45.43	0.07	–61:07:09.4	0.06	2.08	0.1	2.88	0.14	2.944	0.022	18.31	0.11	G	15
G294.9720+0.4846	11:44:18.22	0.06	–61:20:43.2	0.07	1.84	0.1	1.69	0.1	2.398	0.017	15.67	0.12	G	16
G294.9850–0.5357	11:42:08.91	0.7	–62:19:59.6	2.78	1.24	0.03	5.66	2.02	11.478	0.221	11.3	0.11	P	9
G295.0100+0.8398	11:45:21.57	0.57	–61:00:45.5	0.45	1.8	0.04	7.64	1.62	14.848	0.176	21.23	0.09	P	14
G295.0150+0.8400	11:45:23.74	0.08	–61:00:44.9	0.12	1.16	0.1	1.1	0.11	2.436	0.035	12.04	0.1	G	14
G295.0230–0.9266	11:41:33.79	0.02	–62:43:13.5	0.02	5.78	0.11	5.68	0.11	2.478	0.003	53.75	0.1	G	11
G295.0290–0.9857	11:41:28.64	0.28	–62:46:42.9	0.16	1.41	0.03	2.93	1.38	8.087	0.219	11.75	0.12	P	11
G295.0440–0.7431	11:42:10.00	0.08	–62:32:57.2	0.1	1.27	0.11	1.05	0.09	2.273	0.032	10.22	0.12	G	10

Continued on next page

Table B.3 – continued from previous page

sSource Name	RA J2000	σ_{ra} $''$	DEC J2000	σ_{dec} $''$	Peak mJy/bm	σ_{peak} mJy/bm	S mJy	σ_S mJy	ϑ $''$	σ_ϑ $''$	SNR	rms mJy/bm	Type	Tile
G295.0480+0.2072	11:44:19.10	0.11	–61:37:58.4	0.11	0.87	0.1	0.57	0.07	2.026	0.035	8.25	0.11	G	17
G295.0570+1.0169	11:46:06.07	0.04	–60:51:07.2	0.03	3.34	0.11	3.08	0.1	2.4	0.006	29.6	0.11	G	24
G295.0600+0.4868	11:45:00.70	0.02	–61:21:56.3	0.03	7.14	0.52	8.38	1.23	8.228	0.057	66.29	0.11	P	16
G295.1080+0.7668	11:45:59.35	0.09	–61:06:24.5	0.13	1.04	0.09	1.09	0.1	2.552	0.04	11.94	0.09	G	25
G295.1080–0.7271	11:42:44.38	0.12	–62:33:02.6	0.12	0.78	0.1	0.5	0.06	2.006	0.033	7.95	0.1	G	10
G295.1180+0.0949	11:44:38.81	0.02	–61:45:33.9	0.03	5.17	0.1	5.9	0.14	2.671	0.005	44.97	0.11	G	17
G295.1180+0.0965	11:44:39.17	0.3	–61:45:28.6	0.35	0.69	0.09	2.45	0.45	4.711	0.407	20.29	0.1	G	17
G295.1200+0.1023	11:44:40.81	0.04	–61:45:10.9	0.04	5.86	0.36	10.85	1.71	10.588	0.081	54.8	0.11	P	17
G295.1330+0.9898	11:46:38.91	0.34	–60:53:49.9	0.2	0.79	0.09	2.42	0.45	4.372	0.296	7.24	0.1	G	23
G295.1350+0.1995	11:45:00.81	0.07	–61:39:45.5	0.08	1.45	0.1	1.05	0.08	2.123	0.018	11.69	0.11	G	17
G295.1380+0.1299	11:44:53.27	0.01	–61:43:50.4	0.01	10.02	0.11	9.77	0.12	2.468	0.002	73.07	0.13	G	17
G295.1380+0.9996	11:46:42.56	0.18	–60:53:20.2	0.19	0.83	0.1	1.41	0.21	3.266	0.142	7.72	0.1	G	24
G295.1520–0.5882	11:43:25.25	0.01	–62:25:41.1	0.01	21.51	0.17	22.84	0.2	2.576	0.003	79.88	0.25	G	19
G295.1560+0.4219	11:45:38.80	0.07	–61:27:09.8	0.05	4.14	0.18	9.33	1.2	7.844	0.052	39.66	0.11	P	16
G295.1670–0.5795	11:43:34.13	0.17	–62:25:25.2	0.14	1.41	0.11	4.44	0.43	4.442	0.156	9.84	0.14	G	19
G295.1750+0.0099	11:44:55.77	0.11	–61:51:24.1	0.16	4.31	0.2	21.65	2.51	22.557	0.123	45.03	0.1	P	17
G295.1750–0.8496	11:43:01.25	0.03	–62:41:11.0	0.03	4.3	0.11	4.98	0.14	2.691	0.005	41.15	0.1	G	10
G295.1760+0.2283	11:45:24.23	0.04	–61:38:41.9	0.04	2.69	0.11	2.28	0.09	2.303	0.007	24.59	0.1	G	17
G295.1760–0.5744	11:43:38.87	0.64	–62:25:17.4	0.44	3.85	0.16	48.41	5.77	25.935	0.137	31.32	0.13	P	19
G295.1770+0.5729	11:46:08.38	0.04	–61:18:42.5	0.04	3.3	0.11	2.98	0.1	2.375	0.006	27.37	0.11	G	26
G295.1790–0.6444	11:43:31.18	0.06	–62:29:21.9	0.06	1.96	0.11	1.58	0.09	2.241	0.008	21.83	0.09	G	20
G295.2090–0.7448	11:43:32.61	0.03	–62:35:38.7	0.03	4.71	0.1	6.24	0.14	2.877	0.005	48.83	0.09	G	20
G295.2100–0.7089	11:43:37.88	0.0	–62:33:34.6	0.0	38.91	0.15	39.04	0.15	2.504	0.002	166.13	0.23	G	20
G295.2300–0.2259	11:44:52.13	0.11	–62:05:52.9	0.12	0.86	0.1	0.57	0.08	2.036	0.039	7.68	0.11	G	18

Continued on next page

Table B.3 – continued from previous page

sSource Name	RA J2000	σ_{ra} $''$	DEC J2000	σ_{dec} $''$	Peak mJy/bm	σ_{peak} mJy/bm	S mJy	σ_S mJy	ϑ $''$	σ_ϑ $''$	SNR	rms mJy/bm	Type	Tile
G295.2330–1.0573	11:43:01.85	0.0	–62:54:07.0	0.01	53.75	28.94	60.07	2.87	9.564	0.019	250.48	0.21	P	11
G295.2500–0.6212	11:44:10.14	0.08	–62:29:07.7	0.1	1.17	0.11	0.81	0.08	2.083	0.027	9.85	0.12	G	20
G295.2840+0.0257	11:45:51.44	0.04	–61:52:06.2	0.04	3.1	0.1	2.76	0.09	2.361	0.005	30.42	0.1	G	28
G295.3140–0.6677	11:44:35.72	0.16	–62:32:47.8	0.12	0.79	0.1	0.61	0.08	2.185	0.047	7.84	0.1	G	20
G295.3230–0.4447	11:45:09.88	0.09	–62:20:00.0	0.11	1.16	0.1	1.19	0.12	2.535	0.032	12.62	0.09	G	19
G295.3380–0.9840	11:44:05.67	0.1	–62:51:31.3	0.11	0.99	0.1	0.75	0.09	2.175	0.031	9.37	0.1	G	21
G295.3480–0.5033	11:45:14.63	0.09	–62:23:46.7	0.11	1.08	0.1	0.81	0.09	2.174	0.019	11.36	0.08	G	19
G295.3530+0.1725	11:46:44.18	0.1	–61:44:36.6	0.15	1.06	0.11	0.99	0.12	2.417	0.059	9.27	0.11	G	27
G295.3580–0.5753	11:45:10.29	0.1	–62:28:06.9	0.1	1.04	0.11	0.66	0.07	1.999	0.017	10.0	0.09	G	20
G295.3650+0.5488	11:47:36.36	0.03	–61:22:53.6	0.03	3.7	0.11	3.51	0.1	2.434	0.006	32.3	0.12	G	26
G295.3900–0.1740	11:46:18.25	0.02	–62:05:17.6	0.02	7.87	0.11	8.36	0.13	2.578	0.003	66.38	0.11	G	28
G295.3960–0.0645	11:46:35.46	0.09	–61:59:01.6	0.08	1.53	0.1	1.94	0.13	2.814	0.037	13.17	0.11	G	28
G295.4000–0.4813	11:45:43.70	0.11	–62:23:17.8	0.16	0.91	0.11	0.79	0.11	2.327	0.043	8.88	0.09	G	19
G295.4030+0.1206	11:47:02.06	0.12	–61:48:22.0	0.09	1.09	0.1	1.05	0.12	2.454	0.041	10.62	0.1	G	27
G295.4030–0.0775	11:46:36.99	0.12	–61:59:52.6	0.11	1.05	0.1	1.02	0.1	2.468	0.044	10.57	0.1	G	28
G295.4100+0.8470	11:48:34.34	0.03	–61:06:11.9	0.04	3.28	0.1	3.17	0.1	2.459	0.006	33.28	0.1	G	35
G295.4120+0.2713	11:47:25.04	0.09	–61:39:43.6	0.09	1.09	0.1	0.7	0.07	2.0	0.02	10.7	0.1	G	27
G295.4150–0.5477	11:45:42.46	0.08	–62:27:22.5	0.08	1.39	0.1	1.27	0.09	2.383	0.017	14.28	0.09	G	20
G295.4180+1.1396	11:49:13.11	0.07	–60:49:16.4	0.05	3.43	0.21	2.56	0.16	2.158	0.013	15.8	0.22	G	34
G295.4290+1.1378	11:49:17.87	0.1	–60:49:31.6	0.09	2.05	0.2	1.58	0.16	2.196	0.029	10.42	0.2	G	34
G295.4600–0.0482	11:47:09.11	0.01	–61:59:01.6	0.01	11.24	0.1	15.64	0.14	2.948	0.003	100.47	0.11	G	28
G295.4660–0.0486	11:47:12.06	0.05	–61:59:08.3	0.04	3.34	0.1	5.3	0.17	3.15	0.013	27.22	0.12	G	28
G295.4700+0.0013	11:47:20.40	0.03	–61:56:18.0	0.04	3.91	0.09	9.0	0.2	3.794	0.012	41.86	0.1	G	28
G295.4860–0.4879	11:46:26.01	0.07	–62:24:58.4	0.07	1.54	0.1	1.44	0.11	2.422	0.016	16.57	0.09	G	29

Continued on next page

Table B.3 – continued from previous page

sSource Name	RA J2000	σ_{ra} $''$	DEC J2000	σ_{dec} $''$	Peak mJy/bm	σ_{peak} mJy/bm	S mJy	σ_S mJy	ϑ $''$	σ_ϑ $''$	SNR	rms mJy/bm	Type	Tile
G295.5040–0.1665	11:47:16.03	0.07	–62:06:33.3	0.07	1.61	0.1	1.71	0.12	2.581	0.014	18.29	0.08	G	28
G295.5080+0.6675	11:49:00.25	0.04	–61:18:03.8	0.03	3.2	0.1	3.13	0.09	2.472	0.005	32.56	0.09	G	36
G295.5220+0.5962	11:48:58.49	0.01	–61:22:25.1	0.01	16.11	0.11	16.19	0.11	2.506	0.002	127.36	0.12	G	36
G295.5260–0.8062	11:46:04.57	0.02	–62:44:03.6	0.02	7.23	0.1	9.35	0.13	2.842	0.003	68.45	0.1	G	21
G295.5280–0.8055	11:46:05.53	0.22	–62:44:02.7	0.15	1.46	0.03	2.09	0.79	5.812	0.111	16.11	0.09	P	21
G295.5440–0.8352	11:46:09.95	0.13	–62:46:00.8	0.13	0.75	0.1	0.57	0.07	2.171	0.035	8.09	0.08	G	31
G295.5460–0.6555	11:46:34.35	0.1	–62:35:36.1	0.1	0.89	0.1	0.57	0.07	2.0	0.034	7.5	0.11	G	30
G295.5530+0.2629	11:48:33.44	0.01	–61:42:16.7	0.01	12.32	0.1	12.29	0.1	2.497	0.002	124.77	0.09	G	37
G295.5640+0.0222	11:48:09.47	0.11	–61:56:27.7	0.11	0.82	0.1	0.54	0.07	2.023	0.024	9.08	0.08	G	28
G295.5740–0.1923	11:47:47.33	0.11	–62:09:04.5	0.13	0.85	0.1	0.63	0.08	2.152	0.03	9.05	0.08	G	29
G295.5800–0.7954	11:46:33.63	0.06	–62:44:15.0	0.06	1.88	0.1	1.91	0.1	2.518	0.01	21.95	0.08	G	31
G295.5950+0.8641	11:50:05.65	0.09	–61:07:50.7	0.11	1.1	0.1	0.9	0.09	2.261	0.038	10.1	0.11	G	35
G295.6220+0.4711	11:49:32.58	0.05	–61:31:09.0	0.06	2.05	0.1	2.04	0.11	2.494	0.012	21.41	0.1	G	36
G295.6350+0.6857	11:50:04.29	0.03	–61:18:49.1	0.03	3.49	0.09	3.21	0.09	2.397	0.004	35.83	0.09	G	36
G295.6560–0.5267	11:47:46.33	0.05	–62:29:44.2	0.06	1.84	0.1	1.45	0.08	2.221	0.011	17.72	0.1	G	30
G295.6660–0.5262	11:47:51.33	0.02	–62:29:51.1	0.02	5.37	0.1	6.12	0.11	2.67	0.004	50.1	0.11	G	30
G295.6970–0.5719	11:48:01.27	0.01	–62:32:58.0	0.01	11.27	0.11	11.27	0.11	2.501	0.002	90.59	0.12	G	30
G295.6980+0.3020	11:49:49.55	0.02	–61:42:05.0	0.02	6.96	0.1	7.65	0.11	2.621	0.003	63.98	0.11	G	37
G295.7030+0.2984	11:49:51.33	0.11	–61:42:21.5	0.1	1.02	0.1	0.85	0.08	2.273	0.031	10.4	0.1	G	37
G295.7210–0.2115	11:48:58.51	0.12	–62:12:20.1	0.13	1.06	0.09	1.61	0.14	3.084	0.076	10.4	0.1	G	39
G295.7220–0.2164	11:48:58.15	0.01	–62:12:37.5	0.02	7.49	0.1	7.32	0.1	2.471	0.003	69.49	0.1	G	39
G295.7270–0.1112	11:49:13.71	0.08	–62:06:34.4	0.09	1.36	0.09	1.46	0.12	2.591	0.026	13.15	0.09	G	38
G295.7300+0.5888	11:50:39.23	0.12	–61:25:48.4	0.13	0.8	0.1	0.57	0.07	2.11	0.03	8.52	0.08	G	36
G295.7340–0.1135	11:49:17.14	0.11	–62:06:49.0	0.09	1.16	0.09	1.48	0.13	2.826	0.038	13.21	0.09	G	38

Continued on next page

Table B.3 – continued from previous page

sSource Name	RA J2000	σ_{ra} $''$	DEC J2000	σ_{dec} $''$	Peak mJy/bm	σ_{peak} mJy/bm	S mJy	σ_S mJy	ϑ $''$	σ_ϑ $''$	SNR	rms mJy/bm	Type	Tile
G295.7460+0.3397	11:50:17.40	0.05	–61:40:33.4	0.05	2.16	0.1	1.8	0.09	2.282	0.01	19.09	0.11	G	37
G295.7460–0.4069	11:48:46.79	0.0	–62:24:04.3	0.0	41.14	0.15	41.51	0.17	2.511	0.002	205.04	0.19	G	39
G295.7490–0.2072	11:49:13.21	0.72	–62:12:29.5	0.3	0.57	0.07	3.12	0.39	5.834	0.785	7.04	0.1	G	39
G295.7520–0.7137	11:48:11.16	0.08	–62:42:01.4	0.08	1.38	0.1	1.29	0.1	2.418	0.018	14.73	0.09	G	30
G295.7540+0.0673	11:49:48.70	0.02	–61:56:32.9	0.02	5.54	0.1	5.41	0.09	2.471	0.003	51.29	0.1	G	38
G295.7570+0.8945	11:51:27.38	0.01	–61:08:19.9	0.01	17.78	0.11	21.0	0.13	2.717	0.003	117.11	0.15	G	45
G295.8140–0.0170	11:50:08.69	0.05	–62:02:19.6	0.05	2.23	0.1	2.03	0.1	2.386	0.009	22.89	0.1	G	38
G295.8160–0.5941	11:48:58.69	0.03	–62:35:59.1	0.03	3.49	0.1	3.16	0.11	2.379	0.005	30.8	0.11	G	40
G295.8500+0.9809	11:52:22.56	0.11	–61:04:34.4	0.13	0.94	0.1	0.77	0.08	2.264	0.048	8.4	0.11	G	45
G295.8530+0.9276	11:52:17.76	0.03	–61:07:43.3	0.04	3.08	0.1	2.84	0.09	2.398	0.006	28.21	0.1	G	45
G295.8530–0.6888	11:49:05.59	0.46	–62:42:03.2	0.48	0.72	0.01	0.8	0.76	5.561	0.261	7.74	0.09	P	40
G295.8650–0.4570	11:49:40.71	0.02	–62:28:42.3	0.02	5.08	0.09	5.0	0.09	2.48	0.003	50.39	0.1	G	40
G295.8750+0.7436	11:52:07.45	0.07	–61:18:46.1	0.06	1.62	0.1	1.29	0.08	2.233	0.008	19.41	0.07	G	46
G295.9000+0.6643	11:52:10.83	0.08	–61:23:44.8	0.07	1.65	0.1	1.88	0.11	2.666	0.022	16.12	0.1	G	46
G295.9020+0.7644	11:52:22.95	0.05	–61:17:55.2	0.06	1.85	0.11	1.29	0.07	2.086	0.008	17.65	0.09	G	46
G295.9040–0.3910	11:50:08.36	0.09	–62:25:24.1	0.12	0.95	0.1	0.7	0.09	2.152	0.022	10.1	0.08	G	39
G295.9420–0.9867	11:49:13.50	0.0	–63:00:39.4	0.0	54.24	0.15	54.94	0.15	2.516	0.002	281.49	0.18	G	42
G295.9440–0.6501	11:49:56.77	0.03	–62:41:04.6	0.03	4.26	0.1	4.06	0.11	2.442	0.003	44.78	0.08	G	40
G295.9580–0.0366	11:51:17.90	0.08	–62:05:28.5	0.09	1.33	0.1	1.16	0.1	2.339	0.021	13.49	0.1	G	48
G295.9650+0.1262	11:51:40.49	0.09	–61:56:03.9	0.11	0.97	0.1	0.73	0.07	2.168	0.033	9.36	0.1	G	48
G295.9700–0.0316	11:51:24.55	0.01	–62:05:21.1	0.01	11.51	0.11	11.1	0.12	2.455	0.002	95.36	0.12	G	48
G295.9830+0.0359	11:51:38.80	0.07	–62:01:35.1	0.08	1.58	0.1	1.65	0.12	2.552	0.02	16.47	0.1	G	48
G295.9890–0.4401	11:50:45.16	0.06	–62:29:27.5	0.06	1.53	0.1	0.98	0.07	2.003	0.012	14.01	0.11	G	40
G296.0140–0.5935	11:50:39.26	0.04	–62:38:46.1	0.04	3.83	0.16	4.49	1.28	7.646	0.12	32.31	0.12	P	40

Continued on next page

Table B.3 – continued from previous page

sSource Name	RA J2000	σ_{ra} $''$	DEC J2000	σ_{dec} $''$	Peak mJy/bm	σ_{peak} mJy/bm	S mJy	σ_S mJy	ϑ $''$	σ_ϑ $''$	SNR	rms mJy/bm	Type	Tile
G296.0160–0.5961	11:50:40.09	0.14	–62:38:56.6	0.2	0.88	0.1	1.64	0.22	3.406	0.206	7.16	0.12	G	40
G296.0450–0.4654	11:51:10.28	0.09	–62:31:42.7	0.12	1.01	0.1	0.8	0.08	2.236	0.031	10.24	0.09	G	40
G296.0810–0.2727	11:51:51.47	0.01	–62:20:57.2	0.01	26.41	0.13	27.61	0.16	2.556	0.002	147.46	0.18	G	49
G296.1350+0.8657	11:54:28.00	0.02	–61:15:07.2	0.02	5.58	0.1	5.54	0.12	2.49	0.003	49.36	0.11	G	55
G296.1390+0.4142	11:53:39.91	0.07	–61:41:35.8	0.09	1.33	0.1	1.04	0.08	2.208	0.018	12.89	0.09	G	57
G296.1410+0.9089	11:54:35.47	0.15	–61:12:42.3	0.11	2.35	0.07	9.64	2.08	13.181	0.152	22.83	0.1	P	55
G296.1480–0.7356	11:51:30.12	0.15	–62:48:54.7	0.14	0.79	0.1	0.63	0.09	2.233	0.039	8.34	0.08	G	51
G296.1670+0.5372	11:54:07.13	0.06	–61:34:45.5	0.06	1.9	0.1	1.84	0.11	2.462	0.012	19.03	0.09	G	56
G296.1740–0.7723	11:51:39.13	0.02	–62:51:25.2	0.02	4.81	0.1	4.41	0.09	2.394	0.003	48.88	0.1	G	51
G296.1780+0.0755	11:53:20.50	0.12	–62:01:55.2	0.15	0.76	0.1	0.57	0.09	2.157	0.036	8.55	0.08	G	48
G296.1820–0.5909	11:52:05.09	0.01	–62:40:56.1	0.01	100.01	100.23	104.56	6.25	11.57	0.032	222.56	0.45	P	50
G296.1940+0.1268	11:53:34.60	0.12	–61:59:08.4	0.13	0.76	0.1	0.52	0.07	2.061	0.027	8.21	0.08	G	58
G296.2080–1.1104	11:51:15.38	0.03	–63:11:37.5	0.03	11.3	0.3	11.16	0.35	2.484	0.005	33.27	0.33	G	42
G296.2240+1.0899	11:55:35.06	0.09	–61:03:08.2	0.08	2.04	0.16	1.74	0.13	2.309	0.021	12.12	0.15	G	55
G296.2240+1.0913	11:55:35.45	0.02	–61:03:03.7	0.02	9.51	0.16	8.99	0.15	2.43	0.003	60.92	0.14	G	55
G296.2530+0.8001	11:55:18.03	0.04	–61:20:29.5	0.04	2.63	0.1	2.35	0.09	2.364	0.006	26.7	0.09	G	56
G296.2670–0.2383	11:53:29.14	0.03	–62:21:27.7	0.03	4.4	0.1	4.31	0.11	2.474	0.003	47.31	0.08	G	49
G296.2950+0.8645	11:55:45.78	0.02	–61:17:16.0	0.03	5.37	0.09	9.03	0.18	3.24	0.006	53.95	0.1	G	65
G296.3070+0.5674	11:55:19.44	0.04	–61:34:49.5	0.04	2.62	0.1	2.34	0.09	2.364	0.007	26.05	0.1	G	57
G296.3430–0.9692	11:52:42.27	0.08	–63:05:13.5	0.07	1.72	0.1	1.99	0.11	2.689	0.022	16.4	0.1	G	52
G296.3450–0.9692	11:52:43.31	0.1	–63:05:15.2	0.08	1.4	0.09	1.9	0.13	2.915	0.051	11.33	0.11	G	52
G296.3460–0.1016	11:54:24.88	0.18	–62:14:31.0	0.11	0.76	0.1	0.64	0.09	2.305	0.065	8.28	0.1	G	59
G296.3480+0.4891	11:55:31.06	0.08	–61:39:56.7	0.09	1.13	0.1	0.81	0.07	2.118	0.023	11.13	0.1	G	57
G296.3520–0.4585	11:53:46.97	0.11	–62:35:28.9	0.14	0.83	0.1	0.67	0.09	2.258	0.042	8.16	0.09	G	50

Continued on next page

Table B.3 – continued from previous page

sSource Name	RA J2000	σ_{ra} $''$	DEC J2000	σ_{dec} $''$	Peak mJy/bm	σ_{peak} mJy/bm	S mJy	σ_S mJy	ϑ $''$	σ_ϑ $''$	SNR	rms mJy/bm	Type	Tile
G296.3610+0.5270	11:55:41.84	0.07	–61:37:53.7	0.07	1.48	0.09	1.43	0.09	2.454	0.013	17.67	0.08	G	57
G296.3780–0.6070	11:53:43.16	0.03	–62:44:31.1	0.03	4.14	0.09	4.53	0.1	2.614	0.005	40.84	0.1	G	51
G296.3780–0.8607	11:53:13.31	0.08	–62:59:21.5	0.08	1.14	0.09	0.91	0.08	2.229	0.018	13.11	0.08	G	51
G296.3840–0.1385	11:54:39.61	0.03	–62:17:10.6	0.03	4.19	0.09	5.81	0.12	2.945	0.007	43.35	0.1	G	59
G296.3850–0.2816	11:54:23.88	0.06	–62:25:33.7	0.08	1.35	0.09	1.09	0.09	2.245	0.015	14.55	0.08	G	59
G296.4020–0.9975	11:53:09.68	0.04	–63:07:41.1	0.06	2.42	0.09	2.87	0.11	2.724	0.014	24.06	0.1	G	52
G296.4030–1.0189	11:53:07.61	0.1	–63:08:56.8	0.12	1.38	0.09	2.64	0.21	3.461	0.064	12.34	0.11	G	52
G296.4110+0.0011	11:55:09.07	0.16	–62:09:21.4	0.09	1.13	0.09	1.99	0.15	3.309	0.067	13.44	0.09	G	59
G296.4190+0.0043	11:55:13.65	0.27	–62:09:15.6	0.19	0.9	0.02	1.52	0.95	7.013	0.21	10.13	0.09	P	59
G296.4330–0.9748	11:53:28.23	0.02	–63:06:46.1	0.02	5.84	0.09	8.0	0.13	2.926	0.004	55.55	0.1	G	52
G296.4360–0.9457	11:53:33.17	0.05	–63:05:06.1	0.07	1.81	0.09	1.65	0.09	2.381	0.011	20.15	0.09	G	52
G296.4400–0.5836	11:54:17.24	0.02	–62:43:57.7	0.02	5.88	0.1	5.48	0.09	2.414	0.003	55.4	0.1	G	61
G296.4450+0.4707	11:56:17.42	0.08	–61:42:16.3	0.06	1.9	0.1	2.8	0.14	3.03	0.024	18.81	0.1	G	67
G296.4690+0.6983	11:56:53.37	0.09	–61:29:13.5	0.09	1.21	0.09	1.2	0.11	2.492	0.028	13.12	0.09	G	66
G296.4880+0.8041	11:57:13.72	0.01	–61:23:15.2	0.01	8.6	0.1	8.18	0.1	2.439	0.002	74.27	0.12	G	66
G296.4890+0.2937	11:56:20.15	0.2	–61:53:12.5	0.12	0.69	0.09	0.67	0.09	2.463	0.068	8.18	0.08	G	68
G296.4890–0.0106	11:55:46.78	0.03	–62:11:02.7	0.04	2.7	0.09	2.42	0.08	2.368	0.005	31.72	0.07	G	59
G296.4990+0.8624	11:57:25.14	0.01	–61:19:58.3	0.01	18.48	0.11	18.25	0.11	2.485	0.002	147.41	0.12	G	66
G296.5030–0.2695	11:55:25.24	0.02	–62:26:24.5	0.02	10.49	1.11	12.7	1.2	9.077	0.043	108.17	0.1	P	60
G296.5150–0.4649	11:55:09.19	0.13	–62:37:59.8	0.09	0.91	0.09	0.74	0.09	2.251	0.049	8.76	0.11	G	60
G296.5200–0.6469	11:54:51.14	0.14	–62:48:43.6	0.1	1.02	0.09	1.21	0.11	2.727	0.057	10.89	0.1	G	61
G296.5210–0.2866	11:55:32.25	0.06	–62:27:37.6	0.08	1.59	0.09	1.68	0.1	2.568	0.016	17.61	0.09	G	60
G296.5230–0.0130	11:56:03.62	0.13	–62:11:37.2	0.17	0.87	0.09	1.28	0.13	3.034	0.064	10.9	0.08	G	59
G296.5270+0.3665	11:56:46.77	0.05	–61:49:25.3	0.05	2.01	0.1	1.64	0.09	2.257	0.007	21.98	0.08	G	67

Continued on next page

Table B.3 – continued from previous page

sSource Name	RA J2000	σ_{ra} $''$	DEC J2000	σ_{dec} $''$	Peak mJy/bm	σ_{peak} mJy/bm	S mJy	σ_S mJy	ϑ $''$	σ_ϑ $''$	SNR	rms mJy/bm	Type	Tile
G296.6110+0.2237	11:57:13.21	0.1	–61:58:51.0	0.19	0.78	0.1	0.77	0.09	2.473	0.112	7.24	0.11	G	68
G296.6240+0.6606	11:58:05.83	0.12	–61:33:22.2	0.11	1.05	0.1	1.22	0.13	2.698	0.036	12.12	0.08	G	66
G296.6260+0.0961	11:57:06.91	0.02	–62:06:31.3	0.02	6.44	0.1	6.2	0.11	2.453	0.003	61.38	0.1	G	68
G296.6350+0.5856	11:58:03.41	0.09	–61:37:54.7	0.09	1.16	0.1	0.92	0.08	2.233	0.025	11.3	0.1	G	67
G296.6650–0.3920	11:56:33.78	0.09	–62:35:39.0	0.13	1.01	0.1	0.96	0.11	2.432	0.037	10.36	0.09	G	70
G296.6840+0.7379	11:58:43.09	0.08	–61:29:33.6	0.1	1.04	0.1	0.79	0.08	2.171	0.024	11.73	0.09	G	76
G296.6870+0.5749	11:58:27.67	0.08	–61:39:10.0	0.11	1.04	0.1	0.82	0.08	2.217	0.02	12.46	0.08	G	67
G296.7160–0.0319	11:57:38.68	0.04	–62:15:09.7	0.04	2.74	0.09	2.55	0.08	2.411	0.006	29.64	0.09	G	69
G296.7280+1.0286	11:59:33.90	0.03	–61:13:00.2	0.03	3.93	0.1	4.68	0.13	2.727	0.006	37.37	0.1	G	75
G296.7300+1.0366	11:59:35.58	0.06	–61:12:33.4	0.05	2.2	0.1	2.87	0.15	2.858	0.016	21.84	0.1	G	75
G296.7310–0.6637	11:56:37.50	0.09	–62:52:24.9	0.09	1.15	0.1	0.89	0.09	2.196	0.018	12.03	0.09	G	61
G296.7320–0.1675	11:57:32.50	0.03	–62:23:19.3	0.03	3.65	0.1	3.11	0.1	2.307	0.004	34.85	0.1	G	69
G296.7610–0.2476	11:57:38.58	0.08	–62:28:23.3	0.1	1.14	0.1	0.82	0.08	2.125	0.026	10.57	0.11	G	70
G296.7710–0.2112	11:57:47.61	0.08	–62:26:22.4	0.07	1.63	0.1	1.73	0.1	2.578	0.015	18.38	0.08	G	70
G296.7710–0.3551	11:57:31.89	0.08	–62:34:49.0	0.09	1.12	0.1	0.76	0.08	2.055	0.021	10.78	0.1	G	70
G296.7800–0.5068	11:57:20.16	0.0	–62:43:49.9	0.0	34.95	0.15	34.82	0.15	2.495	0.002	163.09	0.2	G	71
G296.7900–0.0855	11:58:10.39	0.11	–62:19:13.4	0.1	1.03	0.09	0.98	0.1	2.439	0.041	10.39	0.1	G	69
G296.8210–0.6112	11:57:29.60	0.06	–62:50:28.1	0.06	1.74	0.09	1.75	0.1	2.507	0.014	19.17	0.09	G	71
G296.8310+0.4935	11:59:30.89	0.04	–61:45:42.1	0.05	2.68	0.09	4.17	0.16	3.12	0.016	25.79	0.1	G	77
G296.8320+0.4911	11:59:31.21	0.03	–61:45:51.3	0.04	3.55	0.09	4.94	0.15	2.947	0.009	31.48	0.11	G	77
G296.8320–0.4610	11:57:51.43	0.09	–62:41:47.1	0.14	0.93	0.1	0.78	0.1	2.292	0.035	9.5	0.09	G	70
G296.8330–0.9549	11:56:57.84	0.03	–63:10:47.1	0.03	3.24	0.09	3.08	0.1	2.438	0.005	33.08	0.09	G	72
G296.8400–0.0107	11:58:43.62	0.11	–62:15:26.5	0.1	1.28	0.09	2.12	0.15	3.216	0.049	13.71	0.09	G	69
G296.8420–0.0067	11:58:45.19	0.22	–62:15:14.0	0.13	0.8	0.09	1.21	0.14	3.078	0.097	10.22	0.08	G	69

Continued on next page

Table B.3 – continued from previous page

sSource Name	RA J2000	σ_{ra} $''$	DEC J2000	σ_{dec} $''$	Peak mJy/bm	σ_{peak} mJy/bm	S mJy	σ_S mJy	ϑ $''$	σ_ϑ $''$	SNR	rms mJy/bm	Type	Tile
G296.8540+0.1000	11:59:02.01	0.11	–62:09:06.1	0.12	1.1	0.11	1.01	0.11	2.404	0.046	9.36	0.12	G	79
G296.8600–0.0615	11:58:48.34	0.06	–62:18:40.2	0.07	1.95	0.1	2.13	0.13	2.615	0.015	19.38	0.1	G	69
G296.8870–0.1000	11:58:58.03	0.06	–62:21:15.6	0.06	1.87	0.1	1.62	0.1	2.329	0.009	19.04	0.09	G	79
G296.9040+0.1411	11:59:31.54	0.0	–62:07:17.5	0.0	125.94	0.35	193.12	0.61	3.096	0.003	187.99	0.68	G	78
G296.9040+0.8494	12:00:42.67	0.1	–61:25:38.2	0.08	1.08	0.1	0.81	0.07	2.166	0.014	13.39	0.07	G	76
G296.9180–0.6942	11:58:10.55	0.07	–62:56:32.4	0.09	1.31	0.1	1.05	0.09	2.234	0.021	12.96	0.1	G	71
G296.9340+0.9763	12:01:09.61	0.15	–61:18:31.0	0.1	1.02	0.09	1.44	0.13	2.98	0.086	10.13	0.09	G	86
G296.9580+0.5462	12:00:39.59	0.17	–61:44:06.8	0.12	0.75	0.09	0.74	0.11	2.484	0.075	8.38	0.09	G	77
G297.0090–1.0159	11:58:23.12	0.11	–63:16:33.4	0.14	1.07	0.1	1.31	0.15	2.765	0.046	11.13	0.09	G	72
G297.0160+0.6541	12:01:18.78	0.04	–61:38:26.0	0.05	2.38	0.1	1.97	0.08	2.271	0.007	23.62	0.1	G	87
G297.0240+0.3760	12:00:55.16	0.06	–61:54:53.5	0.09	1.63	0.08	2.87	0.14	3.318	0.042	17.2	0.1	G	78
G297.0280+1.0242	12:02:00.47	0.11	–61:16:47.0	0.08	1.35	0.1	1.65	0.15	2.761	0.034	13.96	0.1	G	85
G297.0840+0.1516	12:01:02.96	0.03	–62:08:47.7	0.03	3.34	0.1	2.94	0.1	2.348	0.004	36.45	0.09	G	78
G297.1120–0.6787	11:59:52.70	0.1	–62:57:58.8	0.1	0.9	0.09	0.58	0.07	1.999	0.016	10.02	0.08	G	81
G297.1180–1.0344	11:59:18.06	0.04	–63:18:58.2	0.04	2.7	0.1	2.31	0.08	2.311	0.004	31.77	0.08	G	73
G297.1210–0.7794	11:59:46.55	0.16	–63:04:00.4	0.14	0.72	0.09	0.66	0.09	2.395	0.053	9.19	0.07	G	82
G297.1460+0.6422	12:02:22.08	0.11	–61:40:37.4	0.12	0.76	0.1	0.48	0.06	2.0	0.035	7.9	0.1	G	87
G297.1690+0.0374	12:01:34.86	0.03	–62:16:30.8	0.04	3.11	0.09	3.04	0.09	2.472	0.005	36.25	0.08	G	89
G297.2070–0.2985	12:01:20.52	0.0	–62:36:43.6	0.0	45.48	0.15	46.97	0.18	2.541	0.002	184.22	0.23	G	80
G297.2110+0.3738	12:02:28.94	0.2	–61:57:10.8	0.13	0.73	0.1	0.81	0.1	2.62	0.112	7.6	0.1	G	88
G297.2150+0.1252	12:02:06.52	0.01	–62:11:51.9	0.01	22.78	0.13	22.26	0.13	2.471	0.002	118.28	0.19	G	89
G297.2340–0.8709	12:00:35.86	0.07	–63:10:43.6	0.08	1.17	0.09	0.81	0.07	2.076	0.016	12.9	0.09	G	82
G297.2530–0.7540	12:00:57.87	0.06	–63:04:04.3	0.07	3.08	0.13	5.41	0.22	3.316	0.037	17.22	0.19	G	82
G297.2880–0.8909	12:01:02.03	0.06	–63:12:32.5	0.09	1.46	0.1	1.31	0.1	2.363	0.024	14.3	0.1	G	82

Continued on next page

Table B.3 – continued from previous page

sSource Name	RA J2000	σ_{ra} $''$	DEC J2000	σ_{dec} $''$	Peak mJy/bm	σ_{peak} mJy/bm	S mJy	σ_S mJy	ϑ $''$	σ_ϑ $''$	SNR	rms mJy/bm	Type	Tile
G297.2890+0.6424	12:03:33.21	0.08	–61:42:12.8	0.08	1.8	0.09	3.29	0.17	3.384	0.031	17.95	0.1	G	87
G297.2910+0.6412	12:03:34.04	0.05	–61:42:18.6	0.06	2.08	0.11	1.81	0.09	2.331	0.013	15.38	0.12	G	87
G297.2930+0.6414	12:03:35.20	0.06	–61:42:19.1	0.06	2.5	0.09	5.1	0.19	3.571	0.019	27.2	0.09	G	97
G297.3030+0.2280	12:03:01.10	0.04	–62:06:48.3	0.04	2.95	0.1	3.23	0.12	2.616	0.006	33.09	0.08	G	88
G297.3100+0.6351	12:03:43.18	0.08	–61:42:53.1	0.09	1.19	0.1	0.87	0.08	2.137	0.019	12.42	0.1	G	97
G297.3120+0.4816	12:03:29.75	0.15	–61:51:57.3	0.13	0.86	0.09	1.2	0.13	2.955	0.074	9.85	0.09	G	88
G297.3180+0.2059	12:03:06.34	0.07	–62:08:16.2	0.11	1.21	0.1	1.06	0.1	2.342	0.021	13.96	0.08	G	88
G297.3230–0.8496	12:01:24.71	0.11	–63:10:31.2	0.11	0.86	0.1	0.55	0.07	2.0	0.029	8.55	0.1	G	82
G297.3300–0.7266	12:01:40.93	0.06	–63:03:21.2	0.07	1.45	0.1	0.96	0.07	2.037	0.013	13.89	0.1	G	82
G297.3310–1.1034	12:01:02.36	0.02	–63:25:32.6	0.02	10.4	0.16	10.37	0.19	2.496	0.003	55.83	0.18	G	83
G297.3610+0.0215	12:03:10.44	0.01	–62:19:37.3	0.01	18.63	0.12	19.83	0.14	2.58	0.002	127.42	0.15	G	89
G297.3610–0.9875	12:01:30.32	0.13	–63:19:04.5	0.12	1.08	0.14	0.75	0.1	2.085	0.013	8.1	0.07	G	84
G297.3850+1.0806	12:05:00.68	0.07	–61:17:24.5	0.08	1.68	0.13	1.25	0.11	2.158	0.011	15.82	0.1	G	95
G297.3940–0.6347	12:02:23.29	0.96	–62:58:42.8	1.28	0.94	0.02	7.08	2.62	16.23	0.339	9.77	0.1	P	91
G297.4160+0.8674	12:04:56.75	0.01	–61:30:19.3	0.01	10.0	0.1	9.97	0.12	2.497	0.002	88.21	0.11	G	96
G297.4500–0.4286	12:03:12.42	0.15	–62:47:08.9	0.12	0.71	0.1	0.52	0.07	2.128	0.049	7.2	0.09	G	91
G297.4570–0.7628	12:02:43.06	0.02	–63:06:55.8	0.02	5.33	0.1	5.56	0.11	2.553	0.004	46.93	0.11	G	92
G297.4590–0.9024	12:02:30.02	0.04	–63:15:10.6	0.06	2.04	0.1	1.7	0.09	2.282	0.008	22.42	0.09	G	92
G297.4750+0.6681	12:05:08.39	0.09	–61:42:43.7	0.11	1.25	0.08	2.09	0.16	3.227	0.059	13.19	0.1	G	97
G297.4890+0.4751	12:04:57.91	0.04	–61:54:16.4	0.05	2.45	0.1	2.25	0.09	2.395	0.005	30.97	0.07	G	98
G297.4930+1.0446	12:05:50.88	0.04	–61:20:41.3	0.05	2.92	0.11	2.88	0.11	2.48	0.008	25.15	0.11	G	96
G297.4990–0.0541	12:04:13.50	0.03	–62:25:36.4	0.03	3.4	0.1	3.07	0.1	2.377	0.004	34.48	0.09	G	99
G297.5000–0.4306	12:03:38.03	0.11	–62:47:49.5	0.09	1.05	0.1	0.79	0.08	2.171	0.026	10.84	0.09	G	91
G297.5100–0.7749	12:03:09.83	0.14	–63:08:13.6	0.19	4.0	0.18	35.14	4.07	17.938	0.096	30.66	0.13	P	92

Continued on next page

Table B.3 – continued from previous page

sSource Name	RA J2000	σ_{ra} $''$	DEC J2000	σ_{dec} $''$	Peak mJy/bm	σ_{peak} mJy/bm	S mJy	σ_S mJy	ϑ $''$	σ_ϑ $''$	SNR	rms mJy/bm	Type	Tile
G297.5150–0.0014	12:04:26.85	0.03	–62:22:40.7	0.03	3.85	0.1	3.58	0.11	2.413	0.004	37.62	0.1	G	99
G297.5320–0.8223	12:03:16.46	0.01	–63:11:17.3	0.01	38.37	14.77	151.11	5.91	19.518	0.03	175.2	0.22	P	92
G297.5360–0.8283	12:03:17.84	0.01	–63:11:40.6	0.01	24.51	0.19	38.29	0.34	3.125	0.003	113.7	0.21	G	92
G297.5410–0.9376	12:03:09.83	0.11	–63:18:10.6	0.12	0.84	0.09	0.62	0.07	2.153	0.026	9.71	0.08	G	93
G297.5420+0.8887	12:06:00.96	0.02	–61:30:24.2	0.02	6.63	0.1	6.37	0.11	2.449	0.003	62.5	0.1	G	106
G297.5790–0.0650	12:04:53.62	0.02	–62:27:07.3	0.02	6.64	0.1	6.56	0.1	2.486	0.003	59.42	0.1	G	100
G297.5810+0.9983	12:06:29.87	0.11	–61:24:20.3	0.08	1.27	0.09	1.76	0.12	2.942	0.037	15.05	0.09	G	106
G297.5880+0.4587	12:05:45.87	0.04	–61:56:17.5	0.04	2.57	0.09	2.19	0.08	2.311	0.006	26.98	0.1	G	98
G297.5890+0.5426	12:05:53.73	0.01	–61:51:20.7	0.01	18.12	0.12	18.46	0.14	2.523	0.002	107.37	0.16	G	97
G297.5900+0.1560	12:05:19.28	0.01	–62:14:11.4	0.02	7.73	0.1	7.78	0.1	2.507	0.003	67.42	0.12	G	99
G297.5960+0.9703	12:06:35.25	0.02	–61:26:09.4	0.03	4.59	0.1	4.4	0.11	2.447	0.004	43.44	0.11	G	106
G297.6270–0.9029	12:03:57.59	0.8	–63:17:08.0	0.78	1.61	0.04	27.2	4.21	23.06	0.188	16.62	0.1	P	93
G297.6540–0.1105	12:05:27.72	0.04	–62:30:36.9	0.04	2.82	0.1	2.5	0.09	2.355	0.006	27.24	0.1	G	100
G297.6560–1.0128	12:04:02.95	0.04	–63:23:53.1	0.04	3.43	0.13	3.12	0.12	2.384	0.005	31.62	0.11	G	93
G297.6590–0.9720	12:04:07.76	0.03	–63:21:37.0	0.03	23.97	5.77	82.89	8.71	30.58	0.27	151.77	0.16	P	93
G297.6620–0.9763	12:04:09.74	0.09	–63:21:48.1	0.11	2.66	0.19	3.87	0.28	3.017	0.073	10.78	0.25	G	93
G297.6650+0.7660	12:06:51.46	0.01	–61:38:56.8	0.01	588.74	3471.45	704.35	74.51	25.162	0.088	254.35	2.32	P	107
G297.6650–0.0103	12:05:42.49	0.01	–62:24:48.3	0.01	46.32	21.54	46.83	3.65	8.81	0.032	154.36	0.3	P	99
G297.6680+0.0798	12:05:52.00	0.04	–62:19:30.8	0.05	2.43	0.09	2.54	0.11	2.556	0.008	26.48	0.09	G	99
G297.6680+0.9566	12:07:09.72	0.02	–61:27:42.7	0.02	4.89	0.1	4.52	0.11	2.405	0.004	40.27	0.12	G	106
G297.7190+0.9604	12:07:35.22	0.14	–61:28:00.3	0.14	0.73	0.1	0.55	0.08	2.174	0.06	7.54	0.1	G	106
G297.7400–0.3076	12:05:53.31	0.05	–62:43:09.2	0.07	1.66	0.1	1.29	0.08	2.202	0.008	18.82	0.08	G	101
G297.7570–0.5090	12:05:43.51	0.08	–62:55:13.9	0.11	1.07	0.09	0.93	0.09	2.328	0.029	12.41	0.09	G	101
G297.7890–1.0065	12:05:13.46	0.08	–63:24:56.9	0.08	1.14	0.1	0.74	0.07	2.011	0.025	7.58	0.12	G	93

Continued on next page

Table B.3 – continued from previous page

sSource Name	RA J2000	σ_{ra} $''$	DEC J2000	σ_{dec} $''$	Peak mJy/bm	σ_{peak} mJy/bm	S mJy	σ_S mJy	ϑ $''$	σ_ϑ $''$	SNR	rms mJy/bm	Type	Tile
G297.7920+0.3720	12:07:20.96	0.04	–62:03:32.3	0.05	2.52	0.1	2.58	0.11	2.526	0.009	24.66	0.1	G	108
G297.7980+0.3180	12:07:19.13	0.11	–62:06:47.5	0.17	0.78	0.09	0.69	0.1	2.358	0.042	8.92	0.07	G	108
G297.8310–0.7754	12:05:57.32	0.02	–63:11:44.9	0.02	6.11	0.1	5.94	0.11	2.465	0.003	52.0	0.12	G	102
G297.8490+0.7561	12:08:22.30	0.05	–61:41:23.6	0.05	1.92	0.1	1.43	0.08	2.159	0.01	17.93	0.1	G	107
G297.8630–1.0323	12:05:50.04	0.05	–63:27:15.7	0.07	2.38	0.14	1.85	0.12	2.204	0.015	15.7	0.15	G	103
G297.8680+0.9443	12:08:47.55	0.04	–61:30:26.7	0.05	2.39	0.09	2.58	0.12	2.598	0.012	23.59	0.1	G	116
G297.9000–0.9636	12:06:16.11	0.52	–63:23:35.4	0.29	1.08	0.13	6.24	0.76	6.023	0.545	7.02	0.16	G	104
G297.9020–0.2147	12:07:25.46	0.09	–62:39:21.1	0.09	0.98	0.1	0.63	0.07	1.999	0.023	9.53	0.1	G	110
G297.9090–0.9665	12:06:20.80	0.01	–63:23:51.6	0.01	104.95	110.2	109.23	7.16	22.64	0.049	428.63	0.24	P	103
G297.9110–0.4606	12:07:07.90	0.48	–62:53:58.5	0.65	0.58	0.08	1.97	0.44	4.612	0.518	7.23	0.09	G	101
G297.9200+0.8287	12:09:03.99	0.02	–61:37:48.2	0.02	4.98	0.1	5.1	0.1	2.531	0.004	46.67	0.1	G	117
G297.9750+0.8834	12:09:35.79	0.02	–61:35:07.2	0.02	6.89	0.49	12.25	1.22	8.178	0.05	65.13	0.11	P	117
G297.9830+0.5066	12:09:08.42	0.11	–61:57:28.7	0.12	0.8	0.1	0.52	0.06	2.016	0.026	9.17	0.09	G	118
G297.9830–0.5969	12:07:33.50	0.05	–63:02:46.6	0.05	1.97	0.1	1.66	0.08	2.297	0.009	20.51	0.09	G	102
G297.9980+1.0087	12:09:57.42	0.12	–61:27:54.3	0.17	0.73	0.09	0.64	0.09	2.334	0.077	7.71	0.1	G	116
G298.0150–0.8759	12:07:24.77	0.1	–63:19:35.8	0.08	1.42	0.09	2.27	0.15	3.159	0.051	12.88	0.11	G	103
G298.0350–0.2902	12:08:27.36	0.18	–62:45:09.2	0.21	1.05	0.12	1.94	0.23	3.396	0.14	9.06	0.12	G	111
G298.0530+1.0267	12:10:26.23	0.13	–61:27:22.0	0.11	0.96	0.1	0.99	0.12	2.534	0.041	11.87	0.09	G	116
G298.0580+0.0194	12:09:05.51	0.01	–62:27:03.2	0.01	11.43	0.1	11.61	0.1	2.52	0.002	128.25	0.08	G	110
G298.0660–1.0717	12:07:33.83	0.05	–63:31:40.0	0.07	5.84	0.36	11.2	1.65	7.643	0.059	40.3	0.15	P	103
G298.0710–0.4577	12:08:31.43	0.03	–62:55:25.4	0.03	3.81	0.11	3.46	0.11	2.384	0.005	33.13	0.11	G	111
G298.0750–0.4257	12:08:36.40	0.01	–62:53:34.4	0.01	25.28	0.16	25.6	0.18	2.516	0.002	130.73	0.19	G	111
G298.0840–0.0243	12:09:15.13	0.05	–62:29:53.7	0.05	1.94	0.09	1.64	0.08	2.297	0.008	22.6	0.09	G	110
G298.1120+0.2886	12:09:55.62	0.23	–62:11:38.5	0.13	0.66	0.09	0.68	0.1	2.53	0.111	7.48	0.09	G	119

Continued on next page

Table B.3 – continued from previous page

sSource Name	RA J2000	σ_{ra} $''$	DEC J2000	σ_{dec} $''$	Peak mJy/bm	σ_{peak} mJy/bm	S mJy	σ_S mJy	ϑ $''$	σ_ϑ $''$	SNR	rms mJy/bm	Type	Tile
G298.1200–0.9352	12:08:14.63	0.12	–63:24:09.6	0.12	0.78	0.09	0.56	0.07	2.116	0.045	7.79	0.1	G	113
G298.1300–1.0056	12:08:13.73	0.05	–63:28:25.6	0.07	1.72	0.1	1.4	0.09	2.256	0.015	16.67	0.11	G	113
G298.1480+0.0512	12:09:54.86	0.06	–62:26:02.4	0.04	3.53	0.13	7.23	1.23	11.857	0.113	43.34	0.08	P	120
G298.1510+1.0711	12:11:18.15	0.19	–61:25:39.0	0.11	0.89	0.12	0.8	0.1	2.365	0.074	7.99	0.11	G	125
G298.1620–0.3171	12:09:30.63	0.23	–62:47:59.7	0.12	1.62	0.13	5.07	0.41	4.416	0.165	11.67	0.15	G	111
G298.1670–0.5285	12:09:15.12	0.07	–63:00:33.5	0.09	1.2	0.1	0.87	0.07	2.133	0.017	11.8	0.09	G	112
G298.1680+0.1651	12:10:13.93	0.06	–62:19:29.6	0.07	1.78	0.09	2.02	0.12	2.663	0.019	17.69	0.1	G	119
G298.1820–0.7849	12:09:01.32	0.02	–63:15:57.5	0.02	197.41	390.18	1545.15	50.82	36.032	0.045	284.09	0.7	P	112
G298.1880–0.4013	12:09:36.99	0.15	–62:53:14.0	0.22	1.0	0.14	1.22	0.2	2.756	0.106	8.39	0.12	G	111
G298.1910+0.3398	12:10:40.06	0.13	–62:09:21.7	0.11	0.78	0.1	0.56	0.07	2.107	0.028	9.13	0.08	G	119
G298.2000+0.3539	12:10:45.59	0.08	–62:08:36.5	0.08	1.21	0.1	0.77	0.07	1.999	0.011	12.48	0.08	G	118
G298.2000–1.0724	12:08:45.27	0.07	–63:33:04.8	0.08	1.56	0.1	1.48	0.11	2.436	0.016	16.42	0.09	G	113
G298.2050–0.6003	12:09:28.77	0.06	–63:05:10.5	0.04	2.92	0.09	5.43	0.17	3.408	0.019	25.52	0.11	G	112
G298.2170–0.3344	12:09:57.67	0.13	–62:49:30.8	0.13	232.59	542.01	1007.65	28.24	18.139	0.027	229.69	1.01	P	121
G298.2200–0.3397	12:09:58.93	0.43	–62:49:55.3	1.86	91.55	114.96	738.53	167.52	18.06	0.177	16.58	5.58	P	121
G298.2240–0.3391	12:10:01.19	0.02	–62:49:54.0	0.01	724.32	5.01	2972.37	20.59	5.064	0.008	154.05	4.98	G	121
G298.2290+0.2655	12:10:53.58	0.1	–62:14:07.7	0.12	0.89	0.1	0.63	0.07	2.101	0.031	8.93	0.1	G	119
G298.2390–0.3494	12:10:07.90	0.08	–62:50:38.9	0.08	5.48	0.22	15.99	0.65	4.272	0.024	29.65	0.19	G	121
G298.2460–0.2831	12:10:17.24	0.03	–62:46:47.5	0.02	6.72	0.14	7.03	0.15	2.557	0.004	45.6	0.15	G	121
G298.2500–0.7476	12:09:40.05	0.41	–63:14:20.7	0.35	0.74	0.1	3.39	0.72	5.356	0.579	7.29	0.12	G	112
G298.2550+0.5044	12:11:25.60	0.05	–62:00:12.3	0.04	2.91	0.09	4.36	0.14	3.062	0.013	29.61	0.1	G	118
G298.2550–0.2759	12:10:22.25	0.26	–62:46:26.7	0.21	1.02	0.13	2.58	0.32	3.984	0.216	8.31	0.13	G	121
G298.2640–0.3384	12:10:21.88	0.1	–62:50:14.2	0.07	3.51	0.17	7.85	0.38	3.738	0.06	15.49	0.23	G	121
G298.2670–0.7556	12:09:48.07	0.01	–63:14:58.5	0.01	17.99	0.1	20.93	0.14	2.697	0.002	153.39	0.11	G	112

Continued on next page

Table B.3 – continued from previous page

sSource Name	RA J2000	σ_{ra} $''$	DEC J2000	σ_{dec} $''$	Peak mJy/bm	σ_{peak} mJy/bm	S mJy	σ_S mJy	ϑ $''$	σ_ϑ $''$	SNR	rms mJy/bm	Type	Tile
G298.2780+0.6214	12:11:46.29	0.1	–61:53:28.8	0.14	1.02	0.09	1.32	0.12	2.851	0.043	12.66	0.08	G	128
G298.2900+1.0961	12:12:29.08	0.02	–61:25:26.8	0.02	16.41	0.24	17.06	0.25	2.549	0.003	59.66	0.28	G	125
G298.2930–0.1172	12:10:55.17	0.03	–62:37:24.4	0.03	4.4	0.1	4.34	0.12	2.481	0.005	33.62	0.13	G	120
G298.2950+0.7944	12:12:08.19	0.01	–61:43:22.8	0.01	10.92	0.1	12.94	0.12	2.722	0.003	88.83	0.12	G	127
G298.3080–0.0391	12:11:09.34	0.03	–62:32:55.4	0.04	3.46	0.1	3.39	0.1	2.475	0.006	33.04	0.1	G	120
G298.3170+0.6558	12:12:08.95	0.05	–61:51:48.3	0.05	2.03	0.1	1.66	0.09	2.262	0.006	23.78	0.08	G	127
G298.3180–0.2645	12:10:55.82	0.02	–62:46:22.0	0.02	6.5	0.11	6.36	0.11	2.474	0.004	47.75	0.13	G	121
G298.3230–0.1630	12:11:07.03	0.11	–62:40:24.2	0.23	0.93	0.09	2.0	0.23	3.666	0.169	9.5	0.1	G	120
G298.3230–0.4102	12:10:46.50	0.28	–62:55:03.0	0.22	0.61	0.08	1.38	0.25	3.75	0.251	7.52	0.09	G	121
G298.3270–0.0578	12:11:17.49	0.1	–62:34:12.1	0.1	0.93	0.1	0.62	0.07	2.039	0.031	8.89	0.11	G	120
G298.3330–0.3811	12:10:54.03	0.13	–62:53:24.9	0.1	0.93	0.11	0.71	0.1	2.177	0.041	8.49	0.11	G	121
G298.3420–0.5329	12:10:46.47	0.02	–63:02:30.3	0.02	4.99	0.09	5.37	0.09	2.592	0.004	52.46	0.09	G	122
G298.3440+0.1466	12:11:42.23	0.21	–62:22:14.9	0.35	0.74	0.01	1.3	0.81	7.132	0.223	9.8	0.08	P	119
G298.3440–1.0381	12:10:04.74	0.07	–63:32:27.1	0.09	1.5	0.12	1.16	0.1	2.192	0.017	12.02	0.11	G	113
G298.3480–0.1955	12:11:17.10	0.19	–62:42:33.5	0.16	0.73	0.11	0.72	0.11	2.493	0.082	7.46	0.1	G	121
G298.3530–0.2023	12:11:19.29	0.42	–62:43:00.7	0.36	0.98	0.02	1.45	1.05	6.283	0.232	8.74	0.11	P	121
G298.3650–0.3638	12:11:12.11	0.22	–62:52:41.5	0.16	0.8	0.12	0.83	0.15	2.553	0.107	7.29	0.11	G	121
G298.3660–0.2672	12:11:20.58	0.07	–62:46:58.6	0.07	1.56	0.1	1.34	0.09	2.315	0.016	15.96	0.1	G	121
G298.3720+0.4088	12:12:17.64	0.12	–62:06:57.4	0.08	1.4	0.08	3.27	0.24	3.817	0.045	17.69	0.08	G	128
G298.3740–1.0373	12:10:20.78	0.13	–63:32:41.3	0.12	0.85	0.11	0.55	0.09	2.018	0.033	7.68	0.1	G	113
G298.3800–0.1742	12:11:35.43	0.06	–62:41:35.8	0.11	1.64	0.09	2.77	0.18	3.248	0.043	16.64	0.1	G	120
G298.3840+0.9619	12:13:05.67	0.07	–61:34:15.1	0.08	1.46	0.1	1.32	0.11	2.374	0.012	17.54	0.08	G	125
G298.3920–0.2025	12:11:39.30	0.12	–62:43:23.1	0.22	0.66	0.09	0.7	0.11	2.58	0.109	7.35	0.08	G	120
G298.3940–1.0021	12:10:34.23	0.06	–63:30:47.6	0.09	1.65	0.1	2.0	0.14	2.75	0.023	17.47	0.1	G	124

Continued on next page

Table B.3 – continued from previous page

sSource Name	RA J2000	σ_{ra} $''$	DEC J2000	σ_{dec} $''$	Peak mJy/bm	σ_{peak} mJy/bm	S mJy	σ_S mJy	ϑ $''$	σ_ϑ $''$	SNR	rms mJy/bm	Type	Tile
G298.3950+0.9452	12:13:10.01	0.03	–61:35:20.3	0.04	3.21	0.1	2.98	0.09	2.409	0.005	30.31	0.1	G	127
G298.3980–0.1559	12:11:45.92	0.27	–62:40:40.2	0.34	0.62	0.08	2.02	0.36	4.515	0.269	8.64	0.08	G	120
G298.4030+0.8736	12:13:08.53	0.06	–61:39:39.3	0.08	1.46	0.1	1.19	0.08	2.253	0.017	13.85	0.1	G	127
G298.4100–0.1240	12:11:54.75	0.02	–62:38:53.4	0.02	6.33	0.1	6.03	0.11	2.439	0.004	46.84	0.14	G	120
G298.4110–0.1409	12:11:54.14	0.11	–62:39:54.8	0.81	1.63	0.04	3.37	1.43	7.67	0.168	13.01	0.12	P	120
G298.4170–0.5304	12:11:25.83	0.01	–63:03:03.3	0.01	11.44	0.1	11.27	0.1	2.482	0.002	91.63	0.12	G	122
G298.4280+0.9996	12:13:30.39	0.21	–61:32:24.1	0.12	0.86	0.1	1.16	0.2	2.905	0.097	9.23	0.09	G	135
G298.4290–0.4043	12:11:42.10	0.23	–62:55:41.5	0.38	0.94	0.02	1.48	0.97	6.669	0.213	9.78	0.1	P	121
G298.4400–0.3169	12:11:55.30	0.01	–62:50:36.7	0.01	305.56	933.74	345.13	16.55	35.704	0.039	1067.0	0.29	P	121
G298.4500–0.4862	12:11:46.46	0.07	–63:00:44.2	0.07	1.69	0.09	2.09	0.11	2.784	0.016	20.41	0.08	G	122
G298.4750–0.9950	12:11:18.15	0.03	–63:31:08.2	0.03	4.26	0.11	4.12	0.12	2.46	0.005	35.49	0.11	G	124
G298.4810–0.4390	12:12:06.33	0.02	–62:58:13.1	0.02	5.16	0.1	4.9	0.11	2.436	0.003	55.02	0.09	G	121
G298.5100–0.5719	12:12:10.83	0.05	–63:06:21.9	0.07	1.8	0.1	1.5	0.08	2.283	0.012	18.13	0.09	G	122
G298.5310–0.4540	12:12:31.26	0.05	–62:59:33.6	0.06	1.9	0.1	1.68	0.1	2.352	0.01	21.42	0.08	G	121
G298.5360–0.0602	12:13:05.14	0.08	–62:36:15.0	0.07	1.29	0.1	0.94	0.08	2.134	0.018	12.65	0.1	G	130
G298.5370+0.3090	12:13:33.59	0.01	–62:14:20.5	0.01	14.88	0.11	14.89	0.11	2.501	0.002	100.48	0.14	G	129
G298.5430+0.7116	12:14:06.61	0.03	–61:50:30.0	0.03	3.94	0.1	3.63	0.1	2.398	0.004	36.64	0.1	G	137
G298.5560+0.2467	12:13:38.82	0.08	–62:18:12.7	0.08	1.23	0.1	0.78	0.07	2.0	0.018	11.36	0.11	G	129
G298.5730+0.1673	12:13:41.35	0.04	–62:23:04.3	0.04	2.93	0.1	2.32	0.09	2.227	0.005	29.8	0.1	G	129
G298.5790–0.3620	12:13:03.64	0.05	–62:54:32.1	0.06	1.99	0.1	1.52	0.09	2.183	0.011	17.47	0.11	G	131
G298.6050–0.2939	12:13:22.68	0.05	–62:50:43.6	0.04	2.53	0.11	2.32	0.1	2.394	0.01	21.2	0.12	G	131
G298.6130+0.7173	12:14:42.47	0.06	–61:50:46.1	0.08	1.39	0.09	1.13	0.09	2.262	0.012	17.0	0.08	G	137
G298.6200–0.4727	12:13:16.27	0.13	–63:01:27.2	0.18	1.4	0.03	2.34	1.17	8.054	0.234	14.45	0.1	P	132
G298.6220+0.8097	12:14:53.48	0.08	–61:45:21.1	0.11	1.06	0.09	0.95	0.09	2.356	0.037	11.18	0.1	G	137

Continued on next page

Table B.3 – continued from previous page

sSource Name	RA J2000	σ_{ra} $''$	DEC J2000	σ_{dec} $''$	Peak mJy/bm	σ_{peak} mJy/bm	S mJy	σ_S mJy	ϑ $''$	σ_ϑ $''$	SNR	rms mJy/bm	Type	Tile
G298.6300+0.4811	12:14:33.60	0.07	–62:04:56.0	0.07	1.58	0.1	1.48	0.1	2.422	0.017	15.46	0.1	G	139
G298.6350–0.5164	12:13:21.09	0.08	–63:04:11.9	0.07	1.23	0.09	0.86	0.07	2.097	0.017	12.54	0.1	G	132
G298.6460+0.2307	12:14:23.30	0.02	–62:19:56.4	0.02	6.08	0.11	5.84	0.12	2.451	0.003	53.3	0.11	G	129
G298.6520–0.1304	12:13:59.68	0.06	–62:41:26.4	0.06	1.85	0.1	1.62	0.1	2.342	0.009	20.46	0.08	G	130
G298.6590–0.1220	12:14:03.87	0.12	–62:40:59.7	0.12	0.77	0.1	0.5	0.07	2.02	0.028	8.27	0.09	G	130
G298.6660–0.0100	12:14:15.92	0.11	–62:34:24.4	0.16	0.86	0.1	0.72	0.1	2.298	0.06	8.21	0.1	G	130
G298.6760+1.0317	12:15:36.22	0.05	–61:32:37.1	0.04	2.9	0.1	3.68	0.15	2.818	0.007	35.02	0.08	G	135
G298.6820+0.1317	12:14:34.66	0.01	–62:26:07.7	0.01	15.41	0.11	15.64	0.12	2.519	0.002	118.18	0.12	G	130
G298.7140+0.3104	12:15:04.06	0.01	–62:15:47.4	0.01	18.71	0.12	19.32	0.12	2.54	0.002	105.54	0.17	G	140
G298.7150+0.3891	12:15:10.42	0.01	–62:11:07.5	0.0	34.4	0.12	48.92	0.17	2.981	0.003	199.74	0.17	G	140
G298.7570–0.9991	12:13:47.50	0.06	–63:33:54.8	0.07	1.72	0.11	1.55	0.1	2.371	0.012	18.41	0.09	G	136
G298.7630+0.0191	12:15:08.12	0.01	–62:33:30.1	0.01	43.42	18.9	39.73	3.26	10.058	0.04	193.18	0.22	P	141
G298.7860–0.1212	12:15:09.53	0.09	–62:42:02.0	0.1	1.06	0.11	0.75	0.08	2.106	0.024	10.24	0.1	G	141
G298.8060–0.3461	12:15:02.84	0.45	–62:55:33.9	0.3	1.39	0.03	8.94	2.79	14.799	0.28	12.01	0.12	P	131
G298.8100–0.4218	12:14:59.60	0.22	–63:00:05.4	0.13	1.32	0.11	4.0	0.35	4.355	0.107	13.35	0.1	G	132
G298.8110–0.5752	12:14:49.12	0.09	–63:09:12.8	0.09	0.99	0.09	0.64	0.07	2.0	0.022	10.21	0.1	G	132
G298.8120–0.3946	12:15:02.87	0.17	–62:58:29.4	0.25	0.82	0.11	1.47	0.24	3.356	0.096	10.8	0.08	G	131
G298.8140–0.3676	12:15:05.94	0.3	–62:56:54.5	0.29	0.76	0.09	2.74	0.48	4.762	0.255	9.4	0.09	G	142
G298.8180–1.0544	12:14:16.11	0.01	–63:37:44.0	0.01	10.46	0.1	10.66	0.11	2.523	0.002	98.66	0.1	G	136
G298.8220–1.0536	12:14:18.33	0.02	–63:37:43.2	0.02	4.88	0.1	4.82	0.1	2.485	0.004	43.98	0.11	G	136
G298.8230–0.4080	12:15:07.67	0.2	–62:59:22.9	0.23	1.52	0.15	5.16	0.68	4.598	0.169	9.6	0.15	G	131
G298.8300–0.3321	12:15:16.97	0.14	–62:54:55.9	0.15	1.01	0.13	0.99	0.15	2.476	0.037	8.99	0.09	G	142
G298.8320+0.1270	12:15:51.56	0.01	–62:27:40.4	0.01	48.81	0.16	108.03	0.35	3.719	0.004	240.29	0.19	G	141
G298.8320–0.4070	12:15:12.56	0.13	–62:59:24.1	0.21	1.86	0.17	4.74	0.52	3.993	0.188	8.17	0.21	G	131

Continued on next page

Table B.3 – continued from previous page

sSource Name	RA J2000	σ_{ra} $''$	DEC J2000	σ_{dec} $''$	Peak mJy/bm	σ_{peak} mJy/bm	S mJy	σ_S mJy	ϑ $''$	σ_ϑ $''$	SNR	rms mJy/bm	Type	Tile
G298.8380–0.3388	12:15:20.73	0.03	–62:55:25.4	0.03	11.29	1.3	35.34	2.89	11.171	0.056	67.86	0.17	P	142
G298.8390–0.3356	12:15:21.71	0.06	–62:55:12.2	0.03	9.38	0.91	32.2	4.45	17.172	0.109	53.53	0.18	P	142
G298.8450+0.1836	12:16:02.18	0.02	–62:24:24.9	0.02	5.11	0.09	4.87	0.1	2.439	0.003	59.34	0.08	G	140
G298.8480–0.3319	12:15:26.19	0.11	–62:55:03.9	0.13	1.51	0.14	1.98	0.21	2.865	0.038	12.97	0.11	G	142
G298.8600–0.4348	12:15:24.46	0.05	–63:01:26.4	0.06	137.43	190.5	2305.17	69.4	28.296	0.046	108.27	1.28	P	132
G298.8680–0.5172	12:15:23.06	0.13	–63:06:14.6	0.14	1.23	0.1	2.75	0.22	3.736	0.125	9.93	0.13	G	132
G298.8770–0.6319	12:15:19.34	0.02	–63:13:08.2	0.02	6.38	0.08	12.63	0.19	3.517	0.005	81.22	0.08	G	132
G298.8790–0.3065	12:15:44.47	0.21	–62:53:49.2	0.24	0.68	0.08	1.76	0.26	4.02	0.246	7.92	0.09	G	142
G298.8790–0.3550	12:15:41.04	0.1	–62:56:42.4	0.13	1.8	0.09	7.25	0.44	5.026	0.119	14.07	0.14	G	142
G298.8820–0.6325	12:15:21.82	0.05	–63:13:12.8	0.07	2.51	0.07	10.02	0.31	4.996	0.035	29.71	0.09	G	132
G298.8930–0.1711	12:16:01.43	0.07	–62:45:53.1	0.07	1.39	0.1	0.96	0.07	2.082	0.013	13.34	0.1	G	142
G298.8940–0.5067	12:15:37.45	0.18	–63:05:50.2	0.25	0.74	0.08	2.06	0.22	4.185	0.298	7.42	0.1	G	143
G298.8960+1.0858	12:17:29.56	0.05	–61:31:10.7	0.06	3.0	0.13	3.34	0.17	2.641	0.015	20.65	0.15	G	144
G298.9040–0.8363	12:15:18.50	0.05	–63:25:30.4	0.06	1.62	0.1	1.11	0.07	2.074	0.01	16.03	0.1	G	134
G298.9160+1.0896	12:17:40.35	0.46	–61:31:10.2	0.55	3.46	0.15	28.46	4.81	18.665	0.164	21.3	0.16	P	144
G298.9260–0.6128	12:15:46.68	0.1	–63:12:24.5	0.11	1.07	0.09	1.45	0.14	2.918	0.048	13.06	0.09	G	143
G298.9260–0.7908	12:15:33.30	0.08	–63:22:59.2	0.07	1.42	0.09	1.29	0.08	2.378	0.017	14.91	0.09	G	134
G298.9430+1.0130	12:17:48.19	0.09	–61:35:52.8	0.08	1.22	0.09	1.14	0.09	2.412	0.017	14.78	0.08	G	146
G298.9520–0.0715	12:16:39.36	0.05	–62:40:27.1	0.06	1.89	0.09	1.65	0.09	2.337	0.008	21.06	0.08	G	141
G298.9560–0.3472	12:16:21.65	0.09	–62:56:52.2	0.08	1.08	0.09	0.9	0.08	2.285	0.029	10.96	0.1	G	142
G298.9570–0.3907	12:16:19.16	0.51	–62:59:28.0	0.32	0.71	0.08	4.38	0.94	6.2	0.584	7.43	0.11	G	142
G298.9650+0.7774	12:17:43.57	0.12	–61:50:03.8	0.15	0.68	0.09	0.52	0.08	2.178	0.042	7.81	0.08	G	146
G298.9750–0.0818	12:16:50.48	0.03	–62:41:15.0	0.03	4.01	0.1	3.72	0.11	2.408	0.004	37.24	0.1	G	141
G298.9840+0.5534	12:17:38.58	0.04	–62:03:32.5	0.04	2.85	0.1	2.8	0.11	2.478	0.007	27.87	0.1	G	148

Continued on next page

Table B.3 – continued from previous page

sSource Name	RA J2000	σ_{ra} $''$	DEC J2000	σ_{dec} $''$	Peak mJy/bm	σ_{peak} mJy/bm	S mJy	σ_S mJy	ϑ $''$	σ_ϑ $''$	SNR	rms mJy/bm	Type	Tile
G298.9860–0.0714	12:16:56.87	0.11	–62:40:43.1	0.13	0.85	0.1	0.65	0.08	2.18	0.023	10.85	0.07	G	141
G298.9980+0.3357	12:17:30.92	0.03	–62:16:35.9	0.03	4.77	0.09	6.35	0.12	2.884	0.006	44.08	0.11	G	150
G298.9990–0.6827	12:16:20.27	0.01	–63:17:10.2	0.01	10.36	0.1	10.27	0.1	2.49	0.002	97.2	0.1	G	145
G298.9990–0.7953	12:16:11.88	0.12	–63:23:51.4	0.12	0.77	0.1	0.51	0.07	2.031	0.036	7.85	0.1	G	145
G299.0080–1.0386	12:15:58.73	0.21	–63:38:23.4	0.2	0.78	0.11	1.05	0.16	2.911	0.144	7.57	0.11	G	136
G299.0120+0.1287	12:17:24.06	0.65	–62:29:04.0	1.56	2.23	0.06	36.77	4.75	26.791	0.145	24.75	0.09	P	141
G299.0500–0.7359	12:16:43.38	0.07	–63:20:44.6	0.07	1.49	0.1	1.32	0.09	2.346	0.02	14.58	0.11	G	145
G299.0530+0.5791	12:18:15.04	0.1	–62:02:32.8	0.12	0.84	0.1	0.59	0.08	2.106	0.043	7.83	0.11	G	148
G299.0690+0.0213	12:17:46.33	0.05	–62:35:51.6	0.05	2.04	0.1	1.48	0.08	2.126	0.008	19.27	0.11	G	151
G299.0870+0.6136	12:18:34.58	0.06	–62:00:46.8	0.05	3.56	0.14	5.24	1.6	11.27	0.217	36.01	0.1	P	148
G299.0920–0.6069	12:17:14.52	0.01	–63:13:24.0	0.01	26.65	0.15	26.57	0.17	2.496	0.002	145.13	0.18	G	143
G299.1190–0.0588	12:18:06.65	0.05	–62:41:01.0	0.04	2.35	0.1	2.08	0.1	2.355	0.006	25.79	0.08	G	151
G299.1230+0.3134	12:18:33.33	0.01	–62:18:53.7	0.01	18.76	0.11	29.2	0.2	3.119	0.003	112.3	0.16	G	150
G299.1390–1.0963	12:17:04.60	0.04	–63:42:52.8	0.05	6.34	0.32	4.31	0.24	2.06	0.007	19.93	0.31	G	147
G299.1440+0.4357	12:18:52.36	0.15	–62:11:46.9	0.13	0.73	0.1	0.54	0.08	2.144	0.058	7.29	0.1	G	150
G299.1520+0.0088	12:18:28.59	0.23	–62:37:16.1	0.55	2.23	0.06	18.83	2.13	14.519	0.077	26.27	0.09	P	151
G299.1620+0.1048	12:18:40.00	0.05	–62:31:36.8	0.06	1.75	0.1	1.42	0.08	2.25	0.014	15.78	0.11	G	151
G299.1660+0.3958	12:19:00.72	0.12	–62:14:18.9	0.12	0.75	0.1	0.48	0.06	1.999	0.038	7.62	0.1	G	150
G299.1700–0.4202	12:18:08.77	0.13	–63:02:54.6	0.15	0.79	0.09	0.77	0.09	2.476	0.054	9.16	0.08	G	143
G299.2090+0.0117	12:18:58.11	0.08	–62:37:30.4	0.07	1.61	0.1	1.72	0.13	2.585	0.023	16.08	0.11	G	151
G299.2090+0.5574	12:19:33.31	0.03	–62:05:01.4	0.04	4.27	0.1	5.5	0.15	2.839	0.009	32.55	0.13	G	158
G299.2090+0.5599	12:19:33.20	0.02	–62:04:52.2	0.03	5.51	0.1	6.58	0.14	2.731	0.005	40.39	0.13	G	158
G299.2390+0.4708	12:19:42.92	0.13	–62:10:23.7	0.1	0.93	0.1	0.72	0.08	2.198	0.03	9.46	0.09	G	160
G299.2400+0.8305	12:20:05.63	0.02	–61:48:58.7	0.02	6.79	0.11	6.71	0.12	2.484	0.003	56.58	0.12	G	156

Continued on next page

Table B.3 – continued from previous page

sSource Name	RA J2000	σ_{ra} $''$	DEC J2000	σ_{dec} $''$	Peak mJy/bm	σ_{peak} mJy/bm	S mJy	σ_S mJy	ϑ $''$	σ_ϑ $''$	SNR	rms mJy/bm	Type	Tile
G299.2470–0.4106	12:18:49.77	0.11	–63:02:55.6	0.09	0.96	0.09	0.76	0.07	2.231	0.034	10.01	0.1	G	153
G299.2610+0.8502	12:20:17.61	0.01	–61:47:57.7	0.01	8.99	0.1	8.99	0.12	2.5	0.003	74.98	0.12	G	156
G299.2710+0.9080	12:20:25.97	0.1	–61:44:35.3	0.14	1.2	0.08	3.48	0.27	4.259	0.121	11.69	0.1	G	156
G299.2760–0.5389	12:18:56.28	0.11	–63:10:47.0	0.29	0.69	0.07	1.5	0.21	3.684	0.268	8.96	0.09	G	153
G299.2760–0.7910	12:18:39.51	0.01	–63:25:47.1	0.01	110.78	122.92	108.42	12.9	17.613	0.078	254.75	0.43	P	155
G299.2770+0.2550	12:19:48.95	0.01	–62:23:31.9	0.01	9.07	0.1	11.4	0.14	2.803	0.003	84.63	0.1	G	160
G299.3070–0.5057	12:19:14.85	0.02	–63:09:02.3	0.02	7.03	0.11	6.74	0.12	2.448	0.003	55.32	0.12	G	153
G299.3150+0.3173	12:20:11.92	0.03	–62:20:05.6	0.03	4.23	0.1	3.9	0.11	2.4	0.004	36.63	0.11	G	160
G299.3200+0.5752	12:20:30.65	0.05	–62:04:46.0	0.06	2.08	0.1	1.86	0.1	2.361	0.012	18.65	0.11	G	158
G299.3220+0.5177	12:20:28.05	0.1	–62:08:12.4	0.1	1.3	0.1	1.77	0.16	2.918	0.031	14.6	0.09	G	158
G299.3250–0.8116	12:19:04.26	0.01	–63:27:23.3	0.01	13.5	0.12	13.24	0.13	2.476	0.002	92.57	0.15	G	155
G299.3550–0.2731	12:19:54.96	0.35	–62:55:33.3	0.49	1.79	0.05	10.28	3.11	15.883	0.253	14.45	0.13	P	152
G299.3640+0.5231	12:20:50.08	0.13	–62:08:11.3	0.15	0.77	0.1	0.67	0.1	2.335	0.045	8.48	0.08	G	158
G299.3700+0.8571	12:21:13.04	0.07	–61:48:19.6	0.11	1.18	0.1	0.96	0.09	2.258	0.034	10.29	0.11	G	156
G299.3730–0.8628	12:19:26.12	0.09	–63:30:47.2	0.11	1.15	0.1	1.18	0.11	2.532	0.04	11.07	0.1	G	155
G299.3760+0.1715	12:20:34.66	0.09	–62:29:13.2	0.07	1.24	0.09	1.14	0.09	2.4	0.025	12.8	0.09	G	161
G299.3890–0.5112	12:19:58.14	0.09	–63:09:58.7	0.12	1.13	0.09	1.42	0.13	2.808	0.055	11.53	0.1	G	153
G299.4070–0.2371	12:20:24.86	0.01	–62:53:46.6	0.01	11.61	0.1	15.63	0.16	2.901	0.003	99.16	0.11	G	152
G299.4130–0.2373	12:20:28.20	0.05	–62:53:50.1	0.04	3.14	0.1	5.71	0.21	3.374	0.015	29.01	0.11	G	152
G299.4180+0.0844	12:20:50.83	0.06	–62:34:42.5	0.08	1.47	0.1	1.09	0.09	2.151	0.017	12.82	0.11	G	161
G299.4210+0.4794	12:21:16.42	0.11	–62:11:11.5	0.11	0.83	0.1	0.53	0.07	1.999	0.024	9.01	0.09	G	160
G299.4230–0.8932	12:19:51.29	0.04	–63:32:58.6	0.05	2.53	0.11	2.38	0.11	2.426	0.008	23.81	0.1	G	155
G299.4290–0.9027	12:19:53.81	0.07	–63:33:35.2	0.07	1.48	0.11	1.1	0.09	2.157	0.012	14.94	0.09	G	155
G299.4310–1.1274	12:19:39.68	0.07	–63:46:58.6	0.08	4.96	0.3	4.92	0.35	2.49	0.019	16.3	0.31	G	157

Continued on next page

Table B.3 – continued from previous page

sSource Name	RA J2000	σ_{ra} $''$	DEC J2000	σ_{dec} $''$	Peak mJy/bm	σ_{peak} mJy/bm	S mJy	σ_S mJy	ϑ $''$	σ_ϑ $''$	SNR	rms mJy/bm	Type	Tile
G299.4400+0.3105	12:21:16.34	0.13	–62:21:23.4	0.12	1.6	0.04	2.99	1.1	7.392	0.144	15.55	0.1	P	160
G299.4590+0.6598	12:21:46.36	0.02	–62:00:42.2	0.02	5.64	0.1	5.52	0.1	2.474	0.003	54.68	0.09	G	158
G299.4600–0.7961	12:20:17.22	0.01	–63:27:27.5	0.01	17.81	0.12	17.38	0.13	2.469	0.002	107.28	0.16	G	155
G299.4680–0.7135	12:20:26.92	0.06	–63:22:36.0	0.06	1.97	0.09	3.06	0.14	3.114	0.024	18.17	0.1	G	155
G299.4900–0.2527	12:21:07.28	0.1	–62:55:18.0	0.09	1.01	0.1	0.74	0.08	2.143	0.021	11.62	0.09	G	162
G299.4950+0.9862	12:22:23.44	0.06	–61:41:29.5	0.05	1.92	0.1	1.64	0.08	2.311	0.013	17.31	0.11	G	165
G299.4960+0.0337	12:21:28.22	0.09	–62:38:16.6	0.06	1.46	0.09	1.49	0.11	2.531	0.026	14.23	0.1	G	161
G299.4970+0.3278	12:21:46.14	0.13	–62:20:45.4	0.25	0.7	0.1	0.79	0.14	2.659	0.134	7.57	0.1	G	160
G299.5010–1.0331	12:20:23.84	0.01	–63:41:52.3	0.01	9.24	0.1	9.95	0.11	2.594	0.003	78.86	0.11	G	157
G299.5060–0.7809	12:20:42.71	0.1	–63:26:53.0	0.13	0.96	0.1	0.79	0.1	2.274	0.043	8.89	0.1	G	155
G299.5090–0.0750	12:21:28.05	0.01	–62:44:50.6	0.01	9.92	0.1	10.05	0.1	2.517	0.002	93.52	0.1	G	162
G299.5110–1.1026	12:20:24.69	0.01	–63:46:05.2	0.01	25.69	0.16	46.85	0.34	3.376	0.004	122.96	0.22	G	157
G299.5120–1.1093	12:20:24.50	0.06	–63:46:29.2	0.07	3.32	0.2	2.66	0.18	2.24	0.015	15.18	0.22	G	157
G299.5120–1.1154	12:20:24.02	0.02	–63:46:51.0	0.03	11.47	0.14	44.11	0.65	4.902	0.015	48.7	0.23	G	157
G299.5490–0.1348	12:21:45.56	0.03	–62:48:41.3	0.03	3.4	0.1	3.15	0.09	2.406	0.006	30.02	0.11	G	162
G299.5500+0.2856	12:22:10.97	0.01	–62:23:38.1	0.01	17.2	0.12	17.21	0.13	2.5	0.002	142.44	0.11	G	160
G299.5580+0.7116	12:22:39.58	0.09	–61:58:17.4	0.1	1.04	0.1	0.75	0.07	2.126	0.023	10.54	0.09	G	167
G299.5590–0.8061	12:21:09.13	0.13	–63:28:45.6	0.09	1.03	0.1	0.89	0.1	2.331	0.032	10.88	0.09	G	155
G299.5620–0.2251	12:21:46.95	0.01	–62:54:09.5	0.01	14.69	0.11	14.12	0.13	2.451	0.002	100.1	0.14	G	162
G299.5650+0.3711	12:22:23.53	0.11	–62:18:38.3	0.08	1.05	0.09	0.9	0.1	2.308	0.027	12.18	0.09	G	169
G299.5820–1.0490	12:21:06.31	0.03	–63:43:23.9	0.02	6.72	0.14	6.76	0.17	2.509	0.004	43.44	0.15	G	157
G299.5970–0.0875	12:22:13.14	0.04	–62:46:11.6	0.04	2.82	0.09	2.67	0.09	2.432	0.006	30.26	0.1	G	162
G299.6050–0.2192	12:22:09.59	0.04	–62:54:06.1	0.04	2.9	0.1	2.73	0.1	2.424	0.006	29.89	0.09	G	162
G299.6090+0.5335	12:22:55.63	0.08	–62:09:15.1	0.07	1.52	0.1	1.4	0.09	2.396	0.015	15.94	0.09	G	169

Continued on next page

Table B.3 – continued from previous page

sSource Name	RA	σ_{ra}	DEC	σ_{dec}	Peak	σ_{peak}	S	σ_S	ϑ	σ_ϑ	SNR	rms	Type	Tile
	J2000	$''$	J2000	$''$	mJy/bm	mJy/bm	mJy	mJy	$''$	$''$		mJy/bm		
G299.6160+0.5247	12:22:58.81	0.09	–62:09:49.3	0.1	1.19	0.11	0.94	0.09	2.219	0.021	12.29	0.09	G	169
G299.6290–0.4284	12:22:09.65	0.05	–63:06:44.0	0.04	3.13	0.09	5.95	0.17	3.446	0.015	29.82	0.1	G	163
G299.6440–0.3172	12:22:24.18	0.09	–63:00:12.2	0.09	1.48	0.1	2.14	0.14	3.004	0.033	15.7	0.1	G	163
G299.6460+0.6929	12:23:23.09	0.06	–61:59:59.0	0.06	2.11	0.09	2.95	0.13	2.952	0.023	17.64	0.11	G	167
G299.6500+0.6934	12:23:25.32	0.1	–61:59:58.9	0.13	0.88	0.1	0.67	0.08	2.187	0.045	8.17	0.1	G	167
G299.6520–0.1463	12:22:38.68	0.09	–62:50:04.4	0.1	1.14	0.1	1.0	0.09	2.343	0.032	11.34	0.1	G	162
G299.6530+0.6941	12:23:26.88	0.1	–61:59:57.6	0.07	1.59	0.09	2.57	0.15	3.184	0.04	16.29	0.1	G	167
G299.6580+0.3044	12:23:07.53	0.08	–62:23:13.8	0.1	1.14	0.1	0.87	0.09	2.181	0.024	11.81	0.1	G	169
G299.6630+0.3575	12:23:13.37	0.14	–62:20:06.0	0.14	0.88	0.09	1.11	0.14	2.803	0.09	8.94	0.11	G	169
G299.6710–1.0057	12:21:56.66	0.12	–63:41:25.9	0.13	0.81	0.1	0.53	0.07	2.032	0.03	8.23	0.09	G	168
G299.6800+0.9996	12:23:57.37	0.02	–61:41:54.5	0.02	6.09	0.1	6.73	0.11	2.629	0.003	59.87	0.1	G	175
G299.6870–0.4954	12:22:36.37	0.05	–63:11:07.2	0.06	1.92	0.1	1.61	0.1	2.293	0.013	16.46	0.11	G	163
G299.6880+0.6691	12:23:43.28	0.04	–62:01:40.6	0.05	2.65	0.1	2.91	0.13	2.621	0.013	21.28	0.12	G	167
G299.6880–0.8866	12:22:13.56	0.06	–63:34:27.1	0.07	1.73	0.09	2.15	0.11	2.787	0.014	21.97	0.08	G	168
G299.6910–0.4884	12:22:38.95	0.03	–63:10:43.9	0.04	3.2	0.1	2.78	0.1	2.328	0.005	29.87	0.11	G	163
G299.7110+0.4619	12:23:43.47	0.01	–62:14:10.9	0.01	13.68	0.11	15.54	0.12	2.665	0.003	99.52	0.13	G	169
G299.7120+0.1142	12:23:24.73	0.18	–62:34:56.1	0.15	0.76	0.1	0.85	0.13	2.643	0.08	8.44	0.09	G	171
G299.7180–0.4287	12:22:56.84	0.05	–63:07:21.1	0.05	2.24	0.1	2.24	0.1	2.5	0.011	21.74	0.1	G	163
G299.7200+0.0592	12:23:25.98	0.03	–62:38:16.1	0.03	4.28	0.1	4.23	0.11	2.486	0.005	39.34	0.11	G	171
G299.7320+0.1725	12:23:38.21	0.12	–62:31:34.8	0.16	0.8	0.1	0.63	0.08	2.22	0.044	8.13	0.09	G	171
G299.7400–0.2664	12:23:17.58	0.07	–62:57:48.8	0.08	1.71	0.1	1.84	0.13	2.593	0.016	18.45	0.09	G	172
G299.7430+0.9785	12:24:27.86	0.01	–61:43:34.0	0.01	11.13	0.11	11.02	0.12	2.487	0.002	87.5	0.12	G	175
G299.7470+0.4163	12:23:59.58	0.04	–62:17:08.3	0.05	2.14	0.1	1.55	0.08	2.128	0.009	18.26	0.11	G	169
G299.7490+0.2478	12:23:51.42	0.05	–62:27:12.1	0.05	2.29	0.1	1.99	0.09	2.333	0.007	23.92	0.09	G	171

Continued on next page

Table B.3 – continued from previous page

sSource Name	RA J2000	σ_{ra} $''$	DEC J2000	σ_{dec} $''$	Peak mJy/bm	σ_{peak} mJy/bm	S mJy	σ_S mJy	ϑ $''$	σ_ϑ $''$	SNR	rms mJy/bm	Type	Tile
G299.7520+0.3022	12:23:56.15	0.08	–62:23:58.6	0.08	1.26	0.1	0.83	0.08	2.033	0.012	13.24	0.09	G	169
G299.7680–0.4146	12:23:23.63	0.11	–63:06:50.0	0.08	1.22	0.1	1.03	0.09	2.299	0.022	12.3	0.09	G	163
G299.7740–0.2126	12:23:38.61	0.01	–62:54:49.8	0.01	11.92	0.11	12.03	0.12	2.512	0.002	94.55	0.12	G	172
G299.7770+0.4745	12:24:18.00	0.1	–62:13:51.0	0.1	0.89	0.09	0.57	0.06	2.0	0.025	9.5	0.09	G	169
G299.7890–0.6951	12:23:18.65	0.01	–63:23:42.2	0.01	8.46	0.1	8.23	0.1	2.465	0.002	79.55	0.11	G	166
G299.7950–0.7309	12:23:19.60	0.12	–63:25:52.8	0.09	0.98	0.1	0.79	0.08	2.241	0.031	10.8	0.09	G	166
G299.7970–0.8938	12:23:11.15	0.05	–63:35:36.2	0.06	1.71	0.1	1.27	0.07	2.156	0.008	18.91	0.08	G	168
G299.8230+0.0769	12:24:20.43	0.07	–62:37:52.4	0.09	1.6	0.1	1.99	0.14	2.789	0.025	16.68	0.1	G	171
G299.8340–0.5281	12:23:52.21	0.08	–63:14:01.9	0.08	1.08	0.1	0.69	0.07	1.999	0.016	11.51	0.09	G	174
G299.8460+0.8828	12:25:15.12	0.08	–61:49:54.9	0.09	1.29	0.1	1.08	0.1	2.293	0.018	13.47	0.09	G	175
G299.8550+0.3058	12:24:49.13	0.05	–62:24:24.7	0.05	2.08	0.1	1.89	0.1	2.385	0.011	19.09	0.1	G	169
G299.8810+1.0712	12:25:42.05	0.01	–61:38:51.6	0.01	18.13	3.31	23.35	2.19	10.347	0.049	126.79	0.14	P	175
G299.8840+0.6445	12:25:21.62	0.01	–62:04:21.9	0.01	23.4	5.51	22.2	1.9	7.679	0.031	130.45	0.18	P	177
G299.8850+1.0781	12:25:44.66	0.01	–61:38:29.6	0.01	15.07	0.12	17.37	0.14	2.684	0.002	113.46	0.13	G	175
G299.8920–0.8993	12:24:01.83	0.12	–63:36:32.8	0.16	0.7	0.09	0.54	0.07	2.194	0.061	7.67	0.1	G	168
G299.9110–0.8687	12:24:13.83	0.06	–63:34:50.9	0.06	1.73	0.1	1.36	0.08	2.222	0.008	18.84	0.08	G	168
G299.9200–0.3364	12:24:48.13	0.01	–63:03:07.7	0.01	22.1	4.91	33.1	2.04	9.034	0.026	146.35	0.15	P	174
G299.9290+0.3332	12:25:28.52	0.05	–62:23:13.2	0.04	2.43	0.1	2.13	0.1	2.338	0.007	24.73	0.1	G	179
G299.9540–0.3915	12:25:03.05	0.09	–63:06:38.0	0.11	1.0	0.1	0.85	0.08	2.302	0.031	10.72	0.09	G	174
G299.9880+0.8949	12:26:27.51	0.09	–61:50:02.4	0.13	0.96	0.09	0.91	0.1	2.433	0.038	11.31	0.08	G	175
G299.9930–0.8829	12:24:56.89	0.14	–63:36:12.1	0.12	0.8	0.09	0.67	0.08	2.286	0.042	9.35	0.09	G	178
G300.0110+0.4465	12:26:16.58	0.02	–62:16:58.5	0.02	6.87	0.48	10.14	1.41	9.628	0.092	62.86	0.11	P	179
G300.0180–0.8837	12:25:10.40	0.07	–63:36:24.1	0.07	1.38	0.1	1.04	0.07	2.171	0.017	13.52	0.1	G	178
G300.0300+0.0938	12:26:08.88	0.01	–62:38:07.3	0.01	40.02	16.06	38.12	2.51	8.276	0.026	193.38	0.21	P	181

Continued on next page

Table B.3 – continued from previous page

sSource Name	RA J2000	σ_{ra} $''$	DEC J2000	σ_{dec} $''$	Peak mJy/bm	σ_{peak} mJy/bm	S mJy	σ_S mJy	ϑ $''$	σ_ϑ $''$	SNR	rms mJy/bm	Type	Tile
G300.0440–0.3163	12:25:54.84	0.09	–63:02:41.4	0.08	1.19	0.1	0.99	0.08	2.271	0.023	12.54	0.1	G	174
G300.0460+0.4450	12:26:34.40	0.01	–62:17:14.2	0.01	22.62	0.14	22.8	0.16	2.51	0.002	113.63	0.19	G	179
G300.0470–0.3446	12:25:55.09	0.09	–63:04:24.0	0.1	0.98	0.1	0.66	0.06	2.046	0.023	10.72	0.1	G	174
G300.0720–0.0335	12:26:23.79	0.06	–62:45:57.9	0.06	1.94	0.11	1.58	0.09	2.258	0.011	17.6	0.11	G	182
G300.0810–0.0377	12:26:28.42	0.14	–62:46:16.1	0.13	0.76	0.1	0.55	0.07	2.116	0.048	7.14	0.1	G	182
G300.0870–0.0143	12:26:32.74	0.08	–62:44:54.6	0.08	1.29	0.11	0.84	0.07	2.023	0.012	12.7	0.09	G	182
G300.1080+0.2013	12:26:54.57	0.15	–62:32:09.1	0.13	0.7	0.09	0.63	0.08	2.372	0.068	7.21	0.09	G	181
G300.1310–0.8980	12:26:10.27	0.12	–63:37:56.0	0.09	0.96	0.1	0.73	0.07	2.177	0.029	10.37	0.09	G	178
G300.1360–0.8087	12:26:17.81	0.11	–63:32:38.0	0.21	0.73	0.09	0.72	0.12	2.484	0.062	8.52	0.08	G	176
G300.1370–0.9410	12:26:11.05	0.03	–63:40:30.6	0.04	5.66	0.33	11.64	1.22	7.969	0.046	54.24	0.1	P	178
G300.1450+1.0350	12:27:53.18	0.01	–61:42:34.1	0.01	24.85	6.2	34.66	2.45	10.808	0.04	167.21	0.15	P	185
G300.1480–0.7439	12:26:27.55	0.07	–63:28:50.1	0.08	1.42	0.1	1.25	0.1	2.347	0.013	15.71	0.08	G	176
G300.1500+0.4335	12:27:27.60	0.12	–62:18:31.1	0.18	1.03	0.09	2.45	0.25	3.857	0.099	11.15	0.09	G	189
G300.1510+0.4308	12:27:27.83	0.16	–62:18:40.2	0.4	1.02	0.02	1.89	0.89	6.961	0.169	11.98	0.08	P	189
G300.1540–1.0664	12:26:14.05	0.05	–63:48:07.8	0.05	2.83	0.12	2.68	0.13	2.435	0.008	25.86	0.11	G	178
G300.1730–1.1078	12:26:21.90	0.08	–63:50:42.6	0.1	2.96	0.21	3.63	0.29	2.771	0.022	17.58	0.17	G	178
G300.1800–0.9543	12:26:33.70	0.15	–63:41:34.9	0.14	0.87	0.11	0.87	0.11	2.502	0.075	7.76	0.11	G	178
G300.1860+0.8920	12:28:07.28	0.09	–61:51:19.2	0.09	1.1	0.1	0.74	0.08	2.05	0.014	12.08	0.08	G	185
G300.2020+0.1218	12:27:39.29	0.07	–62:37:25.7	0.08	1.4	0.1	1.17	0.09	2.287	0.016	14.38	0.09	G	181
G300.2100–0.9505	12:26:50.16	0.04	–63:41:31.8	0.04	2.55	0.1	2.36	0.09	2.406	0.008	23.97	0.1	G	178
G300.2270–0.5128	12:27:21.41	0.03	–63:15:28.7	0.03	3.15	0.09	2.74	0.09	2.331	0.004	36.61	0.08	G	184
G300.2370–0.9933	12:27:02.65	0.01	–63:44:14.5	0.01	13.16	0.12	12.99	0.13	2.484	0.002	89.67	0.14	G	178
G300.2480–0.0135	12:27:57.47	0.06	–62:45:41.2	0.05	5.32	0.29	38.41	3.23	22.527	0.109	51.37	0.1	P	182
G300.2620–0.5874	12:27:36.66	0.1	–63:20:08.1	0.11	1.16	0.1	1.46	0.12	2.806	0.056	10.13	0.11	G	186

Continued on next page

Table B.3 – continued from previous page

sSource Name	RA J2000	σ_{ra} $''$	DEC J2000	σ_{dec} $''$	Peak mJy/bm	σ_{peak} mJy/bm	S mJy	σ_S mJy	ϑ $''$	σ_ϑ $''$	SNR	rms mJy/bm	Type	Tile
G300.2690–0.2383	12:27:57.24	0.04	–62:59:18.7	0.04	2.41	0.1	1.85	0.09	2.191	0.005	25.99	0.08	G	182
G300.2770+0.1609	12:28:20.24	0.03	–62:35:30.3	0.03	4.09	0.1	4.15	0.12	2.518	0.005	34.66	0.12	G	191
G300.2780+0.6616	12:28:43.97	0.01	–62:05:35.1	0.01	37.63	0.17	67.09	0.35	3.338	0.003	163.4	0.23	G	187
G300.2870+0.6090	12:28:45.98	0.06	–62:08:46.4	0.07	1.88	0.11	1.77	0.12	2.426	0.011	19.15	0.09	G	187
G300.2870–0.6388	12:27:47.05	0.06	–63:23:20.2	0.08	1.48	0.1	1.11	0.08	2.171	0.017	13.06	0.11	G	186
G300.2910–0.5125	12:27:55.27	0.02	–63:15:48.8	0.02	5.59	0.11	5.26	0.11	2.426	0.003	49.31	0.11	G	184
G300.3140–1.0107	12:27:43.46	0.26	–63:45:41.9	0.17	0.94	0.02	1.36	1.07	7.05	0.261	9.39	0.1	P	188
G300.3220+0.6135	12:29:04.15	0.07	–62:08:41.6	0.06	1.78	0.1	1.69	0.11	2.438	0.014	17.48	0.1	G	187
G300.3270–0.9963	12:27:50.83	0.08	–63:44:55.0	0.12	1.11	0.1	0.96	0.1	2.325	0.037	10.6	0.1	G	188
G300.3290+0.8834	12:29:19.54	0.05	–61:52:35.7	0.05	1.83	0.1	1.28	0.07	2.092	0.007	19.31	0.09	G	187
G300.3320+0.8075	12:29:17.60	0.04	–61:57:08.7	0.03	3.06	0.09	2.65	0.08	2.326	0.003	41.11	0.07	G	187
G300.3440+0.9433	12:29:29.72	0.1	–61:49:05.5	0.19	0.8	0.09	0.8	0.11	2.498	0.075	8.68	0.09	G	195
G300.3850+0.3396	12:29:24.46	0.12	–62:25:23.3	0.12	0.87	0.11	0.6	0.09	2.082	0.031	8.37	0.1	G	189
G300.3890+0.8229	12:29:47.54	0.09	–61:56:30.9	0.08	1.09	0.1	0.71	0.07	2.019	0.021	10.33	0.1	G	197
G300.3960+0.6266	12:29:42.31	0.01	–62:08:17.1	0.01	9.48	0.11	9.04	0.12	2.442	0.002	81.03	0.11	G	197
G300.4010+0.5461	12:29:41.70	0.02	–62:13:07.7	0.02	7.6	0.08	26.84	0.28	4.697	0.01	73.8	0.12	G	189
G300.4010–0.8043	12:28:39.99	0.08	–63:33:50.8	0.07	1.63	0.1	1.71	0.11	2.557	0.019	17.23	0.09	G	188
G300.4070+0.4896	12:29:42.29	0.15	–62:16:31.9	0.13	0.82	0.1	0.72	0.09	2.344	0.069	7.42	0.11	G	189
G300.4090–0.7721	12:28:45.85	0.02	–63:31:57.6	0.02	8.07	0.11	9.26	0.14	2.679	0.003	74.61	0.1	G	186
G300.4130+0.4613	12:29:43.83	0.09	–62:18:15.2	0.09	1.12	0.1	0.8	0.07	2.109	0.024	9.97	0.11	G	189
G300.4130–0.2910	12:29:10.75	0.09	–63:03:14.0	0.07	1.37	0.1	1.17	0.09	2.31	0.022	13.05	0.1	G	194
G300.4200+0.4132	12:29:45.77	0.03	–62:21:10.0	0.03	3.86	0.1	3.53	0.11	2.389	0.004	40.34	0.09	G	189
G300.4290–0.9820	12:28:46.82	0.02	–63:44:36.9	0.02	6.49	0.1	8.43	0.14	2.849	0.004	63.06	0.1	G	188
G300.4300+1.0104	12:30:16.12	0.09	–61:45:30.6	0.08	1.56	0.09	2.52	0.17	3.178	0.038	16.23	0.1	G	195

Continued on next page

Table B.3 – continued from previous page

sSource Name	RA J2000	σ_{ra} $''$	DEC J2000	σ_{dec} $''$	Peak mJy/bm	σ_{peak} mJy/bm	S mJy	σ_S mJy	ϑ $''$	σ_ϑ $''$	SNR	rms mJy/bm	Type	Tile
G300.4320+0.2725	12:29:45.59	0.09	–62:29:38.2	0.08	1.2	0.1	0.9	0.08	2.172	0.025	11.07	0.11	G	191
G300.4640–0.9831	12:29:05.80	0.16	–63:44:53.1	0.13	3.04	0.11	10.88	3.29	13.072	0.213	20.57	0.15	P	188
G300.4690–0.9861	12:29:08.11	0.01	–63:45:04.2	0.01	26.59	0.13	34.26	0.19	2.838	0.003	137.67	0.19	G	188
G300.4730–0.9398	12:29:12.83	0.12	–63:42:18.2	0.13	1.57	0.04	2.76	1.33	7.332	0.19	13.57	0.12	P	188
G300.4800+0.9245	12:30:37.80	0.11	–61:50:53.2	0.12	0.99	0.11	0.78	0.1	2.215	0.025	10.17	0.09	G	195
G300.4970+0.6916	12:30:36.96	0.05	–62:04:55.5	0.06	6.06	0.43	8.45	3.65	10.255	0.243	23.55	0.26	P	197
G300.4990+0.6874	12:30:37.58	0.01	–62:05:09.7	0.01	38.35	0.18	38.36	0.21	2.5	0.002	151.72	0.25	G	197
G300.5020–0.1830	12:30:02.66	1.26	–62:57:17.9	0.31	1.42	0.03	16.7	5.18	24.881	0.417	12.46	0.12	P	192
G300.5050–0.1732	12:30:04.03	0.04	–62:56:39.0	0.04	5.18	0.05	61.12	0.72	8.584	0.037	44.16	0.12	G	192
G300.5070+0.1637	12:30:20.03	0.07	–62:36:31.2	0.09	1.75	0.1	2.31	0.16	2.873	0.024	18.16	0.1	G	191
G300.5120–0.6835	12:29:45.39	0.08	–63:27:12.1	0.07	1.48	0.1	1.46	0.11	2.482	0.021	15.04	0.1	G	196
G300.5150+1.0454	12:31:00.62	0.11	–61:43:49.8	0.09	1.3	0.1	1.58	0.15	2.76	0.044	12.61	0.11	G	195
G300.5220–0.5436	12:29:56.72	0.17	–63:18:52.9	0.1	0.9	0.1	0.88	0.1	2.472	0.049	10.38	0.08	G	196
G300.5350+0.2646	12:30:38.65	0.04	–62:30:37.4	0.04	2.73	0.1	2.59	0.09	2.434	0.007	27.69	0.1	G	200
G300.5360+0.3595	12:30:43.41	0.11	–62:24:57.2	0.16	0.83	0.1	0.75	0.1	2.383	0.036	10.63	0.07	G	198
G300.5560–0.1664	12:30:31.44	0.08	–62:56:30.0	0.11	1.04	0.1	0.8	0.08	2.19	0.023	12.25	0.09	G	192
G300.5670+0.6314	12:31:10.30	0.21	–62:08:50.1	0.24	0.71	0.09	1.48	0.25	3.609	0.186	8.28	0.09	G	197
G300.5710–0.3575	12:30:31.31	0.06	–63:07:59.9	0.06	1.76	0.09	1.6	0.09	2.388	0.011	20.3	0.09	G	194
G300.5720+0.6372	12:31:13.11	0.25	–62:08:32.2	0.25	0.93	0.02	1.84	0.95	7.364	0.194	11.51	0.08	P	197
G300.5760+0.0926	12:30:52.85	0.04	–62:41:06.4	0.04	2.87	0.1	3.21	0.13	2.646	0.008	28.76	0.09	G	200
G300.5820–0.3066	12:30:39.30	0.07	–63:05:00.5	0.06	1.58	0.1	1.17	0.08	2.15	0.013	14.84	0.1	G	194
G300.5860–0.6468	12:30:26.64	0.13	–63:25:22.3	0.14	0.73	0.1	0.49	0.07	2.054	0.047	7.24	0.1	G	196
G300.5890–1.1087	12:30:07.54	0.01	–63:53:00.5	0.02	21.18	0.15	79.84	0.66	4.854	0.008	101.27	0.21	G	190
G300.5930+0.2155	12:31:06.71	0.25	–62:33:50.0	0.18	0.68	0.1	0.88	0.13	2.831	0.175	7.09	0.11	G	200

Continued on next page

Table B.3 – continued from previous page

sSource Name	RA J2000	σ_{ra} $''$	DEC J2000	σ_{dec} $''$	Peak mJy/bm	σ_{peak} mJy/bm	S mJy	σ_S mJy	ϑ $''$	σ_ϑ $''$	SNR	rms mJy/bm	Type	Tile
G300.5940+0.2210	12:31:07.41	0.15	–62:33:28.9	0.39	1.41	0.03	4.69	1.61	9.691	0.159	12.93	0.11	P	200
G300.6050+0.6334	12:31:29.84	0.01	–62:08:53.4	0.01	14.06	0.11	14.68	0.11	2.555	0.002	124.25	0.11	G	198
G300.6150+0.0553	12:31:11.74	0.17	–62:43:31.3	0.13	0.78	0.1	0.62	0.09	2.241	0.042	8.51	0.08	G	203
G300.6200+0.5886	12:31:35.48	0.11	–62:11:38.5	0.19	0.78	0.1	0.71	0.09	2.381	0.096	7.24	0.11	G	198
G300.6330–0.1786	12:31:11.59	0.0	–62:57:35.9	0.0	65.72	0.2	77.97	0.27	2.723	0.002	234.38	0.26	G	203
G300.6390–0.5386	12:30:59.27	0.03	–63:19:09.4	0.03	3.97	0.1	4.12	0.1	2.546	0.005	34.37	0.1	G	196
G300.6410–0.5360	12:31:00.61	0.1	–63:19:00.8	0.08	1.11	0.1	0.84	0.08	2.166	0.026	9.93	0.1	G	196
G300.6520–0.4127	12:31:11.57	0.01	–63:11:41.2	0.0	467.34	2186.01	527.35	25.16	13.397	0.021	338.12	1.38	P	194
G300.6580–0.8111	12:30:58.21	0.13	–63:35:32.9	0.19	0.77	0.1	0.75	0.1	2.472	0.062	8.07	0.09	G	199
G300.6770+0.6178	12:32:06.18	0.09	–62:10:09.4	0.13	0.98	0.1	0.88	0.09	2.372	0.032	10.94	0.09	G	198
G300.6770–0.0709	12:31:38.87	0.04	–62:51:21.3	0.04	3.06	0.09	4.77	0.17	3.122	0.013	27.27	0.11	G	203
G300.6810+0.5192	12:32:04.45	0.09	–62:16:04.5	0.11	1.1	0.11	0.8	0.08	2.134	0.03	8.9	0.11	G	198
G300.6910+0.1051	12:31:52.86	0.21	–62:40:51.1	0.39	1.61	0.03	9.59	2.95	20.694	0.262	17.09	0.09	P	200
G300.6990–0.6522	12:31:26.53	0.14	–63:26:14.1	0.12	0.91	0.1	0.82	0.11	2.379	0.052	8.61	0.1	G	196
G300.7130+0.2719	12:32:11.14	0.14	–62:31:00.7	0.11	0.97	0.11	0.81	0.09	2.288	0.042	8.76	0.1	G	200
G300.7490+0.3715	12:32:33.84	0.1	–62:25:12.7	0.17	0.92	0.1	0.96	0.12	2.565	0.058	9.55	0.09	G	198
G300.7600+0.6952	12:32:51.75	0.07	–62:05:53.4	0.13	1.08	0.1	1.01	0.1	2.42	0.037	11.32	0.09	G	206
G300.7630+0.0630	12:32:29.27	0.05	–62:43:44.2	0.07	1.81	0.1	1.72	0.1	2.44	0.011	20.51	0.08	G	203
G300.7750–0.0151	12:32:32.69	0.08	–62:48:27.6	0.11	1.15	0.1	0.92	0.08	2.233	0.029	11.19	0.1	G	203
G300.7840+0.5831	12:32:59.80	0.03	–62:12:42.1	0.04	3.38	0.11	2.75	0.09	2.254	0.005	29.76	0.11	G	208
G300.7950+0.5707	12:33:04.78	0.03	–62:13:29.4	0.03	4.91	0.09	10.82	0.19	3.711	0.01	41.87	0.11	G	208
G300.7990–1.0920	12:32:02.62	0.01	–63:53:00.7	0.02	22.29	5.0	25.76	2.88	11.051	0.049	115.45	0.19	P	201
G300.8130+0.0369	12:32:54.20	0.08	–62:45:30.7	0.08	1.69	0.11	1.86	0.12	2.62	0.029	13.73	0.12	G	203
G300.8250+0.0522	12:33:01.31	0.03	–62:44:39.0	0.03	4.94	0.11	5.78	0.13	2.703	0.005	41.83	0.11	G	203

Continued on next page

Table B.3 – continued from previous page

sSource Name	RA J2000	σ_{ra} $''$	DEC J2000	σ_{dec} $''$	Peak mJy/bm	σ_{peak} mJy/bm	S mJy	σ_S mJy	ϑ $''$	σ_ϑ $''$	SNR	rms mJy/bm	Type	Tile
G300.8340–0.4842	12:32:45.72	0.02	–63:16:47.5	0.03	5.15	0.11	5.78	0.14	2.649	0.005	43.58	0.11	G	205
G300.8350–0.4812	12:32:46.08	0.13	–63:16:37.0	0.23	0.96	0.09	2.26	0.28	3.827	0.23	7.54	0.12	G	205
G300.8440–0.4728	12:32:51.16	0.13	–63:16:09.0	0.11	1.04	0.12	0.82	0.11	2.221	0.037	8.59	0.11	G	205
G300.8490–0.4736	12:32:54.07	0.02	–63:16:13.4	0.02	6.7	0.11	6.18	0.12	2.401	0.003	49.22	0.13	G	205
G300.8500–0.6443	12:32:47.60	0.03	–63:26:26.2	0.04	3.36	0.1	3.08	0.1	2.395	0.006	28.76	0.12	G	207
G300.8520+1.0297	12:33:50.24	0.01	–61:46:15.9	0.01	42.77	18.35	47.39	3.52	10.737	0.033	185.63	0.23	P	204
G300.8770+0.3816	12:33:40.38	0.06	–62:25:09.1	0.09	1.8	0.1	2.33	0.15	2.845	0.025	18.47	0.1	G	208
G300.8780–0.4677	12:33:09.65	0.03	–63:15:59.6	0.03	4.22	0.1	5.56	0.15	2.869	0.007	37.3	0.11	G	205
G300.8840+0.6062	12:33:51.80	0.13	–62:11:44.2	0.14	0.81	0.1	0.7	0.09	2.332	0.054	8.21	0.1	G	208
G300.8900+0.9838	12:34:07.69	0.01	–61:49:09.8	0.01	91.49	83.86	97.77	5.83	10.393	0.028	230.34	0.4	P	204
G300.8900–0.6897	12:33:07.43	0.12	–63:29:19.9	0.16	0.89	0.1	0.93	0.12	2.561	0.072	8.69	0.1	G	207
G300.9520–0.9771	12:33:30.21	0.01	–63:46:47.5	0.01	11.7	0.12	11.49	0.13	2.478	0.002	80.59	0.14	G	209
G300.9680–0.1043	12:34:10.29	0.09	–62:54:36.8	0.1	1.01	0.1	0.7	0.08	2.081	0.028	8.72	0.11	G	213
G300.9690+1.1475	12:34:52.85	0.02	–61:39:38.3	0.02	146.02	213.36	372.0	20.44	31.041	0.092	382.92	0.38	P	214
G300.9800+1.1455	12:34:58.63	0.75	–61:39:47.9	0.24	10.26	1.16	140.46	14.64	24.66	0.123	31.77	0.33	P	214
G300.9940–0.9143	12:33:54.96	0.18	–63:43:12.2	0.16	0.7	0.1	0.66	0.11	2.415	0.079	7.19	0.1	G	209
G301.0100+0.9811	12:35:08.95	0.1	–61:49:47.5	0.12	0.96	0.1	0.76	0.09	2.227	0.029	10.35	0.09	G	214
G301.0220+0.7608	12:35:07.49	0.04	–62:03:01.4	0.05	2.53	0.11	2.41	0.12	2.443	0.011	20.76	0.12	G	216
G301.0340+0.4981	12:35:05.28	0.06	–62:18:48.3	0.09	1.6	0.1	1.4	0.1	2.34	0.02	14.25	0.1	G	208
G301.0380+0.0982	12:34:54.01	0.1	–62:42:45.7	0.13	0.92	0.1	0.72	0.09	2.204	0.03	9.47	0.09	G	210
G301.0540+0.3903	12:35:12.03	0.14	–62:25:20.1	0.12	0.82	0.1	0.77	0.11	2.413	0.044	9.22	0.08	G	208
G301.0580–0.0821	12:34:58.30	0.04	–62:53:38.2	0.05	2.6	0.1	2.34	0.1	2.37	0.008	22.7	0.11	G	213
G301.0640+0.7410	12:35:28.41	0.04	–62:04:22.0	0.09	2.23	0.08	4.03	0.17	3.364	0.035	21.48	0.1	G	216
G301.0770+0.4177	12:35:24.69	0.02	–62:23:46.7	0.03	4.61	0.1	4.07	0.1	2.348	0.003	44.5	0.09	G	218

Continued on next page

Table B.3 – continued from previous page

sSource Name	RA J2000	σ_{ra} $''$	DEC J2000	σ_{dec} $''$	Peak mJy/bm	σ_{peak} mJy/bm	S mJy	σ_S mJy	ϑ $''$	σ_ϑ $''$	SNR	rms mJy/bm	Type	Tile
G301.0840–0.4329	12:35:00.03	0.04	–63:14:42.4	0.05	4.23	0.19	9.75	1.57	9.337	0.086	35.83	0.12	P	215
G301.0840–0.4364	12:35:00.38	0.02	–63:14:57.2	0.02	6.14	0.09	11.88	0.21	3.478	0.007	50.28	0.11	G	215
G301.1050–0.8011	12:34:59.17	0.12	–63:36:52.0	0.12	0.89	0.1	0.71	0.08	2.229	0.035	9.19	0.09	G	209
G301.1150+0.9621	12:36:02.50	0.36	–61:51:22.8	0.27	15.4	2.49	277.77	19.98	29.667	0.081	45.48	0.34	P	214
G301.1160+0.9724	12:36:02.49	0.6	–61:50:40.7	0.31	6.04	0.43	70.41	11.15	27.909	0.224	24.86	0.25	P	214
G301.1260+0.8154	12:36:02.77	0.01	–62:00:08.4	0.01	11.03	0.12	10.94	0.11	2.49	0.002	85.81	0.13	G	216
G301.1270–0.4848	12:35:21.46	0.14	–63:18:00.7	0.1	1.24	0.1	1.88	0.15	3.076	0.058	11.88	0.1	G	217
G301.1290+0.7409	12:36:01.79	0.03	–62:04:36.8	0.04	3.38	0.1	3.15	0.11	2.412	0.006	31.27	0.11	G	216
G301.1300–0.0865	12:35:36.12	0.05	–62:54:10.1	0.04	8.57	0.17	35.16	0.85	5.063	0.014	52.05	0.16	G	213
G301.1310–0.6464	12:35:18.52	0.05	–63:27:42.2	0.06	2.18	0.1	2.06	0.11	2.432	0.012	20.14	0.11	G	217
G301.1340–0.0894	12:35:38.28	0.01	–62:54:21.4	0.01	39.47	0.26	41.33	0.32	2.558	0.002	93.8	0.41	G	213
G301.1350+0.5845	12:35:59.95	0.03	–62:14:00.1	0.04	2.97	0.11	2.64	0.1	2.354	0.007	26.5	0.11	G	218
G301.1360–0.2236	12:35:35.18	0.01	–63:02:27.6	0.01	148.8	221.52	318.69	12.19	20.914	0.04	441.37	0.34	P	215
G301.1370–0.0922	12:35:39.96	0.0	–62:54:32.3	0.0	78.79	0.25	105.89	0.39	2.898	0.003	208.5	0.37	G	213
G301.1690+0.1487	12:36:04.20	0.1	–62:40:13.4	0.17	1.16	0.09	2.22	0.2	3.462	0.104	12.66	0.1	G	220
G301.1730–0.4665	12:35:46.50	0.1	–63:17:05.0	0.1	1.11	0.11	0.88	0.08	2.226	0.026	10.04	0.1	G	217
G301.1860+0.1129	12:36:12.05	0.0	–62:42:25.8	0.0	47.77	0.17	49.17	0.2	2.536	0.002	168.21	0.26	G	220
G301.2040+0.0811	12:36:20.17	0.1	–62:44:23.7	0.08	1.3	0.1	1.21	0.1	2.412	0.021	13.5	0.09	G	213
G301.2070+0.8225	12:36:44.33	0.08	–62:00:00.0	0.1	1.23	0.1	0.97	0.08	2.217	0.026	10.76	0.11	G	216
G301.2460+0.1482	12:36:44.45	0.04	–62:40:31.4	0.05	3.0	0.12	2.54	0.11	2.298	0.008	20.53	0.13	G	220
G301.2610+0.3082	12:36:56.87	0.01	–62:30:59.8	0.01	87.98	77.5	97.62	7.63	19.031	0.044	303.24	0.29	P	220
G301.2780+1.0002	12:37:25.17	0.07	–61:49:35.5	0.07	1.8	0.11	1.54	0.11	2.313	0.013	15.98	0.1	G	224
G301.3100–0.4865	12:36:58.87	0.02	–63:18:45.7	0.03	4.23	0.1	4.36	0.1	2.54	0.004	45.15	0.09	G	217
G301.3110–0.8596	12:36:48.35	0.07	–63:41:07.0	0.12	1.3	0.1	1.24	0.1	2.438	0.041	11.13	0.11	G	219

Continued on next page

Table B.3 – continued from previous page

sSource Name	RA J2000	σ_{ra} $''$	DEC J2000	σ_{dec} $''$	Peak mJy/bm	σ_{peak} mJy/bm	S mJy	σ_S mJy	ϑ $''$	σ_ϑ $''$	SNR	rms mJy/bm	Type	Tile
G301.3140+0.2541	12:37:22.71	0.04	–62:34:24.5	0.07	2.46	0.09	3.9	0.17	3.15	0.022	22.51	0.1	G	220
G301.3160–0.5575	12:37:00.15	0.06	–63:23:02.4	0.08	1.47	0.1	1.16	0.08	2.226	0.018	13.59	0.1	G	217
G301.3300+0.1974	12:37:29.79	0.12	–62:37:51.4	0.09	1.19	0.1	1.28	0.14	2.596	0.04	11.37	0.1	G	220
G301.3750–0.9634	12:37:19.89	0.08	–63:47:33.0	0.08	1.21	0.1	0.86	0.08	2.108	0.019	11.52	0.1	G	219
G301.3840+0.5079	12:38:06.32	0.12	–62:19:25.7	0.15	0.77	0.1	0.58	0.09	2.166	0.046	7.85	0.09	G	228
G301.3910+0.8219	12:38:17.92	0.06	–62:00:37.8	0.07	1.75	0.11	1.43	0.09	2.259	0.015	14.43	0.11	G	226
G301.4170+0.7982	12:38:30.46	0.06	–62:02:07.9	0.09	1.47	0.1	1.3	0.1	2.348	0.02	14.46	0.1	G	226
G301.4230–0.8274	12:37:49.87	0.01	–63:39:33.5	0.01	14.26	0.12	14.32	0.12	2.506	0.002	98.09	0.14	G	219
G301.4320–1.0536	12:37:48.05	0.07	–63:53:08.2	0.07	1.42	0.12	0.91	0.08	2.0	0.011	13.87	0.1	G	221
G301.4370–0.6397	12:38:02.47	0.41	–63:28:20.9	0.3	1.13	0.03	3.17	1.64	9.198	0.227	9.79	0.11	P	227
G301.4400+0.3484	12:38:30.68	0.1	–62:29:09.1	0.13	0.89	0.1	0.68	0.08	2.184	0.041	7.71	0.1	G	230
G301.4430+0.6059	12:38:39.08	0.15	–62:13:43.8	0.12	1.05	0.1	1.43	0.14	2.909	0.09	9.36	0.11	G	228
G301.4460+0.9433	12:38:49.16	0.04	–61:53:31.5	0.04	3.38	0.11	3.54	0.11	2.561	0.006	32.67	0.1	G	226
G301.4520–0.6499	12:38:10.27	0.07	–63:29:00.5	0.11	1.35	0.11	1.18	0.11	2.336	0.037	10.65	0.12	G	227
G301.4660–0.6589	12:38:17.89	0.03	–63:29:35.6	0.04	3.56	0.1	5.21	0.16	3.025	0.01	31.25	0.11	G	227
G301.4950+0.3275	12:38:58.97	0.01	–62:30:34.1	0.01	24.79	0.14	24.84	0.14	2.503	0.002	111.96	0.21	G	230
G301.5010+0.1250	12:38:56.95	0.02	–62:42:43.3	0.02	5.54	0.1	5.07	0.11	2.391	0.003	58.78	0.09	G	230
G301.5120–0.7308	12:38:40.56	0.05	–63:34:02.4	0.05	2.24	0.1	1.99	0.09	2.356	0.009	20.22	0.1	G	229
G301.5650+0.3911	12:39:37.03	0.08	–62:26:57.5	0.08	1.57	0.1	1.86	0.12	2.725	0.024	15.13	0.1	G	230
G301.5650+0.3930	12:39:37.04	0.04	–62:26:50.5	0.04	3.25	0.1	3.92	0.12	2.745	0.008	28.02	0.11	G	230
G301.5690+0.7056	12:39:46.52	0.22	–62:08:05.8	0.2	0.83	0.02	1.17	0.84	6.35	0.233	9.04	0.09	P	226
G301.5820–0.6237	12:39:21.05	0.02	–63:27:49.6	0.03	4.86	0.11	4.78	0.12	2.481	0.004	41.86	0.11	G	227
G301.6080–1.0238	12:39:24.89	0.06	–63:51:52.6	0.06	1.99	0.1	1.95	0.1	2.476	0.011	19.89	0.09	G	231
G301.6190+1.1394	12:40:21.48	0.18	–61:42:14.7	0.12	1.59	0.21	1.41	0.19	2.355	0.069	7.73	0.2	G	233

Continued on next page

Table B.3 – continued from previous page

sSource Name	RA J2000	σ_{ra} $''$	DEC J2000	σ_{dec} $''$	Peak mJy/bm	σ_{peak} mJy/bm	S mJy	σ_S mJy	ϑ $''$	σ_ϑ $''$	SNR	rms mJy/bm	Type	Tile
G301.6250–0.2912	12:39:52.11	0.03	–63:08:01.0	0.04	3.01	0.1	2.49	0.08	2.275	0.005	28.41	0.1	G	234
G301.6280+1.1033	12:40:25.44	0.14	–61:44:25.9	0.07	2.34	0.18	2.96	0.23	2.812	0.133	8.16	0.28	G	233
G301.6300+0.5209	12:40:13.46	0.08	–62:19:21.1	0.1	1.15	0.1	0.84	0.08	2.132	0.017	11.84	0.09	G	228
G301.6300+1.1034	12:40:26.78	0.01	–61:44:27.3	0.01	49.33	24.42	73.78	4.33	13.244	0.05	171.52	0.29	P	233
G301.6670+0.0137	12:40:21.12	0.02	–62:49:50.8	0.02	7.35	0.11	7.31	0.11	2.492	0.003	56.91	0.13	G	232
G301.6720+0.5038	12:40:34.72	0.03	–62:20:28.0	0.03	7.99	0.65	20.13	1.57	9.882	0.047	76.05	0.1	P	237
G301.6750+1.0883	12:40:48.91	0.18	–61:45:27.0	0.11	1.3	0.17	1.14	0.15	2.339	0.059	7.15	0.15	G	222
G301.6830–0.9005	12:40:08.58	0.04	–63:44:41.5	0.04	3.15	0.1	3.31	0.13	2.563	0.008	27.47	0.12	G	229
G301.7020+0.2483	12:40:44.59	0.1	–62:35:52.5	0.11	1.48	0.08	4.52	0.29	4.367	0.052	19.05	0.08	G	230
G301.7040–0.8200	12:40:21.72	0.01	–63:39:55.3	0.01	13.08	0.11	13.28	0.12	2.519	0.002	103.9	0.13	G	229
G301.7090–0.0562	12:40:42.27	0.3	–62:54:10.3	0.54	1.31	0.03	8.6	2.87	16.606	0.297	12.35	0.11	P	232
G301.7210–0.9947	12:40:27.10	0.13	–63:50:26.1	0.14	1.01	0.1	1.44	0.17	2.995	0.069	10.68	0.1	G	229
G301.7240+0.8981	12:41:09.43	0.01	–61:56:58.2	0.01	32.25	10.45	33.47	2.61	8.707	0.03	143.29	0.23	P	235
G301.7270–0.2571	12:40:47.06	0.06	–63:06:14.1	0.08	1.68	0.11	1.46	0.09	2.331	0.022	13.47	0.12	G	234
G301.7310+1.1032	12:41:17.59	0.12	–61:44:41.7	0.27	12.63	0.97	51.72	3.96	5.058	0.045	43.46	0.49	G	222
G301.7310+1.1035	12:41:17.60	0.03	–61:44:40.6	0.04	21.37	0.46	46.23	1.0	3.677	0.01	41.85	0.51	G	233
G301.7870–0.4898	12:41:13.64	0.06	–63:20:19.9	0.08	1.73	0.11	1.58	0.1	2.389	0.02	14.67	0.12	G	236
G301.8020+0.6807	12:41:45.33	0.1	–62:10:11.4	0.09	1.04	0.1	0.72	0.07	2.085	0.019	10.92	0.09	G	237
G301.8140+0.7823	12:41:53.64	0.17	–62:04:07.9	0.27	3.14	0.11	32.86	3.63	18.765	0.091	29.71	0.11	P	235
G301.8340–0.8631	12:41:31.10	0.02	–63:42:49.5	0.02	6.87	0.1	6.72	0.12	2.471	0.003	60.1	0.11	G	238
G301.8480+0.4743	12:42:04.96	0.1	–62:22:40.0	0.15	0.88	0.1	0.7	0.1	2.217	0.048	8.4	0.11	G	237
G301.8500+1.0649	12:42:16.76	0.06	–61:47:15.5	0.07	1.95	0.12	1.54	0.09	2.226	0.013	16.09	0.12	G	242
G301.8780–0.6274	12:41:59.86	0.05	–63:28:47.5	0.09	1.98	0.1	2.67	0.16	2.901	0.03	17.81	0.12	G	236
G301.9290+0.3437	12:42:44.92	0.09	–62:30:40.2	0.08	1.45	0.1	1.68	0.12	2.684	0.029	14.15	0.1	G	239

Continued on next page

Table B.3 – continued from previous page

sSource Name	RA J2000	σ_{ra} $''$	DEC J2000	σ_{dec} $''$	Peak mJy/bm	σ_{peak} mJy/bm	S mJy	σ_S mJy	ϑ $''$	σ_ϑ $''$	SNR	rms mJy/bm	Type	Tile
G301.9590+0.8985	12:43:09.54	0.06	–61:57:27.2	0.08	1.74	0.11	1.45	0.09	2.285	0.015	15.58	0.11	G	244
G301.9730–0.9322	12:42:45.21	0.12	–63:47:15.9	0.14	0.75	0.1	0.53	0.08	2.099	0.052	7.19	0.1	G	238
G301.9810–0.2219	12:43:02.39	0.02	–63:04:41.5	0.03	4.57	0.11	3.86	0.09	2.297	0.004	35.08	0.12	G	243
G302.0030+0.2300	12:43:21.36	0.06	–62:37:37.9	0.06	2.37	0.12	2.45	0.15	2.541	0.016	18.16	0.13	G	239
G302.0050+0.7322	12:43:30.65	0.09	–62:07:31.1	0.1	1.13	0.11	0.81	0.09	2.115	0.019	11.28	0.09	G	244
G302.0070+1.0875	12:43:37.12	0.08	–61:46:12.7	0.08	1.9	0.13	2.01	0.14	2.573	0.024	15.19	0.13	G	242
G302.0220+0.2539	12:43:31.51	0.0	–62:36:13.8	0.0	77.43	0.22	97.02	0.32	2.798	0.002	240.56	0.31	G	239
G302.0320–0.0605	12:43:31.77	0.01	–62:55:06.4	0.01	278.58	0.86	932.2	3.35	4.573	0.006	259.8	1.04	G	241
G302.0460–1.0735	12:43:22.21	0.21	–63:55:54.3	0.16	1.17	0.03	2.72	1.46	9.009	0.251	10.26	0.11	P	240
G302.0500–0.1376	12:43:40.32	0.36	–62:59:44.9	0.81	0.89	0.02	4.78	3.03	15.496	0.421	7.72	0.11	P	241
G302.0760–0.9473	12:43:40.82	0.05	–63:48:22.0	0.06	2.0	0.11	1.54	0.1	2.192	0.008	18.22	0.1	G	248
G302.0880–0.1490	12:43:59.82	0.14	–63:00:30.8	0.13	0.74	0.11	0.47	0.07	1.999	0.029	8.8	0.09	G	243
G302.0890+0.9208	12:44:16.15	0.01	–61:56:21.2	0.01	19.18	0.12	20.27	0.13	2.57	0.002	126.35	0.15	G	244
G302.1480+0.3739	12:44:38.99	0.03	–62:29:15.1	0.03	3.67	0.09	3.49	0.09	2.438	0.005	34.3	0.11	G	247
G302.1520–0.9487	12:44:22.30	0.04	–63:48:34.7	0.04	5.13	0.27	40.99	2.48	16.652	0.044	56.25	0.09	P	248
G302.1540–0.3726	12:44:31.66	0.1	–63:14:02.2	0.14	0.92	0.09	0.95	0.11	2.534	0.057	9.33	0.1	G	243
G302.1550+0.7689	12:44:47.75	0.05	–62:05:34.3	0.05	2.13	0.1	1.97	0.11	2.404	0.008	22.05	0.09	G	244
G302.1610–0.5635	12:44:32.49	0.05	–63:25:29.8	0.06	1.86	0.1	1.43	0.09	2.192	0.01	18.51	0.1	G	245
G302.1730–0.9329	12:44:33.86	0.04	–63:47:40.2	0.04	3.07	0.1	3.65	0.13	2.724	0.009	28.83	0.1	G	248
G302.1770–0.1053	12:44:47.38	0.07	–62:58:02.1	0.13	1.05	0.09	1.01	0.1	2.456	0.03	12.25	0.08	G	250
G302.1800–0.8303	12:44:38.83	0.09	–63:41:31.7	0.09	1.05	0.1	0.7	0.07	2.042	0.022	10.14	0.1	G	248
G302.2000–0.3655	12:44:56.39	0.02	–63:13:40.9	0.02	6.2	0.1	6.05	0.11	2.469	0.003	57.36	0.1	G	243
G302.2070–0.5082	12:44:58.11	0.09	–63:22:15.0	0.08	1.63	0.1	2.54	0.15	3.116	0.04	14.45	0.11	G	245
G302.2280–0.3156	12:45:11.71	0.1	–63:10:43.9	0.16	1.07	0.09	1.63	0.17	3.081	0.082	10.79	0.1	G	253

Continued on next page

Table B.3 – continued from previous page

sSource Name	RA J2000	σ_{ra} $''$	DEC J2000	σ_{dec} $''$	Peak mJy/bm	σ_{peak} mJy/bm	S mJy	σ_S mJy	ϑ $''$	σ_ϑ $''$	SNR	rms mJy/bm	Type	Tile
G302.2300–0.1358	12:45:15.27	0.03	–62:59:56.7	0.03	4.25	0.1	3.99	0.09	2.421	0.004	38.1	0.11	G	253
G302.2400–0.0030	12:45:21.96	0.01	–62:51:59.8	0.01	10.88	0.1	10.72	0.12	2.482	0.002	92.16	0.12	G	250
G302.2570+0.0014	12:45:31.24	0.13	–62:51:45.3	0.15	0.77	0.1	0.66	0.1	2.311	0.064	7.59	0.1	G	250
G302.2740–0.9696	12:45:28.08	0.02	–63:50:01.9	0.02	13.46	1.82	17.16	1.55	10.557	0.041	124.54	0.11	P	248
G302.2820+1.0894	12:45:56.50	0.01	–61:46:31.7	0.01	22.07	0.13	23.4	0.14	2.574	0.002	106.15	0.2	G	249
G302.2830–0.9713	12:45:32.90	0.03	–63:50:08.3	0.03	4.82	0.11	4.64	0.12	2.455	0.003	47.27	0.1	G	248
G302.2840+1.0908	12:45:57.32	0.02	–61:46:26.5	0.02	10.41	0.14	10.38	0.14	2.497	0.003	52.26	0.19	G	249
G302.2900–0.1452	12:45:46.99	0.04	–63:00:35.6	0.04	2.95	0.1	2.5	0.09	2.3	0.006	26.83	0.1	G	253
G302.3110–0.1553	12:45:57.79	0.02	–63:01:13.8	0.03	4.63	0.1	4.49	0.1	2.46	0.003	47.62	0.09	G	253
G302.3190–0.7429	12:45:55.13	0.11	–63:36:29.2	0.18	0.76	0.1	0.65	0.08	2.324	0.067	7.93	0.1	G	248
G302.3210–0.6004	12:45:57.82	0.04	–63:27:56.2	0.04	2.71	0.1	2.5	0.1	2.4	0.006	28.5	0.09	G	255
G302.3460+0.6339	12:46:24.42	0.03	–62:13:55.6	0.04	3.0	0.09	2.94	0.09	2.474	0.007	29.93	0.1	G	254
G302.3500+0.6689	12:46:27.00	0.03	–62:11:50.0	0.03	4.3	0.1	3.93	0.09	2.389	0.004	40.4	0.1	G	254
G302.3590–0.6893	12:46:17.59	0.02	–63:33:19.1	0.02	4.9	0.09	4.95	0.11	2.513	0.003	55.31	0.08	G	255
G302.3850+1.0089	12:46:47.93	0.02	–61:51:28.6	0.03	4.51	0.1	4.06	0.11	2.371	0.003	42.62	0.1	G	249
G302.3870+0.7311	12:46:46.51	0.11	–62:08:08.5	0.25	0.84	0.09	1.25	0.17	3.046	0.138	8.72	0.09	G	252
G302.3890+0.0521	12:46:41.00	0.06	–62:48:52.8	0.07	1.46	0.09	1.12	0.07	2.192	0.013	14.71	0.09	G	250
G302.3900+0.2791	12:46:43.60	0.01	–62:35:15.6	0.01	16.94	0.06	158.95	0.69	7.658	0.019	116.2	0.15	G	256
G302.3920–1.0584	12:46:31.28	0.07	–63:55:30.0	0.08	2.65	0.15	3.7	0.24	2.956	0.029	15.7	0.16	G	251
G302.3950–1.0581	12:46:32.91	0.12	–63:55:29.2	0.13	1.59	0.15	2.12	0.23	2.882	0.067	9.91	0.16	G	251
G302.4060–0.4252	12:46:45.39	0.22	–63:17:31.8	0.2	0.79	0.09	1.88	0.22	3.847	0.164	8.7	0.09	G	255
G302.4280–0.9764	12:46:51.90	0.01	–63:50:37.3	0.01	9.51	0.11	9.38	0.12	2.483	0.002	83.43	0.11	G	257
G302.4330–0.4878	12:46:59.47	0.12	–63:21:19.0	0.12	0.81	0.1	0.52	0.07	1.999	0.034	7.98	0.1	G	255
G302.4340–0.5914	12:46:58.79	0.02	–63:27:31.9	0.03	4.46	0.1	4.01	0.1	2.372	0.004	44.51	0.1	G	255

Continued on next page

Table B.3 – continued from previous page

sSource Name	RA J2000	σ_{ra} $''$	DEC J2000	σ_{dec} $''$	Peak mJy/bm	σ_{peak} mJy/bm	S mJy	σ_S mJy	ϑ $''$	σ_ϑ $''$	SNR	rms mJy/bm	Type	Tile
G302.4470+0.5029	12:47:15.29	0.06	–62:21:53.7	0.07	1.76	0.11	1.38	0.1	2.215	0.013	15.71	0.11	G	254
G302.4600–0.6487	12:47:12.16	0.06	–63:30:59.7	0.06	1.76	0.09	1.68	0.1	2.448	0.013	18.74	0.09	G	255
G302.4750–0.9802	12:47:17.40	0.16	–63:50:53.8	0.13	0.71	0.1	0.52	0.08	2.137	0.04	7.89	0.08	G	260
G302.4810–0.4213	12:47:25.45	0.01	–63:17:22.4	0.01	8.54	0.1	8.02	0.1	2.422	0.002	73.61	0.11	G	255
G302.4840–0.5679	12:47:25.74	0.07	–63:26:10.2	0.06	1.42	0.09	1.0	0.08	2.104	0.014	13.59	0.1	G	255
G302.4870–0.0316	12:47:31.79	0.01	–62:53:59.7	0.02	11.51	0.09	26.72	0.25	3.809	0.006	86.42	0.14	G	259
G302.4890–0.2176	12:47:31.28	0.11	–63:05:09.4	0.11	0.79	0.1	0.51	0.06	1.999	0.022	8.88	0.08	G	253
G302.5130–0.6880	12:47:40.51	0.1	–63:33:24.1	0.09	1.01	0.1	0.68	0.07	2.052	0.017	11.02	0.08	G	255
G302.5640+0.5413	12:48:16.32	0.05	–62:19:41.4	0.07	2.37	0.1	3.36	0.16	2.981	0.02	20.96	0.11	G	263
G302.5640+0.5452	12:48:16.31	0.05	–62:19:27.4	0.07	2.2	0.1	3.12	0.16	2.975	0.018	21.27	0.1	G	263
G302.5670+0.5679	12:48:18.05	0.07	–62:18:05.7	0.08	1.56	0.1	1.38	0.09	2.352	0.012	17.19	0.08	G	263
G302.5810–0.4053	12:48:18.76	0.05	–63:16:29.4	0.05	3.63	0.14	6.73	1.14	7.842	0.081	36.28	0.1	P	262
G302.5990+0.7829	12:48:35.59	0.06	–62:05:13.3	0.06	1.79	0.1	1.54	0.1	2.318	0.014	16.74	0.11	G	261
G302.6470+0.1551	12:48:57.31	0.04	–62:42:54.9	0.04	3.05	0.1	3.19	0.1	2.558	0.006	34.39	0.08	G	259
G302.6570+0.9199	12:49:05.74	0.04	–61:57:02.2	0.04	2.9	0.11	2.37	0.09	2.258	0.006	25.13	0.11	G	261
G302.6570+0.9214	12:49:05.95	0.11	–61:56:56.9	0.11	0.92	0.11	0.59	0.07	2.0	0.032	7.71	0.11	G	261
G302.6620+0.7558	12:49:07.59	0.02	–62:06:53.2	0.02	7.55	0.11	7.24	0.12	2.447	0.003	59.61	0.12	G	261
G302.6670+0.3844	12:49:08.59	0.08	–62:29:10.4	0.07	1.24	0.1	0.82	0.06	2.035	0.013	12.46	0.09	G	265
G302.6740–0.8750	12:49:06.45	0.02	–63:44:44.2	0.02	5.64	0.1	5.08	0.1	2.372	0.003	53.85	0.1	G	266
G302.6810–0.3549	12:49:12.64	0.1	–63:13:32.1	0.09	1.15	0.1	1.0	0.1	2.332	0.033	10.7	0.11	G	262
G302.6970+0.6467	12:49:25.33	0.06	–62:13:27.0	0.06	1.7	0.09	1.56	0.09	2.389	0.016	16.67	0.1	G	263
G302.7060+0.5180	12:49:29.67	0.02	–62:21:10.4	0.02	4.96	0.1	5.45	0.13	2.619	0.004	44.91	0.11	G	263
G302.7070–0.0618	12:49:27.41	0.03	–62:55:57.8	0.04	3.08	0.1	2.69	0.1	2.339	0.005	31.65	0.09	G	259
G302.7090+0.9294	12:49:32.46	0.04	–61:56:29.7	0.05	2.46	0.09	2.53	0.1	2.532	0.008	26.3	0.09	G	261

Continued on next page

Table B.3 – continued from previous page

sSource Name	RA J2000	σ_{ra} $''$	DEC J2000	σ_{dec} $''$	Peak mJy/bm	σ_{peak} mJy/bm	S mJy	σ_S mJy	ϑ $''$	σ_ϑ $''$	SNR	rms mJy/bm	Type	Tile
G302.7170–0.6104	12:49:30.75	0.05	–63:28:52.7	0.06	1.84	0.11	1.37	0.09	2.155	0.014	15.77	0.12	G	264
G302.7210–0.2153	12:49:34.58	0.02	–63:05:10.7	0.02	5.37	0.11	5.02	0.1	2.415	0.004	45.28	0.12	G	262
G302.7300+0.1143	12:49:40.54	0.02	–62:45:24.5	0.01	13.03	0.12	29.42	0.28	3.756	0.006	77.94	0.16	G	268
G302.7350–0.1200	12:49:42.63	0.08	–62:59:30.2	0.07	2.72	0.08	10.88	1.89	16.261	0.146	30.79	0.09	P	268
G302.7410+0.8670	12:49:48.59	0.02	–62:00:14.9	0.02	5.78	0.11	5.29	0.11	2.392	0.003	50.81	0.11	G	261
G302.7660+0.0876	12:49:59.15	0.08	–62:47:00.4	0.08	2.61	0.08	3.87	1.04	6.544	0.098	24.17	0.11	P	268
G302.7730–0.7207	12:50:00.48	0.07	–63:35:31.2	0.08	1.4	0.1	1.31	0.09	2.412	0.013	16.46	0.07	G	266
G302.7740–0.5357	12:50:01.57	0.07	–63:24:25.4	0.08	1.59	0.11	1.4	0.09	2.345	0.017	15.2	0.1	G	264
G302.7830+0.2954	12:50:08.86	0.07	–62:34:33.4	0.08	1.41	0.1	1.12	0.09	2.226	0.017	13.74	0.1	G	265
G302.8060–0.2552	12:50:19.32	0.06	–63:07:36.1	0.08	1.43	0.1	1.1	0.08	2.193	0.011	15.42	0.08	G	271
G302.8090+0.3441	12:50:22.58	0.01	–62:31:38.5	0.01	18.27	0.13	17.8	0.12	2.468	0.002	110.37	0.16	G	265
G302.8390–0.9781	12:50:35.61	0.05	–63:50:59.0	0.07	1.76	0.11	1.31	0.08	2.156	0.012	15.88	0.11	G	269
G302.8640+0.0309	12:50:50.64	0.05	–62:50:26.9	0.06	2.17	0.1	2.04	0.09	2.425	0.01	21.0	0.1	G	268
G302.8770+0.1995	12:50:57.37	0.08	–62:40:19.8	0.08	1.13	0.1	0.78	0.07	2.083	0.015	12.26	0.08	G	265
G302.9230+0.3373	12:51:21.39	0.14	–62:32:03.9	0.13	0.88	0.09	1.06	0.11	2.74	0.048	10.42	0.08	G	265
G302.9410+0.5285	12:51:30.88	0.05	–62:20:34.7	0.07	3.23	0.12	5.6	1.16	7.512	0.085	30.93	0.1	P	272
G302.9520–0.2757	12:51:36.84	0.09	–63:08:50.8	0.11	1.09	0.1	0.86	0.09	2.218	0.028	10.8	0.1	G	271
G302.9570+0.7802	12:51:39.19	0.07	–62:05:29.6	0.09	1.37	0.1	1.12	0.1	2.264	0.023	13.17	0.1	G	270
G302.9610–0.4930	12:51:41.82	0.06	–63:21:53.0	0.07	1.54	0.11	1.08	0.07	2.095	0.013	14.43	0.11	G	273
G303.0420–0.0123	12:52:24.24	0.18	–62:53:01.9	0.21	0.74	0.09	1.32	0.2	3.342	0.173	7.68	0.1	G	277
G303.0450–0.6951	12:52:27.39	0.01	–63:34:00.0	0.01	13.19	0.12	14.29	0.13	2.602	0.002	98.54	0.13	G	275
G303.0470–0.6937	12:52:28.35	0.02	–63:33:54.8	0.02	8.91	0.12	11.0	0.15	2.777	0.003	62.85	0.13	G	275
G303.0540+0.6952	12:52:28.91	0.08	–62:10:34.6	0.12	1.39	0.09	2.48	0.16	3.34	0.041	17.19	0.09	G	272
G303.0630–0.2129	12:52:35.57	0.06	–63:05:03.7	0.07	1.38	0.1	0.95	0.07	2.073	0.013	14.01	0.1	G	271

Continued on next page

Table B.3 – continued from previous page

sSource Name	RA J2000	σ_{ra} $''$	DEC J2000	σ_{dec} $''$	Peak mJy/bm	σ_{peak} mJy/bm	S mJy	σ_S mJy	ϑ $''$	σ_ϑ $''$	SNR	rms mJy/bm	Type	Tile
G303.0730–0.9087	12:52:42.79	0.04	–63:46:48.3	0.04	2.95	0.1	2.69	0.1	2.39	0.007	27.42	0.11	G	275
G303.0860+0.6025	12:52:45.81	0.11	–62:16:07.8	0.08	1.07	0.09	0.87	0.08	2.261	0.029	10.97	0.09	G	272
G303.0860–0.9153	12:52:49.90	0.04	–63:47:12.0	0.04	3.45	0.1	3.7	0.13	2.591	0.007	30.35	0.11	G	275
G303.1090–0.3410	12:53:00.77	0.01	–63:12:44.0	0.01	8.01	0.1	8.03	0.11	2.503	0.002	81.72	0.09	G	280
G303.1150–0.1686	12:53:02.93	0.13	–63:02:23.2	0.12	0.71	0.09	0.49	0.06	2.081	0.029	8.2	0.08	G	280
G303.1170–0.9714	12:53:07.19	0.0	–63:50:33.2	0.01	235.67	0.72	479.21	1.69	3.565	0.004	197.13	1.16	G	275
G303.1240+0.9334	12:53:04.28	0.01	–61:56:16.0	0.01	18.99	0.12	19.08	0.13	2.506	0.002	114.49	0.16	G	279
G303.1340+0.3066	12:53:11.52	0.02	–62:33:52.2	0.02	6.26	0.09	8.29	0.14	2.878	0.005	52.89	0.12	G	274
G303.1340+1.0180	12:53:09.15	0.03	–61:51:11.1	0.03	3.86	0.1	3.71	0.11	2.453	0.004	43.94	0.08	G	276
G303.1510+0.2330	12:53:20.61	0.1	–62:38:16.5	0.1	0.95	0.1	0.68	0.08	2.111	0.037	8.43	0.11	G	274
G303.1560+0.3606	12:53:22.28	0.01	–62:30:35.3	0.02	12.17	1.49	25.33	1.8	11.393	0.059	106.67	0.11	P	274
G303.1570+0.9381	12:53:21.13	0.12	–61:55:58.2	0.12	1.2	0.1	2.09	0.17	3.307	0.091	10.57	0.12	G	279
G303.1940+0.3986	12:53:42.19	0.05	–62:28:19.3	0.06	1.96	0.1	1.54	0.08	2.222	0.013	16.0	0.12	G	274
G303.1940+0.4917	12:53:42.17	0.03	–62:22:44.1	0.03	3.84	0.1	3.57	0.11	2.412	0.004	38.34	0.1	G	281
G303.1960+0.6558	12:53:42.15	0.07	–62:12:53.3	0.11	1.26	0.1	1.13	0.09	2.365	0.034	11.51	0.11	G	281
G303.2110–0.4640	12:53:55.70	0.23	–63:20:03.7	0.2	0.76	0.1	1.15	0.15	3.073	0.136	8.95	0.1	G	282
G303.2280–0.6215	12:54:05.31	0.26	–63:29:30.3	0.46	0.61	0.07	2.61	0.47	5.177	0.522	7.57	0.09	G	282
G303.2360–0.8751	12:54:11.00	0.05	–63:44:42.8	0.07	1.84	0.1	1.56	0.09	2.305	0.013	17.1	0.1	G	275
G303.2440–0.0750	12:54:10.71	0.08	–62:56:42.4	0.08	1.12	0.1	0.73	0.07	2.02	0.016	11.53	0.09	G	277
G303.2450+0.7885	12:54:06.72	0.04	–62:04:53.7	0.05	2.6	0.09	2.97	0.12	2.672	0.009	26.8	0.09	G	279
G303.2490+0.1856	12:54:12.22	0.05	–62:41:04.0	0.05	2.3	0.1	2.01	0.1	2.34	0.007	23.39	0.09	G	283
G303.2610+0.4910	12:54:16.52	0.04	–62:22:44.2	0.05	2.63	0.11	2.3	0.11	2.335	0.008	23.86	0.11	G	281
G303.2650+1.0194	12:54:15.61	0.03	–61:51:01.9	0.04	3.58	0.11	4.27	0.15	2.729	0.007	33.24	0.1	G	276
G303.2720–0.0347	12:54:25.22	0.04	–62:54:16.3	0.05	2.78	0.11	2.36	0.1	2.304	0.008	23.72	0.12	G	277

Continued on next page

Table B.3 – continued from previous page

sSource Name	RA J2000	σ_{ra} $''$	DEC J2000	σ_{dec} $''$	Peak mJy/bm	σ_{peak} mJy/bm	S mJy	σ_S mJy	ϑ $''$	σ_ϑ $''$	SNR	rms mJy/bm	Type	Tile
G303.2790+0.8782	12:54:23.77	0.07	–61:59:29.5	0.1	1.34	0.11	1.09	0.09	2.255	0.026	11.65	0.11	G	279
G303.2830–0.7986	12:54:36.22	0.01	–63:40:05.6	0.02	8.64	0.11	8.23	0.1	2.44	0.002	75.99	0.11	G	285
G303.2990+0.5118	12:54:36.53	0.02	–62:21:28.1	0.02	14.73	2.21	21.15	2.94	9.458	0.068	71.81	0.21	P	281
G303.3040+0.5103	12:54:39.01	0.01	–62:21:32.9	0.01	20.07	0.16	24.27	0.22	2.749	0.003	91.49	0.21	G	281
G303.3110–0.9462	12:54:52.66	0.02	–63:48:55.4	0.02	4.77	0.1	4.31	0.1	2.374	0.003	46.85	0.1	G	285
G303.3240+1.1466	12:54:45.00	0.04	–61:43:21.3	0.04	7.31	0.24	7.92	0.26	2.602	0.006	34.8	0.2	G	284
G303.3290+0.8225	12:54:49.62	0.05	–62:02:47.8	0.06	2.4	0.13	1.86	0.11	2.199	0.01	17.78	0.13	G	279
G303.3370+0.8188	12:54:54.36	0.03	–62:03:01.4	0.04	11.69	1.38	28.14	3.1	18.692	0.153	95.57	0.12	P	279
G303.3430+0.3604	12:54:59.96	0.04	–62:30:30.8	0.06	2.3	0.1	1.89	0.09	2.267	0.012	18.55	0.12	G	283
G303.3470+0.7275	12:54:59.25	0.1	–62:08:29.1	0.15	0.85	0.1	0.73	0.1	2.323	0.045	9.6	0.09	G	279
G303.3530–0.8898	12:55:14.83	0.09	–63:45:30.4	0.11	1.03	0.1	0.77	0.08	2.159	0.023	11.29	0.09	G	285
G303.3570+0.8849	12:55:03.38	0.05	–61:59:01.9	0.05	2.04	0.11	1.43	0.07	2.095	0.005	22.01	0.08	G	279
G303.3620–0.5671	12:55:16.93	0.02	–63:26:08.2	0.03	5.11	0.11	4.73	0.12	2.407	0.004	38.1	0.13	G	282
G303.3760+0.9063	12:55:12.84	0.06	–61:57:43.8	0.05	2.46	0.1	3.13	0.13	2.818	0.013	23.95	0.1	G	279
G303.3840+0.9757	12:55:16.70	0.14	–61:53:33.7	0.13	0.94	0.1	1.01	0.11	2.586	0.045	10.38	0.09	G	287
G303.3900–0.1089	12:55:28.47	0.06	–62:58:37.5	0.07	1.48	0.1	1.05	0.08	2.098	0.011	14.67	0.09	G	286
G303.4090–0.3055	12:55:40.03	0.07	–63:10:23.9	0.1	1.3	0.1	1.06	0.1	2.258	0.02	12.58	0.09	G	289
G303.4650–0.5044	12:56:11.91	0.03	–63:22:16.3	0.04	2.9	0.1	2.57	0.09	2.351	0.006	28.15	0.1	G	282
G303.4680+0.8542	12:56:00.49	0.05	–62:00:45.9	0.07	1.99	0.1	2.07	0.12	2.55	0.014	20.34	0.1	G	287
G303.4840+0.4679	12:56:12.06	0.11	–62:23:55.4	0.12	0.94	0.1	0.75	0.1	2.227	0.034	9.68	0.1	G	290
G303.4840–0.4601	12:56:21.49	0.04	–63:19:35.6	0.04	4.83	0.08	21.4	0.35	5.264	0.018	42.07	0.11	G	282
G303.5180+0.8235	12:56:26.13	0.02	–62:02:33.3	0.02	6.46	0.12	5.68	0.12	2.345	0.003	47.6	0.14	G	287
G303.5200+0.5508	12:56:30.23	0.11	–62:18:54.5	0.12	0.77	0.1	0.49	0.07	2.0	0.031	8.77	0.09	G	290
G303.5300+0.5348	12:56:35.63	0.01	–62:19:51.6	0.01	16.1	0.15	15.5	0.16	2.453	0.002	83.41	0.19	G	290

Continued on next page

Table B.3 – continued from previous page

sSource Name	RA J2000	σ_{ra} $''$	DEC J2000	σ_{dec} $''$	Peak mJy/bm	σ_{peak} mJy/bm	S mJy	σ_S mJy	ϑ $''$	σ_ϑ $''$	SNR	rms mJy/bm	Type	Tile
G303.5350–0.5970	12:56:50.31	0.03	–63:27:44.0	0.06	5.93	0.37	9.55	1.9	9.597	0.096	45.45	0.13	P	291
G303.5530+0.7735	12:56:44.83	0.12	–62:05:30.5	0.14	0.78	0.1	0.54	0.08	2.087	0.048	7.2	0.11	G	287
G303.5540+0.7748	12:56:45.12	0.09	–62:05:25.8	0.13	1.1	0.1	1.25	0.13	2.661	0.058	10.36	0.1	G	287
G303.5710+1.1092	12:56:50.33	0.02	–61:45:21.1	0.02	8.85	0.15	8.35	0.14	2.429	0.003	52.69	0.15	G	284
G303.5760–0.3823	12:57:09.63	0.03	–63:14:48.9	0.03	3.79	0.11	3.05	0.1	2.244	0.004	35.43	0.1	G	289
G303.5920+1.0352	12:57:01.91	0.08	–61:49:45.8	0.15	1.48	0.13	1.73	0.17	2.701	0.047	11.56	0.11	G	284
G303.5950+0.3298	12:57:11.50	0.09	–62:32:04.4	0.09	1.12	0.1	0.72	0.07	2.013	0.018	10.67	0.1	G	292
G303.6000+1.0440	12:57:05.82	0.11	–61:49:13.6	0.12	1.6	0.16	1.61	0.18	2.513	0.056	9.19	0.17	G	293
G303.6210+1.0541	12:57:16.26	0.01	–61:48:34.8	0.01	73.49	54.05	87.34	7.35	20.026	0.053	328.48	0.22	P	293
G303.6510–0.9569	12:57:57.65	0.1	–63:49:10.3	0.14	1.06	0.09	1.78	0.17	3.24	0.063	11.87	0.09	G	294
G303.6660+0.9404	12:57:40.37	0.02	–61:55:20.7	0.02	7.83	0.12	7.37	0.11	2.426	0.003	54.1	0.14	G	287
G303.7030–0.0222	12:58:12.54	0.02	–62:53:01.6	0.02	6.27	0.11	5.73	0.12	2.389	0.003	51.74	0.12	G	295
G303.7070+0.3792	12:58:09.08	0.06	–62:28:56.6	0.08	1.46	0.1	1.08	0.07	2.145	0.015	14.23	0.1	G	292
G303.7080+0.2366	12:58:11.27	0.01	–62:37:29.9	0.01	9.71	0.12	9.36	0.13	2.455	0.002	74.83	0.13	G	292
G303.7160+0.5012	12:58:11.73	0.01	–62:21:37.1	0.02	12.0	0.11	23.62	0.25	3.507	0.006	95.8	0.15	G	290
G303.7310–0.2277	12:58:29.95	0.1	–63:05:18.4	0.1	1.06	0.11	0.8	0.08	2.171	0.028	9.45	0.1	G	298
G303.7340–0.2110	12:58:31.29	0.11	–63:04:18.0	0.12	0.85	0.1	0.59	0.07	2.08	0.036	7.58	0.1	G	298
G303.7540–0.7252	12:58:50.05	0.01	–63:35:06.6	0.01	14.66	0.13	14.37	0.12	2.475	0.002	100.21	0.14	G	294
G303.7800–1.0873	12:59:09.88	0.07	–63:56:46.7	0.07	2.9	0.15	4.18	0.24	2.999	0.022	19.32	0.15	G	297
G303.7880+0.0204	12:58:56.28	0.01	–62:50:19.9	0.01	14.27	0.12	14.06	0.12	2.481	0.002	88.67	0.16	G	295
G303.8070–0.2077	12:59:09.79	0.03	–63:03:58.9	0.03	3.69	0.11	3.54	0.1	2.447	0.006	30.87	0.12	G	298
G303.8350+0.5896	12:59:11.99	0.09	–62:16:06.7	0.1	1.2	0.1	1.04	0.09	2.331	0.029	11.11	0.1	G	299
G303.8380–0.7892	12:59:36.20	0.12	–63:38:47.5	0.12	0.73	0.1	0.47	0.06	1.999	0.042	7.27	0.1	G	294
G303.8740–0.4586	12:59:50.01	0.02	–63:18:54.1	0.02	5.0	0.1	5.88	0.11	2.71	0.004	56.56	0.09	G	300

Continued on next page

Table B.3 – continued from previous page

sSource Name	RA J2000	σ_{ra} $''$	DEC J2000	σ_{dec} $''$	Peak mJy/bm	σ_{peak} mJy/bm	S mJy	σ_S mJy	ϑ $''$	σ_ϑ $''$	SNR	rms mJy/bm	Type	Tile
G303.8760–0.3734	12:59:49.13	0.12	–63:13:47.3	0.11	0.98	0.09	1.0	0.11	2.529	0.055	9.45	0.1	G	298
G303.8800–0.5168	12:59:54.01	0.18	–63:22:22.5	0.13	0.96	0.08	2.18	0.19	3.774	0.14	10.61	0.1	G	300
G303.8870–0.9066	13:00:04.91	0.01	–63:45:44.3	0.01	14.95	0.12	15.49	0.14	2.545	0.002	107.95	0.14	G	303
G303.8960+0.7194	12:59:41.59	0.05	–62:08:13.3	0.06	2.89	0.09	3.07	0.87	6.586	0.099	31.43	0.09	P	296
G303.8980–0.8620	13:00:09.85	0.04	–63:43:02.7	0.05	2.56	0.11	2.11	0.1	2.27	0.007	24.31	0.1	G	303
G303.9120+0.4687	12:59:53.85	0.01	–62:23:11.2	0.01	65.86	43.43	115.68	3.3	9.481	0.016	276.31	0.24	P	299
G303.9290+0.3597	13:00:04.36	0.01	–62:29:43.1	0.01	16.98	0.13	17.02	0.13	2.503	0.002	106.12	0.15	G	301
G303.9300–0.6878	13:00:24.07	0.01	–63:32:31.7	0.01	15.33	0.14	16.0	0.16	2.554	0.002	107.86	0.13	G	300
G303.9380+0.7698	13:00:02.04	0.09	–62:05:06.4	0.11	1.04	0.11	0.77	0.09	2.147	0.038	9.13	0.12	G	296
G303.9390–0.6895	13:00:28.77	0.01	–63:32:36.8	0.01	28.27	0.12	38.38	0.19	2.913	0.003	176.66	0.15	G	300
G303.9400+0.1603	13:00:13.58	0.08	–62:41:39.3	0.09	1.2	0.1	0.82	0.08	2.062	0.013	12.1	0.09	G	301
G303.9440+0.3841	13:00:11.94	0.07	–62:28:13.5	0.07	1.38	0.1	0.9	0.07	2.015	0.016	10.65	0.11	G	301
G303.9450–1.0232	13:00:38.66	0.09	–63:52:36.5	0.09	1.09	0.1	0.78	0.07	2.115	0.021	10.3	0.1	G	297
G303.9520–0.1572	13:00:25.80	0.06	–63:00:40.2	0.07	1.6	0.09	1.61	0.09	2.502	0.01	21.49	0.07	G	298
G303.9530–0.4040	13:00:30.92	0.05	–63:15:28.0	0.06	2.23	0.11	2.11	0.11	2.431	0.007	26.32	0.08	G	298
G303.9550+0.7506	13:00:11.20	0.01	–62:06:13.7	0.01	18.93	0.12	21.84	0.16	2.685	0.002	127.24	0.14	G	296
G303.9560–0.6707	13:00:37.56	0.05	–63:31:27.1	0.05	1.88	0.1	1.23	0.07	2.025	0.005	20.84	0.08	G	300
G303.9580–0.4449	13:00:34.36	0.01	–63:17:54.3	0.01	10.48	0.11	10.24	0.11	2.472	0.002	107.49	0.09	G	300
G303.9860–0.3971	13:00:48.31	0.01	–63:14:58.9	0.01	10.55	0.11	10.55	0.13	2.499	0.002	94.77	0.1	G	298
G303.9980+0.2801	13:00:41.63	0.02	–62:34:20.9	0.02	6.5	0.06	34.7	0.33	5.776	0.016	59.3	0.11	G	301
G304.0060–0.2913	13:00:57.06	0.11	–63:08:35.4	0.1	0.94	0.11	0.6	0.07	2.003	0.023	8.52	0.09	G	298
G304.0320–0.0320	13:01:05.69	0.06	–62:52:59.1	0.07	1.87	0.1	2.05	0.13	2.611	0.02	16.72	0.11	G	304
G304.0330+0.2129	13:01:01.48	0.07	–62:38:18.0	0.09	1.46	0.11	1.24	0.11	2.306	0.022	13.15	0.11	G	301
G304.0860–0.0124	13:01:33.55	0.04	–62:51:41.2	0.04	2.8	0.11	2.52	0.11	2.369	0.008	24.07	0.11	G	304

Continued on next page

Table B.3 – continued from previous page

sSource Name	RA J2000	σ_{ra} $''$	DEC J2000	σ_{dec} $''$	Peak mJy/bm	σ_{peak} mJy/bm	S mJy	σ_S mJy	ϑ $''$	σ_ϑ $''$	SNR	rms mJy/bm	Type	Tile
G304.1160–0.6568	13:02:03.42	0.01	–63:30:14.9	0.01	10.7	0.12	10.43	0.13	2.469	0.002	71.09	0.13	G	309
G304.1210–0.8932	13:02:11.56	0.09	–63:44:24.2	0.11	1.43	0.11	1.73	0.16	2.745	0.042	12.33	0.12	G	303
G304.1260+0.3054	13:01:48.18	0.02	–62:32:32.3	0.02	8.68	0.12	11.2	0.16	2.839	0.004	59.44	0.14	G	301
G304.1430+1.0155	13:01:42.08	0.08	–61:49:55.7	0.09	1.63	0.11	1.97	0.16	2.752	0.025	15.98	0.1	G	302
G304.1440–0.2345	13:02:08.75	0.12	–63:04:51.9	0.13	0.92	0.12	0.66	0.08	2.117	0.042	7.8	0.11	G	307
G304.1470–1.1354	13:02:31.27	0.05	–63:58:51.4	0.05	8.8	0.37	7.84	0.38	2.36	0.008	23.08	0.37	G	306
G304.1560–0.3326	13:02:17.31	0.09	–63:10:43.0	0.11	1.24	0.12	0.99	0.11	2.236	0.038	9.79	0.13	G	307
G304.1690–0.8254	13:02:35.59	0.15	–63:40:13.2	0.09	1.25	0.1	2.02	0.16	3.182	0.071	11.5	0.1	G	303
G304.1690–0.9930	13:02:39.52	0.14	–63:50:16.1	0.2	1.0	0.11	1.91	0.25	3.46	0.114	10.47	0.1	G	312
G304.1830–0.9096	13:02:45.26	0.09	–63:45:13.8	0.08	1.4	0.11	1.06	0.1	2.175	0.019	11.44	0.11	G	312
G304.1840–0.9917	13:02:47.66	0.06	–63:50:08.9	0.07	1.74	0.12	1.28	0.1	2.146	0.013	13.95	0.11	G	312
G304.2000+0.3364	13:02:25.67	0.12	–62:30:29.9	0.16	1.0	0.12	1.07	0.13	2.586	0.085	7.92	0.13	G	310
G304.2010–0.1003	13:02:35.88	0.05	–62:56:40.4	0.06	5.06	0.15	12.95	0.45	3.999	0.021	31.34	0.17	G	304
G304.2040–0.1094	13:02:37.97	0.01	–62:57:14.1	0.01	32.69	10.79	58.38	3.89	8.835	0.036	103.59	0.32	P	304
G304.2060–0.1187	13:02:39.53	5.5	–62:57:40.0	1.11	2.02	0.09	12.2	5.4	15.497	0.38	9.06	0.22	P	313
G304.2080–0.1190	13:02:40.21	1.34	–62:57:44.2	4.7	1.59	0.05	10.46	3.96	14.839	0.319	10.02	0.16	P	313
G304.2170–1.1407	13:03:09.58	0.15	–63:58:59.5	0.19	2.87	0.41	2.63	0.43	2.395	0.096	7.23	0.4	G	306
G304.2240–0.1078	13:02:48.36	0.06	–62:57:03.6	0.08	2.11	0.13	2.01	0.15	2.441	0.016	16.01	0.12	G	313
G304.2540+1.0552	13:02:37.61	0.06	–61:47:16.0	0.06	2.7	0.15	2.65	0.17	2.48	0.017	16.84	0.16	G	311
G304.2740+0.3180	13:03:04.63	0.01	–62:31:24.0	0.01	19.13	3.72	18.96	3.28	9.193	0.072	79.91	0.24	P	310
G304.3060–0.8913	13:03:51.42	0.05	–63:43:47.6	0.05	2.48	0.12	2.2	0.12	2.351	0.01	20.65	0.12	G	312
G304.3080–0.7963	13:03:50.36	0.15	–63:38:05.7	0.16	0.94	0.12	0.99	0.13	2.572	0.076	7.89	0.12	G	312
G304.3270–0.4541	13:03:51.62	0.02	–63:17:32.0	0.02	7.83	0.13	7.42	0.12	2.434	0.003	52.93	0.13	G	309
G304.3320–0.6792	13:03:59.99	0.05	–63:31:00.5	0.06	2.49	0.12	2.14	0.11	2.318	0.009	21.22	0.11	G	309

Continued on next page

Table B.3 – continued from previous page

sSource Name	RA J2000	σ_{ra} $''$	DEC J2000	σ_{dec} $''$	Peak mJy/bm	σ_{peak} mJy/bm	S mJy	σ_S mJy	ϑ $''$	σ_ϑ $''$	SNR	rms mJy/bm	Type	Tile
G304.3340–0.0691	13:03:45.42	0.1	–62:54:26.3	0.14	1.16	0.13	0.92	0.12	2.228	0.047	8.66	0.14	G	313
G304.3380+0.2399	13:03:39.75	0.17	–62:35:54.6	0.18	0.88	0.11	0.97	0.14	2.62	0.132	7.45	0.12	G	310
G304.3530+0.1973	13:03:48.91	0.03	–62:38:25.1	0.04	3.81	0.12	3.54	0.13	2.411	0.007	27.22	0.14	G	310
G304.3650+0.1087	13:03:57.15	0.08	–62:43:41.6	0.09	1.73	0.12	1.9	0.13	2.617	0.023	14.19	0.11	G	313
G304.3650+0.5381	13:03:46.61	0.07	–62:17:57.5	0.06	2.19	0.12	2.09	0.13	2.438	0.011	18.82	0.1	G	317
G304.3680+0.1148	13:03:58.52	0.04	–62:43:19.0	0.04	3.45	0.12	3.64	0.12	2.569	0.006	32.27	0.1	G	313
G304.3690+0.1507	13:03:58.22	0.08	–62:41:09.8	0.08	1.36	0.12	0.89	0.09	2.026	0.018	10.88	0.12	G	310
G304.3740+0.1581	13:04:00.83	0.1	–62:40:42.2	0.11	1.17	0.11	1.06	0.12	2.375	0.033	10.88	0.11	G	310
G304.3920+0.7769	13:03:54.45	0.06	–62:03:34.0	0.08	1.69	0.12	1.43	0.11	2.304	0.021	13.48	0.12	G	314
G304.4090+0.0180	13:04:22.37	0.04	–62:48:59.8	0.04	3.63	0.12	3.68	0.13	2.519	0.008	26.26	0.14	G	313
G304.4230–1.1312	13:05:01.61	0.09	–63:57:48.9	0.12	3.78	0.3	4.69	0.43	2.782	0.056	11.35	0.34	G	315
G304.4680+1.0616	13:04:26.13	0.11	–61:46:16.7	0.13	1.44	0.17	1.05	0.14	2.132	0.039	8.3	0.17	G	311
G304.5060+0.7922	13:04:52.22	0.13	–62:02:18.6	0.15	1.01	0.13	0.82	0.12	2.249	0.069	7.71	0.14	G	314
G304.5120–0.6759	13:05:36.85	0.01	–63:30:15.2	0.02	51.03	26.37	79.75	8.12	10.057	0.043	89.14	0.57	P	319
G304.5240+0.4874	13:05:09.65	0.05	–62:20:30.8	0.06	2.66	0.13	2.16	0.12	2.253	0.011	18.01	0.14	G	317
G304.5300+1.0033	13:04:59.03	0.07	–61:49:35.2	0.09	2.1	0.12	3.15	0.2	3.067	0.026	17.57	0.11	G	321
G304.5370+1.0068	13:05:01.94	0.21	–61:49:21.8	0.13	1.41	0.04	2.06	1.31	7.026	0.233	11.04	0.13	P	321
G304.5420+0.4071	13:05:21.07	0.05	–62:25:16.2	0.06	2.71	0.14	2.37	0.13	2.336	0.01	19.5	0.13	G	317
G304.5470–1.0667	13:06:07.24	0.38	–63:53:33.7	0.69	2.68	0.11	4.47	1.87	6.436	0.137	13.8	0.19	P	315
G304.5490–1.1552	13:06:11.15	0.11	–63:58:50.2	0.11	11.82	1.44	7.79	1.07	2.029	0.029	8.51	1.33	G	315
G304.5510–1.1557	13:06:12.25	0.13	–63:58:51.8	0.11	11.36	1.4	7.9	1.0	2.085	0.032	8.33	1.27	G	315
G304.5550–0.8365	13:06:04.65	0.06	–63:39:43.7	0.07	2.61	0.13	3.38	0.17	2.846	0.03	15.51	0.17	G	322
G304.5560+0.3275	13:05:31.02	0.02	–62:29:59.5	0.02	15.17	0.13	83.34	0.7	5.859	0.015	69.1	0.23	G	320
G304.5570–0.8347	13:06:05.42	0.07	–63:39:36.7	0.05	2.91	0.13	3.85	0.18	2.878	0.031	16.11	0.19	G	322

Continued on next page

Table B.3 – continued from previous page

sSource Name	RA J2000	σ_{ra} $''$	DEC J2000	σ_{dec} $''$	Peak mJy/bm	σ_{peak} mJy/bm	S mJy	σ_S mJy	ϑ $''$	σ_ϑ $''$	SNR	rms mJy/bm	Type	Tile
G304.5650+0.8402	13:05:21.22	0.03	–61:59:14.6	0.03	6.59	0.16	6.42	0.15	2.467	0.004	37.89	0.16	G	314
G304.5710+0.7160	13:05:27.86	0.01	–62:06:39.8	0.01	30.92	0.24	41.3	0.37	2.889	0.003	78.09	0.38	G	314
G304.5790+0.3850	13:05:41.34	0.1	–62:26:28.2	0.12	1.37	0.13	1.29	0.12	2.427	0.041	10.18	0.13	G	320
G304.5850+0.5813	13:05:38.65	0.46	–62:14:41.9	0.53	0.92	0.02	1.36	1.23	6.471	0.257	7.2	0.13	P	317
G304.5880–0.1382	13:06:01.24	0.04	–62:57:47.0	0.05	3.32	0.15	2.88	0.14	2.327	0.009	18.96	0.16	G	323
G304.5960+0.4796	13:05:47.20	0.02	–62:20:44.8	0.03	6.77	0.15	6.92	0.18	2.528	0.005	35.28	0.19	G	317
G304.6260+0.0372	13:06:15.65	0.07	–62:47:08.7	0.08	1.91	0.12	2.08	0.13	2.614	0.028	13.92	0.13	G	323
G304.6480+0.5140	13:06:13.00	0.1	–62:18:30.7	0.08	1.9	0.12	2.73	0.21	2.997	0.033	15.72	0.12	G	317
G304.6800–0.0198	13:06:45.88	0.13	–62:50:22.3	0.15	1.17	0.14	1.21	0.14	2.539	0.064	8.63	0.13	G	323
G304.6870+0.6567	13:06:28.83	0.09	–62:09:49.7	0.12	1.4	0.14	1.24	0.12	2.354	0.032	9.93	0.12	G	326
G304.6950–0.8200	13:07:19.45	0.01	–63:38:13.6	0.02	65.93	43.9	83.53	13.9	16.177	0.104	100.12	0.66	P	322
G304.7820–0.0264	13:07:39.55	0.01	–62:50:23.5	0.02	16.6	0.2	16.9	0.2	2.522	0.003	66.28	0.24	G	323
G304.7860–1.0418	13:08:16.61	0.01	–63:51:10.0	0.01	153.88	237.68	190.34	17.92	13.518	0.05	163.32	0.94	P	327
G304.7870–0.0094	13:07:41.81	0.06	–62:49:21.2	0.06	3.25	0.14	4.94	0.21	3.083	0.021	18.99	0.16	G	323
G304.8190–0.6108	13:08:19.21	0.03	–63:25:14.2	0.04	5.18	0.16	4.99	0.15	2.454	0.007	26.92	0.19	G	331
G304.8430+0.0844	13:08:07.75	0.2	–62:43:31.4	0.23	0.99	0.14	1.54	0.21	3.121	0.163	7.16	0.14	G	333
G304.8450–0.2159	13:08:19.00	0.1	–63:01:29.8	0.16	1.19	0.14	1.04	0.12	2.337	0.057	8.13	0.14	G	325
G304.8610+0.0513	13:08:18.50	0.09	–62:45:26.2	0.18	1.38	0.14	1.71	0.17	2.778	0.087	9.89	0.14	G	333
G304.8730–1.0572	13:09:04.25	0.12	–63:51:44.8	0.14	1.54	0.2	1.13	0.17	2.138	0.03	9.03	0.16	G	338

References

Achterberg, A. (2000). Particle Acceleration at Astrophysical Shocks. In P.C.H. Martens, S. Tsuruta & M.A. Weber, eds., *Highly Energetic Physical Processes and Mechanisms for Emission from Astrophysical Plasmas*, vol. 195 of *IAU Symposium*, 291. 29

Acker, A., Marcout, J., Ochsenbein, F., Stenholm, B., Tylenda, R. & Schohn, C. (1992). *The Strasbourg-ESO Catalogue of Galactic Planetary Nebulae. Parts I, II.*. 24, 82, 84, 208

Akashi, M. (2009). Shaping Planetary Nebulae by Jets. *Astrophysics and Space Science Proceedings*, **13**, 507–510. 11

Akashi, M. & Soker, N. (2013). Impulsive ejection of gas in bipolar planetary nebulae. *MNRAS*, **436**, 1961–1967. 11

Akras, S., Leal-Ferreira, M.L., Guzman-Ramirez, L. & Ramos-Larios, G. (2019). A machine learning approach for identification and classification of symbiotic stars using 2MASS and WISE. *MNRAS*, **483**, 5077–5104. 140

Ali, A., El-Nawawy, M.S. & Pfleiderer, J. (2000). Statistical and physical study of one-sided planetary nebulae. *Ap&SS*, **271**, 245–258. 13

Ali, A., Sabin, L., Snaid, S. & Basurah, H.M. (2012). Interacting planetary nebulae. I. Classification and orientation. *A&A*, **541**, A98. 13

Aller, L.H. & Minkowski, R. (1956). The Interpretation of the Spectrum of NGC 7027. *ApJ*, **124**, 110. 1

Amiri, N., Vlemmings, W. & van Langevelde, H.J. (2010). The magnetic field of the evolved star W43A. *A&A*, **509**, A26. 12

Anderson, L.D., Bania, T.M., Balser, D.S. & Rood, R.T. (2011). The Green Bank Telescope H II Region Discovery Survey. II. The Source Catalog. *ApJS*, **194**, 32. 106

Anderson, L.D., Zavagno, A., Barlow, M.J., García-Lario, P. & Noriega-Crespo, A. (2012). Distinguishing between HII regions and planetary nebulae with Hi-GAL, WISE, MIPSGAL, and GLIMPSE. *A&A*, **537**, A1. xxi, 23, 37, 42, 70, 71, 72, 98, 139, 142, 209

Anderson, L.D., Armentrout, W.P., Johnstone, B.M., Bania, T.M., Balser, D.S., Wenger, T.V. & Cunningham, V. (2015). Finding Distant Galactic HII Regions. *ApJS*, **221**, 26. 106

Anderson, L.D., Wang, Y., Bihr, S., Rugel, M., Beuther, H., Bigiel, F., Churchwell, E., Glover, S.C.O., Goodman, A.A., Henning, T., Heyer, M., Klessen, R.S., Linz, H., Longmore, S.N., Menten, K.M., Ott, J., Roy, N., Soler, J.D., Stil, J.M. & Urquhart, J.S. (2017). Galactic supernova remnant candidates discovered by THOR. *A&A*, **605**, A58. 91

Andrae, R., Schulze-Hartung, T. & Melchior, P. (2010). Dos and don'ts of reduced chi-squared. *arXiv preprint, arXiv:1012.03754*. 183

Balick, B. (1987). The evolution of planetary nebulae. I - Structures, ionizations, and morphological sequences. *AJ*, **94**, 671–678. 7, 10

Balick, B. & Frank, A. (2002). Shapes and Shaping of Planetary Nebulae. *ARA&A*, **40**, 439–486. 4, 5, 7, 11, 13

Balick, B., Preston, H.L. & Icke, V. (1987). The evolution of planetary nebulae. II - Dynamical evolution of elliptical PNs and collimated outflows. *AJ*, **94**, 1641–1652. 10

Ball, N.M., Brunner, R.J., Myers, A.D. & Tcheng, D. (2006). Robust machine learning applied to astronomical data sets. i. star-galaxy classification of the sloan digital sky survey dr3 using decision trees. *ApJ*, **650**, 497. 216

Banerji, M., Lahav, O., Lintott, C.J., Abdalla, F.B., Schawinski, K., Bamford, S.P., Andreescu, D., Murray, P., Raddick, M.J., Slosar, A., Szalay, A., Thomas, D. & Vand enberg, J. (2010). Galaxy Zoo: reproducing galaxy morphologies via machine learning. *MNRAS*, **406**, 342–353. 216

Barentsen, G., Farnhill, H.J., Drew, J.E., González-Solares, E.A., Greimel, R., Irwin, M.J., Miszalski, B., Ruhland, C., Groot, P., Mampaso, A., Sale, S.E., Henden, A.A., Aungwerojwit, A., Barlow, M.J., Carter, P.J., Corradi, R.L.M., Drake, J.J., Eislöffel, J., Fabregat, J., Gänsicke, B.T., Gentile Fusillo, N.P., Greiss, S., Hales, A.S., Hodgkin, S., Huckvale, L., Irwin, J., King, R., Knigge, C., Kupfer, T., Lagadec, E., Lennon, D.J., Lewis, J.R., Mohr-Smith, M., Morris, R.A.H., Naylor, T., Parker, Q.A., Phillipps, S., Pyrzas, S., Raddi, R., Roelofs, G.H.A., Rodríguez-Gil, P., Sabin, L., Scaringi, S., Steeghs, D., Suso, J., Tata, R., Unruh, Y.C., van Roestel, J., Viironen, K., Vink, J.S., Walton, N.A., Wright, N.J. & Zijlstra, A.A. (2014). The second data release of the INT Photometric Hα Survey of the Northern Galactic Plane (IPHAS DR2). *MNRAS*, **444**, 3230–3257. 41

Barlow, M.J. (1983). Observations of dust in planetary nebulae. In D.R. Flower, ed., *Planetary Nebulae*, vol. 103 of *IAU Symposium*, 105–127. 6

Barlow, M.J. (1993). Planetary Nebulae and Related Objects. In S. Kwok, ed., *Astronomical Infrared Spectroscopy: Future Observational Directions*, vol. 41 of *Astronomical Society of the Pacific Conference Series*, 97. 6

Bear, E. & Soker, N. (2017). Planetary Nebulae that Cannot Be Explained by Binary Systems. *ApJ*, **837**, L10. 16

Becker, R.H., White, R.L., Helfand, D.J. & Zoonematkermani, S. (1994). A 5 GHz VLA survey of the galactic plane. *ApJS*, **91**, 347–387. 106

Benjamin, R.A., Churchwell, E., Babler, B.L., Bania, T.M., Clemens, D.P., Cohen, M., Dickey, J.M., Indebetouw, R., Jackson, J.M., Kobulnicky, H.A., Lazarian, A., Marston, A.P., Mathis, J.S., Meade, M.R., Seager, S., Stolovy, S.R., Watson, C., Whitney, B.A., Wolff, M.J. & Wolfire, M.G. (2003). GLIMPSE. I. An SIRTF Legacy Project to Map the Inner Galaxy. *PASP*, **115**, 953–964. 40

Bietenholz, M.F., Kassim, N., Frail, D.A., Perley, R.A., Erickson, W.C. & Hajian, A.R. (1997). The Radio Spectral Index of the Crab Nebula. *ApJ*, **490**, 291–301. 91

Blackman, E.G., Frank, A., Markiel, J.A., Thomas, J.H. & Van Horn, H.M. (2001). Dynamos in asymptotic-giant-branch stars as the origin of magnetic fields shaping planetary nebulae. *Nature*, **409**, 485–487. 12

Blandford, R.D. & Payne, D.G. (1982). Hydromagnetic flows from accretion discs and the production of radio jets. *MNRAS*, **199**, 883–903. 12

Bloecker, T. (1995). Stellar evolution of low- and intermediate-mass stars. II. Post-AGB evolution. *A&A*, **299**, 755. 1, 5, 172, 173, 174, 175, 176, 182, 190, 205, 215

Bloecker, T. & Schoenberner, D. (1990). On the fading of massive AGB remnants. *A&A*, **240**, L11–L14. 166

Bobylev, V.V. & Bajkova, A.T. (2017). Vertical distribution and kinematics of protoplanetary nebulae in the galaxy. *Astronomy Letters*, **43**, 452–463. 170, 183

Bojičić, I.S., Parker, Q.A., Filipović, M.D. & Frew, D.J. (2011). Radio-continuum detections of Galactic Planetary Nebulae - I. MASH PNe detected in large-scale radio surveys. *MNRAS*, **412**, 223–245. 89

Bond, H.E. (2000). Binarity of Central Stars of Planetary Nebulae. In J.H. Kastner, N. Soker & S. Rappaport, eds., *Asymmetrical Planetary Nebulae II: From Origins to Microstructures*, vol. 199 of *Astronomical Society of the Pacific Conference Series*, 115. 17

Borkowski, K.J., Sarazin, C.L. & Soker, N. (1990). Interaction of planetary nebulae with the interstellar medium. *ApJ*, **360**, 173–183. 12, 13

Bovy, J., Rix, H.W., Schlafly, E.F., Nidever, D.L., Holtzman, J.A., Shetrone, M. & Beers, T.C. (2016). The Stellar Population Structure of the Galactic Disk. *ApJ*, **823**, 30. 182, 183

Bozzetto, L.M., Filipović, M.D., Vukotić, B., Pavlović, M.Z., Urošević, D., Kavanagh, P.J., Arbutina, B., Maggi, P., Sasaki, M., Haberl, F., Crawford, E.J., Roper, Q., Grieve, K. & Points, S.D. (2017). Statistical Analysis of Supernova Remnants in the Large Magellanic Cloud. *ApJS*, **230**, 2. 91

Briggs, D.S. (1995). *High Fidelity Interferometric Imaging: Robust Weighting and NNLS Deconvolution*. Ph.D. thesis. 117

Briggs, D.S., Schwab, F.R. & Sramek, R.A. (1999). Imaging. In G.B. Taylor, C.L. Carilli & R.A. Perley, eds., *Synthesis Imaging in Radio Astronomy II*, vol. 180 of *Astronomical Society of the Pacific Conference Series*, 127. 32

Bujarrabal, V. (2016). Molecular line mapping of (young) planetary nebulae. In *Journal of Physics Conference Series*, vol. 728 of *Journal of Physics Conference Series*, 032010. 19

Bujarrabal, V., Alcolea, J. & Planesas, P. (1992). The molecular emission of young preplanetary nebulae. *A&A*, **257**, 701–714. 8

Bujarrabal, V., Castro-Carrizo, A., Alcolea, J. & Sánchez Contreras, C. (2001). The origin of the high-velocity bipolar outflows in protoplanetary nebulae. In G.L. Pilbratt, J. Cernicharo, A.M. Heras, T. Prusti & R. Harris, eds., *The Promise of the Herschel Space Observatory*, vol. 460 of *ESA Special Publication*, 253. 5, 8, 11

Burke, B. & Graham-Smith, F. (2010). *An Introduction to Radio Astronomy*. Cambridge University Press. 25, 27

Buss, R.H., Jr., Tielens, A.G.G.M., Cohen, M., Werner, M.W., Bregman, J.D. & Witteborn, F.C. (1993). Infrared spectra of transition objects and the composition and evolution of carbon dust. *ApJ*, **415**, 250–257. 6

Cahn, J.H., Kaler, J.B. & Stanghellini, L. (1992). A catalogue of absolute fluxes and distances of planetary nebulae. *A&AS*, **94**, 399–452. 80

Cami, J., Bernard-Salas, J., Peeters, E. & Malek, S.E. (2010). Detection of C_{60} and C_{70} in a Young Planetary Nebula. *Science*, **329**, 1180. 6

Cardelli, J.A., Clayton, G.C. & Mathis, J.S. (1989). The relationship between infrared, optical, and ultraviolet extinction. *ApJ*, **345**, 245–256. 64, 73

Carey, S.J., Noriega-Crespo, A., Mizuno, D.R., Shenoy, S., Paladini, R., Kraemer, K.E., Price, S.D., Flagey, N., Ryan, E., Ingalls, J.G., Kuchar, T.A., Pinheiro Gonçalves, D., Indebetouw, R., Billot, N., Marleau, F.R., Padgett, D.L., Rebull, L.M., Bressert, E., Ali, B., Molinari, S., Martin, P.G., Berriman, G.B., Boulanger, F., Latter, W.B., Miville-Deschenes, M.A., Shipman, R. & Testi, L. (2009). MIPSGAL: A Survey of the Inner Galactic Plane at 24 and 70 μm. *PASP*, **121**, 76–97. 40, 108

Caswell, J.L. (2001). Maser emission from OH at the 6035-MHz transition. *MNRAS*, **326**, 805–820. 106

Cerrigone, L., Hora, J.L., Umana, G. & Trigilio, C. (2009). Spitzer Detection of Polycyclic Aromatic Hydrocarbons and Silicate Features in Post-AGB Stars and Young Planetary Nebulae. *ApJ*, **703**, 585–600. 58

Chabrier, G. (2003). Galactic Stellar and Substellar Initial Mass Function. *PASP*, **115**, 763–795. 174

Chang, C.K., Ko, C.M. & Peng, T.H. (2011). Information on the Milky Way from the Two Micron All Sky Survey Whole Sky Star Count: The Structure Parameters. *ApJ*, **740**, 34. 167

Chen, B.Q., Liu, X.W., Yuan, H.B., Robin, A.C., Huang, Y., Xiang, M.S., Wang, C., Ren, J.J., Tian, Z.J. & Zhang, H.W. (2017). Constraining the Galactic structure parameters with the XSTPS-GAC and SDSS photometric surveys. *MNRAS*, **464**, 2545–2556. 167

Chen, X., Wang, S., Deng, L. & de Grijs, R. (2018). An Extremely Low Mid-infrared Extinction Law toward the Galactic Center and 4% Distance Precision to 55 Classical Cepheids. *ApJ*, **859**, 137. 170

Choi, Y.C., Lee, S.J. & Hyung, S. (2008). Expansion Velocity Investigation of the Elliptical Planetary Nebula NGC 6803. *Journal of Korean Astronomical Society*, **41**, 163–172. 1, 215

Chong, S.N., Kwok, S., Imai, H., Tafoya, D. & Chibueze, J. (2012). Multipolar Planetary Nebulae: Not as Geometrically Diversified as Thought. *ApJ*, **760**, 115. 7

Chu, Y.H., Guerrero, M.A. & Gruendl, R.A. (2000). X-rays from Planetary Nebulae. In J.H. Kastner, N. Soker & S. Rappaport, eds., *Asymmetrical Planetary Nebulae II: From Origins to Microstructures*, vol. 199 of *Astronomical Society of the Pacific Conference Series*, 419. 88

Churchwell, E., Babler, B.L., Meade, M.R., Whitney, B.A., Benjamin, R., Indebetouw, R., Cyganowski, C., Robitaille, T.P., Povich, M., Watson, C. & Bracker, S. (2009). The Spitzer/GLIMPSE Surveys: A New View of the Milky Way. *PASP*, **121**, 213–230. 22, 40, 108

Ciardullo, R. (2006). Planetary Nebulae as Probes of Stellar Populations. In M.J. Barlow & R.H. Méndez, eds., *Planetary Nebulae in our Galaxy and Beyond*, vol. 234 of *IAU Symposium*, 325–332. 2

Ciardullo, R., Bond, H.E., Sipior, M.S., Fullton, L.K., Zhang, C.Y. & Schaefer, K.G. (1999). A HUBBLE SPACE TELESCOPE Survey for Resolved Companions of Planetary Nebula Nuclei. *AJ*, **118**, 488–508. 80

Clark, D.M., García-Díaz, M.T., López, J.A., Steffen, W.G. & Richer, M.G. (2010). SHAPING THE GLOWING EYE PLANETARY NEBULA, NGC 6751. *ApJ*, **722**, 1260–1268. 14

Claussen, M.J., Goss, W.M., Frail, D.A. & Seta, M. (1999). No Water Masers Associated with Supernova Remnants. *AJ*, **117**, 1387–1391. 91

Cohen, M. & Green, A.J. (2001). Extended Galactic emission at l = 312deg: a comparison of mid-infrared and radio continuum (843 MHz) images. *MNRAS*, **325**, 531–544. 37

Cohen, M. & Parker, Q.A. (2003). Refining the UKST Hα Survey's PN Database Using MSX. In S. Kwok, M. Dopita & R. Sutherland, eds., *Planetary Nebulae: Their Evolution and Role in the Universe*, vol. 209 of *IAU Symposium*, 33. 37

Cohen, M., Parker, Q.A., Green, A.J., Murphy, T., Miszalski, B., Frew, D.J., Meade, M.R., Babler, B., Indebetouw, R., Whitney, B.A., Watson, C., Churchwell, E.B. & Watson, D.F. (2007). Spitzer IRAC Observations of Newly Discovered Planetary Nebulae from the Macquarie-AAO-Strasbourg Hα Planetary Nebula Project. *ApJ*, **669**, 343–362. 58, 59

Cohen, M., Parker, Q.A., Green, A.J., Miszalski, B., Frew, D. & Murphy, T. (2011). Multiwavelength diagnostic properties of Galactic planetary nebulae detected by the GLIMPSE-I. *MNRAS*, **413**, 514–542. xxi, 23, 37, 59, 60, 67, 69, 85, 95

Condon, J.J. (1997). Errors in Elliptical Gaussian FITS. *PASP*, **109**, 166–172. 130

Condon, J.J. & Kaplan, D.L. (1998). Planetary Nebulae in the NRAO VLA Sky Survey. *ApJS*, **117**, 361–385. 24

Condon, J.J., Cotton, W.D., Greisen, E.W., Yin, Q.F., Perley, R.A., Taylor, G.B. & Broderick, J.J. (1998). The NRAO VLA Sky Survey. *AJ*, **115**, 1693–1716. 24, 33

Condon, J.J., Kaplan, D.L. & Terzian, Y. (1999). Infrared Planetary Nebulae in the NRAO VLA Sky Survey. *ApJS*, **123**, 219–232. 24, 106

Cooper, H.D.B., Lumsden, S.L., Oudmaijer, R.D., Hoare, M.G., Clarke, A.J., Urquhart, J.S., Mottram, J.C., Moore, T.J.T. & Davies, B. (2013). The RMS survey: near-IR spectroscopy of massive young stellar objects. *MNRAS*, **430**, 1125–1157. 89

Cordes, J.M. & Lazio, T.J.W. (2002). NE2001.I. A New Model for the Galactic Distribution of Free Electrons and its Fluctuations. *arXiv preprint astro-ph/0207156*. 171, 172

Cornwell, T., Braun, R. & Briggs, D.S. (1999). Deconvolution. In G.B. Taylor, C.L. Carilli & R.A. Perley, eds., *Synthesis Imaging in Radio Astronomy II*, vol. 180 of *Astronomical Society of the Pacific Conference Series*, 151. 31, 33

Corradi, R.L.M. & Schwarz, H.E. (1995a). *A&A*, **293**. 169

Corradi, R.L.M. & Schwarz, H.E. (1995b). Morphological populations of planetary nebulae: which progenitors? I. Comparative properties of bipolar nebulae. *A&A*, **293**, 871–888. 7, 8, 170

Corradi, R.L.M., Rodríguez-Flores, E.R., Mampaso, A., Greimel, R., Viironen, K., Drew, J.E., Lennon, D.J., Mikolajewska, J., Sabin, L. & Sokoloski, J.L. (2008). IPHAS and the symbiotic stars. I. Selection method and first discoveries. *A&A*, **480**, 409–419. 62, 63, 64, 67, 69, 140

Corradi, R.L.M., Valentini, M., Munari, U., Drew, J.E., Rodríguez-Flores, E.R., Viironen, K., Greimel, R., Santander-García, M., Sabin, L., Mampaso, A., Parker, Q., DePew, K., Sale, S.E., Unruh, Y.C., Vink, J.S., Rodríguez-Gil, P., Barlow, M.J., Lennon, D.J., Groot, P.J., Giammanco, C., Zijlstra, A.A. & Walton, N.A. (2010).

IPHAS and the symbiotic stars . II. New discoveries and a sample of the most common mimics. *A&A*, **509**, A41. 63, 64, 91

Costa, R.D.D. & Maciel, W.J. (2006). Planetary nebulae as probes for galactic chemical evolution. In M.J. Barlow & R.H. Méndez, eds., *Planetary Nebulae in our Galaxy and Beyond*, vol. 234 of *IAU Symposium*, 243–250. 2

Cox, N.L.J., García-Hernández, D.A., García-Lario, P. & Manchado, A. (2011). Far-infrared Imaging of Post-asymptotic Giant Branch Stars and (Proto)-planetary Nebulae with the AKARI Far-Infrared Surveyor. *AJ*, **141**, 111. 70

Cox, N.L.J., Pilleri, P., Berné, O., Cernicharo, J. & Joblin, C. (2016). Polycyclic aromatic hydrocarbons and molecular hydrogen in oxygen-rich planetary nebulae: the case of NGC 6720. *MNRAS*, **456**, L89–L93. 59

Curtis, H.D. (1918). The Planetary Nebulae. *Publications of Lick Observatory*, **13**, 55–74. 7

Danilovich, T., Bergman, P., Justtanont, K., Lombaert, R., Maercker, M., Olofsson, H., Ramstedt, S. & Royer, P. (2014). Detailed modelling of the circumstellar molecular line emission of the S-type AGB star W Aquilae. *A&A*, **569**, A76. 7

Davies, B., Hoare, M.G., Lumsden, S.L., Hosokawa, T., Oudmaijer, R.D., Urquhart, J.S., Mottram, J.C. & Stead, J. (2011). The Red MSX Source survey: critical tests of accretion models for the formation of massive stars. *MNRAS*, **416**, 972–990. 171, 172

de Gregorio-Monsalvo, I., Gómez, Y., Anglada, G., Cesaroni, R., Miranda, L.F., Gómez, J.F. & Torrelles, J.M. (2004). A Survey for Water Maser Emission toward Planetary Nebulae: New Detection in IRAS 17347-3139. *ApJ*, **601**, 921–929. 11

de Jong, J.T.A., Yanny, B., Rix, H.W., Dolphin, A.E., Martin, N.F. & Beers, T.C. (2010). Mapping the Stellar Structure of the Milky Way Thick Disk and Halo Using SEGUE Photometry. *ApJ*, **714**, 663–674. 167

De Marco, O. (2009). The Origin and Shaping of Planetary Nebulae: Putting the Binary Hypothesis to the Test. *PASP*, **121**, 316–342. 15

De Marco, O., Long, J., Jacoby, G.H., Hillwig, T., Kronberger, M., Howell, S.B., Reindl, N. & Margheim, S. (2015a). Identifying close binary central stars of PN with Kepler. *MNRAS*, **448**, 3587–3602. 16

De Marco, O., Long, J., Jacoby, G.H., Hillwig, T., Kronberger, M., Howell, S.B., Reindl, N. & Margheim, S. (2015b). Identifying close binary central stars of PN with Kepler. *MNRAS*, **448**, 3587–3602. 17

Desmurs, J.F. (2012). In R.S. Booth, W.H.T. Vlemmings & E.M.L. Humphreys, eds., *Cosmic Masers - from OH to H0*, vol. 287 of *IAU Symposium*, 217–224. 11

Dgani, R. & Soker, N. (1998a). Instabilities in Moving Planetary Nebulae. *ApJ*, **495**, 337–345. 13

Dgani, R. & Soker, N. (1998b). Nonthermal Radio Emission from Planetary Nebulae. *ApJ*, **499**, L83–L86. 29

Dijkstra, C. & Speck, A.K. (2006). Shaping Bipolar Planetary Nebulae: How Mass Loss Leads to Waistline Development. *ApJ*, **651**, 288–293. 15

Drew, J.E., Greimel, R., Irwin, M.J., Aungwerojwit, A., Barlow, M.J., Corradi, R.L.M., Drake, J.J., Gänsicke, B.T., Groot, P., Hales, A., Hopewell, E.C., Irwin, J., Knigge, C., Leisy, P., Lennon, D.J., Mampaso, A., Masheder, M.R.W., Matsuura, M., Morales-Rueda, L., Morris, R.A.H., Parker, Q.A., Phillipps, S., Rodriguez-Gil, P., Roelofs, G., Skillen, I., Sokoloski, J.L., Steeghs, D., Unruh, Y.C., Viironen, K., Vink, J.S., Walton, N.A., Witham, A., Wright, N., Zijlstra, A.A. & Zurita, A. (2005). The INT Photometric Hα Survey of the Northern Galactic Plane (IPHAS). *MNRAS*, **362**, 753–776. 20, 41

Drew, J.E., Gonzalez-Solares, E., Greimel, R., Irwin, M.J., Küpcü Yoldas, A., Lewis, J., Barentsen, G., Eislöffel, J., Farnhill, H.J., Martin, W.E., Walsh, J.R., Walton, N.A., Mohr-Smith, M., Raddi, R., Sale, S.E., Wright, N.J., Groot, P., Barlow, M.J., Corradi, R.L.M., Drake, J.J., Fabregat, J., Frew, D.J., Gänsicke, B.T., Knigge, C., Mampaso, A., Morris, R.A.H., Naylor, T., Parker, Q.A., Phillipps, S., Ruhland, C., Steeghs, D., Unruh, Y.C., Vink, J.S., Wesson, R. & Zijlstra, A.A. (2014). The VST Photometric Hα Survey of the Southern Galactic Plane and Bulge (VPHAS+). *MNRAS*, **440**, 2036–2058. 108

Ducati, J.R., Bevilacqua, C.M., Rembold, S.B. & Ribeiro, D. (2001). Intrinsic Colors of Stars in the Near-Infrared. *ApJ*, **558**, 309–322. 61, 63, 139, 143

Durand, S., Acker, A. & Zijlstra, A. (1998). The kinematics of 867 galactic planetary nebulae. *A&AS*, **132**, 13–20. 2

Dyson, J.E. & Redman, M.P. (2000). Mass-loaded Jet Models of FLIERS in Planetary Nebulae. In J.H. Kastner, N. Soker & S. Rappaport, eds., *Asymmetrical Planetary Nebulae II: From Origins to Microstructures*, vol. 199 of *Astronomical Society of the Pacific Conference Series*, 367. 11

Eisenhauer, F., Schödel, R., Genzel, R., Ott, T., Tecza, M., Abuter, R., Eckart, A. & Alexander, T. (2003). A Geometric Determination of the Distance to the Galactic Center. *ApJ*, **597**, L121–L124. 170

Engels, D. (2005). AGB and post-AGB stars . *Mem. Soc. Astron. Italiana*, **76**, 441. 3, 4

Fadely, R., Hogg, D.W. & Willman, B. (2012). Star-galaxy classification in multi-band optical imaging. *ApJ*, **760**, 15. 216

Faulkner, D.J. (1970). The Ejection of Planetary-Nebula Shells. *ApJ*, **162**, 513. 4

Felli, M., Testi, L., Schuller, F. & Omont, A. (2002). Young massive stars in the ISOGAL survey. II. The catalogue of bright YSO candidates. *A&A*, **392**, 971–990. 106

Filipović, M.D., Cohen, M., Reid, W.A., Payne, J.L., Parker, Q.A., Crawford, E.J., Bojičić, I.S., de Horta, A.Y., Hughes, A., Dickel, J. & Stootman, F. (2009a). Radio planetary nebulae in the Magellanic Clouds. *MNRAS*, **399**, 769–777. 23

Filipović, M.D., Cohen, M., Reid, W.A., Payne, J.L., Parker, Q.A., Crawford, E.J., Bojičić, I.S., de Horta, A.Y., Hughes, A., Dickel, J. & Stootman, F. (2009b). Radio planetary nebulae in the Magellanic Clouds. *MNRAS*, **399**, 769–777. 59

Fragkou, V., Bojičić, I., Frew, D. & Parker, Q. (2017). Planetary Nebula Candidates Uncovered with the HASH Research Platform. In X. Liu, L. Stanghellini & A. Karakas, eds., *Planetary Nebulae: Multi-Wavelength Probes of Stellar and Galactic Evolution*, vol. 323 of *IAU Symposium*, 329–330. 94, 137

Frank, A. (1994). The unity and diversity of Planetary or Nebulae radiation-gasdynamics of PNe, 2. *AJ*, **107**, 261–275. 10

Freeman, M., Montez, J., R., Kastner, J.H., Balick, B., Frew, D.J., Jones, D., Miszalski, B., Sahai, R., Blackman, E., Chu, Y.H., De Marco, O., Frank, A., Guerrero, M.A., Lopez, J.A., Zijlstra, A., Bujarrabal, V., Corradi, R.L.M., Nordhaus, J., Parker, Q.A., Sandin, C., Schönberner, D., Soker, N., Sokoloski, J.L., Steffen, M., Toalá, J.A., Ueta, T. & Villaver, E. (2014). The Chandra Planetary Nebula Survey (CHANPLANS). II. X-Ray Emission from Compact Planetary Nebulae. *ApJ*, **794**, 99. 88

Frew, D.J. (2008). *Planetary Nebulae in the Solar Neighbourhood: Statistics, Distance Scale and Luminosity Function*. Ph.D. thesis, Department of Physics, Macquarie University, NSW 2109, Australia. 80, 169, 170

Frew, D.J. & Parker, Q.A. (2010). Planetary Nebulae: Observational Properties, Mimics and Diagnostics. *PASA*, **27**, 129–148. 21, 36

Frew, D.J., Bojičić, I.S., Parker, Q.A., Pierce, M.J., Gunawardhana, M.L.P. & Reid, W.A. (2014). Flux calibration of the AAO/UKST SuperCOSMOS Hα Survey. *MNRAS*, **440**, 1080–1094. 20

Frew, D.J., Parker, Q.A. & Bojičić, I.S. (2016). The Hα surface brightness-radius relation: a robust statistical distance indicator for planetary nebulae. *MNRAS*, **455**, 1459–1488. 80, 98

Froebrich, D., Davis, C.J., Ioannidis, G., Gledhill, T.M., Takami, M., Chrysostomou, A., Drew, J., Eislöffel, J., Gosling, A., Gredel, R., Hatchell, J., Hodapp, K.W., Kumar, M.S.N., Lucas, P.W., Matthews, H., Rawlings, M.G., Smith, M.D., Stecklum, B., Varricatt, W.P., Lee, H.T., Teixeira, P.S., Aspin, C., Khanzadyan, T., Karr, J., Kim, H.J., Koo, B.C., Lee, J.J., Lee, Y.H., Magakian, T.Y., Movsessian, T.A., Nikogossian, E.H., Pyo, T.S. & Stanke, T. (2011). UWISH2 - the UKIRT Widefield Infrared Survey for H_2. *MNRAS*, **413**, 480–492. 23

Froebrich, D., Makin, S.V., Davis, C.J., Gledhill, T.M., Kim, Y., Koo, B.C., Rowles, J., Eislöffel, J., Nicholas, J., Lee, J.J., Williamson, J. & Buckner, A.S.M. (2015). Extended H_2 emission line sources from UWISH2. *MNRAS*, **454**, 2586–2605. 23

Gaensler, B.M. & Slane, P.O. (2006). The Evolution and Structure of Pulsar Wind Nebulae. *ARA&A*, **44**, 17–47. 91

García-Hernández, D.A., Manchado, A., García-Lario, P., Stanghellini, L., Villaver, E., Shaw, R.A., Szczerba, R. & Perea-Calderón, J.V. (2010). Formation of Fullerenes in H-containing Planetary Nebulae. *ApJ*, **724**, L39–L43. 6

Garcia-Lario, P., Manchado, A. & Pottasch, S.R. (1993). Planetary and Proto-Planetary Nebulae in the IRAS Two-Colour Diagram. In R. Weinberger & A. Acker, eds., *Planetary Nebulae*, vol. 155 of *IAU Symposium*, 331. 21

Garcia-Lario, P., Manchado, A., Pych, W. & Pottasch, S.R. (1997). Near infrared photometry of IRAS sources with colours like planetary nebulae. III. *A&AS*, **126**. 21, 60, 61

García-Segura, G., Langer, N., Różyczka, M. & Franco, J. (1999). Shaping Bipolar and Elliptical Planetary Nebulae: Effects of Stellar Rotation, Photoionization Heating, and Magnetic Fields. *ApJ*, **517**, 767–781. 10, 15

García-Segura, G., López, J.A. & Franco, J. (2005). Magnetically Driven Winds from Post-Asymptotic Giant Branch Stars: Solutions for High-Speed Winds and Extreme Collimation. *ApJ*, **618**, 919–925. 11, 12, 15

Gathier, R., Pottasch, S.R. & Pel, J.W. (1986). Distances to planetary nebulae. I - The reddening-distance method. *A&A*, **157**, 171–190. 80

Gesicki, K. & Zijlstra, A.A. (2007). White dwarf masses derived from planetary nebula modelling. *A&A*, **467**, L29–L32. 174, 182

Gesicki, K., Zijlstra, A.A., Hajduk, M. & Szyszka, C. (2014). Accelerated post-AGB evolution, initial-final mass relations, and the star-formation history of the Galactic bulge. *A&A*, **566**, A48. 173, 174, 190

Gesicki, K., Zijlstra, A.A. & Miller Bertolami, M.M. (2018). The mysterious age invariance of the planetary nebula luminosity function bright cut-off. *Nature Astronomy*, **2**, 580–584. 1, 18

Gilmore, G. & Reid, N. (1983). New light on faint stars. III - Galactic structure towards the South Pole and the Galactic thick disc. *MNRAS*, **202**, 1025–1047. 167

Glassgold, A.E. & Huggins, P.J. (1983). Atomic and molecular hydrogen in the circumstellar envelopes of late-type stars. *MNRAS*, **203**, 517–532. 5

Gledhill, T.M., Froebrich, D., Campbell-White, J. & Jones, A.M. (2018). Planetary nebulae in the UWISH2 survey. *MNRAS*, **479**, 3759–3777. 23

Gómez, J.F., Rizzo, J.R., Suárez, O., Miranda, L.F., Guerrero, M.A. & Ramos-Larios, G. (2011). IRAS 18113-2503: The Water Fountain with the Fastest Jet? *ApJ*, **739**, L14. 89

Gómez, J.F., Suárez, O., Bendjoya, P., Rizzo, J.R., Miranda, L.F., Green, J.A., Uscanga, L., García-García, E., Lagadec, E., Guerrero, M.A. & Ramos-Larios, G. (2015). The First "Water Fountain" Collimated Outflow in a Planetary Nebula. *ApJ*, **799**, 186. 29

Gómez, J.F., Niccolini, G., Suárez, O., Miranda, L.F., Rizzo, J.R., Uscanga, L., Green, J.A. & de Gregorio-Monsalvo, I. (2018). ALMA imaging of the nascent planetary nebula IRAS 15103-5754. *MNRAS*, **480**, 4991–5009. 30, 89

Gómez, Y., Tafoya, D., Suárez, O., Gómez, J.F., Miranda, L.F., Anglada, G., Torrelles, J.M. & Vázquez, R. (2012). Imaging the water masers toward the H_2O-PN IRAS 18061-2505. In R.S. Booth, W.H.T. Vlemmings & E.M.L. Humphreys, eds., *Cosmic Masers - from OH to H0*, vol. 287 of *IAU Symposium*, 258–259. 11

Gonidakis, I., Chapman, J.M., Deacon, R.M. & Green, A.J. (2014). Polarization maser observations of late-type stars at OH 1665 and 1667 MHz. *MNRAS*, **443**, 3819–3838. 12, 29

Gonzalez, O.A., Rejkuba, M., Zoccali, M., Valenti, E., Minniti, D., Schultheis, M., Tobar, R. & Chen, B. (2012). Reddening and metallicity maps of the Milky Way bulge from VVV and 2MASS. II. The complete high resolution extinction map and implications for Galactic bulge studies. *A&A*, **543**, A13. 78, 83

González-Solares, E.A., Walton, N.A., Greimel, R., Drew, J.E., Irwin, M.J., Sale, S.E., Andrews, K., Aungwerojwit, A., Barlow, M.J., van den Besselaar, E., Corradi, R.L.M., Gänsicke, B.T., Groot, P.J., Hales, A.S., Hopewell, E.C., Hu, H., Irwin, J., Knigge, C., Lagadec, E., Leisy, P., Lewis, J.R., Mampaso, A., Matsuura, M., Moont, B., Morales-Rueda, L., Morris, R.A.H.,

Naylor, T., Parker, Q.A., Prema, P., Pyrzas, S., Rixon, G.T., Rodríguez-Gil, P., Roelofs, G., Sabin, L., Skillen, I., Suso, J., Tata, R., Viironen, K., Vink, J.S., Witham, A., Wright, N.J., Zijlstra, A.A., Zurita, A., Drake, J., Fabregat, J., Lennon, D.J., Lucas, P.W., Martín, E.L., Phillipps, S., Steeghs, D. & Unruh, Y.C. (2008). Initial data release from the INT Photometric Hα Survey of the Northern Galactic Plane (IPHAS). *MNRAS*, **388**, 89–104. 41, 78

Green, A.J. (1999). The Molonglo Galactic Plane Surveys. In A.R. Taylor, T.L. Landecker & G. Joncas, eds., *New Perspectives on the Interstellar Medium*, vol. 168 of *Astronomical Society of the Pacific Conference Series*, 43. 34, 107

Griffin, M., Ade, P., André, P., Baluteau, J.P., Bock, J., Franceschini, A., Gear, W., Glenn, J., Huang, M., King, K., Lellouch, E., Naylor, D., Oliver, S., Olofsson, G., Page, M., Perez-Fournon, I., Rowan-Robinson, M., Saraceno, P., Sawyer, E., Swinyard, B., Vigroux, L., Wright, G. & Zavagno, A. (2009). The SPIRE Instrument. In L. Pagani & M. Gerin, eds., *EAS Publications Series*, vol. 34 of *EAS Publications Series*, 33–42. 40

Griffiths, M. (2012). *Planetary Nebulae and How to Observe Them*. Astronomers' Observing Guides, Springer. 4

Guerrero, M.A., Villaver, E. & Manchado, A. (1998). On The Kinematics of Multiple-Shell Planetary Nebulae. I. Data and Expansion Velocities. *ApJ*, **507**, 889–908. 13

Guerrero, M.A., Villaver, E., Manchado, A., Garcia-Lario, P. & Prada, F. (2000). H_2 and Brγ Narrowband Imaging of Bipolar Planetary Nebulae. *ApJS*, **127**, 125–140. 23

Gutermuth, R.A. & Heyer, M. (2015). A 24μm Point Source Catalog of the Galactic Plane from Spitzer/MIPSGAL. *AJ*, **149**, 64. 70

Guzman-Ramirez, L., Lagadec, E., Jones, D., Zijlstra, A.A. & Gesicki, K. (2014). PAH formation in O-rich planetary nebulae. *MNRAS*, **441**, 364–377. 58, 59, 70

Habing, H.J. & Olofsson, H. (2004). *Asymptotic Giant Branch Stars*. 2

Hajduk, M., van Hoof, P.A.M., Śniadkowska, K., Krankowski, A., Błaszkiewicz, L., Dąbrowski, B. & Zijlstra, A.A. (2018). Radio observations of planetary nebulae: no evidence for strong radial density gradients. *MNRAS*, **479**, 5657–5677. 191, 214

Hajian, A.R. (2006). Distances to Planetary Nebulae. In M.J. Barlow & R.H. Méndez, eds., *Planetary Nebulae in our Galaxy and Beyond*, vol. 234 of *IAU Symposium*, 41–48. 80

Han, Z., Podsiadlowski, P. & Eggleton, P.P. (1995). The formation of bipolar planetary nebulae and close white dwarf binaries. *MNRAS*, **272**, 800–820. 17

Hancock, P.J., Murphy, T., Gaensler, B.M., Hopkins, A. & Curran, J.R. (2012). Compact continuum source finding for next generation radio surveys. *MNRAS*, **422**, 1812–1824. 123

Hancock, P.J., Trott, C.M. & Hurley-Walker, N. (2018). Source Finding in the Era of the SKA (Precursors): Aegean 2.0. *PASA*, **35**, e011. 123

Hands, A.D.P., Warwick, R.S., Watson, M.G. & Helfand , D.J. (2004). X-ray source populations in the Galactic plane. *MNRAS*, **351**, 31–56. 88

Harris, H.C., Dahn, C.C., Canzian, B., Guetter, H.H., Leggett, S.K., Levine, S.E., Luginbuhl, C.B., Monet, A.K.B., Monet, D.G., Pier, J.R., Stone, R.C., Tilleman, T., Vrba, F.J. & Walker, R.L. (2007). Trigonometric Parallaxes of Central Stars of Planetary Nebulae. *AJ*, **133**, 631–638. 80

Haverkorn, M., Gaensler, B.M., McClure-Griffiths, N.M., Dickey, J.M. & Green, A.J. (2006). The Southern Galactic Plane Survey: Polarized Radio Continuum Observations and Analysis. *ApJS*, **167**, 230–238. 107

Hayden, M.R., Recio-Blanco, A., de Laverny, P., Mikolaitis, S. & Worley, C.C. (2017). The AMBRE project: The thick thin disk and thin thick disk of the Milky Way. *A&A*, **608**, L1. 169

Helfand, D.J., Becker, R.H., White, R.L., Fallon, A. & Tuttle, S. (2006). MAGPIS: A Multi-Array Galactic Plane Imaging Survey. *AJ*, **131**, 2525–2537. 39

Herwig, F. (2005). Evolution of Asymptotic Giant Branch Stars. *ARA&A*, **43**, 435–479. 2

Hewett, P.C., Warren, S.J., Leggett, S.K. & Hodgkin, S.T. (2006). The UKIRT Infrared Deep Sky Survey ZY JHK photometric system: passbands and synthetic colours. *MNRAS*, **367**, 454–468. 61

Hoare, M., Burton, M., Fender, R., Urquhart, J., Churchwell, E., Lumsden, S., Kurtz, S., Purcell, C., Molinari, S., Wieringa, M., Cotton, B. & Diamond, P. (2009). The Co-Ordinated Radio 'N' Infrared Survey for High-mass star formation - CORNISH-South. ATNF Proposal. 35

Hoare, M.G. (1989). The dust content of planetary nebulae with neutral halos. In S. Torres-Peimbert, ed., *Planetary Nebulae*, vol. 131 of *IAU Symposium*, 202. 70

Hoare, M.G. (1990). The dust content of two carbon-rich planetary nebulae. *MNRAS*, **244**, 193–206. 68

Hoare, M.G. (2002). High-Resolution Radio Observations of Massive Young Stellar Objects. In P. Crowther, ed., *Hot Star Workshop III: The Earliest Phases of Massive Star Birth*, vol. 267 of *Astronomical Society of the Pacific Conference Series*, 137. 23, 94

Hoare, M.G., Roche, P.F. & Clegg, R.E.S. (1992). Millimetre and submillimetre continuum observations of planetary nebulae. *MNRAS*, **258**, 257–269. 70

Hoare, M.G., Drew, J.E., Muxlow, T.B. & Davis, R.J. (1994). Mapping the radio emission from massive young stellar objects. *ApJ*, **421**, L51–L54. 23, 94

Hoare, M.G., Purcell, C.R., Churchwell, E.B., Diamond, P., Cotton, W.D., Chandler, C.J., Smethurst, S., Kurtz, S.E., Mundy, L.G., Dougherty, S.M., Fender, R.P., Fuller, G.A., Jackson, J.M., Garrington, S.T., Gledhill, T.R., Goldsmith, P.F., Lumsden, S.L., Martí, J., Moore, T.J.T., Muxlow, T.W.B., Oudmaijer, R.D., Pand ian, J.D., Paredes, J.M., Shepherd, D.S., Spencer, R.E., Thompson, M.A., Umana, G., Urquhart, J.S. & Zijlstra, A.A. (2012). The Coordinated Radio and Infrared Survey for High-Mass Star Formation (The CORNISH Survey). I. Survey Design. *PASP*, **124**, 939–955. 37, 106, 107, 137

Högbom, J.A. (1974). Aperture Synthesis with a Non-Regular Distribution of Interferometer Baselines. *A&AS*, **15**, 417. 33

Homan, D.C. & Lister, M.L. (2006). MOJAVE: Monitoring of Jets in Active Galactic Nuclei with VLBA Experiments. II. First-Epoch 15 GHz Circular Polarization Results. *AJ*, **131**, 1262–1279. 116

Hoogzaad, S.N., Molster, F.J., Dominik, C., Waters, L.B.F.M., Barlow, M.J. & de Koter, A. (2002). The circumstellar dust shell of the post-AGB star HD 161796. *A&A*, **389**, 547–555. 4

Hora, J.L., Latter, W.B., Allen, L.E., Marengo, M., Deutsch, L.K. & Pipher, J.L. (2004). Infrared Array Camera (IRAC) Observations of Planetary Nebulae. *ApJS*, **154**, 296–301. 67, 69, 140

Hrivnak, B.J., van Winckel, H., van de Steene, G., Bohlender, D., Sperauskas, J. & Lu, W. (2017). Where are the binaries in proto-planetary nebulae? Results of a long-term radial velocity study. In X. Liu, L. Stanghellini & A. Karakas, eds., *Planetary Nebulae: Multi-Wavelength Probes of Stellar and Galactic Evolution*, vol. 323 of *IAU Symposium*, 218–222. 17

Hsia, C.H. & Kwok, S. (2012). A sample of new planetary nebulae in the IPHAS and DSH catalogue. In *IAU Symposium*, vol. 283 of *IAU Symposium*, 388–389. 23

Huggins, P.J., Bachiller, R., Cox, P. & Forveille, T. (1996). The molecular envelopes of planetary nebulae. *A&A*, **315**, 284–302. 187

Hughes, M.P. (1967). Flux Densities of Planetary Nebulae at 5 GHz. *ApJ*, **149**, 377. 33

Iben, I., Jr. (1995). Planetary nebulae and their central stars - origin and evolution. *Phys. Rep.*, **250**, 2–94. 2

Iben, I., Jr. & Livio, M. (1993). Common envelopes in binary star evolution. *PASP*, **105**, 1373–1406. 16

Iben, I., Jr. & Renzini, A. (1983). Asymptotic giant branch evolution and beyond. *ARA&A*, **21**, 271–342. 4

Icke, V., Preston, H.L. & Balick, B. (1989). The evolution of planetary nebulae. III - Position-velocity images of butterfly-type nebulae. *AJ*, **97**, 462–475. 10

Icke, V., Balick, B. & Frank, A. (1992). The hydrodynamics of aspherical planetary nebulae. II - Numerical modelling of the early evolution. *A&A*, **253**, 224–243. 10

Imai, H., Sahai, R. & Morris, M. (2007). *ApJ*, **669**, 424–434. 11

Indebetouw, R., Mathis, J.S., Babler, B.L., Meade, M.R., Watson, C., Whitney, B.A., Wolff, M.J., Wolfire, M.G., Cohen, M., Bania, T.M., Benjamin, R.A., Clemens, D.P., Dickey, J.M., Jackson, J.M., Kobulnicky, H.A., Marston, A.P., Mercer, E.P., Stauffer, J.R., Stolovy, S.R. & Churchwell, E. (2005). The Wavelength Dependence of Interstellar Extinction from 1.25 to 8.0 μm Using GLIMPSE Data. *ApJ*, **619**, 931–938. 69, 140

Isaacman, R. (1979). The interaction of high-velocity planetary nebulae with the interstellar medium. *A&A*, **77**, 327–331. 12

Isaacman, R. (1984). Molecular hydrogen in planetary nebulae. *A&A*, **130**, 151–156. 19

Ivanova, N., Justham, S., Chen, X., De Marco, O., Fryer, C.L., Gaburov, E., Ge, H., Glebbeek, E., Han, Z., Li, X.D., Lu, G., Marsh, T., Podsiadlowski, P., Potter, A., Soker, N., Taam, R., Tauris, T.M., van den Heuvel, E.P.J. & Webbink, R.F. (2013). Common envelope evolution: where we stand and how we can move forward. *A&ARv*, **21**, 59. 16

Ivison, R.J., Bode, M.F., Roberts, J.A., Meaburn, J., Davis, R.J., Nelson, R.F. & Spencer, R.E. (1991). A multi-frequency study of symbiotic stars. I - Near-simultaneous optical and radio observations. *MNRAS*, **249**, 374–384. 91

Jacob, R., Schönberner, D. & Steffen, M. (2013). The evolution of planetary nebulae. VIII. True expansion rates and visibility times. *A&A*, **558**, A78. 1, 4, 182, 215

Jones, D. & Boffin, H.M.J. (2017). Binary stars as the key to understanding planetary nebulae. *Nature Astronomy*, **1**, 0117. 15

Jones, T.J., Hyland, A.R., Wood, P.R. & Gatley, I. (1983). OH/IR massers. IV - Evolution, pulsation, and nature of the sources. *ApJ*, **273**, 669–680. 4

Jurić, M., Ivezić, Ž., Brooks, A., Lupton, R.H., Schlegel, D., Finkbeiner, D., Padmanabhan, N., Bond, N., Sesar, B., Rockosi, C.M., Knapp, G.R., Gunn, J.E., Sumi, T., Schneider, D.P., Barentine, J.C., Brewington, H.J., Brinkmann, J., Fukugita, M., Harvanek, M., Kleinman, S.J., Krzesinski, J., Long, D., Neilsen, E.H., Jr., Nitta, A., Snedden, S.A. & York, D.G. (2008). The Milky Way Tomography with SDSS. I. Stellar Number Density Distribution. *ApJ*, **673**, 864–914. 167

Kahn, F.D. (1989). Models of planetary nebulae: generalisation of the multiple winds model. In S. Torres-Peimbert, ed., *Planetary Nebulae*, vol. 131 of *IAU Symposium*, 411–424. 214

Kahn, F.D. & West, K.A. (1985). Shapes of planetary nebulae. *MNRAS*, **212**, 837–850. 10

Kalcheva, I.E., Hoare, M.G., Urquhart, J.S., Kurtz, S., Lumsden, S.L., Purcell, C.R. & Zijlstra, A.A. (2018). The coordinated radio and infrared survey for high-mass star formation. III. A catalogue of northern ultra-compact H II regions. *A&A*, **615**, A103. 67, 69, 75, 212

Kaler, J.B. (1983). A photometric survey of compact and selected planetary nebulae. *ApJ*, **264**, 594–598. 79

Kamdar, H.M., Turk, M.J. & Brunner, R.J. (2015). Machine learning and cosmological simulations–i. semi-analytical models. *MNRAS*, **455**, 642–658. 216

Kanarek, G., Shara, M., Faherty, J., Zurek, D. & Moffat, A. (2015). A near-infrared survey of the inner Galactic plane for Wolf-Rayet stars - III. New methods: faintest WR stars. *MNRAS*, **452**, 2858–2878. 106

Karakas, A. & Lattanzio, J.C. (2007). Stellar Models and Yields of Asymptotic Giant Branch Stars. *PASA*, **24**, 103–117. 4

Kastner, J.H. (2007). X-ray Emission from Planetary Nebulae and their Central Stars: a Status Report. In *Asymmetrical Planetary Nebulae IV*, 5. 88

Kastner, J.H., Weintraub, D.A., Gatley, I., Merrill, K.M. & Probst, R.G. (1996). H_2 Emission from Planetary Nebulae: Signpost of Bipolar Structure. *ApJ*, **462**, 777. 23

Kastner, J.H., Montez, R., Jr., Balick, B. & De Marco, O. (2008). Serendipitous Chandra X-Ray Detection of a Hot Bubble within the Planetary Nebula NGC 5315. *ApJ*, **672**, 957–961. 88

Kennicutt, R.C., Jr. (1998). The Global Schmidt Law in Star-forming Galaxies. *ApJ*, **498**, 541–552. 171

Kim, E.J. & Brunner, R.J. (2017). Star-galaxy classification using deep convolutional neural networks. *MNRAS*, **464**, 4463–4475. 217

Kim, J., Cho, S.H. & Yoon, D.H. (2016). Monitoring Observatinos of H2O and SiO Masers Toward Post-AGB Stars. *Journal of Korean Astronomical Society*, **49**, 261–288. 5

Kimura, R.K., Gruenwald, R. & Aleman, I. (2012). Molecular chemistry and the missing mass problem in planetary nebulae. *A&A*, **541**, A112. 187

Kippenhahn, R. & Weigert, A. (1994). *Stellar Structure and Evolution*. 3

Kistiakowsky, V. & Helfand, D.J. (1995). The Identification of Galactic Plane Radio Sources: Distant Planetary Nebulae at |b|< 2 Degrees. *AJ*, **110**, 2225. 106

Kohoutek, L. (2001). VizieR Online Data Catalog: Catalogue of Galactic Planetary Nebulae (Kohoutek, 2001). *VizieR Online Data Catalog*, **4024**. 82, 84, 106

Kroupa, P. (2001). On the variation of the initial mass function. *MNRAS*, **322**, 231–246. xviii, 170, 171, 174

Kwok, S. (1975). Radiation pressure on grains as a mechanism for mass loss in red giants. *ApJ*, **198**, 583–591. 4

Kwok, S. (1982). From red giants to planetary nebulae. *ApJ*, **258**, 280–288. 70

Kwok, S. (1985). High-resolution radio observations of compact planetary nebulae. *AJ*, **90**, 49–58. 33, 53

Kwok, S. (1993a). Proto-planetary nebulae. *ARA&A*, **31**, 63–92. 5, 6

Kwok, S. (1993b). Test of planetary nebula evolution models by distance-independent parameters. *Acta Astron.*, **43**, 359–370. 88, 166

Kwok, S. (1994). Planetary nebulae: A modern view. *PASP*, **106**, 344–355. 10, 166, 187

Kwok, S. (2000). A Retrospective: Interacting Winds Theory, Two Decades Later. In J.H. Kastner, N. Soker & S. Rappaport, eds., *Asymmetrical Planetary Nebulae II: From Origins to Microstructures*, vol. 199 of *Astronomical Society of the Pacific Conference Series*, 9. 4, 5, 7, 11

Kwok, S. (2003). Symbiotic Stars and Planetary Nebulae. In R.L.M. Corradi, J. Mikolajewska & T.J. Mahoney, eds., *Symbiotic Stars Probing Stellar Evolution*, vol. 303 of *Astronomical Society of the Pacific Conference Series*, 428. 21

Kwok, S. (2007). The Morphology and 3-D Structures of the Ionized, Molecular, and Dust Components of Planetary Nebulae. In *Asymmetrical Planetary Nebulae IV*. 36

Kwok, S. (2011). Historical overview of planetary nebulae research. In *Planetary Nebulae: An Eye to the Future*, vol. 7 of *Proceedings of the International Astronomical Union*, 1–8. 4

Kwok, S. (2012). Historical overview of planetary nebulae research. In *IAU Symposium*, vol. 283 of *IAU Symposium*, 1–8. 7

Kwok, S., Purton, C.R. & Fitzgerald, P.M. (1978). On the origin of planetary nebulae. *ApJ*, **219**, L125–L127. 4, 8

Kwok, S., Hrivnak, B.J. & Milone, E.F. (1986). Ground-based and IRAS observations of compact planetary nebulae. *ApJ*, **303**, 451–464. 42, 68

Kwok, S., Zhang, Y., Koning, N., Huang, H.H. & Churchwell, E. (2008). Planetary Nebulae Detected in the Spitzer Space Telescope GLIMPSE Legacy Survey. *ApJS*, **174**, 426–454. 22

Kwon, Y.J. & Suh, K.W. (2012). Properties of OH, SiO, and H2O Maser Emission in O-Rich AGB Stars. *Journal of Korean Astronomical Society*, **45**, 139–146. 6

Lacy, M., Baum, S.A., Chandler, C.J., Chatterjee, S., Murphy, E.J., Myers, S.T. & VLASS Survey Science Group (2016). The VLA Sky Survey (VLASS): Description and Science Goals. In *American Astronomical Society Meeting Abstracts #227*, vol. 227 of *American Astronomical Society Meeting Abstracts*, 324.09. 212

Lagadec, E., Verhoelst, T., Mékarnia, D., Suáeez, O., Zijlstra, A.A., Bendjoya, P., Szczerba, R., Chesneau, O., van Winckel, H., Barlow, M.J., Matsuura, M., Bowey, J.E., Lorenz-Martins, S. & Gledhill, T. (2011). A mid-infrared imaging catalogue of post-asymptotic giant branch stars. *MNRAS*, **417**, 32–92. 5

Lakićević, M., van Loon, J.T., Meixner, M., Gordon, K., Bot, C., Roman-Duval, J., Babler, B., Bolatto, A., Engelbracht, C., Filipović, M., Hony, S., Indebetouw, R., Misselt, K., Montiel, E., Okumura, K., Panuzzo, P., Patat, F., Sauvage, M., Seale, J., Sonneborn, G., Temim, T., Urošević, D. & Zanardo, G. (2015). The Influence of Supernova Remnants on the Interstellar Medium in the Large Magellanic Cloud Seen at 20-600 μm Wavelengths. *ApJ*, **799**, 50. 91

Lattanzio, J.C. & Wood, P.R. (2004). *Evolution, Nucleosynthesis, and Pulsation of AGB Stars*, 23–104. 6

Lawrence, A., Warren, S.J., Almaini, O., Edge, A.C., Hambly, N.C., Jameson, R.F., Lucas, P., Casali, M., Adamson, A., Dye, S., Emerson, J.P., Foucaud, S., Hewett, P., Hirst, P., Hodgkin, S.T., Irwin, M.J., Lodieu, N., McMahon, R.G., Simpson, C., Smail, I., Mortlock, D. & Folger, M. (2007). The UKIRT Infrared Deep Sky Survey (UKIDSS). *MNRAS*, **379**, 1599–1617. 22

Lawrence, H. (1991). *Atoms, Stars and Nebulae*. Cambridge Univeristy Press. 25

Leal Ferreira, M.L. (2014). *Magnetic Fields And The Formation Of Aspherical Planetary Nebulae*. Ph.D. thesis, Argelander Institut für Astronomie, University of Bonn, Auf dem Hügel 71, 53121 Bonn, Germany. 11

Leto, P., Umana, G., Trigilio, C., Buemi, C.S., Dolei, S., Manzitto, P., Cerrigone, L. & Siringo, C. (2009). 7 mm continuum observations of ultra compact HII regions. *A&A*, **507**, 1467–1473. 89

Lombaert, R., de Vries, B.L., de Koter, A., Decin, L., Min, M., Smolders, K., Mutschke, H. & Waters, L.B.F.M. (2012). Observational evidence for composite grains in an AGB outflow. MgS in the extreme carbon star LL Pegasi. *A&A*, **544**, L18. 6

Lombaert, R., Decin, L., de Koter, A., Blommaert, J.A.D.L., Royer, P., De Beck, E., de Vries, B.L., Khouri, T. & Min, M. (2013). H_2O vapor excitation in dusty AGB envelopes. A PACS view of OH 127.8+0.0. *A&A*, **554**, A142. 6

López, J.A., Escalante, K. & Riesgo-Tirado, H. (2004). Links between Symbiotic and Planetary Nebulae. In G. Tovmassian & E. Sion, eds., *Revista Mexicana de Astronomia y Astrofisica Conference Series*, vol. 20 of *Revista Mexicana de Astronomia y Astrofisica, vol. 27*, 226–227. 91

Lucas, P.W., Hoare, M.G., Longmore, A., Schröder, A.C., Davis, C.J., Adamson, A., Band yopadhyay, R.M., de Grijs, R., Smith, M., Gosling, A., Mitchison, S., Gáspár, A., Coe, M., Tamura, M., Parker, Q., Irwin, M., Hambly, N., Bryant, J., Collins, R.S., Cross, N., Evans, D.W., Gonzalez-Solares, E., Hodgkin, S., Lewis, J., Read, M., Riello, M., Sutorius, E.T.W., Lawrence, A., Drew, J.E., Dye, S. & Thompson, M.A. (2008). The UKIDSS Galactic Plane Survey. *MNRAS*, **391**, 136–163. 40

Lumsden, S.L., Hoare, M.G., Urquhart, J.S., Oudmaijer, R.D., Davies, B., Mottram, J.C., Cooper, H.D.B. & Moore, T.J.T. (2013). The Red MSX Source Survey: The Massive Young Stellar Population of Our Galaxy. *ApJS*, **208**, 11. 42, 94, 137, 138, 140, 141, 142

Lynds, C.R. (1961). Observations of Planetary Nebulae At Centimeter Wavelengths. In *Publications of The National Radio Astronomy Observatory*, vol. 1 of *5*, 58–98. 33

Maciel, W.J. & Costa, R.D.D. (2003). PN and Galactic Chemical Evolution (invited review). In S. Kwok, M. Dopita & R. Sutherland, eds., *Planetary Nebulae: Their Evolution and Role in the Universe*, vol. 209 of *IAU Symposium*, 551. 6

Maciel, W.J. & Dutra, C.M. (1992). Kinematics of disk planetary nebulae. *A&A*, **262**, 271–280. 169

Maciel, W.J. & Lago, L.G. (2005). A New Determination of the Rotation Curve from Galactic Disk Planetary Nebulae. *Rev. Mex. Astron. Astrofis.*, **41**, 383–388. 2

Maercker, M., Olofsson, H., Eriksson, K., Gustafsson, B. & Schöier, F.L. (2010). The detached dust and gas shells around the carbon star U Antliae. *A&A*, **511**, A37. 4, 5

Malkin, Z. (2013). Statistical analysis of the determinations of the Sun's Galactocentric distance. In R. de Grijs, ed., *Advancing the Physics of Cosmic Distances*, vol. 289 of *IAU Symposium*, 406–409. 170

Mampaso, A., Corradi, R.L.M., Viironen, K., Leisy, P., Greimel, R., Drew, J.E., Barlow, M.J., Frew, D.J., Irwin, J., Morris, R.A.H., Parker, Q.A., Phillipps, S., Rodríguez-Flores, E.R. & Zijlstra, A.A. (2006). The "Príncipes de Asturias" nebula: a new quadrupolar planetary nebula from the IPHAS survey. *A&A*, **458**, 203–212. 41

Manchado, A. (2003). The Correlation of PN Morphology and Parameters (invited review). In S. Kwok, M. Dopita & R. Sutherland, eds., *Planetary Nebulae: Their Evolution and Role in the Universe*, vol. 209 of *IAU Symposium*, 431. 8

Manchado, A., Stanghellini, L. & Guerrero, M.A. (1996). Quadrupolar Planetary Nebulae: A New Morphological Class. *ApJ*, **466**, L95. 7

Manchado, A., Villaver, E., Stanghellini, L. & Guerrero, M.A. (2000). The Morphological and Structural Classification of Planetary Nebulae. In J.H. Kastner, N. Soker & S. Rappaport, eds., *Asymmetrical Planetary*

Nebulae II: From Origins to Microstructures, vol. 199 of *Astronomical Society of the Pacific Conference Series*, 17. 170

Manchado, A., García-Hernández, D.A., Villaver, E. & de Massas, J.G. (2012). Morphological classification of post-AGB stars. In *IAU Symposium*, vol. 283 of *IAU Symposium*, 83–86. 8

Marigo, P., Girardi, L., Groenewegen, M.A.T. & Weiss, A. (2001). Evolution of planetary nebulae. I. An improved synthetic model. *A&A*, **378**, 958–985. 166, 206, 214, 215

Marquez-Lugo, R.A., Guerrero, M.A., Ramos-Larios, G. & Miranda, L.F. (2015). The excitation mechanism of H_2 in bipolar planetary nebulae. *MNRAS*, **453**, 1888–1897. 62

Marten, H. & Schoenberner, D. (1991). On the dynamical evolution of planetary nebulae. *A&A*, **248**, 590–598. 214, 215

Massardi, M., Ekers, R.D., Murphy, T., Mahony, E., Hancock, P.J., Chhetri, R., de Zotti, G., Sadler, E.M., Burke-Spolaor, S., Calabretta, M., Edwards, P.G., Ekers, J.A., Jackson, C.A., Kesteven, M.J., Newton-McGee, K., Phillips, C., Ricci, R., Roberts, P., Sault, R.J., Staveley-Smith, L., Subrahmanyan, R., Walker, M.A. & Wilson, W.E. (2011). The Australia Telescope 20 GHz (AT20G) Survey: analysis of the extragalactic source sample. *MNRAS*, **412**, 318–330. 107

Mastrodemos, N. & Morris, M. (1998). Bipolar Preplanetary Nebulae: Hydrodynamics of Dusty Winds in Binary Systems. I. Formation of Accretion Disks. *ApJ*, **497**, 303–329. 16

Matsuura, M., Zijlstra, A.A., Molster, F.J., Hony, S., Waters, L.B.F.M., Kemper, F., Bowey, J.E., Chihara, H., Koike, C. & Keller, L.P. (2004). Polycyclic Aromatic Hydrocarbons and Crystalline Silicates in the Bipolar Post-Asymptotic Giant Branch Star IRAS 16279-4757. *ApJ*, **604**, 791–799. 59

Matsuura, M., Zijlstra, A.A., Gray, M.D., Molster, F.J. & Waters, L.B.F.M. (2005). The symmetric dust shell and the central star of the bipolar planetary nebula NGC6537. *MNRAS*, **363**, 628–640. 79

Matsuura, M., Indebetouw, R., Kamenetzky, J., McCray, R., Zanardo, G., Barlow, M.J. & Dwek, E. (2015). ALMA Observations of Supernova 1987A. In D. Iono, K. Tatematsu, A. Wootten & L. Testi, eds., *Revolution in Astronomy with ALMA: The Third Year*, vol. 499 of *Astronomical Society of the Pacific Conference Series*, 323. 91

Mauas, P.J.D., Cacciari, C. & Pasquini, L. (2006). Modelling chromospheric line profiles in NGC 2808: evidence of mass loss from RGB stars. *A&A*, **454**, 609–615. 2

McClure-Griffiths, N.M., Dickey, J.M., Gaensler, B.M., Green, A.J., Haverkorn, M. & Strasser, S. (2005). The Southern Galactic Plane Survey: H I Observations and Analysis. *ApJS*, **158**, 178–187. 107

Medina, S.N.X., Urquhart, J.S., Dzib, S.A., Brunthaler, A., Cotton, B., Menten, K.M., Wyrowski, F., Beuther, H., Billington, S.J., Carrasco-Gonzalez, C., Csengeri, T., Gong, Y., Hofner, P., Nguyen, H., Ortiz-León, G.N., Ott, J., Pandian, J.D., Roy, N., Sarkar, E., Wang, Y. & Winkel, B. (2019). GLOSTAR – Radio Source Catalog I: $28^\circ < l < 36^\circ$ and $|b| < 1^\circ$. *arXiv e-prints*, arXiv:1905.09281. 213

Mellema, G. (1995). Radiation gasdynamics of planetary nebulae - VI. The evolution of aspherical planetary nebulae. *MNRAS*, **277**, 173–192. 10

Mellema, G. & Frank, A. (1995). Radiation gasdynamics of planetary nebulae - V. Hot bubble and slow wind dynamics. *MNRAS*, **273**, 401–410. 10, 215

Mendez, R.H., Kudritzki, R.P. & Herrero, A. (1992). On central star luminosities and optical thicknesses in planetary nebulae. *A&A*, **260**, 329–340. 187

Mezger, P.G. & Henderson, A.P. (1967). Galactic H II Regions. I. Observations of Their Continuum Radiation at the Frequency 5 GHz. *ApJ*, **147**, 471. 27

Mikołajewska, J. & Ivison, R.J. (2001). On the radio spectrum of CI Cygni: a test of popular models for symbiotic stars. *MNRAS*, **324**, 1023–1028. 91

Miller Bertolami, M.M. (2016). New models for the evolution of post-asymptotic giant branch stars and central stars of planetary nebulae. *A&A*, **588**, A25. xviii, 173, 174, 175, 176, 177, 178, 181, 182, 183, 184, 185, 186, 187, 188, 189, 192, 193, 196, 197, 198, 199, 200, 201, 202, 203, 204, 205, 206, 210, 211

Minniti, D., Lucas, P.W., Emerson, J.P., Saito, R.K., Hempel, M., Pietrukowicz, P., Ahumada, A.V., Alonso, M.V., Alonso-Garcia, J., Arias, J.I., Bandyopadhyay, R.M., Barbá, R.H., Barbuy, B., Bedin, L.R., Bica, E., Borissova, J., Bronfman, L., Carraro, G., Catelan, M., Clariá, J.J., Cross, N., de Grijs, R., Dékány, I., Drew, J.E., Fariña, C., Feinstein, C., Fernández Lajús, E., Gamen, R.C., Geisler, D., Gieren, W., Goldman, B., Gonzalez, O.A., Gunthardt, G., Gurovich, S., Hambly, N.C., Irwin, M.J., Ivanov, V.D., Jordán, A., Kerins, E., Kinemuchi, K., Kurtev, R., López-Corredoira, M., Maccarone, T., Masetti, N., Merlo, D., Messineo, M., Mirabel, I.F., Monaco, L., Morelli, L., Padilla, N., Palma, T., Parisi, M.C., Pignata, G., Rejkuba, M., Roman-Lopes, A., Sale, S.E., Schreiber, M.R., Schröder, A.C., Smith, M., , L.S., Jr., Soto, M., Tamura, M., Tappert, C., Thompson, M.A., Toledo, I., Zoccali, M. & Pietrzynski, G. (2010). VISTA Variables in the Via Lactea (VVV): The public ESO near-IR variability survey of the Milky Way. *New Astron.*, **15**, 433–443. 22

Minniti, D., Clariá, J.J., Saito, R.K., Hempel, M., Lucas, P.W., Rejkuba, M., Toledo, I., Gonzalez, O.A., Alonso-García, J., Irwin, M.J., Gonzalez-Solares, E., Cross, N., Ivanov, V.D., Soto, M., Dékány, I., Angeloni, R., Catelan, M., Amôres, E.B., Gurovich, S.,

Emerson, J.P., Lewis, J., Hodgkin, S., Pietrukowicz, P., Zoccali, M., Sale, S.E., Barbá, R., Barbuy, B., Beamin, J.C., Helminiak, K., Borissova, J., Folkes, S.L., Gamen, R.C., Geisler, D., Mauro, F., Chené, A.N., Alonso, M.V., Gunthardt, G., Hanson, M., Kerins, E., Kurtev, R., Majaess, D., Martín, E., Masetti, N., Mirabel, I.F., Monaco, L., Moni Bidin, C., Padilla, N., Rojas, A., Pietrzynski, G., Saviane, I., Valenti, E., Weidmann, W., López-Corredoira, M., Ahumada, A.V., Aigrain, S., Arias, J.I., Bica, E., Bandyopadhyay, R.M., Baume, G., Bedin, L.R., Bonatto, C., Bronfman, L., Carraro, G., Contreras, C., Davis, C.J., de Grijs, R., Dias, B., Drew, J.E., Fariña, C., Feinstein, C., Fernández Lajús, E., Gieren, W., Goldman, B., Gosling, A., Hambly, N.C., Hoare, M., Jordán, A., Kinemuchi, K., Maccarone, T., Merlo, D.C., Mennickent, R.E., Morelli, L., Motta, V., Palma, T., Popescu, B., Parisi, M.C., Parker, Q., Pignata, G., Read, M.A., Ruiz, M.T., Roman-Lopes, A., Schreiber, M.R., Schröder, A.C., Smith, M., Sodré, L., Jr., Stephens, A.W., Walton, N.A., Zijlstra, A.A., Tamura, M., Tappert, C., Thompson, M.A. & Vanzi, L. (2011). The VVV Survey of the Milky Way: first year results. *Boletin de la Asociacion Argentina de Astronomia La Plata Argentina*, **54**, 265–276. 108, 139

Miranda, L.F., Gómez, Y., Anglada, G. & Torrelles, J.M. (2001a). *Nature*, **414**, 284–286. 11, 29

Miranda, L.F., Torrelles, J.M., Guerrero, M.A., Vázquez, R. & Gómez, Y. (2001b). Morphological and kinematic signatures of a binary central star in the planetary nebula Hu2-1. *MNRAS*, **321**, 487–496. 16

Miszalski, B., Parker, Q.A., Acker, A., Birkby, J.L., Frew, D.J. & Kovacevic, A. (2008). MASH-II: more planetary nebulae from the AAO/UKST Hα survey. *MNRAS*, **384**, 525–534. 20, 50, 51, 82, 84, 106, 208

Miszalski, B., Acker, A., Moffat, A.F.J., Parker, Q.A. & Udalski, A. (2009). Binary planetary nebulae nuclei towards the Galactic bulge. I. Sample discovery, period distribution, and binary fraction. *A&A*, **496**, 813–825. 17

Miszalski, B., Mikołajewska, J. & Udalski, A. (2013). Symbiotic stars and other Hα emission-line stars towards the Galactic bulge. *MNRAS*, **432**, 3186–3217. 63, 64, 67, 69, 140

Moe, M. & De Marco, O. (2006). Do Most Planetary Nebulae Derive from Binaries? I. Population Synthesis Model of the Galactic Planetary Nebula Population Produced by Single Stars and Binaries. *ApJ*, **650**, 916–932. xxii, 16, 17, 18, 165, 166, 170, 171, 172, 173, 174, 175, 177, 182, 183, 184, 204, 207, 209, 210

Moe, M. & De Marco, O. (2012). Population synthesis of planetary nebulae from binaries. In *IAU Symposium*, vol. 283 of *IAU Symposium*, 111–114. 17, 165, 193, 207, 209, 210

Molinari, S., Swinyard, B., Bally, J., Barlow, M., Bernard, J.P., Martin, P., Moore, T., Noriega-Crespo, A., Plume, R., Testi, L., Zavagno, A., Abergel, A., Ali, B., André, P., Baluteau, J.P., Benedettini, M., Berné, O., Billot, N.P., Blommaert, J., Bontemps, S., Boulanger, F., Brand, J., Brunt, C., Burton, M., Campeggio, L., Carey, S., Caselli, P., Cesaroni, R., Cernicharo, J., Chakrabarti, S., Chrysostomou, A., Codella, C., Cohen, M., Compiegne, M., Davis, C.J., de Bernardis, P., de Gasperis, G., Di Francesco, J., di Giorgio, A.M., Elia, D., Faustini, F., Fischera, J.F., Fukui, Y., Fuller, G.A., Ganga, K., Garcia-Lario, P., Giard, M., Giardino, G., Glenn, J., Goldsmith, P., Griffin, M., Hoare, M., Huang, M., Jiang, B., Joblin, C., Joncas, G., Juvela, M., Kirk, J., Lagache, G., Li, J.Z., Lim, T.L., Lord, S.D., Lucas, P.W., Maiolo, B., Marengo, M., Marshall, D., Masi, S., Massi, F., Matsuura, M., Meny, C., Minier, V., Miville-Deschênes, M.A., Montier, L., Motte, F., Müller, T.G., Natoli, P., Neves, J., Olmi, L., Paladini, R., Paradis, D., Pestalozzi, M., Pezzuto, S., Piacentini, F., Pomarès, M., Popescu, C.C., Reach, W.T., Richer, J., Ristorcelli, I., Roy, A., Royer, P., Russeil, D., Saraceno, P., Sauvage, M., Schilke, P., Schneider-Bontemps, N., Schuller, F., Schultz, B.,

Shepherd, D.S., Sibthorpe, B., Smith, H.A., Smith, M.D., Spinoglio, L., Stamatellos, D., Strafella, F., Stringfellow, G., Sturm, E., Taylor, R., Thompson, M.A., Tuffs, R.J., Umana, G., Valenziano, L., Vavrek, R., Viti, S., Waelkens, C., Ward-Thompson, D., White, G., Wyrowski, F., Yorke, H.W. & Zhang, Q. (2010). Hi-GAL: The Herschel Infrared Galactic Plane Survey. *PASP*, **122**, 314. 22, 41, 108

Molinari, S., Schisano, E., Elia, D., Pestalozzi, M., Traficante, A., Pezzuto, S., Swinyard, B.M., Noriega-Crespo, A., Bally, J., Moore, T.J.T., Plume, R., Zavagno, A., di Giorgio, A.M., Liu, S.J., Pilbratt, G.L., Mottram, J.C., Russeil, D., Piazzo, L., Veneziani, M., Benedettini, M., Calzoletti, L., Faustini, F., Natoli, P., Piacentini, F., Merello, M., Palmese, A., Del Grand e, R., Polychroni, D., Rygl, K.L.J., Polenta, G., Barlow, M.J., Bernard, J.P., Martin, P.G., Testi, L., Ali, B., André, P., Beltrán, M.T., Billot, N., Carey, S., Cesaroni, R., Compiègne, M., Eden, D., Fukui, Y., Garcia-Lario, P., Hoare, M.G., Huang, M., Joncas, G., Lim, T.L., Lord, S.D., Martinavarro-Armengol, S., Motte, F., Paladini, R., Paradis, D., Peretto, N., Robitaille, T., Schilke, P., Schneider, N., Schulz, B., Sibthorpe, B., Strafella, F., Thompson, M.A., Umana, G., Ward-Thompson, D. & Wyrowski, F. (2016). Hi-GAL, the Herschel infrared Galactic Plane Survey: photometric maps and compact source catalogues. First data release for the inner Milky Way: +68 $\geq$ l $\geq$ -70. *A&A*, **591**, A149. 41

Morris, M. (1987). Mechanisms for mass loss from cool stars. *PASP*, **99**, 1115–1122. 4, 12, 16

Murphy, T., Mauch, T., Green, A., Hunstead, R.W., Piestrzynska, B., Kels, A.P. & Sztajer, P. (2007). The second epoch Molonglo Galactic Plane Survey: compact source catalogue. *MNRAS*, **382**, 382–392. 107

Murphy, T., Cohen, M., Ekers, R.D., Green, A.J., Wark, R.M. & Moss, V. (2010). Ultra- and hyper-compact HII regions at 20 GHz. *MNRAS*, **405**, 1560–1572. 107

Natta, A. & Hollenbach, D. (1998). The evolution of the neutral gas in planetary nebulae: theoretical models. *A&A*, **337**, 517–538. 187

Neugebauer, G., Habing, H.J., van Duinen, R., Aumann, H.H., Baud, B., Beichman, C.A., Beintema, D.A., Boggess, N., Clegg, P.E., de Jong, T., Emerson, J.P., Gautier, T.N., Gillett, F.C., Harris, S., Hauser, M.G., Houck, J.R., Jennings, R.E., Low, F.J., Marsden, P.L., Miley, G., Olnon, F.M., Pottasch, S.R., Raimond, E., Rowan-Robinson, M., Soifer, B.T., Walker, R.G., Wesselius, P.R. & Young, E. (1984). The Infrared Astronomical Satellite (IRAS) mission. *ApJ*, **278**, L1–L6. 21

Nordhaus, J. (2010). Magnetic Fields in Low-mass Evolved Stars. In L.M. Stanford, J.D. Green, L. Hao & Y. Mao, eds., *New Horizons in Astronomy: Frank N. Bash Symposium 2009*, vol. 432 of *Astronomical Society of the Pacific Conference Series*, 117. 12

Nordhaus, J. & Blackman, E.G. (2006). Low-mass binary-induced outflows from asymptotic giant branch stars. *MNRAS*, **370**, 2004–2012. 12, 16

Nordhaus, J. & Blackman, E.G. (2007). The Bipolar Engines of post-AGB stars: Transient Dynamos and Common Envelopes. In *Asymmetrical Planetary Nebulae IV*. 12, 16

Nordhaus, J., Blackman, E.G. & Frank, A. (2007). Isolated versus common envelope dynamos in planetary nebula progenitors. *MNRAS*, **376**, 599–608. 12

Norris, R.P., Afonso, J., Appleton, P.N., Boyle, B.J., Ciliegi, P., Croom, S.M., Huynh, M.T., Jackson, C.A., Koekemoer, A.M., Lonsdale, C.J., Middelberg, E., Mobasher, B., Oliver, S.J., Polletta, M., Siana, B.D., Smail, I. & Voronkov, M.A. (2006). Deep ATLAS Radio Observations of the Chandra Deep Field-South/Spitzer Wide-Area Infrared Extragalactic Field. *AJ*, **132**, 2409–2423. 38

Norris, R.P., Afonso, J., Cava, A., Farrah, D., Huynh, M.T., Ivison, R.J., Jarvis, M., Lacy, M., Mao, M., Maraston, C., Mauduit, J.C., Middelberg, E., Oliver, S., Seymour, N. & Surace, J. (2011a). Deep Spitzer Observations of Infrared-faint Radio Sources: High-redshift Radio-loud Active Galactic Nuclei? *ApJ*, **736**, 55. 38

Norris, R.P., Hopkins, A.M., Afonso, J., Brown, S., Condon, J.J., Dunne, L., Feain, I., Hollow, R., Jarvis, M., Johnston-Hollitt, M., Lenc, E., Middelberg, E., Padovani, P., Prandoni, I., Rudnick, L., Seymour, N., Umana, G., Andernach, H., Alexander, D.M., Appleton, P.N., Bacon, D., Banfield, J., Becker, W., Brown, M.J.I., Ciliegi, P., Jackson, C., Eales, S., Edge, A.C., Gaensler, B.M., Giovannini, G., Hales, C.A., Hancock, P., Huynh, M.T., Ibar, E., Ivison, R.J., Kennicutt, R., Kimball, A.E., Koekemoer, A.M., Koribalski, B.S., López-Sánchez, Á.R., Mao, M.Y., Murphy, T., Messias, H., Pimbblet, K.A., Raccanelli, A., Randall, K.E., Reiprich, T.H., Roseboom, I.G., Röttgering, H., Saikia, D.J., Sharp, R.G., Slee, O.B., Smail, I., Thompson, M.A., Urquhart, J.S., Wall, J.V. & Zhao, G.B. (2011b). EMU: Evolutionary Map of the Universe. *PASA*, **28**, 215–248. 216

Oliveira, J.M., van Loon, J.T., Sloan, G.C., Sewiło, M., Kraemer, K.E., Wood, P.R., Indebetouw, R., Filipović, M.D., Crawford, E.J., Wong, G.F., Hora, J.L., Meixner, M., Robitaille, T.P., Shiao, B. & Simon, J.D. (2013). Early-stage young stellar objects in the Small Magellanic Cloud. *MNRAS*, **428**, 3001–3033. 95

Olofsson, H., Eriksson, K. & Gustafsson, B. (1988). SEST CO (J = 1 - 0) observations of carbon-rich circumstellar envelopes. *A&A*, **196**, L1–L4. 6

Orosz, G., Gómez, J.F., Imai, H., Tafoya, D., Torrelles, J.M., Burns, R.A., Frau, P., Guerrero, M.A., Miranda, L.F., Perez-Torres, M.A., Ramos-Larios, G., Rizzo, J.R., Suárez, O. & Uscanga, L. (2018). Rapidly-evolving episodic outflow in IRAS 18113-2503: clues to the ejection mechanism of the fastest water fountain. *MNRAS*. 11

Osterbrock, D. & Ferland, G. (2006). *Astrophysics of Gaseous Nebulae and Active Galactic Nuclei*. University Science Books. 25

Osterbrock, D.E. (1964). Planetary Nebulae. *ARA&A*, **2**, 95. 1

Oudmaijer, R.D., Waters, L.B.F.M., van der Veen, W.E.C.J. & Geballe, T.R. (1995). Near-infrared spectroscopy of post-AGB stars. *A&A*, **299**, 69. 6

Paczyński, B. (1970). Evolution of Single Stars. I. Stellar Evolution from Main Sequence to White Dwarf or Carbon Ignition. *Acta Astron.*, **20**, 47. 1

Paczynskii, B. (1976). Evolution of Binary Systems. In *Bulletin of the American Astronomical Society*, vol. 8 of *BAAS*, 442. 16

Parker, Q.A., Phillipps, S., Pierce, M.J., Hartley, M., Hambly, N.C., Read, M.A., MacGillivray, H.T., Tritton, S.B., Cass, C.P., Cannon, R.D., Cohen, M., Drew, J.E., Frew, D.J., Hopewell, E., Mader, S., Malin, D.F., Masheder, M.R.W., Morgan, D.H., Morris, R.A.H., Russeil, D., Russell, K.S. & Walker, R.N.F. (2005). The AAO/UKST SuperCOSMOS Hα survey. *MNRAS*, **362**, 689–710. 20, 93, 143

Parker, Q.A., Acker, A., Frew, D.J., Hartley, M., Peyaud, A.E.J., Ochsenbein, F., Phillipps, S., Russeil, D., Beaulieu, S.F., Cohen, M., Köppen, J., Miszalski, B., Morgan, D.H., Morris, R.A.H., Pierce, M.J. & Vaughan, A.E. (2006). The Macquarie/AAO/Strasbourg Hα Planetary Nebula Catalogue: MASH. *MNRAS*, **373**, 79–94. 7, 20, 50, 51, 82, 83, 84, 106, 208

Parker, Q.A., Cohen, M., Stupar, M., Frew, D.J., Green, A.J., Bojicic, I., Guzman-Ramirez, L., Sabin, L. & Vogt, F. (2012a). Discovery of planetary nebulae using predictive mid-infrared diagnostics. *MNRAS*, **427**, 3016–3028. xvii, 59, 85, 94, 95, 96, 106

Parker, Q.A., Frew, D.J., Acker, A. & Miszalski, B. (2012b). The past, present and future of Galactic planetary nebula surveys. In *IAU Symposium*, vol. 283 of *IAU Symposium*, 9–16. 23

Parker, Q.A., Bojičić, I. & Frew, D.J. (2017). Exploiting the HASH Planetary Nebula Research Platform. In X. Liu, L. Stanghellini & A. Karakas, eds., *Planetary Nebulae: Multi-Wavelength Probes of Stellar and Galactic Evolution*, vol. 323 of *IAU Symposium*, 36–39. 18, 19, 20, 21, 82, 83, 84, 93, 94, 150, 153, 156, 207, 217

Pascoli, G. (1997). On Circumstellar Envelope Formation. *ApJ*, **489**, 946–950. 4

Peimbert, M. (1978). Chemical abundances in planetary nebulae. In Y. Terzian, ed., *Planetary Nebulae*, vol. 76 of *IAU Symposium*, 215–223. 167, 169, 205, 210

Peimbert, M. (1990). Total number of planetary nebulae in different galaxies and the PN distance scale. *Rev. Mex. Astron. Astrofis.*, **20**, 119. 1

Peimbert, M. & Serrano, A. (1980). On the helium and nitrogen enrichment of the interstellar medium by planetary nebulae. *Rev. Mex. Astron. Astrofis.*, **5**, 9–18. 167

Peimbert, M. & Torres-Peimbert, S. (1983). Type I planetary nebulae. In D.R. Flower, ed., *Planetary Nebulae*, vol. 103 of *IAU Symposium*, 233–241. 169

Pena, M. & Torres-Peimbert, S. (1987). JHK photometry of compact planetary nebulae. *Rev. Mex. Astron. Astrofis.*, **14**, 534–539. 77

Perek, L. & Kohoutek, L. (1967). Catalogue of galactic planetary nebulae. *Publ. House Czech. Acad. Sci.*. 7

Pérez-Sánchez, A.F., Vlemmings, W.H.T., Tafoya, D. & Chapman, J.M. (2013). A synchrotron jet from a post-asymptotic giant branch star. *MNRAS*, **436**, L79–L83. 12, 15, 29, 87

Perinotto, M. (1989). Mass loss rates in central stars of planetary nebulae. In S. Torres-Peimbert, ed., *Planetary Nebulae*, vol. 131 of *IAU Symposium*, 293–300. 5

Phillips, J.P. (2002). The correlation between expansion velocity and morphology in planetary nebulae. *A&A*, **393**, 1027–1033. 182, 202, 215

Phillips, J.P. (2003a). The correlation between planetary nebula morphology and radio brightness temperatures. *A&A*, **412**, 791–798. 88

Phillips, J.P. (2003b). The use of high brightness temperature sources to constrain the scale heights and distances of planetary nebulae. *New Astron.*, **8**, 29–38. 169

Phillips, J.P. (2004). Variation of Central Star Masses in Planetary Nebulae with Height above the Galactic Plane. *Rev. Mex. Astron. Astrofis.*, **40**, 25–30. 169

Phillips, J.P. (2007). Density gradients in Galactic planetary nebulae. *MNRAS*, **378**, 231–238. 91

Phillips, J.P. & Márquez-Lugo, R.A. (2011). Mid- and Far-Infrared Photometry of Galactic Planetary Nebulae with the AKARI All-Sky Survey. *Rev. Mex. Astron. Astrofis.*, **47**, 83–112. 70

Phillips, J.P. & Ramos-Larios, G. (2008). A GLIMPSE of new and possible planetary nebulae at mid-infrared wavelengths. *MNRAS*, **386**, 995–1012. 106

Phillips, J.P. & Ramos-Larios, G. (2009). The mid-infrared colours of Galactic bulge, disc and Magellanic planetary nebulae. *MNRAS*, **396**, 1915–1928. 68

Phillips, J.P. & Zepeda-García, D. (2009). The near- and far-infrared colours of MASH planetary nebulae. *MNRAS*, **394**, 1875–1886. 60, 61, 62

Pinheiro Gonçalves, D., Noriega-Crespo, A., Paladini, R., Martin, P.G. & Carey, S.J. (2011). The MIPSGAL View of Supernova Remnants in the Galactic Plane. *AJ*, **142**, 47. 91

Planck Collaboration, Arnaud, M., Atrio-Barandela, F., Aumont, J., Baccigalupi, C., Banday, A.J., Barreiro, R.B., Battaner, E.,

Benabed, K., Benoit-Lévy, A., Bernard, J.P., Bersanelli, M., Bielewicz, P., Bonaldi, A., Bond, J.R., Borrill, J., Bouchet, F.R., Buemi, C.S., Burigana, C., Cardoso, J.F., Casassus, S., Catalano, A., Cerrigone, L., Chamballu, A., Chiang, H.C., Colombi, S., Colombo, L.P.L., Couchot, F., Crill, B.P., Curto, A., Cuttaia, F., Davies, R.D., Davis, R.J., de Bernardis, P., de Rosa, A., de Zotti, G., Delabrouille, J., Dickinson, C., Diego, J.M., Donzelli, S., Doré, O., Dupac, X., Ensslin, T.A., Eriksen, H.K., Finelli, F., Frailis, M., Franceschi, E., Galeotta, S., Ganga, K., Giard, M., González-Nuevo, J., Górski, K.M., Gregorio, A., Gruppuso, A., Hansen, F.K., Harrison, D.L., Hildebrandt, S.R., Hivon, E., Holmes, W.A., Hora, J.L., Hornstrup, A., Hovest, W., Huffenberger, K.M., Jaffe, T.R., Jones, W.C., Juvela, M., Keihänen, E., Keskitalo, R., Kisner, T.S., Knoche, J., Kunz, M., Kurki-Suonio, H., Lähteenmäki, A., Lamarre, J.M., Lasenby, A., Lawrence, C.R., Leonardi, R., Leto, P., Lilje, P.B., Linden-Vørnle, M., López-Caniego, M., Macías-Pérez, J.F., Maffei, B., Maino, D., Mandolesi, N., Martin, P.G., Masi, S., Massardi, M., Matarrese, S., Mazzotta, P., Mendes, L., Mennella, A., Migliaccio, M., Miville-Deschênes, M.A., Moneti, A., Montier, L., Morgante, G., Mortlock, D., Munshi, D., Murphy, J.A., Naselsky, P., Nati, F., Natoli, P., Noviello, F., Novikov, D., Novikov, I., Pagano, L., Pajot, F., Paladini, R., Paoletti, D., Peel, M., Perdereau, O., Perrotta, F., Piacentini, F., Piat, M., Pietrobon, D., Plaszczynski, S., Pointecouteau, E., Polenta, G., Popa, L., Pratt, G.W., Procopio, P., Prunet, S., Puget, J.L., Rachen, J.P., Reinecke, M., Remazeilles, M., Ricciardi, S., Riller, T., Ristorcelli, I., Rocha, G., Rosset, C., Roudier, G., Rubiño-Martín, J.A., Rusholme, B., Sandri, M., Savini, G., Scott, D., Spencer, L.D., Stolyarov, V., Sutton, D., Suur-Uski, A.S., Sygnet, J.F., Tauber, J.A., Terenzi, L., Toffolatti, L., Tomasi, M., Trigilio, C., Tristram, M., Trombetti, T., Tucci, M., Umana, G., Valiviita, J., Van Tent, B., Vielva, P., Villa, F., Wade, L.A., Wandelt, B.D., Zacchei, A., Zijlstra, A.

& Zonca, A. (2015). Planck intermediate results. XVIII. The millimetre and sub-millimetre emission from planetary nebulae. *A&A*, **573**, A6. 19, 22, 42, 189

Poglitsch, A., Waelkens, C., Bauer, O.H., Cepa, J., Feuchtgruber, H., Henning, T., van Hoof, C., Kerschbaum, F., Krause, O., Renotte, E., Rodriguez, L., Saraceno, P. & Vand enbussche, B. (2008). The Photodetector Array Camera and Spectrometer (PACS) for the Herschel Space Observatory. In *Space Telescopes and Instrumentation 2008: Optical, Infrared, and Millimeter*, vol. 7010 of *Proc. SPIE*, 701005. 40

Pottasch, S.R. (1986). Infrared emission from young planetary nebulae. *Comptes Rendus sur les Journees de Strasbourg*, **8**, 97–111. 68

Pottasch, S.R., Baud, B., Beintema, D., Emerson, J., Harris, S., Habing, H.J., Houck, J., Jennings, R. & Marsden, P. (1984). IRAS measurements of planetary nebulae. *A&A*, **138**, 10–18. 42, 68

Pottasch, S.R., Bignell, C., Olling, R. & Zijlstra, A.A. (1988). Planetary nebulae near the galactic center. I - Method of discovery and preliminary results. *A&A*, **205**, 248–256. 21, 23

Pottasch, S.R., Beintema, D.A. & Feibelman, W.A. (2000). Abundance in the planetary nebulae NGC 6537 and He2-111. *A&A*, **363**, 767–778. 79

Preite-Martinez, A. (1988). Possible new planetary nebulae in the IRAS Point Source Catalogue. *A&AS*, **76**, 317–330. 106

Purcell, C.R., Hoare, M.G., Cotton, W.D., Lumsden, S.L., Urquhart, J.S., Chandler, C., Churchwell, E.B., Diamond, P., Dougherty, S.M., Fender, R.P., Fuller, G., Garrington, S.T., Gledhill, T.M., Goldsmith, P.F., Hindson, L., Jackson, J.M., Kurtz, S.E., Martí, J., Moore, T.J.T., Mundy, L.G., Muxlow, T.W.B., Oudmaijer, R.D., Pandian, J.D., Paredes, J.M., Shepherd, D.S., Smethurst, S., Spencer, R.E., Thompson, M.A., Umana, G. & Zijlstra, A.A. (2013). The Coordinated Radio and Infrared Survey for

High-mass Star Formation. II. Source Catalog. *ApJS*, **205**, 1. 37, 39, 43, 45, 48, 49, 82, 114, 115, 125, 130, 131, 134, 154, 180, 208, 214

Qin, W., Nataf, D.M., Zakamska, N., Wood, P.R. & Casagrande, L. (2018). The Mira-based Distance to the Galactic Center. *ApJ*, **865**, 47. 170

Quireza, C., Rocha-Pinto, H.J. & Maciel, W.J. (2007). Bayesian posterior classification of planetary nebulae according to the Peimbert types. *A&A*, **475**, 217–231. 167, 169, 205, 210

Ramos-Larios, G. & Phillips, J.P. (2005). An analysis of 2MASS near-infrared photometry for galactic planetary nebulae. *MNRAS*, **357**, 732–752. 60, 61, 75, 78, 86

Ramos-Larios, G. & Phillips, J.P. (2009). The haloes of planetary nebulae in the mid-infrared: evidence for interaction with the interstellar medium. *MNRAS*, **400**, 575–588. 14

Ramos-Larios, G., Guerrero, M.A., Sabin, L. & Santamaría, E. (2017). Pushing the limits: detecting H_2 emission from faint bipolar planetary nebulae in the IPHAS sample. *MNRAS*, **470**, 3707–3719. 23, 36

Ratag, M.A. & Pottasch, S.R. (1991). Planetary nebulae near the Galactic center. III - The WSRT measurements. *A&AS*, **91**, 481–486. 106

Rauch, T. (2003). Calculation of Synthetic Ionizing Spectra for Planetary Nebulae. In S. Kwok, M. Dopita & R. Sutherland, eds., *Planetary Nebulae: Their Evolution and Role in the Universe*, vol. 209 of *IAU Symposium*, 191. 166

Reach, W.T., Megeath, S.T., Cohen, M., Hora, J., Carey, S., Surace, J., Willner, S.P., Barmby, P., Wilson, G., Glaccum, W., Lowrance, P., Marengo, M. & Fazio, G.G. (2005). Absolute Calibration of the Infrared Array Camera on the Spitzer Space Telescope. *PASP*, **117**, 978–990. 45

Reach, W.T., Rho, J., Tappe, A., Pannuti, T.G., Brogan, C.L., Churchwell, E.B., Meade, M.R., Babler, B., Indebetouw, R. & Whitney, B.A. (2006). A Spitzer Space Telescope Infrared Survey of Supernova Remnants in the Inner Galaxy. *AJ*, **131**, 1479–1500. 91

Reddy, B.E. & Parthasarathy, M. (1997). CCD photometry and spectroscopy of 14 IRAS sources having far-IR colours similar to Planetary Nebulae. In H.J. Habing & H.J.G.L.M. Lamers, eds., *Planetary Nebulae*, vol. 180 of *IAU Symposium*, 365. 21

Refsdal, S. & Weigert, A. (1970). Shell Source Burning Stars with Highly Condensed Cores. *A&A*, **6**, 426. 2

Reyes-Ruiz, M. & López, J.A. (1999). Accretion Disks in Pre-Planetary Nebulae. *ApJ*, **524**, 952–960. 12

Roberts, J.A., Roger, R.S., Ribes, J.C., Cooke, D.J., Murray, J.D., Cooper, B.F.C. & Biraud, F. (1975). Measurements of the circular polarization of radio sources at frequencies of 0.63, 1.4, 5.0 and 8.9 GHz. *Australian Journal of Physics*, **28**, 325–351. 116

Robitaille, T.P., Meade, M.R., Babler, B.L., Whitney, B.A., Johnston, K.G., Indebetouw, R., Cohen, M., Povich, M.S., Sewilo, M., Benjamin, R.A. & Churchwell, E. (2008). Intrinsically Red Sources Observed by Spitzer in the Galactic Midplane. *AJ*, **136**, 2413–2440. 94, 106

Rodríguez-Flores, E.R., Corradi, R.L.M., Mampaso, A., García-Alvarez, D., Munari, U., Greimel, R., Rubio-Díez, M.M. & Santander-García, M. (2014). IPHAS and the symbiotic stars. III. New discoveries and their IR spectral energy distributions. *A&A*, **567**, A49. 63, 64

Rosen, S.R., Webb, N.A., Watson, M.G., Ballet, J., Barret, D., Braito, V., Carrera, F.J., Ceballos, M.T., Coriat, M., Della Ceca, R., Denkinson, G., Esquej, P., Farrell, S.A., Freyberg, M., Grisé, F., Guillout, P., Heil, L., Koliopanos, F., Law-Green, D., Lamer, G., Lin, D., Martino, R., Michel, L., Motch, C.,

Nebot Gomez-Moran, A., Page, C.G., Page, K., Page, M., Pakull, M.W., Pye, J., Read, A., Rodriguez, P., Sakano, M., Saxton, R., Schwope, A., Scott, A.E., Sturm, R., Traulsen, I., Yershov, V. & Zolotukhin, I. (2016). The XMM-Newton serendipitous survey. VII. The third XMM-Newton serendipitous source catalogue. *A&A*, **590**, A1. 88

Rosolowsky, E., Dunham, M.K., Ginsburg, A., Bradley, E.T., Aguirre, J., Bally, J., Battersby, C., Cyganowski, C., Dowell, D., Drosback, M., Evans, N.J., II, Glenn, J., Harvey, P., Stringfellow, G.S., Walawender, J. & Williams, J.P. (2010). The Bolocam Galactic Plane Survey. II. Catalog of the Image Data. *ApJS*, **188**, 123–138. 106

Ruffle, P.M.E., Zijlstra, A.A., Walsh, J.R., Gray, M.D., Gesicki, K., Minniti, D. & Comeron, F. (2004). Angular diameters, fluxes and extinction of compact planetary nebulae: further evidence for steeper extinction towards the bulge. *MNRAS*, **353**, 796–812. 73, 80

Ryle, M. (1955). The application of interferometric methods in radio astronomy. *Vistas in Astronomy*, **1**, 532–541. 30

Ryle, M. (1968). The Counts of Radio Sources. *ARA&A*, **6**, 249. 30

Ryle, M. & Hewish, A. (1960). The synthesis of large radio telescopes. *MNRAS*, **120**, 220. 30

Sabin, L., Zijlstra, A.A. & Greaves, J.S. (2007). Magnetic fields in planetary nebulae and post-AGB nebulae. In *Asymmetrical Planetary Nebulae IV*, 91. 29

Sabin, L., Corradi, R.L.M., Parker, Q., Mampaso, A. & Zijlstra, A. (2012). New planetary nebulae with ISM interaction discovered with IPHAS. In *IAU Symposium*, vol. 283 of *IAU Symposium*, 492–493. 13

Sabin, L., Parker, Q.A., Corradi, R.L.M., Guzman-Ramirez, L., Morris, R.A.H., Zijlstra, A.A., Bojičić, I.S., Frew, D.J., Guerrero, M., Stupar, M., Barlow, M.J., Cortés Mora, F., Drew, J.E., Greimel,

R., Groot, P., Irwin, J.M., Irwin, M.J., Mampaso, A., Miszalski, B., Olguín, L., Phillipps, S., Santander García, M., Viironen, K. & Wright, N.J. (2014). First release of the IPHAS catalogue of new extended planetary nebulae. *MNRAS*, **443**, 3388–3401. 20, 41, 50, 51, 61, 63, 64, 82, 83, 84, 106, 208

Sahai, R. & Patel, N.A. (2015). An Extreme High-velocity Bipolar Outflow in the Pre-planetary Nebula IRAS 08005-2356. *ApJ*, **810**, L8. 11

Sahai, R. & Trauger, J.T. (1998). *AJ*, **116**, 1357–1366. 11

Sahai, R., Morris, M., Knapp, G.R., Young, K. & Barnbaum, C. (2003). A collimated, high-speed outflow from the dying star V Hydrae. *Nature*, **426**, 261–264. 11

Sahai, R., Morris, M., Sánchez Contreras, C. & Claussen, M. (2007). Preplanetary Nebulae: A Hubble Space Telescope Imaging Survey and a New Morphological Classification System. *AJ*, **134**, 2200–2225. 7, 11

Sahai, R., Morris, M.R. & Villar, G.G. (2011). Young Planetary Nebulae: Hubble Space Telescope Imaging and a New Morphological Classification System. *AJ*, **141**, 134. xv, 7, 8, 9, 11, 42

Saito, R.K., Hempel, M., Minniti, D., Lucas, P.W., Rejkuba, M., Toledo, I., Gonzalez, O.A., Alonso-García, J., Irwin, M.J., Gonzalez-Solares, E., Hodgkin, S.T., Lewis, J.R., Cross, N., Ivanov, V.D., Kerins, E., Emerson, J.P., Soto, M., Amôres, E.B., Gurovich, S., Dékány, I., Angeloni, R., Beamin, J.C., Catelan, M., Padilla, N., Zoccali, M., Pietrukowicz, P., Moni Bidin, C., Mauro, F., Geisler, D., Folkes, S.L., Sale, S.E., Borissova, J., Kurtev, R., Ahumada, A.V., Alonso, M.V., Adamson, A., Arias, J.I., Bandyopadhyay, R.M., Barbá, R.H., Barbuy, B., Baume, G.L., Bedin, L.R., Bellini, A., Benjamin, R., Bica, E., Bonatto, C., Bronfman, L., Carraro, G., Chenè, A.N., Clariá, J.J., Clarke, J.R.A., Contreras, C., Corvillón, A., de Grijs, R., Dias, B., Drew, J.E., Fariña, C., Feinstein, C., Fernández-Lajús, E., Gamen,

R.C., Gieren, W., Goldman, B., González-Fernández, C., Grand, R.J.J., Gunthardt, G., Hambly, N.C., Hanson, M.M., Hełminiak, K.G., Hoare, M.G., Huckvale, L., Jordán, A., Kinemuchi, K., Longmore, A., López-Corredoira, M., Maccarone, T., Majaess, D., Martín, E.L., Masetti, N., Mennickent, R.E., Mirabel, I.F., Monaco, L., Morelli, L., Motta, V., Palma, T., Parisi, M.C., Parker, Q., Peñaloza, F., Pietrzyński, G., Pignata, G., Popescu, B., Read, M.A., Rojas, A., Roman-Lopes, A., Ruiz, M.T., Saviane, I., Schreiber, M.R., Schröder, A.C., Sharma, S., Smith, M.D., Sodré, L., Stead, J., Stephens, A.W., Tamura, M., Tappert, C., Thompson, M.A., Valenti, E., Vanzi, L., Walton, N.A., Weidmann, W. & Zijlstra, A. (2012). VVV DR1: The first data release of the Milky Way bulge and southern plane from the near-infrared ESO public survey VISTA variables in the Vía Láctea. *A&A*, **537**, A107. 139

Santander-García, M., Corradi, R.L.M. & Mampaso, A. (2007). Symbiotic or planetary nebulae? In *Asymmetrical Planetary Nebulae IV*. 91

Sault, R.J. & Conway, J.E. (1999). Multi-Frequency Synthesis. In G.B. Taylor, C.L. Carilli & R.A. Perley, eds., *Synthesis Imaging in Radio Astronomy II*, vol. 180 of *Astronomical Society of the Pacific Conference Series*, 419. 116

Sault, R.J., Teuben, P.J. & Wright, M.C.H. (1995). A Retrospective View of MIRIAD. In R.A. Shaw, H.E. Payne & J.J.E. Hayes, eds., *Astronomical Data Analysis Software and Systems IV*, vol. 77 of *Astronomical Society of the Pacific Conference Series*, 433. 110

Schneider, S.E. & Terzian, Y. (1983). Planetary nebulae and the galactic rotation curve. *ApJ*, **274**, L61–L64. 2

Schoenberner, D. (1983). Late stages of stellar evolution. II - Mass loss and the transition of asymptotic giant branch stars into hot remnants. *ApJ*, **272**, 708–714. 172, 173, 174, 175, 176

Schoenberner, D. (1988). Mass loss and post-asymptotic giant-branch evolution. In L. Bianchi & R. Gilmozzi, eds., *Mass Outflows from Stars and Galactic Nuclei*, vol. 142 of *Astrophysics and Space Science Library*, 137–146. 175

Schonberner, D. & Blocker, T. (1993). Evolution on the AGB and Beyond. In D.D. Sasselov, ed., *Luminous High-Latitude Stars*, vol. 45 of *Astronomical Society of the Pacific Conference Series*, 337. 1

Schönberner, D., Jacob, R., Sandin, C. & Steffen, M. (2010). The evolution of planetary nebulae. VII. Modelling planetary nebulae of distant stellar systems. *A&A*, **523**, A86. 215

Schönberner, D., Jacob, R., Lehmann, H., Hildebrandt, G., Steffen, M., Zwanzig, A., Sandin, C. & Corradi, R.L.M. (2014). A hydrodynamical study of multiple-shell planetary nebulae. III. Expansion properties and internal kinematics: Theory versus observation. *Astronomische Nachrichten*, **335**, 378–408. 1, 4, 215

Schuller, F., Menten, K.M., Contreras, Y., Wyrowski, F., Schilke, P., Bronfman, L., Henning, T., Walmsley, C.M., Beuther, H., Bontemps, S., Cesaroni, R., Deharveng, L., Garay, G., Herpin, F., Lefloch, B., Linz, H., Mardones, D., Minier, V., Molinari, S., Motte, F., Nyman, L.Å., Reveret, V., Risacher, C., Russeil, D., Schneider, N., Testi, L., Troost, T., Vasyunina, T., Wienen, M., Zavagno, A., Kovacs, A., Kreysa, E., Siringo, G. & Weiss, A. (2009). ATLASGAL - The APEX telescope large area survey of the galaxy at 870 μm. *A&A*, **504**, 415–427. 141

Schwarz, H.E., Corradi, R.L.M. & Stanghellini, L. (1993). H alpha Morphological Classification of Planetary Nebulae. In R. Weinberger & A. Acker, eds., *Planetary Nebulae*, vol. 155 of *IAU Symposium*, 214. 7

Seaton, M.J. (1960). HI, HeII, and HeII intensities in planetary nebulae. *MNRAS*, **120**, 326. 1

Sevilla-Noarbe, I. & Etayo-Sotos, P. (2015). Effect of training characteristics on object classification: An application using boosted decision trees. *Astronomy and Computing*, **11**, 64–72. 217

Sewilo, M., Churchwell, E., Kurtz, S., Goss, W.M. & Hofner, P. (2004). Broad Radio Recombination Lines from Hypercompact H II Regions. In *American Astronomical Society Meeting Abstracts*, vol. 36 of *Bulletin of the American Astronomical Society*, 1574. 106

Shklovskii, I.S. (1957). On the Nature of the Optical Emission from the Crab Nebula. *Soviet Ast.*, **1**, 690. 1

Siódmiak, N. & Tylenda, R. (2001). An analysis of the observed radio emission from planetary nebulae. *A&A*, **373**, 1032–1042. 56, 58, 191, 214

Skrutskie, M.F., Cutri, R.M., Stiening, R., Weinberg, M.D., Schneider, S., Carpenter, J.M., Beichman, C., Capps, R., Chester, T., Elias, J., Huchra, J., Liebert, J., Lonsdale, C., Monet, D.G., Price, S., Seitzer, P., Jarrett, T., Kirkpatrick, J.D., Gizis, J.E., Howard, E., Evans, T., Fowler, J., Fullmer, L., Hurt, R., Light, R., Kopan, E.L., Marsh, K.A., McCallon, H.L., Tam, R., Van Dyk, S. & Wheelock, S. (2006a). The Two Micron All Sky Survey (2MASS). *AJ*, **131**, 1163–1183. 22

Skrutskie, M.F., Cutri, R.M., Stiening, R., Weinberg, M.D., Schneider, S., Carpenter, J.M., Beichman, C., Capps, R., Chester, T., Elias, J., Huchra, J., Liebert, J., Lonsdale, C., Monet, D.G., Price, S., Seitzer, P., Jarrett, T., Kirkpatrick, J.D., Gizis, J.E., Howard, E., Evans, T., Fowler, J., Fullmer, L., Hurt, R., Light, R., Kopan, E.L., Marsh, K.A., McCallon, H.L., Tam, R., Van Dyk, S. & Wheelock, S. (2006b). The Two Micron All Sky Survey (2MASS). *AJ*, **131**, 1163–1183. 61

Sloan, G.C., Lagadec, E., Zijlstra, A.A., Kraemer, K.E., Weis, A.P., Matsuura, M., Volk, K., Peeters, E., Duley, W.W., Cami, J., Bernard-Salas, J., Kemper, F. & Sahai, R. (2014). Carbon-rich Dust

Past the Asymptotic Giant Branch: Aliphatics, Aromatics, and Fullerenes in the Magellanic Clouds. *ApJ*, **791**, 28. 7

Smith, H. (1976). Differential deceleration of nebular shells and the displacement of central stars. *MNRAS*, **175**, 419–427. 12

Soker, N. (1992). Planetary nebulae. *SciAm*, **266**, 78–88. 7

Soker, N. (1997). Properties That Cannot Be Explained by the Progenitors of Planetary Nebulae. *ApJS*, **112**, 487–505. 15, 16

Soker, N. (2006). Observed Planetary Nebulae as Descendants of Interacting Binary Systems. *ApJ*, **645**, L57–L60. 17, 18

Soker, N. (2016). Planetary nebula progenitors that swallow binary systems. *MNRAS*, **455**, 1584–1593. 16

Soker, N. & Livio, M. (1989). Interacting winds and the shaping of planetary nebulae. *ApJ*, **339**, 268–278. 10, 16

Soker, N. & Livio, M. (1994). Disks and jets in planetary nebulae. *ApJ*, **421**, 219–224. 12, 16

Soker, N. & Regev, O. (1998). Disturbed FLIERS in Planetary Nebulae. *AJ*, **116**, 2462–2465. 11

Soker, N., Borkowski, K.J. & Sarazin, C.L. (1991). Interaction of planetary nebulae with the interstellar medium - Theory. *AJ*, **102**, 1381–1392. 12

Stanghellini, L. (2004). Magellanic Cloud Planetary Nebulae as Probes of Stellar Evolution and Populations. In M. Meixner, J.H. Kastner, B. Balick & N. Soker, eds., *Asymmetrical Planetary Nebulae III: Winds, Structure and the Thunderbird*, vol. 313 of *Astronomical Society of the Pacific Conference Series*, 10. 2

Stanghellini, L. (2006). Magellanic Cloud planetary nebulae as probes of stellar evolution and populations. In M. Livio & T.M. Brown, eds., *The Local Group as an Astrophysical Laboratory*, vol. 17, 196–207. 2

Stanghellini, L. & Renzini, A. (2000a). Synthetic Post-Asymptotic Giant Branch Evolution: Basic Models and Applications to Disk Populations. *ApJ*, **542**, 308–327. 166, 206

Stanghellini, L. & Renzini, A. (2000b). Synthetic Post-Asymptotic Giant Branch Evolution: Basic Models and Applications to Disk Populations. *ApJ*, **542**, 308–327. 175

Stanghellini, L., Corradi, R.L.M. & Schwarz, H.E. (1993). The correlations between planetary nebula morphology and central star evolution. *A&A*, **279**, 521–528. 7, 8, 21

Stanghellini, L., Villaver, E., Manchado, A. & Guerrero, M.A. (2002). The Correlations between Planetary Nebula Morphology and Central Star Evolution: Analysis of the Northern Galactic Sample. *ApJ*, **576**, 285–293. 8, 21, 35, 51, 169

Stanghellini, L., Shaw, R.A. & Villaver, E. (2008). The Magellanic Cloud Calibration of the Galactic Planetary Nebula Distance Scale. *ApJ*, **689**, 194–202. 83

Stanghellini, L., Shaw, R.A. & Villaver, E. (2016). Compact Galactic Planetary Nebulae: An HST/WFC3 Morphological Catalog, and a Study of Their Role in the Galaxy. *ApJ*, **830**, 33. 7

Stasińska, G. & Tylenda, R. (1994). An extensive study of planetary nebulae in the Galactic bulge. *A&A*, **289**, 225–236. 203, 206

Stasińska, G., Richer, M.G. & McCall, M.L. (1998). The planetary nebulae populations in five galaxies: abundance patterns and evolution. *A&A*, **336**, 667–681. 166

Steggles, H.G. (2016). *Ultra-compact HII regions*. Ph.D. thesis, University of Leeds. 171, 172

Stenborg, T.N. (2017). A New Population of Galactic Bulge Planetary Nebulae. *PASP*, **129**, 067002. 216

Suárez, O., García-Lario, P., Manchado, A., Manteiga, M., Ulla, A. & Pottasch, S.R. (2006a). A spectroscopic atlas of post-AGB stars and planetary nebulae selected from the IRAS point source catalogue. *A&A*, **458**, 173–180. 106

Suárez, O., García-Lario, P. & Manteiga, M. (2006b). Stellar evolution in the Post-AGB stage. *Lecture Notes and Essays in Astrophysics*, **2**, 149–158. 5

Suárez, O., Francisco Gómez, J., Bendjoya, P., Miranda, L.F., Guerrero, M.A., Ramos-Larios, G., Ricardo Rizzo, J. & Uscanga, L. (2012). The first water fountain in a planetary nebula. In R.S. Booth, W.H.T. Vlemmings & E.M.L. Humphreys, eds., *Cosmic Masers - from OH to H0*, vol. 287 of *IAU Symposium*, 230–234. 11

Suárez, O., Gómez, J.F., Bendjoya, P., Miranda, L.F., Guerrero, M.A., Uscanga, L., Green, J.A., Rizzo, J.R. & Ramos-Larios, G. (2015). Time-variable Non-thermal Emission in the Planetary Nebula IRAS 15103-5754. *ApJ*, **806**, 105. 28, 89

Szczerba, R., Siódmiak, N., Stasińska, G. & Borkowski, J. (2007). An evolutionary catalogue of galactic post-AGB and related objects. *A&A*, **469**, 799–806. 106

Tafoya, D., Gómez, Y., Patel, N.A., Torrelles, J.M., Gómez, J.F., Anglada, G., Miranda, L.F. & de Gregorio-Monsalvo, I. (2009). A Collimated, Ionized Bipolar Structure and a High Density Torus in the Planetary Nebula IRAS 17347-3139. *ApJ*, **691**, 611–620. 12

Taylor, A.R., Goss, W.M., Coleman, P.H., van Leeuwen, J. & Wallace, B.J. (1996). A Westerbork Synthesis Radio Telescope 327 MHz Survey of the Galactic Plane. *ApJS*, **107**, 239. 106

Taylor, J.H. & Cordes, J.M. (1993). Pulsar distances and the galactic distribution of free electrons. *ApJ*, **411**, 674–684. 171

Terzian, Y. (1997). Expansion distances of Planetary Nebulae (Invited Review). In H.J. Habing & H.J.G.L.M. Lamers, eds., *Planetary Nebulae*, vol. 180 of *IAU Symposium*, 29. 80

Thompson, A.R. (1986). The interferometer in practice. In R.A. Perley, F.R. Schwab & A.H. Bridle, eds., *Synthesis Imaging*, 9–30. 31

Thompson, A.R., Colvin, R.S. & Stanley, G.J. (1967). Measurements of the Flux Densities, Positions, and Angular Widths of Planetary Nebulae at 10- and 21-CM Wavelengths. *ApJ*, **148**, 429. 33

Thompson, A.R., Moran, J.M. & Swenson, G.W., Jr. (2001). *Interferometry and Synthesis in Radio Astronomy, 2nd Edition*. 31

Thompson, A.R., Moran, J.M. & Swenson, G.W., Jr. (2017). *Interferometry and Synthesis in Radio Astronomy, 3rd Edition*. 31

Thompson, M., Goedhart, S., Goedhart, S., Benaglia, P., Beuther, H., Blomme, R., Chrysostomou, A.C., Clark, J.S., Dickinson, C., Ellingsen, S., Fenech, D., Hindson, L., Longmore, S.N., van Langevelde, H.J., MacLeod, G., Molinari, S., Prinja, R., Purcell, C.R., Stevens, I., Umana, G., Urquhart, J.S., Vlemmings, W., Walsh, A.J., Yang, A.Y. & Zijlstra, A. (2016). MeerGAL: the MeerKAT Galactic Plane Survey. In *Proceedings of MeerKAT Science: On the Pathway to the SKA. 25-27 May, 2016 Stellenbosch, South Africa (MeerKAT2016)*, 15. 212, 213

Tocknell, J., De Marco, O. & Wardle, M. (2014). Constraints on common envelope magnetic fields from observations of jets in planetary nebulae. *MNRAS*, **439**, 2014–2024. 12

Tylenda, R., Acker, A., Stenholm, B. & Koeppen, J. (1992). The extinction constants for galactic planetary nebulae. *A&AS*, **95**, 337–354. 79

Ueta, T., Ladjal, D., Exter, K.M., Otsuka, M., Szczerba, R., Siódmiak, N., Aleman, I., van Hoof, P.A.M., Kastner, J.H., Montez, R., McDonald, I., Wittkowski, M., Sandin, C., Ramstedt,

S., De Marco, O., Villaver, E., Chu, Y.H., Vlemmings, W., Izumiura, H., Sahai, R., Lopez, J.A., Balick, B., Zijlstra, A., Tielens, A.G.G.M., Rattray, R.E., Behar, E., Blackman, E.G., Hebden, K., Hora, J.L., Murakawa, K., Nordhaus, J., Nordon, R. & Yamamura, I. (2014). The Herschel Planetary Nebula Survey (HerPlaNS). I. Data overview and analysis demonstration with NGC 6781. *A&A*, **565**, A36. 187

Umana, G., Cerrigone, L., Trigilio, C. & Zappalà, R. A. (2004). A search for very young planetary nebulae. *A&A*, **428**, 121–129. 11

Urquhart, J.S., Hoare, M.G., Purcell, C.R., Lumsden, S.L., Oudmaijer, R.D., Moore, T.J.T., Busfield, A.L., Mottram, J.C. & Davies, B. (2009a). The RMS survey. 6 cm continuum VLA observations towards candidate massive YSOs in the northern hemisphere. *A&A*, **501**, 539–551. 42

Urquhart, J.S., Hoare, M.G., Purcell, C.R., Lumsden, S.L., Oudmaijer, R.D., Moore, T.J.T., Busfield, A.L., Mottram, J.C. & Davies, B. (2009b). The RMS survey. 6 cm continuum VLA observations towards candidate massive YSOs in the northern hemisphere. *A&A*, **501**, 539–551. 106

Urquhart, J.S., Thompson, M.A., Moore, T.J.T., Purcell, C.R., Hoare, M.G., Schuller, F., Wyrowski, F., Csengeri, T., Menten, K.M., Lumsden, S.L., Kurtz, S., Walmsley, C.M., Bronfman, L., Morgan, L.K., Eden, D.J. & Russeil, D. (2013). ATLASGAL - properties of compact H II regions and their natal clumps. *MNRAS*, **435**, 400–428. 41, 42, 141

Uscanga, L., Gómez, Y., Raga, A.C., Cantó, J., Anglada, G., Gómez, J.F., Torrelles, J.M. & Mirand a, L.F. (2008). Kinematics of the H_2O masers at the centre of the planetary nebula K3-35. *MNRAS*, **390**, 1127–1132. 12

Valenti, E., Zoccali, M., Gonzalez, O.A., Minniti, D., Alonso-García, J., Marchetti, E., Hempel, M., Renzini, A. & Rejkuba, M. (2016). Stellar density profile and mass of the Milky Way bulge from VVV data. *A&A*, **587**, L6. 51

van de Steene, G.C. (2017). Herschel observations of planetary nebulae. In X. Liu, L. Stanghellini & A. Karakas, eds., *Planetary Nebulae: Multi-Wavelength Probes of Stellar and Galactic Evolution*, vol. 323 of *IAU Symposium*, 128–135. 68

van de Steene, G.C. & Pottasch, S.R. (1995). Radio continuum observations of planetary nebula candidates from the northern hemisphere. *A&A*, **299**, 238. 23, 106

van de Steene, G.C., Jacoby, G.H. & Pottasch, S.R. (1996). Optical observations of planetary nebula candidates from the northern hemisphere. *A&AS*, **118**, 243–262. 106

Van de Steene, G.C., van Hoof, P.A.M., Exter, K.M., Barlow, M.J., Cernicharo, J., Etxaluze, M., Gear, W.K., Goicoechea, J.R., Gomez, H.L., Groenewegen, M.A.T., Hargrave, P.C., Ivison, R.J., Leeks, S.J., Lim, T.L., Matsuura, M., Olofsson, G., Polehampton, E.T., Swinyard, B.M., Ueta, T., Van Winckel, H., Waelkens, C. & Wesson, R. (2015). Herschel imaging of the dust in the Helix nebula (NGC 7293). *A&A*, **574**, A134. 68, 70

van Hoof, P.A.M. (2000). Measuring angular diameters of extended sources. *MNRAS*, **314**, 99–108. 49

van Hoof, P.A.M., Oudmaijer, R.D. & Waters, L.B.F.M. (1997). The spectral evolution of post-asymptotic giant branch stars. *MNRAS*, **289**, 371–387. 68

van Marle, A.J., Cox, N.L.J. & Decin, L. (2014). Eyes in the sky. Interactions between asymptotic giant branch star winds and the interstellar magnetic field. *A&A*, **570**, A131. 13

Vassiliadis, E. & Wood, P.R. (1994). Post-asymptotic giant branch evolution of low- to intermediate-mass stars. *ApJS*, **92**, 125–144. xviii, 5, 172, 173, 174, 175, 176, 177, 178, 181, 182, 183, 184, 185, 186, 187, 188, 189, 192, 193, 195, 196, 197, 198, 199, 200, 201, 202, 203, 204, 205, 206, 210, 211

Vennes, S., Smith, R.J., Boyle, B.J., Croom, S.M., Kawka, A., Shanks, T., Miller, L. & Loaring, N. (2002). White dwarfs in the 2dF QSO Redshift Survey - I. Hydrogen-rich (DA) stars. *MNRAS*, **335**, 673–686. 170

Vickers, S.B., Frew, D.J., Parker, Q.A. & Bojičić, I.S. (2015). New light on Galactic post-asymptotic giant branch stars - I. First distance catalogue. *MNRAS*, **447**, 1673–1691. 170

Viironen, K., Greimel, R., Corradi, R.L.M., Mampaso, A., Rodríguez, M., Sabin, L., Delgado-Inglada, G., Drew, J.E., Giammanco, C., González-Solares, E.A., Irwin, M.J., Miszalski, B., Parker, Q.A., Rodríguez-Flores, E.R. & Zijlstra, A. (2009a). Candidate planetary nebulae in the IPHAS photometric catalogue. *A&A*, **504**, 291–301. 23, 62

Viironen, K., Greimel, R., Corradi, R.L.M., Mampaso, A., Rodriguez, M., Sabin, L., Delgado-Inglada, G., Drew, J.E., Giammanco, C., Gonzalez-Solares, E.A., Irwin, M.J., Miszalski, B., Parker, Q.A., Rodriguez-Flores, E.R. & Zijlstra, A. (2009b). VizieR Online Data Catalog: Candidate Planetary Nebulae in IPHAS catalog (Viironen+, 2009). *VizieR Online Data Catalog*, **350**. 41, 61, 63, 64, 82

Viironen, K., Mampaso, A., Corradi, R.L.M., Rodríguez, M., Greimel, R., Sabin, L., Sale, S.E., Unruh, Y., Delgado-Inglada, G., Drew, J.E., Giammanco, C., Groot, P., Parker, Q.A., Sokoloski, J. & Zijlstra, A. (2009c). New young planetary nebulae in IPHAS. *A&A*, **502**, 113–129. 23, 41, 61, 63, 64

Villarreal Hernández, A.C. & Andernach, H. (2018). A Search for Extended Radio Sources in 1.3 sr of the VLA Sky Survey (VLASS). *arXiv e-prints*, arXiv:1808.07178. 212

Villaver, E., García-Segura, G. & Manchado, A. (2002). The Dynamical Evolution of the Circumstellar Gas around Low- and Intermediate-Mass Stars. I. The Asymptotic Giant Branch. *ApJ*, **571**, 880–900. 42, 68

Villaver, E., García-Segura, G. & Manchado, A. (2003). Ram Pressure Stripping in Planetary Nebulae. *ApJ*, **585**, L49–L53. 13

Villaver, E., Manchado, A. & García-Segura, G. (2012). The Interaction of Asymptotic Giant Branch Stars with the Interstellar Medium. *ApJ*, **748**, 94. 13

Villaver, E., Garcia-Segura, G., Manchado, A. & Stanghellini, L. (2014). Nature Versus Nurture: the Influence of the Environment in the Formation of Asymmetries. In *Asymmetrical Planetary Nebulae VI Conference*, 110. 13

Vlemmings, W., Diamond, P. & van Langevelde, H.J. (2005). Circular Polarization of Circumstellar H_2O Masers: Magnetic Fields of AGB Stars. In J. Romney & M. Reid, eds., *Future Directions in High Resolution Astronomy*, vol. 340 of *Astronomical Society of the Pacific Conference Series*, 394. 15

Vlemmings, W.H.T. & Diamond, P.J. (2006). *ApJ*, **648**, L59–L62. 11, 12, 15, 29

Vlemmings, W.H.T., Diamond, P.J. & Imai, H. (2006). A magnetically collimated jet from the evolved star W43A. In M.J. Barlow & R.H. Méndez, eds., *Planetary Nebulae in our Galaxy and Beyond*, vol. 234 of *IAU Symposium*, 267–270. 12, 29

Volk, K. & Kwok, S. (1985). Dynamical evolution of planetary nebulae. *A&A*, **153**, 79–90. 215

Wareing, C.J., O'Brien, T.J., Zijlstra, A.A. & Drew, J.E. (2005). Sh2-188: a model for a speedy planetary nebula . *Mem. Soc. Astron. Italiana*, **76**, 477. 7, 13

Wareing, C.J., O'Brien, T.J., Zijlstra, A.A., Kwitter, K.B., Irwin, J., Wright, N., Greimel, R. & Drew, J.E. (2006). The shaping of planetary nebula Sh2-188 through interactionwith the interstellar medium. *MNRAS*, **366**, 387–396. 13

Wareing, C.J., Zijlstra, A.A. & O'Brien, T.J. (2007). The interaction of planetary nebulae and their asymptotic giant branch progenitors with the interstellar medium. *MNRAS*, **382**, 1233–1245. 13, 14, 187

Waters, L.B.F.M. (1994). Infrared imaging of dust shells around AGB and post-AGB stars: mapping the mass loss history. *J. R. Astron. Soc. Canada*, **88**, 249. 5

Weidmann, W.A., Gamen, R., van Hoof, P.A.M., Zijlstra, A., Minniti, D. & Volpe, M.G. (2013). Near-infrared photometry of Galactic planetary nebulae with the VVV Survey. *A&A*, **552**, A74. 61, 62, 63, 75, 77, 139, 143

Werner, K. & Herwig, F. (2006). The Elemental Abundances in Bare Planetary Nebula Central Stars and the Shell Burning in AGB Stars. *PASP*, **118**, 183–204. 4

White, R.L., Becker, R.H. & Helfand, D.J. (2005). New Catalogs of Compact Radio Sources in the Galactic Plane. *AJ*, **130**, 586–596. 34, 39, 55

Whitelock, P.A. (1985). JHK photometry of planetary nebulae. *MNRAS*, **213**, 59–69. 60

Williams, B.J. & Temim, T. (2016). *Infrared Emission from Supernova Remnants: Formation and Destruction of Dust*. 91

Willner, S.P., Becklin, E.E. & Visvanathan, N. (1972). Observations of Planetary Nebulae at 1.65 to 3.4 Microns. *ApJ*, **175**, 699. 73, 75

Wilson, W.E., Ferris, R.H., Axtens, P., Brown, A., Davis, E., Hampson, G., Leach, M., Roberts, P., Saunders, S., Koribalski, B.S., Caswell, J.L., Lenc, E., Stevens, J., Voronkov, M.A., Wieringa, M.H., Brooks, K., Edwards, P.G., Ekers, R.D., Emonts, B., Hindson, L., Johnston, S., Maddison, S.T., Mahony, E.K., Malu, S.S., Massardi, M., Mao, M.Y., McConnell, D., Norris, R.P., Schnitzeler, D., Subrahmanyan, R., Urquhart, J.S., Thompson, M.A. & Wark, R.M. (2011). The Australia Telescope Compact Array

Broad-band Backend: description and first results. *MNRAS*, **416**, 832–856. 108

Wood, D.O.S. & Churchwell, E. (1989a). Massive stars embedded in molecular clouds - Their population and distribution in the galaxy. *ApJ*, **340**, 265–272. 42

Wood, D.O.S. & Churchwell, E. (1989b). The morphologies and physical properties of ultracompact H II regions. *ApJS*, **69**, 831–895. 42

Woodall, J.M. & Gray, M.D. (2007). A search for 22-GHz H_2O masers in supernova remnants. *MNRAS*, **378**, L20–L23. 91

Wright, E.L., Eisenhardt, P.R.M., Mainzer, A.K., Ressler, M.E., Cutri, R.M., Jarrett, T., Kirkpatrick, J.D., Padgett, D., McMillan, R.S., Skrutskie, M., Stanford, S.A., Cohen, M., Walker, R.G., Mather, J.C., Leisawitz, D., Gautier, T.N., III, McLean, I., Benford, D., Lonsdale, C.J., Blain, A., Mendez, B., Irace, W.R., Duval, V., Liu, F., Royer, D., Heinrichsen, I., Howard, J., Shannon, M., Kendall, M., Walsh, A.L., Larsen, M., Cardon, J.G., Schick, S., Schwalm, M., Abid, M., Fabinsky, B., Naes, L. & Tsai, C.W. (2010). The Wide-field Infrared Survey Explorer (WISE): Mission Description and Initial On-orbit Performance. *AJ*, **140**, 1868–1881. 22, 40

Yao, J.M., Manchester, R.N. & Wang, N. (2017). A New Electron-density Model for Estimation of Pulsar and FRB Distances. *ApJ*, **835**, 29. 171

Yung, B.H.K., Nakashima, J.i., Imai, H., Deguchi, S., Diamond, P.J. & Kwok, S. (2011). High Velocity Precessing Jets from the Water Fountain IRAS 18286-0959 Revealed by Very Long Baseline Array Observations. *ApJ*, **741**, 94. 11

Yung, B.H.K., Nakashima, J.i. & Henkel, C. (2014). Maser and Infrared Studies of Oxygen-rich Late/Post-asymptotic Giant Branch Stars and Water Fountains: Development of a New Identification Method. *ApJ*, **794**, 81. 6

Zhang, C.Y. (1995). A statistical distance scale for Galactic planetary nebulae. *ApJS*, **98**, 659–678. xix, 187, 190, 203

Zhang, C.Y. & Kwok, S. (1991). Spectral energy distribution of compact planetary nebulae. *A&A*, **250**, 179–211. 19

Zhang, C.Y. & Kwok, S. (1993). Trace of planetary nebula evolution by distance-independent parameters. *ApJS*, **88**, 137–167. 187

Zhang, Y. (2017). Molecular studies of Planetary Nebulae. In X. Liu, L. Stanghellini & A. Karakas, eds., *Planetary Nebulae: Multi-Wavelength Probes of Stellar and Galactic Evolution*, vol. 323 of *IAU Symposium*, 141–149. 19

Zijlstra, A.A. (1990). A radio study of planetary nebulae. *A&A*, **234**, 387–395. 83

Zijlstra, A.A. (2007). Binary Central Stars of Planetary Nebulae. *Baltic Astronomy*, **16**, 79–86. 15, 16

Zijlstra, A.A. & Pottasch, S.R. (1991). On the scale height of planetary nebulae. *A&A*, **243**, 478–482. 17, 18, 167, 169, 183, 207

Zijlstra, A.A., van Hoof, P.A.M. & Perley, R.A. (2008a). The Evolution of NGC 7027 at Radio Frequencies: A New Determination of the Distance and Core Mass. *ApJ*, **681**, 1296–1309. 22

Zijlstra, A.A., van Hoof, P.A.M. & Perley, R.A. (2008b). The Evolution of NGC 7027 at Radio Frequencies: A New Determination of the Distance and Core Mass. *ApJ*, **681**, 1296–1309. 172

Zoonematkermani, S., Helfand, D.J., Becker, R.H., White, R.L. & Perley, R.A. (1990). A catalog of small-diameter radio sources in the Galactic plane. *ApJS*, **74**, 181–224. 106